RECRYSTALLIZATION AND TRANSFORMATION IN LOW CARBON Nb AND Nb-B STEELS

by

Deng Qi Bai

A Thesis Submitted to the Faculty of Graduate Studies
and Research in Partial Fulfillment of the Requirements
for the Degree of Doctor of Philosophy

Department of Mining and Metallurgical Engineering
McGill University
Montreal, Canada

December 1995

ISBN 0-612-12328-6

ABSTRACT

The recrystallization behaviour of nine steels containing various combinations of Mo, Nb and B was investigated under continuous cooling conditions. Hot torsion tests were performed using a 17 pass deformation schedule at strain rates of 0.2 to 10 s^{-1}, and interpass times of 0.05 to 150 seconds. After reheating at 1250 or 1200 °C, the first deformation was applied at 1180 °C and the last one at about 700 °C. By plotting the mean flow stress vs. 1000/T, the no-recrystallization temperatures (T_{nr}) were determined, and the effects of chemical composition and the deformation conditions were assessed. Separate empirical equations for the T_{nr} were derived from the data for short and long interpass times. These relations describe the influence of chemical composition and of the pass strain, strain rate, and interpass time under continuous cooling conditions. Furthermore, the relationship between the residual strain ε_r or the residual strain ratio λ (ratio of the residual strain to the total effective strain) and the deformation parameters was also established by analyzing the flow curves. This made it possible to specify the recrystallization limit (RLT) and recrystallization stop (RST) temperatures that apply to each steel and to each combination of rolling conditions.

The occurrence of dynamic and metadynamic recrystallization in three Nb steels (0.023Nb, 0.07Nb and 0.09Nb) was investigated under isothermal conditions. Hot torsion tests were performed using the single pass, double twist and multipass deformation schedules at temperatures of 850 to 1100 °C, strain rates of 0.02 s^{-1} to 10 s^{-1}, and interpass times of 0.05 to 100 seconds. The peak and steady state strains were determined from the flow curves generated from the continuous deformation tests. Two empirical equations were derived describing the effects of the deformation parameters and of the Nb in solution on the peak and steady state strains, respectively. A kinetic model for metadynamic recrystallization was also established which takes the Nb concentration into account. This model can be combined with the conventional static one to judge the relative importance of competing mechanisms such as SRX, DRX and MDRX during hot rolling.

The transformation behaviours of the Mo-Nb-B, Mo-B, Nb-B and boron steels were studied under continuous cooling and isothermal conditions. CCC tests were used to determine the transformation temperatures, while the strain rate change technique was

employed to study the transformation kinetics. The effects of the amount of deformation and of the cooling rate on the final microstructure were also investigated. It was found that the Mo-Nb-B steel is basically a low carbon bainitic steel, and that B_3 microstructures are produced over a large cooling rate range (from 1 °C/s to 50 °C/s). The lengths of the lath-like ferrite sheaths increased and their widths decreased when the cooling rate was increased. The shapes and distributions of the retained austenite changed from being blocky and randomly distributed to fine, more aligned, and needle-like with increasing cooling rate. The precipitates that appeared at 900 °C were examined using a TEM and analyzed with the aid of EDX spectra. Large $Fe_{23}(C,B)_6$ particles were found in the Nb-48B steel after 3600 seconds of holding. These large precipitates are considered to be responsible for increasing the transformation temperature when they appear as well as the proportion of polygonal ferrite in the final microstructure. The mechanism of γ-to-B formation is judged to be displacive in the present case; the serrations evident on the flow curves of the Mo-Nb-B steel are considered to be due to the jerky nature of this transformation.

RESUME

La recristallisation de neufs aciers de différentes teneurs en Mo, Nb et B a été étudiée pour différentes conditions de refroidissement continu. Des tests de torsion à chaud ont été effectués comportant 17 passes de déformation et des temps d'interpasses de 0.05 à 150 secondes, pour des vitesses de déformation de 0.2 à 10 s^{-1} . Après un recuit à 1250°C ou 1200°C, la première déformation est effectuée à 1180°C et la dernière autour de 700°C. En traçant la contrainte d'écoulement en fonction de 1000/T, la température de non recristallisation (T_{nr}) a été déterminée, et les effets de la composition chimique et des conditions de déformation estimés. Des équations empiriques distinctes pour des temps d'interpasse courts ou longs ont alors été obtenues pour T_{nr} à partir des données expérimentales. Ces relations décrivent l'influence de la composition chimique, du chemin de déformation, de la vitesse de déformation et du temps d'interpasse pendant le refroidissement. De plus, les relations entre la déformation résiduelle ε_r ou le rapport de déformation résiduelle λ (rapport de la déformation résiduelle par la déformation effective totale) et les paramètres de déformation ont aussi été étudiées grâce à l'analyse des courbes contrainte-déformation. Cela a permis de déterminer les températures de début de recristallisation complète (RLT) et de fin de recristallisation (RST) pour chaque acier et pour toutes les conditions de laminage investiguées.

La présence de recristallisation dynamique et métadynamique dans trois aciers au Nb (0.023 Nb, 0.07 Nb et 0.09 Nb) a été analysée sous conditions isothermes. Des tests de torsion à chaud d'une seule passe, de double torsion et de multi-passes ont été effectués pour des températures de 850 à 1100°C, des vitesses de déformation de 0.02 à 10 s^{-1}, et des temps d'interpasse de 0.05 à 100 secondes. Le pic et l'état stationnaire ont été déterminés à partir des courbes contrainte-déformation obtenues lors des tests de déformation continue. Deux équations empiriques, pour le pic et l'état stationnaire, ont été proposées pour la description de l'influence des paramètres de déformation et du Nb en solution. Un modèle cinétique pour la recristallisation métadynamique prenant en compte la concentration de Nb a aussi été établi. Ce modèle peut être combiné avec le modèle statique conventionnel afin de comparer l'importance relative des différents mécanismes mis en jeu tels que SRX, DRX et MDRX pendant le laminage à chaud.

Les transformations de phase sous refroidissement continu ou conditions isothermes ont été étudiées pour les aciers Mo-Nb-B, Mo-B, Nb-B et B. Les tests CC ont

été effectués pour déterminer les températures de transformation, alors que la technique des sauts de vitesse a permis d'étudier les cinétiques de transformation. L'influence du taux de déformation et de la vitesse de refroidissement sur la microstructure finale est analysée. Il apparaît que l'acier Mo-Nb-B est fondamentalement un acier bainitique à faible teneur en carbone, et que les microstructures B_3 sont produites pour une large domaine de vitesses de refroidissement (de 1°C/s à 50°C/s). La longueur des lattes de ferrites croit alors que leur largeur diminue lorque la vitesse de refroidissement augmente. De même, les grains d'austénite résiduelle de forme plutôt équiaxe et de distribution aléatoire s'allongent en aiguilles et ont tendance à s'aligner lorsque la vitesse de refroidissement augmente. Les précipités qui apparaissent à 900°C ont été examinés par MET et analysés à l'aide des spectres EDX. De grosses particules de $Fe_{23}(C,B)_6$ sont trouvées dans l'acier Nb-48B après 3600 secondes de maintien. Ces précipités sont supposés responsables de l'augmentation de la température de transformation ainsi que de la présence d'une proportion de ferrite polygonale dans la microstructure finale. Le mécanisme de formation de B à partir de γ est supposé lié au cisaillement dans le cas présent. Les ondulations des courbes contrainte-déformation de l'acier Mo-Nb-B sont interprétées comme étant la conséquence de la nature saccadée de cette transformation.

ACKNOWLEDGMENTS

I would like to express my sincere gratitude to my thesis supervisor, Professor John J. Jonas, for his guidance, encouragement and support through the whole course of this work. His kind nature, unique scientific approach, and hard work have been of themselves an example which I have tried and will emulate in the future.

I am very grateful to Professor S. Yue for his fruitful suggestions and encouragement in my graduate studies. Many thanks are due to Dr. T. Maccagno for his stimulating discussions and for his assistance in modifying the computer programs. I would also like to thank Dr. O.N. Senkov for his beneficial suggestions.

The pleasant and friendly international environment created by my fellow graduate students along with their knowledge and skills are deeply appreciated. Special thanks are due to E. Fernandez who patiently and enormously helped in specimen preparation. I am also very grateful to L. Mello and C. Rousseau for their continuous help in various forms.

I am also very grateful to the Fonds FCAR for awarding me a scholarship during my studies. The financial support received from the Natural Sciences and Engineering Research Council of Canada (NSERC), and the Canadian Steel Industry Research Association (CSIRA) is acknowledged with gratitude.

Last, but not least, I would like to express my sincere gratitude to my wife, Zhiling Zou, and my daughter, Ruoyu, for their selfless patience, continuous support and encouragement. I am also much indebted to my parents and friends for their love and understanding.

TABLE OF CONTENTS

LIST OF FIGURES

LIST OF TABLES

CHAPTER 1

INTRODUCTION

High-strength low-alloy (HSLA) steels are now in wide use as structural materials in shipbuilding, car manufacturing, pressure vessels, pipelines, bridge construction, etc. The development of such steels constitutes a successful metallurgical innovation in that alloying additions and thermomechanical processing methods have been brought together to produce improved combinations of engineering properties. This technology is relatively inexpensive because the alloying elements are only needed in very small concentrations as carbide- or carbonitride-formers and the associated thermomechanical processing precludes the need for further heat treatment.

During the last two decades, much attention has been paid to Nb-bearing steels, and these have been subject to more detailed scientific investigation than any other kind of steel. Their unique combination of properties arises from the precipitation of carbonitrides and from the interaction of these precipitates with the processes of recrystallization and grain growth. A clear understanding of the thermomechanical processing of these materials is therefore essential if the optimum benefit is to be obtained from these interactions.

One excellent representative of the Nb microalloyed steels developed during the last decade is the class of ultralow carbon bainitic steels, to which considerable attention

has been paid by metallurgists. This is because these materials have good combinations of strength, toughness and weldability, which can be achieved by means of thermomechanical processing followed by continuous cooling. The concept of this new design is that the interplate carbides can be reduced in quantity or eliminated completely if the carbon content of the steel is sufficiently low. The production of such steels requires the addition of suitable microalloying elements, and the use of controlled rolling and accelerated cooling to ensure that the hardenability with respect to bainite transformation is good while that with respect to martensite transformation is rather low. Using this principle, it has become possible to obtain virtually fully bainitic steels during continuous cooling transformation.

In the past, numerous investigations have been conducted to study the influence of the microalloying elements and deformation parameters on the kinetics of recrystallization and precipitation. Most of these investigations have involved simple one-hit or double-hit deformations carried out under isothermal conditions, and there exists only limited data regarding the influence of multipass deformation. Under industrial conditions, however, the situation becomes more complicated because as many as twenty-two passes can be applied, and deformation is completed under continuous cooling conditions over a wide temperature range. It is therefore quite difficult to apply such isothermal results to the prediction of industrial schedules. By means of hot torsion tests carried out during cooling, these difficulties can be avoided. The present study was conducted in this way; it was concerned with clarifying some of the issues raised above. Thus the overall aims of the investigation were:

i) To determine the effects of chemical composition and processing variables such as pass strain, strain rate and interpass time on the no-recrystallization temperature, namely, the T_{nr}.

ii) To investigate the effects of these processing variables on strain accumulation.

iii) To follow the evolution of microstructure during multipass deformation under continuous cooling conditions.

iv. To examine the occurrence of dynamic and metadynamic recrystallization in Nb microalloyed steels during short-interpass-time multipass deformation.

Unfortunately, the microstructural definition of ultralow carbon bainitic steels remains unclear and their transformation behaviour is still not completely understood. Much effort is therefore needed to clarify these issues. The aims of the present work were thus extended to include:

i) the microstructural evolution of Nb-B treated steels during isothermal and continuous cooling transformation;

ii) the kinetics of isothermal and continuous cooling transformation;

iii) the effect of deformation and cooling rate on the final microstructure.

To fulfill the above objectives, the present investigation was divided into five parts. A literature review is first presented in Chapter 2. Both the development of bainitic steels and the thermomechanical processing of microalloyed steels are considered. In Chapter 3, the experimental materials and equipment are described, and three methods referred to here as the continuous cooling hot torsion test, continuous cooling compression test, and isothermal compression test are reviewed.

In Chapter 4, the effects of the deformation parameters on the no-recrystallization temperature are presented and discussed. Strain accumulation in the partial recrystallization range is evaluated by measuring the flow curve. The method employed to predict the T_{nr} under continuous cooling conditions in the case of multipass deformation is also presented. In Chapter 5, the occurrence of dynamic and metadynamic recrystallization in Nb microalloyed steels is examined. Empirical equations are derived to describe the kinetics of these behaviours. In Chapter 6, the transformation kinetics and microstructural evolution of Nb-B treated steels are presented and discussed under both isothermal and continuous cooling conditions. Finally, the general conclusions of this research are drawn in Chapter 7.

CHAPTER 2

LITERATURE REVIEW

2.1. Development of Low Carbon Bainitic Steels

2.1.1 Development of Low Carbon Bainitic Steels

In the early 1900's, little importance was attached to weldability, formability, and resistance to brittle fracture. The inexpensive alloying element carbon was employed to achieve the tensile strength required[1]. It was only after World War II that major structural failures were associated with poor weldability and fracture resistance. Requirements regarding the weldability and fracture resistance were therefore added to steel specifications, especially those for shipbuilding[2]. Later, metallurgists and steelmakers found that better weldability and lower impact transition temperatures (ITT) could be obtained by lowering the carbon content of steel and a high yield stress could be more important than a high tensile strength.

In order to improve the strength while not decreasing the toughness, low carbon bainitic steels were developed on a commercial scale simultaneously with ferrite-pearlite HSLA (high-strength low-alloy) steels in the 1950's[3-6]. These steels contained 0.1 to 0.15% carbon, and many combinations of alloying elements were used to produce the required austenite transformation characteristics so that bainitic structures would form during air cooling over a wide range of section sizes. The yield strengths of these steels

ranged from 450 to 900 MPa, depending on the carbon content and temperature of austenite transformation.

These steels had a potential strength advantage over available ferrite-pearlite steels. However, the impact properties of bainitic steels were somewhat inferior. Thus, further lowering of the carbon content was used to improve the toughness through the formation of acicular ferrite and bainitic structures in the late 1960's. The first development of these ultralow carbon bainitic steels was the 0.02% carbon, 3% nickel, 3% molybdenum and niobium, aluminum-treated steels[7, 8]. They had yield strengths of more than 700 MPa and impact transition temperatures below -75 °C. These steels were uneconomical for general structural engineering due to their expensive alloying elements.

With the development of improved steelmaking techniques, the carbon level in steels has been gradually decreased. At the same time, lowering the cost of ultralow carbon bainitic steels was also a goal for steelmakers. In the early 1970's, more commercially attractive alloys based on 0.03% carbon, manganese-molybdenum-niobium were developed in hot-rolled strip for line pipe[9, 10]. This steel can be produced with fully bainitic structures or with very fine polygonal ferrite structures, depending on the finishing rolling temperature and general processing. More recently, boron has been added to the ultralow carbon bainitic steels as it was found that a small addition of boron can effectively prevent the formation of polygonal ferrite, and thereby enhance the formation of bainite[11-17]. Furthermore, using boron can lower the required amount of expensive elements such as molybdenum. Since the 1980's, ultralow carbon bainitic steels have been an attractive subject of investigation for metallurgists and steelmakers because of their excellent combination of toughness, strength and weldability.

2.1.2 Nature of Bainite

The discovery of bainite can be traced back to the 1920's. In their pioneering studies on the isothermal transformation of austenite in steels, Davenport and Bain[18] discovered a new microstructure consisting of an acicular, dark etching product at intermediate temperatures. Since then, many attempts have been made to clarify the characteristic features of this kind of microstructure. However, it was not until 1939 that bainite was well defined. By means of electron microscopy, "upper" and "lower" bainite were distinguished during isothermal transformation by Mehl[19]. It has now been generally agreed that upper bainite consists of a lathlike morphology, and the carbides are

distributed between individual ferrite regions. Lower bainite has a platelike morphology, and the carbides are distributed inside the ferrite.

Most commercial bainitic steels, however, are produced by continuous cooling techniques, and the transformation under these conditions is more complicated. A typical continuous cooling transformation (CCT) diagram for a commercial bainitic steel is shown in Fig. 2.1 to illustrate some of the important features of the bainite transformation in continuously cooled steels[20]. It indicates that bainitic microstructures are generated over a wide range of cooling rates. The microstructures formed from austenite in the bainite bay or nose of the CCT diagram do not consist of a single constituent which can be uniquely termed bainite. These microstructures are quite complex, and may consist of carbides, martensite, and/or austenite in an acicular ferrite matrix. They are not easily classified as upper or lower bainite. In fact, as the terms upper and lower bainite were originally used to describe isothermal transformations in specific temperature regimes, the terminology is probably not suitable for continuously cooled steels.

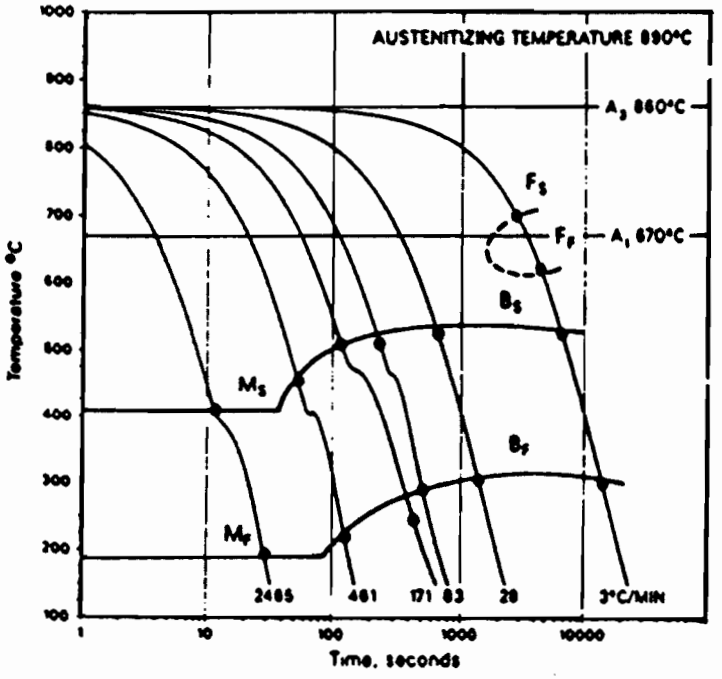

Fig. 2.1 CCT diagram for a Ni-Cr-Mo steel. Composition of steel (wt%): 0.15C, 0.32Mn, 0.31Si, 2.72Ni, 1.52Cr, and 0.41Mo[20].

Bainite was also found in low carbon steels. Early attempts were made by Habraken[21] and Habraken and Economopoulos[22] to define the morphological features of the microstructures present in a number of low carbon Cr-Mo-B steels. In examining surface replicas, they observed the presence of bainite with the classic upper and lower morphologies, but most often a mixture of microstructures was obtained, which contained both acicular and nonacicular components. The former has a carbide-free morphology, the latter, however, consists of a ferrite matrix containing islands of martensite/austenite.

2.1.3 Transformation Mechanism

The kinetics and mechanisms of bainite formation have been widely studied by a number of investigators[23-30]. A generalized microstructural definition strongly supported by Aaronson and co-workers[25-27] is that bainite in steel is a nonlamellar, two-phase eutectoid decomposition product of austenite. Crystals of the two phases form by diffusional nucleation and growth in a noncooperative manner and may have any morphology. The other definition, which considers bainite to be a product of phase transformation characterized by surface relief produced in association with shear, was proposed by Christian and Edmonds, as well as by Olson et al.[28-30]. Although hundreds of papers have been published on this topic, the mechanism of bainite formation is still a matter of controversy and confusion continually arises.

2.1.4 Recent Developments in the Definition of Bainite

For bainite alone, Kennon[31] has compiled a list of 30 different terms that have been used over the years to describe bainitic microstructures. More recently, based on a review of the literature, Bramfitt and Speer[20] have tried to provide a definition which can be applied in a general fashion, regardless of the specific alloy system under consideration. According to their proposal, three types of bainite, named B1, B2 and B3, can be used to describe the following morphological characteristics:

- acicular ferrite associated with the intralath precipitation of iron carbide;
- acicular ferrite associated with interlath particles or interlath films of cementite and/or austenite; and
- acicular ferrite associated with a constituent consisting of discrete islands, or blocky regions of austenite and/or martensite or pearlite.

2.2 Thermomechanical Processing of Low Carbon Steels

Before World War II, hot rolling was traditionally concerned simply with shape changes, and was not used in the production of desirable microstructures. In order to achieve the required strength, the major approach utilized was alloying, e.g. increasing the levels of carbon and manganese[1,32], increasing the levels of elements such as silicon and phosphorus, or adding chromium, nickel or copper[33]. This approach generally gave steels poor toughness, weldability and formability, and increased their cost.

By the early 1950's, it was realized that hot rolling also changed the properties of hot rolled steel. One of the pioneers of this approach was Domnanfvets Jernverk[34] in Sweden in 1940, which employed finish rolling temperatures substantially lower than used conventionally, to refine the ferrite structure and to improve the properties. The advantage of such processing lies in energy savings by minimizing, or even eliminating, heat treatment after hot rolling. Such processing was termed 'controlled rolling' in 1958 by Vanderbeck[34].

During the past twenty years, based on a better understanding of many metallurgical phenomena (such as static and dynamic recrystallization and precipitation), conventional controlled rolling (CCR), recrystallization controlled rolling (RCR) and dynamic recrystallization (DRCR) or metadynamic recrystallization (MDRCR) controlled rolling have been developed[35-38].

The important parameter that separates the RCR and CCR processes from the DRCR and MDRCR processes is the length of the interpass interval. The long interpass time processes are those that involve reversing mills, such as breakdown or plate mills. The interpass times employed in these processes are significantly longer than 1 second. The short interpass time processes are those that involve tandem or continuous mills, particularly when these are located at the finishing end of an operation, so that the stock is moving relatively quickly and the interpass times are usually shorter than 1 second. Hot rolling mills are compared in terms of their ranges of strain rate and interpass time in Table 2.1.

2.2.1 Conventional Controlled Rolling (CCR)

Historically, this was the first type of controlled rolling to come into regular commercial use. This process generally involves control of all four stages of rolling, i.e.:

1) reheating, 2) roughing, 3) finishing, and 4) cooling[39]. An illustration of these four stages is shown in Fig. 2.2.

Table 2.1 Comparison of hot rolling mills in terms of their ranges of strain rate and interpass time

Mill Type	Strain rate range (s^{-1})	Interpass time (s)
Reversing mills (plate, slabbing, roughing, etc.)	1~30	8~20
Hot strip mills	10~200	0.4~4
Wire rod mills	10~1000	0.015~1

2.2.1.1 Reheating

In a conventional controlled rolling schedule, the material is usually reheated to a relatively high temperature, ranging from 1050 °C to 1300 °C. The reheating temperature not only controls the amount of microalloying elements dissolved prior to rolling, but also influences the austenite grain size. On the one hand, it is advantageous to maximize dissolution of the microalloy carbonitrides on reheating, to ensure that the desired austenitic microstructure is developed during rolling. On the other hand, it is also essential to avoid austenitic grain growth as much as possible. A fine, uniform as-reheated austenitic grain size helps minimize the development of a duplex austenitic structure after rolling, thereby leading to improved toughness[40].

2.2.1.2 Roughing

In order to refine the relatively coarse, as-reheated austenitic microstructure, a series of high temperature rolling/recrystallization steps are carried out at temperatures above the no-recrystallization temperature (T_{nr}). Recrystallization at this stage is very rapid and can be followed by some grain growth. If the strain and strain rate of the deformation are properly chosen, complete static recrystallization will take place, and

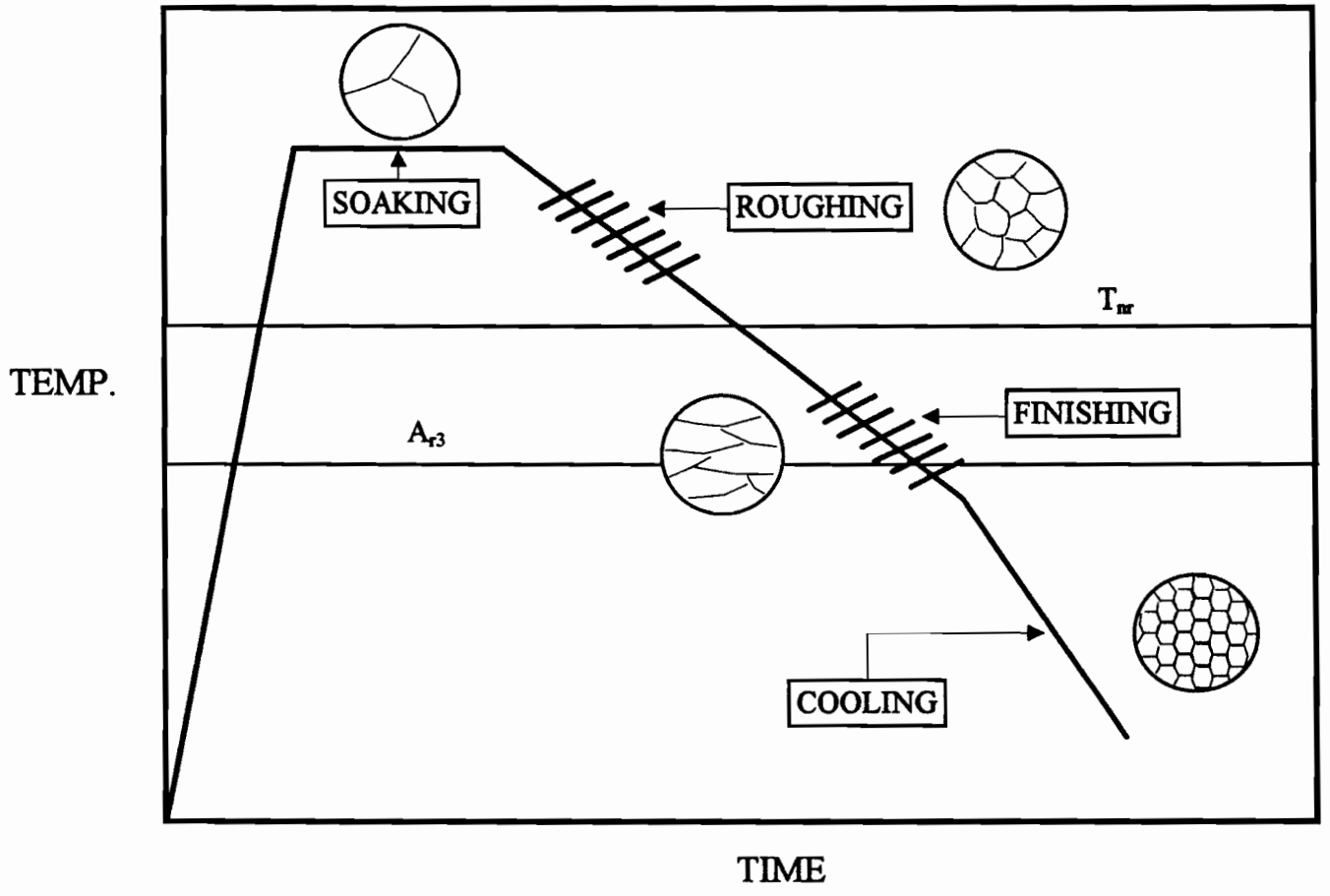

Fig. 2.2 Schematic illustration of controlled rolling and the resulting microstructures
T_{nr}- no-recrystallization temperature;
A_{r3}-start temperature of the austenite-to-ferrite transformation

small austenite grains will result. If the conditions are not well chosen, then static recrystallization will be incomplete. A mixture of recrystallized and non-recrystallized structures will be produced, and this will lead to undesirable duplex structures after transformation.

2.2.1.3 Finishing

Finishing operations are usually conducted at temperatures ranging from the T_{nr} to the start of the austenite-to-ferrite transformation (A_{r3}). Recrystallization is no longer possible and the austenite structure is progressively flattened. This eventually produces a pancaked austenite before the material enters the transformation range[41, 42]. The ratio of grain surface to grain volume (S_v) increases, although the grain volume remains constant. This provides more potential nucleation sites for the austenite-to-ferrite transformation[43].

Other important nucleation sites are deformation bands inside the austenite grains, which are formed during finishing when more than 50% deformation is applied[44]. When such pancaked austenite grains transform, a very fine ferrite grain size is produced because of the large number of nucleation sites available at the surfaces of the pancaked austenite grains and in the deformation bands. This fine ferrite is responsible for the attractive combination of good toughness properties and high yield strengths[45, 46].

2.2.1.4 Cooling

Cooling is a natural and integral part of thermomechanical processing. Its control can yield excellent results in terms of economy, productivity and material properties. Rapid cooling rates during rolling can prevent austenite recrystallization prior to transformation, reduce the extent of carbonitride precipitation in the austenite[47, 48], and lower the transformation temperature (A_{r3}). This increases the breadth of the no-recrystallization zone and therefore decreases the ferrite grain size because, at lower temperatures, ferrite grain growth is more limited. Rapid cooling also limits precipitation in the austenite range and leaves a large proportion of microalloying elements in solution and, as a result, enhanced precipitation occurs in the ferrite range. This is both a source of ferrite grain refinement and improved precipitation strengthening, due to finer precipitate formation at lower temperatures.

Accelerated cooling is a powerful technique for improving the strength of steels and has been widely used in Japan, Europe and North America. This method can be used not only to produce fine ferrite but also to give desired combinations of final

microstructures. The strength can be simultaneously improved in this way, while the toughness may be reduced when the cooling rate is too high. The maximum cooling rate that can be employed depends on whether strength or toughness is the key objective.

2.2.2 Recrystallization Controlled Rolling (RCR)

Controlled rolling, as described above, is generally based on the use of low finishing temperatures, which produces pancaked austenitic structures and leads to fine ferrite grain sizes after transformation. Such a style of finishing, however, is inappropriate for certain products, such as heavy plates and thick-walled seamless tubes, which cannot be finished at relatively low temperatures, due to excessive rolling loads. In such cases, it is possible to produce the fine microstructures required by carefully controlling the recrystallization of austenite and arranging for it to occur at successively lower temperatures during finish rolling[49]. These temperatures are, nevertheless, above 900 °C and thus higher than those employed in conventional controlled rolling (CCR).

In the case of recrystallization controlled rolling, the most important processing parameters are the austenite grain size after rolling and the cooling rate during transformation in terms of producing fine grained ferrite. To obtain fine grained austenite, recrystallization should not be sluggish, so that it can occur at relatively low temperatures. This can be achieved by employing V rather than Nb as an alloying element. On the other hand, grain growth after each cycle of recrystallization should be prevented. For this purpose, Ti is often added to steels to form fine particles of TiN during cooling after continuous casting[50]. When these particles have an appropriate size and frequency distribution, they can effectively prevent the grain growth of austenite after each cycle of recrystallization with the interpass times associated with commercial hot rolling. The fine grained austenite in turn transforms into relatively fine grained ferrite, as long as an appropriate cooling rate is used, leading to mechanical properties of the hot rolled product which are acceptable for many purposes.

2.2.3 Dynamic Recrystallization Controlled Rolling (DRCR)

Although there has been some controversy concerning the possibility of dynamic recrystallization under industrial rolling conditions, Samuel et al.[51] reported that dynamic recrystallization could take place under strip rolling conditions. Pussegoda et al.[52] also reported that dynamic recrystallization can be initiated at relatively high temperatures, as in billet piercing during the manufacture of seamless tubes. In their investigations, strains

as high as 1.5 were applied in a single pass, which was large enough to initiate dynamic recrystallization.

It is generally impossible to reach the critical strain for dynamic recrystallization during single pass deformation for most industrial practices, except in the case of large reduction 'single step' operations, such as extrusion and planetary hot rolling. However, when the interpass time is short, as in rod rolling and hot strip rolling, there is insufficient time for static recrystallization to take place during the interpass delay, especially when Nb is present in solution. For the same reason, the amount of carbonitride precipitation that can take place is also severely limited. As a result, dynamic recrystallization will be initiated by the accumulated strain and will continue over a few passes[53, 54]. At the end of this process, an austenite grain size as fine as 10 μm can be achieved[55].

It is important to note that, under industrial conditions of rolling, CCR, RCR and DRCR can occur to different degrees during a given operation if the processing parameters have not been optimized so as to favor either: i) strain-induced precipitation and austenite pancaking, ii) conventional recrystallization, or iii) dynamic recrystallization, respectively.

To utilize these different thermomechanical processing routes for the production of commercial HSLA steels, it is necessary to have a clear understanding of the basic metallurgical phenomena associated with the controlled rolling of HSLA steels. These are reviewed in the following sections.

2.3 Basic Metallurgical Phenomena in the Controlled Rolling of Steels

Softening and hardening are two major metallurgical phenomena taking place during the hot working of steels. The success of thermomechanical processing is largely dependent on the control of these processes. The types of softening that occur can be divided into five distinct categories: i) static recovery, ii) static recrystallization, iii) dynamic recovery, iv) dynamic recrystallization, and v) metadynamic recrystallization.

2.3.1 Static Recovery

After plastic deformation, the strain energy that is stored within the deformed material will be released by the annihilation and rearrangement of dislocations in individual

events. During the process, no motion of grain boundaries occurs. The sub-boundaries, however, become sharper and the dislocation density within the subgrains is reduced with relatively little change in size or shape of the grains. Temperature, strain, strain rate and the addition of alloying elements all have an influence on the recovery rate. An increase in temperature results in an increase in the rate of recovery because of enhanced thermal activation. Increasing the strain and strain rate also increases the rate of recovery due to dislocation density increases.

Although static recovery is a basic phenomenon which occurs under most rolling conditions, it has been shown that this process only produces up to 25% of total softening in most steels, and is not a dominant factor in controlled rolling.

2.3.2 Static Recrystallization

2.3.2.1 Static Recrystallization Kinetics

As in the case of static recovery, static recrystallization is a softening process that takes place after deformation is interrupted. Static recrystallization can cause 75% softening; therefore, it is one of the more important softening mechanisms involved in controlled rolling. During static recrystallization, the strained grains are gradually replaced by new, strain-free ones by means of nucleation and growth. The rate of static recrystallization is influenced by the strain, strain rate, temperature and grain size. During past decades, numerous investigations[56-71] have been conducted to determine the rate of static recrystallization in plain carbon and microalloyed steels; most of the observed softening curves follow an Avrami equation of the form

$$X_{rex} = 1 - \exp\left[-C(t/t_F)^k\right] \qquad (2.1)$$

where X_{rex} is the fraction recrystallized in time t; t_F is the time for some specified fraction of recrystallization (say 0.5); k is a constant; and C=-ln(1-F).

A fact which should be noted is that there are no simple equations for calculating the fraction of recrystallization from mechanical data. Equation (2.1) was originally used to describe the fractional softening, instead of recrystallization; it was applied to study the changes in yield or flow stress in a double-hit technique. Although it has been reported that the fraction restored is not linearly related to the fraction recrystallized in low alloy steels[72], the assumption that 50% recrystallization = 50% restoration has been widely

adopted by most researchers who have calculated the static recrystallization kinetics. This is probably due to the difficulty of estimating the contribution of static recovery to the softening.

In this way, t_{50}, the time for 50% recrystallization, can be related to the strain (ε), initial grain size (d_0), absolute temperature (T) and Zener-Hollomon parameter (Z). Various empirical relationships have been proposed, and most take the form:

$$t_{50} = B\varepsilon^{-p} d_0^{q} Z^{r} \exp\frac{Q_{rex}}{RT} \qquad (2.2)$$

where R is the gas constant, Q_{rex} is the activation energy for recrystallization, and B, p, q, and r are material dependent constants.

It has been shown that the characteristic time, t_{50}, is strongly strain dependent[73-76]. The lower limit of strain to which the above relationship is applicable is uncertain as the critical strain for static recrystallization has not received systematic study. The data of Morrison[73] indicate that it is <0.05 for low carbon steel at 950 °C, whereas the observations of Djaic and Jonas[74] indicate that a critical strain ~0.08 must be exceeded before recrystallization can begin in a high carbon steel at 780 °C. Nevertheless, a small deformation at high temperatures is detrimental to grain refinement.

The dependence of the recrystallization kinetics on strain rate is not straightforward. Morrison observed that there was no effect of strain rate over the two orders of magnitude studied, while Barraclough and Sellars[72], and Ruibal et al.[77] found a significant effect of strain rate on the recrystallization rate of stainless and low alloy steels.

In general, increasing the strain rate increases the flow stress. Increasing the flow stress is associated with an increase in the dislocation density and a decrease in the subgrain size and hence an increase in the stored energy. The driving force for recrystallization, therefore, will increase. The time for 50% recrystallization will thus decrease with strain rate.

The recrystallization rate also has a strong temperature dependence since it is a process that is diffusion controlled. The presence of the Zener-Hollomon parameter in

equation (2.2) suggests that there is an equivalence between temperature and strain rate during deformation[78, 79]. Many workers do not, however, take appropriate account of this equivalence and tend to have separate strain rate and temperature terms in the recrystallization kinetics equation.

Table 2.2 Recrystallization models reported in the literature

Investigator	Equation
Kwon et al. [60]	$X = 1 - \exp\left[-0.693\left(\frac{t-t_0}{t_{0.5}}\right)^2\right]$ $t_{0.5} = 3.32\times10^{-15} d_0^{1.4145} \varepsilon^{-3.144} Z^{-0.121} \exp\left(\frac{285000}{RT}\right)$ (2.3)
Hodgson and Gibbs [61]	$X = 1 - \exp\left[-0.693\left(\frac{t}{t_{0.5}}\right)^{1.5}\right]$ $t_{0.5} = 3.6\times10^{-12} d_0 \varepsilon^{-2.5} \exp\left(\frac{230000}{RT}\right)$ (2.4)
Roberts et al. [64]	$X = 1 - \exp\left[-0.693\left(\frac{t}{t_{0.5}}\right)^{1.5}\right]$ (2.5) $t_{0.5} = 5.1\times10^{-21} d_0^{2} \varepsilon^{-4} \exp\left(\frac{330000}{RT}\right)$ (2.6)
Yada and Senuma [66]	$X = 1 - \exp\left[-0.693\left(\frac{t-t_0}{t_{0.5}}\right)^2\right]$ (2.7) $t_{0.5} = 2.86\times10^{-8} \varepsilon^{-2} \dot{\varepsilon}^{-0.2} S_v^{-0.5} \exp\left(\frac{150000}{RT}\right)$ (2.8) $S_v = \frac{24}{\pi d_0}\left(0.491\exp\varepsilon + 0.155\exp-\varepsilon + 0.1433\exp-3\varepsilon\right)$ (2.9)
Sellars and Whiteman [68]	$X = 1 - \exp\left[-0.693\left(\frac{t}{t_{0.5}}\right)^2\right]$ (2.10) $t_{0.5} = 2.5\times10^{-19} d_0^{2} \varepsilon^{-4} \exp\left(\frac{300000}{RT}\right)$ (2.11)

The formulas describing the kinetics of static recrystallization employed by various workers for C-Mn steels are summarized in Table 2.2. They all have similar forms, but with different constants. This wide range of constants is difficult to rationalize, and can be due to the different test methods used by the different investigators.

2.3.2.2 Recrystallized Grain Size

In controlled rolling, the recrystallization kinetics are only one of the aspects of importance; the recrystallized grain size is the other. To predict the final microstructure and then the properties of hot rolled materials, a key step is to predict the evolution of microstructure in the austenite range during hot rolling.

The quantitative analysis of the microstructural changes taking place during hot rolling was pioneered by Sellars and co-workers[62, 68]. A power law relationship between the recrystallized grain size and the applied strain was derived by Sellars based on the analysis of literature data. It has the following form:

$$d_{rex} = D d_0^{0.67} \varepsilon^{-1} \qquad \text{(C-Mn, } \varepsilon<\varepsilon_c\text{)} \qquad (2.12)$$

$$d_{rex} = D' d_0^{0.67} \varepsilon^{-0.67} \qquad \text{(Nb, } \varepsilon<\varepsilon_c\text{, T>950 °C)} \qquad (2.13)$$

where D and D' are constants, and d_0 and ε are the initial grain size and applied strain, respectively. These two relationships remain true for strains below a critical value, ε_c, and the predictions are in reasonable agreement with the observations made by some investigators as long as the constants D and D' are varied[43, 57, 62, 80, 81].

The above models do not incorporate a temperature term and some other researchers have noted a similar lack of influence of temperature. In a recent study, however, Hodgson[82] pointed out that the grain size exponent in equation (2.12) might be incorrect, and that temperature plays a significant role in the prediction of recrystallized grain size. Table 2.3 summarizes some models used by different researchers in the past.

Although each research group employed a different equation for the recrystallized grain size, the differences in the final austenite grain sizes are not significant when the models are applied to simulate the multipass hot strip rolling of plain carbon steels. The microstructural evolution predicted using the Sellars model for a Nb steel is presented in

Fig. 2.3. It can be seen that the grain sizes converge to the same value after several passes, even though the difference between initial grain sizes is huge. Similar observations have also been reported by other researchers[84-87].

Table 2.3 Relations for predicting the recrystallized grain size

Investigator	Equation		
Choquet et al. [59]	$d_{rex} = 45\exp(-5793/RT)\varepsilon^{-0.6} d_0^{0.374}\dot{\varepsilon}^{-0.1}$	C-Mn	(2.14)
	$d_{rex} = 472\exp(-11620/RT)\varepsilon^{-0.7} d_0^{0.277}\dot{\varepsilon}^{-0.1}$	Nb	(2.15)
Sellars [62]	$d_{rex} = 0.5 d_0^{0.67}\varepsilon^{-1}$	C-Mn	(2.16)
	$d_{rex} = 1.1 d_0^{0.67}\varepsilon^{-0.67}$	Nb	(2.17)
Roberts et al. [64]	$d_{rex} = 6.2 + 55.7 d_0^{0.15}\varepsilon^{-0.65}\left[\exp\left(\frac{350000}{RT}\right)\right]^{-0.1}$	C-Mn	(2.18)
	$d_{rex} = 4.3 + 195.7 d_0^{0.15}\varepsilon^{-0.57}\left[\exp\left(\frac{350000}{RT}\right)\right]^{-0.1}$	Nb	(2.19)
Suehiro et al. [69]	$d_{rex} = 5/(S_v\varepsilon)^{0.6}$	C-Mn	(2.20)
	$S_v = \frac{24}{\pi D_0}(0.491\exp(\varepsilon) + 0.155\exp(-\varepsilon) + 0.1433\exp(-3\varepsilon))$		(2.21)
Hodgson [82]	$d_{rex} = 343 d_0^{0.4}\varepsilon^{-0.5}\exp(-45000/RT)$	C-Mn	(2.22)
Anelli et al. [83]	$d_{rex} = 75\varepsilon^{-0.6} d_0^{0.39}\exp(-3189/T)$	C-Mn and Nb	(2.23)

2.3.2.3 Grain Growth after Recrystallization

Once recrystallization is complete, further grain growth takes place at a rate that is a function of time and temperature. A relationship derived by Sellars and Whiteman[68] is of the form

$$d^{10} = d_{rex}^{10} + A' t \exp\left(-\frac{Q_{gg}}{RT}\right) \qquad (2.24)$$

where t is defined as the time after a pass minus the time for 95% recrystallization. A' and Q_{gg} are constants. When the temperature is above 1000 °C, the values for A' and Q_{gg} are $3.87\text{x}10^{32}$ and 400 kJ/mol; otherwise, they are $5.02\text{x}10^{53}$ and 914 kJ/mol, respectively.

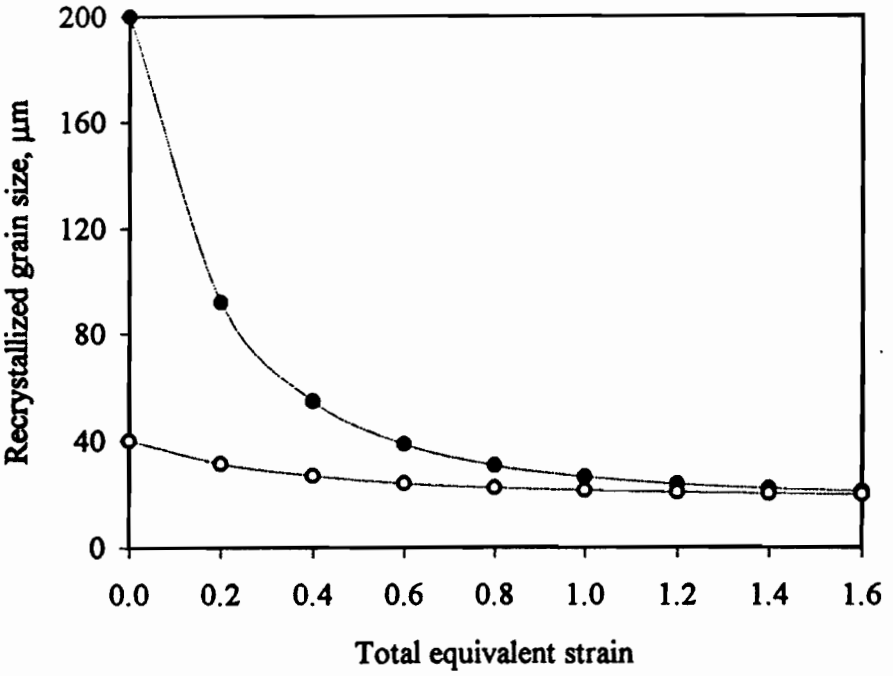

Fig. 2.3 Evolution of the recrystallized grain size during multipass rolling with pass equivalent strains of 0.2; calculated from equation (2.17).

A similar relation but with an exponent of 2 was proposed by Senuma and Yada[70].

$$d^2 = d_{rex}{}^2 + 1.44\times10^{12} t \exp\left(-\frac{266{,}700}{RT}\right) \qquad (2.25)$$

where t is the time after static recrystallization (taken to be 95%). Choquet et al.[65] derived a simpler equation, which is only related to the time after the completion of recrystallization,

$$d = d_{rex}\left(1+\alpha\ln(t/t_{rex})\right) \qquad (2.26)$$

where t_{rex} is the time for complete recrystallization (taken to be 99%), and α is a grain growth parameter that depends on steel composition: α=0.195 for C-Mn steels and α =0.098 for C-Mn-Nb steels.

2.3.3 Dynamic Recovery

In the early stages of hot deformation, the dislocation density increases with strain, but some rearrangement and annihilation of dislocations takes place at the same time. In high stacking fault energy materials, as deformation proceeds, the work hardening rate gradually decreases due to an increase in the annihilation rate of dislocations. When the rate of annihilation of dislocations is equal to the rate of generation of dislocations, a steady state regime is reached. The steady state in hot working is thus characterized by a constant flow stress. In metals and alloys of medium or low stacking fault energy, e.g. austenite, the rate of dislocation annihilation is less than that of dislocation generation and, therefore, the dislocation density increases rapidly during deformation. When the dislocation density reaches a critical value, dynamic recrystallization occurs[88].

2.3.4 Dynamic Recrystallization

This important concept was originally proposed on the basis of the detailed experimental work of Rossard and Blain in 1959[89, 90]. Initially, dynamic recrystallization was considered to be a testing artifact attributable to quenching methods which were insufficiently rapid to prevent new grains from forming by static recrystallization during the cooling period after deformation at elevated temperatures[91]. Later in 1969, it was modeled and interpreted in detail by Luton and Sellars[92]. More recently, Sakui and co-workers[93] and Sakai et al.[94, 95] correlated the shape of dynamic recrystallization flow curves with the microstructure.

Unlike static recrystallization, dynamic recrystallization takes place *during* deformation. The flow curves characteristic of dynamic recrystallization display well-developed peak stresses during one single continuous straining if recrystallization is complete. This particular feature can be also seen by drawing an envelope over several interrupted deformations with very short interpass times.

The predominant nucleation sites for dynamic recrystallization are pre-existing grain boundaries with high dislocation densities[88, 96, 97]. During deformation, when accumulated strains exceed the critical strain ε_c that corresponds to a critical dislocation density, recrystallization is initiated at the austenite grain boundaries and is propagated into the grain interiors by a mechanism known as 'necklacing'[55, 98, 99]. This will progress with continuing deformation until the deformed austenite is entirely replaced by a fine grain size. However, recent work by Sakai et al.[94] and McQueen and co-workers[100-102]

shows that deformation bands and subgrains can also act as nucleation sites, and dynamic recrystallization does not necessarily progress in a necklace manner.

For C-Mn steels, the critical strain may be approximated as a constant fraction (0.8) of the strain to the peak stress, ε_p, or evaluated by the equation:

$$\varepsilon_c = 0.57 d_0^{0.17} \varepsilon_p \qquad (2.27)$$

where the peak strain is easily measured and is a function of initial grain size (d_0) as well as of strain rate and temperature[62, 103]:

$$\varepsilon_p = 6.97 \times 10^{-4} d_0^{0.3} Z^{0.17} \qquad (2.28)$$

where
$$Z = \dot{\varepsilon} \exp\left(\frac{312{,}000}{RT}\right) \qquad (2.29)$$

When the strain exceeds the critical strain for the initiation of dynamic recrystallization, the recrystallization kinetics take the form:

$$t_{0.5} = 1.06 \times 10^{-5} Z^{-0.6} \exp\left(\frac{300{,}000}{RT}\right) \qquad (2.30)$$

The dynamically recrystallized grain size can then be represented by the following equation:

$$d_{rex} = 1.8 \times 10^{3} Z^{-0.15} \qquad (2.31)$$

It is important to note that the grain size obtained by dynamic recrystallization is independent of strain but depends on the Zener-Hollomon parameter.

2.3.5 Metadynamic Recrystallization

Metadynamic recrystallization is another important metallurgical phenomenon involved in hot working. The concept is that when the strain exceeds the peak strain for dynamic recrystallization, many nuclei are produced within the material; these nuclei will

continue growing without an incubation time if the deformation is halted. Hence, it can only occur after dynamic recrystallization has introduced nuclei into the material.

Since the term was first introduced by Petkovic et al.[104, 105], very little further examination of metadynamic recrystallization has been undertaken until recently, when Sakai and co-workers began a very detailed study using TEM (transmission electron microscopy)[106-108]. More recently, systematic studies were carried out by Roucoules at McGill University, Canada[109] and Hodgson at BHP, Australia[82]. Their work shows that the kinetics of metadynamic recrystallization are more rapid than those of static recrystallization and that the grain size produced by metadynamic recrystallization is much finer than that produced by static recrystallization[110-115]. This concept can lead to new thermomechanical processing routes in industrial practice.

The difference between static recrystallization and dynamic or metadynamic recrystallization can be seen from the dependence of the recrystallization rate on the deformation parameters. As mentioned above, the static recrystallization kinetics are strongly dependent on strain and temperature, and somewhat less on strain rate; the dynamic or metadynamic recrystallization kinetics, however, are highly sensitive to strain rate, depend to a lesser degree on temperature, and not at all on strain.

Hodgson[82] reported that the time for 50% softening after dynamic recrystallization in C-Mn steels can be as short as 0.063 seconds for a strain rate of 10 s^{-1} and 0.0016 seconds for a strain rate of 1000 s^{-1} at 900 °C. Interpass times of 0.5 seconds for strip mills and 0.03 seconds for rod mills are long enough for metadynamic recrystallization to be completed during interpass delays. As a result, strain accumulation cannot continue to enable dynamic recrystallization to be completed and work hardening begins anew. For microalloyed steels (e.g. Nb steel), however, post-dynamic recrystallization (either metadynamic or static) is significantly delayed by solute drag or precipitate pinning. The strain can be effectively accumulated from pass to pass, a situation that leads to the completion of dynamic recrystallization.

Dynamic recrystallization is not expected to be a dominant phenomenon in hot strip mills because of the high sensitivity of the rate of metadynamic recrystallization to strain rate and the relatively 'long' interpass times. As soon as dynamic recrystallization is initiated by the accumulated strain, metadynamic recrystallization takes over during unloading.

The lack of experimental work concerning metadynamic recrystallization is obvious, and more investigations are needed to clarify such questions as: Is metadynamic recrystallization simply the growth of dynamic recrystallization nuclei? How do the processing parameters affect the transition between static and metadynamic recrystallization? How does the microstructure change if the process involves both metadynamic and static recrystallization? How does Nb addition affect the metadynamic recrystallization kinetics?

2.4 Role of Microalloying Additions During Controlled Rolling

2.4.1 Effect On Reheated Austenite Grain Size

It is well known that microalloy additions retard grain growth and coarsening during reheating. The effects of microalloying elements, such as Ti, Nb, Al and V, on the reheated grain size and grain coarsening temperature have been reported by some researchers[116-123]. Here, their roles are described as follows.

Ti Ti is the most effective microalloying element with respect to the retardation of grain growth and grain coarsening. Its effect can be extended to very high temperatures because TiN particles are very stable, and these fine particles can effectively retard the migration of grain boundaries, thereby impeding grain coarsening. The effect of Ti addition in steels on the reheated grain size has been reported by several authors[124-126]. The more recent work carried out by Liu and Jonas[123] shows that, at a given reheat temperature, the reheated austenite grain size first decreases with increasing Ti concentration, and then increases when the concentration exceeds 0.15 wt % (see Fig.2.4). This effect depends mainly on the volume fraction of fine TiN particles formed during solidification.

The volume fraction of fine TiN particles can be estimated from the following relation:

$$f_v^s = f_v^o - f_v^L \qquad (2.32)$$

where f_v^o is the equilibrium volume fraction of TiN, and f_v^L and f_v^s are the volume fractions of large and small TiN particles, respectively. Furthermore, the mean diameter of

reheated austenite in the presence of second phase particles can be estimated from the following equation according to the Zener pinning theory[127]:

$$D = Kd / f_v \qquad (2.33)$$

Here K is a constant and d and f_v are the mean particle size and volume fraction of the second phase particles. Liu and Jonas have shown that the volume fraction of small TiN particles first increases then decreases as the Ti concentration is increased, and the maximum value of f_v^s is at a concentration about 0.15 wt%. This provides an explanation of why the reheated austenite grain size is smallest at this concentration.

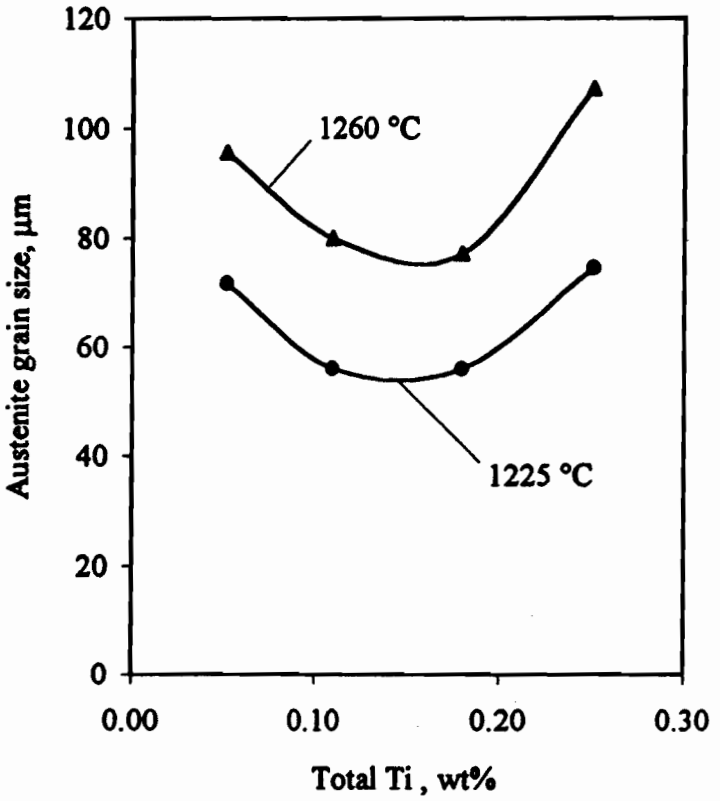

Fig. 2.4 Effect of Ti on reheated austenite grain size[123].

Nb Nb is one of the most favorable alloying elements because of its effect on grain growth, recrystallization and precipitation strengthening. It has been shown that the reheated austenite grain size of Nb treated steels is finer than that of plain carbon steels at temperatures up to 1200 °C; it also decreases with increasing Nb content. This refinement can be achieved while increasing the Nb content up to about the stoichiometric Nb:C ratio

at lower temperatures, ~1050 °C; further increases in the Nb content do not lead to further refinement. At higher temperatures of 1150 °C~1200 °C, however, higher Nb contents slightly coarsen the grain size (see Fig. 2.5)[120].

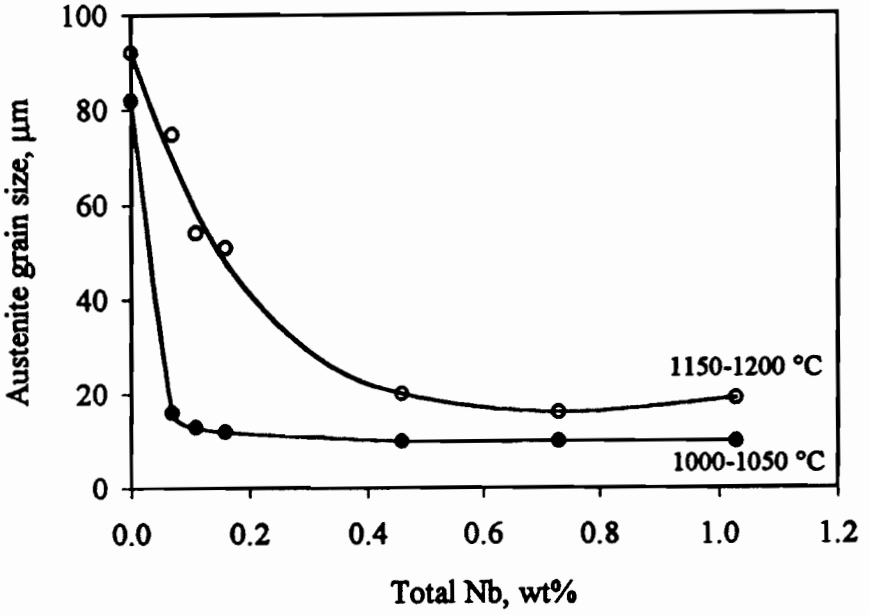

Fig. 2.5 Effect of Nb on reheated austenite grain size in low N steels[120].

It has been reported that grain refinement by Nb addition is due to the presence of undissolved Nb(CN) precipitates during reheating. This effect is strongly related to Nb(CN) particle size and volume fraction. Smaller sizes and higher volume fractions of Nb(CN) lead to greater refinement of the austenite grain size. For a constant volume fraction of Nb(CN), the increasing particle size produced by increasing temperatures results in coarser austenite grain sizes. The effects of volume fraction and particle size of precipitate on the grain size of austenite have been depicted graphically [116, 128].

This effect is also reflected in the grain coarsening temperature. It is shown in Fig. 2.6 that the grain coarsening temperature is a maximum at approximately the stoichiometric Nb:C ratio; this is because the estimated volume fraction of fine Nb(CN) precipitates is a maximum at this ratio. The reason for this is that the temperature dependence of the solubility of Nb(CN) is a maximum at the stoichiometric ratio. A similar effect has been reported for grain coarsening in steels containing AlN[117].

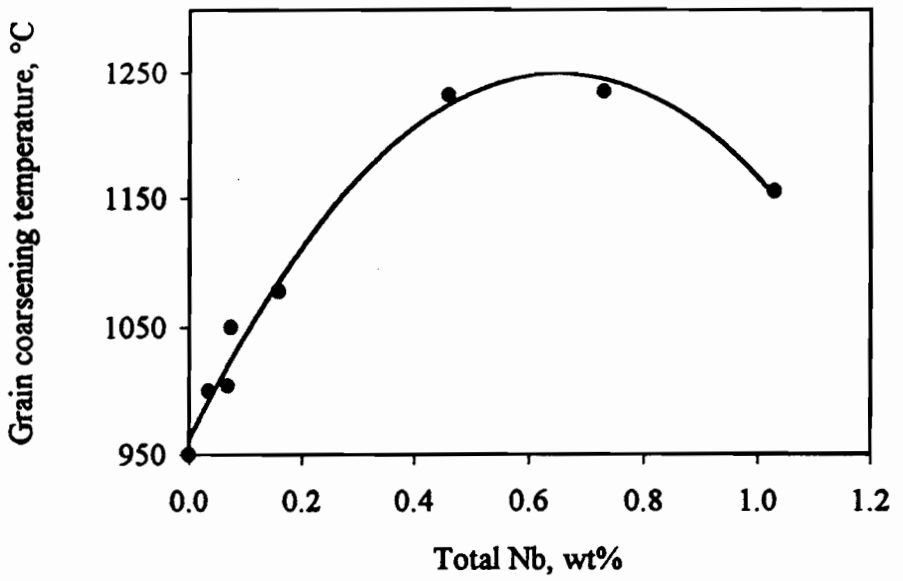

Fig. 2.6 Effect of Nb on austenite grain coarsening temperature[120].

V In the same manner as Ti and Nb, V is also a grain size refiner. The effect of V addition on the reheated austenite grain size, however, is much weaker than those of the former elements. Grain refinement by increasing the V content in steels can be obtained at temperatures up to 1050 °C. Generally there is little effect of V on the grain size at temperatures above 1150 °C due to the fact that the grain coarsening temperature never exceeds 1100 °C. The grain coarsening temperatures of V-N steels are consistently lower than those of the Nb steels.

Because of the increased stability and lower solubility of VN compared to VC, it is the VN that is usually considered to be responsible for pinning the austenite grain boundaries and thereby inhibiting grain growth. It seems likely that the grain coarsening temperature is also controlled by the solubility and coarsening rate of VN in austenite. Erasmus[119] showed that the grain coarsening temperature is always less than the VN solution temperature, due to the temperature dependent growth of VN.

B The effect of boron addition on the reheated austenite grain size has received little attention during past decades. Although Maitrepierre et al.[129] reported that boron has little effect on austenite grain size in low alloy steels, Yamanaka and Ohmori[130-132] and Djahazi[133] demonstrated that boron addition in low carbon low alloy steels raises the reheated austenite grain size. The results of Yamanaka and Ohmori are

reproduced in Fig. 2.7, which shows that the reheated grain size increases with increasing boron content. This can be explained in terms of the effect of BN formation on the volume fraction of AlN particles available to prevent the growth of austenite grains.

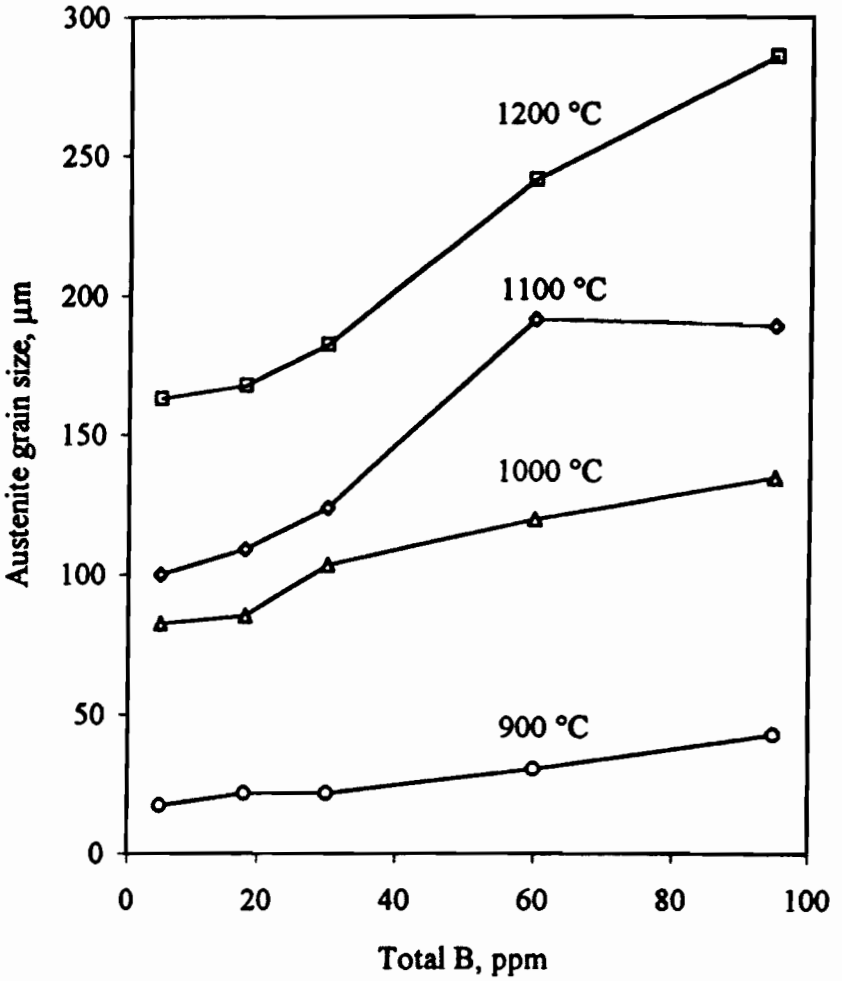

Fig. 2.7 Effect of boron on reheated austenite grain size[130].

When the kinetics of precipitation of AlN and BN are considered in detail, it is found that the precipitation of AlN is preceded by BN formation since boron atoms diffuse more rapidly in austenite than aluminum atoms. Nitrogen atoms are trapped by the boron atoms as BN; the amount of finely-dispersed AlN particles is therefore decreased in this way. Although such excess BN particles can be gradually replaced by AlN rods during lengthy austenitization, the AlN particles formed after precipitation cannot refine the austenite grain size.

2.4.2 Effect On Static Recrystallization

2.4.2.1 Operative Mechanism-Solute Drag or Precipitation?

It is well known that additions of Mo, Nb, Ti, Al and/or V to a plain carbon steel are effective in retarding recovery and recrystallization[134-137]. In the past, most attention was paid to the role of niobium in retarding austenite recrystallization in HSLA steels[138-141]. Previous research suggests that the pinning retardation of austenite recrystallization in Nb-bearing steels results from the pinning of austenite grain boundaries and sub-boundaries by either strain-induced niobium carbonitride precipitates or solute drag. Some investigators have suggested that solute drag effects on austenite recrystallization in Nb-bearing steels are small compared to the effects of strain-induced carbonitride precipitation[142]. Nevertheless, other workers have argued strongly that solute drag controls the recrystallization kinetics under certain conditions[143]. Akben et al. have suggested that the recrystallization kinetics are controlled by both solute drag and precipitation sequentially[144, 145].

It now appears that strain-induced precipitation is the operative mechanism when recrystallization is retarded to very long times at temperatures below 900 °C. However, for the early stages of retardation, there is still a certain amount of debate in recent publications[146-148] regarding the relative contributions of the two mechanisms.

In a recent study, Speer and Hansen[146] suggested that the retardation of recrystallization by solute drag only occurs very rarely, while Nb(CN) precipitates are entirely responsible for the retardation of recrystallization, even at high temperatures. In their work, steels were designed to contain a constant level of 0.05Nb, with the carbon concentration varying from 0.008 to 0.25. These compositions were considered to be able to indicate whether solute drag or precipitate-pinning is more important in controlling the austenite recrystallization kinetics.

The idea was that if the solute drag effect is the dominant factor, the recrystallization kinetics would presumably be identical since the Nb atoms available in solution are same. On the other hand, it is known that the precipitation kinetics depend to a large extent on the supersaturation ratio. The variation in carbon content should lead to differences in the carbonitride precipitation behavior between these steels; differences should therefore be observed in the retardation effect as a result of the differences in the precipitate supersaturation.

Their results are reproduced in Fig. 2.8 and display a continuous increase in the time to 50% recrystallization with increasing carbon content, even at 1066 °C. They therefore concluded that it is Nb(CN) precipitation and not Nb solute drag that is responsible for the retardation of recrystallization. However, this conclusion is weakened by some factors pertaining to their experiments. Firstly, the initial grain size varied widely among the steels, from 88 μm for the steel with a carbon concentration of 0.008 wt% to 1250 μm for the steel with a carbon level of 0.25 wt%. This can lead to a considerable difference in the time to a given fraction of recrystallization by grain size effects alone. Secondly, in the temperature range from 900 °C to 1010 °C, their results also show that the recrystallization rate is much slower in the steel containing 0.008C-0.05Nb than in a plain carbon steel. Yamamoto et al.[148] had a different opinion regarding this observation, although Speer and Hansen argued strongly that Nb(CN) precipitation was still the dominant effect.

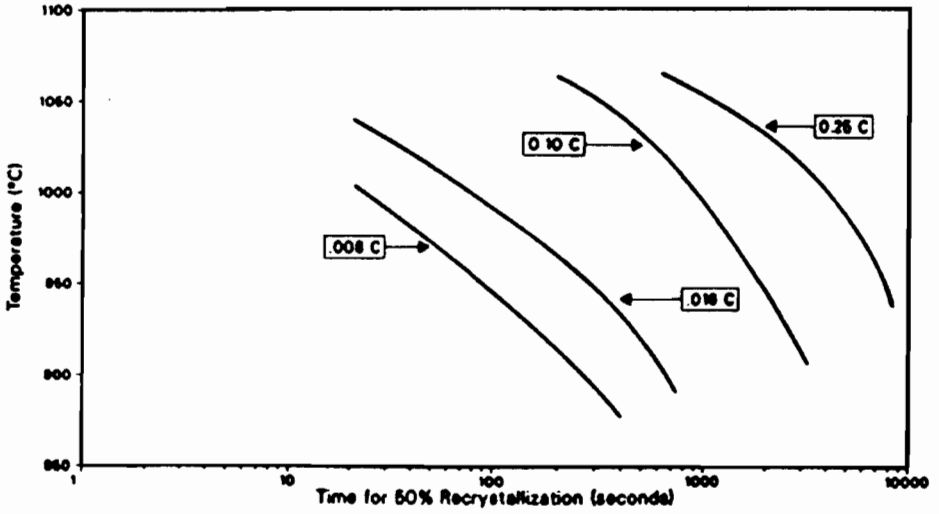

Fig. 2.8 RTT curves for 50% recrystallization in the steels containing 0.05Nb[146].

In their investigation, Yamamoto et al. present a different sceario using a series of steels with the same carbon concentration (0.002 wt%) and varying niobium levels from Nb-free to 0.171 wt %. Their softening curves are presented in Fig. 2.9. It is obvious that the softening process in the 0.097 Nb steel is about three orders of magnitude slower than in the Nb-free steel. They interpreted this as a result of a solute drag effect since the microalloying atoms remained dissolved under all testing conditions. Although a strong retardation effect by Nb(CN) precipitates was observed in the higher carbon steels, they concluded that solute Nb has an important role in retarding the onset of recrystallization so that strain induced precipitation can start before recrystallization is complete.

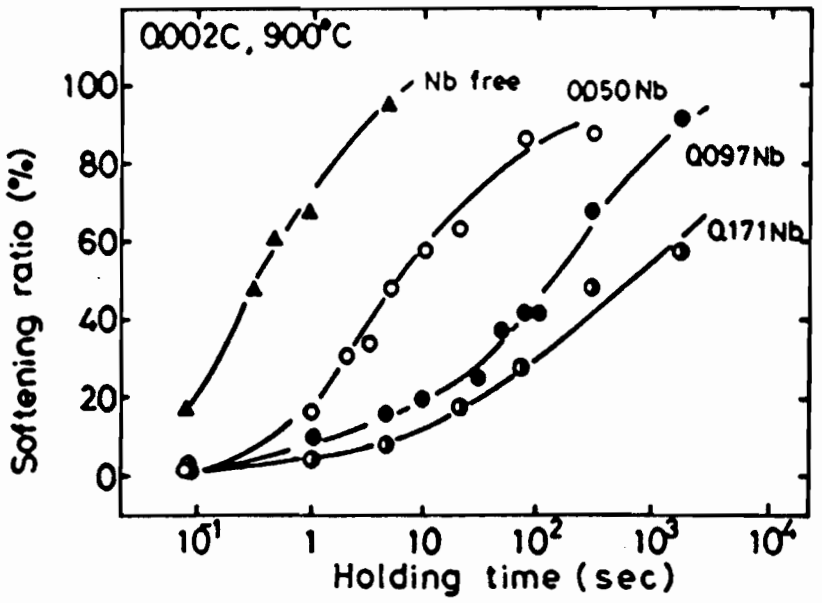

Fig. 2.9 Effect of Nb on softening behavior in 0.002C steels.

2.4.2.2 Precipitation in Ultralow Carbon Microalloyed Steels

Recently, Akamatsu et al.[149] observed that Nb(CN) precipitation is possible in an ultralow carbon (0.006 mass% C) Nb treated steel at a temperature of 950 °C, and that the progress of precipitation is much faster than in a steel with a higher carbon level (0.018 mass%) but the same supersaturation. Their results of the observed mole fractions of Nb(CN) are reproduced in Fig. 2.10. It can be seen that at holding times up to 18000 seconds, the mole fraction of Nb(CN) in the 0.006C steel is much higher than in the 0.018C steel. Their observations are not explained by conventional precipitation models for HSLA steels, and it appears instead that precipitation in ultralow carbon steels is influenced not only by the precipitate-forming atom product [Nb][C], but also by the Nb/C ratio.

The precipitation behavior of ultralow carbon steels, i.e. interstitial free (IF) steels, has not been widely investigated to date. The precipitation kinetics in austenite and ferrite should be studied as a new phenomenon since the conventional models for HSLA steels are not suitable. For instance, the calculated value of $t_{0.05p}$ (precipitation start time) obtained from the Dutta and Sellars model (see later section in this chapter) for the 0.006C steel used in the investigation of Akamatsu et al. and Yamamoto et al. is 7.5×10^{36} seconds. This suggests that Nb(CN) precipitation is impossible in this steel under the

testing conditions used. Such a conclusion is clearly in contradiction with the observations of both research groups.

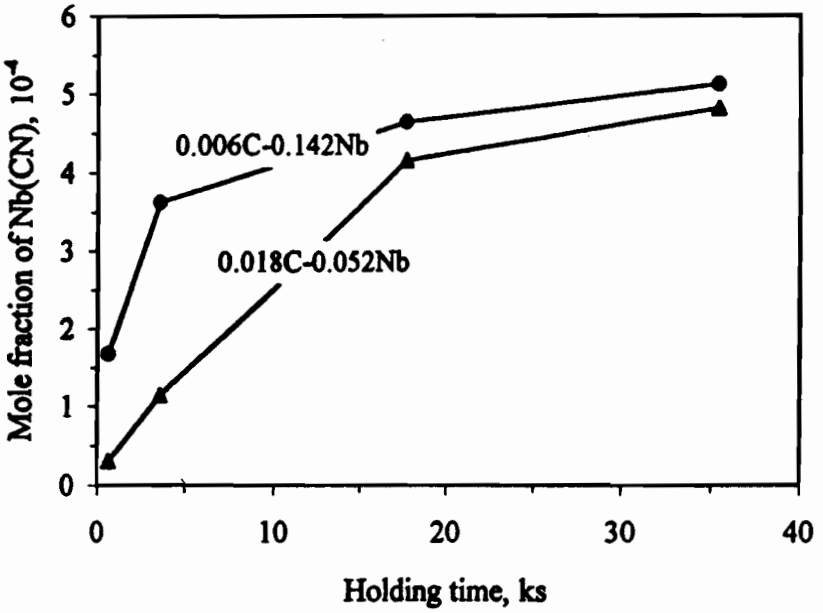

Fig. 2.10 Observed fraction of Nb(CN) precipitates in austenite at 950 °C.

In the production of IF steels, microalloying elements such as Ti and Nb are added to stabilize the interstitial elements, and thereby to promote recrystallization textures that are favorable for deep drawing[150-152]. It is evident that a full understanding of Ti and Nb behavior during the processing of these steels is of considerable importance. Several such investigations have been reported in the past five years[153-163], and most of these are associated with precipitation behavior in the ferrite range during annealing. One of them discussed both precipitation behavior and solute effects in austenite[163].

Tither et al.[163] pointed out that the differences in the precipitation behavior between the HSLA and IF steels could be due to their compositions. A typical HSLA steel might contain 0.05 wt%C, 0.006 wt%N, and 0.006 wt% S, whereas a typical IF steel contains ≤0.003 wt%C, 0.003 wt%N, and 0.006 wt%S. On an atomic weight percent basis, the ratios of C:N:S are consequently much different; i.e., C:N:S=22:2.5:1 for HSLA steels and 1.2:1.2:1 for IF steels. Hence, carbon represents about 86% of the precipitate-forming atoms in HSLA steels but only 35% in IF steels. Similarly, nitrogen represents only 10% of the precipitate-forming atoms in HSLA steels but 35% in IF steels. Sulfur, on the other hand, represents only 4% in HSLA steels but 30% in IF steels.

They observed that in Ti+Nb stabilized steels, if the Ti content satisfies the relation Ti=3.42N+2S, then C is principally removed from solid solution by the formation of $Ti_4C_2S_2$. There is a small percentage of C-bearing precipitates observed and they formed epitaxially on the $Ti_4C_2S_2$ particles. When this stabilization mechanism occurs, there is no further precipitation of particles other than those centered on the original sulfides and nitrides. Unlike HSLA steels, there is no strain-induced precipitation during rolling. In this case, the vast majority of the Nb was in solid solution.

If the IF steel contains less Ti than required for stabilization through the formation of $Ti_4C_2S_2$, the free C would then be available for the formation of a new and additional array of particles formed as strain-induced precipitates in the austenite during rolling or as precipitates in the ferrite during coiling. In Nb-only steels, carbon is picked up by Nb through the formation of Nb(CN), but there are no reported investigations confirming whether the Nb(CN) is formed during hot rolling or during subsequent annealing.

As is evident from the discussion above, the mechanism of retardation by solute drag is not fully understood. Yamamoto et al.[148] suggested that the effect of solute atoms on static recrystallization may be explained by the degree of lattice distortion; furthermore, the degree of lattice distortion can be indirectly detected by the change in the lattice constant. Their results show a consistent correlation between the retardation rate and the change in lattice constant per atomic % of the element in question. Nb, which produces the largest change in lattice constant, has the strongest effect on static recrystallization among the microalloying elements concerned.

The retardation of recrystallization can also be explained by the theory of pinning of grain boundaries by second phase particles. This will be presented in the subsection that follows.

2.4.2.3 Retardation by Precipitate Pinning

(a) Driving force for recrystallization

The strain induced boundary migration model has been widely accepted as one of the mechanisms for the nucleation of recrystallization[164-170]. This model was originally put forward by Beck and Sperry[167, 168] and was subsequently advanced through the work of Bailey and Hirsch[169].

According to this model, the driving force for recrystallization results from the difference in dislocation density between adjacent austenite subgrains[165]. To balance the strain energy, the grain boundaries "bulge" into grains of high dislocation density[166]. Quantitatively, the driving force, F_{RXN}, has been described by[166-169]:

$$F_{RXN} = \frac{\mu b^2 \Delta\rho}{2} \qquad (2.34)$$

where μ is the shear modulus, b is the Burgers vector, and $\Delta\rho$ is the change in dislocation density associated with the motion of the recrystallization front.

(b) Pinning force for recrystallization

Zener originally pointed out that, in the presence of a second phase, grain boundary migration may be inhibited because the second phase particles replace part of the grain boundary; this increment of grain boundary area must be recreated if the boundary is to move away from the particles[171]. Zener's theory was later quantified by Gladman[128], who assumed that the grain boundaries move rigidly through a regular array of spherical particles. The pinning force for each particle can be expressed as

$$F_{PIN} = 4r\gamma N_s \qquad (2.35)$$

where r is the particle radius, γ is the interfacial energy per unit area of boundary, and N_S is the number of particles per unit area of boundary.

For the rigid boundary model, N_S is calculated from $N_s^R = 3f_v / 2\pi r^2$. For the flexible boundary model proposed by Cuddy[84, 85], N_S can be determined from $N_s^F = 3f_v^{2/3} / 4\pi r^2$. The most realistic model was the one proposed by Hansen et al.[142], where N_S is expressed as $N_s^S = 3f_v l / 8\pi r^3$. f_v in the above equation is the precipitate volume fraction.

Substitution of the expressions for N_s^R, N_s^F, and N_s^S into equation (2.35) gives the respective pinning force for each model:

$$F_{PIN}^R = \frac{6f_v\gamma}{\pi r} \qquad (2.36)$$

$$F_{PIN}^{F} = \frac{3f_v^{2/3}\gamma}{\pi r} \qquad (2.37)$$

$$F_{PIN}^{S} = \frac{3f_v\bar{l}\gamma}{2\pi r^2} \qquad (2.38)$$

For hot deformed or cold deformed austenite, if $F_{RXN}<F_{PIN}$, the grain boundaries will be completely arrested, whereas if $F_{RXN}>>F_{PIN}$, the precipitates should not have any significant effect on boundary migration. However, if $F_{RXN}> F_{PIN}$ and the magnitudes are comparable, the boundary may move, but at some reduced velocity.

2.4.2.4 Kinetics of Nb(CN) Precipitation

Precipitation behavior in microalloyed steels has been frequently investigated during the last twenty years[56, 57, 142, 172-183] and a general Avrami type equation has been used to describe isothermal precipitation from supersaturated austenite:

$$Y = 1-\exp\left(-bt^n\right) \qquad (2.39)$$

where Y is the fraction precipitated, b and n are constants, and t is the precipitation time.

Precipitation kinetics in microalloyed steels are largely dependent on temperature, and precipitation-time-temperature diagrams (known as PTT diagrams) are usually of "C" shape. There have not existed any relationships to describe the precipitation behavior quantitatively until recently, when Dutta and Sellars[180] derived a model for strain-induced Nb(CN) precipitation. The model is based on classical nucleation theory and on the solubility products for NbC and NbN in austenite. The precipitation start time, t_{P_S} or $t_{0.05p}$, can be expressed as a function of the supersaturation ratio (k_S), strain (ε), Nb concentration [Nb] and Zener-Hollomon parameter [Z]:

$$t_{0.05p} = A[Nb]^{-1}\varepsilon^{-1}Z^{-0.5}\exp\left(\frac{270{,}000}{RT}\right)\exp\left(\frac{B}{T^3(\ln k_s)^2}\right) \qquad (2.40)$$

Here $t_{0.05p}$ is the time for 5% Nb(CN) precipitation, T is the absolute temperature, and R is the gas constant. A and B are two constants which were obtained by fitting data reported in the literature; these have the values $A=3\times10^{-6}$ and $B=2.5\times10^{10}$. At a

given temperature, the supersaturation ratio is defined as the ratio of the actual amount of [Nb][C+12N/14] in solution to the equilibrium amount, i.e.

$$k_s = \frac{[Nb][C+12N/14]_{soln}}{10^{2.26-6770/T}} \qquad (2.41)$$

This model suggests that the precipitation kinetics of Nb(CN) are dependent not only on the amount of Nb in solution but also on the C concentration that appears in the supersaturation ratio. That is, the supersaturation ratio determines the driving force, and is therefore more important than the concentration of Nb atoms in solution in terms of predicting the kinetics of precipitation.

In 1989, based on their thermodynamic analysis of the system, Liu and Jonas were able to derive an alternative model for titanium carbonitride[181].

$$t_{P_s} = H(\rho X_{Ti})^{-1} \exp\left(\frac{Q}{RT}\right)\exp\left(\frac{\Delta G^*}{kT}\right) \qquad (2.42)$$

The main difference between the D-S and L-J models is in the second exponential term. In the D-S model, the chemical driving force for nucleation is simply related to the solubility product of the precipitating species. By contrast, in the L-J model, the chemical driving force was derived from the free energy change that occurs during precipitation. Every term in the L-J model was given a clear physical and thermodynamic meaning. The D-S model, however, is associated solely with simple processing parameters; these lead to simpler calculations for Nb microalloyed steels and the method is therefore more convenient for practical use.

Later, in 1992, Park, Yue and Jonas modified the L-J model for Nb(CN) precipitation[182], and derived the start time for Nb(CN) precipitation as:

$$t_{P_s} = \frac{N_c a_{Nb(CN)}^3}{D_0 \rho}(X_{Nb})^{-1} \exp\left(\frac{Q}{RT}\right)\exp\left(\frac{\Delta G^*}{kT}\right) \qquad (2.43)$$

where ρ is the dislocation density, and N_c is the critical number of nuclei. Parameters such as the lattice parameter $a_{Nb(CN)}$, activation energy for the diffusion of solute atoms Q, particle/matrix interfacial energy γ, and frequency factor D_0 can be obtained from the literature:

$a_{Nb(CN)}=4.445\times10^{-10}$ m
$Q=266.5$ kJ/mole [184]
$D_0=0.83$ cm^2/s [184]
$\gamma=0.5$ J/m^2 [180]

The critical free energy can be expressed as:

$$\Delta G^* = 16\pi(\xi\gamma)^3 / \left(3(\Delta G_{chem} + \Delta G_\varepsilon)^2\right) \qquad (2.44)$$

where ξ is a modifying factor, ΔG_{chem} is the chemical free energy, and ΔG_ε is the volume strain energy. The latter is very small compared to the chemical driving force for nucleation and is neglected for simplicity.

The chemical free energy can be derived from a thermodynamic analysis of the system. For the complete calculation of the t_{P_S} for Nb(CN) precipitation, however, there are still three unknown parameters; N_c, ρ and ξ, in the P-Y-J model. Values of ξ in the range from 0.19 to 0.55 were reported for Nb(CN) nucleation[180]; it determines the nose temperature of the C curve. According to Park, Yue and Jonas[182], the values for ξ and N_c/ρ were obtained by performing a best fit to the experimental data.

This formulation was then used to model the continuous cooling precipitation behavior by Park, Yue and Jonas, using the additivity rule originally proposed by Scheil in 1935[185]. Their results show that the calculated continuous cooling precipitation diagrams (CCP diagrams) have shapes similar to those of PTT diagrams, but with lower nose temperatures. It appears that, during continuous cooling, the precipitation start and finish coordinates are shifted to longer times and lower temperatures. This occurs because both nucleation and growth of the precipitates are suppressed during cooling, and the effect is more prominent at the higher cooling rates. This is of great interest in the case where the solute Nb available at relatively low temperatures (close to the A_{r3}) is required to suppress the formation of polygonal ferrite in low carbon bainitic steels.

In industrial practice, both continuous cooling and multipass deformation are involved. This could further complicate the situation, and makes modeling very difficult. Not only the precipitation start time but also the rate of particle coarsening are affected by deformation. Weiss and Jonas[186] reported that the coarsening rate under dynamic deformation conditions is accelerated by about two orders of magnitude when compared to the static rate of Ostwald ripening. One must therefore be very careful about applying models developed under isothermal and single-pass deformation conditions to actual industrial rolling practice.

2.4.2.5 Recrystallization Kinetics of Nb Microalloyed Steels

Since Le Bon et al.[57] first presented a recrystallization-temperature-time diagram (RTT diagram) for a Nb microalloyed steel in 1975, numerous investigations have been undertaken to study the recrystallization kinetics of Nb steels. In 1980, based on their experimental observations, Hansen et al.[142] proposed the schematic recrystallization-precipitation-temperature-time diagram (known as an RPTT diagram) shown in Fig. 2.11. It clearly demonstrates the interaction between recrystallization and precipitation over the whole temperature range that may be used in industrial practice. Above T_0 (the equilibrium solution temperature for the operative precipitation process), precipitation is thermodynamically impossible. Below T_0, however, three interaction regions are possible and two important temperatures, RLT and RST, can be identified. In region I (the high temperature region), recrystallization is very rapid and complete before precipitation can start. Therefore, there is no interaction between recrystallization and precipitation. Accordingly, precipitation eventually takes place in recrystallized (strain-free) austenite along the P_s curve. The recrystallization process, which precedes any precipitation in this case, is defined by the R_s (recrystallization start) and R_f (recrystallization finish) curves.

In region II (the intermediate temperature region), as a result of the higher supersaturation ratio and the potent nucleation sites introduced by deformation, the precipitation C curve is shifted to the left (P_s^D). Precipitation takes place after the onset of recrystallization, but before it is complete. Therefore, recrystallization starts along the R_s curve, but ends along the R_f^P curve because of the retardation by precipitation. In region III (the low temperature region), precipitation takes place *before* recrystallization, and now both the start and finish of recrystallization are delayed (to the R_s^P and R_f^P curves).

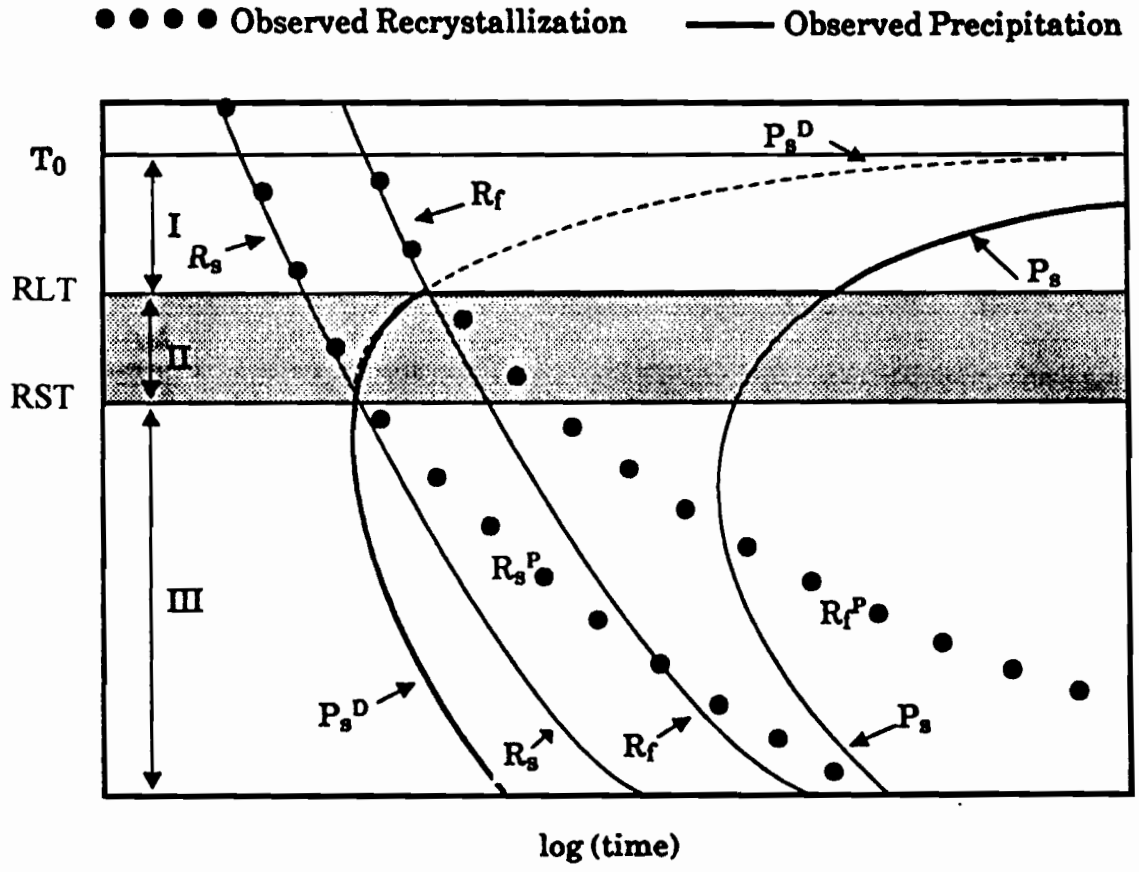

Fig. 2.11 Schematic recrystallization-precipitation-temperature-time (RPTT) diagram.

These interactions between recrystallization and precipitation are affected by steel composition, temperature, deformation and initial austenite grain size. Quantitative relationships for describing the recrystallization rate in Nb microalloyed steels have been reported by several research groups; these have the following general form:

$$t_X = A\varepsilon^p \dot{\varepsilon}^q d_0^s \exp\left(\frac{Q}{RT}\right) \qquad (2.45)$$

where t_x is the time for a given recrystallized volume fraction X, d_0 is the grain size, Q is an activation energy, and A, p, q and s are the constants listed in Table 2.4.

Table 2.4 Parameters used in equation (2.45) by different research groups

Investigator	steel	X	A	s	p	q	Q (J/mol)
Sellars [62]	~0.04Nb	0.5	2.52×10^{-19}	2	-4	0	325000
Laasraoui and Jonas [63]	0.055Nb 0.055Nb-0.003B	0.5 0.5	1.27×10^{-19} 2.86×10^{-24}	0 0	-3.8 -3.55	-0.36 -0.42	404000 436000
Hodgson [82]	0.046Nb	0.5	$(-5.24+550[Nb])\times10^{-18}$	2	-4+77[Nb]	0	330000
Siwecki [187]	≤0.043Nb	0.25	?	2	-4	0	350000
Medina and Mancilla [188]	0.042Nb	0.5	3.943×10^{-13}	1	-1.96	-0.44	262000

It can be seen that strain has a strong effect on the recrystallization kinetics, while strain rate has, if any, a minor effect. Strain rate does not appear in the models of Siwecki[187] and Hodgson[82], but has an exponent about 10 times lower than that of strain in the model of Laasraoui and Jonas[63]. Medina and Mancilla[188] also reported a weak effect of strain rate on the recrystallization kinetics.

Later in 1987, Dutta and Sellars[180] developed a model for the recrystallization kinetics of Nb steels in the absence of strain-induced precipitation, and the change in recrystallization behavior can then be predicted using the strain-induced precipitation

model given in the previous section. In this model, the time for 5% recrystallization is expressed as:

$$t_{0.05x} = 6.75\times10^{-20} d_0^2 \varepsilon^{-4} \exp\left(\frac{300000}{RT}\right)\exp\left(\left(\frac{2.75\times10^5}{T} - 185\right)[Nb]\right) \qquad (2.46)$$

where d_0 is the initial grain size, T is the absolute temperature and [Nb] is the concentration of Nb in solution. The time for 85% recrystallization is $t_{0.85x}$,

$$t_{0.85x} = Ct_{0.05x} \qquad (2.47)$$

where the constant C=6.1 is derived from the Avrami equation using an exponent n=2. By combining these recrystallization models with the one for precipitation, the RPTT diagram can be established quantitatively, as shown in Fig. 2.12. It can be seen that the precipitation curve intersects the recrystallization curves at two points; these define two

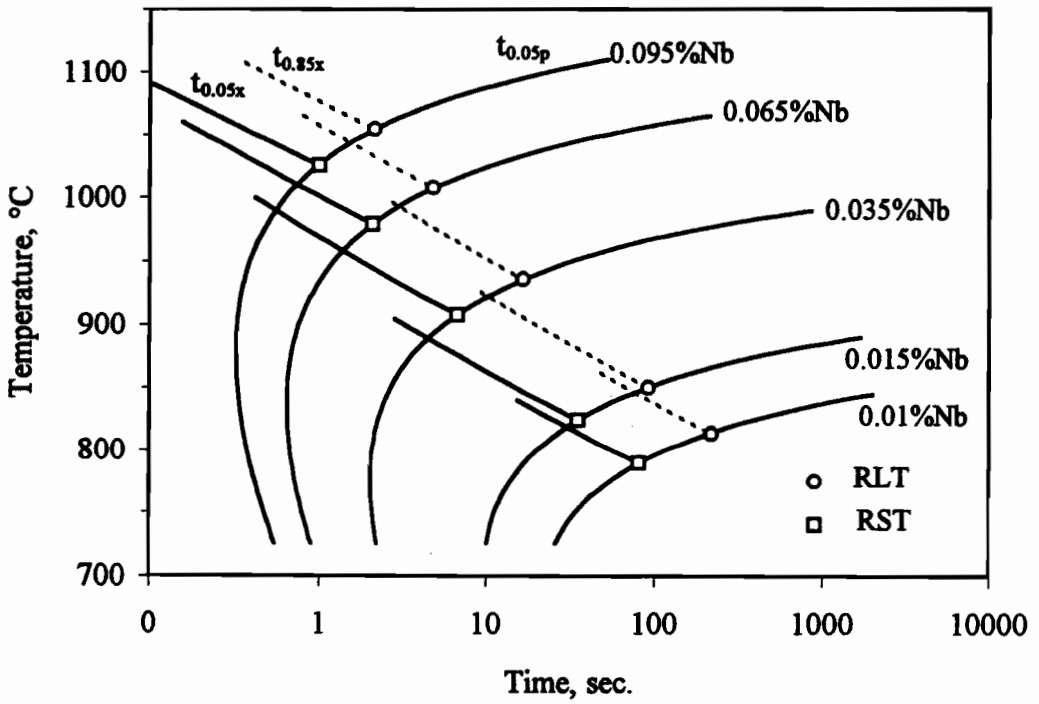

Fig. 2.12 Interaction of recrystallization and strain-induced precipitation as a function of Nb content in 0.07C-0.004N steels rolled by 15 % reduction at $\dot{\varepsilon}$=10 s^{-1}. RLT refers to the lower temperature limit for 'full' (85%) recrystallization and RST refers to the upper temperature limit for the complete arrest of recrystallization.

characteristic temperatures, RLT and RST, named recrystallization limit temperature and recrystallization stop temperature by Dutta and Sellars, respectively.

The term recrystallization limit temperature, or RLT, refers to the lowest possible temperature at which complete recrystallization can take place. This represents the lowest convenient temperature for roughing. In a similar manner, the recrystallization stop temperature or RST is the highest possible temperature at which recrystallization is completely absent. This represents the highest permissible temperature for starting the "pancaking" passes.

The effect of Nb on both the RLT and RST in a 0.07C-0.004N microalloyed steel is evident from Fig. 2.12. The RLT and RST increase according to a power law relationship with respect to the increase in Nb content, reflecting the effect of the greater Nb level on the kinetics of strain-induced Nb(CN) precipitation. At low Nb concentrations, a small addition of Nb can raise the RLT and RST considerably, i.e., the increase in Nb concentration from 0.01 wt% to 0.02 wt% raises the RLT by about 64 °C. This rate of increase decreases at high Nb concentrations. The strong effect of C on the RLT and RST can also be predicted for a given deformation condition, as shown in Fig. 2.13. For C levels above 0.1, the RLT and RST are above 900 °C, and increase by approximately 40 °C per 0.1 wt% C. This relative change in RLT compares favorably with the T_{nr}'s (no-recrystallization temperatures) modeled by Boratto et al.[189] in Nb microalloyed steels.

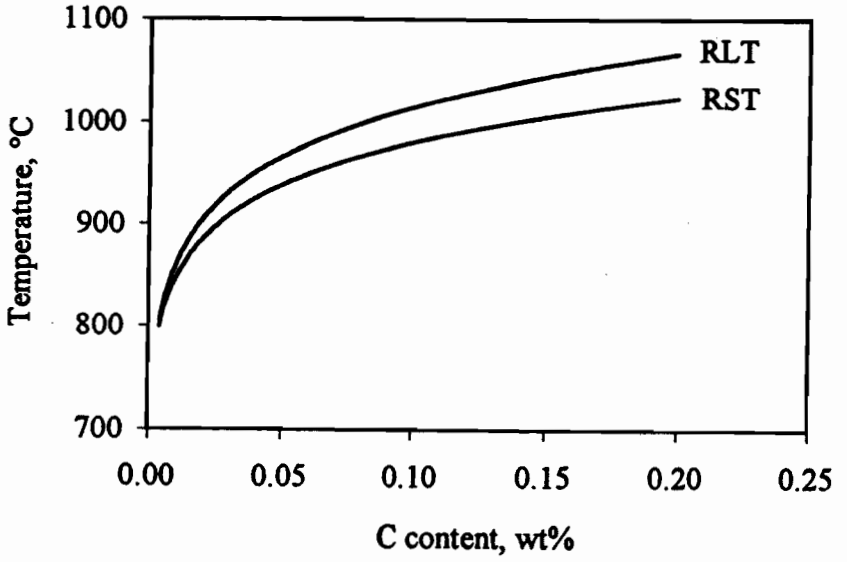

Fig. 2.13 Effect of C on the RLT and RST in a steel containing 0.056Nb.

It is dangerous to extrapolate the predictions described above to very low carbon levels because such a calculation gives an RLT as low as 812 °C for a C level at 0.004 wt%, for example. This is obviously an inappropriate prediction since a T_{nr} of 960 °C was determined experimentally by Najafi-Zadeh et al.[190] for a Nb stabilized IF steel with the same niobium, carbon and nitrogen concentrations. It therefore seems that the Dutta and Sellars model does not apply to ultralow carbon steels; these should instead be studied as a new category, with respect to both their recrystallization and precipitation behaviours. Nevertheless, the Dutta and Sellars models are still useful for predicting the recrystallization and precipitation behaviors of HSLA steels, as long as the carbon level is higher than 0.06 wt% or the atomic ratio Nb/C<1, as suggested by Akamatsu et al[149].

The effect of boron addition on the recrystallization behavior of Nb microalloyed steels has not been intensively investigated until recently. It has been generally observed that the presence of boron in Nb microalloyed steels further retards austenite recrystallization, and that the retarding effect is greater than the sum of their individual effects. Although the mechanism of retardation of recrystallization by boron has not been fully explained, Tamehiro et al.[14, 15] suggest that, because Nb is a strong carbonitride former, adding it to boron steels will tie up the carbon and nitrogen, leaving more boron atoms free to segregate to grain boundaries, thereby retarding recrystallization in this way. However, Djahazi et al.[183] showed that boron addition increases the recrystallization incubation time by enhancing Nb(CN) precipitation (shifting the PTT curve to the left). Other researchers have proposed that the combined addition of Nb and boron has a synergistic effect on recrystallization[191-193].

Based on the above review, it seems that there are limited data concerning the effect of deformation parameters, such as strain, strain rate and interpass interval, on the no-recrystallization temperature under conditions of continuous cooling. Although single pass softening curves can help us to understand recrystallization behavior, they cannot be applied directly to industrial practices that involve both multipass deformation and continuous cooling. The present work therefore focuses on a systematic investigation of the effect of processing parameters on the no-recrystallization temperature, T_{nr}; it also seeks to throw some light on the transformation behavior of Nb-B treated low carbon steels.

CHAPTER 3

EXPERIMENTAL MATERIALS AND TECHNIQUES

3.1 Experimental Materials

In the present work, the influence of processing parameters on the critical temperatures, T_{nr} and A_{r3} (or B_s), were investigated in eleven microalloyed steels. The chemical compositions of these steels are shown in Table 3.1; they can generally be divided into two groups in terms of whether boron is present or absent. In group I, the first three steels contained simple niobium additions of 0.05, 0.07, and 0.09 wt pct. This range of addition, in combination with different levels of carbon and nitrogen, allowed the influence of both solute drag and precipitate pinning to be investigated. To compare the effect of various microalloying elements on the recrystallization of austenite, a titanium and a vanadium steel were also studied. A plain carbon steel was used as a base steel for comparison purposes. In group II, four steels containing binary combinations of Nb and B or Mo and B were investigated so as to determine the influence of boron addition on the no-recrystallization temperature. Finally, a ternary Mo-Nb-B steel and a single B-modified grade were also included, the latter to provide a baseline for the effect of B addition when added alone.

Table 3.1 Chemical compositions of the steels investigated

Group	Steel	C	Si	Mn	Mo	Al	Nb	Ti	V	B	N
I	A (0.05Nb)	0.125	0.33	0.43	0.17	0.035	0.05	-	-	-	0.005
	B (0.07Nb)	0.040	0.31	1.67	0.20	0.038	0.07	0.026	-	-	0.01
	C (0.09Nb)	0.040	0.27	1.53	0.14	0.042	0.09	0.007	-	-	0.008
	D (0.16Ti)	0.055	0.24	1.30	-	0.036	-	0.16	-	-	0.004
	E (0.1V)	0.048	0.22	1.30	-	0.032	-	0.020	0.1	-	0.005
	F (PC)	0.090	0.28	1.44	-	0.020	-	-	-	-	0.007
II	G (Nb-15B)	0.021	0.24	1.75	-	0.030	0.060	0.015	-	0.0015	0.0048
	H (Nb-48B)	0.021	0.12	1.80	-	0.042	0.061	0.017	-	0.0048	0.0030
	I (Nb-64B)	0.020	0.16	1.40	-	0.020	0.055	0.026	-	0.0064	0.0045
	J (Mo-B)	0.030	0.14	1.80	0.35	0.028	-	0.012	-	0.0040	0.0030
	K (Mo-Nb-B)	0.026	0.12	1.70	0.30	0.037	0.059	0.015	-	0.0035	0.0030
	L (B)	0.030	0.18	1.55	-	0.020	-	0.020	-	0.0033	0.0043

All of the steels were cast and hot rolled to plates of 13 mm final thickness at the Metals Technology Laboratories of the Department of Energy, Mines and Resources, CANMET, Ottawa. Each heat was deoxidized with aluminum. In group II, in order to enhance the effect of boron, both titanium and niobium were added to the steels. Niobium is a strong carbide former, and it was added to prevent the formation of $Fe_{23}(CB)_6$. Titanium is an element which has a stronger affinity for nitrogen than boron, and an addition with a ratio of Ti/N>3.4 can effectively tie up the nitrogen and thus prevent the formation of boron nitride. More fresh boron is made available in this way for grain boundary segregation. Among steels G, H, and I, the boron concentration varied from 15 ppm to 64 ppm; this made it possible to investigate the influence of boron level on the grain growth, recrystallization and transformation behavior.

3.2 Specimen Preparation

As mentioned in the introduction, two types of tests, torsion and compression, were performed in the present work. Torsion tests were mainly employed to investigate the influence of processing parameters on the T_{nr} during multipass deformation under continuous cooling conditions. Compression tests were carried out to study transformation behavior in the low carbon niobium and boron treated steels. In the hot torsion tests, torsion specimens with gage lengths of 22.2 mm and diameters of 6.3 mm were used (shown in Fig. 3.1). In the case of the high strain rate tests, the specimens had reduced gage lengths of 10.4 mm, but the same diameters as regular specimens. In the hot compression tests, small cylindrical samples with heights of 11.4 mm and diameters of 7.8 mm were used. All of the torsion and compression samples were machined from the as-received plates, with their longitudinal axes parallel to the rolling direction.

The equilibrium solution temperatures for the present materials were evaluated from the following equation given by Irvine et al.:[135]

$$\log[Nb]\left[C+\frac{12}{14}N\right]=2.26-\frac{6770}{T} \qquad (3.1)$$

These were estimated to be 1240 °C, 1153 °C, and 1187 °C for the 0.05Nb, 0.07Nb, and 0.09Nb steels, respectively. An austenitization temperature of 1250 °C was selected for

these materials. For compositions D to I in Table 3.1, the equilibrium solution temperatures were approximately 1080 °C. An austenitization temperature of 1200 °C was therefore chosen for these grades.

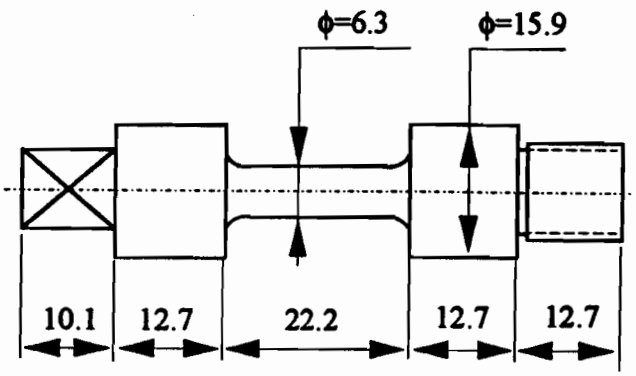

Fig. 3.1 Geometry of the torsion specimen (all dimensions in mm).

3.3 Experimental Equipment

3.3.1 Torsion Testing System

During the past few decades, numerous investigations and hot rolling simulations have been carried out on torsion machines. Although the deformation mode differs from that of rolling (simple shear vs. pure shear), it has been demonstrated that torsion testing is a very powerful tool for simulating industrial processing. The main advantage of torsion testing, as opposed to compression or tensile testing, is that high levels of strain can be readily attained in torsion. The other mechanical tests are limited to strains of about unity, considerably less than those commonly experienced in mills.

3.3.1.1 Torsion Machine

In the present work, the investigations involved large deformations (i.e. strains >1) were carried out on a servo-hydraulic, computer controlled MTS torsion machine; the latter is equipped with a Research Incorporated radiant furnace controlled by a Leeds and Northrup system. Details of the apparatus are shown in Fig. 3.2. A lathe bed was used as

the frame of the torsion machine on which the motor-furnace-torque cell system was mounted longitudinally[194]. This motor is driven by an MTS hydraulic power supply and can develop a maximum torque of 100 N.m and a maximum speed of 628 rpm. The speed and direction of rotation of the motor are controlled by a servovalve that proportions the hydraulic fluid flow to the motor in relation to the magnitude of an electrical signal.

The specimen is held by means of nickel-based superalloy loading bars, which are connected to the motor and torque cell; the latter is mounted on the lathe saddle so that it can be moved axially. The right side of the specimen is screwed into the fixed bar, and the left side of the specimen (with a flat) fits into the slot of the rotating bar. During deformation, the load developed by the test specimen was measured by the torque cell connected to the end of the right-side loading bar, while the displacements, i.e. the angle of twist of the sample, were recorded by the transducer connected to the motor shaft through the rotating bar on the left hand side. In the present study, a 1000 in-lbf (112.98 N-m) capacity torque cell was used, and its associated electronics were calibrated for four ranges (1000, 500, 200, and 100 in-lbf), which correspond to 112.98, 56.49, 22.60, and 11.30 N-m. This relatively low capacity was selected to ensure adequate resolution of the torque measurements obtained from the small samples.

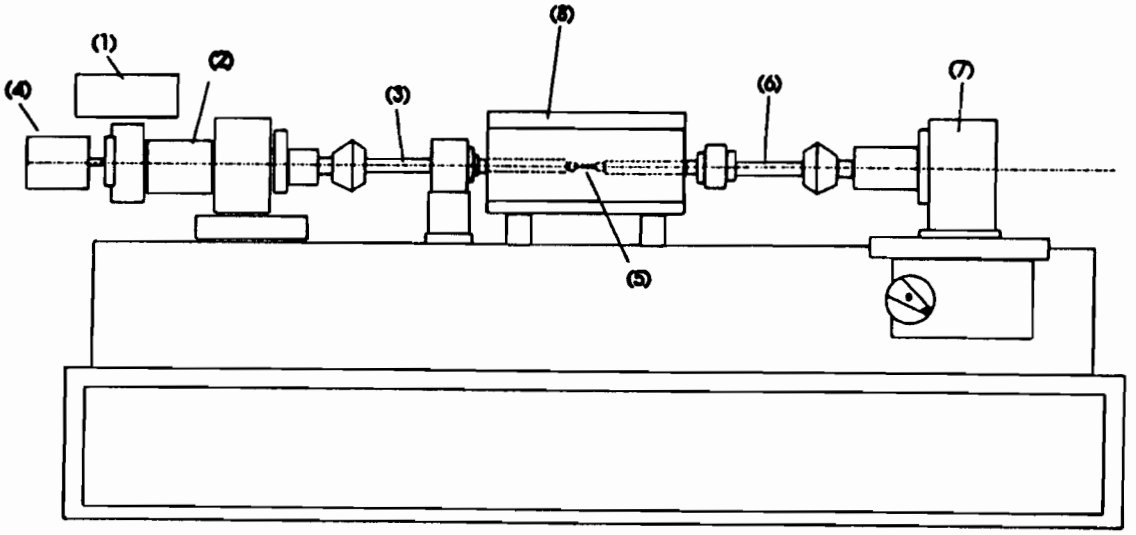

(1) hydraulic servovalve, (2) hydraulic motor, (3) rotating torsion bar, (4) potentiometer, (5) specimen, (6) stationary grip, (7) torque cell, (8) furnace.

Fig. 3.2 The torsion machine.

3.3.1.2 Control System of the Torsion Machine

The torsion machine was linked to a COMPAQ 386 computer which runs on the OS/2 operating system. A new generation of MTS testing software, TestStar, was used to run the testing system, and thereby the torsion tests. The TestStar control system consists of a PC terminal, a digital controller and a load control panel. The digital controller handles all real time activities, such as closed-loop control of the torsion machine, command generation, signal conditioning and data acquisition. The load control panel is used to operate the hydraulic system and position the actuator of the torsion machine. A schematic diagram of the operations involved in running a test is shown in Fig. 3.3.

The MTS BASIC programs employed with the old control system have now been replaced by the current testing programs (or templates), which can be created step by step using the TestWare S/X application software. A typical template window for a 17 pass test is shown in Fig. 3.4. For each step on the left hand column, there are four processes corresponding to the right hand column. These are named DATA, RAMP, BACK/HOLD, and STEP DONE. Once the procedure frame is ready, the testing parameters such as strain, strain rate, and interpass time are input into the template (Fig. 3.5).

The minimum hold time between two deformations (which is termed the interpass time in hot rolling) that can be reached using this type of template is 1 second. By using the file playback command, the hold time can be reduced down to 0.05 seconds. When programming this type of template, a separate file is needed to describe the test parameters (Fig. 3.6).

3.3.1.3 Furnace and Temperature Control

The test specimens were heated by means of a water-cooled four-element radiant furnace, model E4-10PA, which allows transient specimen temperatures of up to 1650 °C (3000 °F) to be reached. The furnace temperature was controlled by a Leeds and Northrup system. A digital industrial temperature controller was used with this system, which is linked to the programmer and the furnace through a thermocouple and a power supply, respectively. The temperature was also read on the computer screen, and could be written onto the hard disk with the other data. A K-type open-ended thermocouple was used to measure the temperature of the test specimen; it was placed on the surface of the specimen in the centre of gage length. Deformation heating, if any, was compensated by

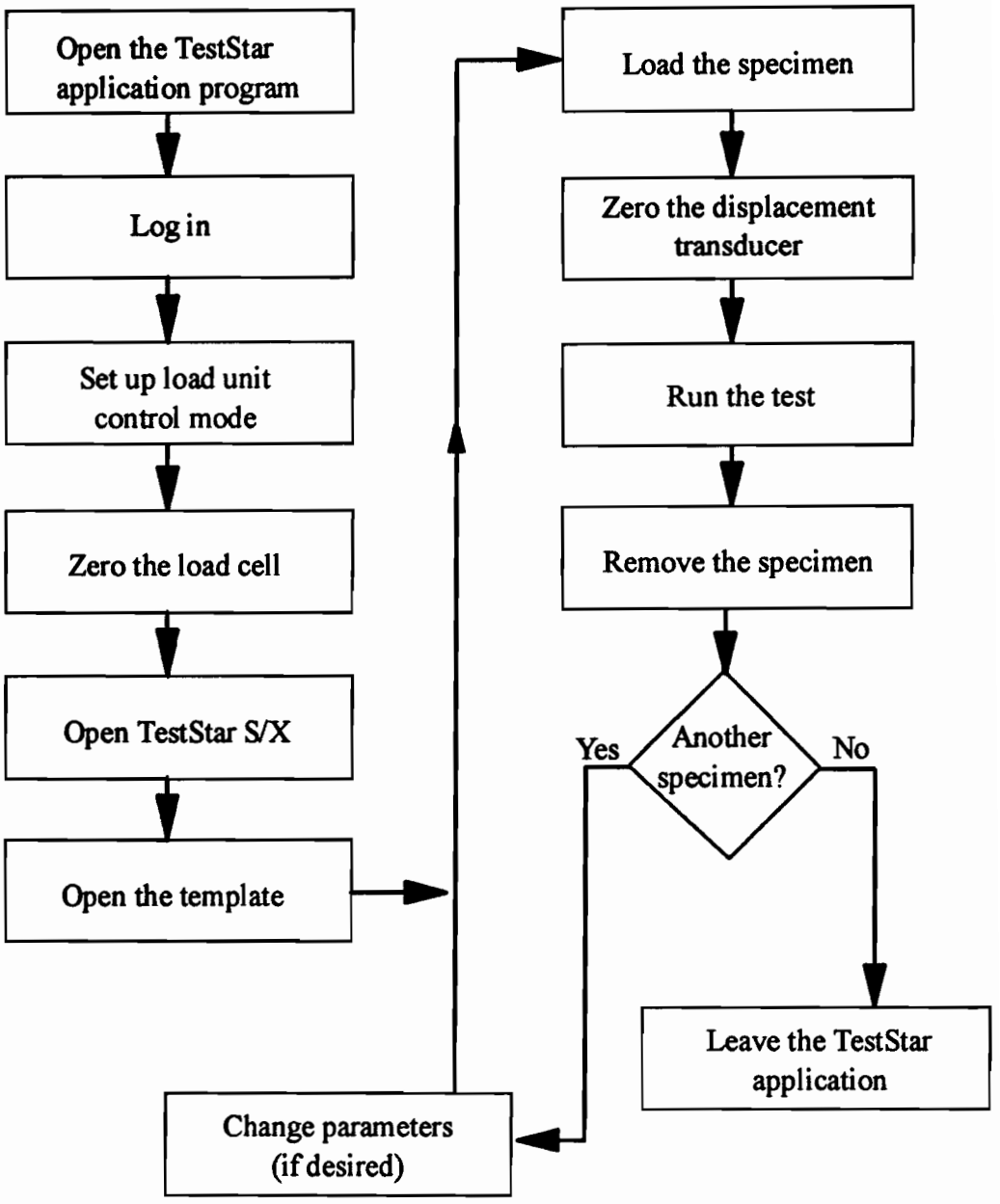

Fig. 3.3 A schematic diagram of the test procedure.

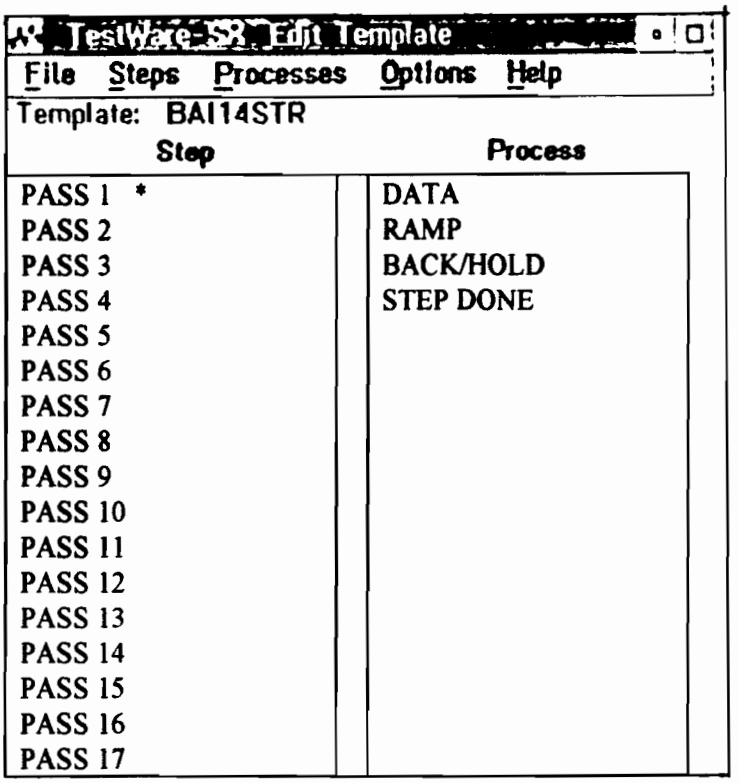

Fig. 3.4 17 pass torsion program, using the MTS TestWare S/X software.

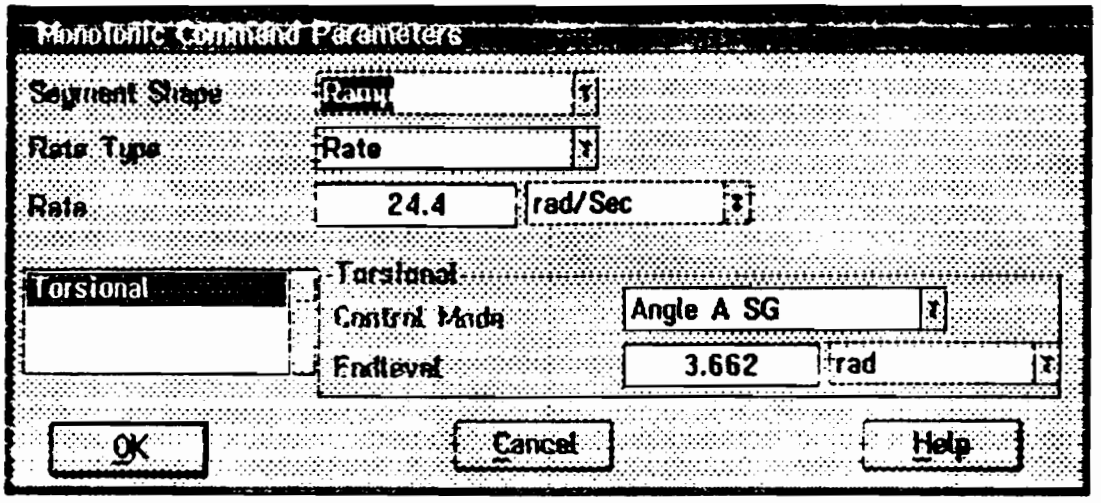

Fig. 3.5 Test parameters.

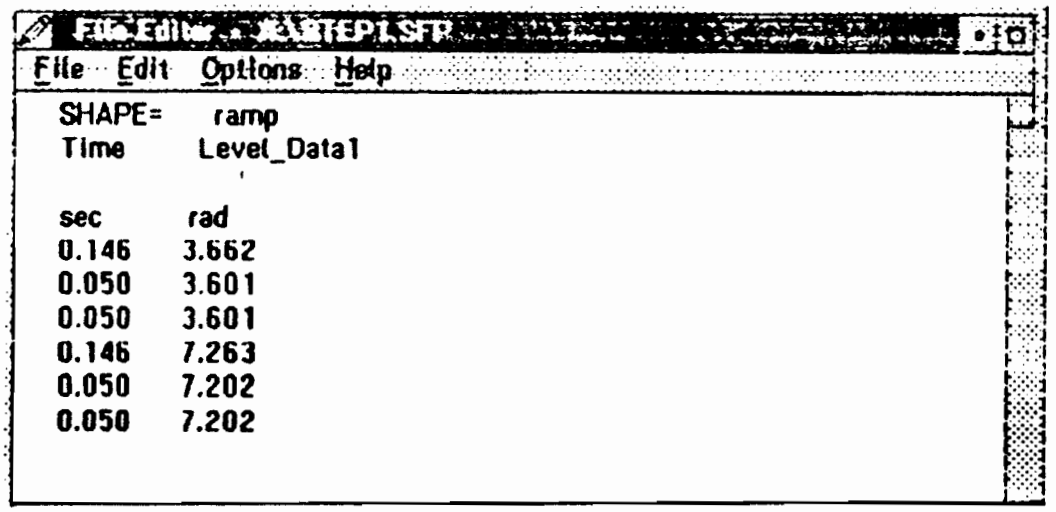

Fig. 3.6 A typical parameter file for the file playback program.

the temperature controller, which reduced the current to the furnace via the power supply. It was detected that, while cooling from a high temperature down to 800 °C, cooling rates of up to 2 °C/s could be accurately controlled by adjusting the power supply automatically. Higher cooling rates were obtained by blowing compressed air into the furnace or by shutting down the power.

As this is a fixed-end torsion machine, the set distance between the two loading bars does not change during reheating and deformation. A gap was therefore left between the test specimen and the left-hand loading bar in order to avoid bending the specimen due to extension during reheating. Oxidation of the specimens at high temperatures was prevented by passing a constant flow of high purity argon through the furnace.

3.3.2 Compression Testing System

As described in the previous section, the torsion test is a very useful method when large deformations (strains > 1) are involved. As with other mechanical testing machines, however, there are some disadvantages to this approach. One is associated with the strain gradient along the radius. This eventually leads to a non-uniform microstructure within the cross section of the specimen, and makes it difficult to analyze the microstructure. In this case, the subsurface tangential microstructure is examined, which can be assumed to represent the test specimen. By contrast, the compression test produces more

homogeneous deformation through the whole volume of the test sample, so that more uniform microstructures are obtained. In the present study, compression tests were used to investigate the transformation kinetics and the influence of the process parameters on the microstructural evolution. The compression testing system is described below.

3.3.2.1 Compression Machine

The equipment used in the compression tests was a model 810 MTS machine. Basically, it is composed of a load frame, a hydraulic power supply, and closed loop servohydraulic and computerized outer loop systems. The control system is a PDP-11 computer running under the RT-11 operating system and interfaced with the servohydraulics through a 468 unit. All the test programs were written in MTS BASIC. The test programs used in the present investigation are listed in Appendix I. The main structure of the programs is similar to that used by other investigators in this research group, but some improvements were made by the present author. One is direct temperature measurement. This was done by converting the test time to temperature through the cooling rate. The approach is only applicable to low cooling rates (cooling rate < 0.5 °C/s), and errors are introduced if higher cooling rates are employed. The present author adapted the third channel in the PDP-11 for temperature measurement. That is, temperature measurements made using the K-type thermocouple contacting the sample were converted into electronic signals and collected in the additional channel. Then the temperature measurement was written directly into the data file. The data file was moved into a Microsoft Excel data file using a commercial package called CrossTalk in PC after each test.

A closer look at the test apparatus is shown in Fig. 3.7. The components contained in the high temperature zone are the upper and lower anvils. They are made of TZM, which is a molybdenum-base alloy containing a dispersion of 0.5% Ti and 0.08% Zr oxides; the latter improve the high temperature strength. A specimen is held on the lower anvil, which is connected to the MTS actuator by means of a stainless steel bar. During testing, the actuator controlled by the servovalve generates the force and the linear displacement; the latter are measured by the load cell and the LVDT (linear variable differential transformer), respectively.

Specimens were reheated by means of a model E4-10 radiant furnace mounted on the columns of the MTS load frame and linked to a Micristar digital controller/programmer. To generate a uniform temperature distribution, it is important to

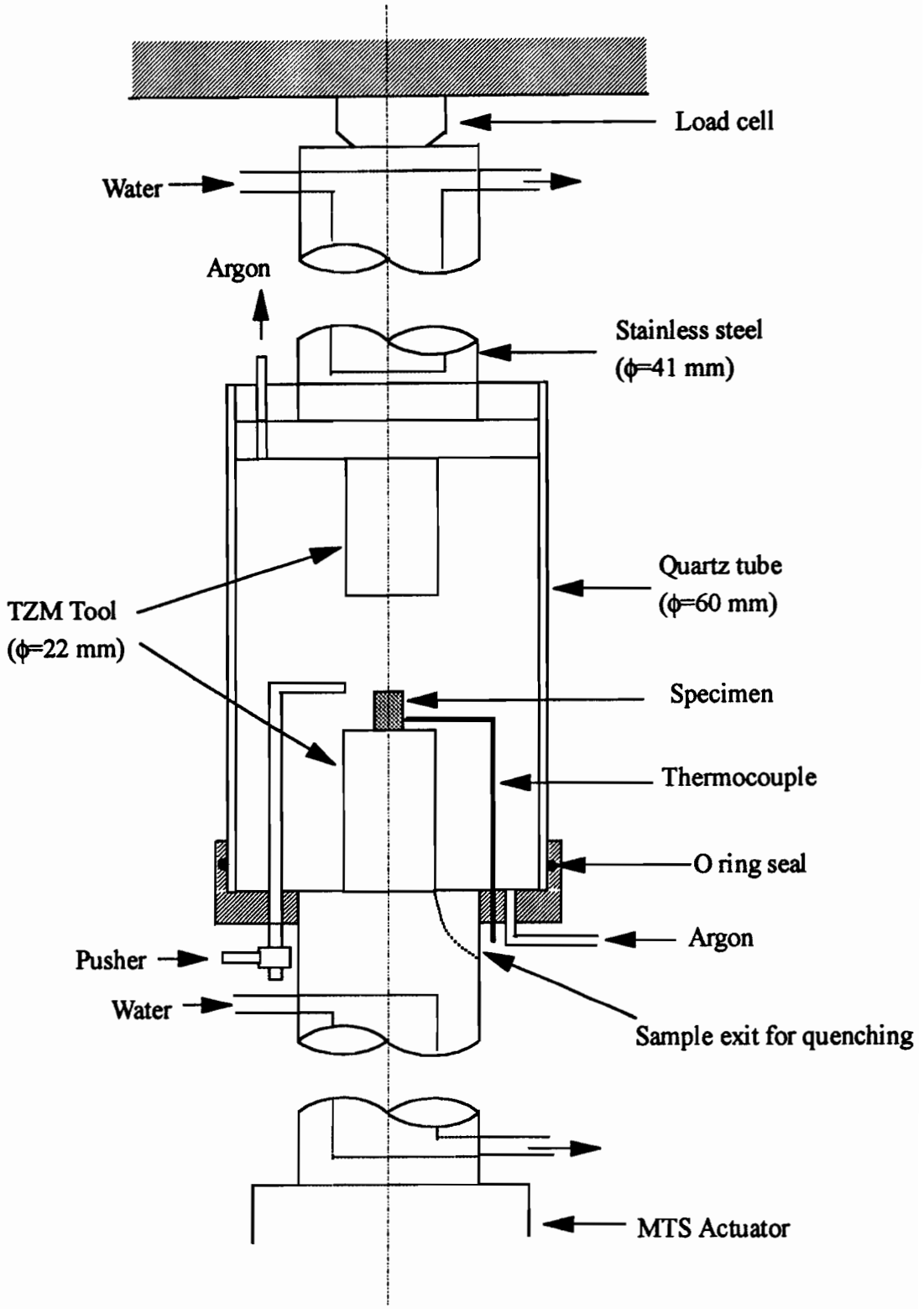

Fig. 3.7 Schematic diagram of the compression testing equipment

align the test specimen with the central axis of the furnace. To minimize oxidation, the specimen and anvils were enclosed in a quartz tube sealed with O-rings in which a high purity argon atmosphere was maintained.

Quenching the samples for metallography was performed by a pusher which can be rotated and moved up and down. When temperature or time reached the set point, the specimen was pushed off the lower anvil, and dropped through a hole in the lower support (between the inside wall of the quartz tube and the lower tool) into a quench cup containing cold water. This sample exit was kept closed during testing and was only opened a few seconds before initiating a quench. Using this system, it was possible to quench deformed specimens in about 1 second.

3.3.2.2 Constant strain rate testing

All the compression tests were carried out under constant strain rate conditions. This is because materials are rate sensitive at high temperatures, and testing at constant crosshead speed makes it difficult to determine if metallurgical changes (e.g. dynamic recrystallization, precipitation, transformation, etc.) are taking place. The compression mode, instead of the tension mode, was used because it avoids the heterogeneous flow due to necking.

In a compression test, an increment of true strain in a specimen deformed from an initial height h is given by:

$$d\varepsilon = \frac{dh}{h} \qquad (3.2)$$

By differentiating with respect to time t, the true strain rate in compression is obtained:

$$\dot{\varepsilon} = (-\frac{1}{h})\frac{dh}{dt} \qquad (3.3)$$

where *dh/dt* is the rate of change of specimen height.

To run a constant true strain rate test, the sample must be deformed at a rate which is proportional to its instantaneous height, h:

$$\frac{dh}{dt} = -\dot{\varepsilon}h \qquad (3.4)$$

By integrating the above equation and setting $h=h_0$ at t=0, the following relation is obtained:

$$h = h_0 \exp(-\dot{\varepsilon} t) \qquad (3.5)$$

With a computer controlled system, true strain rate tests are produced by dividing the entire deformation time into n steps (n=50 in the present test) with intervals of Δt, so that the instantaneous height of the deforming specimen (or the position of the MTS actuator) at time i can be expressed as:

$$h_i = h_0 \exp(-\dot{\varepsilon} i \Delta t) \qquad (3.6)$$

This equation was employed in the program listed in Appendix I to deform the specimen at a constant true strain rate.

During testing, sufficient load and displacement data points were sampled; these were then converted into true stress and true strain by the following equations:

$$\sigma_i = \frac{load}{A_i} \qquad (3.7)$$

$$\varepsilon_i = -\ln(\frac{h_i}{h_0}) \qquad (3.8)$$

where A_i is the instantaneous sample cross section, which was calculated as $A_i=A_0h_0/h_i$. Here A_0 and h_0 are the initial cross sectional area and height of the specimen, respectively, and h_i is the instantaneous height of the specimen.

3.4 Experimental Methods

Two major experimental methods, the continuous cooling torsion test and the continuous cooling compression test, were used in the present investigation. The torsion tests were mainly employed to study the austenite recrystallization behavior as well as to determine the no-recrystallization temperature (known as T_{nr}) and strain accumulation during multipass deformation. The compression tests were employed to study the

austenite-to-ferrite or bainite transformation and the influence of processing parameters on the evolution of the microstructure. These methods are described in the sections that follow.

3.4.1 The Continuous Cooling Torsion Test

3.4.1.1 Calculation of Equivalent Stress and Strain

For the torsion tests, the torque and twist data from the experiments were used to calculate the equivalent stresses and equivalent strains. The equivalent stress at the surface of the specimen is evaluated from the torque T via the relation proposed by Fields and Backofen[195],

$$\sigma_{eq} = \frac{\sqrt{3}T(3+m+n)}{2\pi r^3} \qquad (3.9)$$

and the equivalent strain at the surface is proportional to the measured angle of twist Θ, as given by:

$$\varepsilon_{eq} = \frac{r\Theta}{\sqrt{3}L} \qquad (3.10)$$

Here, r and L are the specimen radius and gage length, respectively, m is the rate sensitivity and n is the work hardening coefficient derived from the torque.

$$m = \partial \ln T / \partial \ln \dot{\Theta} \qquad (3.11)$$

$$n = \partial \ln T / \partial \ln \Theta \qquad (3.12)$$

Although both m and n vary with strain, for the sake of simplicity, constant values of m=0.17, and n=0.13 were employed. The variations in m and n are much smaller than the mean value of the multiplier (3+m+n)=3.3, and the approximations, therefore, do not introduce large errors.

3.4.1.2 Mean Flow Stress vs. Inverse Absolute Temperature Method

Recently, a mean flow stress vs. inverse absolute temperature method for determining the T_{nr} was developed by Boratto and co-workers[189]. They employed this technique to investigate the influence of chemical composition on the T_{nr}. The concept of an "average" simplified rolling schedule was adopted in this method, which is judged to be

characteristic of the mill configuration and product. The method leads to results that are applicable to a broad range of schedule variants[36]. A schematic illustration of this method is given in Fig. 3.8.

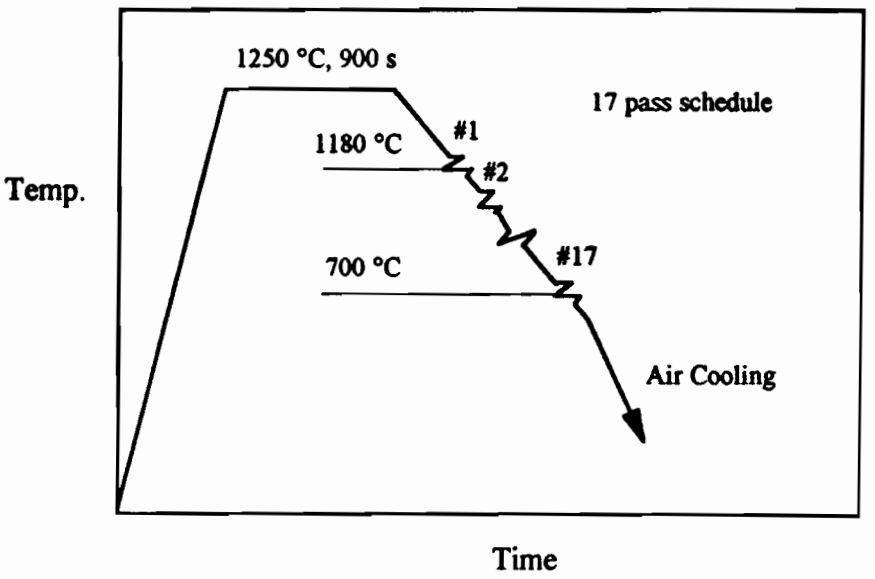

Fig. 3.8 Schedule A employed in the present hot torsion tests.

First of all, a specimen was reheated to a selected solution temperature and soaked at this temperature for 15 minutes: then it was cooled at a constant cooling rate (i.e. 1 °C/s). During cooling, 17 passes with certain interpass delays between the passes were executed at a constant strain rate. For a particular test, the strain per pass, strain rate and interpass time were identical. The stress-strain curves generated from such a test are shown in Fig. 3.9. The mean flow stress of each pass can be calculated using numerical integration, as given by

$$\bar{\sigma}_{eq} = \frac{1}{\varepsilon_b - \varepsilon_a} \sum_a^b \frac{\sigma_{i+1} + \sigma_i}{2} \times (\varepsilon_{i+1} - \varepsilon_i) \qquad (3.13)$$

$$\bar{\sigma}_{eq} = \frac{1}{\varepsilon_b - \varepsilon_a} \int_{\varepsilon_a}^{\varepsilon_b} \sigma_{eq} d\varepsilon_{eq} \qquad (3.14)$$

Here $\overline{\sigma}_{eq}$ is the mean flow stress, σ_{eq} is the equivalent flow stress and $(\varepsilon_b - \varepsilon_a)$ is the equivalent strain of the pass of interest. Then the mean flow stresses are plotted against the inverse absolute temperature, leading to the kind of plot demonstrated in Fig. 3.10.

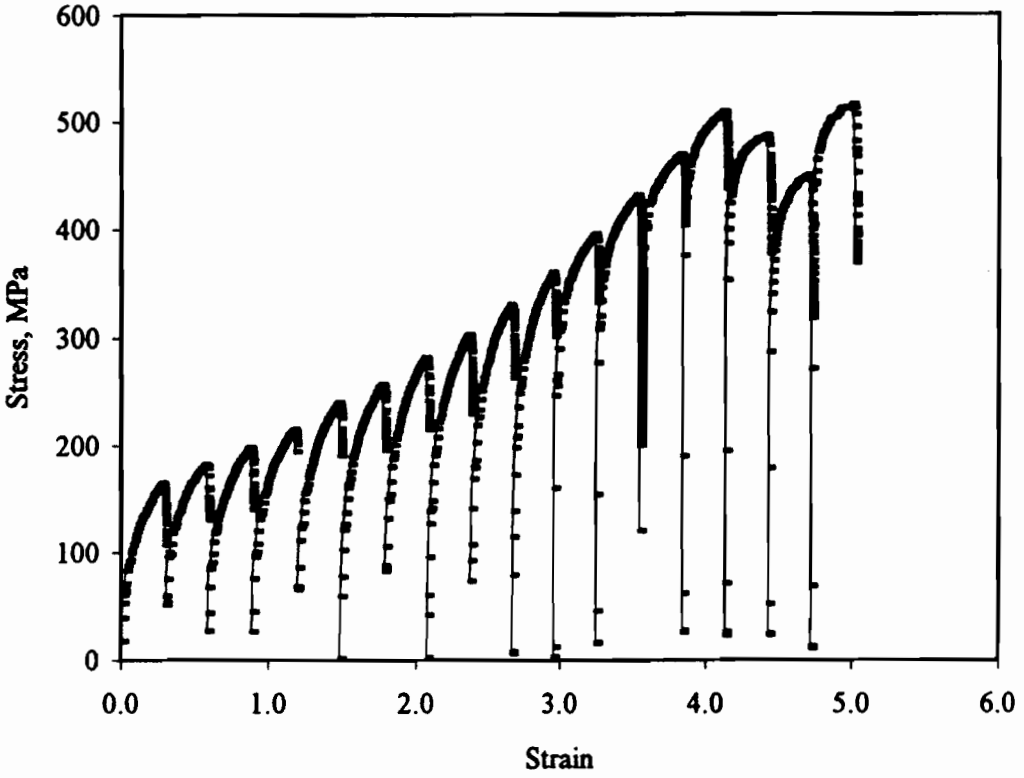

Fig. 3.9 Stress-strain curves for sample deformed using schedule A.

Based on the slope changes that can be seen, processing can be divided approximately into four ranges. In range I (the high temperature range), recrystallization takes place fairly rapidly, so that there is no strain accumulation and no accumulated work hardening; in this case, the mean flow stress depends only on the temperature. The mean flow stress increases slowly with decreasing temperature. In range II (the intermediate temperature range), only partial recrystallization occurs or no recrystallization at all, so the strain is accumulated from pass to pass and continued work hardening is displayed. In this case, the mean flow stress increases more rapidly with decreasing temperature. The cessation of full recrystallization is responsible for the slope change at the intersection of ranges I and II. According to Boratto et al., the temperature that corresponds to this point can be defined as the no-recrystallization temperature (T_{nr}) for plate rolling.

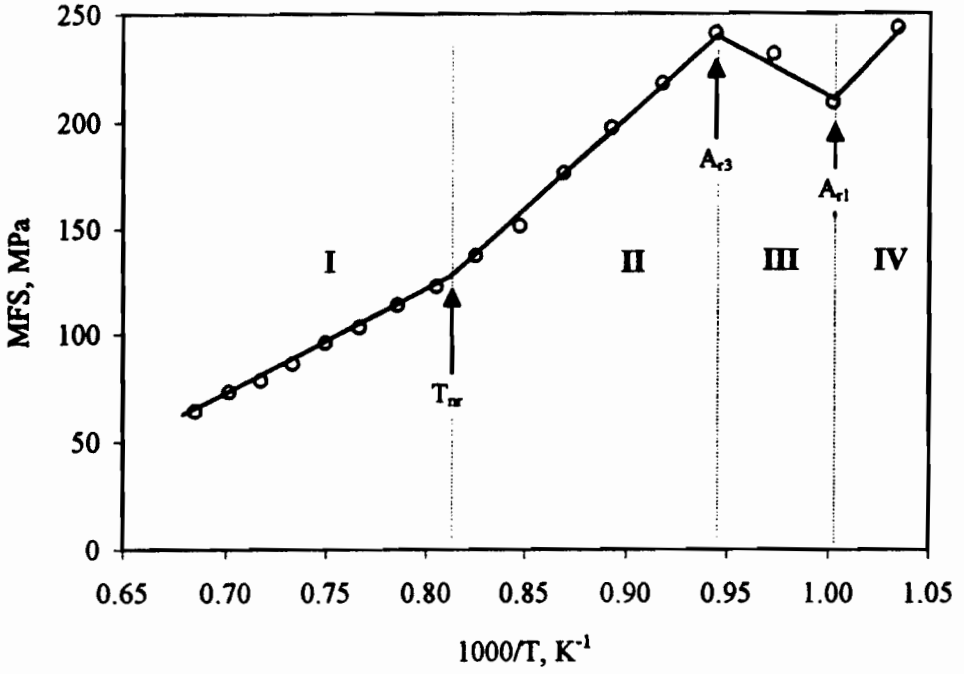

Fig. 3.10 Dependence of the mean flow stress (MFS) on inverse pass temperature.

To verify this definition of the T_{nr}, two samples were tested down to temperatures either above or below the measured T_{nr}, and water quenched. The microstructures observed in this way are presented in Fig. 3.11. It can be seen that the structure above the T_{nr} is recrystallized, while in the case of the sample quenched below the T_{nr}, the structure is pancaked.

When processing is carried out to lower temperatures, the austenite-to-ferrite transformation takes place; this leads to a drop in the mean flow stress because ferrite is softer than austenite. With further continuous increases in the ferrite fraction, the mean flow stress decreases continuously until the transformation is finished; then the mean flow stress increases again. The temperatures that correspond to these two points of further intersection can be defined as the start (A_{r3}) and finish (A_{r1}) temperatures of the austenite-to-ferrite transformation.

(a)

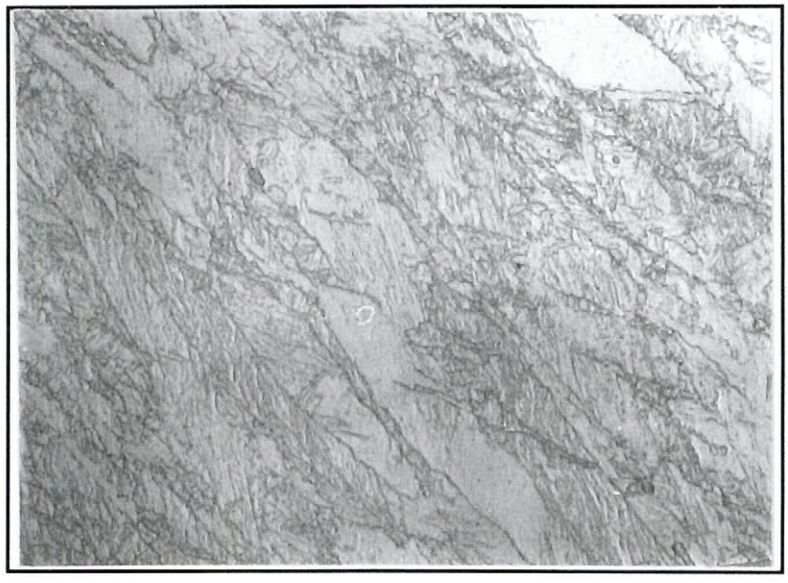

(b)

Fig. 3.11 Microstructures above (a) and below (b) the T_{nr}. x400

3.4.1.3 Mean Flow Stress for Evaluating Fractional Softening

The mean flow stress method described above is applicable to long interpass times. In the case of very short interpass times ($t \leq 1$ second), it is difficult to decrease the temperature appropriately between passes, so that a modified schedule was employed to determine the fractional softening (see Fig. 3.12). Deformation was initiated at 1230 °C (1250 °C for an interpass time of 0.05 second), and a two pass deformation with a short interpass time was performed while the temperature decreased by 15 °C between pairs of deformations.

The mean flow stress method, instead of the offset or back extrapolation method, was used in the present investigation to calculate the fractional softening between passes. The mean flow stresses shown in Fig. 3.13 were calculated using equation (3.14), so that the softening between passes is given by

$$X\% = \frac{\bar{\sigma}_m - \bar{\sigma}}{\bar{\sigma}_m - \bar{\sigma}_0} \times 100\% \qquad (3.15)$$

where $\bar{\sigma}_0$ and $\bar{\sigma}$ are the mean flow stresses in the first and second deformations, respectively; these are measured at equal strains (i.e. ε=0.15). $\bar{\sigma}_m$ is the expected mean flow stress in the second deformation, calculated using the continuous curve which is extrapolated from the data of the first deformation.

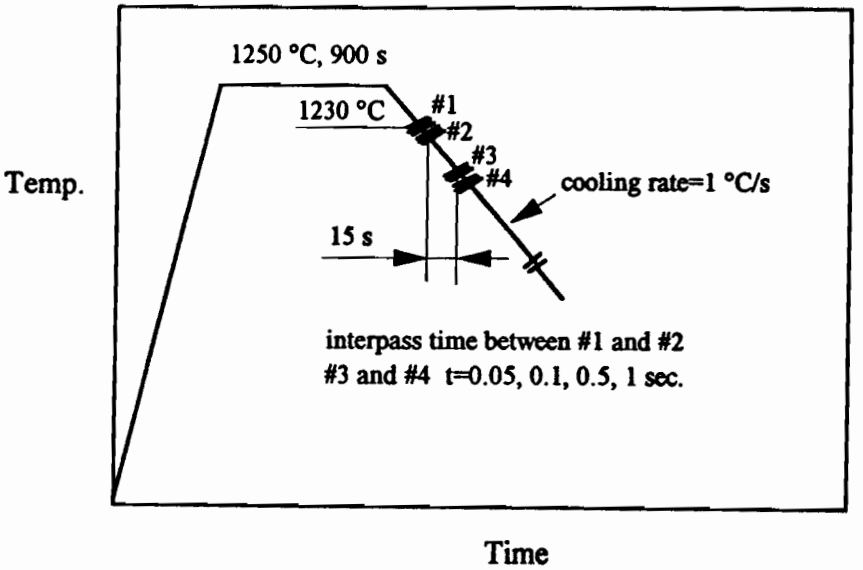

Fig. 3.12 Schedule B employed in the present hot torsion tests.

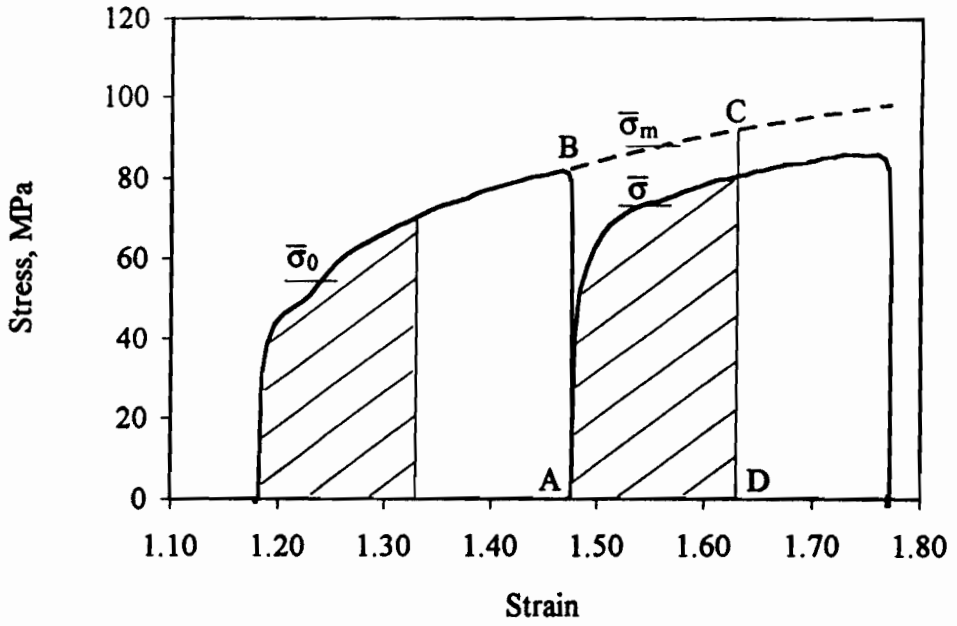

Fig. 3.13 Determination of the mean flow stresses used in the evaluation of interpass softening by the mean flow stress method.

3.4.2 The Continuous Cooling Compression Test

In the past, the dilatometer test was widely used to construct phase transformation diagrams, known as IT (isothermal transformation) and CCT (continuous cooling transformation) diagrams. With respect to thermomechanical processing, this kind of test cannot simulate situations involving large deformations, and thereby the microstructure of interest. This is why alternative methods, such as hot tensile testing[196-198], hot compression testing[199-201] and hot torsion testing[36, 189], have been developed to investigate the transformation behavior in plain carbon and microalloyed steels. The concepts adopted by these three different methods are similar, in that all are based on the analysis of flow curves. The continuous cooling hot torsion test was already presented in the previous section. Here, the continuous cooling compression test developed by Zarei Hanzaki et al.[201] in the CSIRA laboratory is presented in the section that follows.

3.4.2.1 The Basic Concept of the CCC Test

The basic concept adopted in CCC (continuous cooling compression) testing is that different phases react to deformation in different ways. For example, when deformation is being carried out on single phase austenite, the steady state flow stress can be described by the following equation[202]:

$$\dot{\varepsilon} = A[\sinh(\alpha\sigma_s)]^{n'} \exp(\frac{-Q}{RT}) \qquad (3.16)$$

which, on rearrangement, gives

$$\sigma_s = \frac{\sinh^{-1}(X)}{\alpha} \qquad (3.17)$$

$$\text{where, } X = \left[\frac{\dot{\varepsilon}\exp(Q/RT)}{A}\right]^{1/n'}$$

Here $\dot{\varepsilon}$ and σ_s are the strain rate and steady state flow stress, respectively, R is the gas constant, Q is an experimental activation energy considered to be related to the magnitude of the energy barrier opposing the deformation mechanism, and A, α and n' are constants assumed to be independent of the temperature but dependent on the material composition.

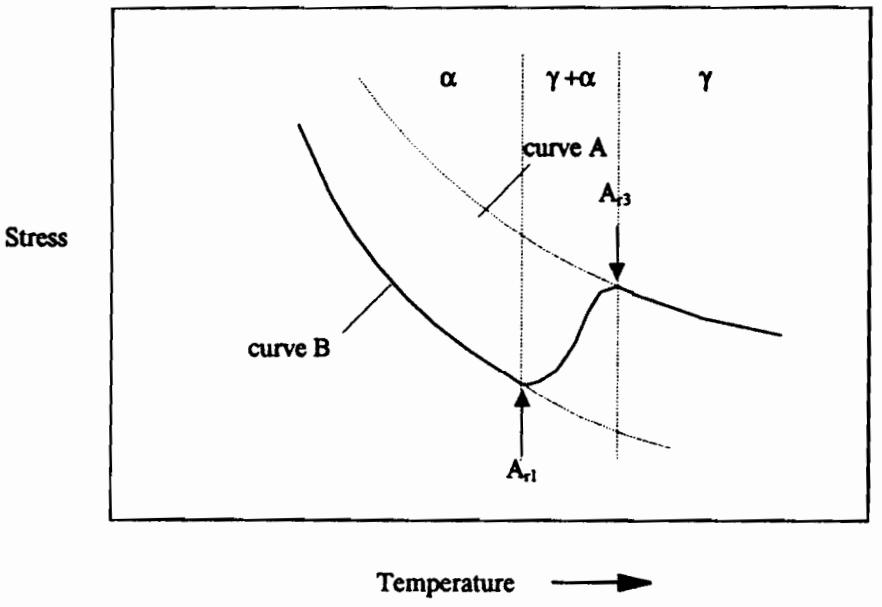

Fig. 3.14 Temperature dependence of the CCC flow stress on cooling.

The stress induced in a deforming specimen increases smoothly with decreasing temperature, as shown on curve A in Fig. 3.14. Any deviation or deflection in the flow stress-temperature curve may be related to a microstructural change. Curve B in Fig. 3.14 is the flow curve pertaining to a specimen being deformed in the single phase ferrite range.

There is a transition range between curves A and B, which represents the flow curve of a material being deformed in the ferrite + austenite range. The temperature corresponding to the first cooling transition point is defined as A_{r3}, the austenite-to-ferrite transformation start temperature. This is verifiable by metallography. Other transformation start temperatures, such as B_s, the austenite-to-bainite transformation start temperature, can also be detected by this method since the two phases have different deformation resistances.

3.4.2.2 Determination of A_{r3} and B_s

A typical temperature and deformation schedule for a CCC test is illustrated in Fig. 3.15. Here, the specimen was reheated to the selected solution temperature of 1200 °C at a heating rate of 1.5 °/s, and soaked at this temperature for 30 minutes. Then, the specimen was cooled to room temperature at a cooling rate of 1 °C/s. When the temperature reached 850 °C, continuous deformation at a constant strain rate of 0.001/s was applied to the specimen during cooling. The true strain and true stress were calculated from the data generated during deformation. Two typical true stress-temperature curves are presented in Fig. 3.16. Curve (a) demonstrates the behavior of an IF steel, and curve (b) was determined on the Mo-Nb-B steel studied in the present investigation.

The transformation temperatures are identified by the arrows on the true stress-temperature curves. It is evident that the transformation kinetics are very different in the two steels. The A_{r3} temperature determined for the IF steel is consistent with that determined by the MFS-1000/T method. The transformation temperature for the Mo-Nb-B steel is quite low compared with that of the IF steel, and the true stress-temperature curve adopts a much higher slope after the second deviation. This suggests that, after the initial transformation, the rest of the austenite transforms to a phase that is harder than polygonal ferrite. This kind of microstructure will be shown below to correspond to low carbon bainite, so that the temperature corresponding to the second deviation can be defined as B_s. More detailed results of this type and further discussion will be presented in Chapter 6. Here, several specimens were tested and water quenched at temperatures in the neighborhood of these deviations so as to identify the causes of the deviations. The microstructures obtained in this way are presented in Fig. 3.17.

It can be seen that at a temperature above the first deviation, the microstructure contains low carbon martensite, while below the deviation, a transformed phase, which

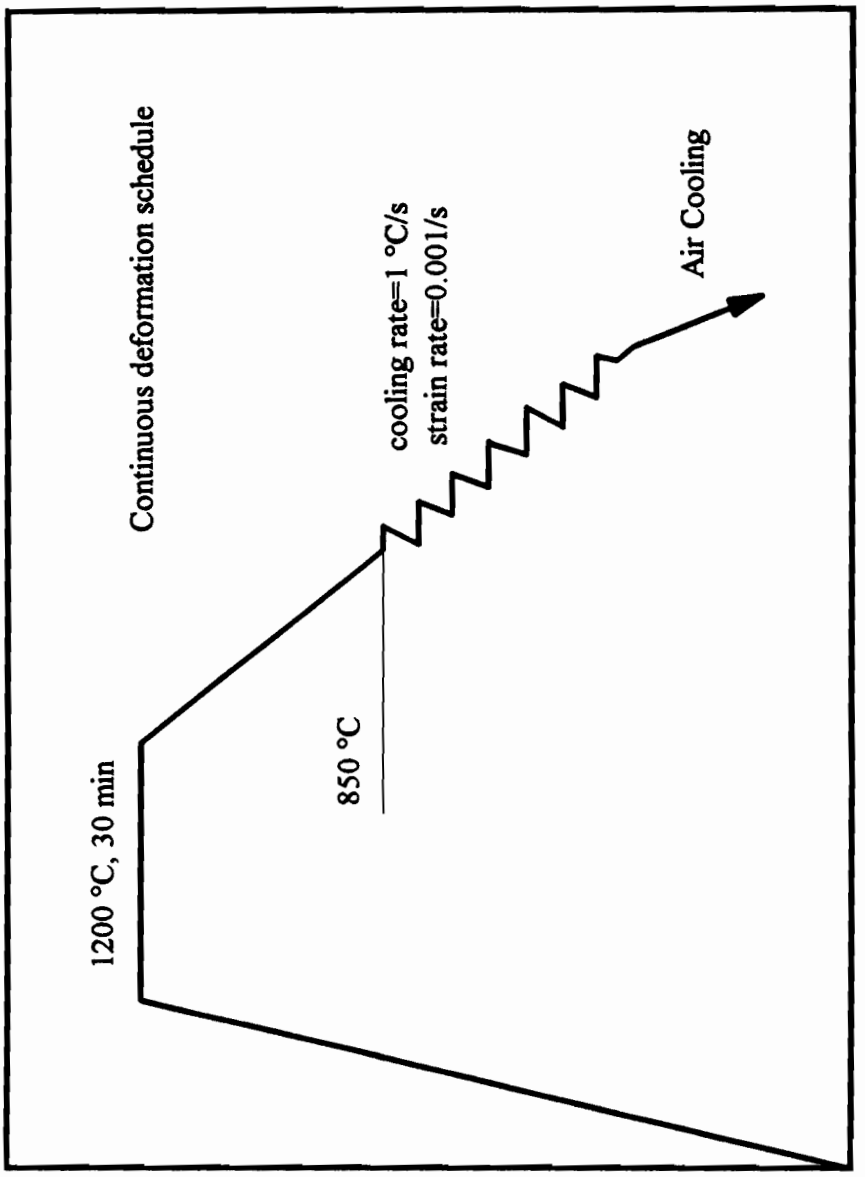

Fig. 3.15 Schedule C used for the continuous cooling compression tests

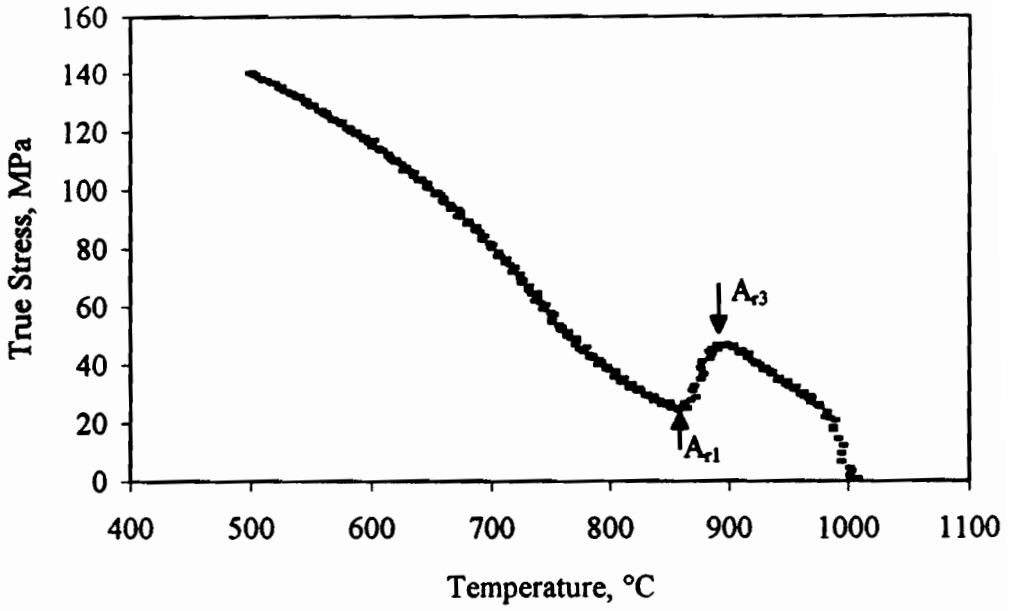

(a)

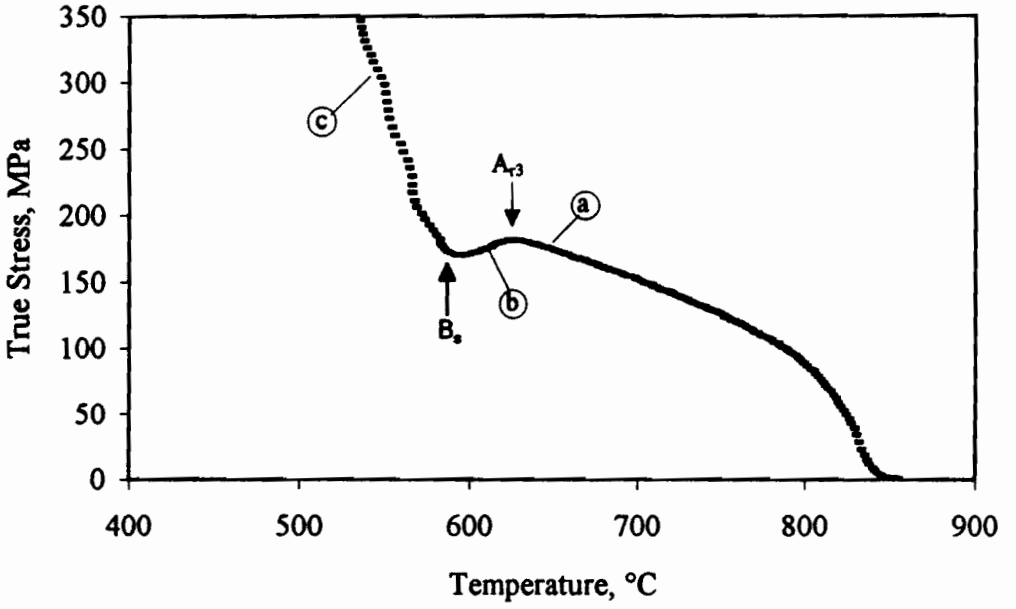

(b)

Fig. 3.16 True stress-temperature curves for the (a) IF and (b) Mo-Nb-B steels.

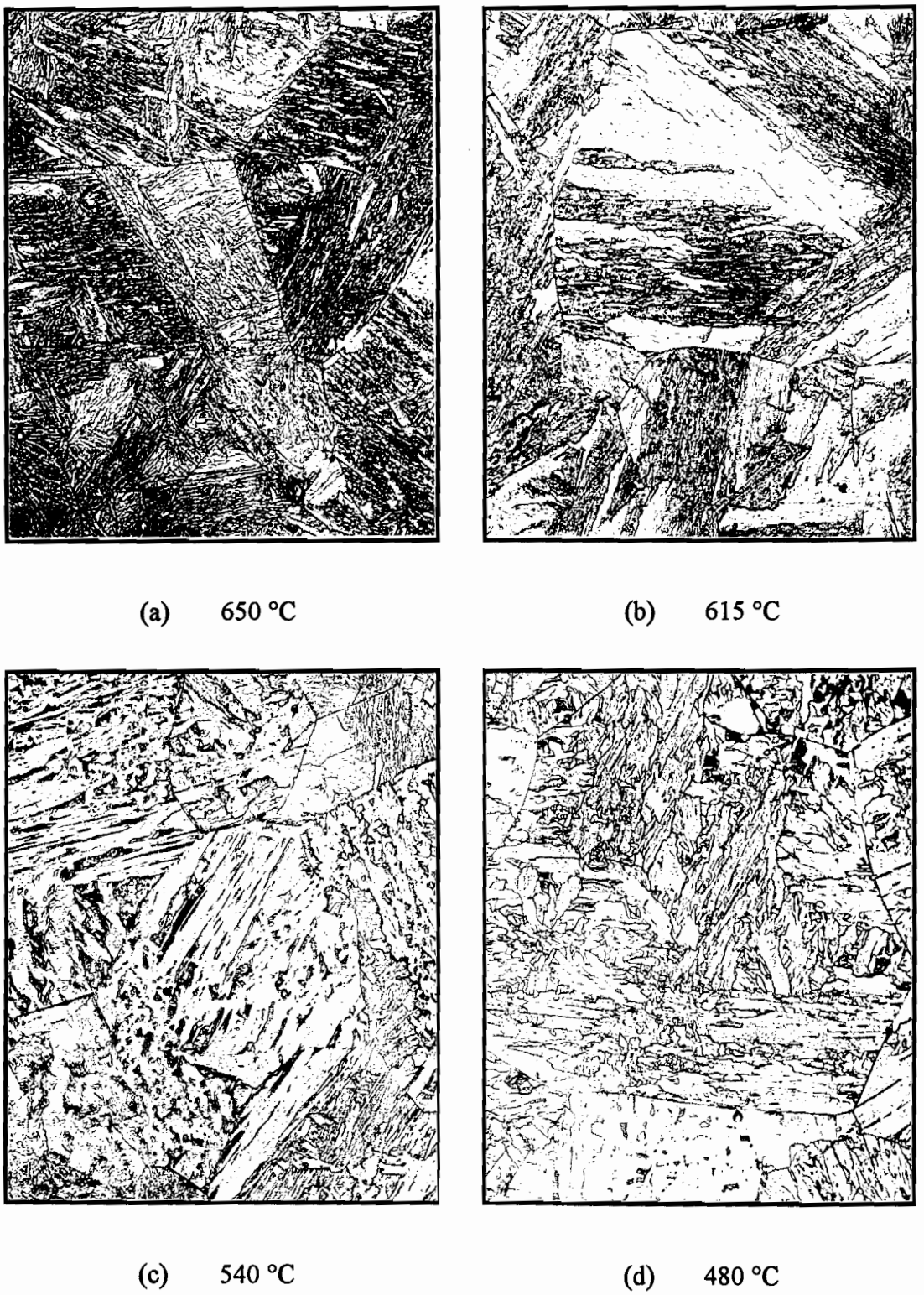

(a) 650 °C (b) 615 °C

(c) 540 °C (d) 480 °C

Fig. 3.17 Microstructural evolution during continuous cooling of the Mo-Nb-B steel. x 500

corresponds to massive ferrite, is observed. The microstructure after the second deviation contains acicular ferrite with some discrete islands or blocky regions which have been identified as retained austenite and/or martensite. This type of microstructure is categorized as class 3 bainite (or B_3). The temperature corresponding to the second deviation in the Mo-Nb-B steel can, therefore, be defined as the B_S.

3.4.2.3 Length Change of the Compression Tooling

During cooling, the lengths of the compression anvils decrease due to thermal contraction. If the contraction rate of the tools is higher than the strain rate employed, no deformation will be applied to the specimen. The strain rate selected for CCC test should therefore be higher than the contraction rate of the compression tools. To determine the contraction behavior of the compression anvils during CCC testing, and hence its effect on the true stress-temperature curve, dummy tests were performed using the same thermal history as the CCC test. A constant load was maintained on an alumina specimen subjected to continuous cooling over the range of test temperatures used in this work. In this way, the displacement of the actuator was taken to be indicative of the contraction of the compression anvils. The contractions detected at different cooling rates are presented in Fig. 3.18. It can be seen that the anvil contraction was linear with temperature decrease over the range used in the present study.

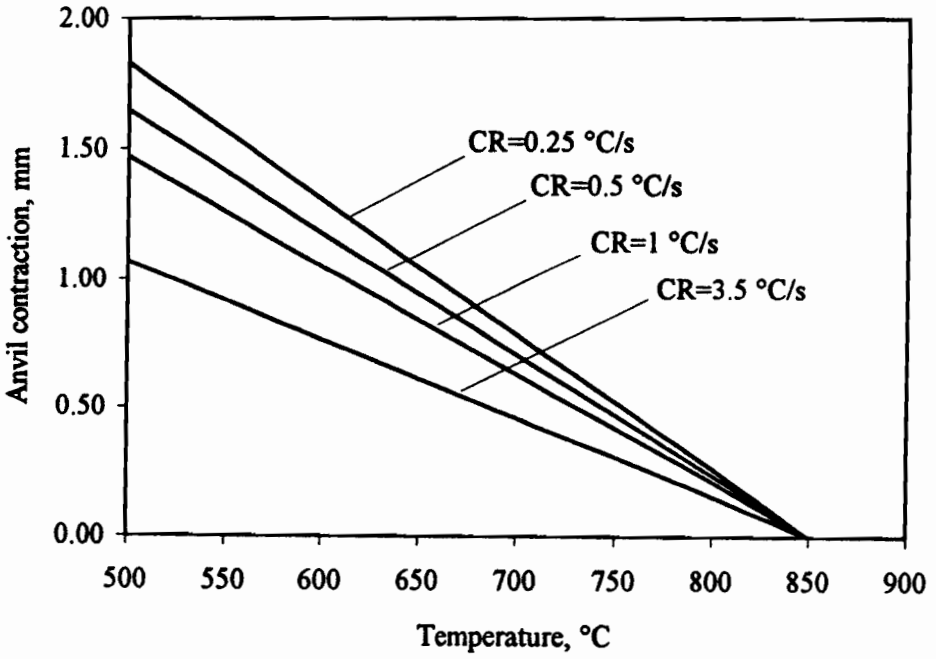

Fig. 3.18 Anvil contraction versus temperature for different cooling rates.

3.4.2.4 Accelerated Cooling

To study the influence of cooling rate on the final microstructures, specimens were first deformed to a given strain , and then different cooling rates ranging from 0.1 °C/s to 50 °C/s were applied. These cooling rates were obtained by cooling the samples in the furnace, in still air, or by means of compressed air or compressed helium. The cooling curves produced by these methods are illustrated in Fig. 3.19.

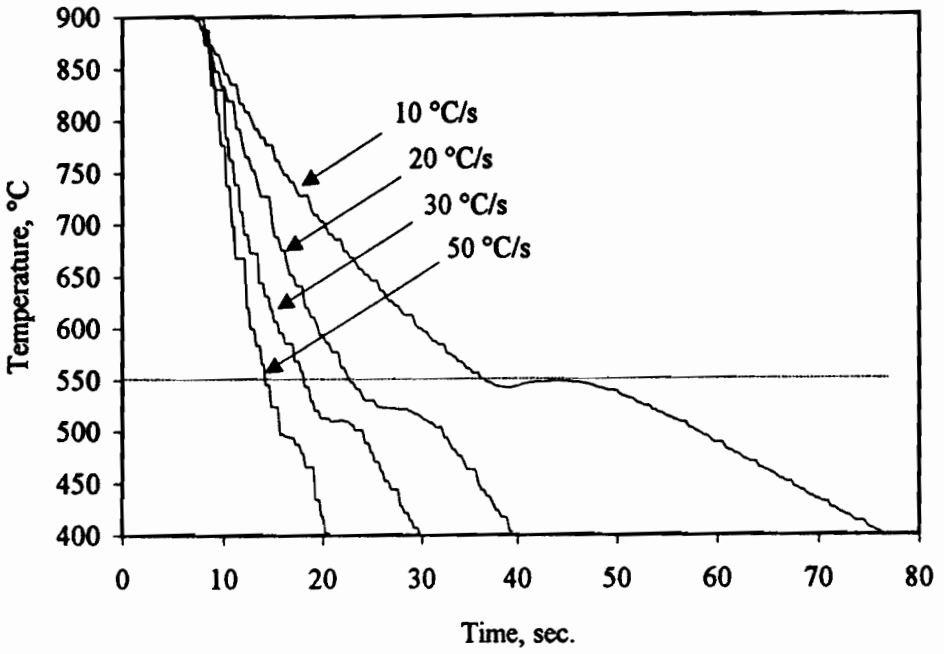

Fig. 3.19 Cooling curves for different cooling rates.

3.4.3 The Isothermal Compression Test

In order to study the isothermal transformation kinetics of low carbon niobium and boron treated steels, the constant strain rate test program was modified. The reheating and soaking processes used for this type of test are similar to those employed for the continuous cooling compression test. The difference is that when the testing temperature was reached, a prestrain of ε=0.1 was applied at a higher strain rate (0.1 s^{-1}), after which the strain rate was reduced to 0.0005 s^{-1}, without unloading the sample.

Two typical stress-strain curves that resulted from the application of this type of test to the Mo-Nb-B and Nb-15B steels are illustrated in Fig. 3.20. The first deformation induces a certain level of stress and strain, then the second flow curve reflects the transformation behavior. On curve A, the true stress drops almost immediately after the low strain rate deformation is commenced; the true stress then remains nearly constant on

further deformation. This curve is indicative of a rapid γ-to-α transformation process at the experimental temperature in this steel. Flow curve B, however, displays a different type of behavior in the second material. The true stress first increases with true strain; then, after about 30 seconds, the true stress decreases with further deformation. When the deformation time reaches about 100 seconds, the true stress increases again. This curve reflects the occurrence of a more complicated transformation phenomenon, one that will be described later (in Chapter 6).

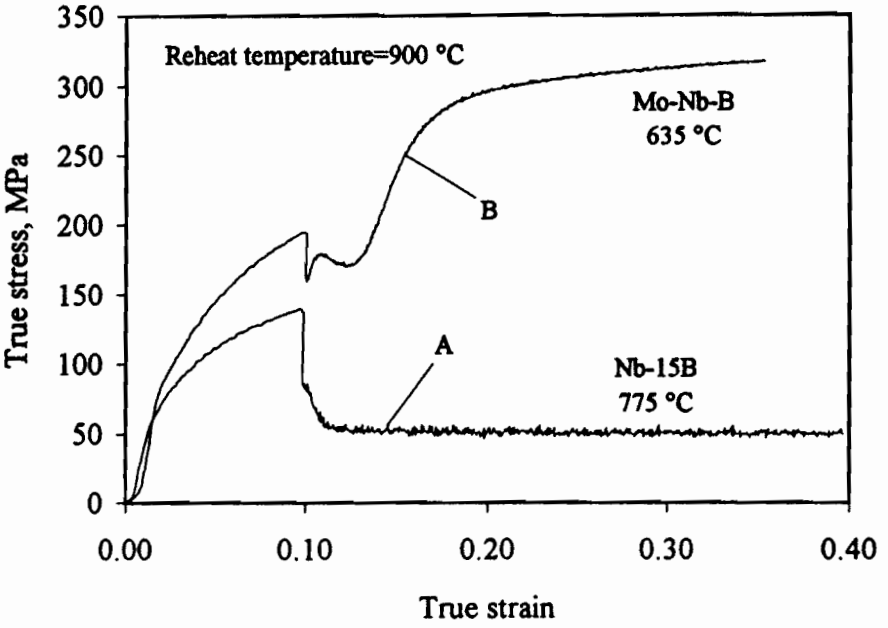

Fig. 3.20 Flow curves generated from the samples tested using the strain rate change technique.

3.4.4 Metallographic Examination

For the torsion specimens, the stresses and strains were always calculated using the maximum radius, and the microstructures were always examined at the specimen subsurface. This is because of the presence of a strain gradient in the solid bar torsion samples. For the compression specimens, the microstructures were examined along the sample axis as seen in a longitudinal cross section.

In order to reveal the prior austenite microstructure, a series of tests was interrupted at selected temperatures, and the specimens were quenched in water. The latter were sectioned and ground using silicon carbide papers and polished with 6 μm diamond paste and 0.05 μm alumina, in sequence. The polished specimens were etched

using a solution based on a saturated aqueous picric acid solution, with small additions of HCl. The composition of the etchant and the etching conditions were varied for specimens deformed under different conditions until the prior-austenite grain structure was revealed. For examination of the microstructures associated with transformed products, 2% nital was generally used. In some cases, the polished sample was first etched with 2% nital for 10-15 seconds in order to reveal the ferrite grain boundaries and then further etched with Marshall's reagent in order to enhance the contrast between the ferrite and the martensite.

3.4.5 Electron Microscopy

3.4.5.1 Carbon Replica

In order to demonstrate the effect of interpass time on precipitation during continuous cooling, a set of specimens was tested using the schedule shown in Fig. 3.8 with interpass times of 5, 30, 80, and 200 seconds. The specimens were water quenched at the selected temperature, and sectioned and polished as described above. Then the polished specimens were lightly etched with 2% nital for about 5~10 s. Carbon was deposited on the etched surfaces using a vacuum evaporator in a vacuum better than $5x10^{-4}$ torr.

Squares approximately 2 mm × 2 mm were scribed on the coated surfaces and removed by electropolishing using a solution of 10% nital. During etching, the current was slowly increased until small bubbles began to form. The removed carbon replicas were washed gently in ethanol and then in a 50-50 mixture of ethanol and distilled water. They were finally mounted on TEM copper grids (3 mm, 200 mesh) and dried. The carbon replicas were examined in a JEM-100 CXII scanning transmission electron microscope fitted with a PGT system IV energy dispersive X-ray spectrometer (EDS) for the chemical analysis of individual particles.

3.4.5.2 Thin Foils

Specimens were quenched at the temperatures of interest, and samples for optical microscopy were prepared using the procedure described in section 3.4.4. Thin slices were then cut from the surfaces of these samples. They were ground down to a thickness of 70 μm using 600 grit silicon carbide paper. A Struers Tenupol 2 was then used for jet thinning with a solution containing 6% perchloric acid in methanol. The voltage was set at 30 V and the flow rate at 3. Liquid nitrogen was used to cool the solution down to -20 °C.

CHAPTER 4

STATIC RECRYSTALLIZATION

The critical temperature below which the "pancaking" of austenite grains can take place is important in the controlled rolling of microalloyed steels. For this reason, the static recrystallization kinetics of steels containing Mo, Nb, Ti, V and B have been measured by a number of means[63, 71, 75, 145, 191, 192, 203-207]. A model has also been developed[180] in which the kinetics of strain-induced precipitation are compared to those of recrystallization. This led to the definition of two critical temperatures known as the recrystallization limit temperature (RLT) and the recrystallization stop temperature (RST). However, the model does not link the RLT or RST directly to continuous cooling conditions. An early attempt was made by Cuddy in 1982[84, 208, 209] to relate chemical composition to the RST (in terms of definition, their RST is equivalent to Dutta and Sellars' RLT), using a five pass deformation schedule under continuous cooling conditions. Later, in 1988, Boratto et al.[189] investigated the effect of chemical composition on a third measure of the pancaking temperature -- the so-called no-recrystallization temperature (T_{nr}).

One main objective of the present work was to investigate the influence of the deformation parameters on the T_{nr} in low carbon Nb and Nb-B bearing steels under continuous cooling conditions. A second aim was to determine the quantitative relationship between the T_{nr} and the deformation parameters.

To accomplish these objectives, several series of hot torsion tests were performed. During testing, all the experimental data were recorded and stored on the hard drive of the

PC computer that was linked to the MTS machine. At the end of each test, the stress-strain curve for each pass was plotted and the mean flow stress was computed. The mean flow stresses were then plotted against the inverse absolute temperature, leading to a series of diagrams similar to Fig. 3.10. Furthermore, the T_{nr}'s were determined by means of the method described in Chapter 3.

4.1 Test Parameters

Specimens were reheated to the selected austenitization temperatures at a reheating rate of about 1.5 °C/s, and soaked at these temperatures for 15 minutes. They were then cooled to 700 °C at cooling rates (CR) specified by the relation

$$CR = 30 / t \qquad (°C/s) \qquad (4.1)$$

where t is the interpass time in seconds. During cooling, 17 passes of identical strains were applied at identical strain rates and followed by identical interpass times. In order to investigate the effect of pass strain on the no-recrystallization temperature, this parameter was increased in steps of 0.1 from 0.1/pass to 0.5/pass. In a similar manner, strain rates of 0.2 s^{-1} to 10 s^{-1} were employed, together with interpass times of 2 seconds to 150 seconds. A schematic representation of the schedule was illustrated in Fig. 3.8. For the interpass times $t \leq 1$ second, a modified schedule (shown in Fig. 3.12) was employed to determine the fractional softening between passes. All the test parameters employed in the present work are summarized in Table 4.1.

Table 4.1 Test parameters for determination of the T_{nr}

Reheat temperature
T= 1200, 1250 °C
Strain/pass
ε=0.1, 0.2, 0.3, 0.4, 0.5, 0.7
Strain rate
$\dot{\varepsilon}$=0.2, 2, 5, 10 s^{-1}
Interpass time
t=0.05, 0.1, 0.5, 1, 2, 5, 7.5, 10, 12.5, 15, 20, 30, 50, 80, 100, 150, 200 s

4.2 Experimental Results

4.2.1 Reheated Austenite Grain Size

Individual specimens were reheated to different austenitization temperatures and held for 15 minutes before quenching. The prior austenite grain boundaries were revealed by etching the specimens in a saturated aqueous picric acid solution at about 80 °C. Figs. 4.1 and 4.2 show the microstructures of the Mo-B and Mo-Nb-B steels, respectively, reheated to 900, 1000, 1100, and 1200 °C. The dependence of initial austenite grain size on reheating temperature and boron concentration is presented in Figs. 4.3 and 4.4, respectively. It can be seen that, in general, the austenite grain size increases with increasing reheat temperature. For the Nb-B and Mo-Nb-B steels, the grain sizes are similar (about 10 μm) at 900 °C; when the reheat temperature is increased to 1000, 1100, and 1200 °C, however, the grain sizes of the former are larger than those of the latter. This difference could result from the boron concentration in these steels. In fact, the boron concentration in the Nb-B steel is higher (48 ppm) than in the Mo-Nb-B steel (35 ppm). It has been reported that higher boron concentrations accelerate the formation of coarse grain boundary $Fe_{23}(B,C)_6$ precipitates, which are ineffective in retarding grain growth during reheating.

Although Tamehiro et al.[14] did not observe $Fe_{23}(B,C)_6$ precipitates in a low carbon Nb treated steel with a boron concentration of 11 ppm, coarse $Fe_{23}((B,C)_6$ precipitates were found on the grain boundaries by Mavropoulos et al.[192] in a low carbon Nb-bearing steel with a boron concentration of 33 ppm. It was therefore expected that coarse $Fe_{23}(B,C)_6$ precipitates would be present in the steels studied in this investigation. The results presented in Fig. 4.4 show that the reheated austenite grain size increased with boron concentration. This observation agrees with that of Yamanaka et al.[130]. They observed that boron addition in low carbon low alloy steels raises the reheated austenite grain size, and that the reheated austenite grain size increases with boron content.

A mixture of fine and large grains with a ratio $d_l/d_s \approx 4$ is illustrated in Fig. 4.5 for the boron only steel. This mixed structure was also observed in the specimens reheated to 1000 and 1100 °C, but not in specimens reheated to 1200 °C. Such microstructures were not observed in the Nb-B steels. This suggests that the grain coarsening temperature of the boron-only steel is lower than that of the Nb-B steel, and that reheating the former at temperatures below 1200 °C might produce a mixed microstructure before rolling.

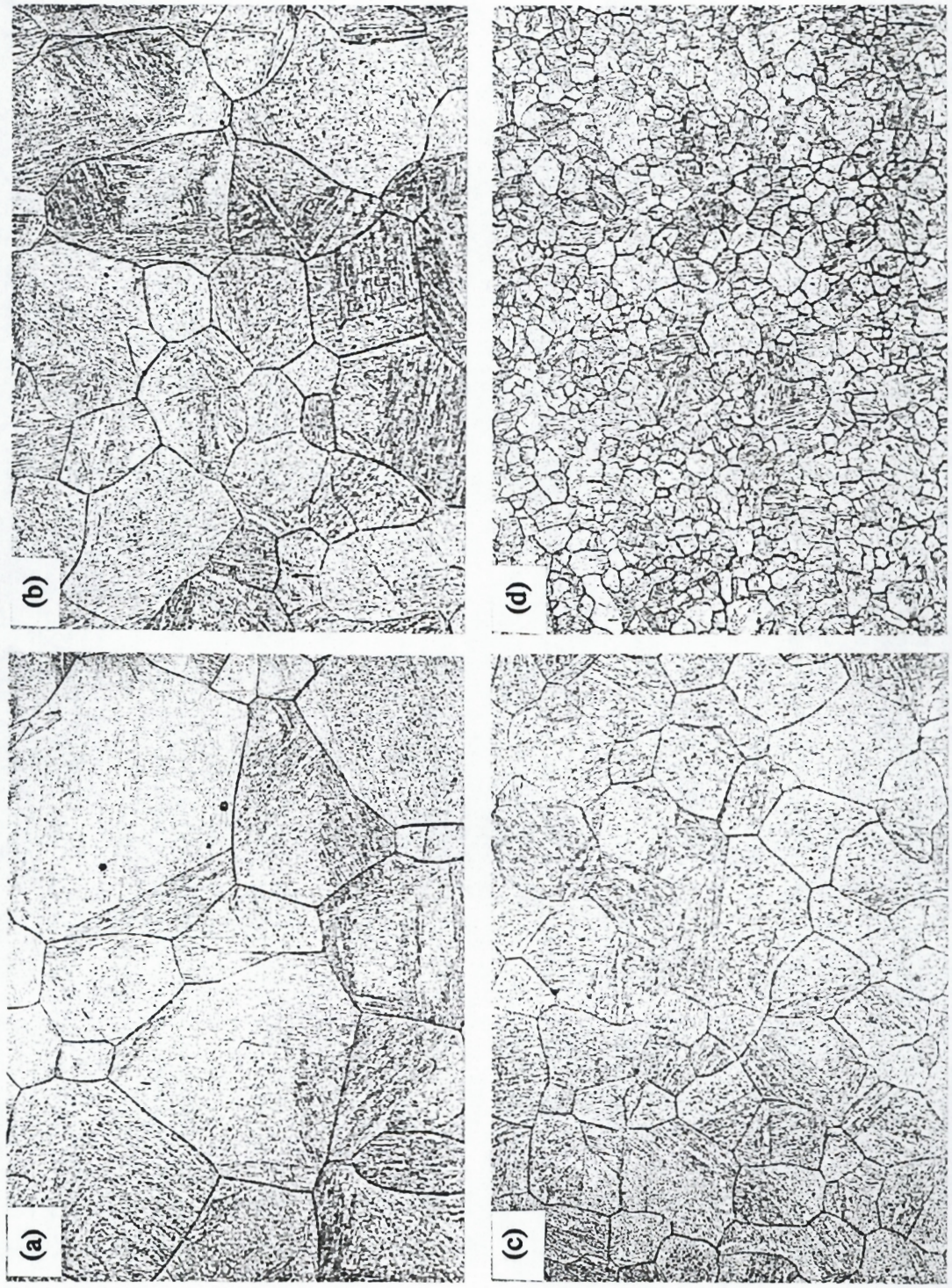

Fig. 4.1 Reheated austenite microstructures of the Mo-Nb-B steel: (a) 1200 °C, (b) 1100 °C, (c) 1000 °C, (d) 900 °C. x400

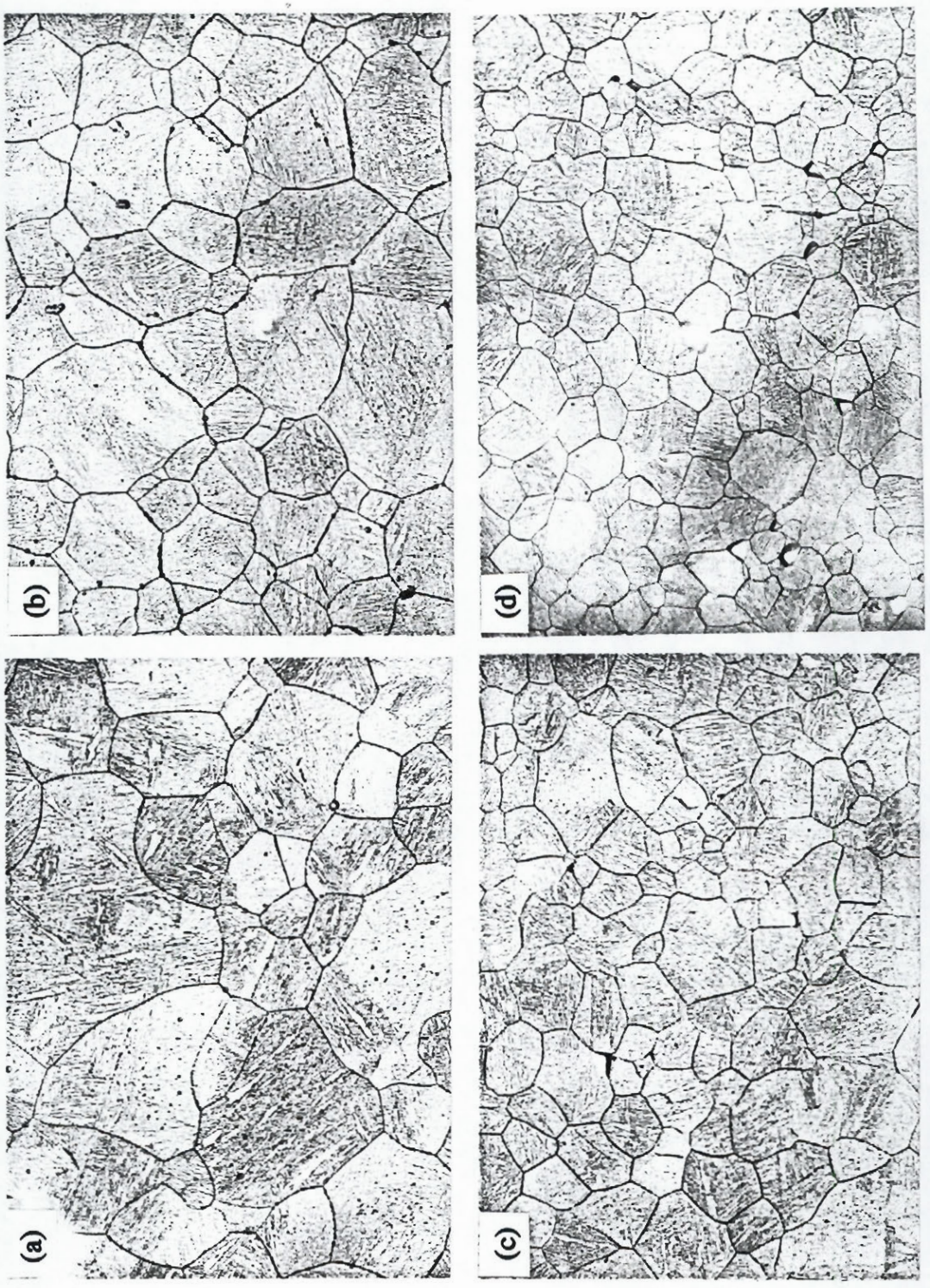

Fig. 4.2 Reheated austenite microstructures of the Mo-B steel: (a) 1200 °C, (b) 1100 °C, (c) 1000 °C, (d) 900 °C. x400

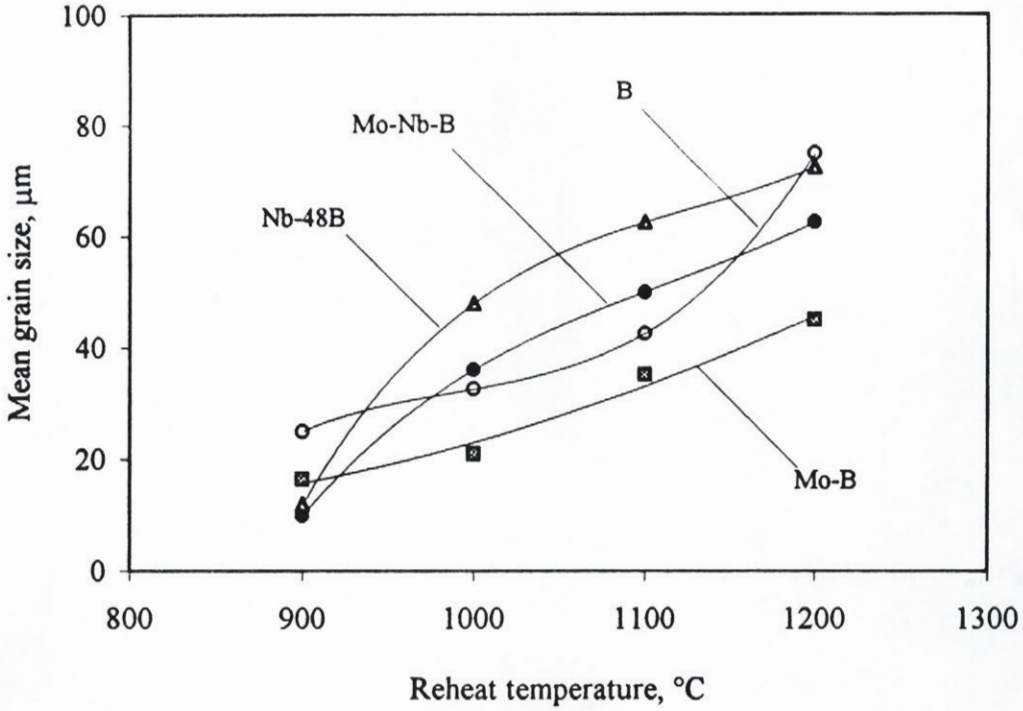

Fig. 4.3 Effect of reheat temperature on grain size.

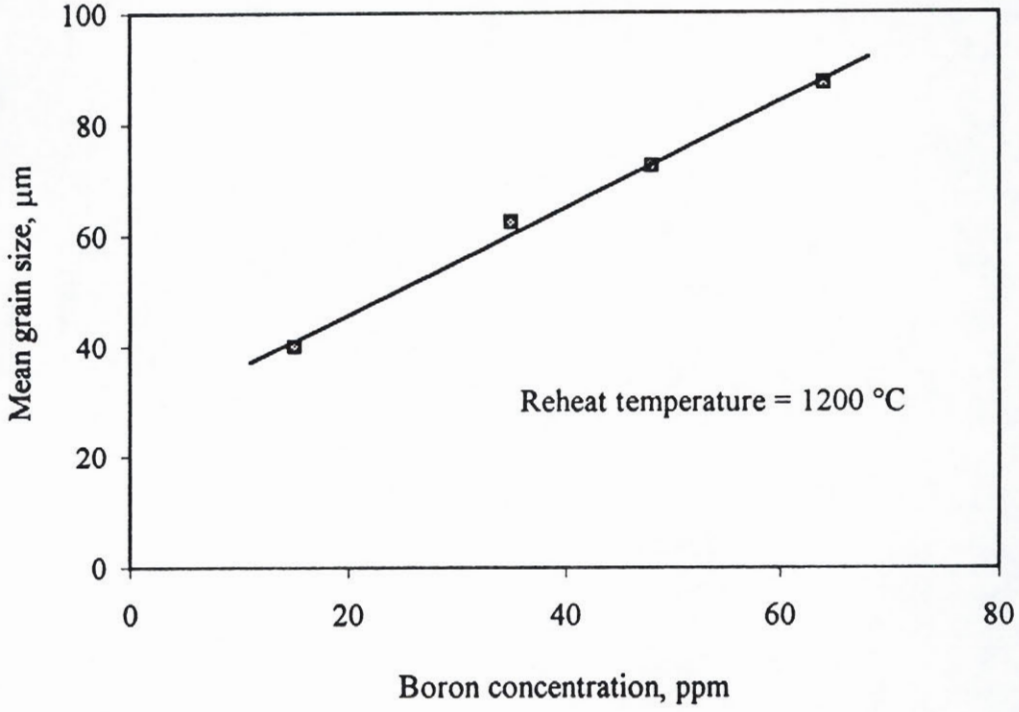

Fig. 4.4 Effect of boron concentration on grain size.

Fig. 4.5 Microstructure of the boron steel reheated at 900 °C. x 400

4.2.2 Effect of Chemical Composition on the T_{nr}

In the present study, three Nb bearing steels, one Ti bearing steel, one V bearing steel, and six boron bearing steels with different combinations of Mo-B, Nb-B, and Mo-Nb-B, were used to investigate the effect of microalloying elements on the no-recrystallization temperature. Fig. 4.6 shows the mean flow stress vs 1000/T curves of the 0.05Nb, 0.1V, and plain carbon steels tested using the same deformation parameters: strain of 0.3/pass, strain rate of 2 s^{-1}, and interpass time of 30 seconds. It can be seen that the mean flow stress of the plain carbon steel is only a function of temperature, and increases linearly with decreasing temperature over the whole austenite range. This suggests that there was no strain accumulation in this material, and that full recrystallization took place between passes. For the 0.05Nb steel, however, the slope of the mean flow stress curve changed at around 980 °C. As mentioned in Chapter 3, this temperature is defined as the no-recrystallization temperature under the present deformation conditions. Compared with the Nb bearing steel, the 0.1V steel has a lower T_{nr}, which is about 840 °C.

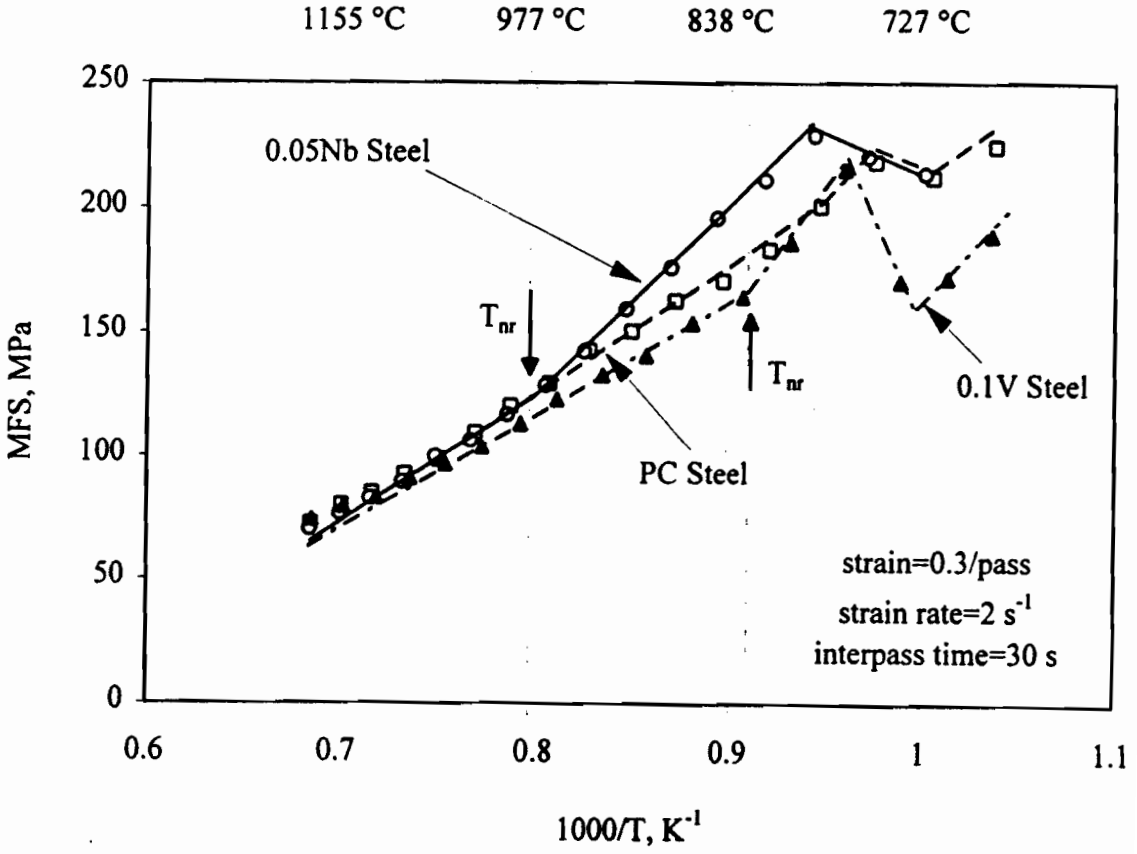

Fig. 4.6 MFS-1000/T diagram, samples deformed according to the 17 pass schedule.

The T_{nr}'s determined in this way are illustrated in Figs. 4.7 and 4.8. From Fig. 4.7(a), it can be seen that among the 0.05Nb, 0.16Ti and 0.1V steels, the Nb bearing grade has the highest T_{nr}'s, while the V bearing one has the lowest T_{nr}'s. The T_{nr}'s for the Ti bearing steel are lower than in the Nb bearing grade, but much higher than in the V bearing steel, even though the atomic concentration of Ti represented by 0.16 wt% is approximately six times the atomic fraction of Nb in the Nb bearing steel. This observation is consistent with that of Cuddy[84]. He demonstrated that the critical temperature, T_{RS}, increased with the initial solute level. The rate of increase, however, varied greatly with the type of solute. Nb, through the formation of Nb(CN), is the most effective in raising the T_{RS}; V, which forms VN in austenite, is the least effective. The increase in the T_{RS} over that of the plain carbon steel $\Delta T_{RS}=(T_{RS}-780)$ is related to the atomic percent of solute X according to:

$$\Delta T_{RS} = \alpha X^{1/2} \qquad (4.2)$$

where α is a measure of the strength of the solute's effect on the T_{RS}. The α values from the present work are presented in Table 4.2 and compared with those determined by Cuddy. It can be seen that the present results follow the same trend as those of Cuddy, although the α for Nb is considerably lower than his value. The lower α value determined here probably results from the lower carbon concentrations of the steels used in this investigation.

Table 4.2 α factors for particular solutes

solute	α °C/(at %)$^{1/2}$	
	present work	Cuddy
Nb	877	1350
Ti	379	410
V	181	200

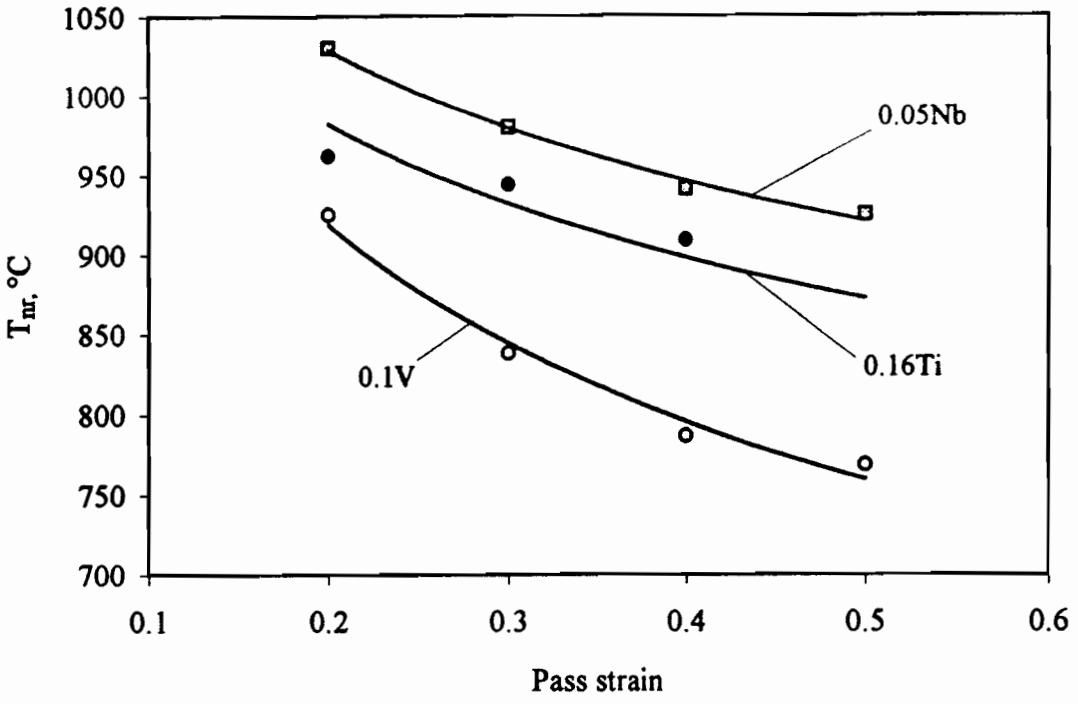

(a)

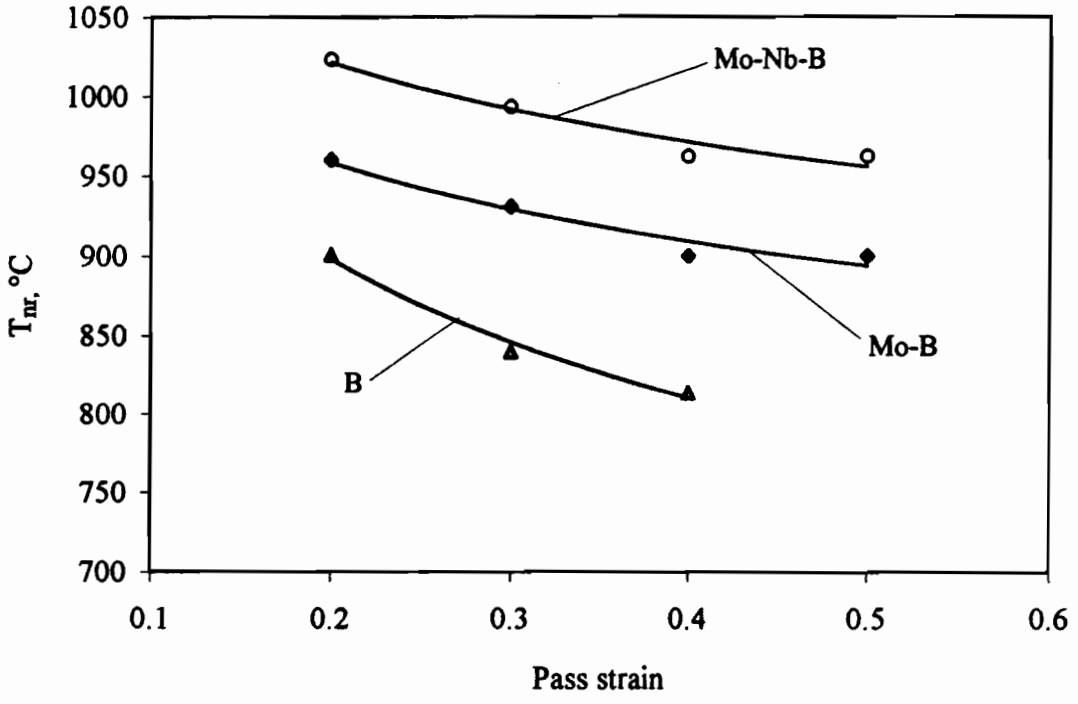

(b)

Fig. 4.7 Dependence of T_{nr} on steel composition.

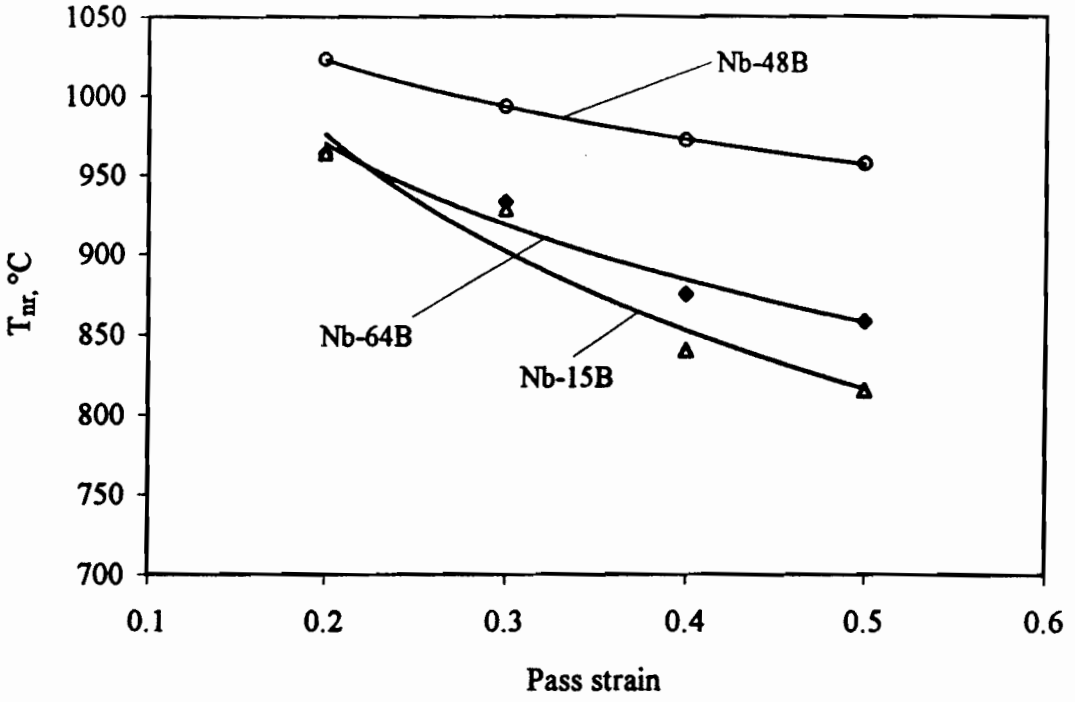

Fig. 4.8 Dependence of T_{nr} on boron concentration.

Fig. 4.7(b) shows the effect of Mo and Nb addition on the T_{nr}. It can be seen that, among these three steels, the Mo-Nb-B steel has the highest T_{nr}'s, which are even higher than those of the 0.09Nb steel (shown later in Fig. 4.10), although the Nb level in this grade is 30 percent lower than that of the 0.09Nb steel. This indicates that boron addition generally raises the no-recrystallization temperature, and that the combination of Nb and B produces the strongest retardation of recrystallization. The mechanisms of the retardation of recrystallization by boron are not fully understood. Tamehiro et al.[14] suggested that the retardation could be due to the strong interaction between boron atoms and lattice defects such as dislocations and vacancies; Mavropoulos et al.[192] proposed that the strong retardation effect produced by the combined addition of Nb and B can be attributed to a synergism between Nb and boron atoms. The effect of boron addition on the kinetics of Nb(CN) precipitation will be discussed in detail later.

The effect of boron concentration on the T_{nr} is demonstrated in Fig. 4.8 (the Nb concentrations of these three steels are about 0.06 wt%). It can be seen that the T_{nr}'s of the steel with 48 ppm boron are higher than those of the steels with either higher (64 ppm) or lower (15 ppm) boron concentration. This shows that there is an optimum boron

concentration which produces the strongest retardation of recrystallization through combination with Nb.

4.2.3 Effect of Deformation Parameters on the T_{nr}

4.2.3.1 Effect of Pass Strain

In order to understand the effect of deformation on the T_{nr}, the MFS vs 1000/T curves are presented in Fig. 4. 9 for specimens tested with pass strains of 0.1, 0.3 and 0.5. For these tests, the strain rate and interpass time were held constant at $\dot{\varepsilon}$=2 s^{-1} and t=30 s. It can be seen from the figure that the MFS increases with increasing pass strain, and that the MFS slope change occurs at higher temperatures when the pass strain is reduced. This indicates that the T_{nr} decreases with increasing pass strain.

The dependence of the T_{nr} on pass strain for the 0.05Nb, 0.07Nb, and 0.09Nb steels is illustrated in Fig. 4.10. The results demonstrate that the T_{nr} decreases with increasing pass strain in all cases, and that the T_{nr} 's in these three steels follow the order 0.05Nb, 0.07Nb, and 0.09Nb; this is in agreement with the supersaturation ratio or [Nb][C] solubility product. In the 0.05Nb steel, the carbon level is 0.125 wt%, which is approximately three times higher than in the 0.09Nb steel. Thus the solubility product of the former ([Nb][C]≈6.25×10^{-3}) is almost twice that of the latter ([Nb][C]≈3.6×10^{-3}) despite the lower Nb concentration. In the 0.07Nb steel, the presence of titanium accelerates the progress of Nb(CN) precipitation[212, 213], and therefore retards recrystallization in this way.

The experimental results of Fig. 4 10 correspond to a relationship between the T_{nr} and the pass strain of the following type

$$T_{nr} \propto \varepsilon^{-0.12} \qquad (4.3)$$

It is evident that a small change in pass strain leads to a significant change in the T_{nr}. When the strain is increased from 0.1 to 0.5, for instance, the T_{nr} in the 0.07Nb steel decreases from 1060 °C to about 900 °C. This is again consistent with the results of Cuddy, who reported that recrystallization is incomplete at about 1075 °C at pass strains of 0.04~0.13, while the temperature for complete recrystallization can be as low as 925 °C when the pass strain is increased to 0.2~0.48.

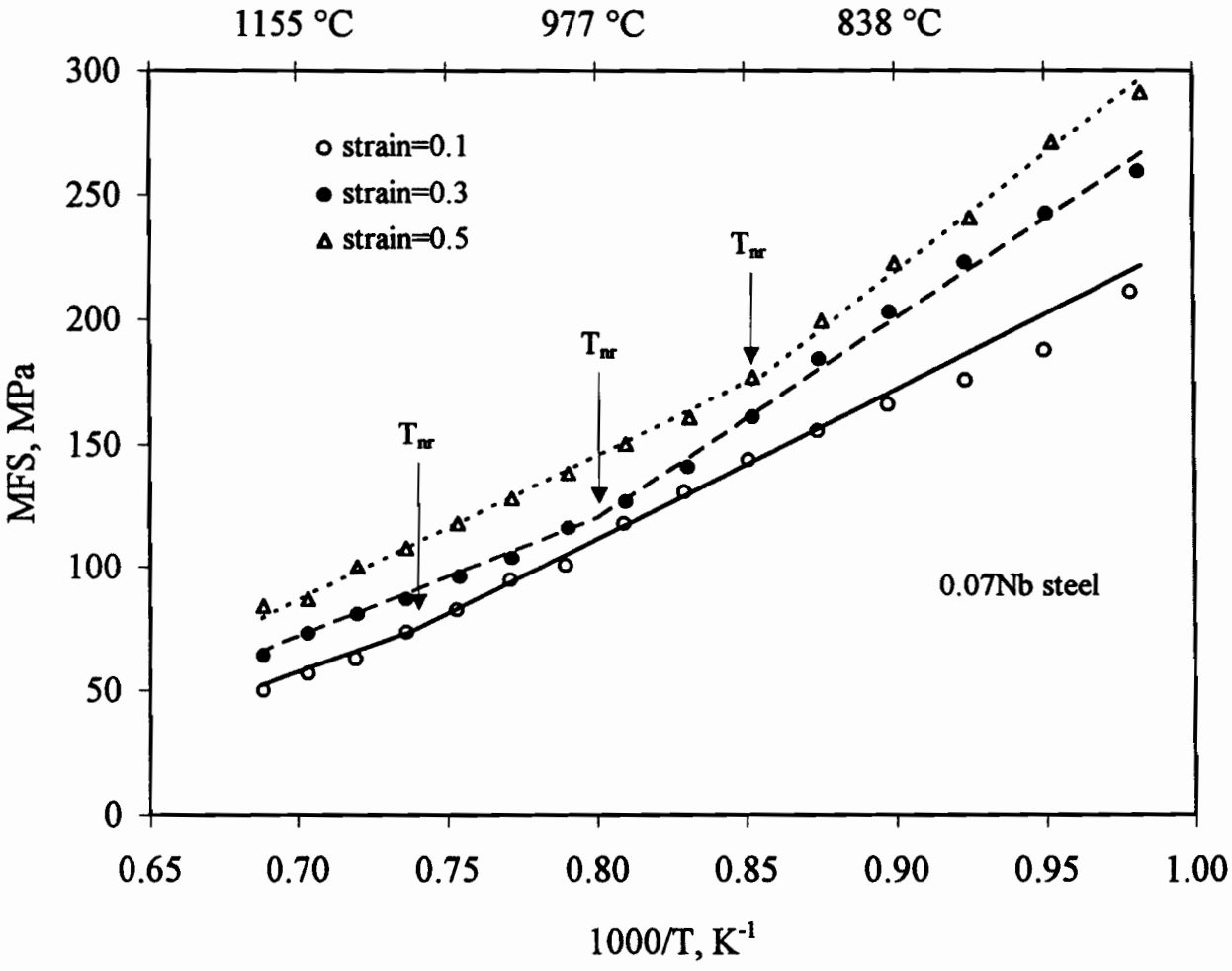

Fig. 4.9 Dependence of the mean flow stress (MFS) on inverse pass temperature for samples deformed according to schedule A; strain rate=2 s^{-1}, t=30 s.

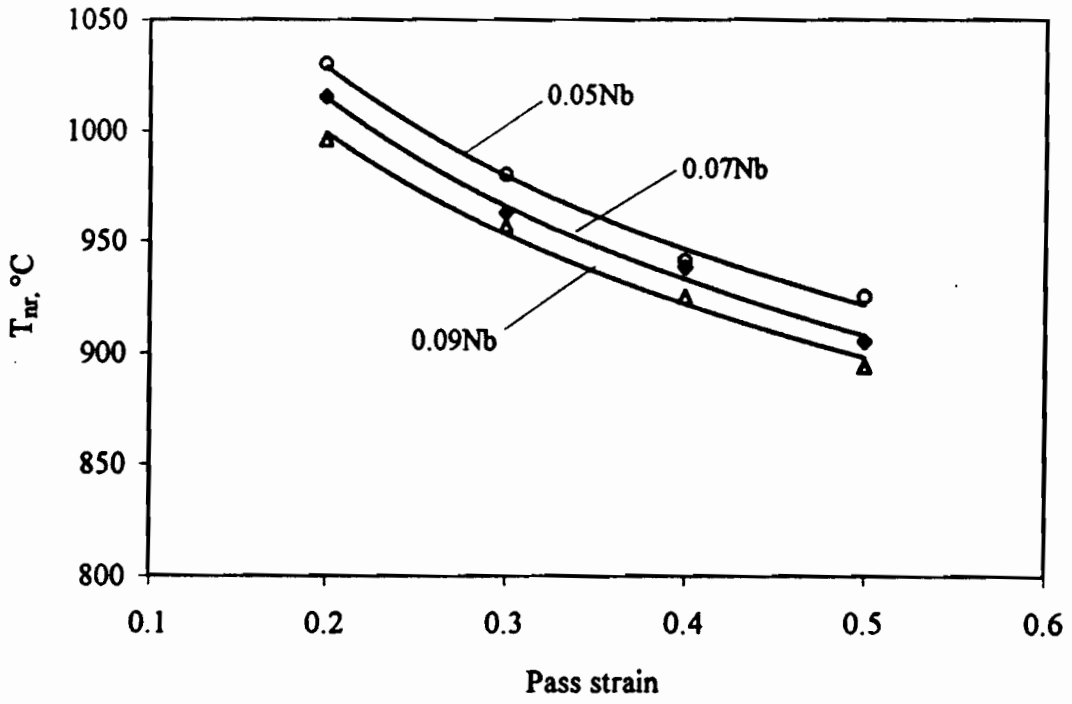

Fig. 4.10 Dependence of T_{nr} on pass strain (strain rate=2 s^{-1}, t=30 s).

Such a dramatic decrease in the T_{nr} with increasing pass strain can be due to several contributing factors:

1). Grain refinement. When the pass strain is increased, finer grain sizes are produced by static recrystallization. Such fine structures supply more nucleation sites for subsequent recrystallization and also soften more quickly.

2). Increased dislocation density. When the pass strain is increased, higher dislocation densities are generated, which also promote more rapid recrystallization. When a fixed interpass time is used, this makes it possible for recrystallization to go to completion at lower temperatures.

3). Precipitate coarsening. When the pass strain is increased, the density of dislocations increases, which leads to more rapid coarsening of the precipitates[9]. These coarsened particles lose their effectiveness in retarding recrystallization, and thus allow recrystallization to continue to take place at lower temperatures.

The TEM micrographs shown in Fig. 4.11 demonstrate the effect of increasing the pass strain on precipitate coarsening. The upper micrograph was obtained from a specimen deformed using a pass strain of 0.3 and quenched at 972 °C (near the T_{nr} for this strain), while the lower micrograph represents a specimen deformed using pass strains of 0.7 and quenched at 860 °C (near the T_{nr} for the increased strain). The mean particle size in the latter case (about 110 nm) is considerably larger than in the former case (about 25 nm); these large particles are thus less effective in retarding recrystallization. Similar observations of precipitate coarsening during hot deformation have been reported by Weiss and Jonas[186], and Speer and Hansen[146].

Equations (2.40) and (2.46) in Chapter 2 are recalled here. For the present purpose, let

$$A = 3\times10^{-6}[Nb]^{-1}Z^{-0.5}\exp\left(\frac{270{,}000}{RT}\right)\exp\left(\frac{2.5\times10^{10}}{T^3(\ln k_s)^2}\right) \qquad (4.4)$$

and $$B = 6.75\times10^{-20}d_0^2\exp\left(\frac{300000}{RT}\right)\exp\left(\left(\frac{2.75\times10^5}{T}-185\right)[Nb]\right) \qquad (4.5)$$

Then

$$t_{0.05p} = A\varepsilon^{-1} \qquad (4.6)$$

$$t_{0.05x} = B\varepsilon^{-4} \qquad (4.7)$$

The rate of change of $t_{0.05p}$ and $t_{0.05x}$ with strain are given by the first partial derivatives of equations (4.6) and (4.7):

$$\frac{\partial t_{0.05p}}{\partial\varepsilon} = -A\varepsilon^{-2} \qquad (4.8)$$

$$\frac{\partial t_{0.05x}}{\partial\varepsilon} = -4B\varepsilon^{-5} \qquad (4.9)$$

As deformation increases the dislocation density, and dislocations act as nucleation sites for both recrystallization and precipitation, increasing the strain increases the rates of both phenomena. The increases are different, however, for the two mechanisms. From equations (4.8) and (4.9), it can be seen that the recrystallization kinetics are more sensitive to strain than the precipitation kinetics, although the difference in sensitivity

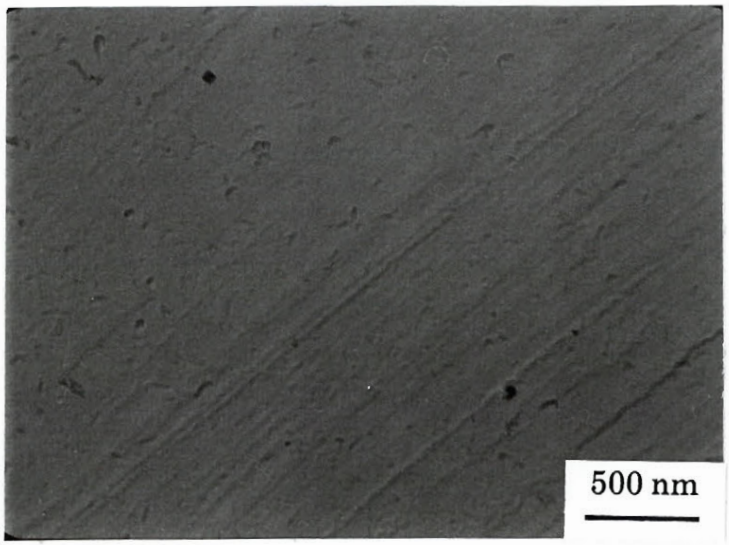

(a) ε=0.3/pass

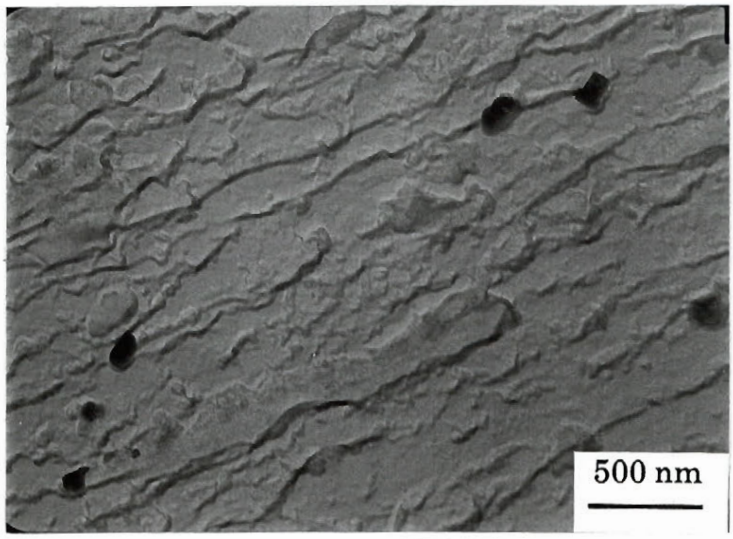

(b) ε=0.7/pass

Fig. 4.11 Carbon extraction replicas showing the influence of deformation on precipitate size. (a) quenched at 972 °C; (b) quenched at 860 °C.

diminishes as the strain approaches unity. Thus, the T_{nr} decreases continuously with strain. As an example, the data for the 0.07Nb steel in Fig. 4.10 show that when the strain is increased from 0.2 to 0.3, the T_{nr} decreases by 52 °C (from 1015 °C to 963 °C). When the strain is increased from 0.4 to 0.5, the T_{nr} decreases by 33 °C (from 938 °C to 905 °C).

4.2.3.2 Effect of Strain Rate

The MFS vs 1000/T curves for specimens tested with strain rates of 0.2, 2 and 10 s^{-1} are presented in Fig. 4.12. For these tests, the pass strain (0.3/pass) and interpass time (30 seconds) were held constant, and only the strain rate was varied from test to test. It can be seen that the mean flow stress increases with increasing strain rate. This is because the amount of restoration caused by dynamic recovery per unit strain decreases as the strain rate is increased. At lower strain rates, the deformation time is longer, which leads to more restoration. When the strain rate is 0.2 s^{-1}, for example, the deformation time is 1.5 seconds for a strain of 0.3. This time is long enough to cause appreciable dynamic restoration, and therefore produces a relatively low mean flow stress. By contrast, a strain rate of 10 s^{-1} leads to a deformation time of 0.03 seconds. This short time will minimize the amount of dynamic restoration, and lead to a higher mean flow stress. Such less restored austenite supplies more driving force for subsequent static recrystallization, which decreases the T_{nr} in this way. The effect of strain rate on the T_{nr} is presented in Fig. 4.13. It can be seen that the T_{nr}'s decrease with increasing strain rate for all values of pass strain.

In general, in the absence of strain induced precipitation, increasing the rate of deformation decreases the incubation time and increases the rate of subsequent recrystallization. This is due to the increase in dislocation density and the decrease in subgrain size that accompanies the strain rate increase, both of which increase the driving force for recrystallization. In the range of temperatures where strain induced precipitation is likely to occur, not only recrystallization but also precipitation are accelerated at high strain rates. There is an interaction between these two processes. When the strain is large, the recrystallization kinetics are accelerated over the precipitation kinetics; this leads to a decrease in the T_{nr}. The decrease in the T_{nr} is more noticeable at lower strain rates. At higher strain rates, however, the T_{nr} changes only slightly with strain rate. This makes it possible to extrapolate the present results to the higher strain rates that are employed in rolling mills. The relationship between T_{nr} and strain rate can be represented in the form of a power function:

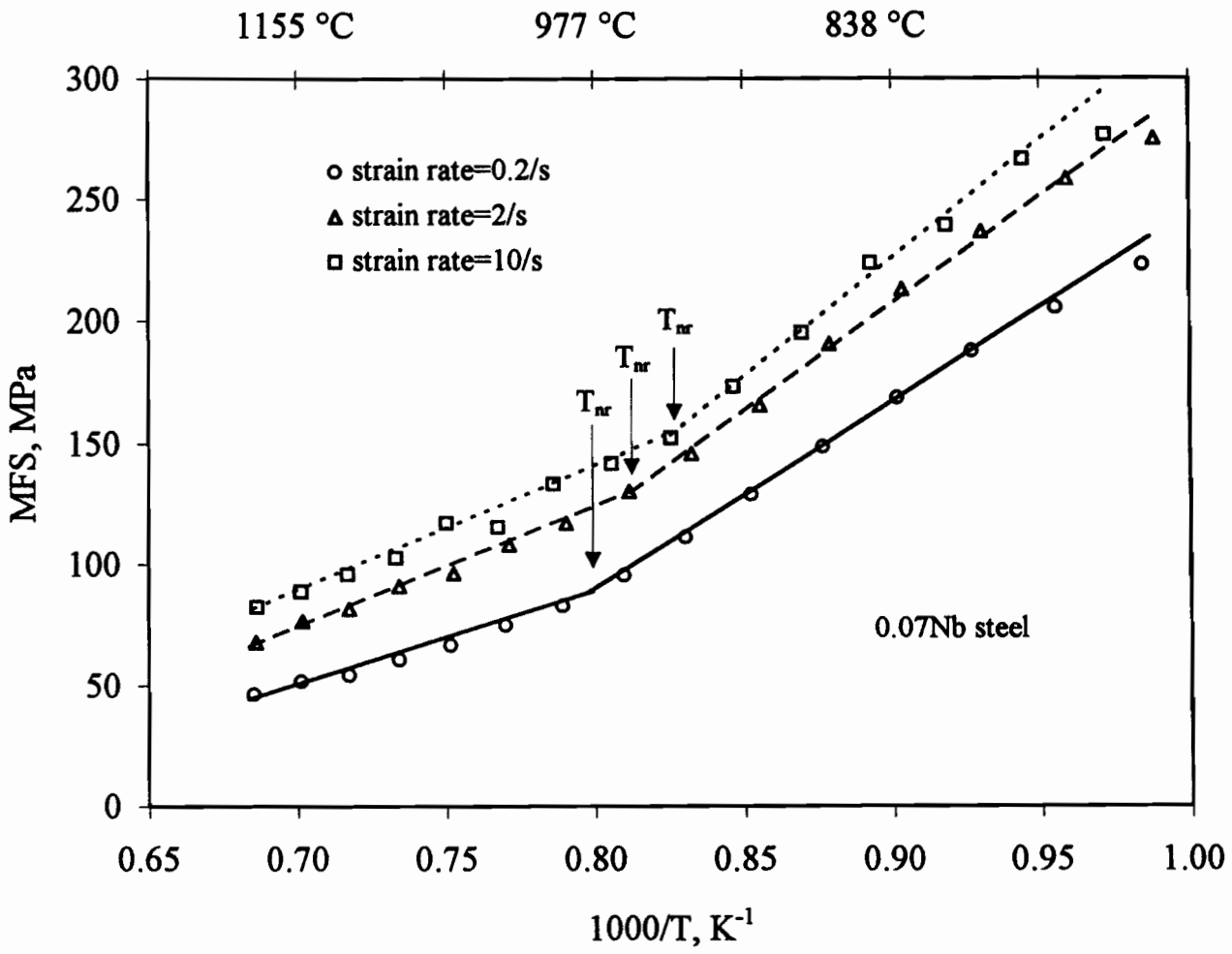

Fig. 4.12 Dependence of the mean flow stress (MFS) on inverse pass temperature for samples deformed according to schedule A; ε=0.3, t=30 s.

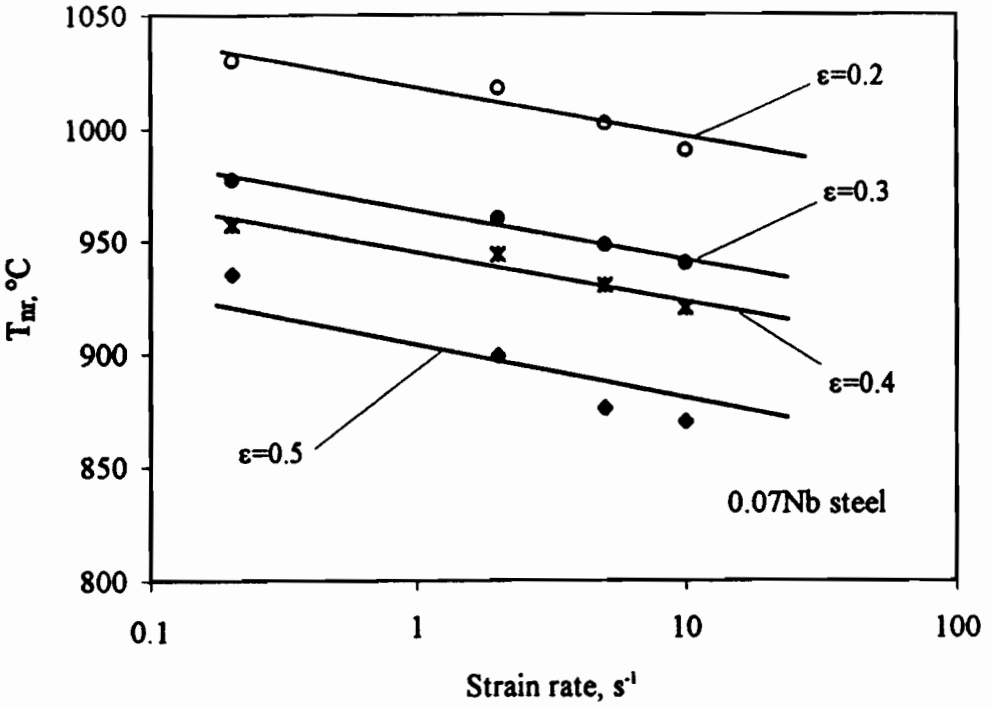

Fig. 4.13 Dependence of T_{nr} on strain rate (interpass time=30 s).

$$T_{nr} \propto \dot{\varepsilon}^{-0.01} \qquad (4.10)$$

As can be seen, the strain rate exponent is about one order of magnitude lower than that of the pass strain. This is consistent with the experimental results reported by Laasraoui and Jonas[63]. In their work, the effect of strain on time for 50% recrystallization was described by a power relation with an exponent of -3.81, while that for the effect of strain rate was again one order lower at -0.36. It can thus be concluded that strain rate does not have a significant effect on either the recrystallization kinetics or the T_{nr}.

4.2.3.3 Effect of Interpass Time

A. Interpass times ≤1 second

In the case of very short interpass times, i.e., t ≤ 1 second, schedule B (pass strain=0.3, and strain rate=2 s^{-1}) was used. The stress-strain curves for samples of the 0.07Nb steel tested with interpass times of t = 0.05, 0.1, 0.5 and 1 second are presented in

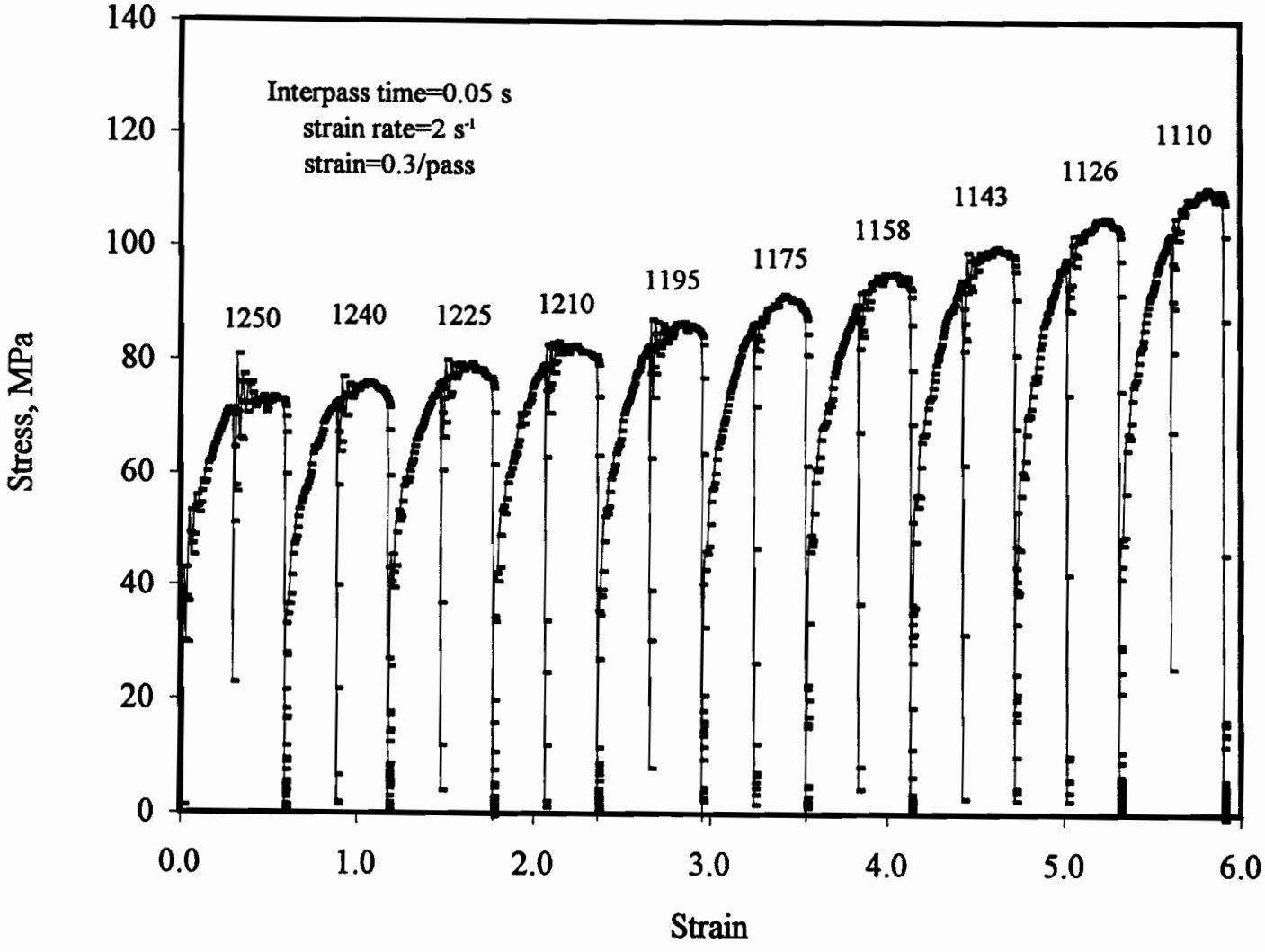

Fig. 4.14 (a) Stress-strain curves for steel B deformed using schedule B for short interpass times.

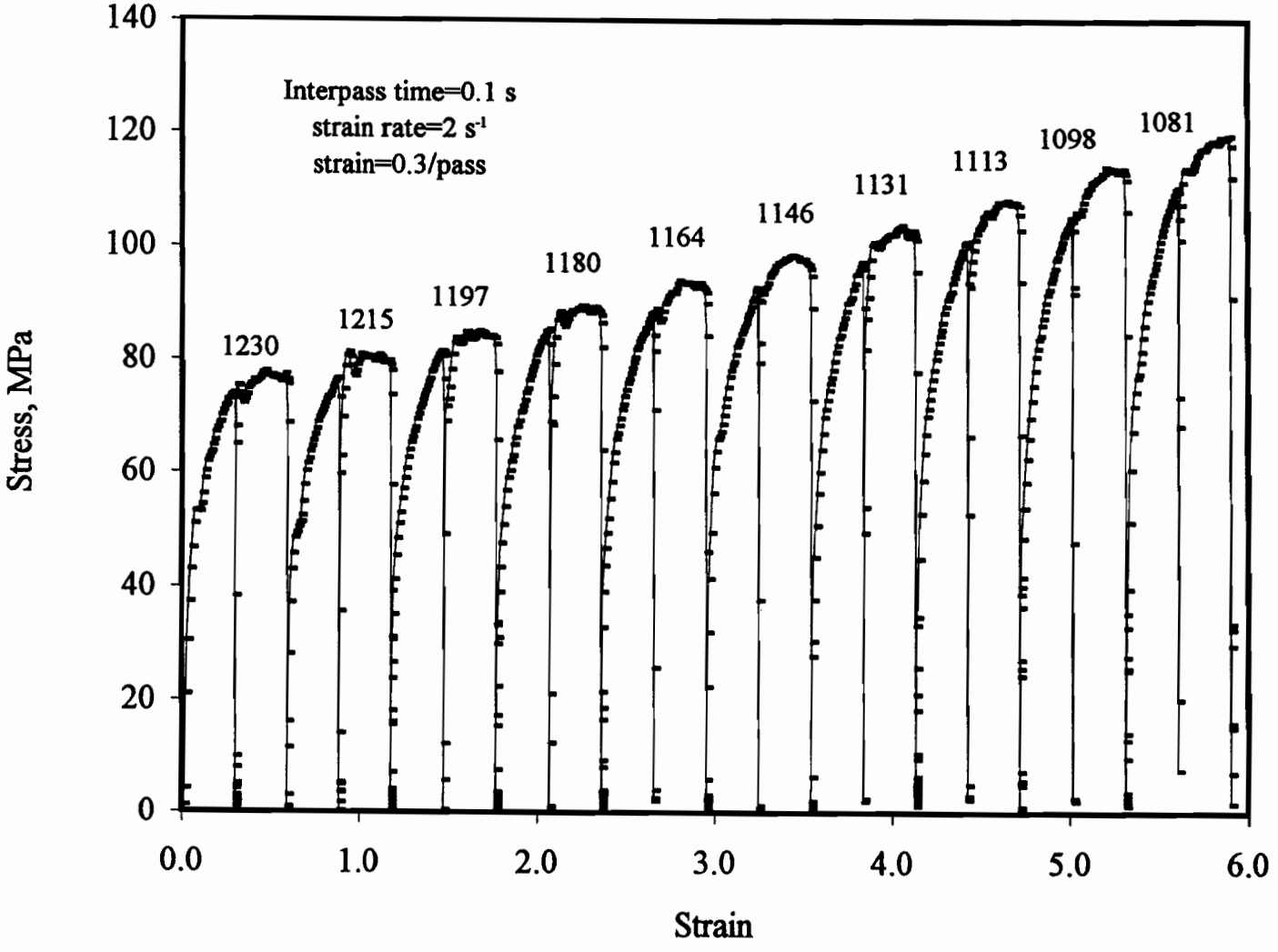

Fig. 4.14 (b) Stress-strain curves for steel B deformed using schedule B for short interpass times.

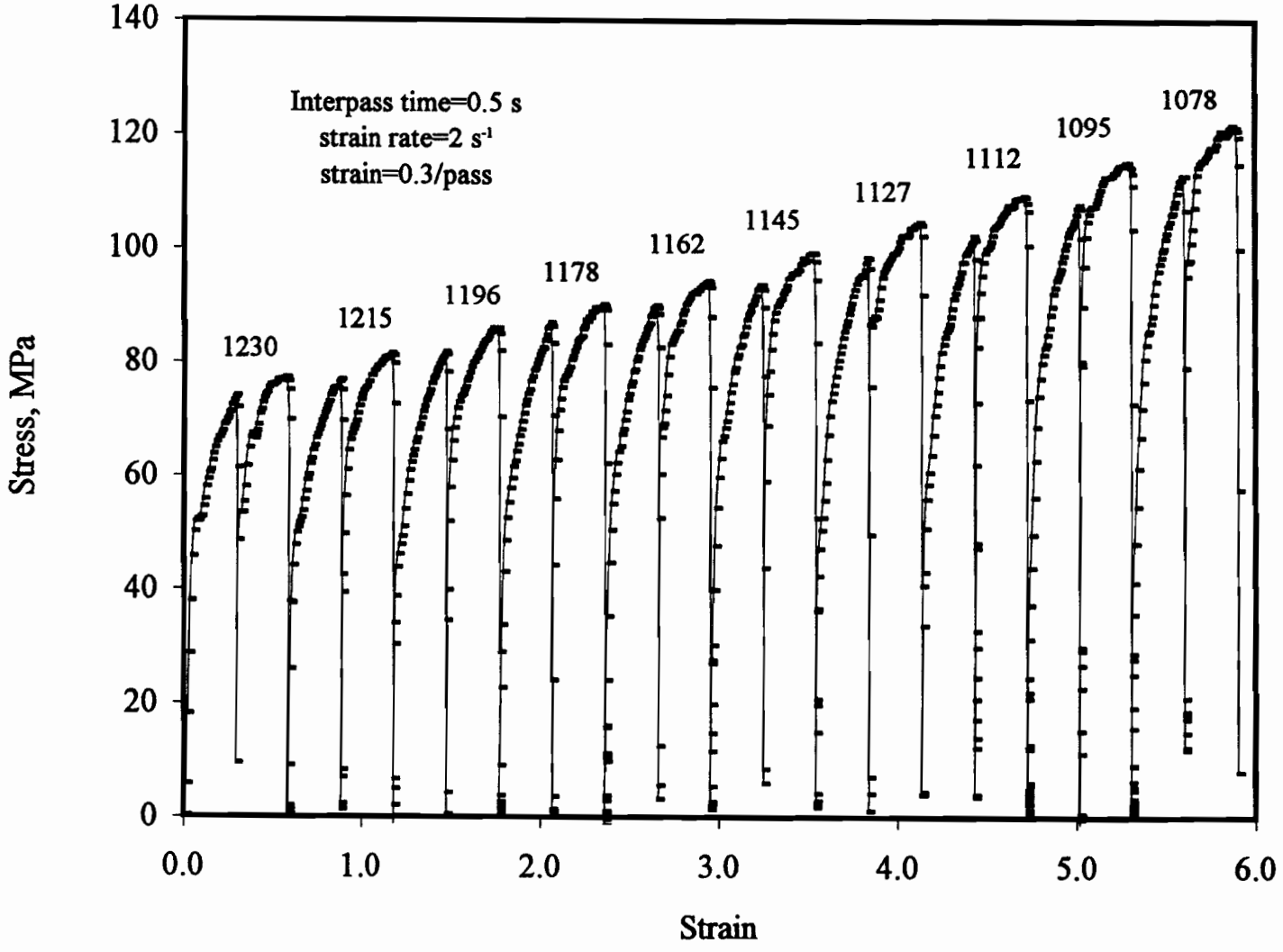

Fig. 4.14 (c) Stress-strain curves for steel B deformed using schedule B for short interpass times.

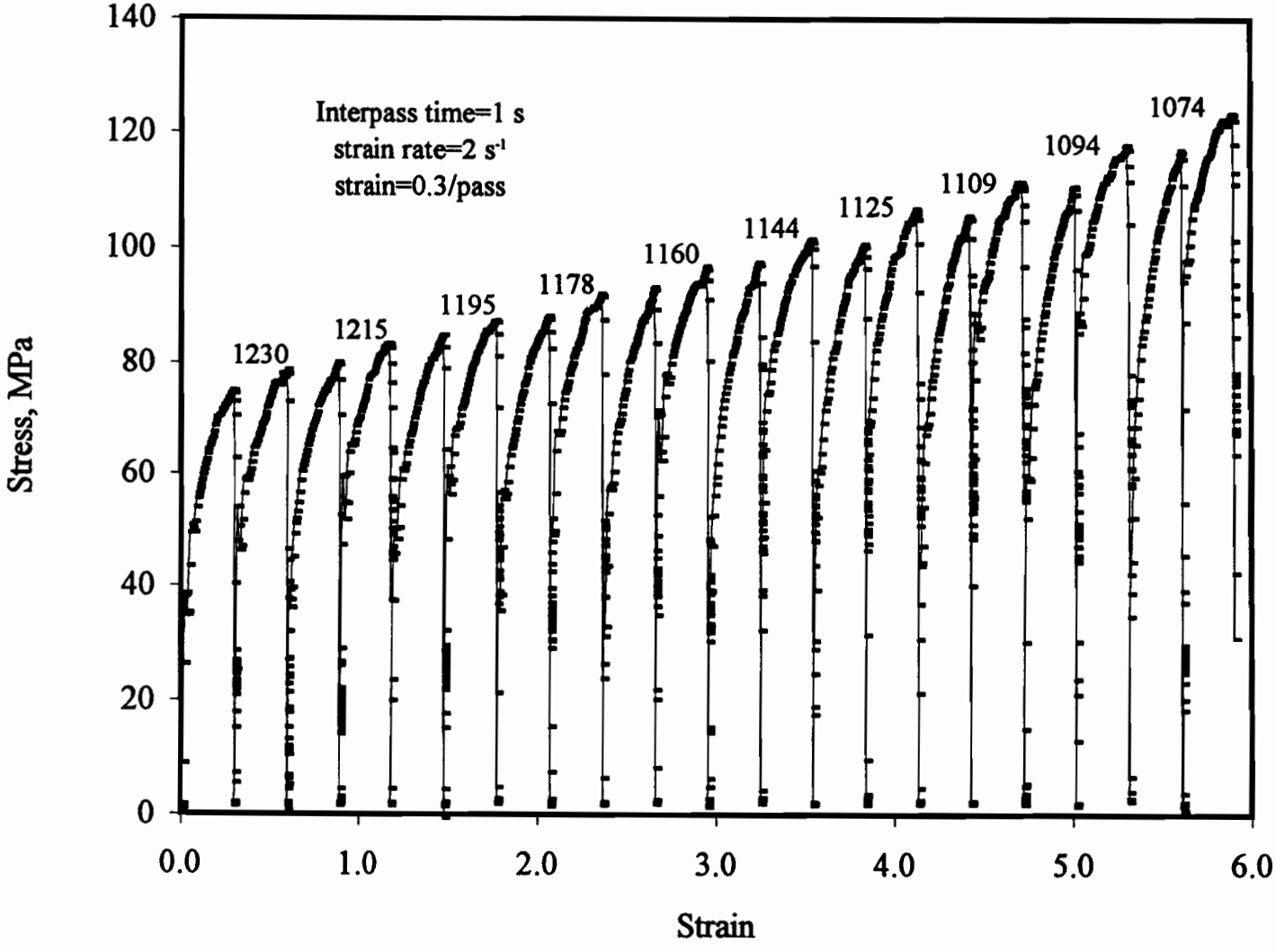

Fig. 4.14 (d) Stress-strain curves for steel B deformed using schedule B for short interpass times.

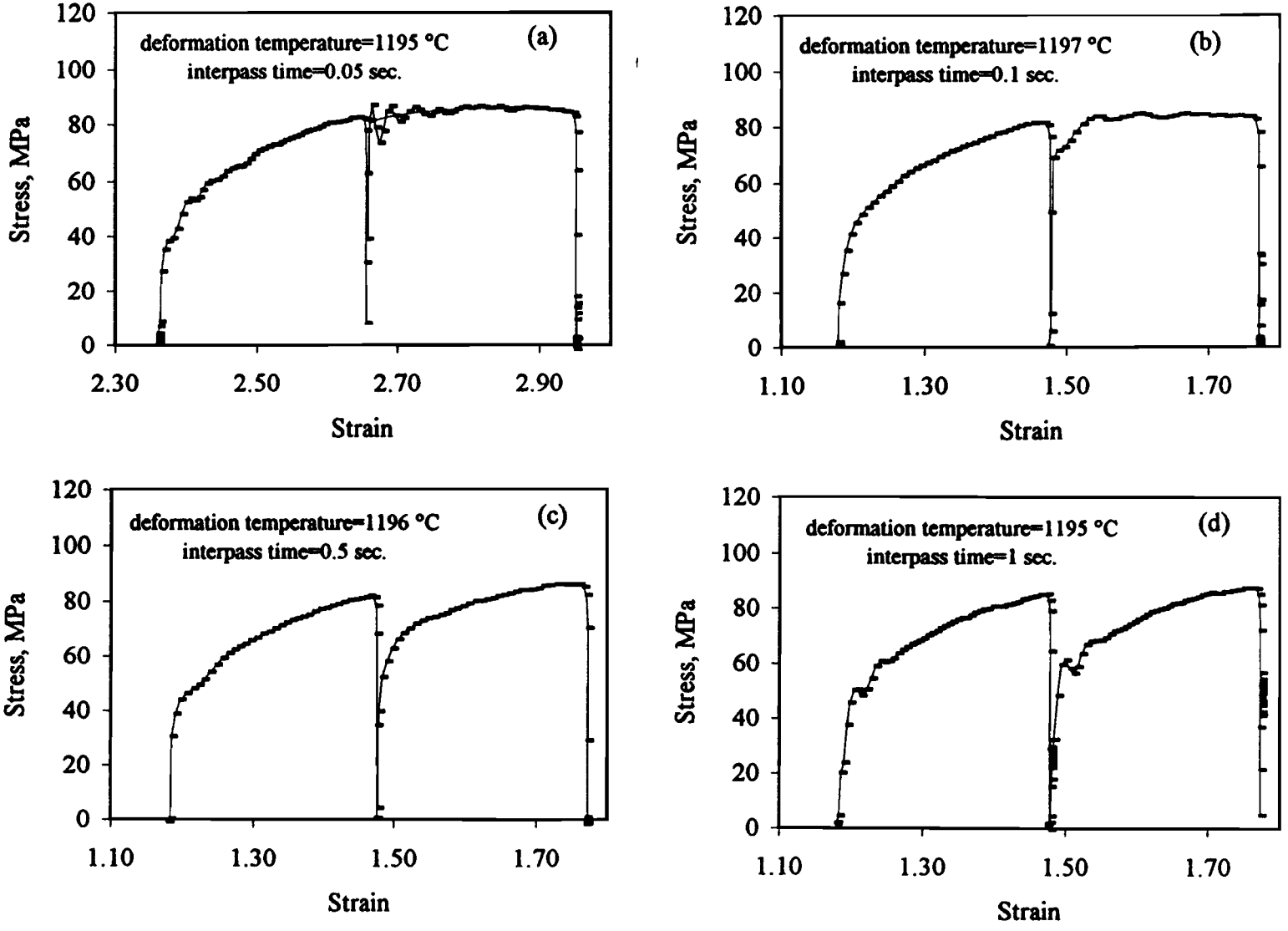

Fig. 4.15 Stress-strain curves determined on steel B showing the softening taking place at temperatures around 1196 °C for different interpass times.

Figs. 4.14 (a), (b), (c) and (d), respectively. The flow curves determined at temperatures around 1196 °C using different interpass times are shown in expanded form in Figs. 4.15 (a)-(d) for steel B. It can be seen that the amount of softening between two deformations increases with the length of the interpass interval. The softening ratios were calculated using equation (3.15), which was introduced in Chapter 3; these results are presented in Fig. 4.16. It is evident that the softening ratios are below 80 % for interpass times < 1 second, even at 1230 °C. In the case of interpass times of t = 0.05 and 0.1 second, the softening ratios are below 20 %. This suggests that recovery alone is responsible for the restoration in such short interpass times. When the interpass time is increased to 1 second, the softening ratio is significantly increased, which indicates that recrystallization starts to play a major role. On the assumption that a decrease in the fractional softening to 75% corresponds to the no-recrystallization temperature, a T_{nr} of 1180 °C can be estimated for this particular interpass time (1 s). By means of similar arguments, the T_{nr} at 0.5 s interpass time can be estimated to be 1230 °C.

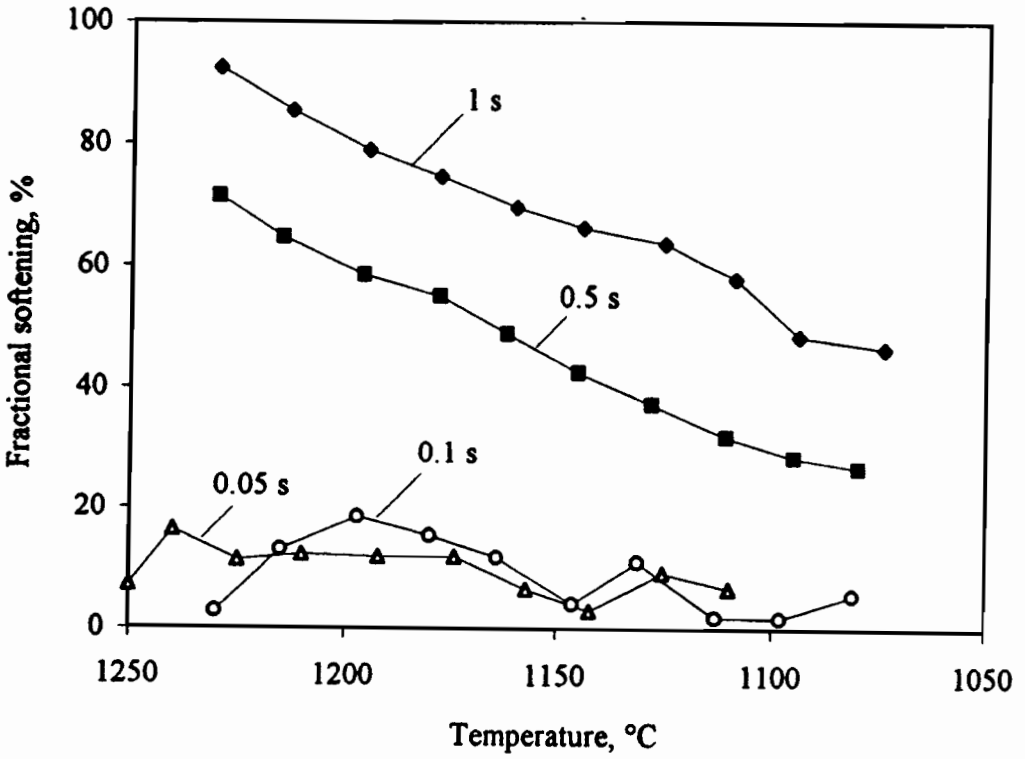

Fig. 4.16 Fractional softening at very short interpass times determined on steel B (strain=0.3/pass, strain rate=2 s^{-1}).

B. Interpass times > 1 second

In the case of interpass time t > 1 second, the MFS vs 1000/T diagram was used to determine the T_{nr}. A set of mean flow stress vs 1000/T curves for the 0.07Nb steel is presented in Fig. 4.17. For the tests shown here, the pass strain (0.3/pass) and strain rate ($\dot{\varepsilon}$=2 s^{-1}) were held constant, and the interpass time was changed from test to test (ranging from 2 to 200 seconds). For a selected test, the individual interpass times were identical. It can be seen that at temperatures above the T_{nr}, the interpass time does not affect the mean flow stress because significant recrystallization takes place, and there is no precipitation strengthening. In this case, the mean flow stress is only a function of temperature.

At temperatures below the T_{nr}, recrystallization is no longer complete, so that strain accumulation takes place. The mean flow stress now increases more quickly with decreasing temperature. The dependence on interpass time of the T_{nr} of the 0.07Nb steel is demonstrated in Fig. 4.18. It can be seen that the effect of interpass time can be divided into three distinct regions: short ($t \leq 12.5$ seconds), medium ($12.5 < t < 50$ seconds), and long ($t > 50$) interpass times. In the range of short interpass times (region I), precipitation is unable to take place or be very effective, so that only solute drag is available for the retardation of recrystallization. In this range, the extent of recrystallization increases with increasing interpass time, thus decreasing the T_{nr}. With further increases in interpass time, if no precipitation were to take place, the T_{nr} would decrease continuously along the broken curve. For the present steels, however, when the interpass time is increased over a critical value (for instance, 12.5 seconds for the 0.07Nb steel), precipitation begins to be effective, and the retardation of recrystallization is mainly attributable to this phenomenon, so that the T_{nr} shifts to the solid curve in this range. In the third region, the interpass time is quite long (> 50 seconds), the precipitates begin to coarsen, and the retardation of recrystallization by precipitates becomes weaker. As a result, the T_{nr} decreases again.

Some typical TEM micrographs of 0.07Nb steel samples processed using different interpass times are presented in Fig. 4.19. The quenching temperature was 910 °C in all cases, but the total times from the solution temperature to the temperature at which quenching was carried out were different because different interpass times were used. The interpass times used for these cases are specified on the micrographs of Fig. 4.19. It can be seen that when the interpass time was increased from 5 to 200 seconds (the total time was increased from 45 to 1800 seconds), the mean particle size increased from 15 to 135 nm. It is evident from the final micrograph that the particle density has decreased,

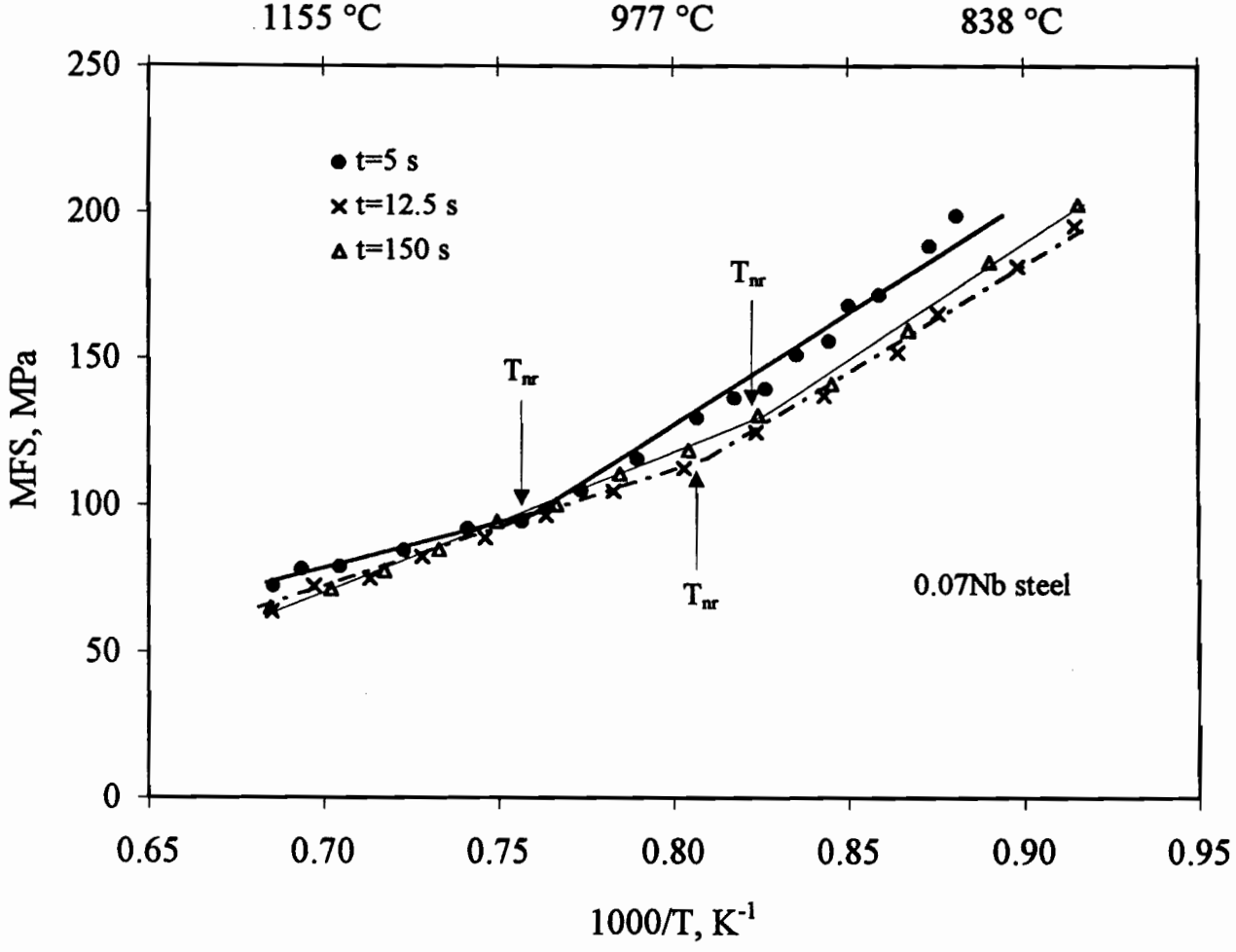

Fig. 4.17 Dependence of the mean flow stress (MFS) on inverse pass temperature for samples deformed according to schedule A; strain=0.3, strain rate=2 s^{-1}.

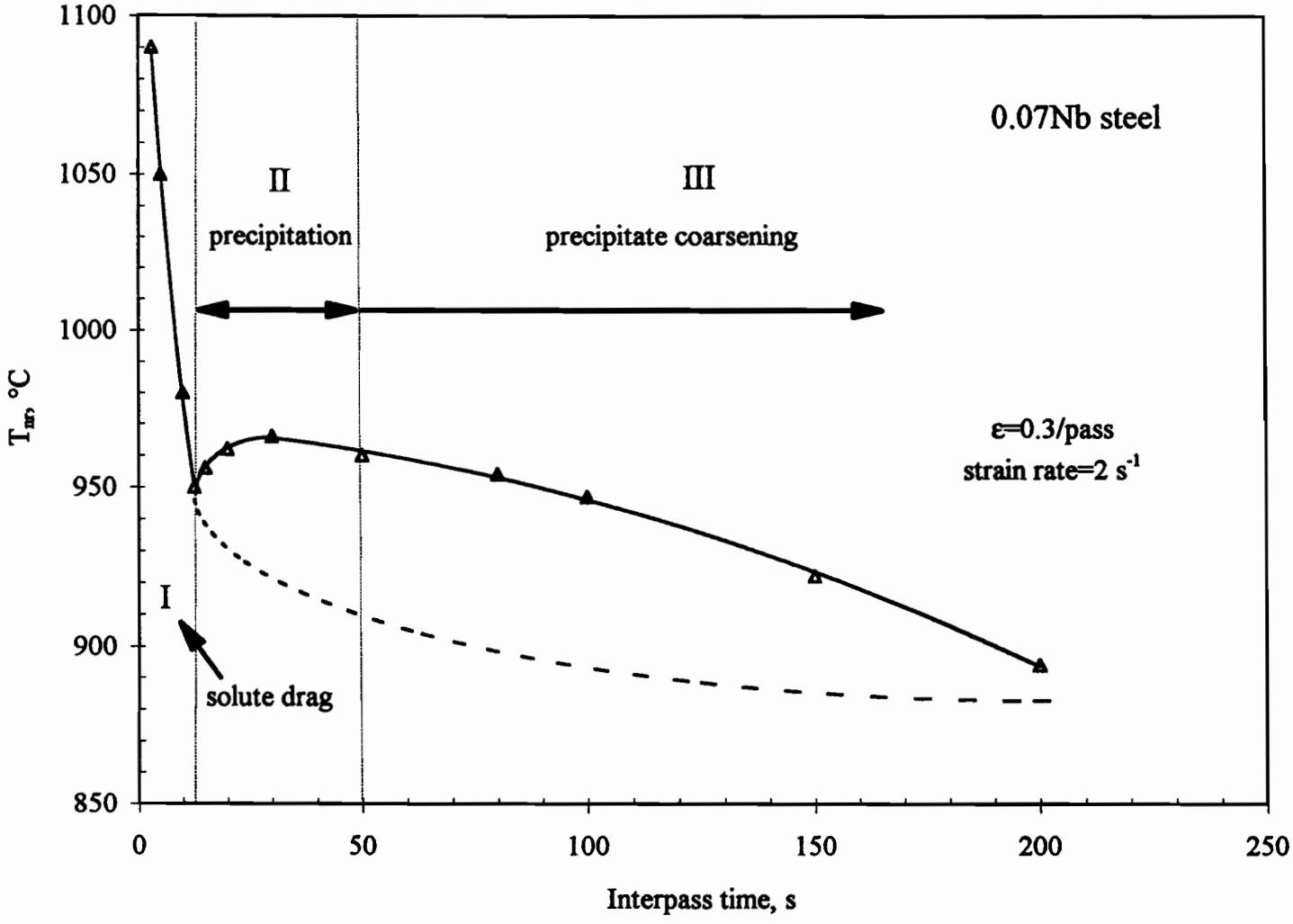

Fig. 4.18 Dependence of the T_{nr} on interpass time.

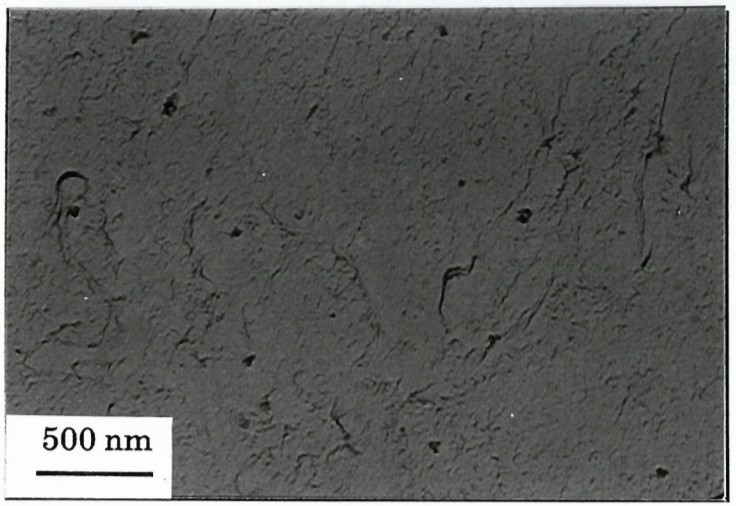

(a) 5 s

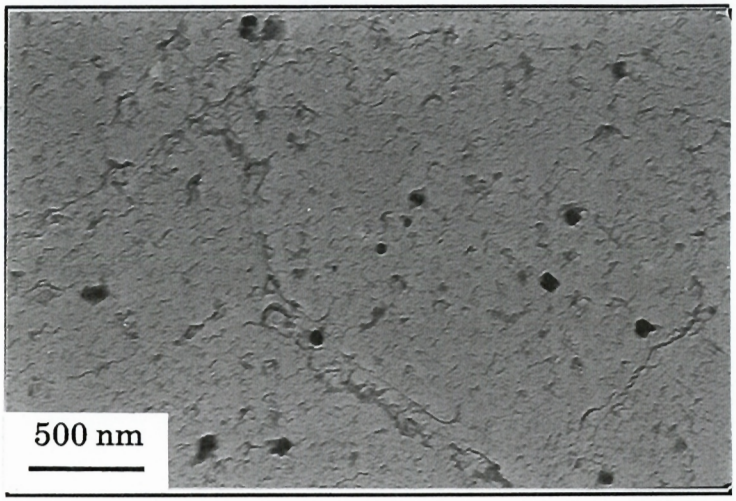

(b) 30 s

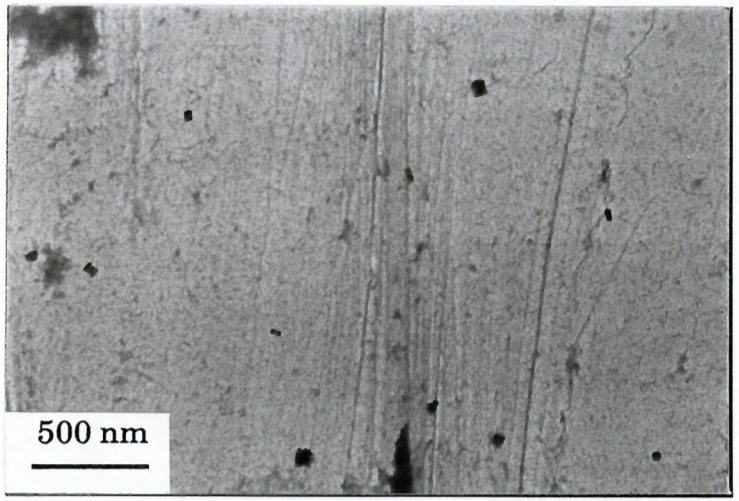

(c) 80 s

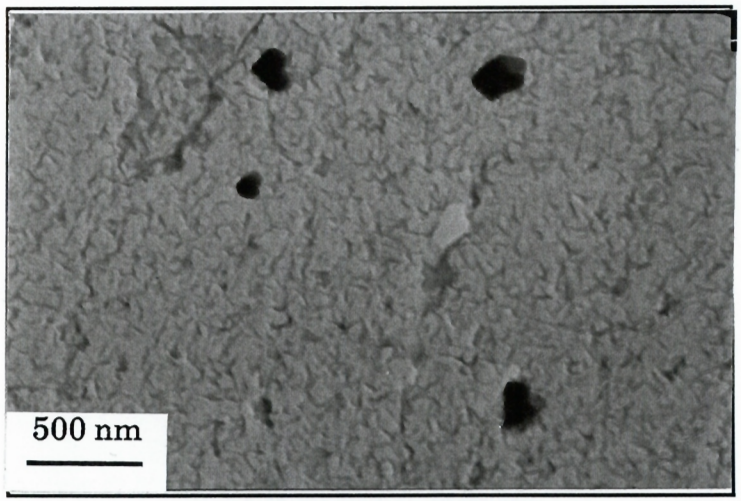

(d) 200 s

Fig. 4.19 Carbon replicas showing the dependence of the morphology of the Nb(CN) precipitates on interpass time in the 0.07Nb steel. All of the specimens were quenched at 910 °C.

indicating that coarsening is taking place. These micrographs are thus consistent with the interpretation given to the mechanical results in this section and support the explanation proposed.

Fig. 4.20 illustrates the dependence of the T_{nr}'s of three Nb-bearing steels (0.05Nb, 0.07Nb and 0.09Nb) on interpass time. It can be seen that precipitation is slightly more rapid in the 0.05Nb and 0.07Nb steels. In the case of the 0.05Nb steel, this is because it has a higher solubility product for C, N, and Nb than the other grades and therefore a higher level of supersaturation ratio at a given deformation temperature. In the 0.07Nb steel, the higher level of titanium addition (0.026 wt%) leads to Ti(CN) precipitation; these particles act as nucleation sites for Nb(CN) precipitation[183, 210, 211] and therefore retard recrystallization in this way. In the short interpass time region, in which solute drag controls the rate of recrystallization, the order of the T_{nr} for these steels is 0.07Nb, 0.09Nb, and 0.05Nb; this is because the 0.07Nb steel contains the highest concentration of Nb plus Ti, whereas the lowest is found in the 0.05Nb steel.

By analyzing the results of Fig. 4.20, the dependence of the T_{nr} on interpass time can generally be described by the following two relationships:

$$T_{nr} \propto t^{-0.1} \qquad t \leq 12.5 \text{ s} \qquad (4.11)$$

$$T_{nr} \propto t^{0.04} \qquad 12.5 \text{ s} < t \leq 30 \text{ s} \qquad (4.12)$$

(a) *Short interpass times ($t \leq 12.5$ seconds)*

The relationship between T_{nr} and the deformation parameters in the short interpass time range can be formulated as follows:

$$T_{nr} = A\varepsilon^{-0.12}\dot{\varepsilon}^{-0.01}t^{-0.1} \qquad (4.13)$$

Here A is a fitting constant related to the chemical composition. It can be evaluated from the work of Cuddy[84, 208, 209], who investigated the influence of Nb, Ti, and Al on the recrystallization stop temperature. His results are reproduced in Fig. 4.21, from which the linear T_{RS}-log[Nb] relationship shown in the figure was derived. [Nb] cannot be zero in the equation, so a value of 0.0032 was chosen to represent the lowest [Nb] concentration in carrying out the fitting. The T_{nr} associated with this [Nb] level is that of a simple C-Mn

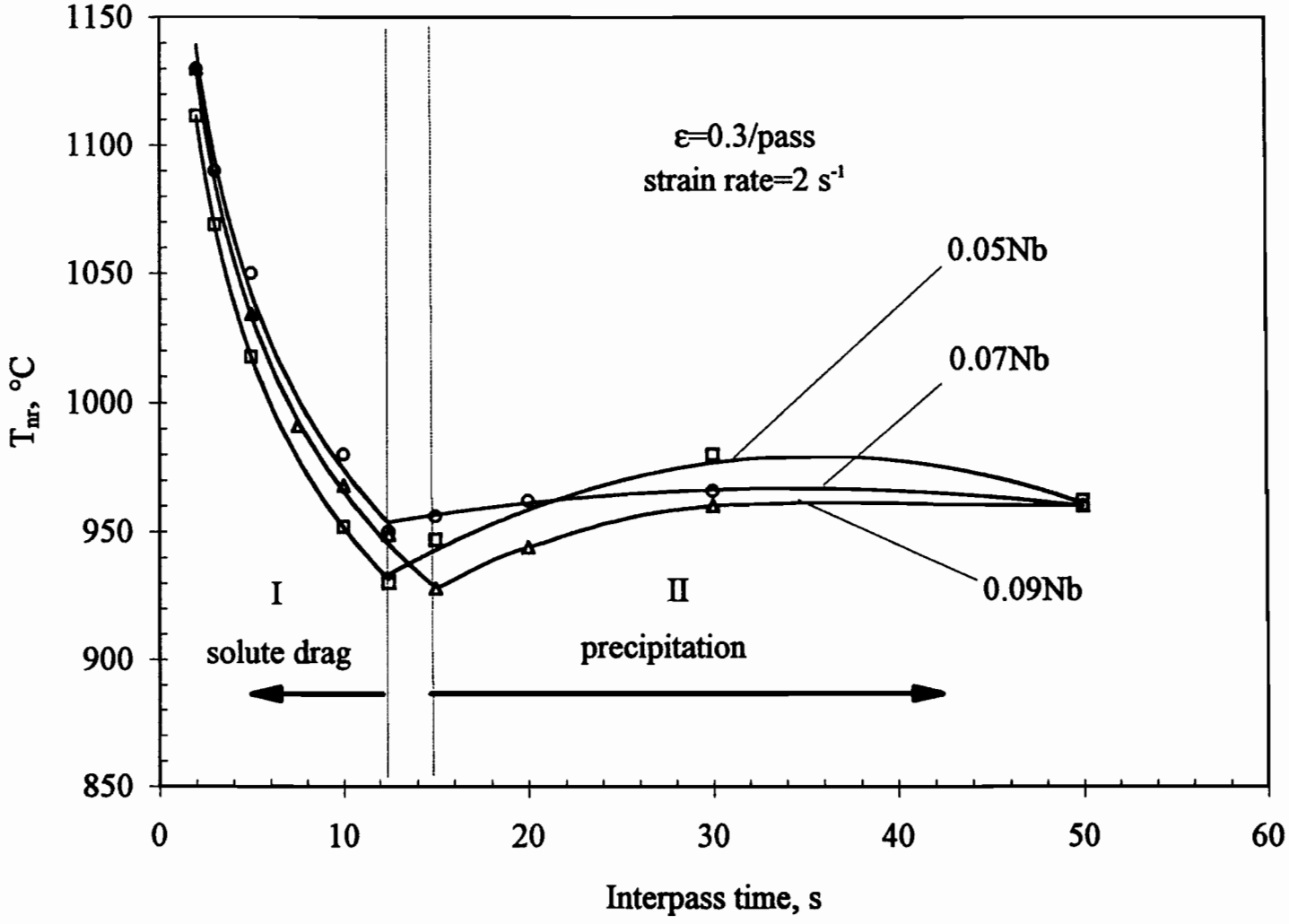

Fig. 4.20 Dependence of T_{nr} on interpass time in three Nb steels.

steel (i.e. ~780 °C). As can also be seen in Fig. 4.21, titanium and aluminum have much weaker effects on the T_{RS}. A similar observation was reported by Boratto et al.[189]. They investigated the effect of chemical composition on the T_{nr}, in the range 0.04~0.17C, 0~0.06Nb, 0~0.06Ti and 0.016~0.052Al, using the same schedule employed in the present work, and obtained the following empirical equation describing the dependence of T_{nr} on chemical composition:

$$T_{nr} = 887 + 464C + \left(6445Nb - 644\sqrt{Nb}\right) + \left(732V - 230\sqrt{V}\right) + 890Ti + 363Al - 357Si \qquad (4.14)$$

From this relationship, it can be seen that each 0.01 percentage increase in the Nb concentration will lead to a 50 °C increase in the T_{nr}, each 0.01 percentage increase in the Ti level will lead to a 10 °C increase in the T_{nr}, while there is only a 4 °C increase for each 0.01% Al concentration increase. This suggests that titanium is only 0.2 times as effective as a recrystallization retardant as niobium, while Al is only about 0.08 times effective as Nb. Thus, as solute drag is considered to be the major factor retarding recrystallization, the equivalent niobium content will be used to express the total solute effect in multiply microalloyed steels, i.e.

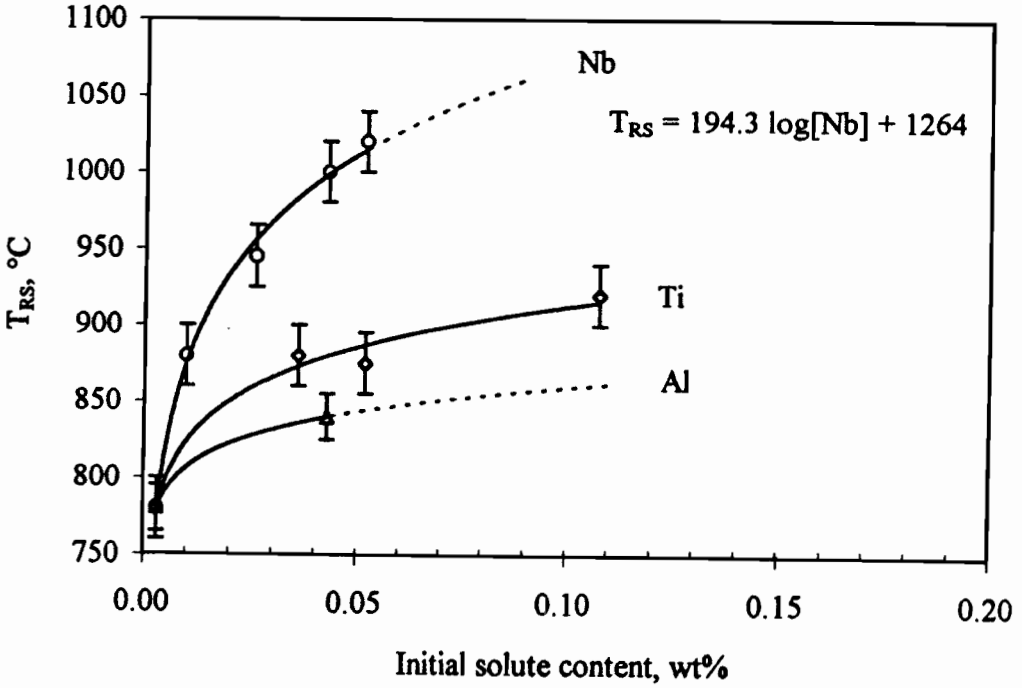

Fig. 4.21 The increase in T_{RS} with increase in the level of microalloy solutes in a 0.07C, 1.4Mn, 0.25Si steel.

$$[Nb]_{eq} = [Nb + 0.22Ti + 0.08Al] \tag{4.15}$$

Then the T_{nr} can be expressed as

$$T_{nr} = \left(A \log[Nb]_{eq} + B\right)\varepsilon^{-0.12}\dot{\varepsilon}^{-0.01}\, t^{-0.1} \tag{4.16}$$

where A=88.1 and B=1156 were derived from the data in Fig. 4.20.

(b) *Long interpass times (t > 12.5 seconds)*

In the long interpass time range, the T_{nr}'s shown in range II of Fig. 4.20 *increase* with interpass time, a dependence that can again be described by a power function.

$$T_{nr} = A'\varepsilon^{-0.12}\dot{\varepsilon}^{-0.01}\, t^{0.04} \tag{4.17}$$

where A' is once more a fitting constant that depends on chemical composition. In this case, it is the solubility product [Nb][C] that is important. Appropriate fitting leads to the following relationship, which is illustrated in Fig. 4.22:

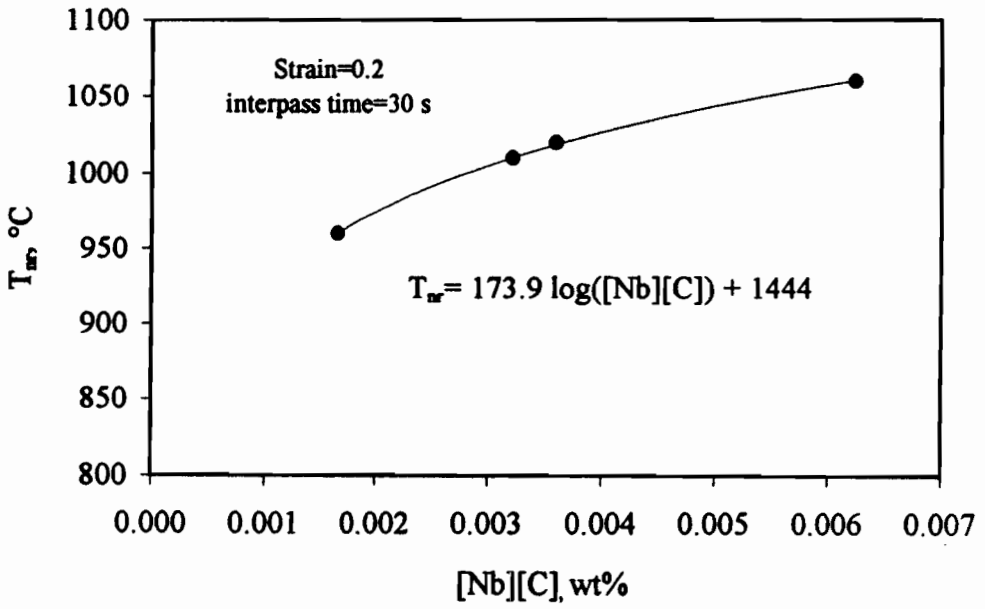

Fig. 4.22 The increase in T_{nr} with increase in the [Nb][C] product.

$$T_{nr} = \left(A' \log([Nb][C]) + B'\right)\varepsilon^{-0.12}\dot{\varepsilon}^{-0.01}t^{0.04} \qquad (4.18)$$

Here A'=63.5 and B'=885. The T_{nr}'s calculated using the above equations are plotted against the measured T_{nr}'s in Fig. 4.23, and good agreement between the two sets of T_{nr}'s is demonstrated.

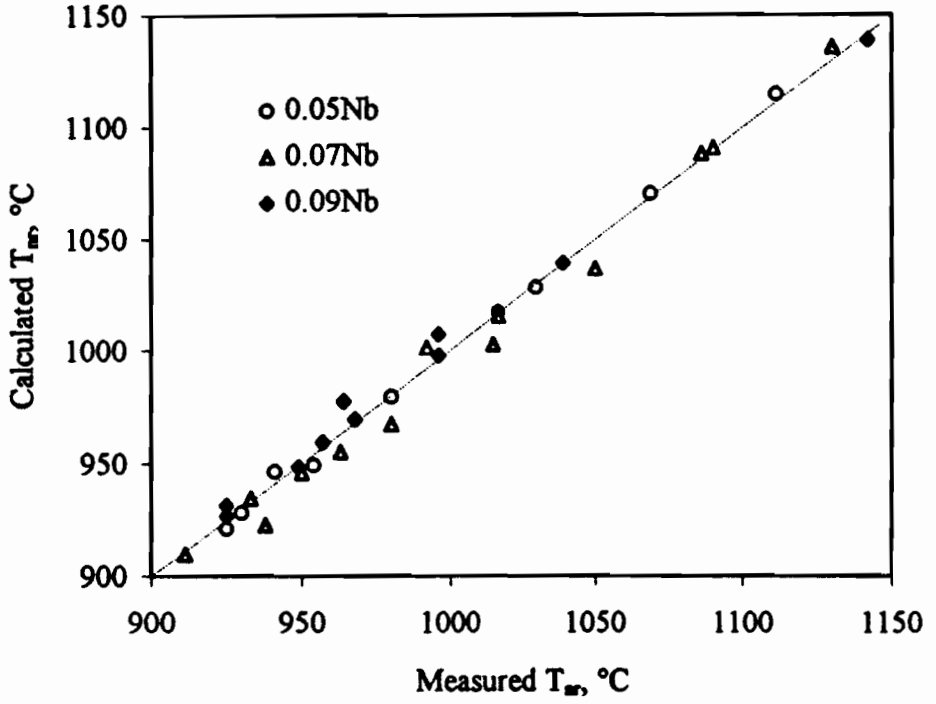

Fig. 4.23 Comparison between predicted and measured T_{nr} values.

A three dimensional plot depicting the dependence of T_{nr} on pass strain and interpass time is presented in Fig. 4. 24. This shows the solution to equation (4.16) for a given composition (Nb=0.09) and strain rate ($\dot{\varepsilon}$=2 s^{-1}). It can be seen that long interpass times together with large pass strains produce lower T_{nr}'s, while short interpass times combined with small pass strains lead to higher T_{nr}'s. Most mill schedules fall between these two extremes. For instance, rolling schedules for hot strip, rod and bar mills consist of short interpass times and fairly large pass strains (and there is also a possibility of strain accumulation), while those for plate mills involve long interpass times and smaller pass strains. In this case, although strain accumulation (pancaking) occurs, dynamic recrystallization is prevented by the copious precipitation that takes place in Nb microalloyed steels. It is of interest to see from Fig. 4. 20 that the T_{nr}'s for hot strip mills are generally higher than for plate mills. *This implies that strain accumulation begins at*

higher temperatures in hot strip than in plate mills. Fig. 4.25 collects the results of two sets of cross sections of Fig. 4.24. In Fig. 4.25(a), where the cross sections are taken at increasing interpass times, the dependence of T_{nr} on pass strain is represented by a set of interpass time contour lines. Fig. 4.25(b) shows the dependence of T_{nr} on interpass time at different strain levels. It can be seen that when the interpass time is less than 5 seconds, the T_{nr} increases significantly when the interpass time is reduced. Equation (4.16) also describes the effect of Nb concentration on the T_{nr}, and it is evident that a small amount of Nb addition to a plain carbon steel is expected to raise the T_{nr} considerably.

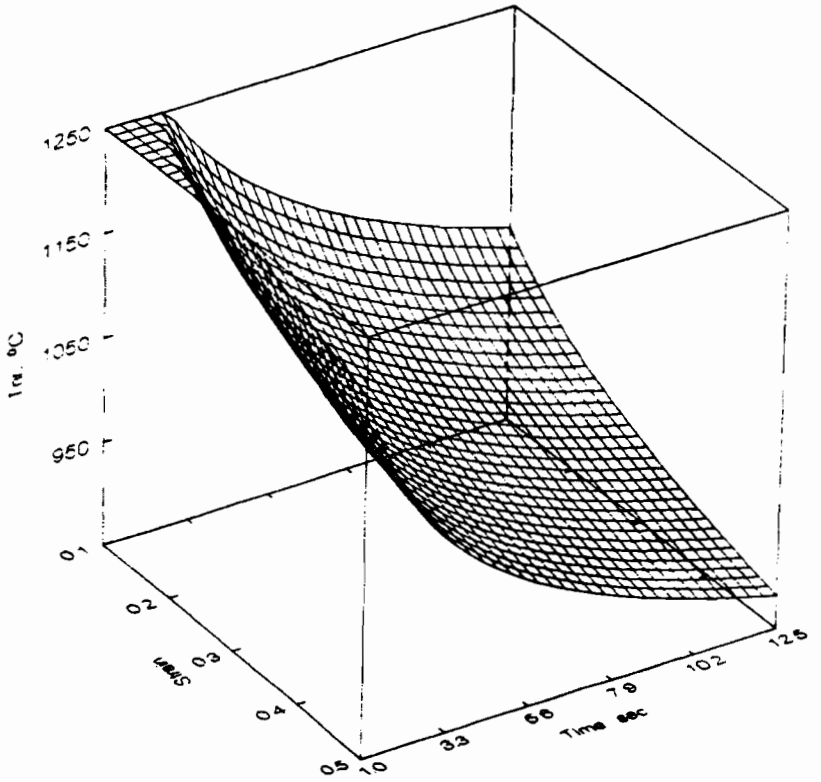

Fig. 4.24 Three dimensional plot of equation (4. 16) corresponding to the condition: strain ≥ 0.05, strain rate = 2 s^{-1}, interpass time ≥ 0.05 second.

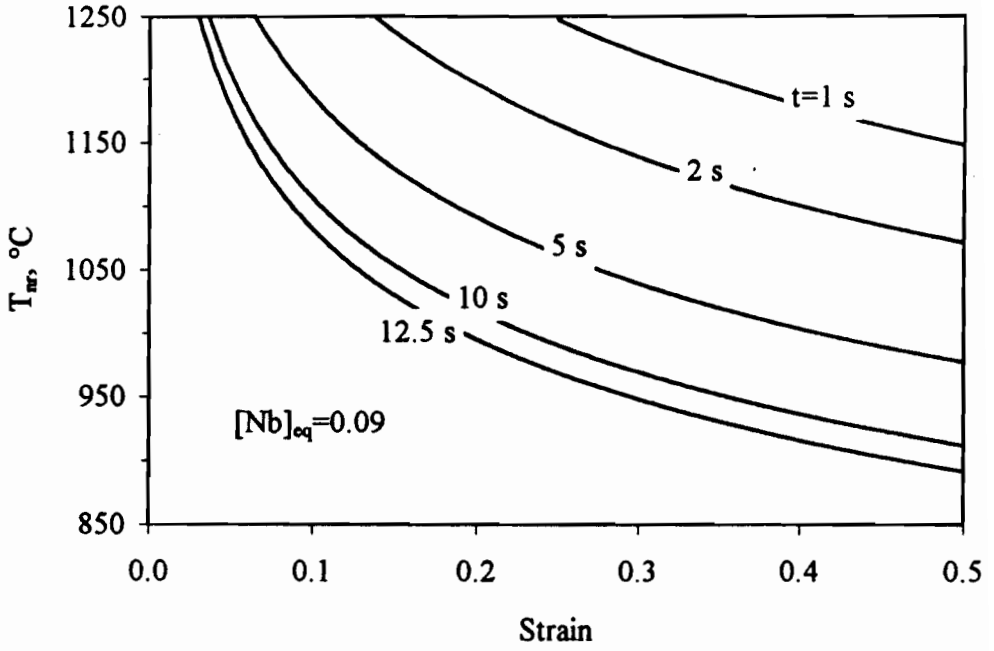

(a)

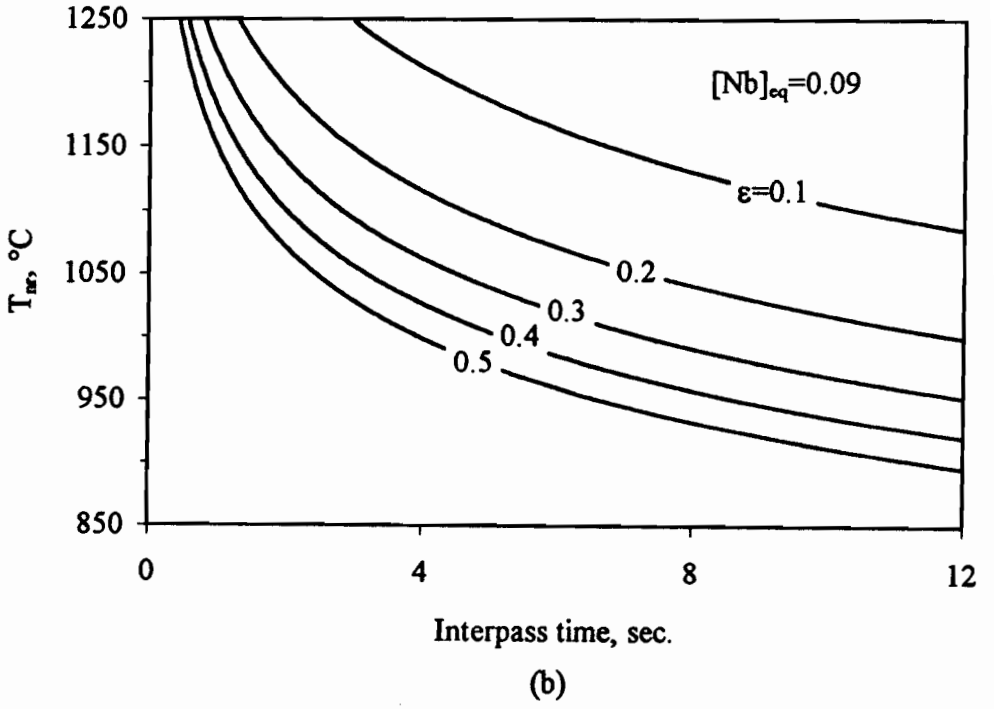

(b)

Fig. 4.25 Dependence of the T_{nr} on (a) strain at different interpass times; (b) interpass times at different strains. On these plots, the results of two sets of cross sections of Fig. 4.24 are collected.

4.3 Discussion

4.3.1 Determination of the Residual Strain

At high deformation temperatures (above the T_{nr}), recrystallization takes place very quickly between passes. Under these conditions, the mean flow stress depends only on temperature, and increases linearly with the inverse absolute temperature (solid line in range I of Fig. 3.10). Below the T_{nr}, the dependence of the mean flow stress on deformation temperature is described by the solid line in range II. Here the residual strain due to incomplete recrystallization (or even the complete absence of recrystallization) is accumulated from pass to pass, and is responsible for the pancaked structure present in the material before the γ-to-α transformation. Knowledge of the residual strain remaining in the material after each pass in range II is important because it affects the ferrite grain size after transformation, and also determines the rolling load in the subsequent pass.

In the partial recrystallization range, the cumulative strain present at the end of the i-th pass, ε^e_i, is given by

$$\varepsilon_i^e = \varepsilon_{i-1}^r + \varepsilon_i \qquad (4.19)$$

where the residual strain that is retained after the (i-1)-th pass is ε^r_{i-1} and ε_i is the strain applied in the pass under consideration. In a similar manner, the residual strain ratio λ that is applicable to the i-th interpass interval can be expressed as

$$\lambda = \frac{\varepsilon_i^r}{\varepsilon_i^e} = \frac{\varepsilon_i^r}{\varepsilon_{i-1}^r + \varepsilon_i} \qquad (4.20)$$

where ε^r_i is now the residual strain retained after the i-th pass.

Two methods have been used in the literature to calculate the residual strain ratio λ. That of Choquet et al.[65] is based on fractional softening. It was derived by measuring the average grain sizes of partially recrystallized structures and comparing the results with the progress of softening in annealed structures. By this means, Choquet et al. derived the following relation between the residual strain and the fraction recrystallized:

$$\lambda = \frac{\varepsilon^r}{\varepsilon^e} = D(1 - X_a) \qquad (4.21)$$

Here X_a is the fraction recrystallized and D is a constant that takes the value 1 when X_a is less than 0.1 and 0.5 when X_a falls between 0.1 and 1. This relation is illustrated schematically in Fig. 4.26.

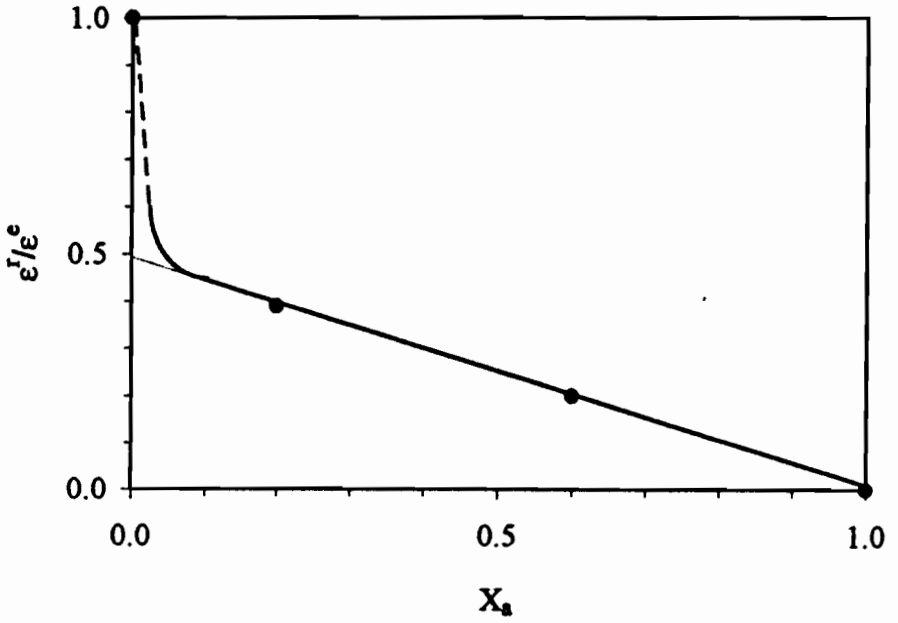

Fig. 4.26 Influence of fractional recrystallization X_a on the residual strain ε^r (ε^e represents the strain applied in the first pass)[65].

The second method, employed by Ouchi et al.[212], is based on the flow curve and is represented schematically in Fig. 4.27. Here the residual strain ratios λ_2 and λ_3 can be calculated from the function $\sigma = f(\varepsilon)$, that represents a single uninterrupted deformation. The residual strain ε^r retained from the first deformation can be obtained by satisfying the relation $f(\varepsilon^r_1+\varepsilon_2)=\sigma_2$. In this case, the residual strain ratio varies from 0 to 1, where λ=0 corresponds to the absence of residual strain and λ=1 represents the absence of softening. However, as shown by Ouchi et al., there is softening by recovery prior to recrystallization. Their results indicate that recovery alone can produce a loss of about 40% in the residual strain, so that λ=0.6 is approximately equivalent to the initiation of static recrystallization. Therefore, the RLT can be identified with λ=0 (i.e. the lowest possible temperature at which complete recrystallization takes place). The RST can in

turn be identified with λ=0.6 (i.e. the highest possible temperature at which recrystallization is completely absent).

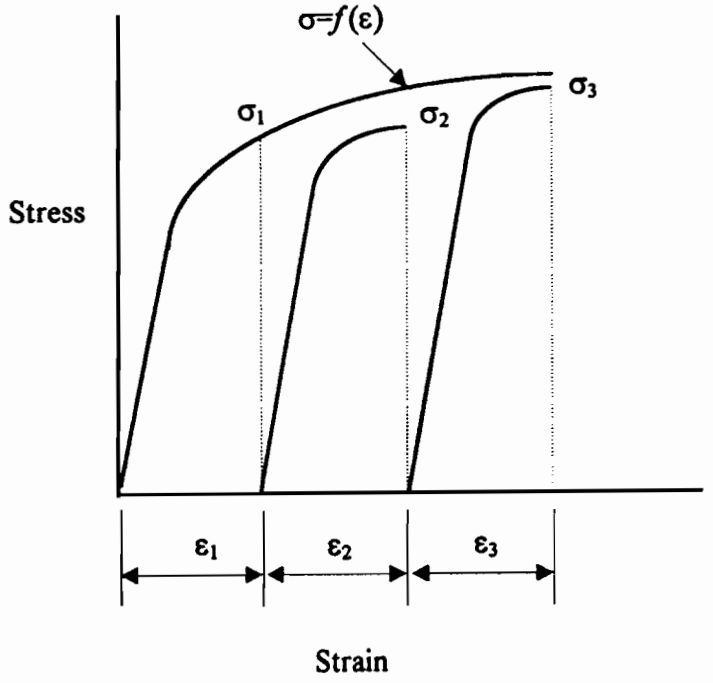

Fig. 4.27 Schematic diagram showing the method used to determine the residual strain by Ouchi et al.[212].

In the present work, a new approach is introduced, which is illustrated in Figs. 4.28 and 4.29. Returning to the 17 pass deformation schedule of Fig. 3.8, the maximum stress for each pass can be plotted against 1000/T in a manner similar to that of the mean flow stress vs. 1000/T diagram of Fig. 3.10. As shown in Fig. 4.28, σ_i^{max} increases linearly with inverse absolute temperature at high temperatures. Under these conditions, the σ_i^{max} vs. 1000/T plot can be described by the linear relation

$$\sigma_o^{max} = a(1000/T)+b \qquad (4.22)$$

where a and b are constants. When the deformation temperature drops below the T_{nr}, the σ_i^{max} vs. 1000/T plot is displaced to the solid line of higher slope because of the retained work hardening.

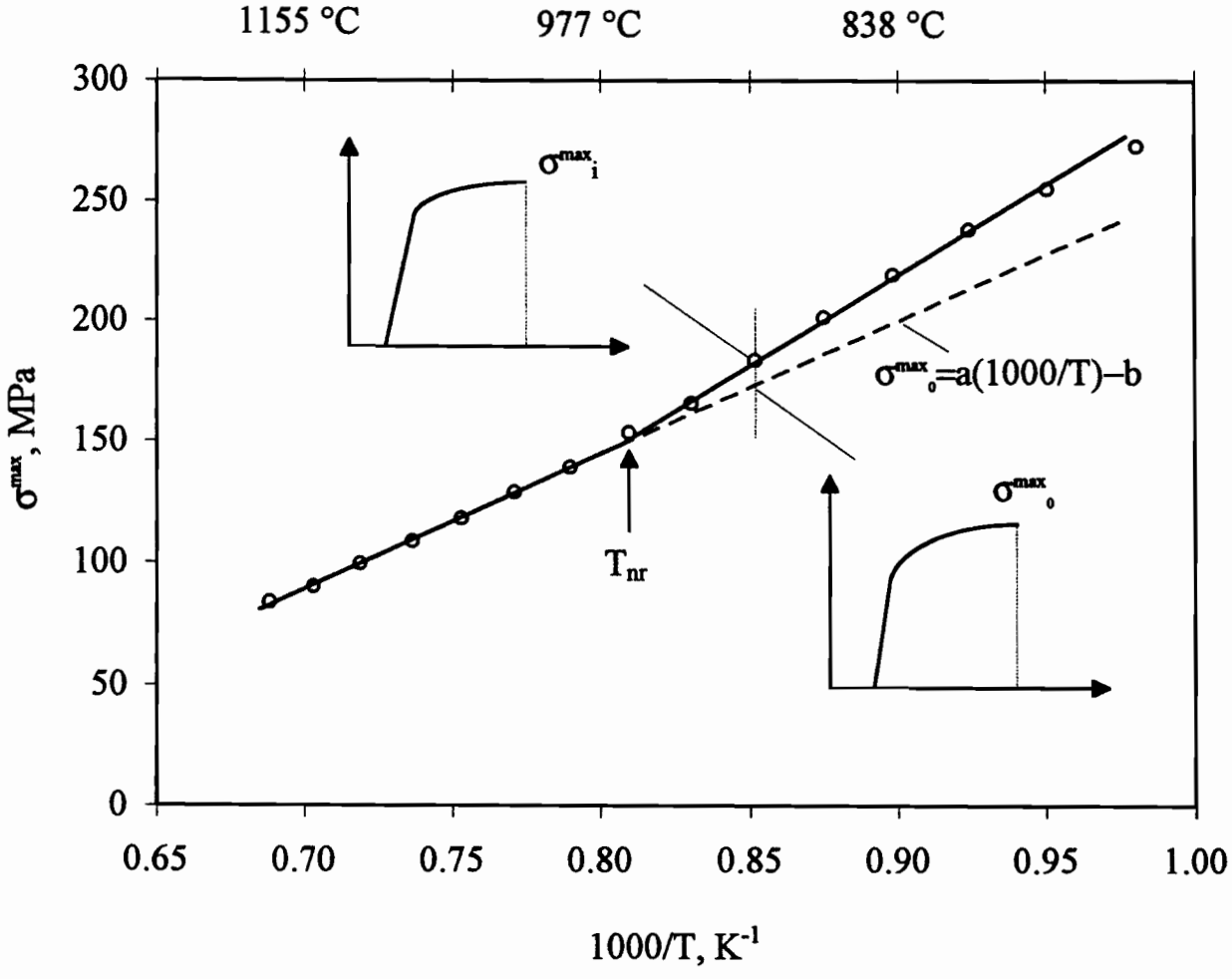

Fig. 4.28 Dependence of the maximum stress on inverse absolute pass temperature.

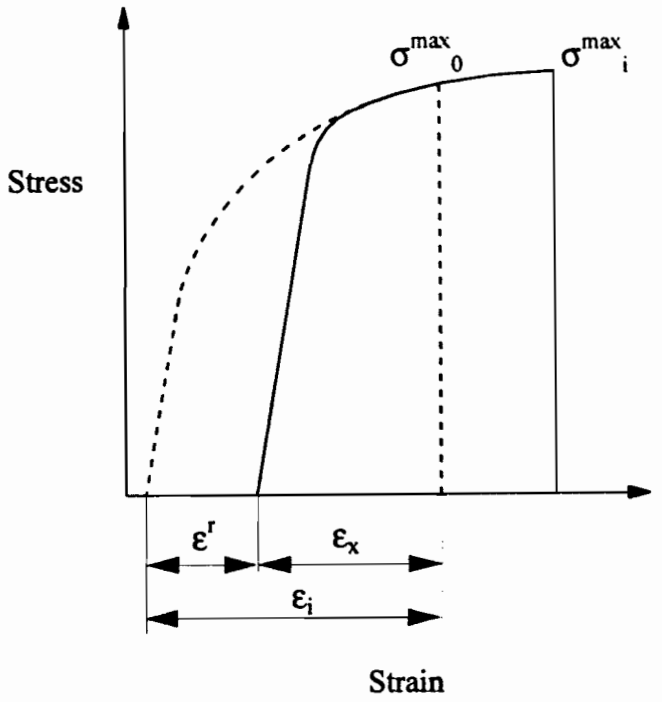

Fig. 4.29 Schematic illustration of the flow curve method for determining the residual strain in 17 pass hot torsion testing. The broken curve represents the absence of residual strain, while the solid curve represents the flow behaviour when there is retained work hardening.

Flow curves corresponding to the presence and absence of retained work hardening are shown in Fig. 4.29. The broken curve represents the absence of residual strain, so that σ^{max}_o at the end of loading is given by equation (4.22); by contrast, the solid curve represents the flow behaviour determined when there is retained work hardening at the same temperature. By marking the point on the solid curve that is equal to σ^{max}_o, the strain ε_x associated with σ^{max}_o is determined. Then, the residual strain ε^r is equal to:

$$\varepsilon^r = \varepsilon_i - \varepsilon_x \qquad (4.23)$$

where ε_i is the pass strain.

The dependence on temperature of the residual strain calculated in this way is shown in Fig. 4.30 for pass strains of 0.3. It can be seen that the residual strain increases almost linearly with decreasing temperature. The residual strain ratio, which is expressed

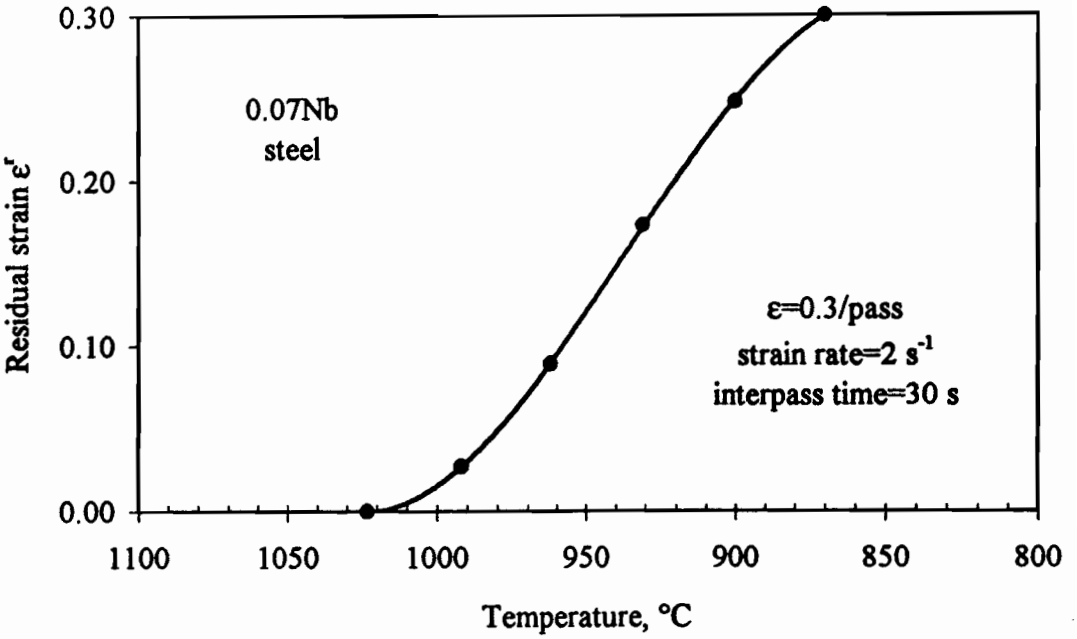

Fig. 4.30 Dependence of residual strain on deformation temperature.

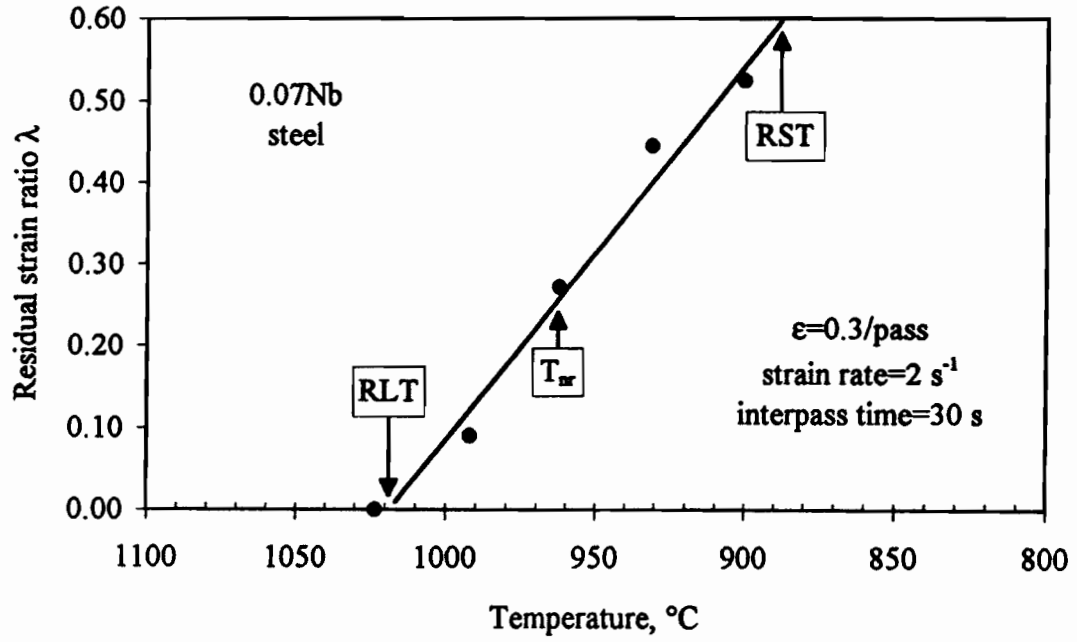

Fig. 4.31 Effect of deformation temperature on the residual strain ratio λ.

as $\lambda = \varepsilon_i^r / \left(\varepsilon_{i-1}^r + \varepsilon_i \right)$, is plotted against temperature in Fig. 4.31. As indicated above, the critical temperatures, RLT and RST, can be determined from Fig. 4.31 by setting λ=0 and λ=0.6, respectively. The RLT and RST temperatures determined in this way are indicated by arrows in the figure. It can be seen that the experimentally measured T_{nr} lies between RLT and RST.

4.3.2. Dependence of the Residual Strain Ratio on Chemical Composition and the Deformation Parameters

The dependence of the residual strain ratio on chemical composition is displayed in Fig. 4.32(a). It can be seen that all the steels have the same temperature dependence (in terms of the slope), although they have different intercepts. The latter generalization is related to the observation that each steel has a different T_{nr}; the effect of steel chemistry can thus be eliminated by normalizing for the effect of composition using the T_{nr}. This is done in Fig. 4.32(b); here T_i/T_{nr} is employed in place of the experimental temperature T_i and the T_{nr} selected is the one that corresponds to the pass strain, strain rate, and interpass time of interest. It is evident that the residual strain ratio only depends on T_i/T_{nr}.

The dependences of the residual strain ratio on the deformation parameters are presented in Fig. 4.33 for the 0.07Nb steel. It can be seen that strain rate does not have a large influence on the residual strain ratio (see Fig. 4.33(a)), whereas the interpass time and pass strain have somewhat greater effects, see Figs. 4.33(b) and (c). These differences can again be reduced by plotting the data against T_i/T_{nr} (see Fig. 4.34). As can be seen from Fig. 4.34(a), the effect of strain rate can be represented by a single straight line (except for the 0.2 s^{-1} data, which are not of interest in hot rolling). A similar insensitivity to interpass time can be deduced from Fig. 4.34(b), as long as the range is restricted to 10 to 30 seconds. The data for 5 seconds, however, lie on a different line, indicating that the dependence of residual strain ratio on temperature must be determined separately when mills with short interpass times are being modelled. The effect of strain is somewhat more complex, although there is not much variation in the strain range 0.3 to 0.5. It can be seen that the *slope* α of the temperature dependence, Fig. 4.34(c), increases with strain, an effect that can be described by the linear relation

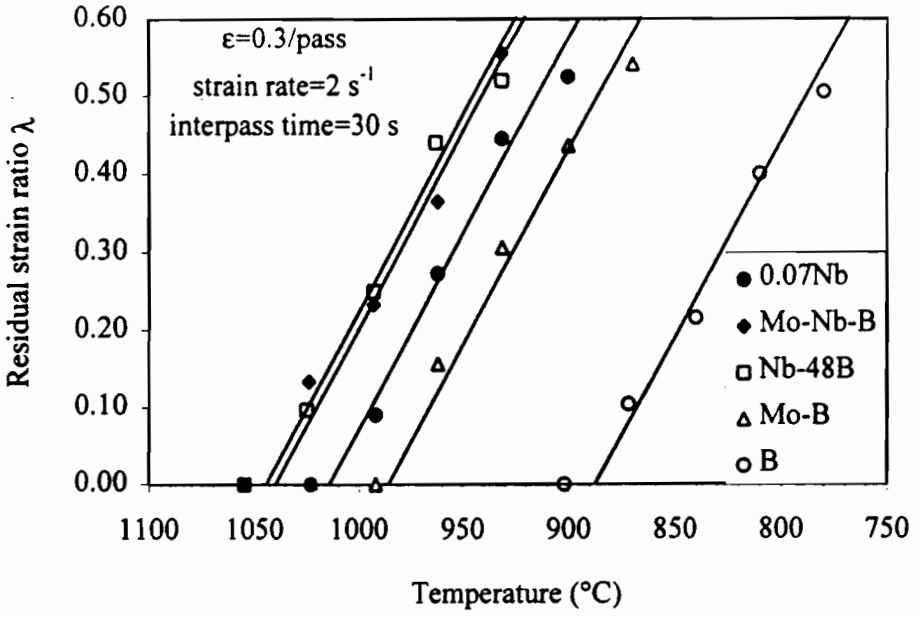

(a)

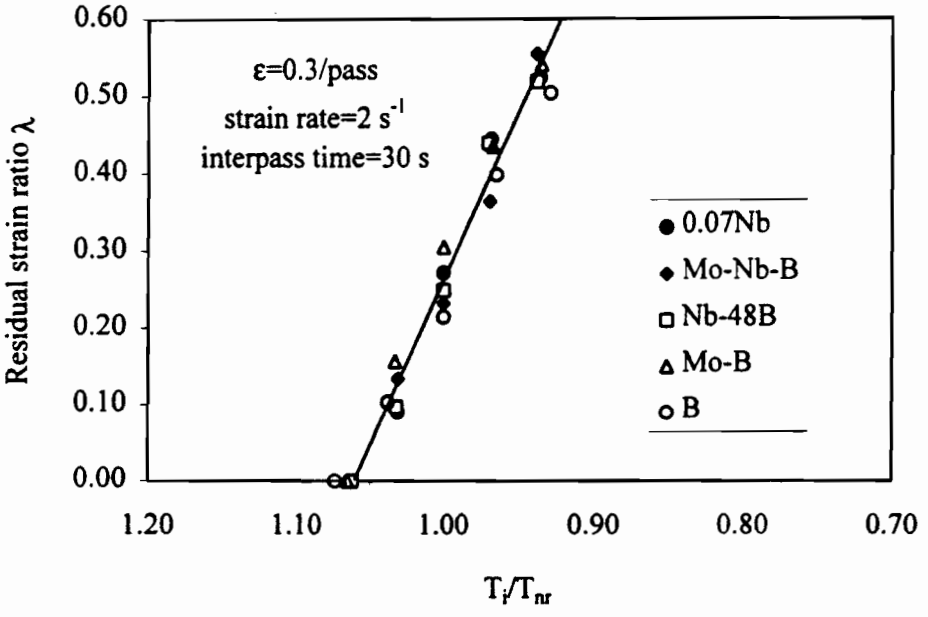

(b)

Fig. 4.32 (a) Effect of chemical composition on the residual strain ratio λ.
(b) Use of the T_{nr}-corrected temperature to represent the effect of chemical composition.

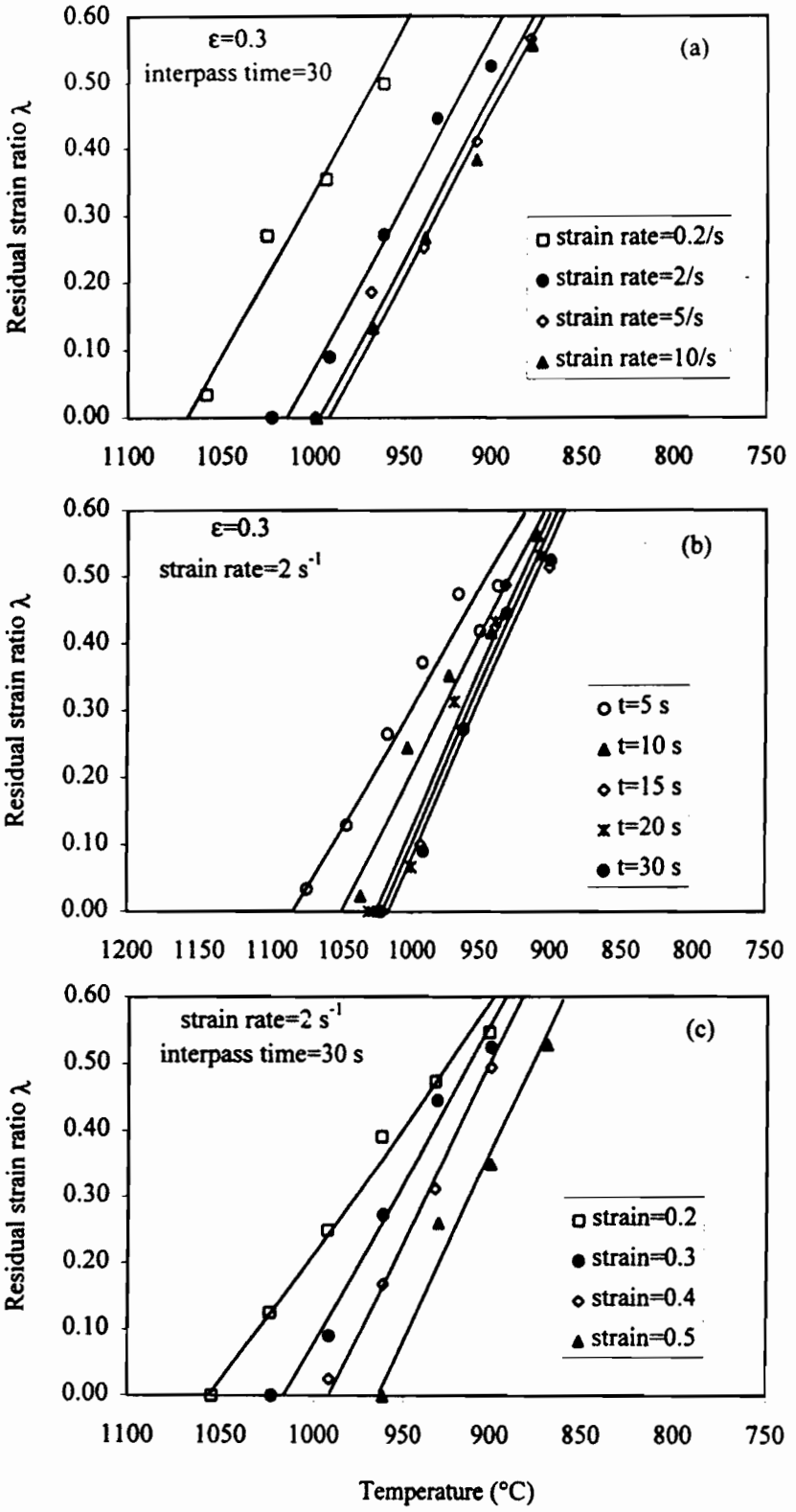

Fig. 4.33 Effect of (a) strain rate, (b) interpass time, (c) pass strain on the residual strain ratio λ in the 0.07Nb steel.

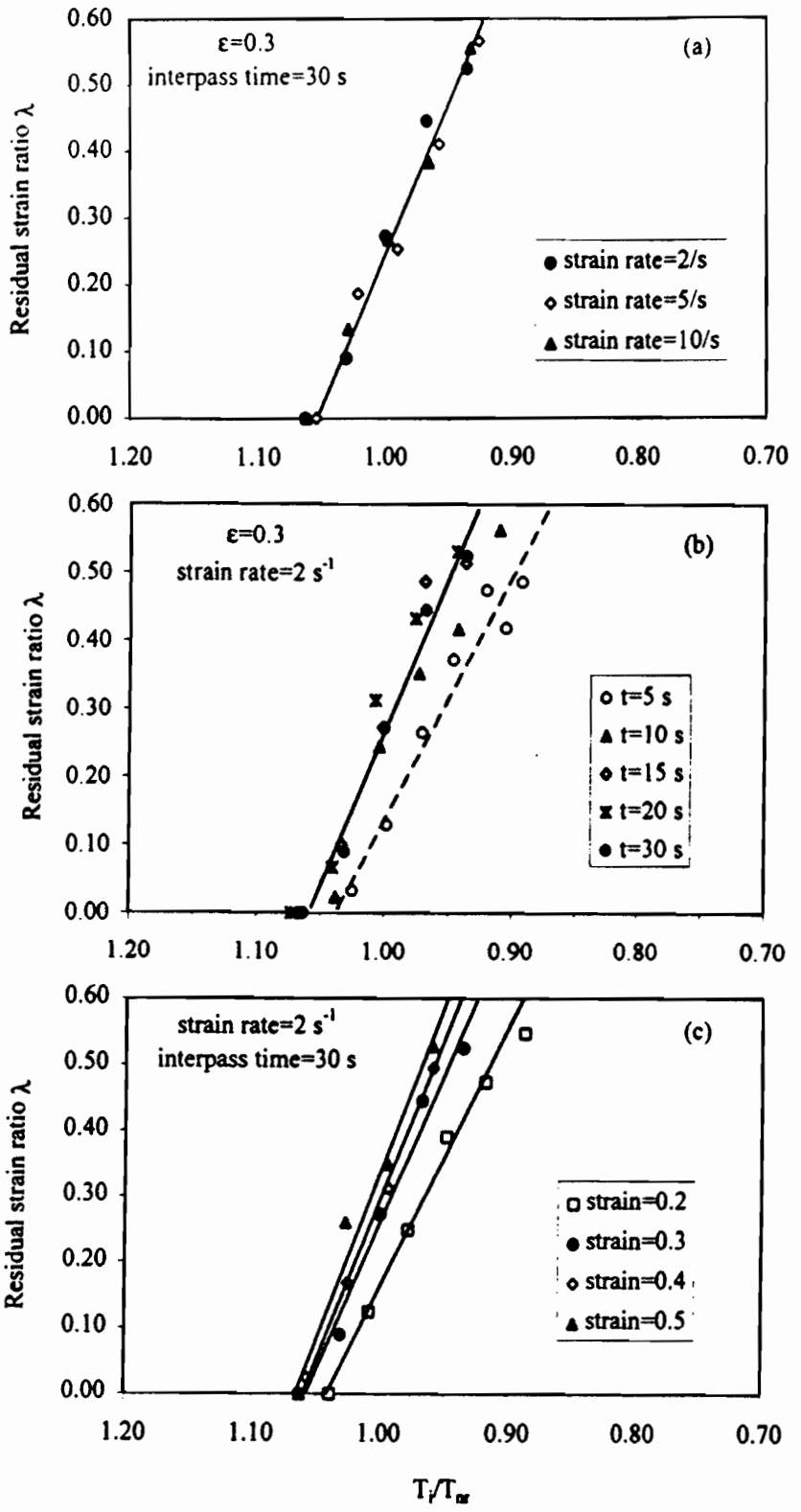

Fig. 4.34 Effect of (a) strain rate, (b) interpass time, (c) pass strain on the T_i/T_{nr} dependence of the residual strain ratio λ in the 0.07Nb steel.

$$\lambda = \alpha(\varepsilon, t_i)\frac{T_i}{T_{nr}} + \beta(\varepsilon, t_i) \qquad (4.24)$$

where $\beta(\varepsilon, t_i)$ represents the intercept. For short interpass times, the dependences of α and β on pass strain can be expressed as:

$$\alpha(\varepsilon) = -(3.1\log(\varepsilon) + 4.95) \qquad t < 10\ s \qquad (4.25)$$

$$\beta(\varepsilon) = 3.52\log(\varepsilon) + 5.3 \qquad t < 10\ s \qquad (4.26)$$

In the interpass time range 10~30 seconds, the dependences of α and β on pass strain can be expressed as:

$$\alpha(\varepsilon) = -(3.1\log(\varepsilon) + 5.93) \qquad 10\ s \le t \le 30\ s \qquad (4.27)$$

$$\beta(\varepsilon) = 3.52\log(\varepsilon) + 6.4 \qquad 10\ s \le t \le 30\ s \qquad (4.28)$$

This approach leads to the following empirical equations for calculating the residual strain ratio:

$$\lambda = (3.52\log(\varepsilon) + 5.3) - (3.1\log(\varepsilon) + 4.95)\frac{T_i}{T_{nr}} \qquad t < 10\ s \qquad (4.29)$$

$$\lambda = (3.52\log(\varepsilon) + 6.4) - (3.1\log(\varepsilon) + 5.93)\frac{T_i}{T_{nr}} \qquad 10\ s \le t \le 30\ s \qquad (4.30)$$

The values of λ calculated using the above equations are plotted in Fig. 4.35 against the λ ratios measured from the flow curves. It can be seen that most of the points fall between two lines with slopes of 0.82 and 1.13 (i.e. within about ±15%). The dependences of RLT and RST on pass strain calculated in this way for the 0.07 Nb steel are presented in Fig. 4.36, together with the T_{nr}'s determined experimentally. It is evident that the T_{nr}'s fall between RLT and RST in the pass strain range 0.2~0.5. The spread of 100 to 150 °C between these two temperatures indicates the range over which duplex microstructures can be produced by partial recrystallization. Equations (4.29) and (4.30) can be used in grain size and rolling load predictions when the hot rolling of Nb steels is being modelled.

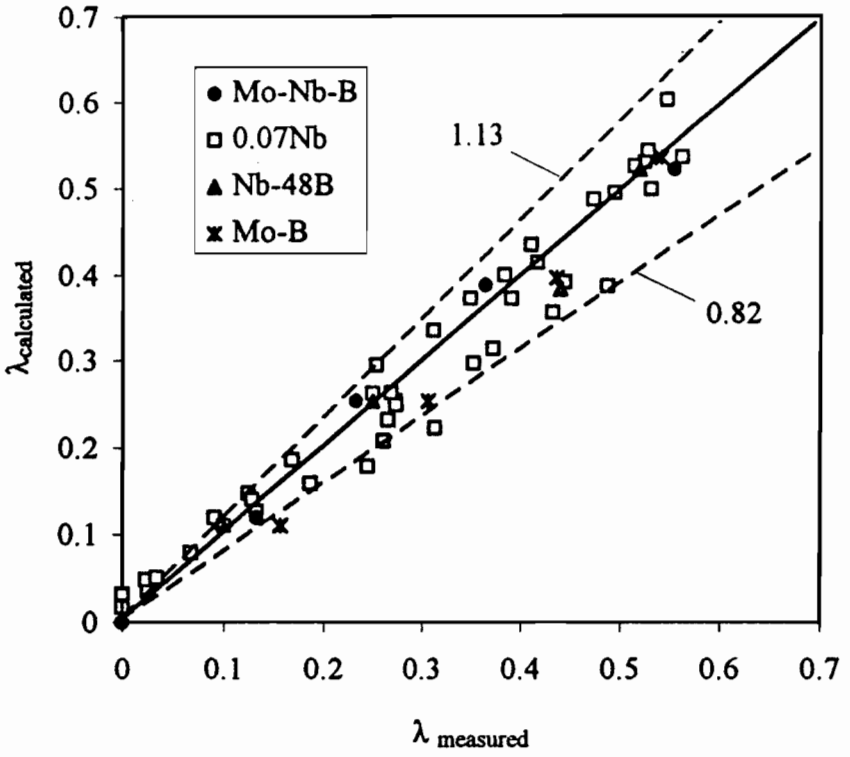

Fig. 4.35 Comparison between measured and calculated λ values.

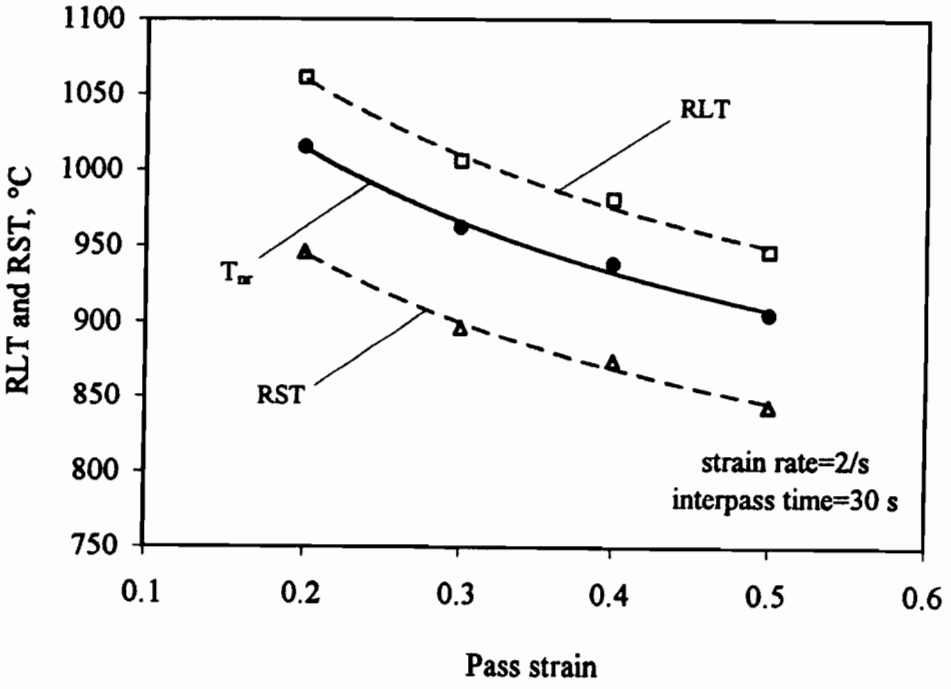

Fig. 4.36 Calculated values of RLT and RST in the 0.07Nb steel compared with the experimentally determined T_{nr}'s.

Fig. 4.37 shows more λ-T plots determined experimentally on the 0.07Nb steel. The change in slope of the residual strain ratio in the figure can be interpreted in terms of the occurrence of precipitation. Park and Jonas[182] calculated the precipitation kinetics during continuous cooling from isothermal data, and showed that the higher the cooling rate, the lower the precipitation start temperature (T_{Ps}) and the shorter the precipitation start time (t_{Ps}). For instance, they showed that the T_{Ps} decreases from 955 °C to 910 °C when the cooling rate increases from 0.2 °C/s to 1.5 °C/s in a 0.07C-0.04Nb steel.

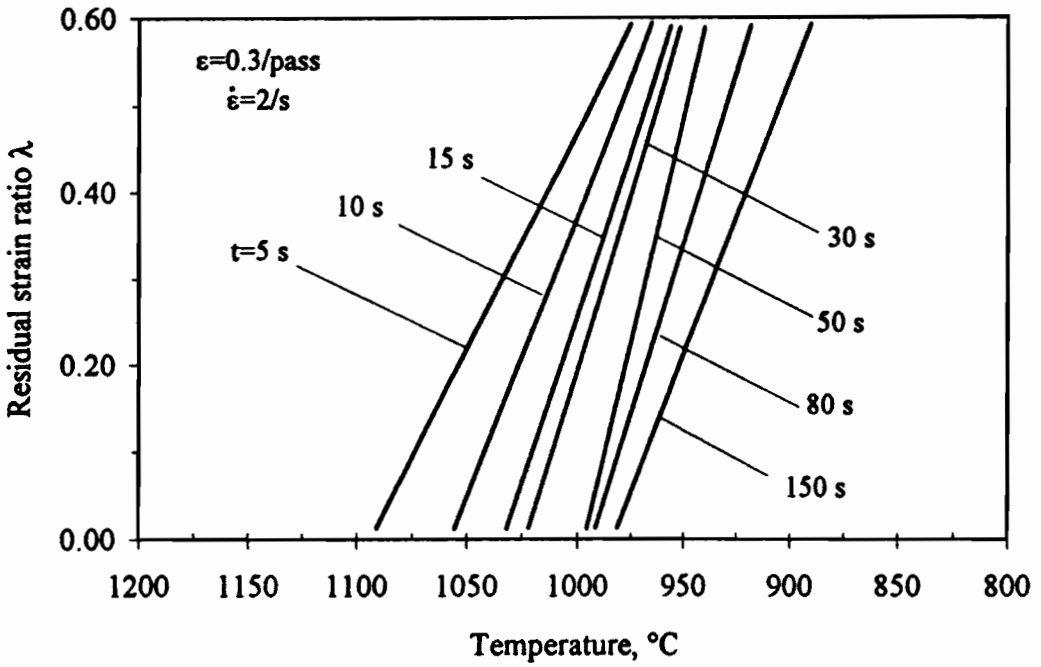

Fig.4.37 Effect of interpass time on the residual strain ratio in the 0.07Nb steel.

The cooling rate employed in the present work ranged from 6 °C/s (in the case of the 5 s interpass times) to 0.2 °C/s (in the case of the 150 s interpass times). The estimated T_{Ps} is about 910 °C when the cooling rate is 6 °C/s; thus rises to 958 °C when the cooling rate is decreased to 0.6 °C/s. Therefore, in the case of short interpass times (or high cooling rates), there is no interaction between recrystallization and precipitation since the T_{Ps} is lower than the RST. Thus, the recrystallization process is controlled mainly by solute drag, and the residual strain is accumulated at a lower rate. In the longer interpass time range (or at lower cooling rates), the T_{Ps}'s are higher and well above the calculated RST; an interaction between recrystallization and precipitation is therefore expected to take place. The recrystallization process is slowed down by freshly precipitated Nb(CN); this leads to a higher rate of strain accumulation. The interaction is reflected by the

increase in the slope of the residual strain ratio as the interpass time is increased (or the cooling rate is decreased) in Fig. 4.32. A very long interpass time (e.g. 150 seconds), however, leads to precipitate coarsening. This weakens the retardation of recrystallization by the precipitates and consequently leads once again to a slower rate of strain accumulation (reflected by the decrease in the slope of the residual strain ratio at $t \geq 80$ seconds).

It can be concluded that at temperatures above the RLT, full recrystallization takes place and there is no strain accumulation. At temperatures between the RLT and RST, i.e. in the partial recrystallization region, the strain accumulates at the rate described by equations (4.29) and (4.30). Finally, at temperatures below the RST, recrystallization is stopped completely, and the strain is accumulated fully (simply by adding the pass strains).

4.3.3 Prediction of the T_{nr}

When "long" interpass times are involved, the T_{nr} is a result of the retardation of recrystallization by Nb(CN) precipitation. It is therefore important to model Nb(CN) precipitation in order to predict the T_{nr} under these conditions. The following subsections deal with this matter.

4.3.3.1 Kinetics of Nb(CN) Precipitation

The precipitation of Nb(CN) in HSLA steels has been widely investigated during the past twenty years. It has been shown that the steady state nucleation rate of Nb(CN) follows the classical nucleation theory and can be expressed as[213]

$$J = N\frac{DX}{a^2}\exp\left(-\frac{\Delta G^*}{kT}\right) \qquad (4.31)$$

where D and X are the diffusivity and concentration of the element that is rate controlling the nucleation process, a is the lattice parameter of the austenite, N is the number of potential nucleation sites per unit volume of the matrix, ΔG^* is the critical free energy for nucleation, and finally k and T have their usual meanings. Since the diffusivity of Nb in austenite is much lower than those of C and N, the former is assumed to be rate controlling with regard to Nb(CN) nucleation. Kurokawa et al.[214] have shown that the diffusion coefficient of Nb in austenite is independent of steel composition and the values

they reported of D_0=1.4x10^{-4} m^{2}s^{-1} and Q=270 kJ/mol can be used to calculate the diffusivity D in equation (4.31).

Following Aaronson and Lee[215], the critical free energy in equation (4.31) can be expressed as

$$\Delta G^* = \frac{16\pi(\xi\gamma)^3}{3(\Delta G_{chem})^2} \qquad (4.32)$$

where ΔG_{chem} is the chemical free energy change (often termed chemical driving force), γ is the unit interfacial energy of the nucleus-matrix interface, and ξ is a γ modifier which takes into account the interaction energy associated with nucleation on dislocations.

According to Dutta and Sellars[180], the chemical free energy can be related to the supersaturation ratio, k_s as follows:

$$\Delta G_{chem} = -\left(\frac{RT}{V_m}\right)\ln k_s \qquad (4.33)$$

where V_m is the mole fraction of Nb(CN), and the value V_m=1.28x10^{-5} m^3/mol is used in the calculation. In deformed austenite, dislocations are preferred nucleation sites for strain-induced Nb(CN) precipitation, and the potential nucleus site density can be estimated from[213]

$$N = \frac{\rho}{a} \qquad (4.34)$$

where ρ is the dislocation density. Then, equation (4.31) can be rewritten for Nb(CN) precipitation as

$$J = \frac{\rho D_0}{a^3}[Nb]\exp\left(-\frac{Q}{RT}\right)\exp\left(-\frac{16\pi(\xi\gamma)^3 V_m{}^2}{3kT\left(-RT\ln k_s\right)^2}\right) \qquad (4.35)$$

The number of nuclei per unit volume formed during a time interval t can thus be expressed as

$$N = \int_0^t J dt \tag{4.36}$$

Considering that the critical number of nuclei per unit volume (N_c) must be available at $t=P_s$ for precipitation to be detectable (often referred to as the time for 5% volume fraction of precipitation), then

$$P_s = \frac{N_c}{J} \tag{4.37}$$

The combination of equations (4.35) and (4.37) leads to

$$P_s = C[Nb]^{-1} \exp\left(\frac{270000}{RT}\right) \exp\left(\frac{B}{T^3(\ln k_s)^2}\right) \tag{4.38}$$

where $C=N_c a^3/\rho D_0$, and $B=16\pi(\xi\gamma)^3 V_m/3kR^2$. The generation of dislocations by deformation is related to the strain, strain rate and deformation temperature; thus the constant C can be further expressed as a function of strain and Zener-Hollomon parameter. According to Dutta and Sellars[180], the constant C has the following form:

$$C = A\varepsilon^{-1}Z^{-0.5} \tag{4.39}$$

Replacing P_s in equation (4.38) by $t_{0.05p}$, i.e. the time for 5% precipitation, leads to

$$t_{0.05p} = A\varepsilon^{-1}Z^{-0.5}[Nb]^{-1} \exp\left(\frac{270000}{RT}\right) \exp\left(\frac{B}{T^3(\ln k_s)^2}\right) \tag{4.40}$$

The constants A and B can be obtained by fitting experimental data, and $A=3\times10^{-6}$ and $B=2.5\times10^{10}$ were reported for steels in the composition range 0.03~0.084 wt% Nb, 0.06~0.17 wt% C, and 0.005~0.015 wt% N[180]. For steels with lower carbon concentrations, the reported values of A and B are entirely unsatisfactory. Taking the results of Yamamoto et al.[148] as an example (see Fig. 4.38), the predicted PTT curve using the

above values of A and B is shifted down and to the left compared to the measured one. A better fit was obtained with $A=3.5\times10^{-4}$ and $B=0.25\times10^{10}$.

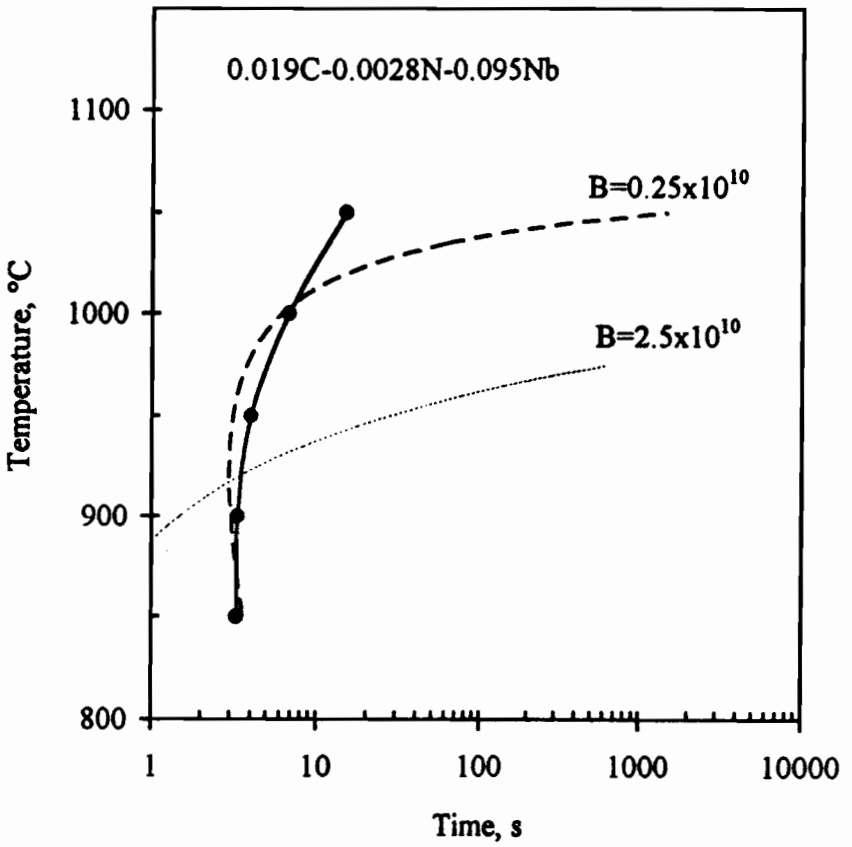

Fig.4.38 Comparison of observed PTT curve[148] with curve calculated from equation (4.40).

The results in Fig. 4.38 indicate that the constants A and B are likely to be composition dependent. Some authors have indeed suggested that the solubility product equation of Irvine et al. might not be applicable to ultralow carbon steels[148, 180]. Furthermore, Akamatsu et al.[149] have indicated that the kinetics of MC precipitation are influenced, not only by the precipitate-forming atom product, M×C, but also by the ratio, M/C. Since no solubility product equation for ultralow carbon microalloyed steels is available in the literature, the suggestion by Akamatsu et al. is taken into account in the present work. This is further demonstrated in Fig. 4.39 by comparing the observed PTT curve of Djahazi[133] with the one calculated from equation (4.40). The calculated PTT

curve is in reasonable agreement with the measured one when the constants A and B take the values 3.6×10^{-5} and 1.1×10^{10}, respectively.

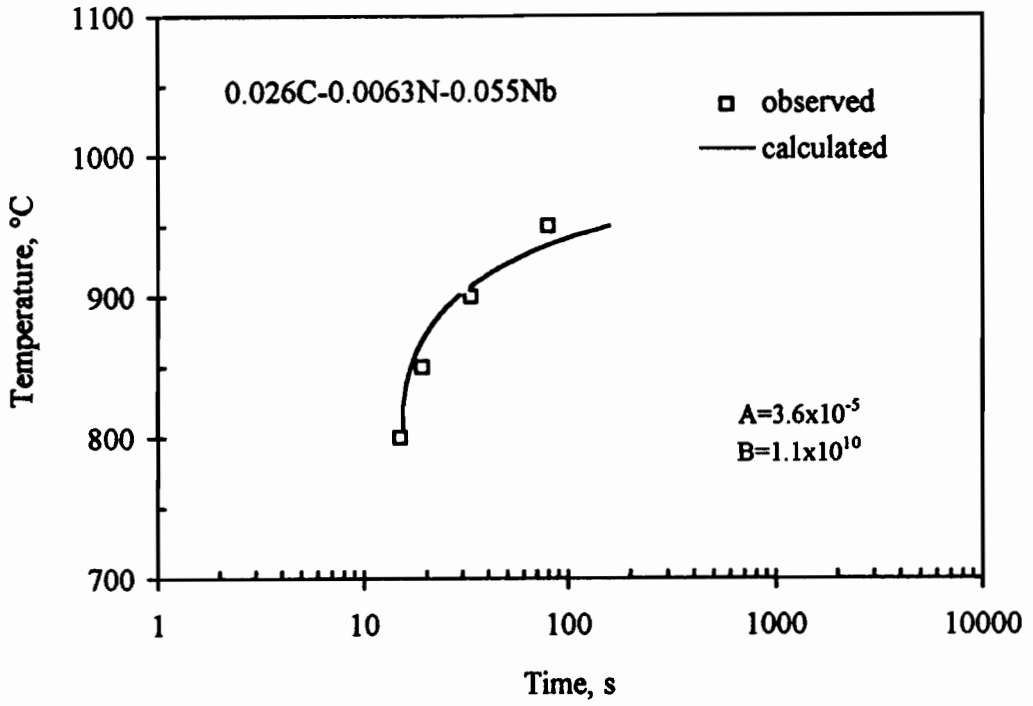

Fig. 4.39 Comparison of observed PTT curve[133] with curve calculated from equation (4.40).

Table 4.3 Evaluation of the constants A and B in equation (4.40)

Author	Steel	Nb/C (atomic ratio)	Condition	A $\times10^{-6}$	B $\times10^{10}$
Ouchi et al.[174]	0.16C-0.05N-0.031Nb	0.025	deformed (ε=0.8)	10	2.5
Weiss and Jonas[216]	0.05C-0.04N-0.035Nb	0.09	deformed (ε=0.06)	2	1.2
Hansen et al.[142]	0.1C-0.01N-0.095Nb	0.122	deformed (ε=0.8)	10	1.5
Watanabe et al.[175]	0.08C-0.015N-0.06Nb	0.172	deformed (ε=0.41)	25	4
Djahazi [133]	0.026C-0.0063N-0.055Nb	0.273	deformed (ε=0.33)	36	1.1
Yamamoto et al.[148]	0.019C-0.0028N-0.095Nb	0.645	deformed (ε=0.69)	310	0.25

Table 4.3 summarizes the values of the constants A and B that were used in this investigation to fit the experimental data reported by the authors in the table. The test conditions and Nb/C atomic ratios are also listed in this table. It can be seen that the constant A generally increases with Nb/C ratio, while the constant B decreases with increases in the ratio. These trends are further illustrated in Figs. 4.40 (a) and (b); the dependences of A and B on the Nb/C ratio shown there can be expressed as:

$$A = 3.17 \times 10^{-6} \exp(7.5Nb/C) \tag{4.41}$$

$$B = 2.95 \times 10^{10} \exp(-3.6Nb/C) \tag{4.42}$$

There are no obvious physical meanings for the constants A and B. In the original derivation, the constant A included the critical number of nuclei per unit volume (N_C^*), which was treated as composition independent by Dutta and Sellars. In fact, the number of nuclei provided by composition fluctuations in the material can be expected to be associated with the density of Nb atoms available. A higher niobium concentration could supply more Nb atoms (or clusters) in a given material, so that, at a given interaction time, the probability of more nuclei emerging in the material will be higher. In other words, for a given volume fraction of precipitation (e.g. 5%), the interaction time could be shorter in high Nb than in low Nb steels. Akamatsu et al. suggested that a local equilibrium might apply when the Nb/C ratio is high. Furthermore, they applied this concept to the evaluation of Nb(CN) precipitation in ultralow carbon Nb steels (with atomic ratios of Nb/C > 1).

The constant B includes the interfacial energy (γ) and a modifier (ξ). The interfacial energy γ is usually constant for a particular type of interface (e.g. γ=0.5 Jm^{-2} for incoherent interfaces[217]). The modifier ξ is a measure of the interaction energy between the surface of a nucleus and the surrounding dislocations. It is unity when nucleation is homogeneous and less than unity when nucleation is heterogeneous. Values ranging from 0.19 to 0.55 were reported by Dutta and Sellars for Nb(CN) nucleation[180], and values ranging from 0.35 to 0.51 were reported by Liu and Jonas for Ti(CN) nucleation[181]. Furthermore, Djahazi et al. reported that the ξ value decreased from 0.41 to 0.38 when boron was added to a niobium bearing steel[183]. Table 4.4 summarizes the ξ values reported in the literature.

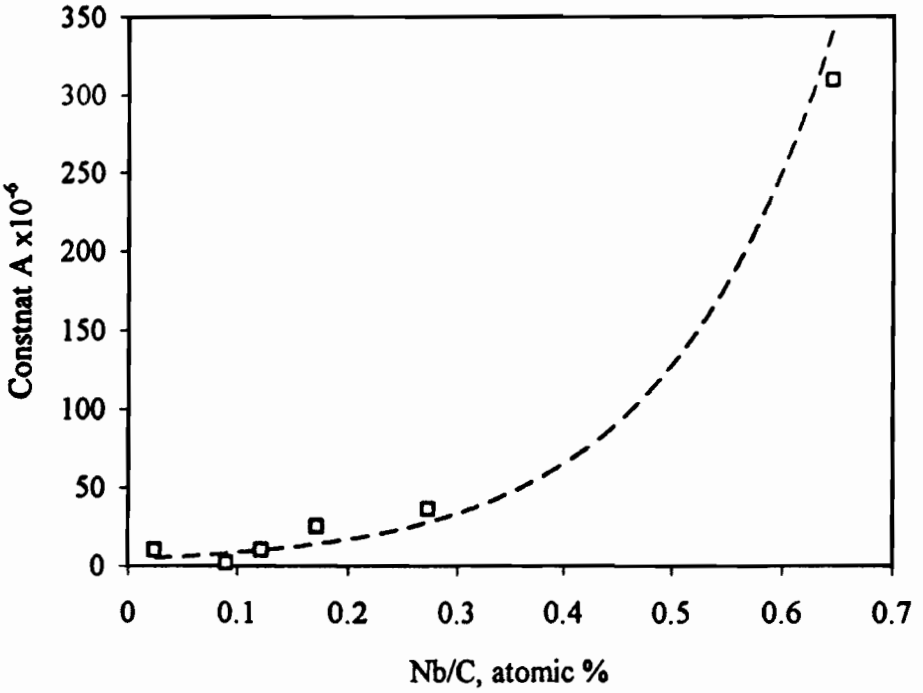

(a)

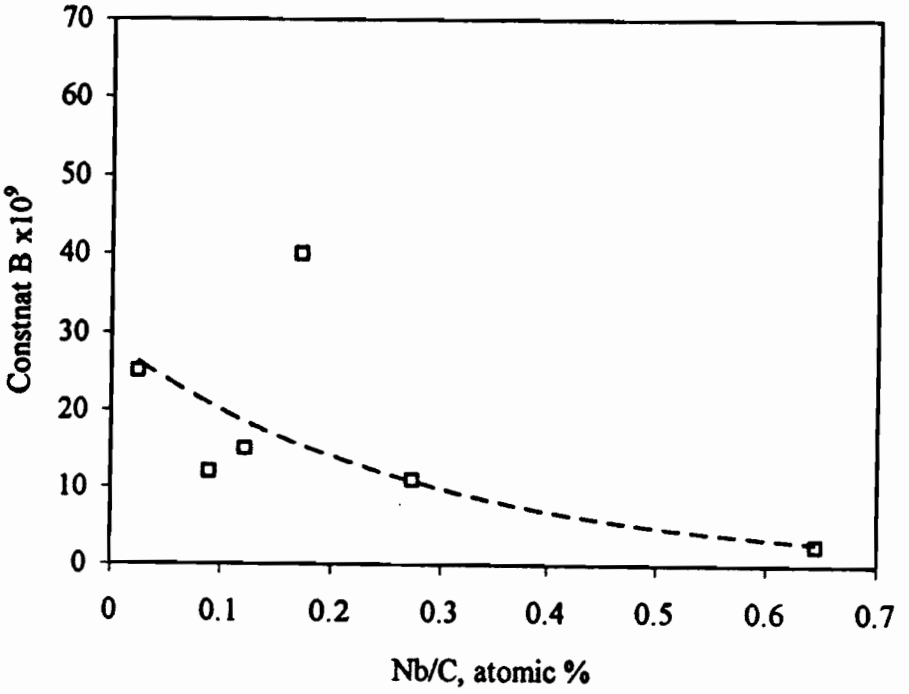

(b)

Fig.4.40 Effect of Nb/C atomic ratio on the (a) constant A and (b) constant B in equation (4.40).

Table 4.4 Values of the modifier ξ reported in the literature

Author	Steel	M/C, atomic ratio	ξ
Le Bon et al.[57]	0.17C-0.011N-0.04Nb	0.030	0.55
Watanabe et al.[175]	0.08C-0.015N-0.06Nb	0.172	0.48
Djahazi et al.[133]	0.026C-0.0063N-0.055Nb	0.273	0.31
Yamamoto et al.[148]	0.019C-0.0028N-0.095Nb	0.645	0.19
Liu and Jonas[181]	0.071C-0.026Ti	0.091	0.51
	0.057C-0.066Ti	0.289	0.35
	0.066C-0.102Ti	0.386	0.37
	0.041C-0.177Ti	1.079	0.38

Liu and Jonas suggested that the high ξ value for their 0.026Ti steel might be attributable to the inaccurate measurement of t_{Ps} because of the lack of data points. Dutta and Sellars, on the other hand, attributed the differences to the different methods used for the detection of precipitation by different authors. Nevertheless, the tendency demonstrated by the data in Table 4.4 implies that the value of the modifier ξ is related to the atomic ratio of the precipitate forming elements in the steel: the higher the atomic ratio, the lower the value of ξ will be. This is probably responsible for the variation in the constant B with steel composition.

The A's and B's determined from equations (4.41) and (4.42) for the 0.05Nb and 0.09Nb steels are listed in Table 4.5, and will be used in the calculations that follow.

Table 4.5 Constants A and B used in equation (4.40)

Steel	A	B
0.05Nb	4.6×10^{-6}	2.45×10^{10}
0.09Nb	2.8×10^{-5}	1.0×10^{10}

4.3.3.2 Modifying the Recrystallization Kinetics of Nb Steels

(a) Microstructural evolution during multipass deformation

At temperatures above the T_{nr}, the austenite grain size is refined by repeated recrystallization, and the recrystallized grain size is described by the equation:

$$d_{rex} = A d_0^p \varepsilon^{-q} \qquad (4.43)$$

where A, p, and q are constants. Values for A, p, and q reported in the literature range from 0.33 to 1.8, 0.15 to 1, and 0.5 to 0.7, respectively. In the present work, it was found that the grain sizes predicted using the models proposed by Sellars for Nb steels are finer than the measured ones (see Fig. 4.41). To obtain better predictions for multipass deformation, A=1.3 was employed for the 0.09Nb steel and A=1.6 for the 0.05Nb steel.

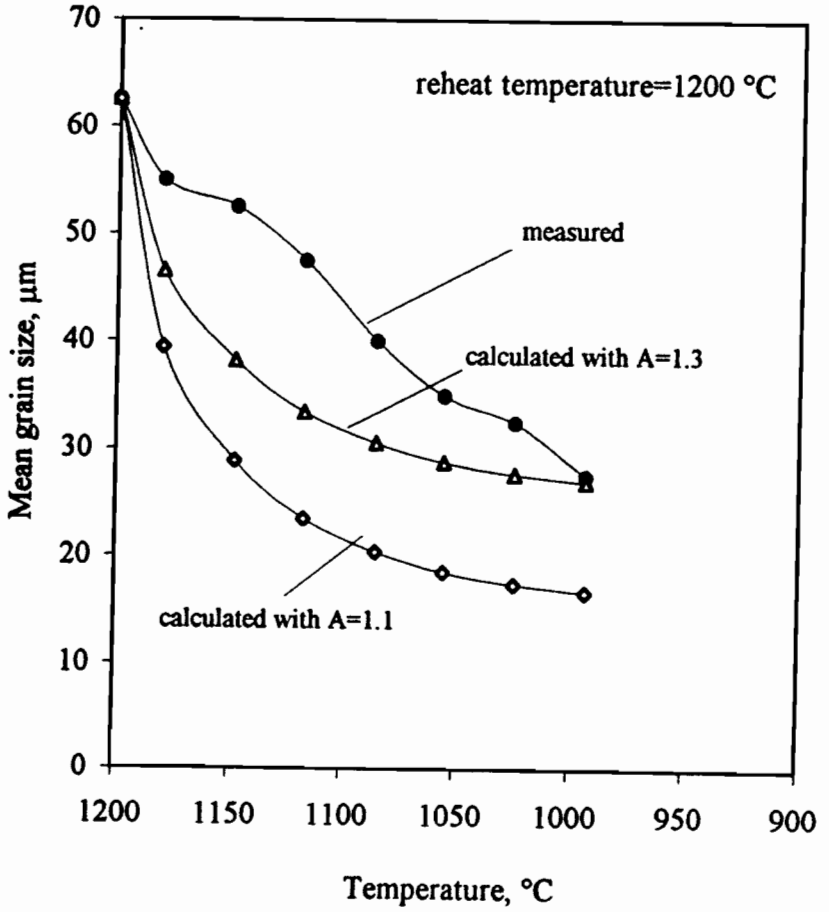

Fig. 4.41 Grain size evolution during multipass deformation in the Mo-Nb-B steel, strain=0.3/pass, strain rate=2 s^{-1}, and interpass time=30 s.

(b) Dependence of the recrystallization kinetics on strain

The model proposed by Sellars for the recrystallization kinetics in the solute drag region was already presented in the review of Chapter 2 and is recalled here:

$$t_{0.05x} = Ad_0^2\varepsilon^{-p}\exp\left(\frac{300000}{RT}\right)\exp\left(\left(\frac{2.75\times10^5}{T}-185\right)[Nb]\right) \qquad (4.44)$$

It was found that the calculated values of $t_{0.05x}$ using the model are generally less than the measured ones. For instance, at 1150 °C and a strain of 0.3, the calculated $t_{0.05x}$ is 0.004 seconds for the 0.07Nb steel, while the measured $t_{0.05x}$ is 0.1 second. This discrepancy could result from the strain term in the model. In fact, the strain exponent p in the $t_{0.5}$ models reported in the literature changes from one author to another. An exponent of 4 was originally proposed for C-Mn steels by Sellars. Then lower values of 2.8[218], 1.96[188] and 3.8[63] were used by other authors. Recently, Hodgson Gibbs[219] suggested that the strain exponent could be Nb concentration dependent (their equation was listed in Table 2.4). Although their model only applies to steels with Nb ≤ 0.03 wt%, the approach shows that the value of p decreases with increasing Nb concentration.

4.3.3.3 Calculation of the T_{nr} by the Additivity Rule

(a) The additivity rule

The additivity rule was originally proposed by Scheil[185]. The concept of the rule is that the reaction starts when the sum of the ratios of reaction time to reaction start time (τ_0) reaches unity.

$$\sum_{i=1}^{n}\frac{\Delta t_i}{\tau_0(T_i)} = 1 \qquad (4.45)$$

This rule has been widely used to predict the start time of phase transformations. Umemoto et al.[220-224] extended this method to predict the time when the reaction reaches x%. The additivity rule, in this case, can be rewritten as:

$$\sum_{i=1}^{n}\frac{\Delta t_i}{\tau_x(T_i)} = \sum_{i=1}^{n}\frac{1}{\tau_x(T_i)}\frac{\Delta t_i}{\Delta T_i}\Delta T_i = 1 \qquad (4.46)$$

where $\tau_x(T_i)$ is the time when the reaction reaches x% at temperature T_i, Δt_i is the incremental hold time at temperature T_i, and $\Delta t_i/\Delta T_i$ is the inverse of the cooling rate. If the cooling curve is divided into sufficiently small steps, then the equation can be expressed as an integral:

$$\int_{T_e}^{T} \frac{1}{\tau_x(T_i)} \frac{dt}{dT} dT = 1 \qquad (4.47)$$

where T_e is the equilibrium temperature at which the reaction is initiated.

It has been shown that the CCT (continuous-cooling transformation) behavior predicted from IT (isothermal-transformation) data using the additivity rule was in reasonable agreement with the experimental results when the calculations were carried out for the proeutectoid ferrite, pearlite and bainite transformations[220, 222, 223]. Park et al.[182] applied the additivity rule successfully to calculate the CCP (continuous-cooling-precipitation) curve using isothermal (PTT) data. Since recrystallization is a kind of phase transformation, it should be possible to predict the CCR (continuous-cooling-recrystallization) behavior using the same rule. This calculation was performed in the present study and is described below.

(b) Calculation of CCR and CCP curves

The following assumptions were made in this case: (1) after each deformation, the occurrence of recrystallization and precipitation can be modeled separately; and (2) at the i-th pass, the deformation temperature can be used in place of T_e in equation (4.47).

The cooling curves were divided into 0.01 °C increments, and τ_x and Δt_i were calculated at each temperature. The recrystallization finish and precipitation start times for each pass were then evaluated from the times when the sums of the reaction time ratios $\Delta t_i/\tau_x$ reached unity.

In the calculation, $t_{0.75x}$ was used to represent the time for recrystallization, instead of t_{100x}, since the recrystallized fraction at the T_{nr} is roughly 75% not 100%. It is then assumed that the $t_{0.75x}$ is proportional to the $t_{0.05x}$ and can be expressed as

$$t_{0.75x} = Ct_{0.05x} \qquad (4.48).$$

The constant C can be derived from the Avrami equation using an exponent n=1:

$$C = \frac{t_{0.75x}}{t_{0.05x}} = \left[\frac{\ln(1-0.75)}{\ln(1-0.05)}\right]^{\frac{1}{n}} \qquad (4.49)$$

This leads to

$$t_{0.75x} = 27.17 \times t_{0.05x} \qquad (4.50)$$

For the calculation of $t_{0.75x}$ for the i-th pass, the recrystallized grain size after the (i-1)-th pass was taken equal to the initial grain size of the i-th pass. It can be evaluated from equation (4.43). Bearing in mind the effect of composition on the strain exponent, the constant A and strain exponent p in equation (4.44) were chosen to give reasonable agreement between the predicted and measured T_{nr}'s. The recrystallization-precipitation-temperature-time (RPTT) diagrams calculated in this way are presented in Fig. 4.42. The broken curves represent $t_{0.75x}$, and the solid ones represent $t_{0.05p}$ for four increasing pass strains ($\dot{\varepsilon} = 2\,s^{-1}$ and interpass time = 30 s). The open circles identify the points of intersection of the $t_{0.75x}$ and $t_{0.05p}$ curves. The temperatures that correspond to these points are the predicted T_{nr}'s, and the predictions made in this way for the 0.05Nb and 0.09Nb steels for four pass strains are presented as examples in Fig. 4.43. It can be seen that the T_{nr} can be predicted using Sellars' model by applying the additivity rule to continuous cooling conditions. In this case, equation (4.44) can be rewritten as:

$$t_{0.05x} = Ad_0^2\varepsilon^{-2.5}\exp\left(\frac{300000}{RT}\right)\exp\left(\left(\frac{2.75\times10^5}{T} - 185\right)[Nb]\right) \qquad (4.51)$$

where $A=4.52\times10^{-20}$ for the 0.09Nb steel and 1.27×10^{-19} for the 0.05Nb steel.

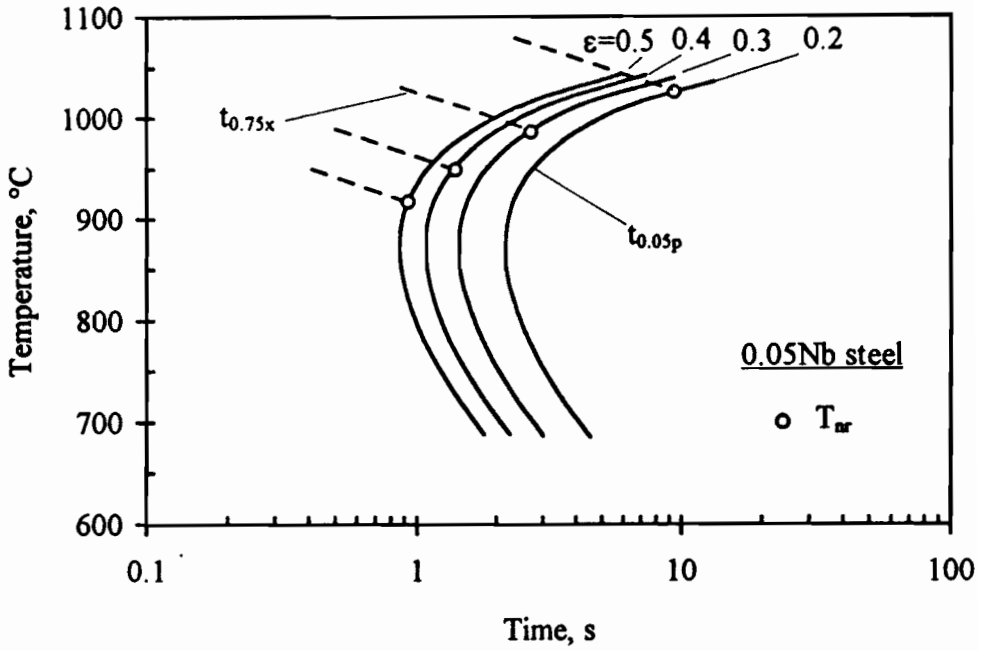

(a)

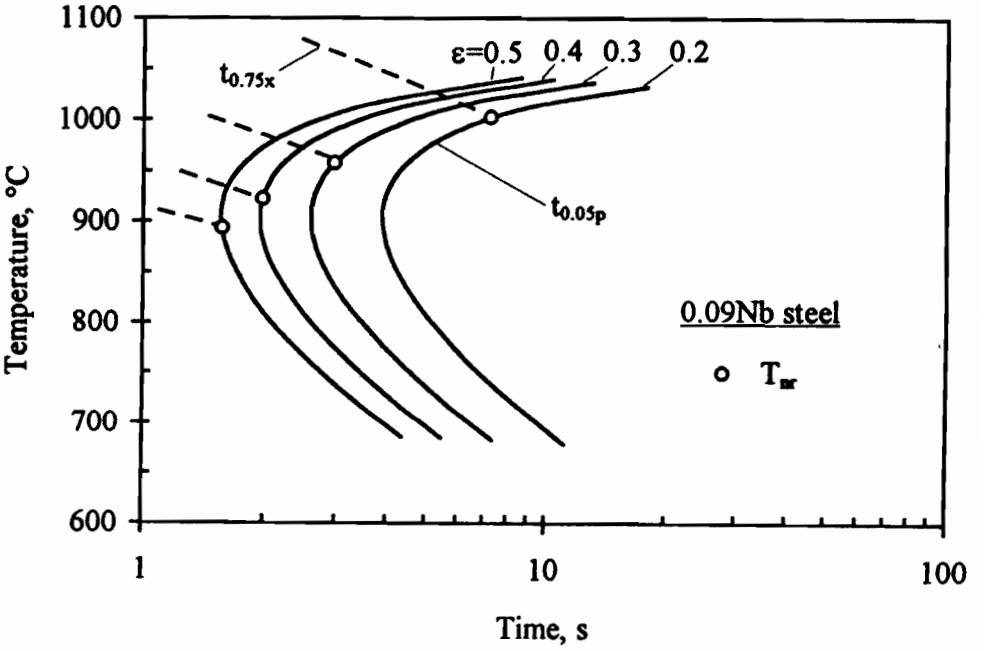

(b)

Fig. 4.42 RPTT diagrams pertaining to (a) the 0.05Nb steel and (b) the 0.09Nb steel processed under continuous cooling conditions (strain rate=2 s^{-1}, interpass time=30 s).

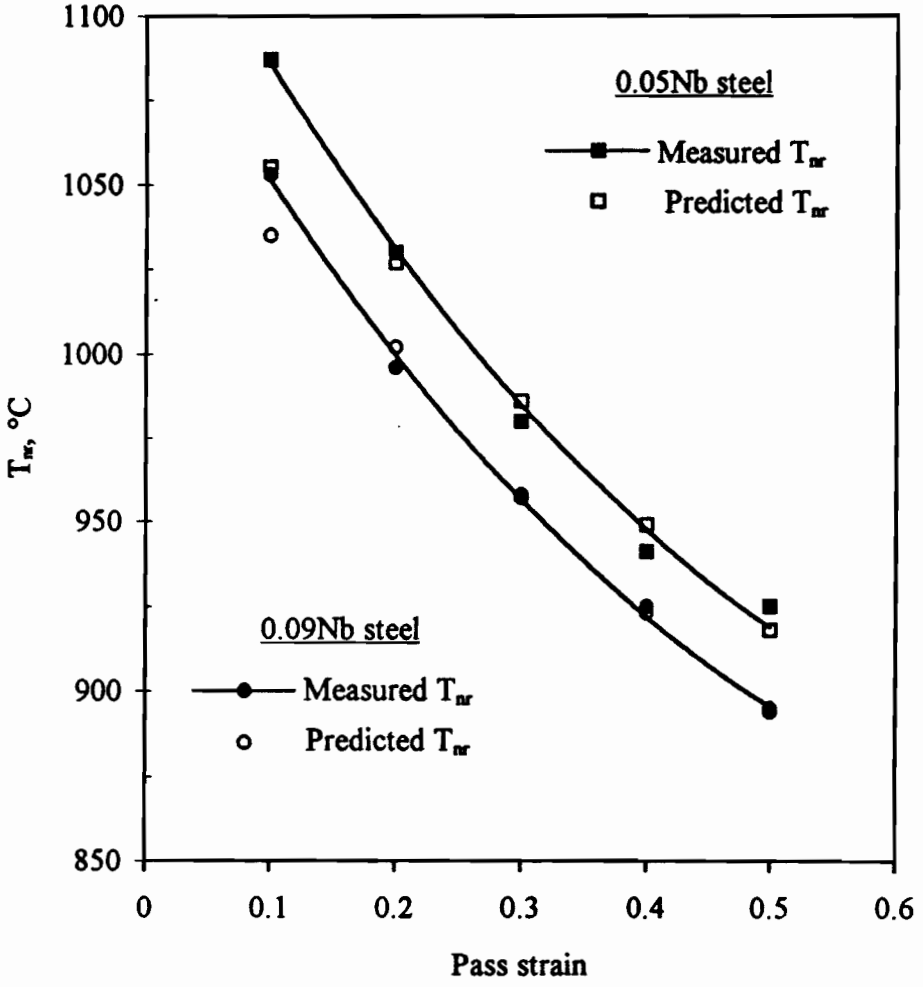

Fig. 4.43 Comparison of measured and predicted T_{nr}'s for the two steels of Fig. 4.42 (strain rate=2 s^{-1}, interpass time=30 s).

4.3.4. Effect of Boron Addition on the T_{nr}

The effect of boron addition on the T_{nr} in the Nb-bearing steels was presented in Figs. 4.13(b) and 4.14. It was seen that the addition of boron increases the T_{nr}, but weakens the dependence of the T_{nr} on pass strain. This effect can be explained in part in terms of the influence of boron on the precipitation kinetics of Nb(CN); a contribution may also be made by the non-equilibrium segregation of boron to austenite grain boundaries[183, 192, 193]. The results of Djahazi[133] are reproduced in Fig. 4.44. It can be seen that boron addition accelerates the precipitation process by increasing T_{Ps} and decreasing t_{Ps}; as a result, the PTT curves for the 0.055Nb steel are shifted to the upper left by the addition of boron. This indicates that precipitation is capable of retarding recrystallization at higher temperatures than in steels containing Nb only. The T_{nr} is increased by boron addition in this way, i.e. by accelerating the precipitation kinetics.

The effect of prestrain on the P_s curves is shown in Fig. 4.44(b). It is worth noting that the P_s curve of the Nb-B steel is shifted to the left by increasing the prestrain from 5% to 25%; the P_s curve of the Nb steel, however, remains almost unchanged. This suggests that the precipitation kinetics in Nb-B steels are more sensitive to deformation; that is, they are accelerated to a greater extent by the increase in prestrain. This can be explained by the different effects of deformation on Nb(CN) precipitation in Nb-only and Nb-B steels. As analyzed in §4.2.3.1 for the Nb-only steel, both recrystallization and precipitation are accelerated by increasing the pass strain; the rate of recrystallization, however, is increased to a greater extent than that of precipitation. The overall interaction between these two processes therefore brings about a significant decrease in the T_{nr} with increasing pass strain. In the Nb-B steel, both the non-equilibrium grain boundary segregation of boron and the Nb(CN) precipitation are accelerated by increasing pass strain. Therefore, the retardation of recrystallization is enhanced in this way.

It is reported in the literature[193, 225-228] that boron forms complexes with vacancies. These vacancy-solute complexes diffuse faster than single vacancies or boron atoms (according to Williams et al.[228], the vacancy diffusion coefficient $D_v=0.5\exp(-2.7/kT)$, the boron diffusion coefficient $D_i=2\times10^{-3}\exp(-0.91/kT)$, and the complex diffusion coefficient $D_c=0.5\exp(-0.91/kT)$). The migration of complexes to boundaries, where they deposit the boron, is therefore taken to be responsible for the non-equilibrium segregation of boron to austenite grain boundaries. This mechanism also involves the motion of the vacancies liberated at the boundaries away from these interfaces. Thus the flux of boron atoms to the boundaries is sensitive to cooling rate and the amount of

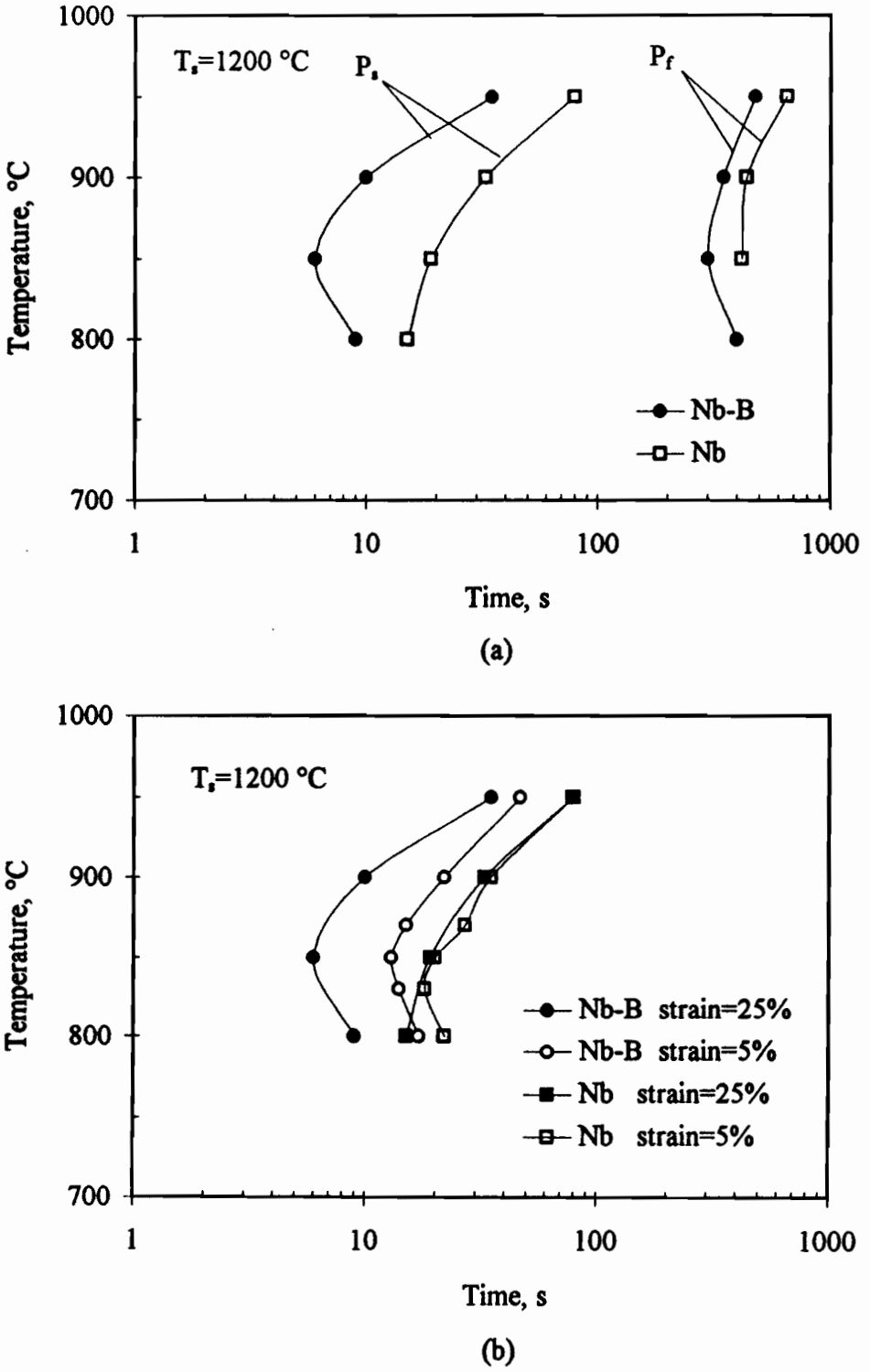

Fig. 4.44 Effect of (a) boron addition and (b) amount of deformation on the precipitation kinetics in a 0.055Nb steel[133].

deformation. At a given cooling rate, the greater the deformation, the higher the excess vacancy concentration; thus more vacancies are available to form the vacancy-solute complexes that transport the boron to the boundaries. Once the complexes have reached the grain boundaries, the latter act as vacancy sinks, releasing the boron. These segregated boron atoms can retard the motion of grain boundaries, so that recrystallization is retarded by the increased solute drag.

The presence of boron also increases the Nb diffusion rate and decreases the interfacial energy modifier ξ as a result of the segregation of the vacancy-boron complexes to dislocations and grain boundaries[183, 229]. This leads to the decrease in the precipitation start time discussed above, and shifts the PTT curves to the upper left, and eventually raises the T_{nr}.

The dependence of the T_{nr} on boron concentration is illustrated in Fig. 4.45 by replotting the results of Fig. 4.14 for a given deformation condition (ε=0.3, $\dot{\varepsilon} = 2\,s^{-1}$, and interpass time = 30 s). It can be seen that there is a boron concentration at which the T_{nr} has the highest value. Both increasing and decreasing the boron content from this concentration will lead to a decrease in the T_{nr}. In the case of low boron concentrations, either the non-equilibium segregation of boron to boundaries or the acceleration of Nb(CN) precipitation by boron addition is less effective because of lower boron concentration. In the case of high boron concentrations, the lower T_{nr} is due to both an acceleration of the recrystallization kinetics and Nb(CN) precipitate coarsening. First, when the boron concentration is high, borocarbide precipitation can take place during cooling and deformation. This type of precipitate was observed by Taylor and Hansen in 0.2C-0.033 Ti steels with boron concentrations of 50-100 ppm[230, 231], as well as by Mavropoulos et al.[191] and Djahazi et al.[133, 192] in a 0.03C-0.02Ti-0.055Nb-0.003B steel. These precipitates are usually 0.1~1 μm in size; they are thus less able to retard recrystallization and may even accelerate it by acting as nucleation sites. Secondly, the precipitate coarsening of Nb(CN) is accelerated by the presence of large borocarbide particles. These coarsened Nb(CN) particles lose their effectiveness with regard to retarding recrystallization, thus decreasing the T_{nr} in this way.

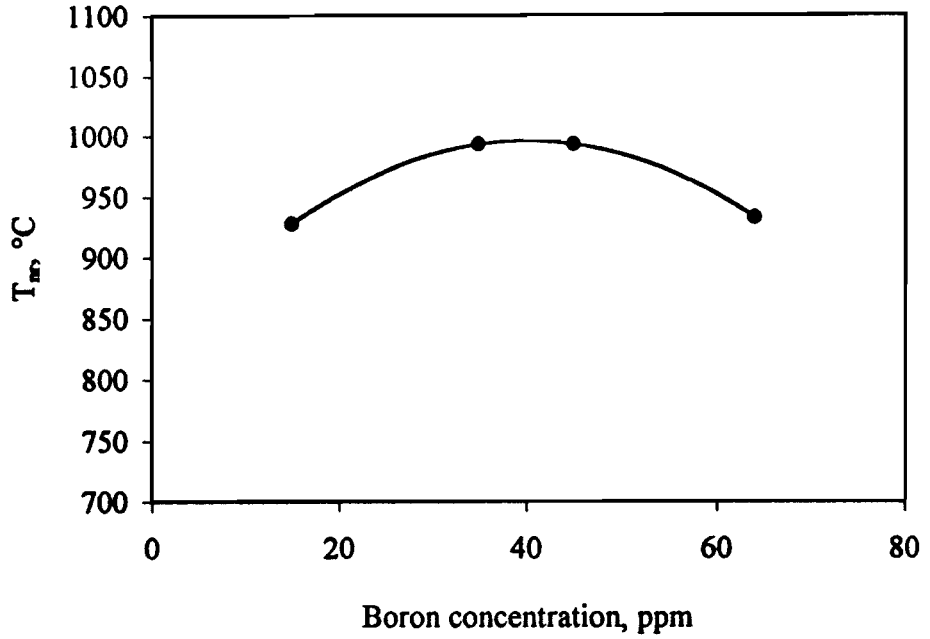

Fig. 4.45 Effect of boron concentration on the T_{nr} in the steels containing 0.06Nb. (deformation condition: $\varepsilon = 0.3$/pass, $\dot{\varepsilon} = 2\ s^{-1}$, and interpass time = 30 s).

4.4 Summary

The recrystallization behaviors of eleven steels containing different microalloying additions were investigated under continuous cooling conditions. Hot torsion tests were performed using a 17 pass deformation schedule at strain rates of 0.2 s^{-1} to 10 s^{-1}, and interpass times of 0.05 to 150 seconds. After reheating at 1250 °C or 1200 °C, the first deformation was applied at 1180 °C and the last one at about 700 °C. By means of mean flow stress vs. 1000/T diagrams, the effects on the T_{nr} of chemical composition and of the deformation conditions were determined. Separate empirical equations for the T_{nr} were derived from the data for short and long interpass times. These relations describe the influence of chemical composition and of pass strain, strain rate, and interpass time under continuous cooling conditions. Furthermore, the dependence of the residual strain ε_r or the residual strain ratio λ on the deformation parameters was also investigated by analyzing the flow curves, and a relationship between λ and the T_{nr} was established. This made it possible to interpret the significance of both the recrystallization limit temperature (RLT) and the recrystallization stop temperature (RST) in greater detail than previously.

CHAPTER 5

DYNAMIC AND METADYNAMIC RECRYSTALLIZATION

It has been recognized that dynamic and metadynamic recrystallization can take place in cases involving large pass strains ($\varepsilon > \varepsilon_p$) or short interpass times ($t < 1$ s). Although the mechanisms and kinetics of both processes have been studied for decades, accurate quantitative descriptions of these processes are still lacking, especially for microalloyed steels. In the present work, one low carbon low niobium steel was used, together with two previous low carbon high niobium steels, to study the kinetics of dynamic and metadynamic recrystallization at high temperatures. The compositions of the two high niobium steels were presented in Chapter 3; they are referred to here as the 0.07Nb and 0.09Nb steels. The main alloying elements of interest in the low niobium steel are 0.06C-0.55Mn-0.023Nb. The experimental results concerning dynamic and metadynamic recrystallization are presented in the first part of this chapter; these are then followed by analysis and discussion. Simulations of rod and hot strip mills are presented in the third part, and the chapter ends with a brief summary.

5.1 Test Schedules

In order to study the occurrence of dynamic and metadynamic recrystallization in the present Nb treated steels and to simulate multipass deformation, three hot torsion test schedules were employed in the present investigation. These schedules are illustrated schematically in Fig. 5.1, and will be referred to as schedules D (single pass deformation), E (double twist), and F (multipass deformation), respectively. In the case of single pass deformation, the strains were chosen to be large enough to produce peak shaped flow curves. The double twist schedule was used to study the kinetics of recrystallization after the tests were interrupted at different strains: e.g. strains below the critical strain, strains greater than the critical strain but less than the peak strain, the peak strain, strains greater than the peak strain but less than the steady state strain, and the steady state strain. The multipass deformation schedule was employed to investigate softening between passes and strain accumulation at different deformation temperatures and interpass times. The experimental results will be presented in the sections that follow.

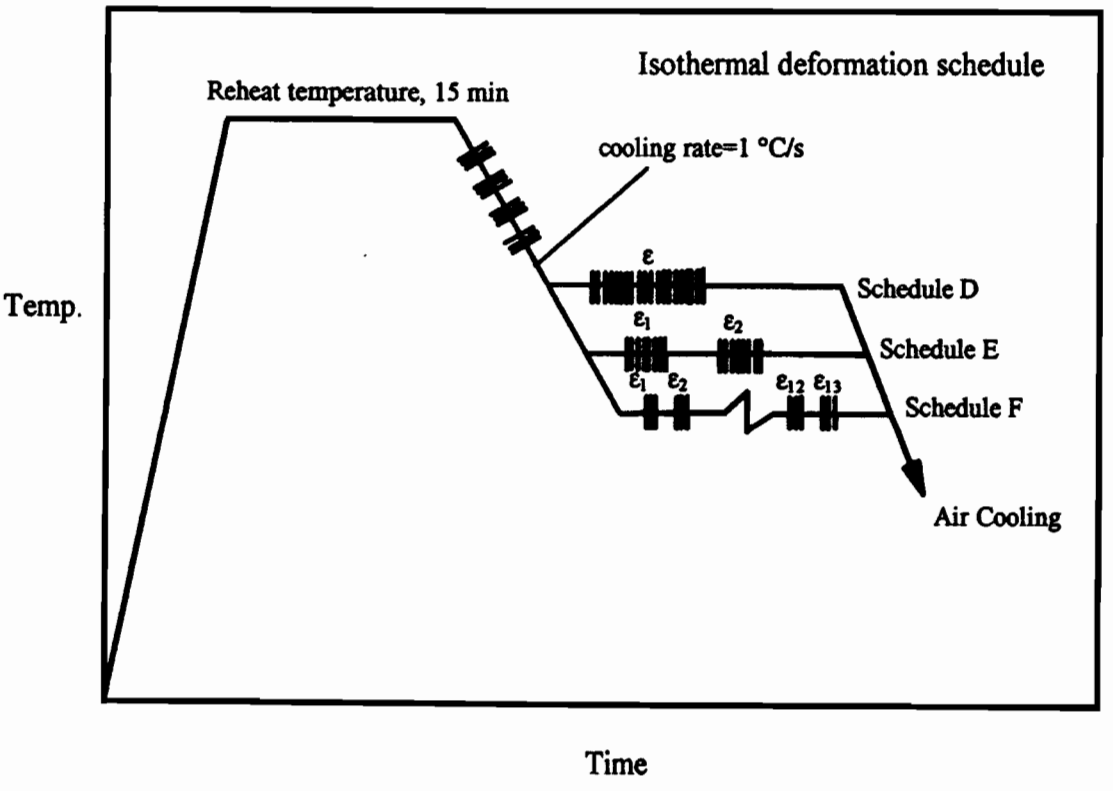

Fig. 5.1 Schedules used for the single pass, double twist, and 13 finishing pass tests.

5.2 Results

5.2.1 Flow Curves of the Continuous Hot Torsion Tests

The test schedule used for generating a series of single peaked flow curves was presented in Fig. 5.1. Four roughing passes with identical pass strains of 0.3 were used to break down the reheated austenite structure. The refined grain size was about 50 μm and acted as the initial grain size in the later single pass deformation. Specimens were continuously cooled to deformation temperatures ranging from 850 °C to 1090 °C. After 20 seconds of homogenizing, one single-pass deformation with large strains and different strain rates ranging from 0.02 s^{-1} to 10 s^{-1} was performed at the selected temperatures. A typical flow curve generated from this kind of test is shown in Fig. 5.2. The method of measuring the peak and steady state strains is also demonstrated in this figure.

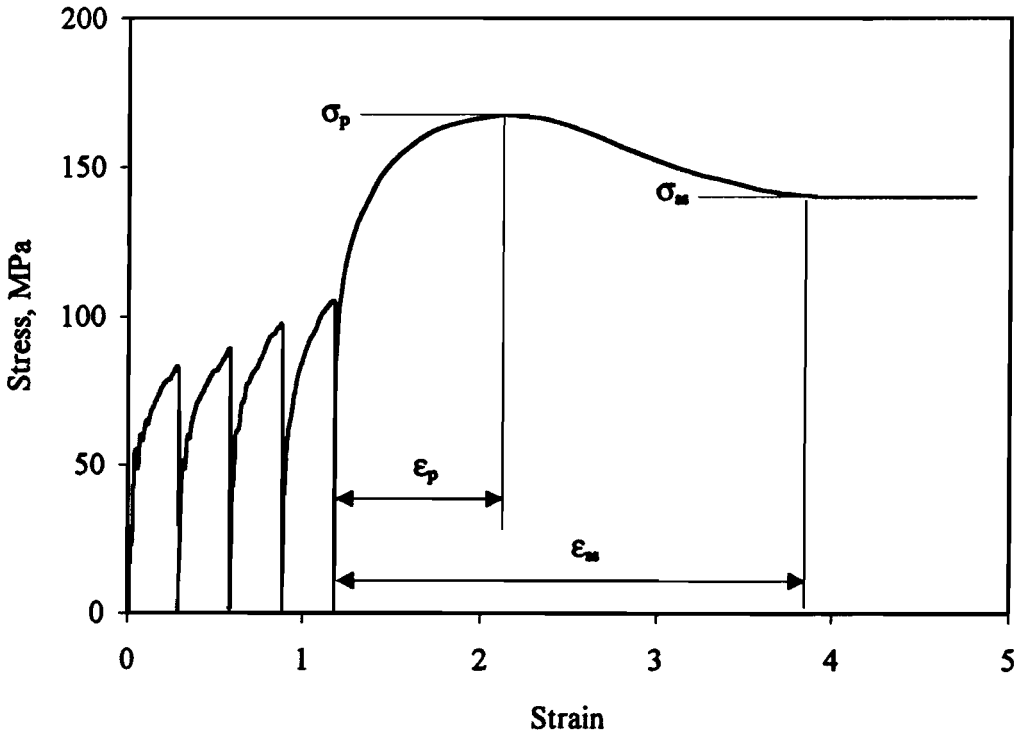

Fig. 5.2 Example of single pass deformation after roughing.

5.2.1.1 Dependence of the Peak and Steady State Strains on Deformation Temperature

The flow curves generated at the same strain rate (2 s^{-1}) but different deformation temperatures for both the 0.023Nb and 0.07Nb steels are presented in Figs. 5.3 (a) and (b). It is evident from these curves that the peak and steady state strains increase with

decreasing temperature, and that the peak strains of the 0.07Nb steel are greater than those of the 0.023Nb steel at the same temperature. It can also be seen that, at 940 and 970 °C, the peak stresses for the 0.07Nb steel, 190 and 170 MPa, are appreciably higher than the 143 and 135 MPa observed for the 0.023Nb steel at the same two temperatures. Another feature of the curves shown is that the peak becomes flatter and broader with decreasing deformation temperature. In order to describe this phenomenon, a horizontal line is drawn at a stress $\sigma = \sigma_p - \Delta\sigma/3$, where $\Delta\sigma = \sigma_{ss} - \sigma_p$. This stress level defines the strains ε_1 and ε_2, as shown in Fig. 5.3 (b). The strain interval $\Delta\varepsilon$ is then defined as $\Delta\varepsilon = \varepsilon_2 - \varepsilon_1$. The interval $\Delta\varepsilon$ increases from 0.8 to 1.23 when the deformation temperature is decreased from 1000 °C to 940 °C. Further, $\Delta\varepsilon$ increases from 1.23 to 2.05 when the deformation temperature is decreased from 940 °C to 850 °C. The same trend can also be observed when the niobium content is increased from 0.023 wt% to 0.07 wt%. Compared with the deformation temperature, however, Nb has much less influence on the shape of the flow curve.

The dependence of the peak strain on deformation temperature is presented in Fig. 5.4 (a). It can be seen that the peak strains of all three steels increase with decreasing deformation temperature. The slopes of the ε_p - 1/T plots for these steels are approximately equal at the higher temperatures and shift to higher values (the broken lines) at about 940 °C for the 0.07Nb and 0.09Nb steels and at 900 °C for the 0.023Nb steel. This abrupt change in slope can be attributed to the influence of niobium carbonitride precipitation on dynamic recrystallization. Therefore, as in the case of the MFS - 1/T plots presented in Chapter 4, the dependence of peak strain on deformation temperature can be divided into two ranges. In range I, the high temperature range, the solute drag of Nb atoms plays a role in retarding the onset of dynamic recrystallization. The peak strain is only a function of temperature and increases gently as the deformation temperature is decreased. As soon as the deformation temperature drops below the Nb(CN) precipitation start temperature T_{Ps}, in range II, the initiation of dynamic recrystallization becomes more difficult because of the stronger retarding effect of the Nb(CN) particles. A higher strain is therefore needed to initiate the recrystallization process and to provide the driving force. It can also be seen from Fig. 5.4 (a) that the peak strains of the 0.07Nb steel are slightly higher than those of the 0.09Nb steel. This is probably because the former contains a higher concentration of Nb plus Ti (0.07Nb plus 0.026Ti) than the latter; as a result, a stronger overall retarding effect was found in the former than in the latter steel.

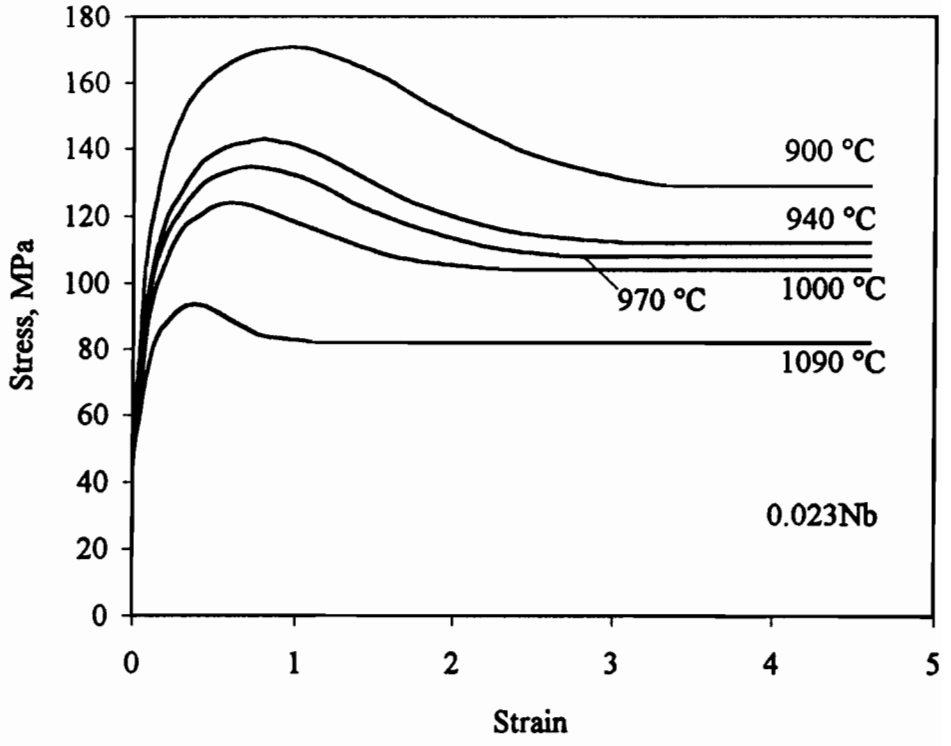

(a)

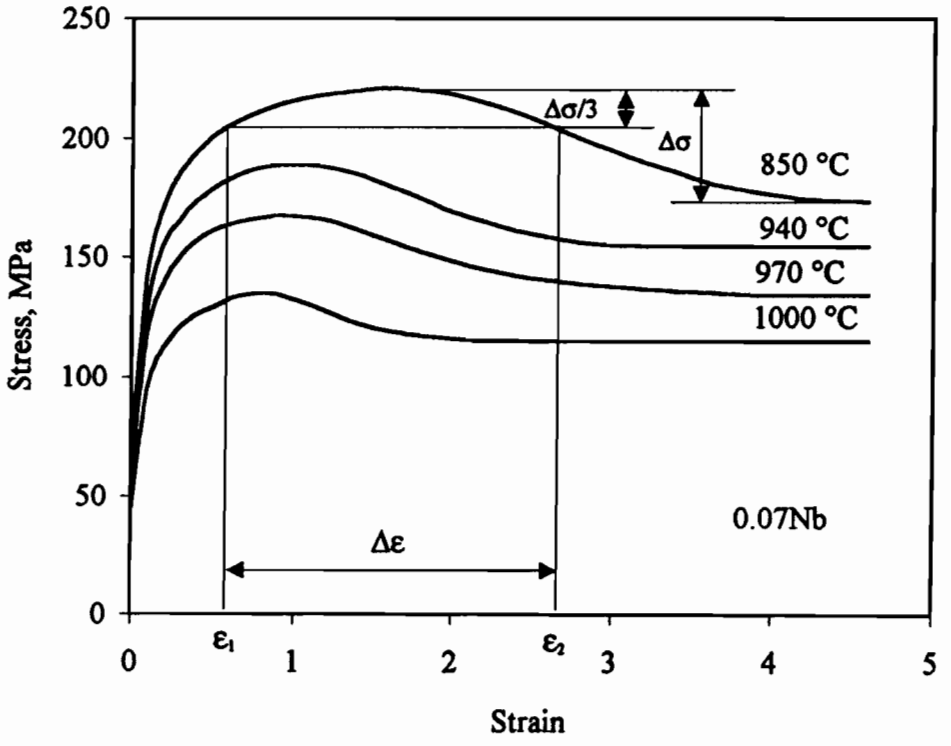

(b)

Fig. 5.3 Stress-strain curves for the two steels, strain rate = 2 s^{-1}.

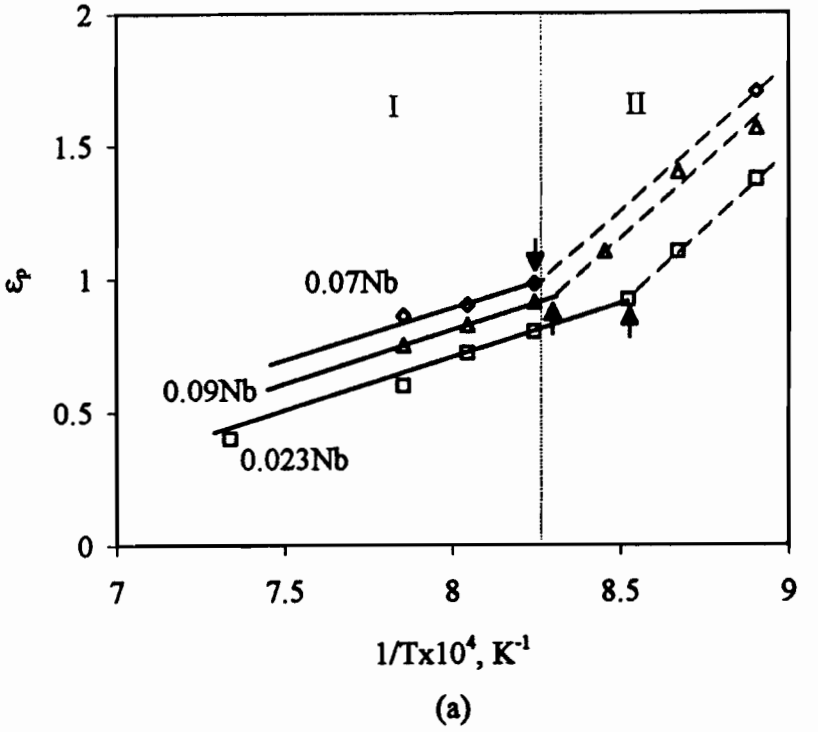

(a)

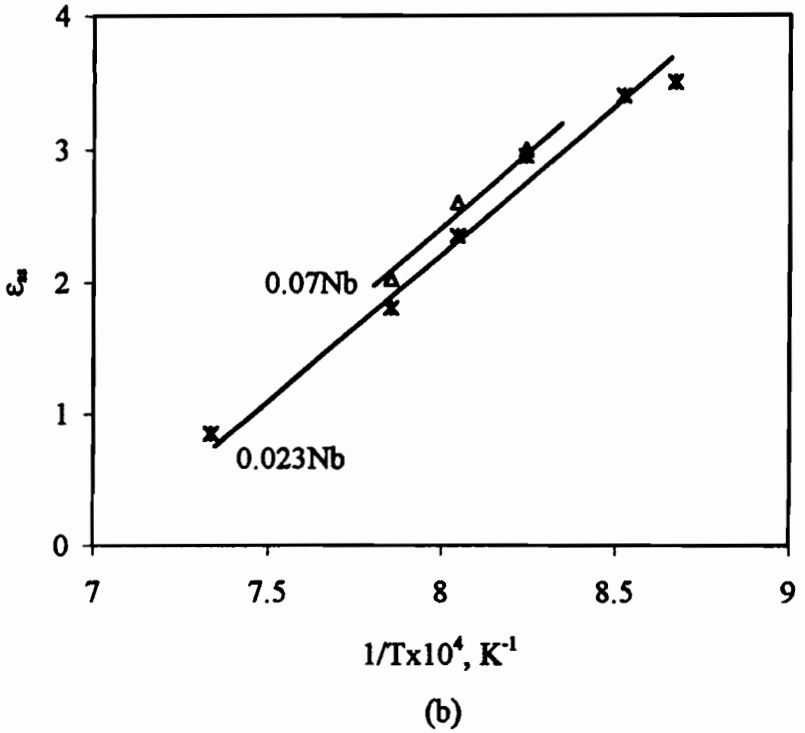

(b)

Fig. 5.4 Dependence of (a) peak strain and (b) steady state strain on the inverse absolute temperature.

The dependence of the steady state strain on deformation temperature is presented in Fig. 5.4 (b). Here it can be seen that the steady state strains (ε_{ss}) of both steels increase with decreasing deformation temperature, and that the values for the 0.07Nb steel are slightly higher than the ones for the 0.023Nb steel. The absence of data points at the lower temperatures, however, prevents the drawing of any conclusions regarding a break at T_{Ps}.

5.2.1.2 Dependence of the Peak and Steady State Strains on Strain Rate

In this set of tests, the deformation temperatures were kept at 970 °C for the 0.07Nb steel and at 900 °C for the 0.023Nb steel, while the strain rates were varied in steps from 0.02 s^{-1} to 10 s^{-1}. Selected flow curves for both steels are presented in Figs. 5.5 (a) and (b). It can be seen that the peak and steady state strains of both steels increase with strain rate. This dependence is presented in more detail in Figs. 5.6 (a) and (b). When the strain rate was increased from 0.02 s^{-1} to 10 s^{-1}, the peak strain increased from 0.42 to 1.3. The rate of increase in peak strain with strain rate is more pronounced at higher than at lower strain rates. For instance, at 970 °C, the peak strain increased from 0.42 to 0.6 when the strain rate was increased from 0.02 s^{-1} to 0.2 s^{-1}, one order of magnitude, in the 0.07Nb steel. When the strain rate was increased from 2 s^{-1} to 10 s^{-1}, a factor of 5, however, the peak strain increased from 0.9 to 1.3. It is also evident in Fig. 5.6 (a) that the peak strains of the 0.023Nb steel at 900 °C are approximately the same as those of the 0.07Nb steel at 970 °C. This implies that the retarding effect of 0.023 wt% Nb at 900 °C on the onset of dynamic recrystallization is equivalent to that of 0.07 wt% Nb at 970 °C on a basis of solute drag. In Fig. 5.6 (b), the dependence of the steady state strain on strain rate and Nb content displays a similar trend.

It should be mentioned here that, at the strain rates of 0.02 and 0.2 s^{-1}, the temperature rise due to deformation heating can be neglected. At higher strain rates, especially at 10 s^{-1}, however, the temperature rise during deformation is significant and cannot be ignored. The effect of temperature rise on the flow stress was evaluated using the following expression derived by Laasraoui and Jonas[232],

$$\delta\sigma_i = \left[\frac{\partial\sigma}{\partial(1/T)}\right]_{\delta\epsilon,\dot{\epsilon}}\left[\frac{1}{T_{iso}+\delta T} - \frac{1}{T_{iso}}\right] \qquad (5.1)$$

The flow curves presented in Figs. 5.3 and 5.5 have been corrected in this way and represent the calculated "isothermal" behaviour.

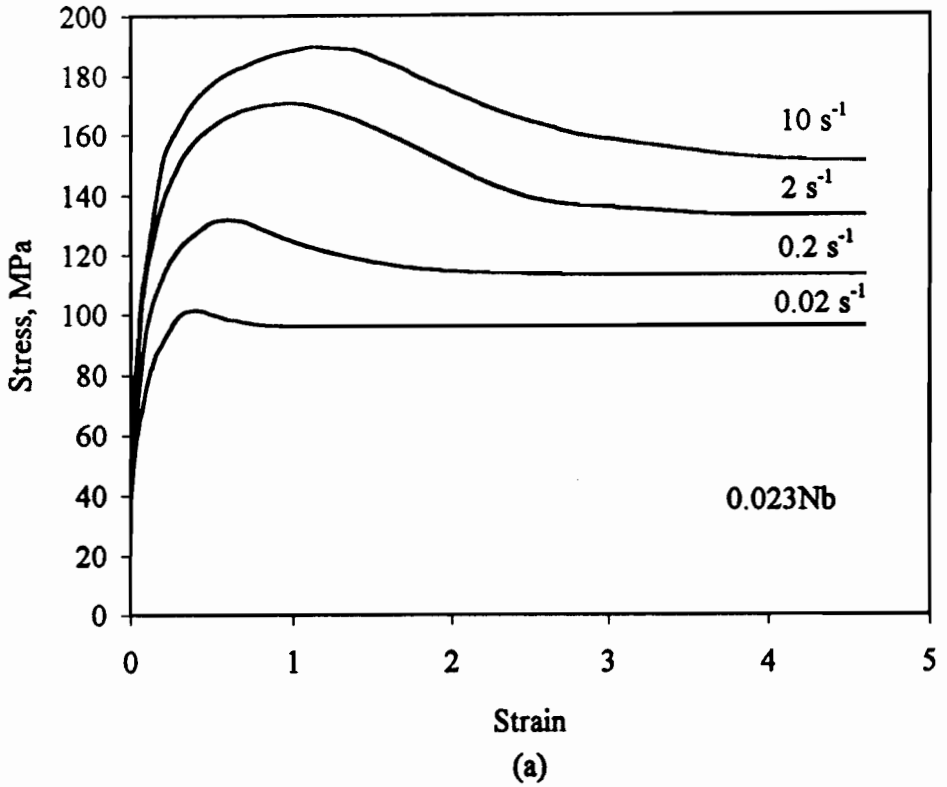

(a)

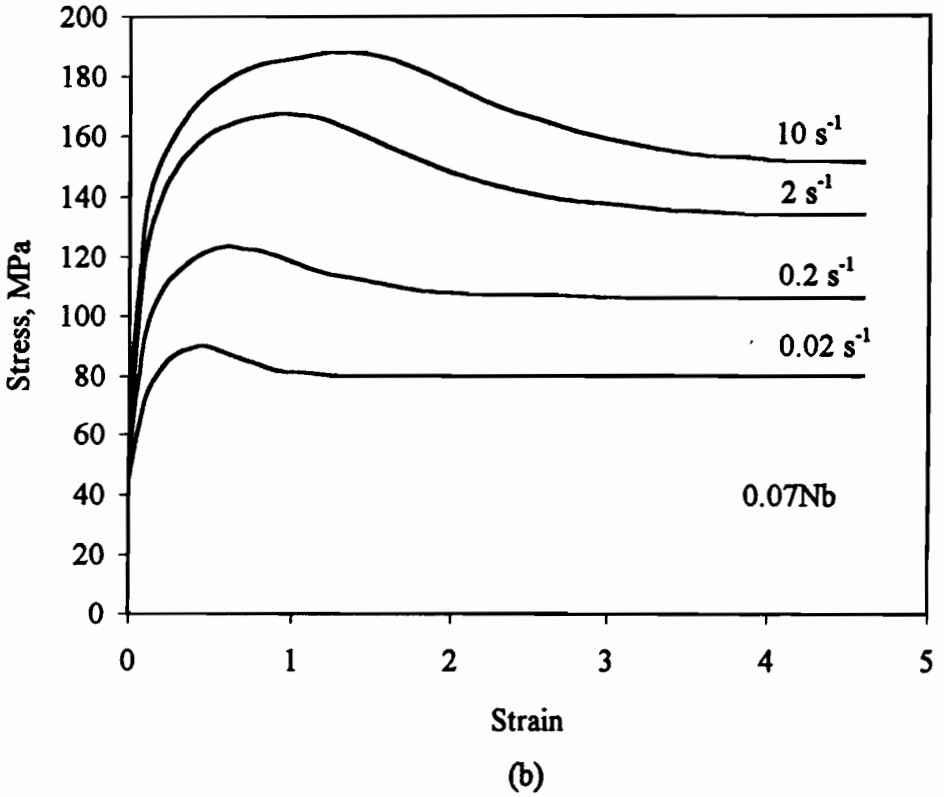

(b)

Fig. 5.5 Stress-strain curves for the two steels, (a) T=900 °C, (b) T=970 °C.

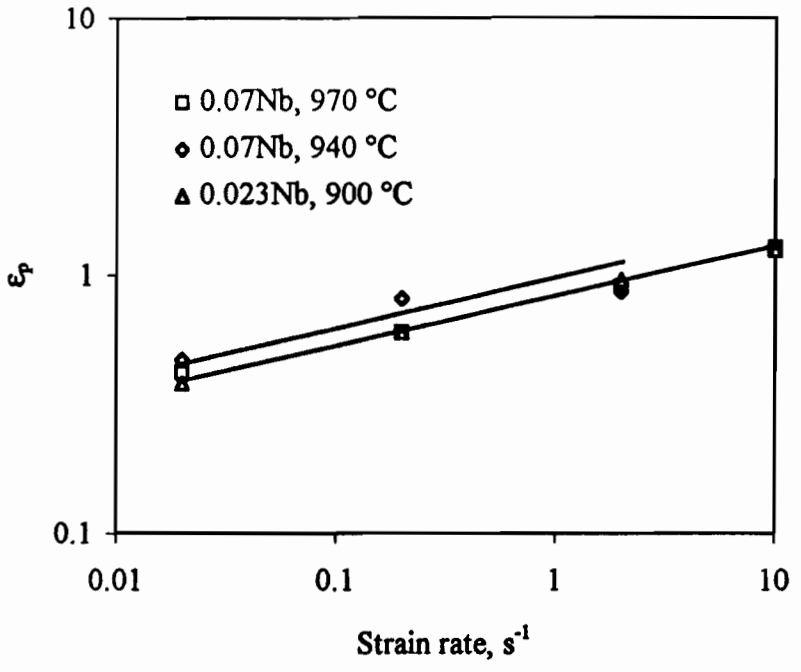

(a)

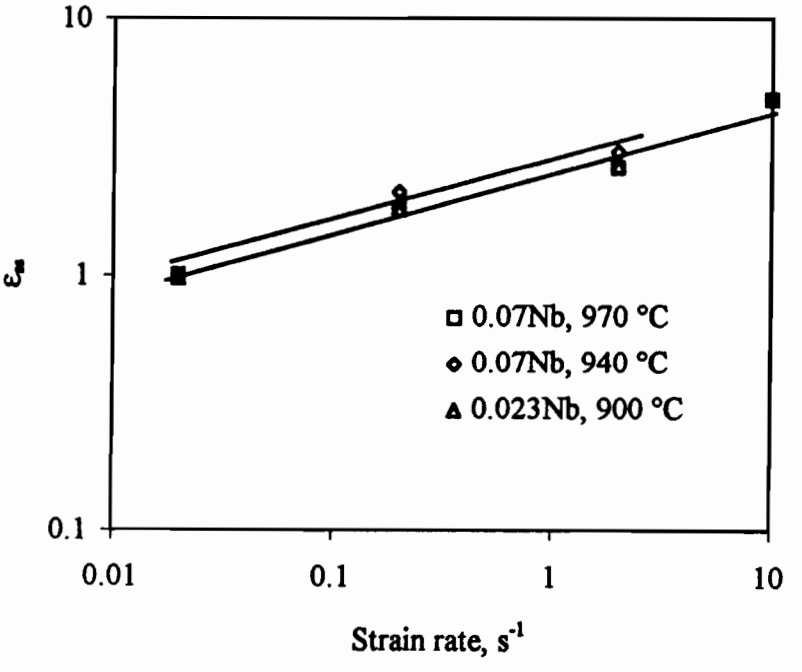

(b)

Fig. 5.6 Dependence of (a) peak strain and (b) steady state strain on strain rate.

The effect of initial grain size on the peak strain has been described by different authors in the literature. Sah et al.[98] reported that the peak strain in nickel deformed at 0.65 s^{-1} and 880 °C increased from 1.16 to 1.73 as the initial grain size was increased from 60 μm to 470 μm. Roberts et al.[99] observed that the peak strain of an austenitic stainless steel deformed at 0.5 s^{-1} and 1150 °C increased from 0.38 to 0.73 as the initial grain size was increased from 75 μm to 225 μm. Ouchi and Okita[233] demonstrated a very weak dependence of the peak strain on initial grain size in a 0.03Nb steel deformed at 950 °C and a low strain rate of 2.1 x 10^{-3} s^{-1}. In an investigation of the hot deformation of ETP copper by Petkovic et al.[234], a prestrain applied at different strain rates was employed to produce initial grain sizes ranging from 56 μm to 200 μm. They observed a weak initial grain size dependence of the peak strain when the samples were deformed at 0.08 s^{-1} and 540 °C.

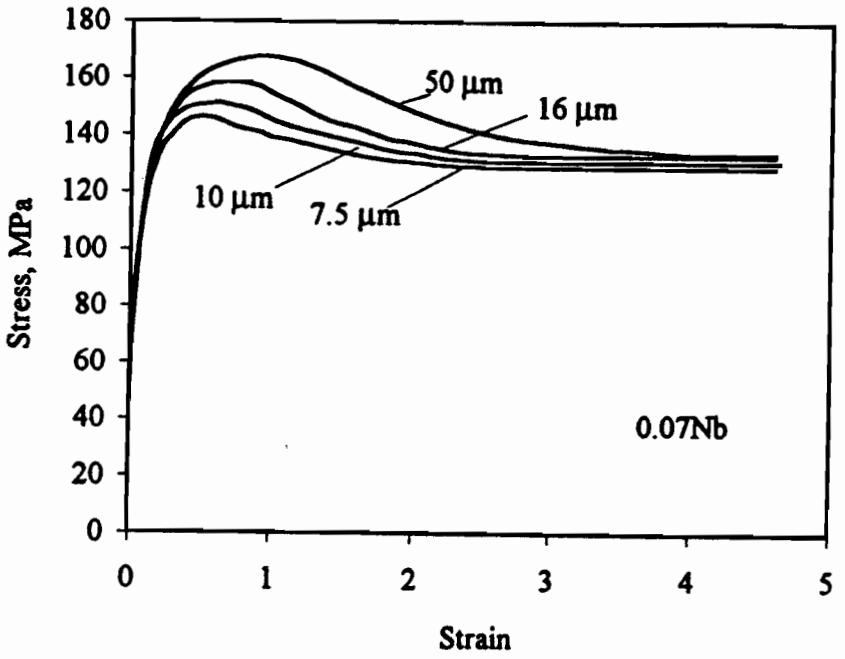

Fig. 5.7 Stress-strain curves of the 0.07Nb steel, deformed at a strain rate of 2 s^{-1}, and T = 970 °C.

In the present investigation, following Petkovic et al., a prestrain was applied at strain rates ranging from 0.02 s^{-1} to 2 s^{-1} to produce initial grain sizes ranging from 7.5 μm to 50 μm in the 0.07Nb steel. The flow curves determined at 2 s^{-1} and 970 °C are shown in Fig. 5.7. The peak strain increased from 0.5 to 0.9 when the initial grain size

was increased from 7.5 μm to 50 μm. The dependence displayed in Fig. 5.8 can be expressed in the form of a power function:

$$\varepsilon_p \propto D_0^p \qquad (5.2)$$

The exponent p was found to be 0.31 and is close to the one given by Hodgson[82]; it is less than that reported by Sellars[62]. It is also of interest to note that the steady state stress is independent of D_0. This is consistent with the findings of Sah et al.[98].

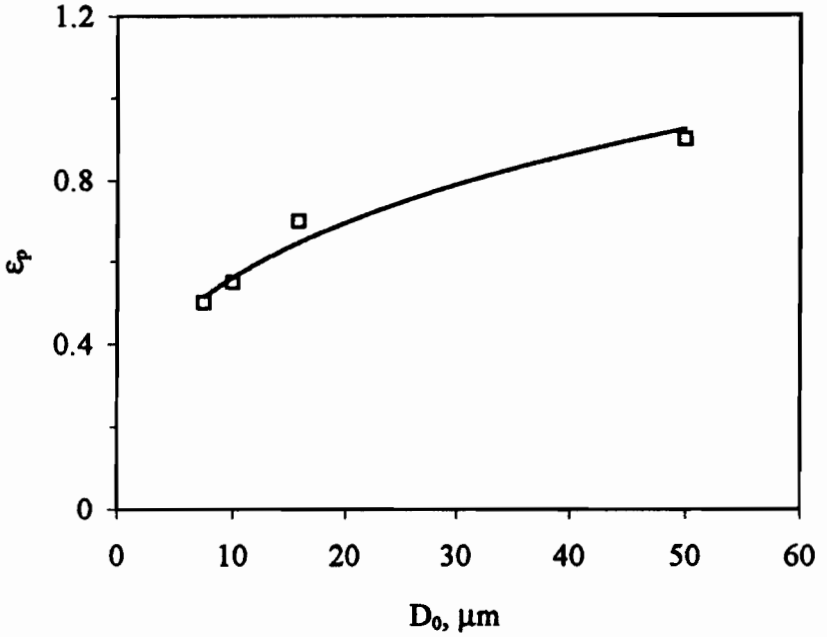

Fig. 5.8 Dependence of peak strain on initial grain size.

5.2.2 Flow Curves of the Interrupted Hot Torsion Tests

In order to study the kinetics of metadynamic recrystallization, the double twist technique was used in the present investigation. The schedule designed for this purpose was presented in Fig. 5.1 and is referred to as Schedule E. Four roughing passes were employed at higher temperatures to break down the coarse grain structure of the reheated austenite. The specimens were then continuously cooled to selected deformation temperatures ranging from 900 °C to 1090 °C. At these temperatures, double twists were executed at a constant strain rate. The first deformation was interrupted at strains well after the peak (these strains were determined from the continuous deformation flow curves shown in Fig. 5.3 (b)). The second deformation (ε=0.3) was applied after an interpass

delay with time intervals ranging from 0.05 seconds to 100 seconds. The fractional softening was estimated using the method presented in Chapter 3. Fig. 5.9 shows one set of the flow curves generated from this kind of test.

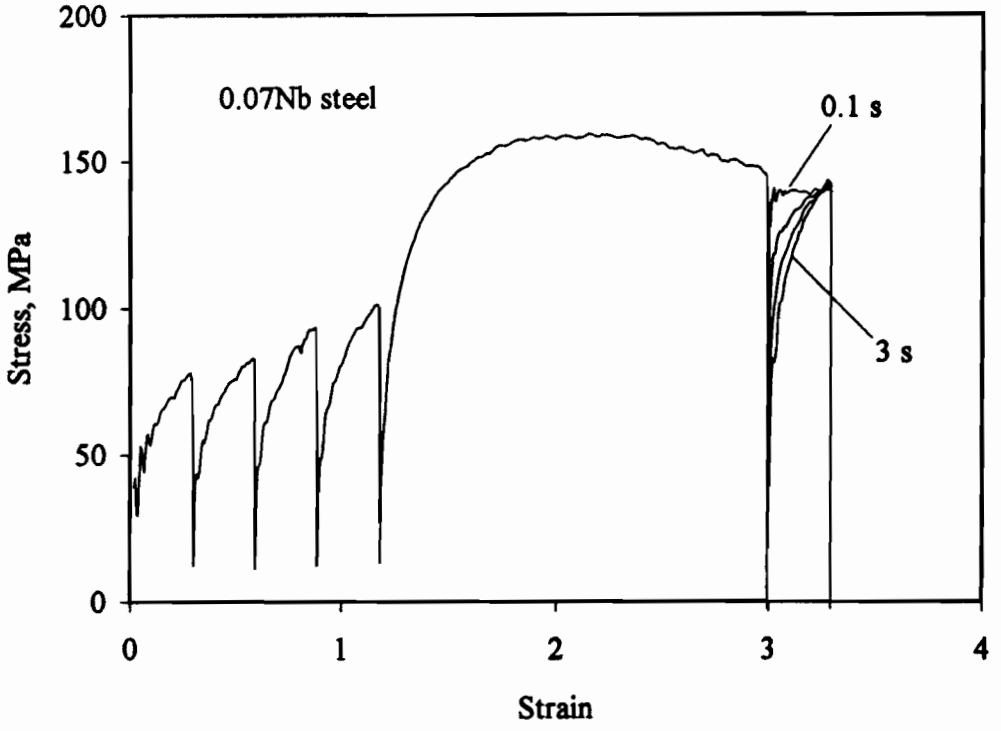

Fig. 5.9 Examples of double twist flow curves.

5.2.2.1 Influence of Strain on Softening

It has been recognized that the kinetics of static recrystallization are strongly strain dependent, while those of metadynamic recrystallization are strain independent. In order to investigate the effect of strain on the kinetics of metadynamic recrystallization in the steels studied in the present work, the first twist of the double twist tests was chosen to correspond to strains ranging from ones below the critical strain ε_c to others at the steady state strain ε_{ss}. The estimated fractional softening at different strains is presented in Figs. 5.10 (a) and (b). The interpass intervals were identical (1 second) for all the tests, except for those at 1000 °C for the 0.023Nb steel and 10 s^{-1} for the 0.07Nb steel. In these two cases, the interpass intervals were reduced to 0.5 and 0.3 seconds in order to observe the transition point at which the rate of softening changes from being strain dependent to being strain independent. The following features are to be noted from these figures.

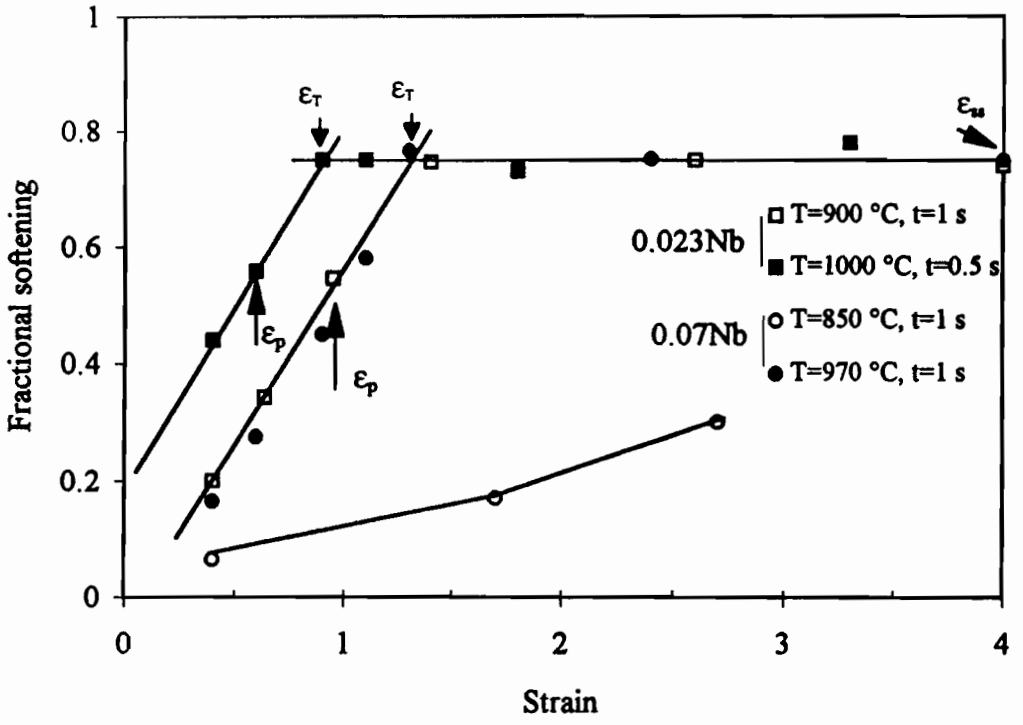

(a)

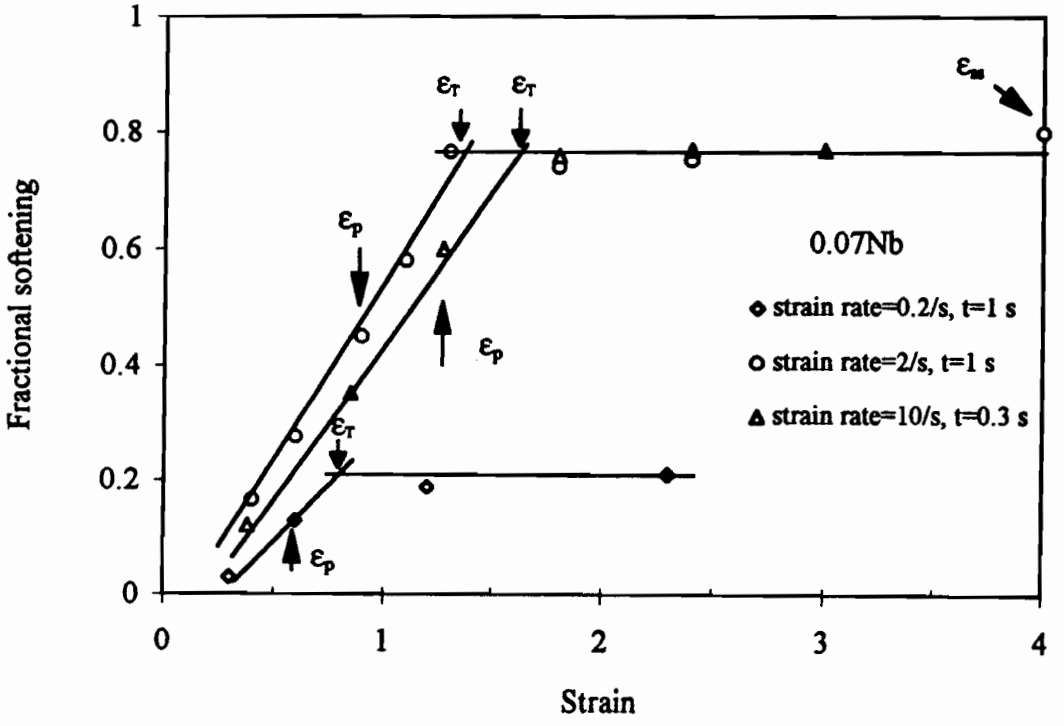

(b)

Fig. 5.10 Effect of strain on softening in the two steels, (a) strain rate = 2 s^{-1} (b) T = 970 °C.

(a) There is a transition strain ε_T which separates the softening behaviour into the strain dependent and strain independent ranges. The values for ε_T are approximately 1.5 ε_p. This transition strain differs somewhat from those reported by other authors in modelling recrystallization kinetics, and will be discussed later.

(b) At strains below ε_T, the amount of fractional softening increases linearly with strain for a given holding time. At strains above ε_T, however, the amount of fractional softening remains constant at about 75%. This maximum softening is insensitive to temperature, strain rate and composition, except at the low strain rate of 0.2 s^{-1} and the low temperature of 850 °C.

(c) The softening rate of the 0.023Nb steel at 900 °C is similar to that of the 0.07Nb steel at 970 °C.

5.2.2.2 Influence of Strain Rate on Softening

At strains below the critical strain ε_c, the effect of strain rate on static recrystallization is small and is usually neglected in kinetics models. Although some authors have considered the effect of strain rate, its exponent is 6~10 times lower than that of the strain. The effect of strain rate on the recrystallization rate at the steady state strain in C-Mn steels has been studied by Hodgson and Gibbs[219] Recently, the effect of strain rate at the peak strain in a Mo, a Ti and a Nb low carbon microalloyed steel was investigated by Roucoules et al.[235]. Both groups reported a strong dependence on strain rate of the rate of metadynamic recrystallization. In the present work, the effect of strain rate on the recrystallization rate at strains slightly higher than ε_T in the 0.023Nb steel was studied at strain rates ranging from 0.02 s^{-1} to 10 s^{-1}.

The measured fractional softening at different strain rates is plotted vs. the logarithm of the holding time in Fig. 5.11. These plots (except for the 0.02 s^{-1} one) have a sigmoidal appearance. From this figure, the effect of strain rate is obvious. At a strain rate of 0.02 s^{-1}, the softening rate is very slow and only reaches about 35 % at a holding time of 100 seconds. As the strain rate is increased to 0.2 s^{-1}, the softening process reaches its maximum value (~85%) in 30 seconds. When the strain rate is further increased to 2 s^{-1} and 10 s^{-1}, the fractional softening reaches its maximum value in about 3 and 0.5 seconds, respectively. The measured $t_{0.5}$, time to 50% softening, decreases from 4.1 seconds to 0.17 seconds as the strain rate is increased from 0.2 s^{-1} to 10 s^{-1}. This is about a 24 fold decrease in the $t_{0.5}$, which is much higher than that reported by

Laasraoui[236] for the fractional softening brought about by static recrystallization (the ratio is about 6.3) in a Nb-B steel deformed to a true strain of 0.25 at 1000 °C.

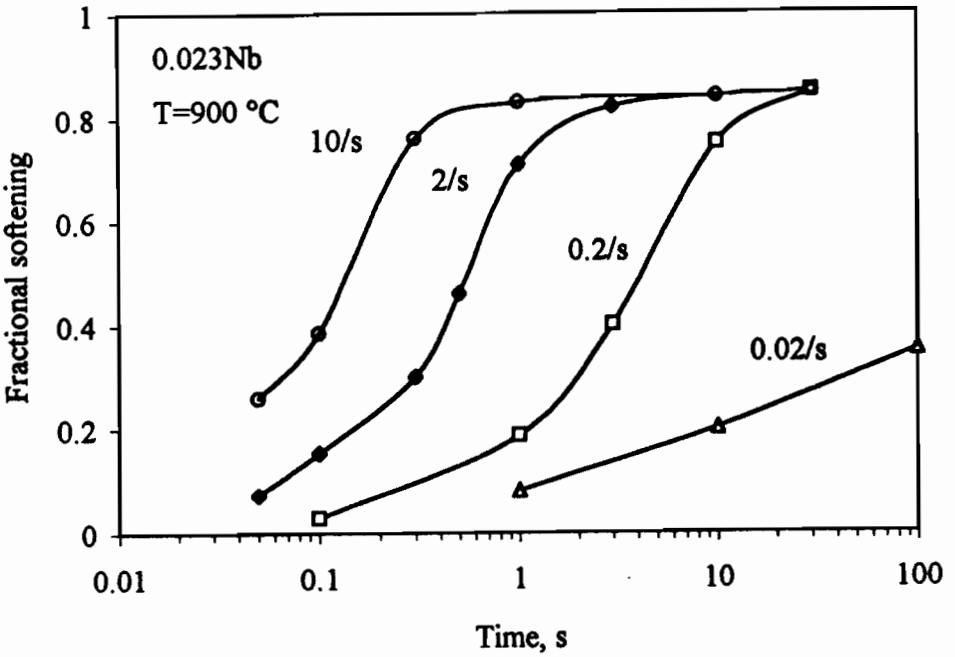

Fig. 5.11 Effect of strain rate on softening in the 0.023Nb steel.

It is also of interest to note that unlike static recrystallization, the softening process in the present case does not go to completion on further increases in holding time. The maximum fractional softening is around 85%. This incomplete softening phenomenon has also been observed by other authors, and Sakai et al.[106, 107] attributed it to the presence of metadynamically recovered grains. These grains have a dislocation density that is not high enough for nucleation, but which nevertheless increases the yield stress of the second deformation in the double twist tests. This leads to the yield stresses of the second twist always being higher than those of the first one, leading to the values of softening below 100% calculated in the present investigation. In addition to the strong strain rate dependence, the incomplete softening behaviour is another factor which must be accounted for in differentiating between conventional static and metadynamic recrystallization.

The temperature rise due to deformation heating was considered in estimating the fractional softening taking place in the 10 s^{-1} tests. The mean flow stress method used by

Laasraoui[236] was employed in the present work, and the fractional softening was calculated using the following expression:

$$X_{corrected} = \frac{\overline{\sigma}_m(T_1) - \overline{\sigma}(T_1)}{\overline{\sigma}_m(T_1) - \overline{\sigma}_0(T_1)} \qquad (5.3)$$

Here T_1 is the measured temperature, which is higher than the isothermal temperature T_0. The yield stress $\overline{\sigma}_0(T_1)$ can be estimated from the following relation:

$$\overline{\sigma}_0(T_1) = \frac{\overline{\sigma}_0(T_0)}{K_S} \qquad (5.4)$$

where K_s is a conversion factor estimated to be 1.17 from the mean flow stress-temperature relationship. The estimated difference between the corrected and uncorrected fractional softening is about 11~16 %. The fractional softening data in Fig. 5.11 are displayed after correction.

5.2.2.3 Influence of Deformation Temperature on Softening

The effect of deformation temperature on the fractional softening of metadynamic recrystallization is shown in Fig. 5.12. In this case, the strain rate was held constant, while the deformation temperature was varied. Both steels show that the amount of softening increases with increasing temperature. In the 0.023Nb steel (Fig. 5.12(a)), the $t_{0.5}$ decreases from 0.57 to 0.3 seconds when the deformation temperature is increased from 900 to 1000 °C; it further decreases to 0.15 seconds when the temperature is raised to 1090 °C. In the 0.07Nb steel (Fig. 5.12(b)), the $t_{0.5}$ decreases from 0.57 to 0.28 seconds when the deformation temperature is increased from 970 to 1070 °C. These decreases in $t_{0.5}$ correspond to a factor of about 2 for each 100 °C increase in deformation temperature in the testing range. This is significantly smaller than the ratio that applies to static recrystallization. In fact, factors of 7.1~10 have been reported by several authors for the decrease in the $t_{0.5}$ with each 50 °C increase in deformation temperature over the range 950 to 1100 °C for static recrystallization in Nb steels. The present observations are in good agreement with those reported by Hodgson[82] and Roucoules[109]. It can therefore be concluded that the kinetics of metadynamic recrystallization are relatively temperature insensitive. This is another difference between metadynamic and conventional static recrystallization.

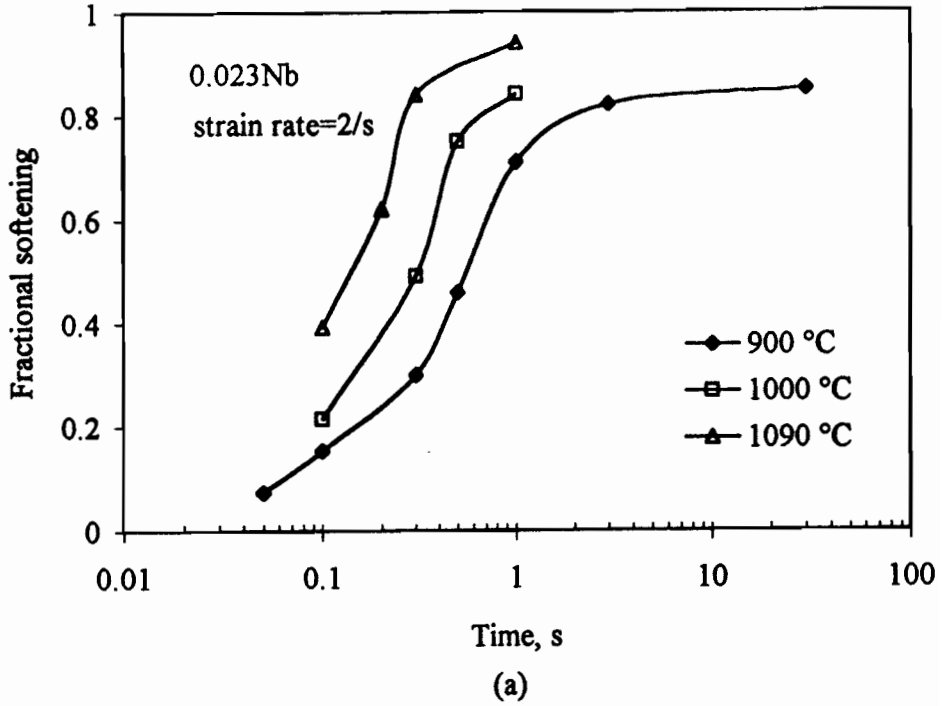

(a)

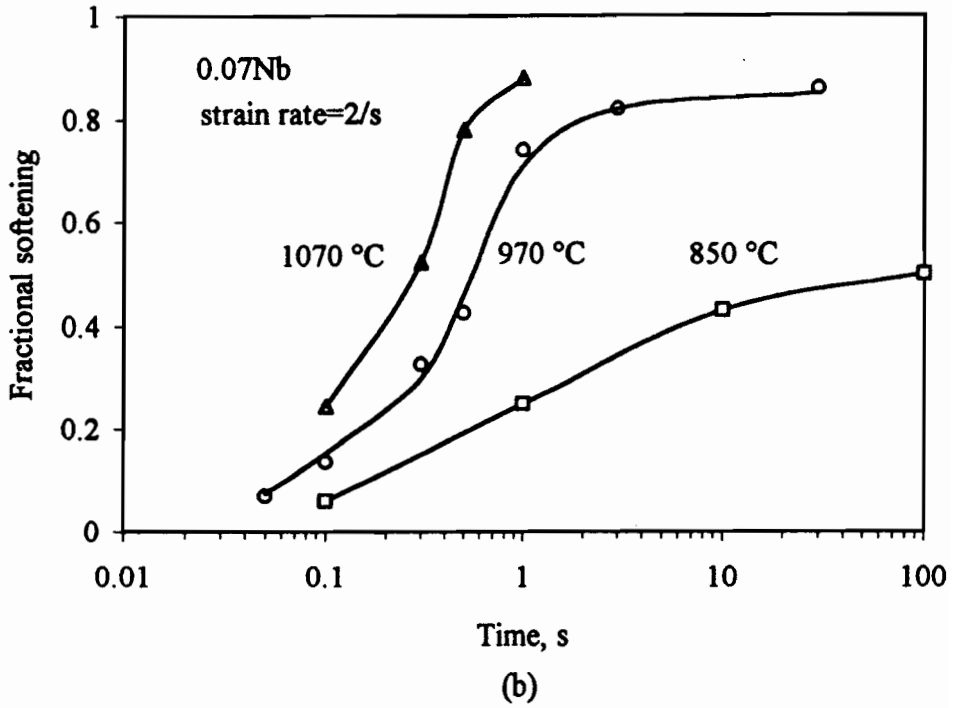

(b)

Fig. 5.12 Effect of temperature on softening in the two steels.

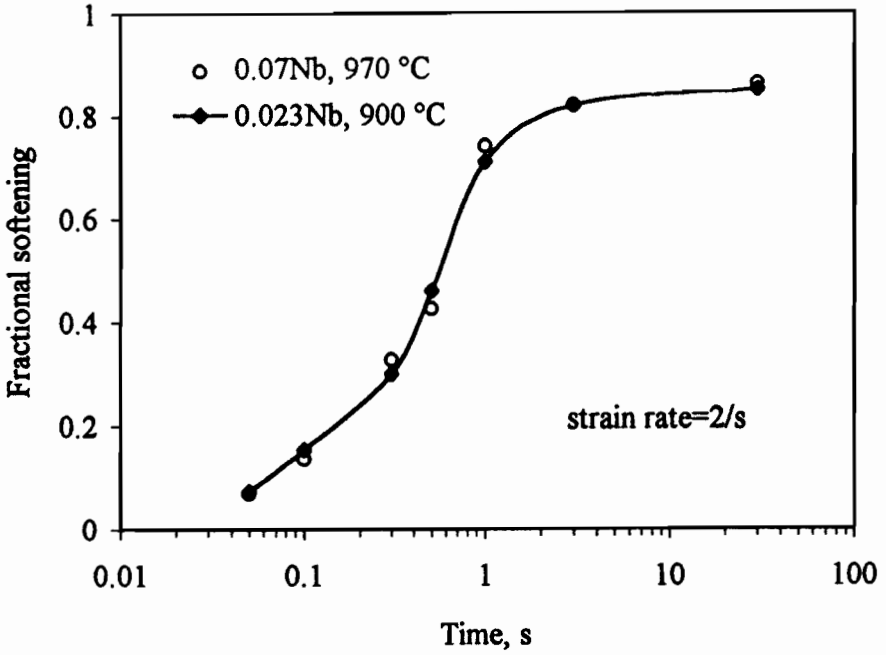

Fig. 5.13 Effect of Nb in solution on softening.

However, it should be pointed out that the above statement is only true in the solute drag range. As soon as Nb(CN) precipitation takes place, the rate of recrystallization is slowed down significantly. The softening curve of the 0.07Nb steel at 850 °C (Fig. 5.12 (b)) illustrates this phenomenon very well. Incomplete softening behaviour is also displayed by the softening curve at 970 °C.

It is also of interest to note that the softening curve of the 0.07Nb steel at 970 °C is nearly the same as that of the 0.023Nb steel at 900 °C (shown in Fig. 5.13). On the one hand, the peak strains for these two steels are quite close to one another at the temperatures given above. This suggests that they have nearly the same nucleus densities, or that the same numbers of nuclei are growing. On the other hand, it also reflects the effect of Nb in solution on the rate of recrystallization in terms of grain growth: for the same rate, the temperatures for the higher Nb steels are higher than those for the lower Nb steels.

5.2.3 Simulations of Rod and Hot Strip Mills

In order to simulate rod and hot strip mills, an "average" multipass deformation schedule was designed; this was presented in Fig. 5.1 and referred to as Schedule F. Four

passes with pass strains of 0.3 and interpass times of 30 seconds were employed at relatively high temperatures to simulate roughing. The specimens were then cooled to selected temperatures ranging from 850 °C to 970 °C and thirteen passes with identical pass strains were executed at these temperatures to simulate finish rolling. The interpass times were changed from 0.05 to 8 seconds while the strain rates were maintained at 2 s^{-1}.

5.2.3.1 Simulations Carried Out on the 0.023Nb Steel

The 0.023Nb steel flow curves generated using multipass deformation are presented in Fig. 5.14. In this case, the deformation temperature was held constant at 850 °C, while the interpass times were increased from 0.05 to 8 seconds. It can be seen that in the case of the 0.05 second test (Fig. 5.14 (a)), little conventional static or metadynamic recrystallization could take place because of the short interpass time. There was essentially no interpass softening. This led to a well developed peak shaped envelope of flow curves that fitted the one generated by single pass deformation. This indicates that dynamic recrystallization took place under these conditions.

When the interpass time was increased to 0.5 seconds (Fig. 5.14 (b)), a peak shaped envelope of flow curves was still observed, but the envelope lies slightly above the single pass flow curve after the 6th pass. The estimated level of interpass softening from the 5th to the 13th pass falls between 20 to 25% (see Fig. 5.15). This suggests that metadynamic recrystallization has now started to contribute to the interpass softening.

When the interpass time was increased to 1 second (Fig. 5.14(c)), little interpass softening was observed after the first three passes and the strain was largely accumulated. Much of the accumulated strain was released after the 4th pass, however, as indicated by the appreciable interpass softening. Under these conditions, the accumulated strain never reached the peak strain (measured as 1.35 from the single pass flow curve). As a result, the flow curve envelope did not follow the single pass one.

When the interpass time was further increased to 8 seconds, only the first pass strain was significantly accumulated. The interpass softening then ranged between 30 and 40 % from the third pass to the 13th pass and the individual flow curves display similar shapes and work hardening rates. No peak is evident on the flow curve envelope, and conventional static recrystallization is believed to be responsible for the interpass softening.

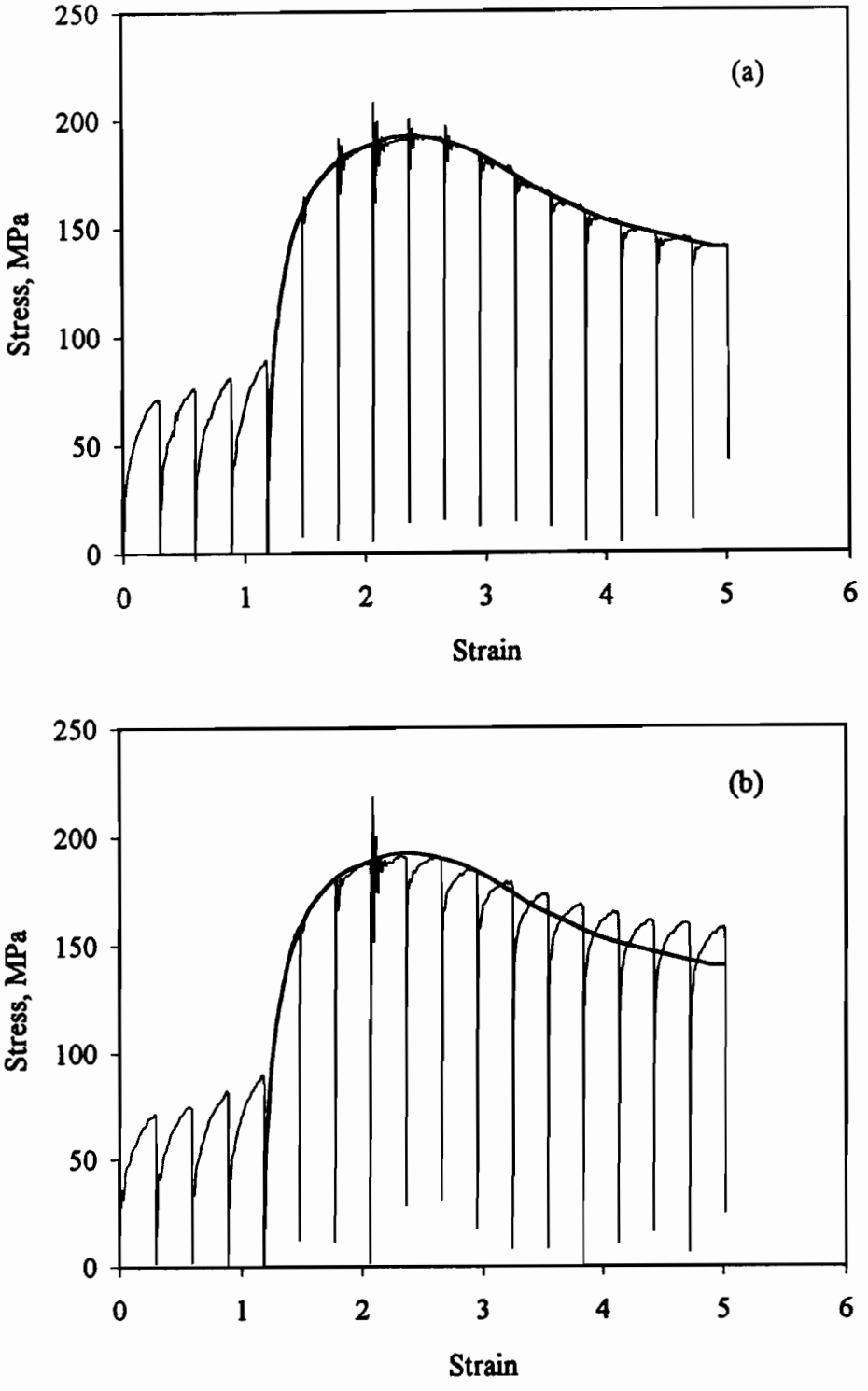

Fig. 5.14 Effect of interpass time on the 0.023Nb steel flow curves determined at 850 °C and a strain rate of 2 s^{-1}: (a) t=0.05 s, (b) t=0.5 s, (c) t=1 s, (d) t=8 s.

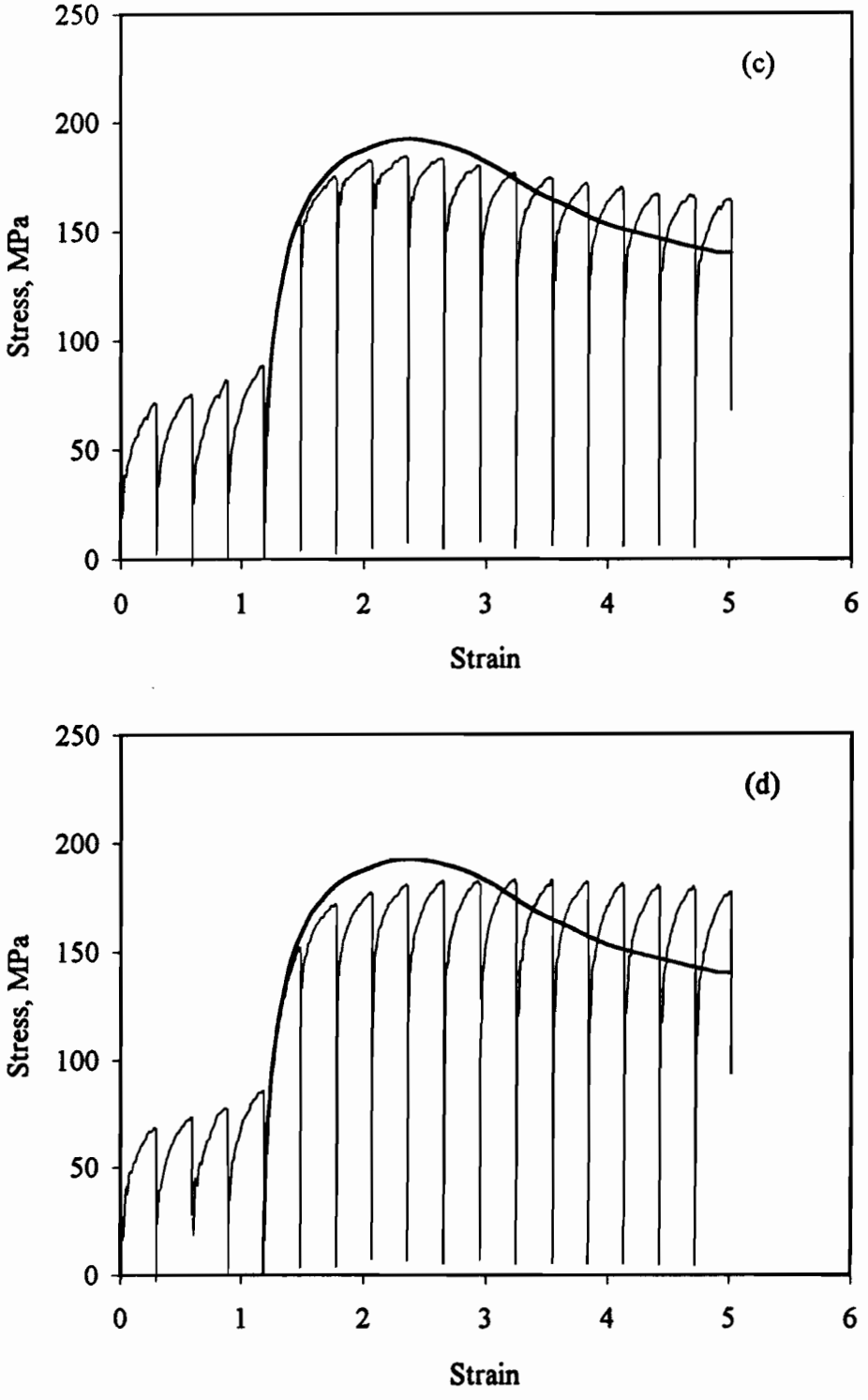

Fig. 5.14 Effect of interpass time on the 0.023Nb steel flow curves determined at 850 °C and a strain rate of 2 s^{-1}: (a) t=0.05 s, (b) t=0.5 s, (c) t=1 s, (d) t=8 s.

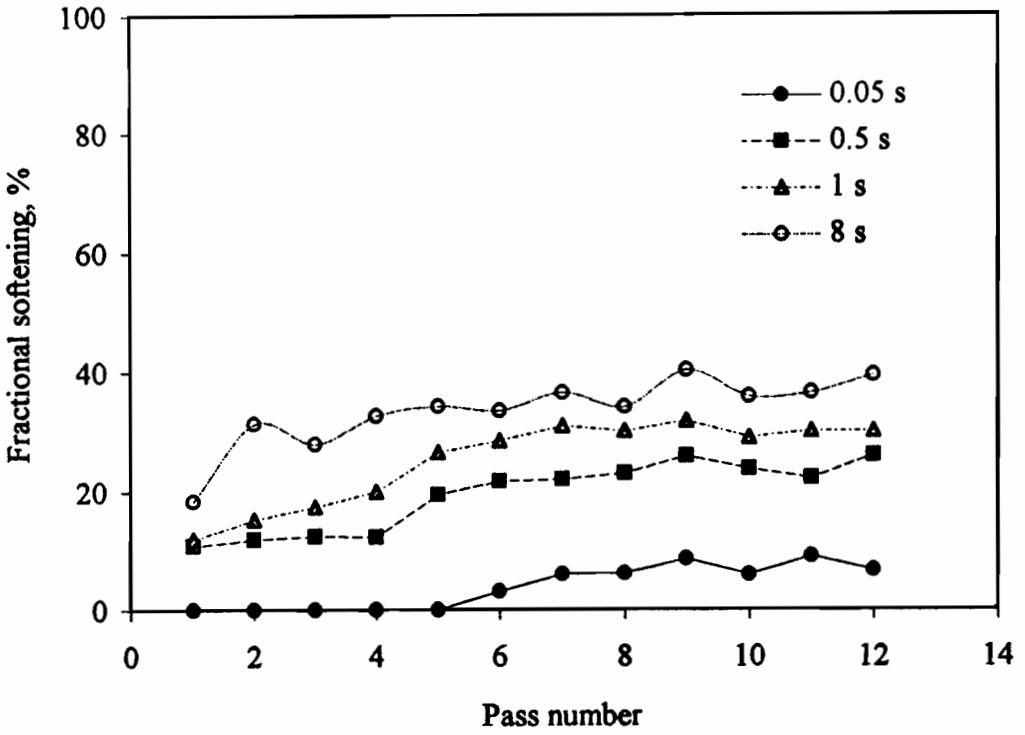

Fig. 5.15 Fractional softening determined from the flow curves shown in Fig. 5.14.

Similar simulations were carried out at 880, 940 and 970 °C. The flow curves observed are presented in Figures. 5.16 through to 5.18. In the case of the 0.05 second tests, all three temperature simulations demonstrate a well developed peak shaped flow curve envelope. All the flow curves after the second pass have a lower work hardening rate and display "stair-like" softening behaviour. This suggests that the dislocation structures were not significantly changed during the interpass delays, and that recovery was largely responsible for the small degree of interpass softening (the estimated interpass softening was below 20%). Neither static nor metadynamic recrystallization seems to take place. It is also interesting to note that the "stair-like" softening was triggered at earlier passes when the deformation temperature was increased. For instance, the beginning of the stair is advanced from the 5th pass to the second pass when the deformation temperature is increased from 880 to 970 °C. This also indicates that recovery is more rapid at higher than at lower temperatures.

In the case of the 0.5 second tests, an increase in deformation temperature leads to more and more interpass softening. As shown in Fig. 5.19, the fractional softening

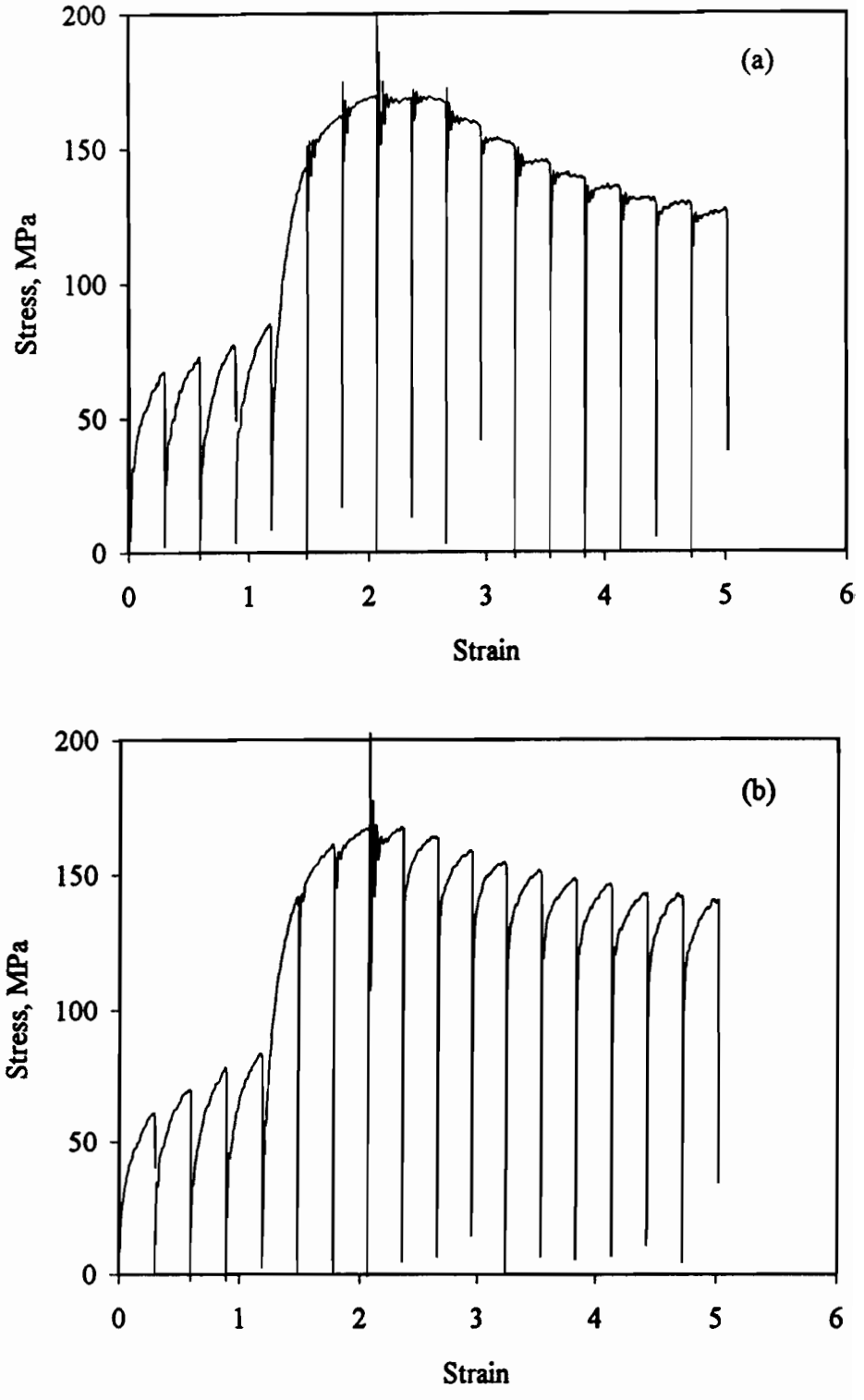

Fig. 5.16 Effect of interpass time on the 0.023Nb steel flow curves determined at 880 °C and a strain rate of 2 s^{-1}: (a) t=0.05 s, (b) t=0.5 s.

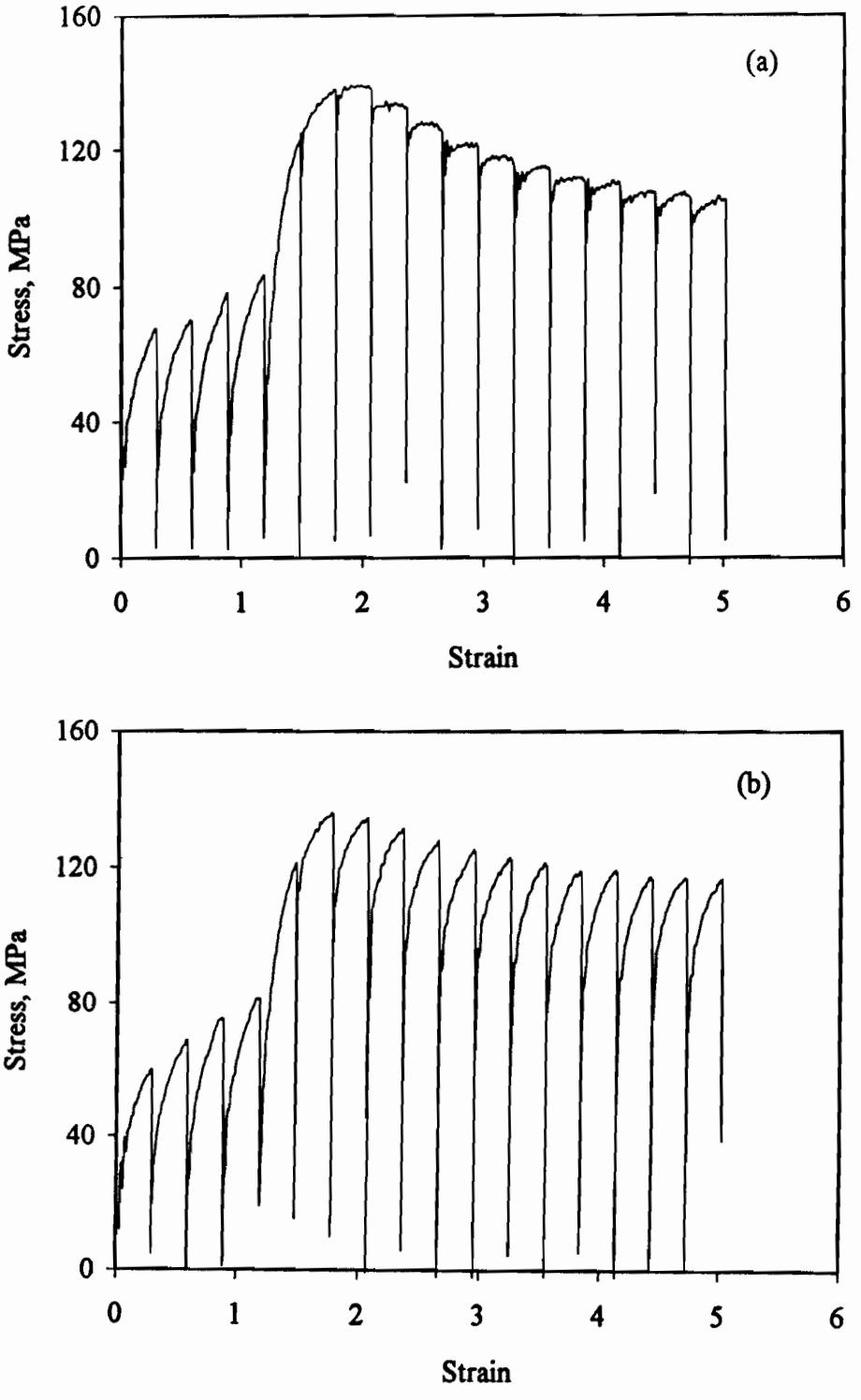

Fig. 5.17 Effect of interpass time on the 0.023Nb steel flow curves determined at 940 °C and a strain rate of 2 s^{-1}: (a) t=0.05 s, (b) t=0.5 s.

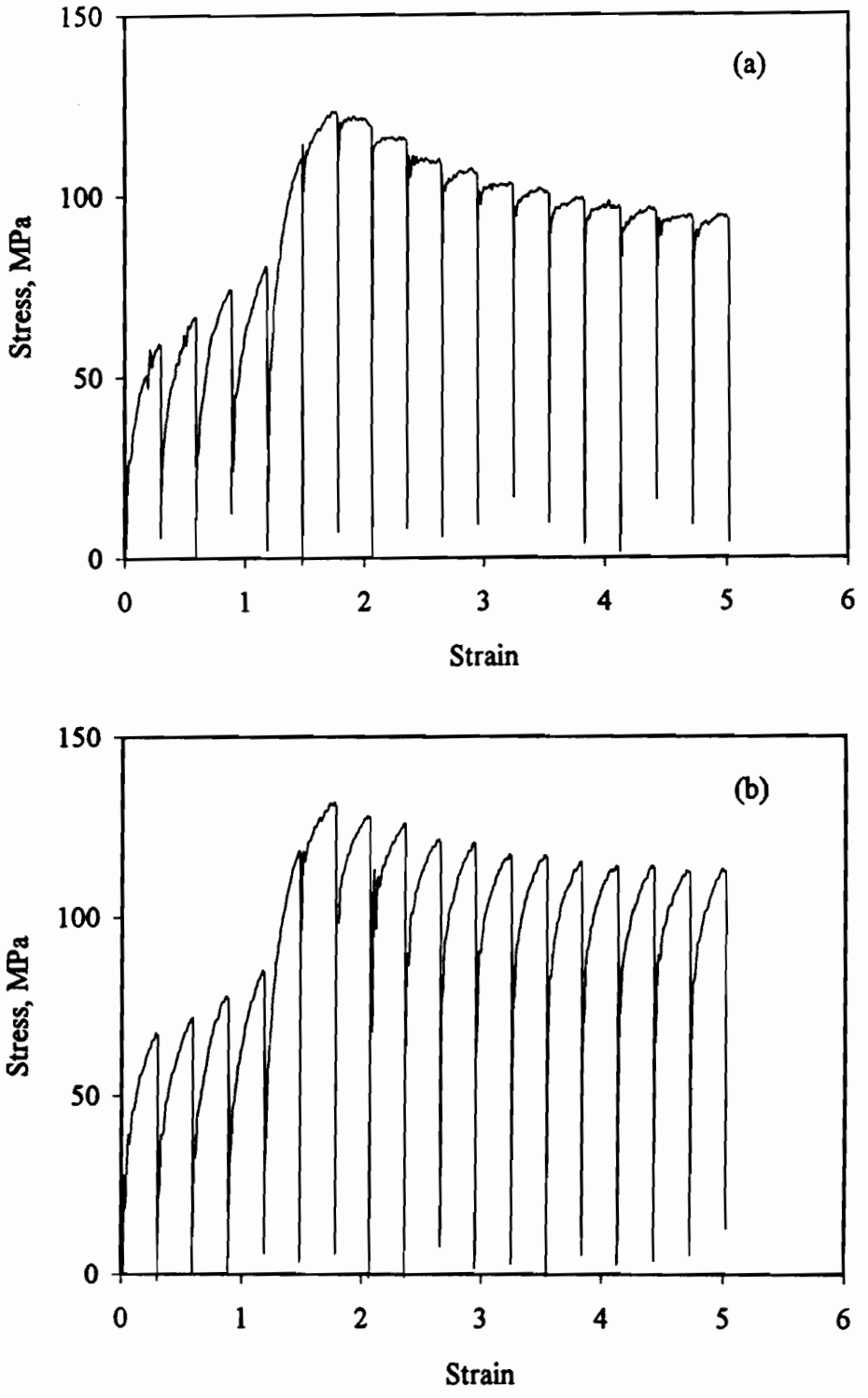

Fig. 5.18 Effect of interpass time on the 0.023Nb steel flow curves determined at 970 °C and a strain rate of 2 s^{-1}: (a) t=0.05 s, (b) t=0.5 s.

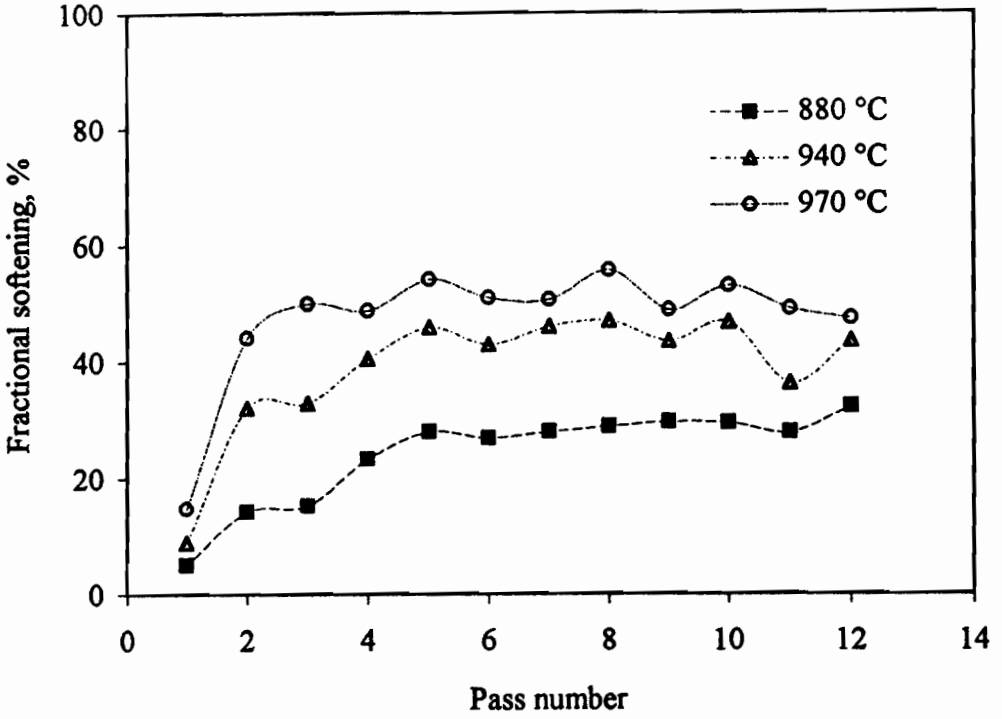

Fig. 5.19 Fractional softening determined from the flow curves shown in Figures 5.16 through to 5.18, t=0.5 s.

increases from 28% to 54% when the deformation temperature is increased from 880 to 970 °C. All the fractional softening vs. strain plots display "oscillations". This suggests that a repeated strain accumulation-strain release process was involved in these cases and that the evolution of the microstructure is more difficult to predict because of partial recrystallization.

5.2.3.2 Simulations Carried Out on the 0.07Nb Steel

The flow curves determined on the 0.07Nb steel are presented in Figs. 5.20 and 5.21. The measured levels of interpass softening are shown in Fig. 5.22. It can be seen from Fig. 5.20 (a) that there is full strain accumulation from pass to pass, and the peak shape is well developed. The "stair" heights are smaller than in the 0.023Nb steel. This suggests that the higher Nb concentration does strongly retard both recovery and recrystallization, as further demonstrated in Figs 5.20 (b) and (c). Compared with the 0.05 second flow curves, the 0.5 and 1 second flow curve envelopes are flatter but still display a peak. The levels of interpass softening are below 15%, and are about 10% lower than in the 0.023Nb steel. Based on these observations, it can be concluded that

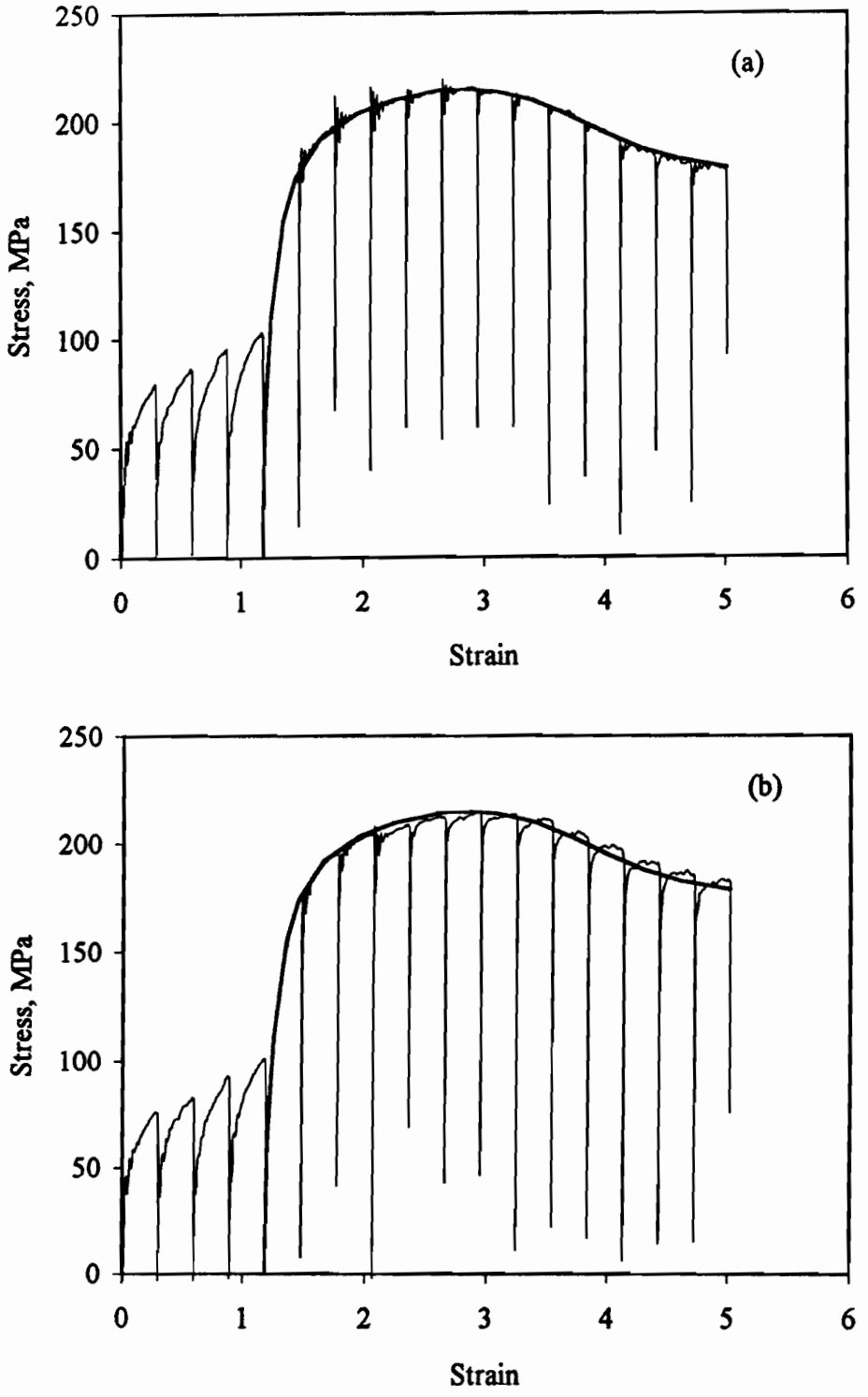

Fig. 5.20 Effect of interpass time on the 0.07Nb steel flow curves determined at 850 °C and a strain rate of 2 s^{-1}: (a) t=0.05 s, (b) t=0.5 s, (c) t=1 s, (d) t=8 s.

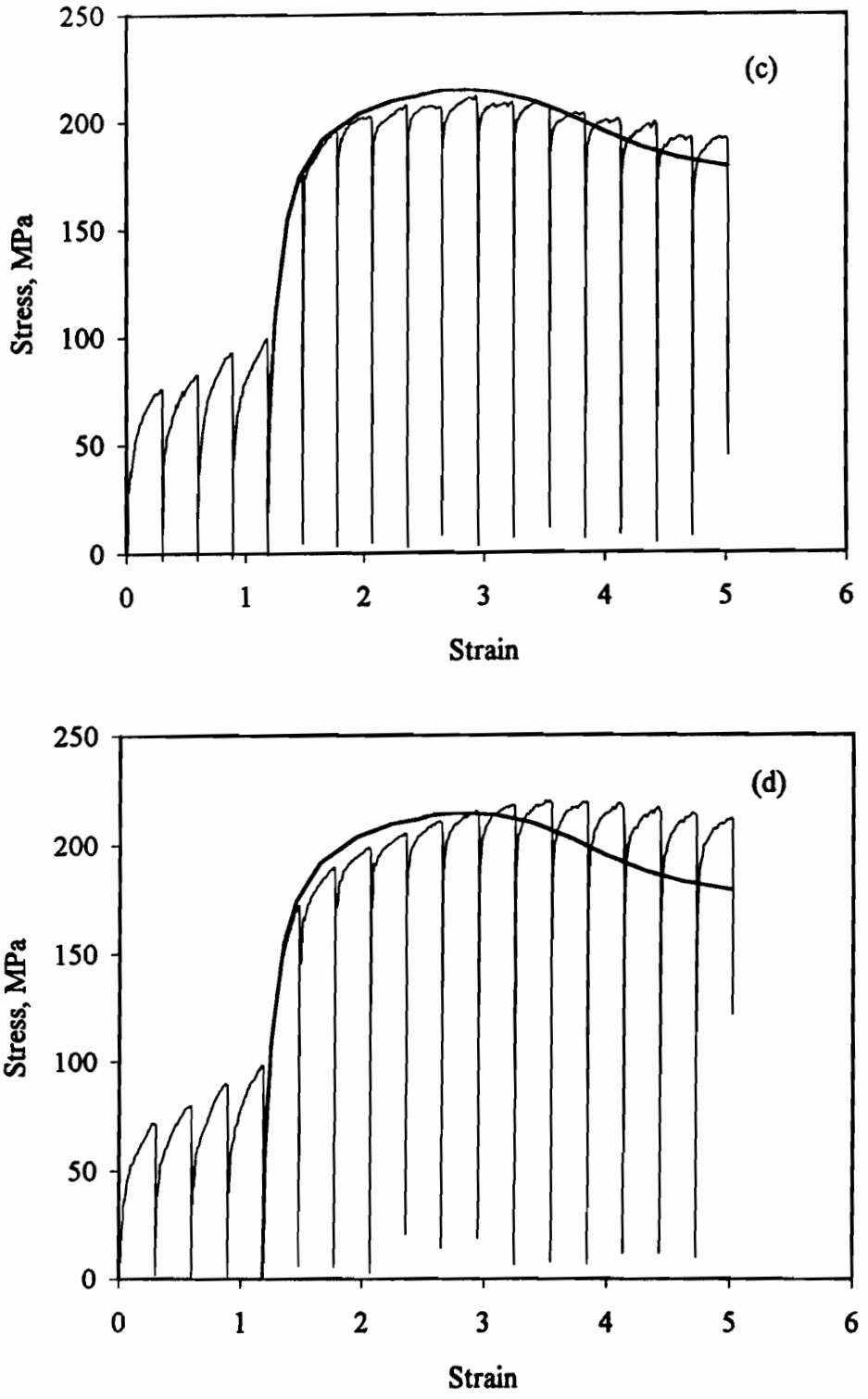

Fig. 5.20 Effect of interpass time on the 0.07Nb steel flow curves determined at 850 °C and a strain rate of 2 s^{-1}: (a) t=0.05 s, (b) t=0.5 s, (c) t=1 s, (d) t=8 s.

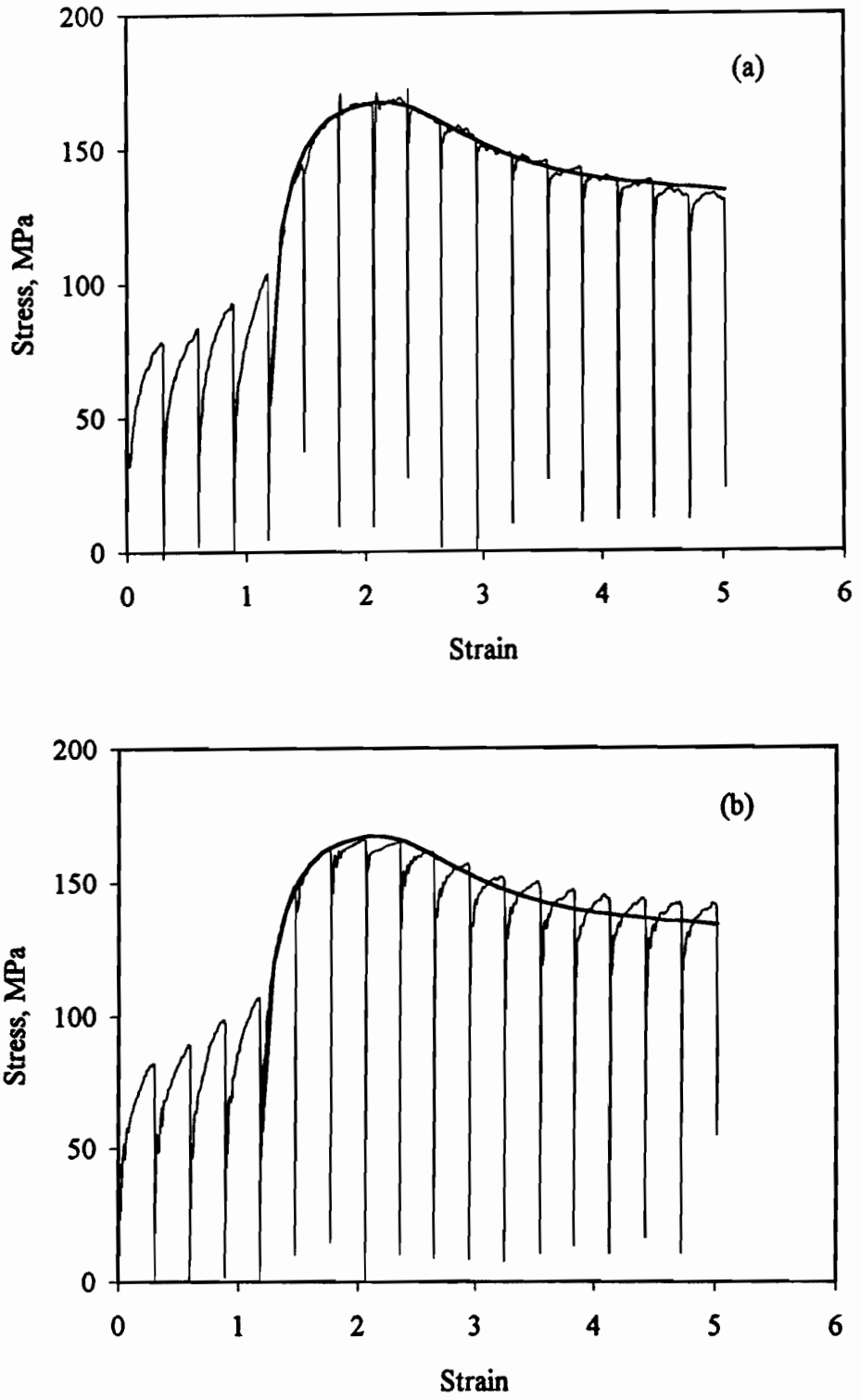

Fig. 5.21 Effect of interpass time on the 0.07Nb steel flow curves determined at 970 °C and a strain rate of 2 s^{-1}: (a) t=0.05 s, (b) t=0.5 s, (c) t=1 s, (d) t=8 s.

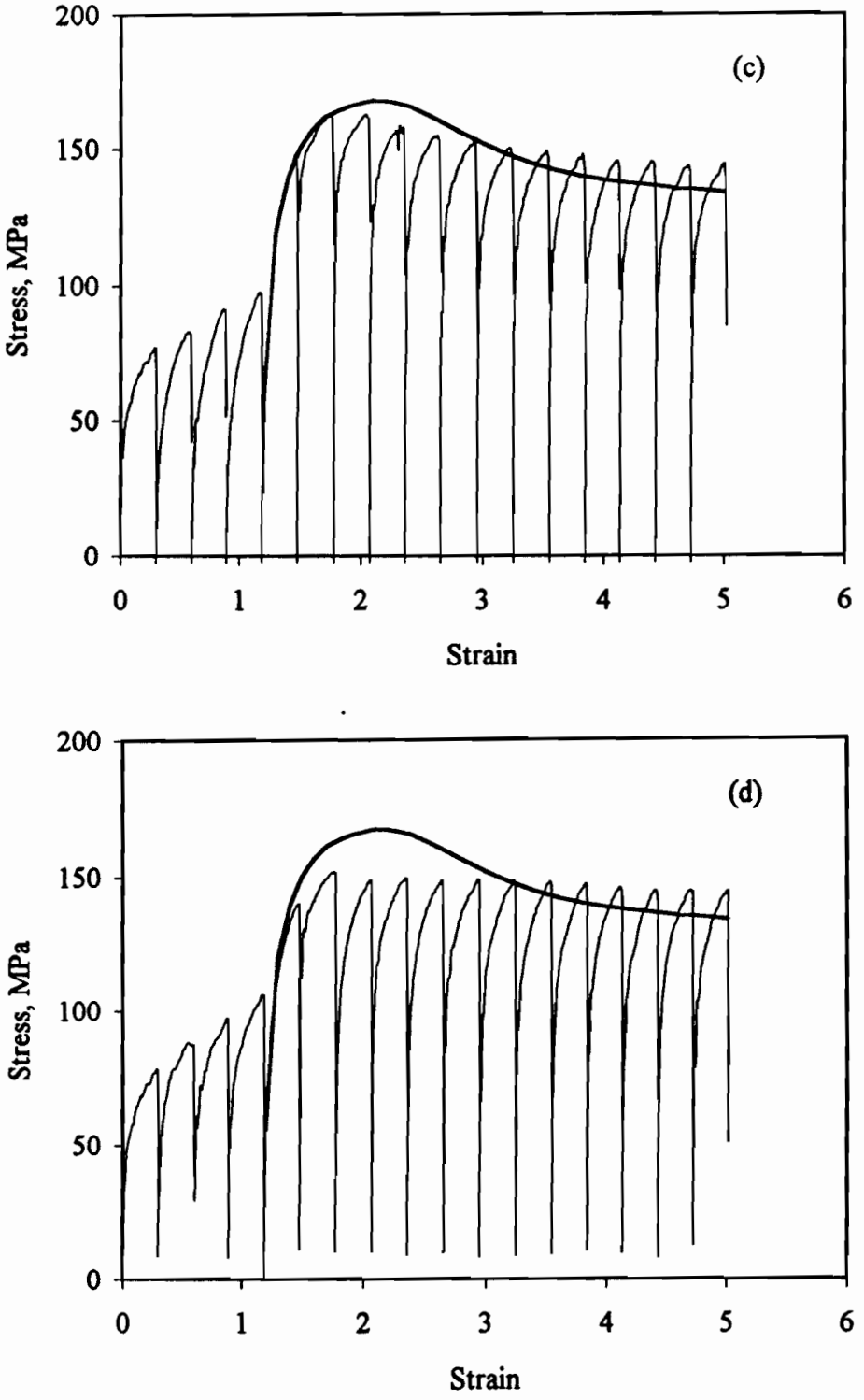

Fig. 5.21 Effect of interpass time on the 0.07Nb steel flow curves determined at 970 °C and a strain rate of 2 s^{-1}: (a) t=0.05 s, (b) t=0.5 s, (c) t=1 s, (d) t=8 s.

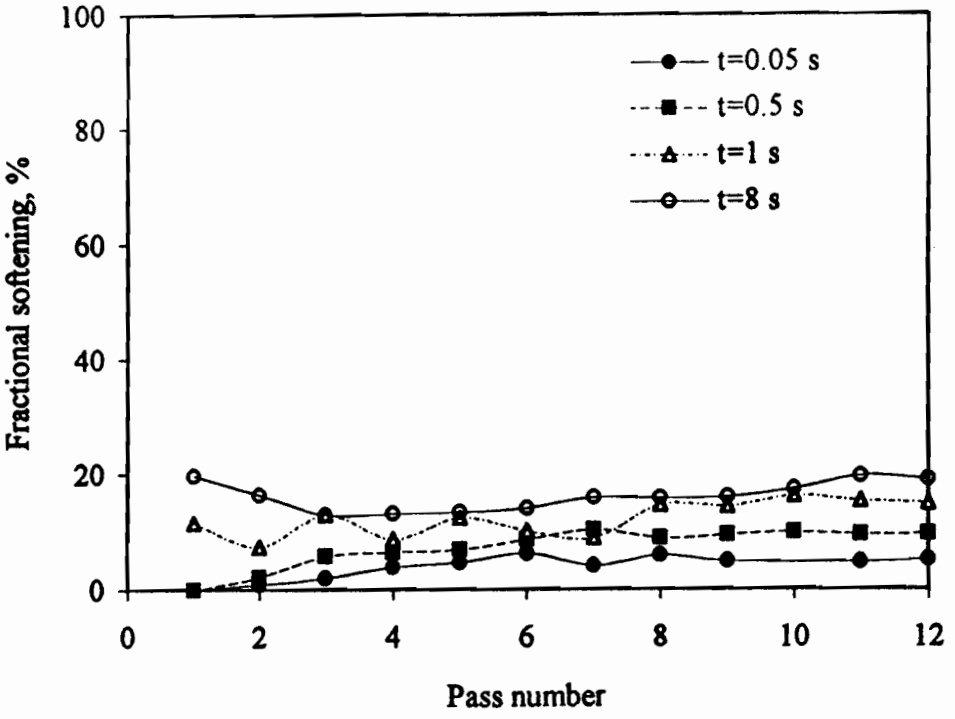

(a)

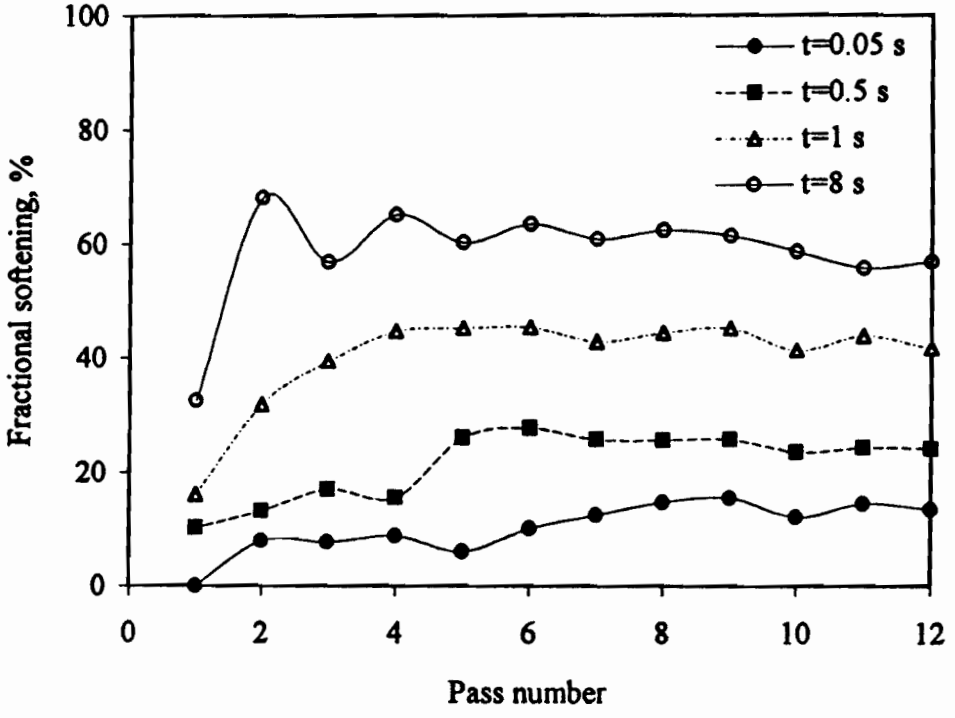

(b)

Fig. 5.22 Fractional softening measured from the flow curves shown in Figs. 5.20 and 5.21: (a) at 850 °C, (b) at 970 °C.

dynamic recrystallization was initiated in these samples. In the case of the 8 second tests, it is not clear whether dynamic recrystallization was initiated or not, since there was somewhat more interpass softening than in the 0.05, 0.5 and 1 second tests. Furthermore the peak on the flow curve envelope is not that obvious in this case.

At 970 °C, only the 0.05 second flow curve envelope follows the single pass flow curve (Fig. 5.21(a)). In the case of the 0.5 second tests (Fig. 5.21(b)), although the envelope displays a peak, it does not conform closely to the shape of the single pass one. The level of interpass softening after the 4th pass was about 25%. This amount of softening can be attributed to recovery and metadynamic recrystallization since the accumulated strain is greater than the peak strain.

When the interpass time was increased to 1 second, only the first pass strain was fully accumulated. There was about 32% softening between the second and third passes, and this gradually increased to 45% after the further passes (Fig. 5.22(b)). Under these circumstances, the accumulated pass strain was never large enough to initiate dynamic recrystallization. The interpass softening was therefore judged to be due largely to recovery and static recrystallization. When the interpass time was further increased to 8 seconds, the extent of interpass softening became more visible. The fractional softening reached 67% at the second pass, then decreased to 60% at the third pass and maintained a level of 60% for the remainder of the passes (Fig. 5.22(b)). As a result, the maximum flow stresses remained nearly the same from the third to the 13th pass. It is clear that static recrystallization was responsible for the interpass softening in the case of the long interpass times.

5.3 Analysis and Discussion

In this part, the experimental results will be analyzed and such important parameters as the activation energies of deformation, dynamic recrystallization and metadynamic recrystallization will be derived. Finally, empirical equations for predicting the peak and steady state strains will be deduced, and a kinetic model for metadynamic recrystallization in Nb steels will be proposed.

5.3.1 Modelling Dynamic Recrystallization

5.3.1.1 Activation Energy of Deformation

Various empirical equations have been proposed to describe the thermally activated process of hot deformation. The one used most frequently was suggested by Sellars and Tegart in 1966[202]. In their proposal, the steady state flow stress at high temperatures can be correlated with the strain rate and deformation temperature using the following relation:

$$\dot{\varepsilon} = A\left[\sinh\left(\alpha\sigma_s\right)\right]^{n'} \exp\left(\frac{-Q_{def}}{RT}\right) \qquad (5.5)$$

where $\dot{\varepsilon}$ is the strain rate, σ_s is the steady state stress, A, α and n' are constants independent of the temperature, R is the gas constant, T is the absolute temperature, and Q_{def} is the activation energy of deformation.

In the present work, Q_{def} was determined in two steps. First, the peak stresses from the results presented above were plotted vs. the logarithm of the strain rate, as shown in Fig. 5.23. This gives the relationship between the peak stress and the strain rate at constant temperature. It can be seen that, at 940 °C and 970 °C, the peak stresses are linearly related to $\log(\dot{\varepsilon})$. The slopes for the two straight lines are approximately equal, although the intercepts are different. The strain rates at selected peak strains can now be recalculated from these relations. Using these derived data, the logarithm of the strain rate at the selected peak stress is plotted vs. the inverse absolute temperature (see Fig. 5.24). These plots have slopes that vary little as the peak stress is increased from 140 to 160 MPa. The activation energy of deformation can then be determined from these slopes as follows:

$$Q_{def} = -R\frac{\partial(\ln\dot{\varepsilon})}{\partial(1/T)}\Big|_{\sigma_p} \qquad (5.6)$$

The Q_{def} determined in this way is about 370 kJ/mol for the peak stresses in the range 140 to 160 MPa. This value compares well with that (375 kJ/mol) reported by Roucoules et al.[235] for a 0.061C-1.2Mn-0.039Nb steel and is somewhat higher than that observed by Laasraoui and Jonas[232] for a 0.026C-1.42Mn-0.055Nb steel.

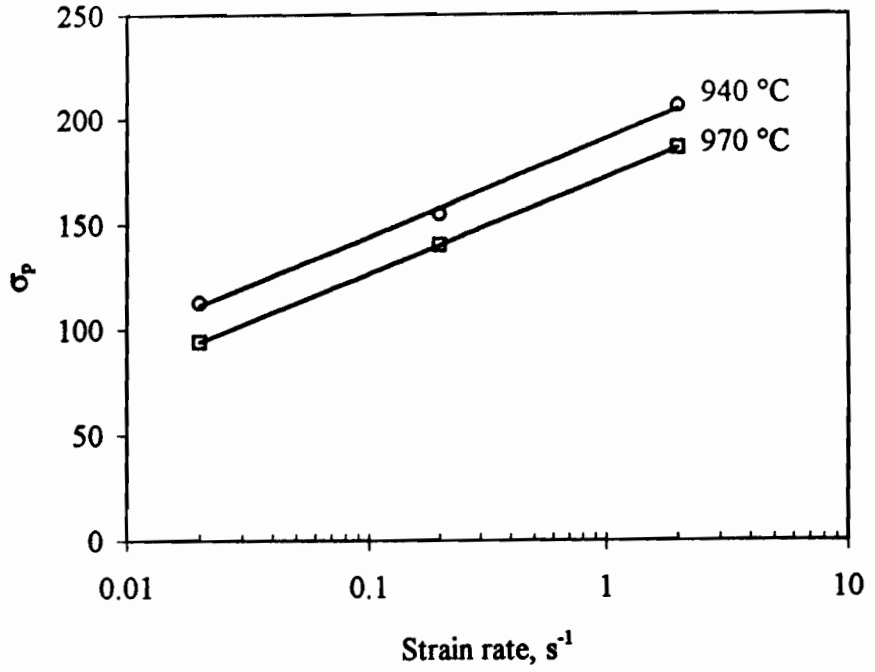

Fig. 5.23 Dependence of peak stress on strain rate in the 0.07Nb steel.

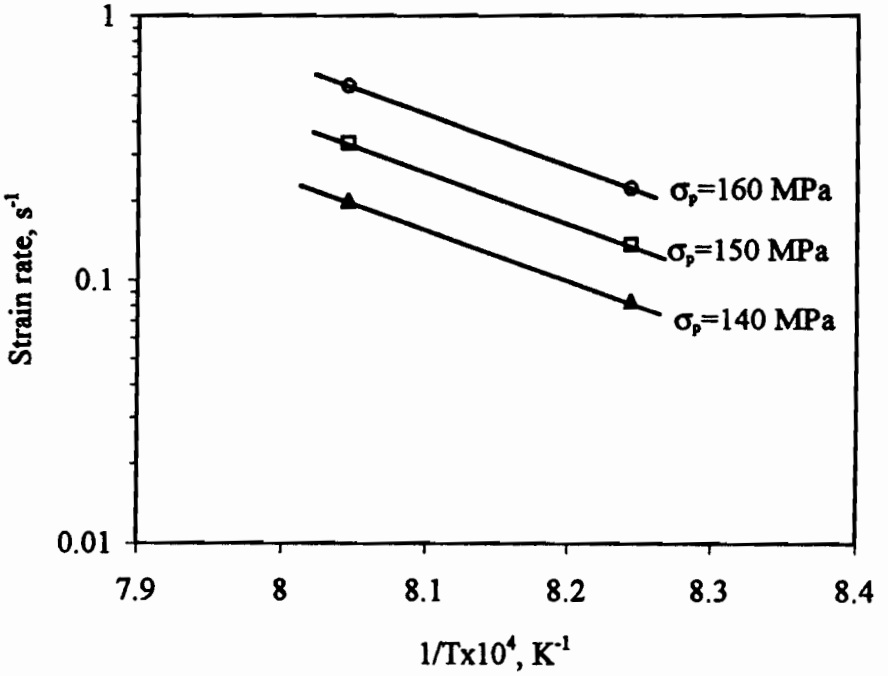

Fig. 5.24 Temperature dependence of the strain rate at constant peak strain in the 0.07Nb steel.

5.3.1.2 Correlation of the Peak Strain with Nb Concentration and the Deformation Parameters

As reviewed in Chapter 2, dynamic recrystallization is initiated at the critical strain, which is less than the peak strain. The measurement of this critical strain is difficult and it is commonly estimated instead from the peak strain by multiplying by a constant. The peak strain can be measured directly from the flow curve, and has been related to the initial grain size D_0 and the Zener-Hollomon parameter Z by the following expression:

$$\varepsilon_p = A_{\varepsilon_p} D_0^p Z^n \qquad (5.7)$$

where A_{ε_p}, p and n are constants. The subscript ε_p is used to avoid confusion from other constant A's, which will be introduced later. The exponent p is reported to be 0.5 by Sellars[62], and 0.3 by Hodgson[82]. From the present results, it was determined to be 0.31, a value that compares well with that of Hodgson.

Some $\log(\varepsilon_p)$-$\log(Z)$ plots were prepared from these data; they are shown in Fig. 5.25. In order to relate the peak strain to the Nb content, results from Roucoules[109] (the 0.039Nb steel) and Mavropoulos[237] (the 0.055Nb steel) are also presented in this figure. It can be seen that these plots are straight lines and the slopes are approximately equal. The Z exponent in equation (5.7) was determined by taking the average value of these slopes; the latter turned out to be 0.17. This is in good agreement with the values observed by Hodgson[82] and Roucoules[109]. The values of the constant A_{ε_p} can be determined from the following expression:

$$A_{\varepsilon_p} = D_0^{-0.31} 10^{A'} \qquad (5.8)$$

Here A' is the intercept of the $\log(\varepsilon_p)$-$\log(Z)$ plot. The dependence of A_{ε_p} on the Nb content can now be determined, as shown in Fig. 5.26. Here it can be seen that there is a linear relation between the peak strain and log[Nb]. The final form of equation (5.7) with the effect of Nb taken into consideration therefore is the following:

$$\varepsilon_p = (3.34 \log[Nb] + 9.79) \times 10^{-4} D_0^{0.31} Z^{0.17} \qquad (5.9)$$

Predicted and measured ε_p's are compared in Fig. 5.27 and good agreement is displayed.

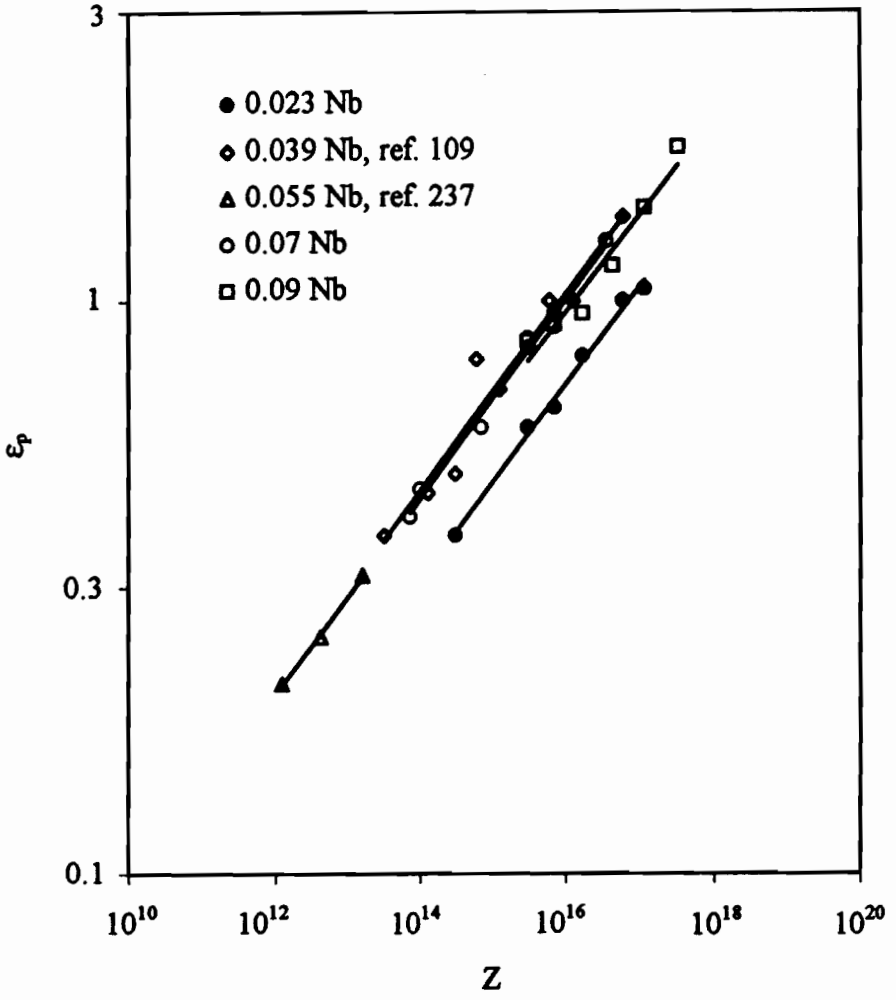

Fig. 5.25 Dependence of peak strain on the Zener-Hollomon parameter in the five Nb steels.

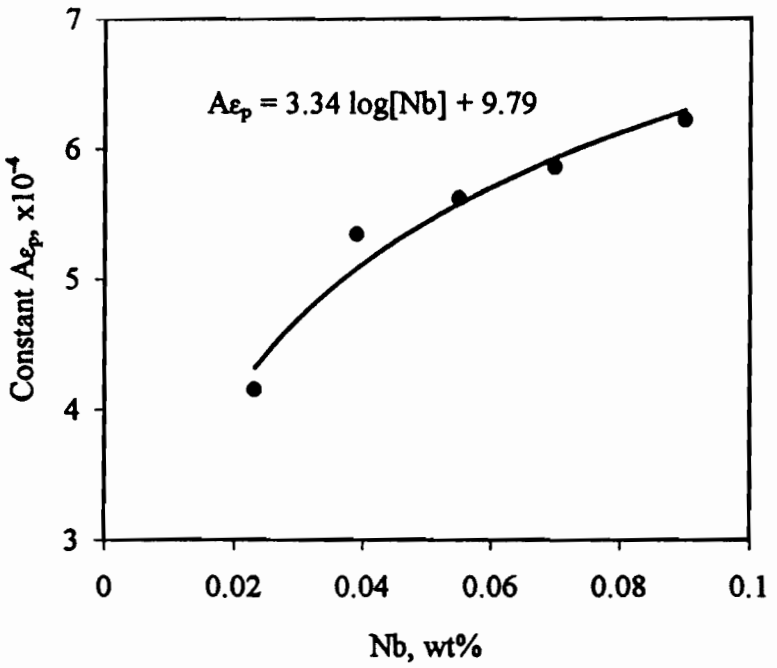

Fig. 5.26 Effect of Nb in solution on the constant A_{ε_p}.

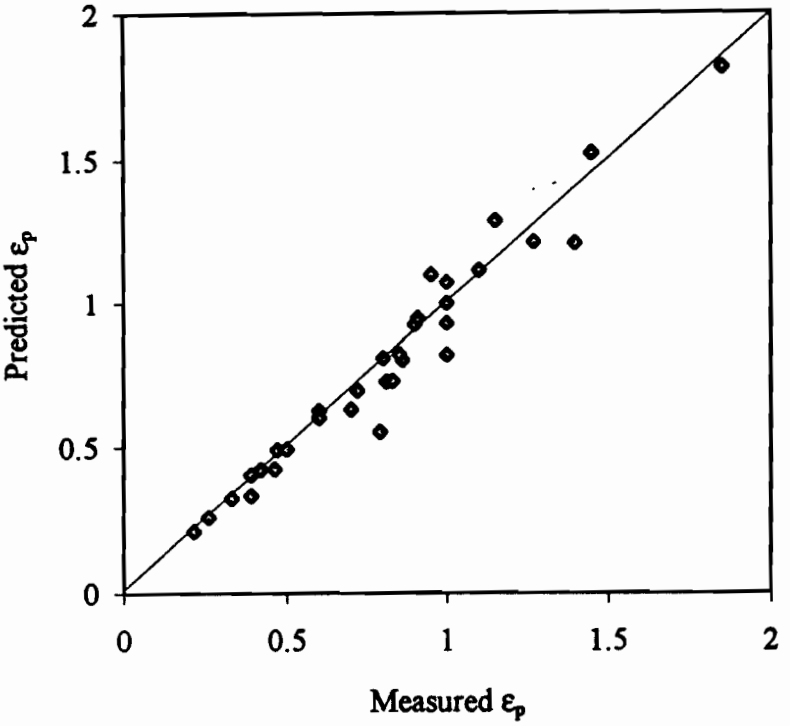

Fig. 5.27 Comparison between predicted and measured ε_p values.

5.3.1.3 Dynamic Recrystallization Kinetics

Static and metadynamic recrystallization are restoration processes that take place *after deformation*. The fractional softening produced by these processes can therefore be estimated by studying the reloading flow curves. Dynamic recrystallization, by contrast, takes place *during deformation*. This makes it difficult to estimate the fractional softening produced by this process. The basic method used for this purpose is metallography; however, this involves a number of difficulties. One is that the microstructure must be frozen in order for the fraction recrystallized to be measured. The fraction recrystallized at the peak strain is thought to be 5%~10%, while that at the steady state strain is about 80~90%[99, 109]. It has also been observed that the fraction recrystallized increases in direct proportion to the strain (ε-ε_c) until a considerable fraction of the microstructure is recrystallized; after this, the rate of recrystallization tends to decrease.

In the present work, it was assumed that the levels of fractional softening at the peak and steady state strains are 5% and 85%. The time required to deform from ε_p to ε_{ss} is defined as $t_{0.8}$ and can be calculated from the following expression:

$$t_{0.8} = \frac{\varepsilon_{ss} - \varepsilon_p}{\dot{\varepsilon}} \qquad (5.10)$$

From the results presented in §5.2.1, it can be seen that the peak and steady state strains depend on strain rate and deformation temperature. The values of $t_{0.8}$ can also be correlated with the strain rate or Zener-Hollomon parameter. Such an approach has been used by other several authors to model the kinetics of metadynamic recrystallization. One of the expressions employed has the following form:

$$t_{0.8} = A_{dyn} Z^{n_{dyn}} \exp\left(\frac{Q_{dyn}}{RT}\right) \qquad (5.11)$$

where A_{dyn}, and n_{dyn} are constants, Q_{dyn} is the activation energy of dynamic recrystallization, T is the absolute temperature, and R is the gas constant. The Z exponent can be obtained from the $\log(t_{0.8}) - \log(\dot{\varepsilon})$ plots. It is clear that all the plots in Fig. 5.28 are described by linear relationships and that the slopes of these plots are approximately equal. Then the exponent n_{dyn} can be evaluated by averaging these slopes. This leads to a

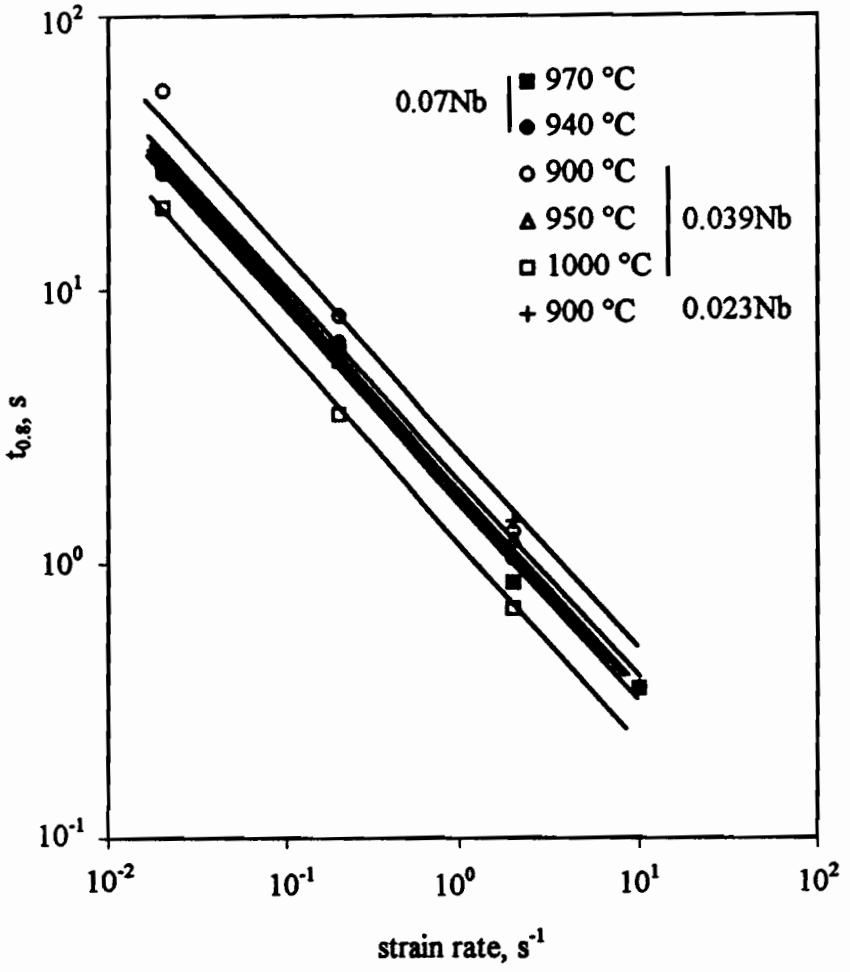

Fig. 5.28 Dependence of $t_{0.8}$ (time of deformation from peak to steady state) on strain rate in three Nb steels.

value of -0.73. No comparisons with other results can be made at this stage since no $t_{0.8}$ or $t_{0.5}$ data are currently available from the literature concerning the kinetics of dynamic recrystallization. However, it is interesting to note that the present value is close to that observed by Hodgson and Gibbs[219] for metadynamic recrystallization, and is somewhat higher than that reported by Roucoules et al.[235] It is also worth noting that the strain rate (or Z) exponent associated with dynamic recrystallization is about twice as high as

those for static recrystallization reported in the literature[63, 72, 238, 239]. It can thus be concluded that dynamic recrystallization displays a strain rate dependence about twice as high as that of static recrystallization.

The other features that can be observed in Fig. 5.28 are the following. (a) At a given deformation temperature, the $t_{0.8}$ is not particularly sensitive to Nb content. For instance, at 900 °C, the data for the 0.023Nb steel are quite close to (although below) those for the 0.039Nb steel. Similar remarks apply to the 0.039Nb and 0.07Nb steels at 950 °C if the 10 °C difference in temperature is ignored. (b) At a given deformation temperature, the $t_{0.8}$ decreases rapidly with increasing strain rate, while at a given strain rate, the $t_{0.8}$ increases slowly with decreasing temperature. This suggests that dynamic recrystallization is only weakly temperature dependent.

Alternatively, equation (5.11) can be rewritten as follows:

$$\frac{t_{0.8}}{Z^{-0.73}} = A_{dyn} \exp\left(\frac{Q_{dyn}}{RT}\right) \qquad (5.12)$$

Taking natural logarithms of both sides, we have

$$\ln\left(\frac{t_{0.8}}{Z^{-0.73}}\right) = \ln\left(A_{dyn}\right) + \frac{Q_{dyn}}{RT} \qquad (5.13)$$

It is clear that the logarithm of the Z-compensated $t_{0.8}$ is a linear function of the inverse absolute temperature. This is further illustrated in Fig. 5.29, and again a weak Nb effect is observed. The values for A_{dyn} and Q_{dyn} were determined from the slope and intercept; this procedure led to 1.5×10^{-5} and 392 kJ/mol, respectively. A comparison between the predicted and measured values of $t_{0.8}$ is presented in Fig. 5.30 and it can be seen that there is reasonable agreement.

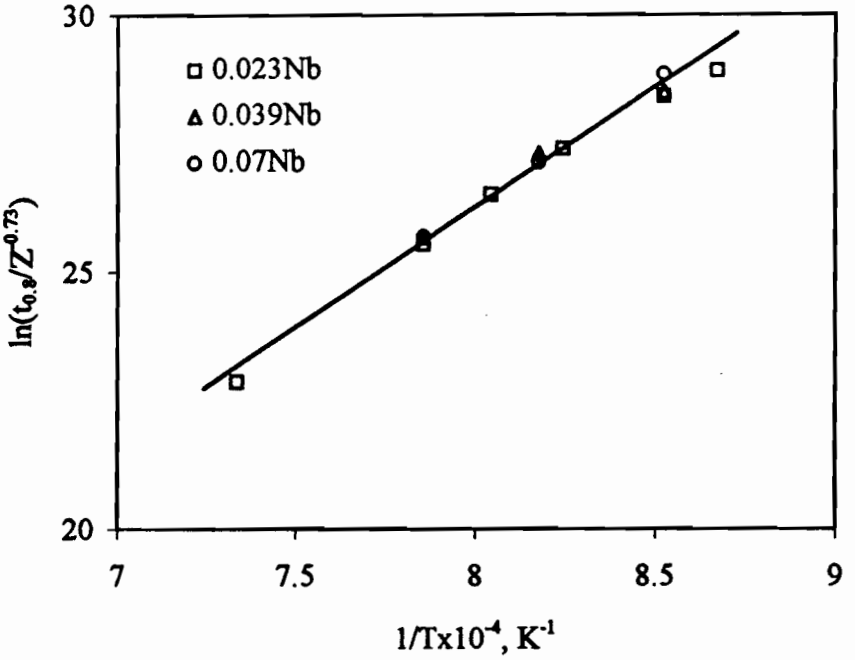

Fig. 5.29 Dependence of Z-compensated $t_{0.8}$ on inverse temperature.

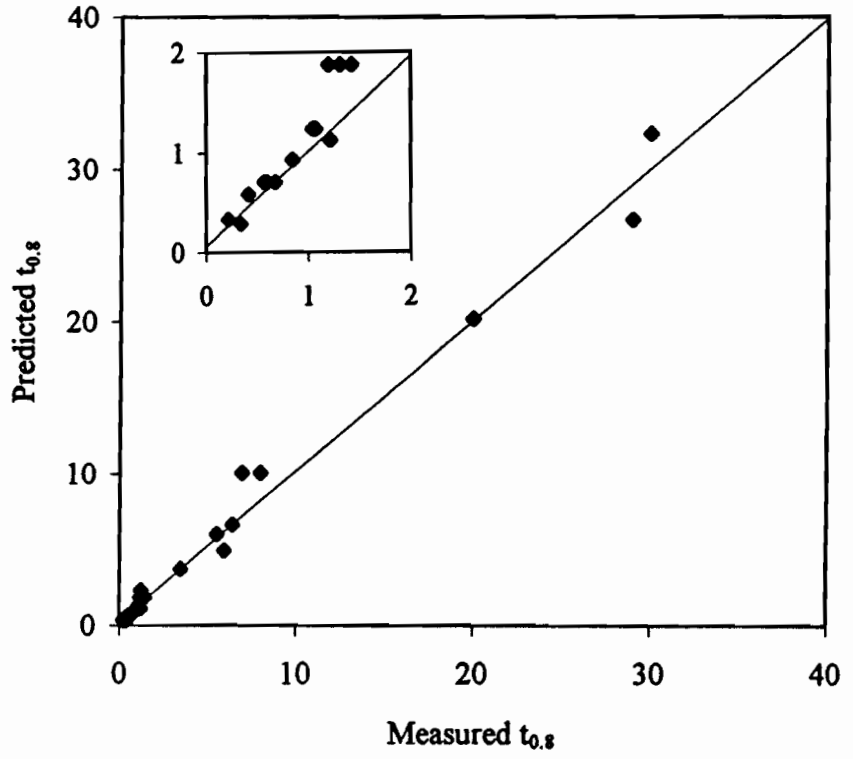

Fig. 5.30 Comparison between predicted and measured $t_{0.8}$ values.

It has been suggested that the kinetics of dynamic recrystallization can also be described using the Avrami equation[99, 109, 240, 241]:

$$X_{dyn} = 1 - \exp\left(-k_{dyn} t^{n_{dyn}}\right) \qquad (5.14)$$

where k_{dyn} and n_{dyn} are constants. The latter can be evaluated by plotting $\log(\ln(1/(1-X_{dyn})))$ against $\log(t/t_{0.8})$. Some examples are shown in Fig. 5.31. In the present work, the exponent n_{dyn} fell between 1.1 and 1.9 for the steels investigated. An average value of 1.7 compares well with those reported by Laasraoui[236] for C-Mn steels (1.5 to 1.6), but is somewhat higher than those observed by Roberts et al.[99] for stainless steels (1.2 to 1.4). Similarly, an average value of 0.8 was determined for the constant k_{dyn}. As long as $t_{0.8}$ is determined using equation (5.11), the steady state strain can be estimated from equation (5.10). The fractions recrystallized at strains between the peak and steady state values can then be readily estimated from plots similar to the one illustrated in Fig. 5.32. For instance, the fraction recrystallized at the transition strain ε_T was estimated to be 20%~30%.

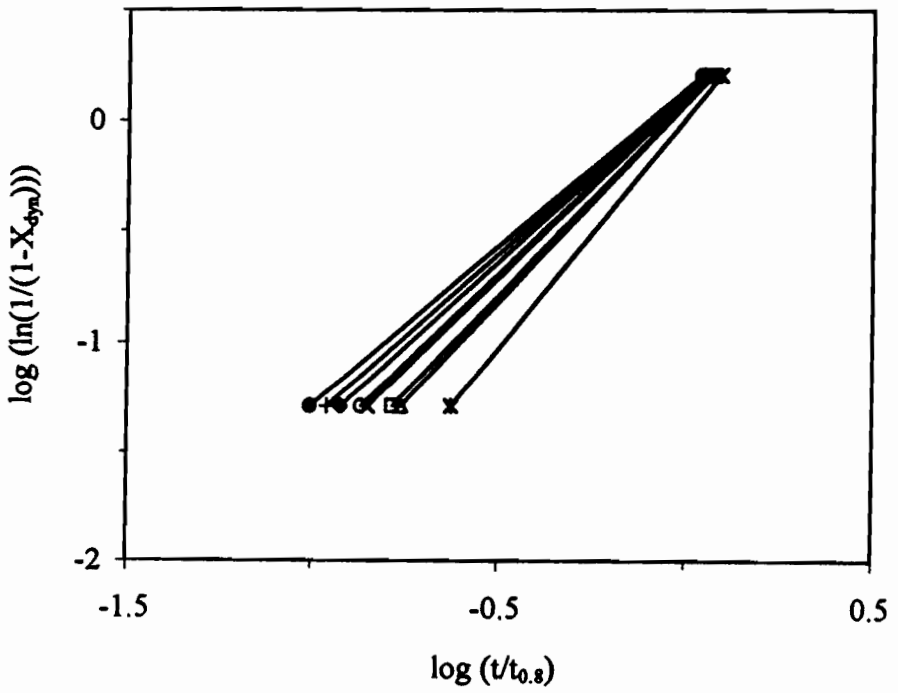

Fig. 5.31 Avrami plots of the dynamic recrystallization kinetics for the 0.023Nb and 0.07Nb steels.

Surprisingly, the relative insensitivity of $t_{0.8}$ to Nb content stands in sharp contrast to the effect of Nb on the kinetics of static recrystallization, $t_{0.5}$, reported in the literature. This seems to suggest that dynamic recrystallization is a nucleation rate controlled event, and that the process is completed by repeated nucleation and limited grain growth. By contrast, static recrystallization is mainly controlled by grain growth. In fact, Nb solutes, in common with other microalloying elements, can retard both nucleation and grain growth effectively.

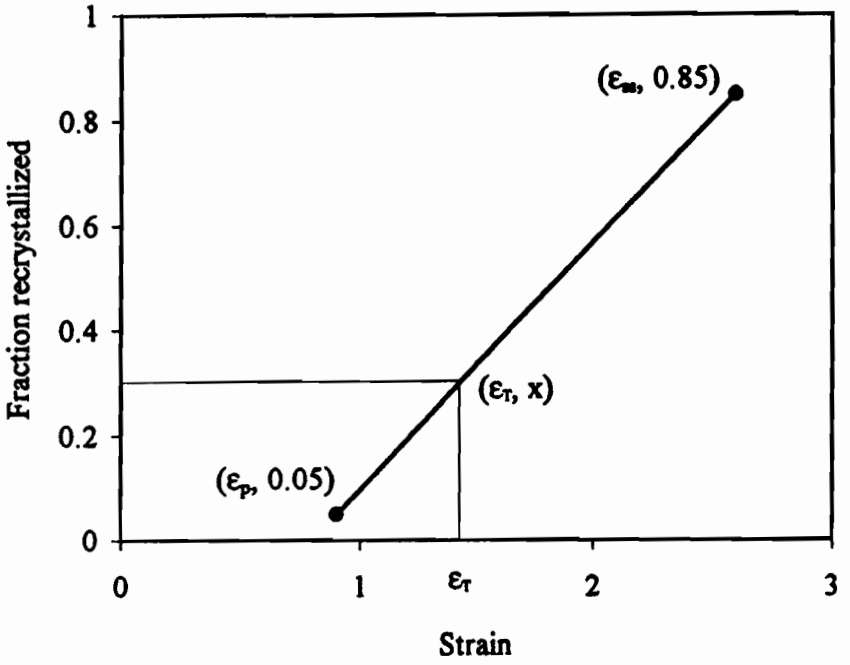

Fig. 5.32 Effect of strain on dynamic recrystallization.

5.3.2 Modelling Metadynamic Recrystallization

Petkovic et al.[104] observed that the softening rate after unloading at strains beyond the peak strain is much higher than after unloading at lower strains. They gave the name metadynamic recrystallization to this process. Later, Sellars proposed the first mathematical model relating the time for 50% recrystallization to the deformation parameters[62]. Recently, more extensive investigations concerning metadynamic recrystallization in C-Mn and microalloyed steels were carried out by Hodgson[82] and Roucoules[109]. The kinetics model for C-Mn steels is now well established. However, that of Roucoules et al.[235] is the only model available to date for Nb microalloyed steels. The problem with this model is that it was based on a single composition. It is difficult to apply this model to prediction of the $t_{0.5}$ for other compositions since Nb affects the rate

of recrystallization. Therefore, it is important to add the effect of Nb to the model. This is one of the aims of the present work.

It has been found that the kinetics of metadynamic recrystallization can also be described by the Avrami equation:

$$X_{mdrx} = 1 - \exp\left(-k_{mdrx}\left(\frac{t}{t_{0.5}}\right)^{n_{mdrx}}\right) \qquad (5.15)$$

Here $t_{0.5}$ is the time for 50% recrystallization, n_{mdrx} is a constant, and k_{mdrx} is equal to $-\ln(1-0.5)$. The exponent n_{mdrx} describes the rate of recrystallization (i.e. the slope) and $t_{0.5}$ represents the position of the line. The recrystallization kinetics can be completely described once n_{mdrx} and $t_{0.5}$ are known.

5.3.2.1 Avrami Plots

In order to determine the exponent n_{mdrx} in equation (5.15), the softening results for the 0.023Nb steel were drawn up as $\log(\ln(1/(1-X_{mdrx})))$ vs. log(time) plots, as shown in Fig. 5.33. Three different sets of slopes can be distinguished. The two ranges of low slope (the broken lines) are associated with recovery and the completion of recrystallization. At the very beginning of holding, dislocation rearrangement and slight changes of substructure led to some degree of softening. This event was immediately followed by recrystallization, which took place by growth of the dynamic nuclei into the deformed structure. This involved the disappearance of a large number of dislocations so that a higher softening rate was observed. When recrystallization was close to completion, the softening rate slowed down again because of impingement, and because the main contributor to softening at this stage was grain growth, which is slow.

The exponent n_{mdrx} for the present case was found to be 1. This is the value reported by Roucoules et al.[235] for microalloyed steels, but it is lower than that observed for C-Mn steels by Hodgson and Gibbs[219]. The softening curves predicted by equation (5.15) using the present n_{mdrx} and measured $t_{0.5}$ are plotted in Fig. 5.34 for comparison with those measured experimentally (the broken lines). It can be seen that the present model represents the main part of the softening curves very well but not the data above X = 85%. This is because incomplete softening is a feature of metadynamic recrystallization.

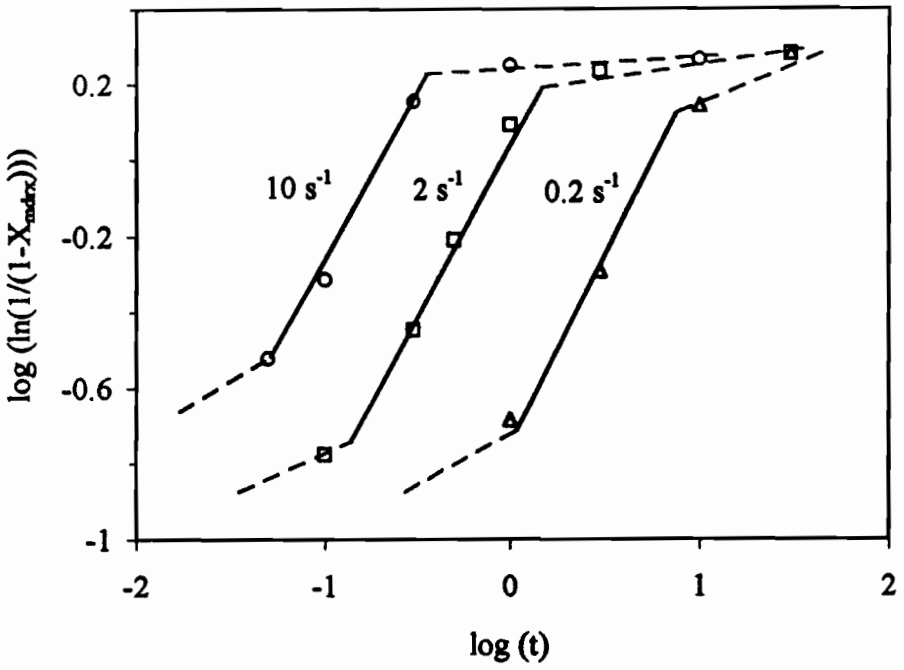

Fig. 5.33 Avrami plots of metadynamic recrystallization in the 0.023Nb steel.

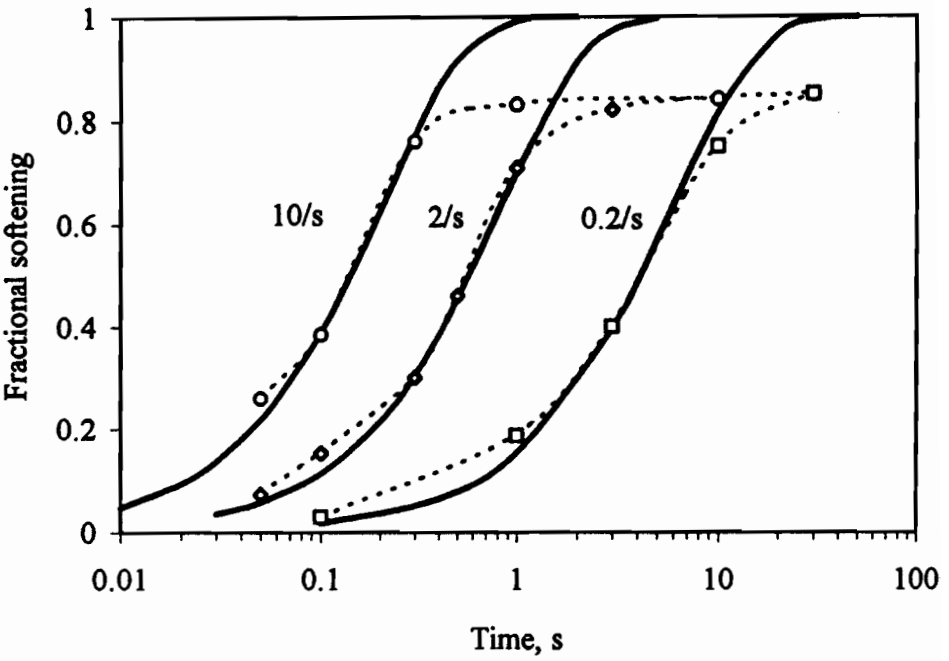

Fig. 5.34 Comparison between predicted and measured softening curves for the 0.023Nb steel.

5.3.2.2 Mathematical Expression for $t_{0.5}$

In equation (5.15), the exponent n_{mdrx} and constant k_{mdrx} do not vary much with the deformation parameters as long as the behaviour remains in the solute drag range. The $t_{0.5}$, however, was found to depend significantly on strain rate, deformation temperature and Nb content in solution. The equation for specifying $t_{0.5}$ in C-Mn steels was derived by Sellars and has the form:

$$t_{0.5} = A_{mdrx} Z^{n_{mdrx}} \exp\left(\frac{Q_{mdrx}}{RT}\right) \qquad (5.16)$$

where A_{mdrx} and n_{mdrx} are constants, Z is the Zener-Hollomon parameter, and Q_{mdrx} is the activation energy of metadynamic recrystallization.

In order to determine the Z exponent n_{mdrx}, the $t_{0.5}$ results determined from the softening curves were plotted on a $\log(t_{0.5}) - \log(\dot{\varepsilon})$ basis in Fig. 5.35. The results obtained by Roucoules on a 0.039Nb steel are also plotted in this figure in order to display the effect of Nb. The slopes of the plots for both steels are similar and the average value of n_{mdrx} is -0.84. This compares well with that (n_{mdrx}=-0.8) obtained by Hodgson

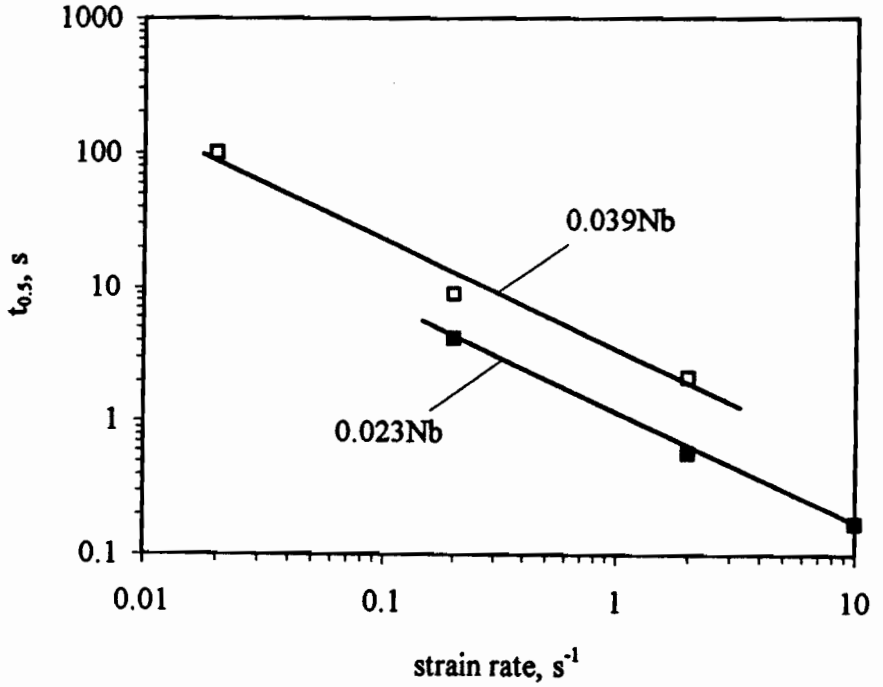

Fig. 5.35 Effect of strain rate on the metadynamic $t_{0.5}$.

and Gibbs[219], but is somewhat higher than those (n_{mdrx}=-0.6) observed by Sellars[62] and Roucoules et al.[235]. Nevertheless, like dynamic recrystallization, this value is about twice as high as those reported for static recrystallization. It can therefore be concluded that metadynamic recrystallization is clearly a strain rate dependent event.

The logarithm of the Z-compensated $t_{0.5}$ is plotted against the inverse absolute temperature in Fig. 5.36. Q_{mdrx} and A_{mdrx} can be determined from the slopes and intercepts of these plots. A similar value of Q_{mdrx}=403 kJ/mol was found for the three steels, while A_{mdrx} varied with the Nb content. The dependence of A_{mdrx} on Nb concentration is illustrated in Fig. 5.37, and the following linear relation was observed to hold:

$$A_{mdrx} = \left(12[Nb] + 0.5\right) \times 10^{-4} \qquad (5.17)$$

In the final formulation, the dependence of $t_{0.5}$ on Nb concentration, Zener-Hollomon parameter, and deformation temperature can be expressed as follows:

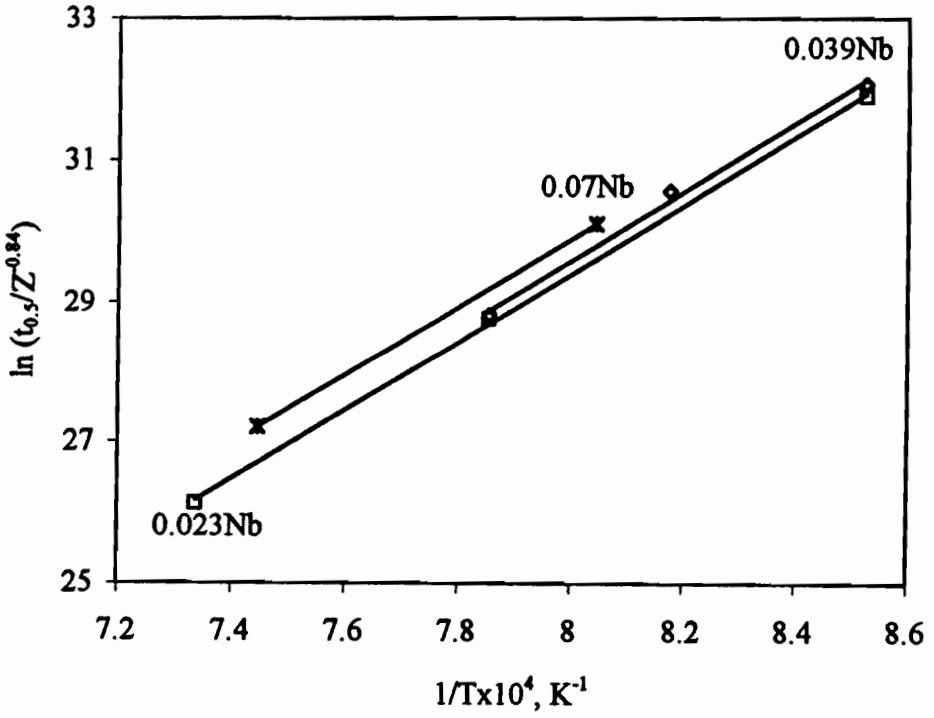

Fig. 5.36 Effect of temperature on the Z-compensated metadynamic $t_{0.5}$.

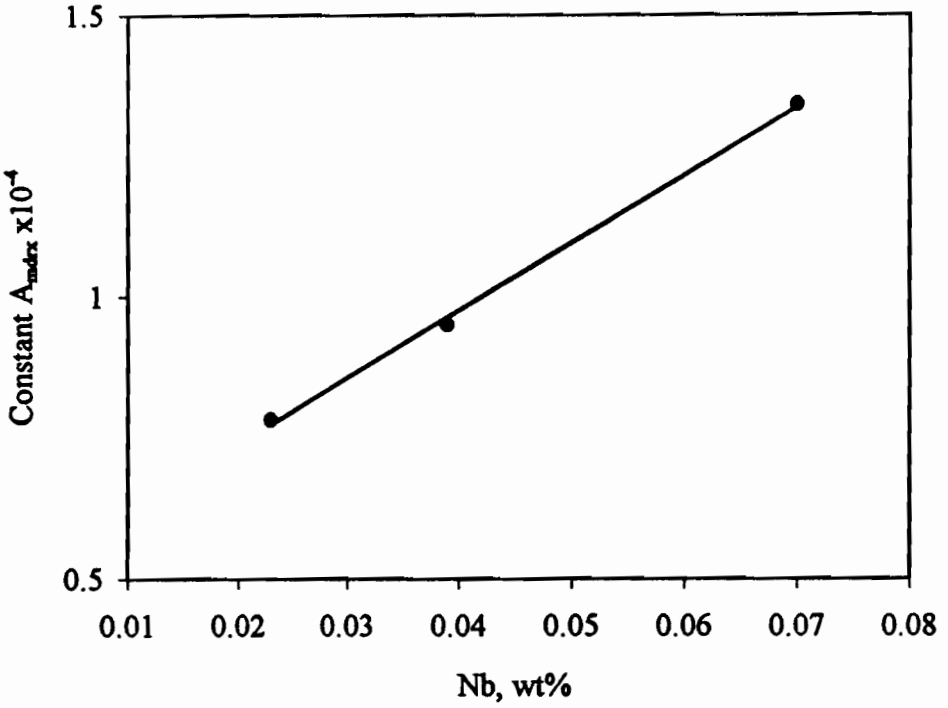

Fig. 5.37 Effect of Nb in solution on the constant A_{mdrx}.

$$t_{0.5} = \left(12[Nb] + 0.5\right) \times 10^{-4} Z^{-0.84} \exp\left(\frac{403{,}000}{RT}\right) \qquad (5.18)$$

The overall temperature dependence of $t_{0.5}$ was obtained by combining the temperature term in Z with the recrystallization activation energy, i.e.

$$Q_{app} = Q_{mdrx} - 0.84 Q_{def} \qquad (5.19)$$

Here Q_{app} is the overall apparent activation energy, which works out in the present case to be 92 kJ/mol. This is much lower than for conventional static recrystallization and indicates that metadynamic recrystallization is only weakly temperature dependent. The present observation is in good agreement with the findings of Hodgson and Gibbs[219] and Roucoules et al.[235].

It should be pointed out that some authors prefer to use separate strain rates and deformation temperatures in their models. If the two exponential terms (one in the Z expression) are combined, equation (5.18) can be rewritten as follows:

$$t_{0.5} = \left(12[Nb] + 0.5\right) \times 10^{-4} \dot{\varepsilon}^{-0.84} \exp\left(\frac{92200}{RT}\right) \qquad (5.20)$$

This expression is similar to the one used by Roucoules et al.[235]. Mathematically, equation (5.20) is more logical, although thermodynamically, equation (5.18) has more physical meaning in the interpretation of metadynamic recrystallization. The Zener-Hollomon parameter here is associated with nucleation, although this occurs during deformation rather than after. This can be understood by considering that higher nucleus densities are associated with higher Z values. The exponential term describes the growth rate.

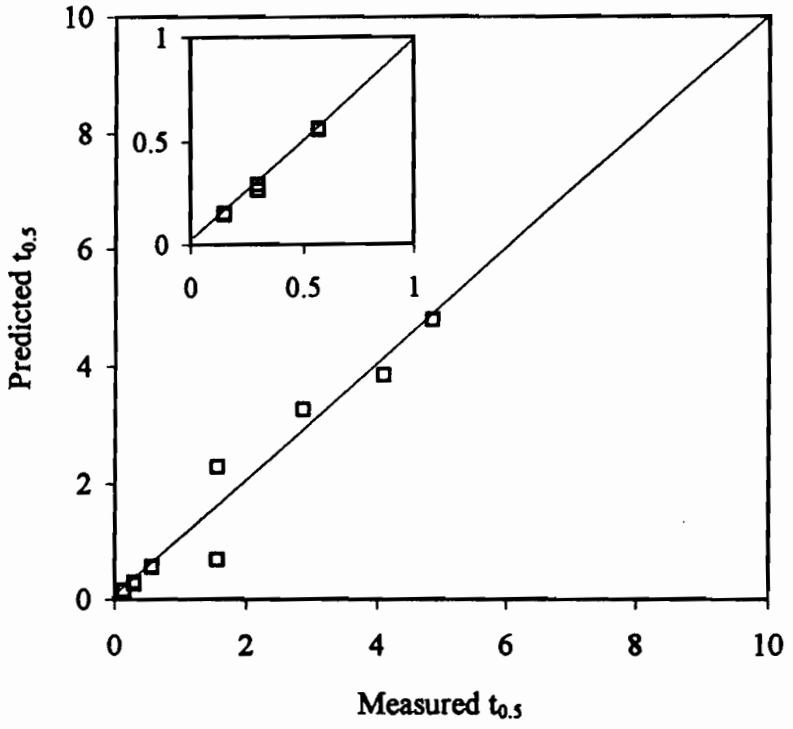

Fig. 5.38 Comparison between predicted and measured $t_{0.5}$ values.

A comparison between the predicted and measured values of $t_{0.5}$ is made in Fig. 5.38. There is good agreement between the two sets of $t_{0.5}$. It should be pointed out that the present work is the first attempt to put the effect of Nb into a metadynamic recrystallization model, although clearly more experimental data are needed to validate the model.

5.3.3 Comparison between Static and Dynamic or Metadynamic Recrystallization

Although the detailed definition of metadynamic recrystallization is still under discussion, there is a significant difference between the kinetics of this process and that of conventional static recrystallization. The latter is strongly strain and temperature dependent, while dynamic and metadynamic recrystallization are strongly strain rate or Z dependent processes. The kinetics of the latter do not depend on strain as long as deformation is interrupted beyond the transition strain (ε_T).

These differences have their parallels in the Nb dependences of their kinetics, as illustrated in Fig. 5.39. In this comparison, the $t_{0.5}$ values were calculated for a strain rate of 2 s^{-1}, T = 970 °C and ε = 0.4. The strain was chosen to give a reasonable driving force but not to exceed the peak strain for a given level of Nb addition. The temperature was chosen to be above the T_{nr} for all Nb compositions and thus to keep the comparison in the solute drag range. It can be seen that the calculated values of $t_{0.5}$ for static recrystallization are higher than the others. By contrast, those for metadynamic recrystallization are the lowest. Overall, the effectiveness of Nb in solution follows the decreasing order: static recrystallization-dynamic recrystallization-metadynamic recrystallization.

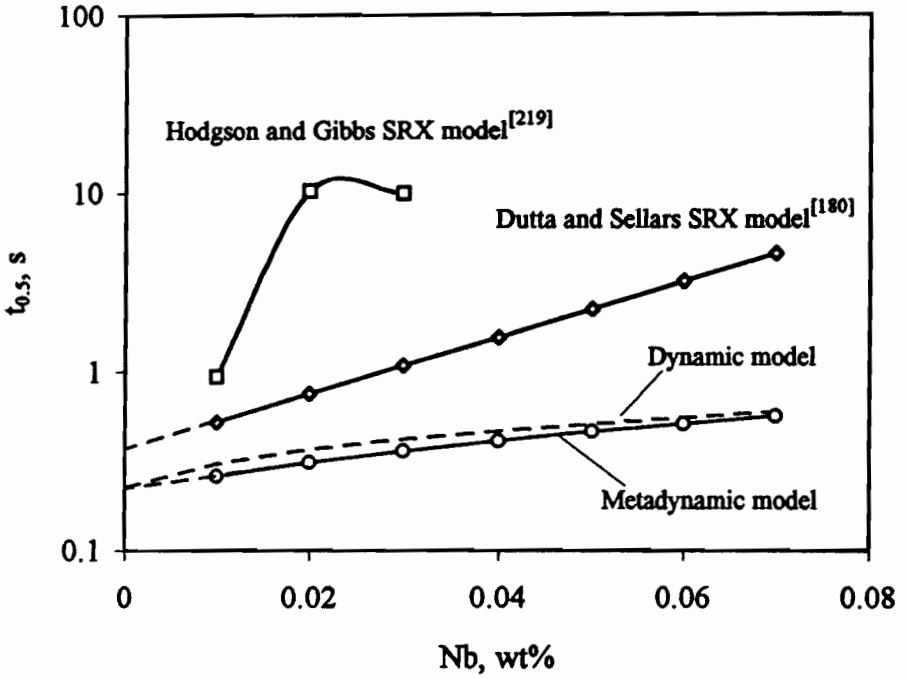

Fig. 5.39 Comparison between the kinetics of conventional static and dynamic and metadynamic recrystallization.

The kinetics of dynamic recrystallization depend only slightly on the Nb concentration, as mentioned in the previous subsection. It can also be seen that the values of $t_{0.5}$ calculated using the equation of Hodgson and Gibbs[219] are much higher than those obtained from the Dutta and Sellars model[180] in the Nb range 0.01 to 0.03 wt%. However, there is a transition in the Nb dependence at 0.02 wt% in the curve of Hodgson and Gibbs, leading to the suggestion of a different dependence in the higher Nb range. It should be noted that Hodgson and Gibbs derived their model over the experimental range 0.01 to 0.03 wt% Nb. Thus the application of this model to higher Nb concentrations is not appropriate.

The much higher values of $t_{0.5}$ calculated using the equation of Hodgson and Gibbs can be explained as follows. First, the strain exponent in their equation, which is linearly related to the Nb content, was deduced using only two compositions. Therefore, the form of the dependence of the strain exponent on Nb concentration may not be very accurate. Secondly, in the case of the 0.03Nb steel (this is one of the compositions used by those authors), deformation and holding at 900 °C probably produced a certain amount of Nb(CN) precipitation since the calculated t_{Ps} is only 1.32 seconds[82]. The softening process in this case was likely to have been controlled by the pinning of Nb(CN) precipitates and not by solute drag. Thus, it is inappropriate to use these data to derive an equation for softening in the solute drag range.

It is of interest to note that, despite the trends displayed in Fig. 5.39, the time for the completion of dynamic recrystallization is less than that for the completion of metadynamic recrystallization. In other words, the time of deformation from the peak to the steady state strain is shorter than that required for 85% metadynamic recrystallization. By contrast, the $t_{0.5}$ for dynamic recrystallization can be seen to be slightly longer than for metadynamic recrystallization in Fig. 5.39. This is because the Avrami exponent for dynamic recrystallization (evaluated to be 1.7) is higher than for metadynamic recrystallization (evaluated to be 1). The differences between the $t_{0.85}$ values for dynamic and metadynamic recrystallization are illustrated in Fig. 5.40 for the 0.07Nb steel deformed at 970 °C. It can be seen that at 0.02 s^{-1}, the $t_{0.85}$ for metadynamic recrystallization is about twice that for dynamic recrystallization, and that this difference gradually decreases with increasing strain rate. By the time the industrial range of strain rates is reached (1 to 10^3 s^{-1}), there is essentially no difference between the two recrystallization times.

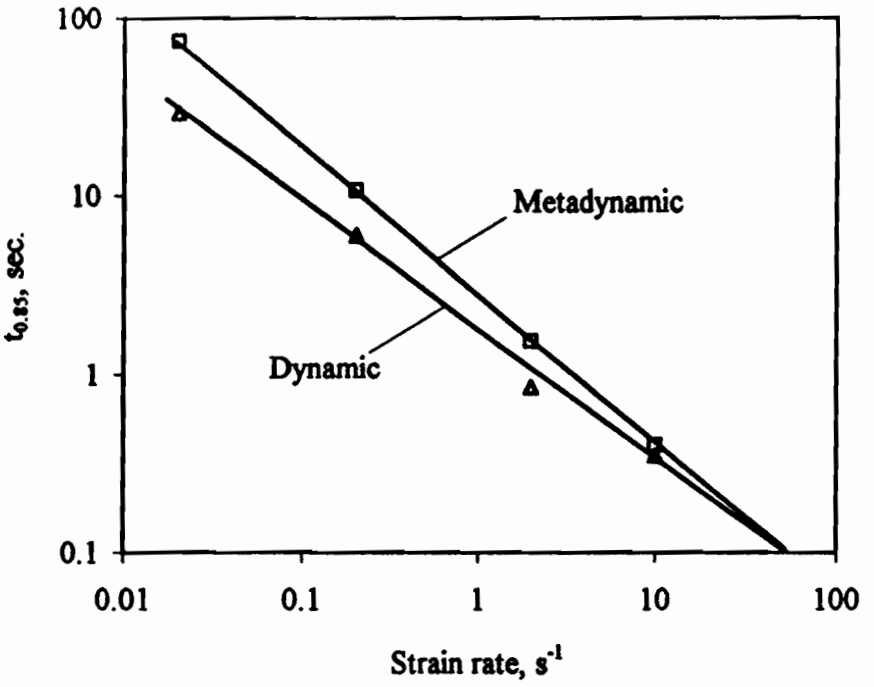

Fig. 5.40 Comparison between the recrystallization times for dynamic and metadynamic recrystallization.

A different conclusion was drawn by Hodgson[82] for C-Mn steels tested at strain rates of 0.03 to 3 s^{-1}. He found that metadynamic softening occurs over time intervals that are similar to the time of deformation from the peak to the steady state strain. The difference could result from the Nb effect in the present steel. In fact, 970 °C is quite close to the T_{nr} for this steel, at which Nb(CN) precipitation may commence. The volume fraction of Nb(CN) precipitates increases with holding and testing time, and these freshly formed precipitates can slow down the growth rate of dynamically formed nuclei. They can therefore delay the completion of the process. This is especially true at low strain rates, where the rate of recrystallization is low.

The strain at which there is a transition from static to metadynamic recrystallization is different for different authors. In the earlier studies, Morrison[73], Glover and Sellars[242, 243], English and Backofen[244], and Djaic and Jonas[74], all reported a fourth power dependence of softening rate on prior strain. This power relation breaks down at large strains, because the softening rate becomes strain independent in this range. This transition must take place no later than at ε_{ss} (the steady state strain), as

demonstrated by Glover and Sellars[242] in their study of the recrystallization kinetics of α iron, in which dynamic recovery is the only restoration process during deformation. The transition at the steady state strain was also observed by Djaic and Jonas[74] in their investigation of the recrystallization behaviour of high carbon steel, in which dynamic recrystallization takes place during deformation.

In his later analysis, Sellars proposed that there are two separate kinetics models, one for strains below, and another for strains above a critical strain ε_c. He did not take ε_{ss} as the transition point in his interpretation and also considered that the transition strain ε_{ss} shown in Djaic and Jonas' diagram was actually ε_p. Sellars did not give any reasons for this change, but probably simply concluded that the transition takes place at strains less than the steady state strain. For simplicity, he took ε_c as the transition point in his models since there were no data available indicating a more accurate value for this point.

In more recent observations, Hodgson[82] showed that the softening rate in the steady state range is strain independent, while Roucoules[109] demonstrated that the recrystallization kinetics convert from being strain dependent to strain independence at ε_p. By carefully checking Roucoules' data, the author finds that there is about a 10% difference between the softening rate after deforming to the peak strain and to strains after the peak. This suggests that the transition occurs beyond the peak strain. In the present work, it was shown that the fractional softening increases *linearly* with the strain until $1.5\varepsilon_p$ (named ε_T in the previous subsection) is attained. It therefore seems desirable to use ε_T instead of ε_p as the transition point between the two mechanisms in modelling the recrystallization kinetics.

5.3.4 The Mechanism of Dynamic Recrystallization

During the past twenty years, the mechanisms of dynamic recrystallization have been studied by numerous authors[55, 98-100, 102, 245-248]. Although some experimental results have demonstrated that multiple twinning occurs frequently during the growth of dynamic grains in copper and nickel single crystals[55, 245-248], it has been generally accepted that the bulge mechanism plays a more important role in the nucleation of dynamic recrystallization in polycrystals. Dynamic recrystallization is initiated at the critical strain, and progresses by repeated nucleation and limited grain growth, i.e. in a "necklace" or "cascade" manner. The necklace mechanism has been experimentally detected by several authors, and is commonly adopted to describe dynamic

recrystallization in different metals. A schematic illustration of dynamic recrystallization by this means is presented in Fig. 5.41.

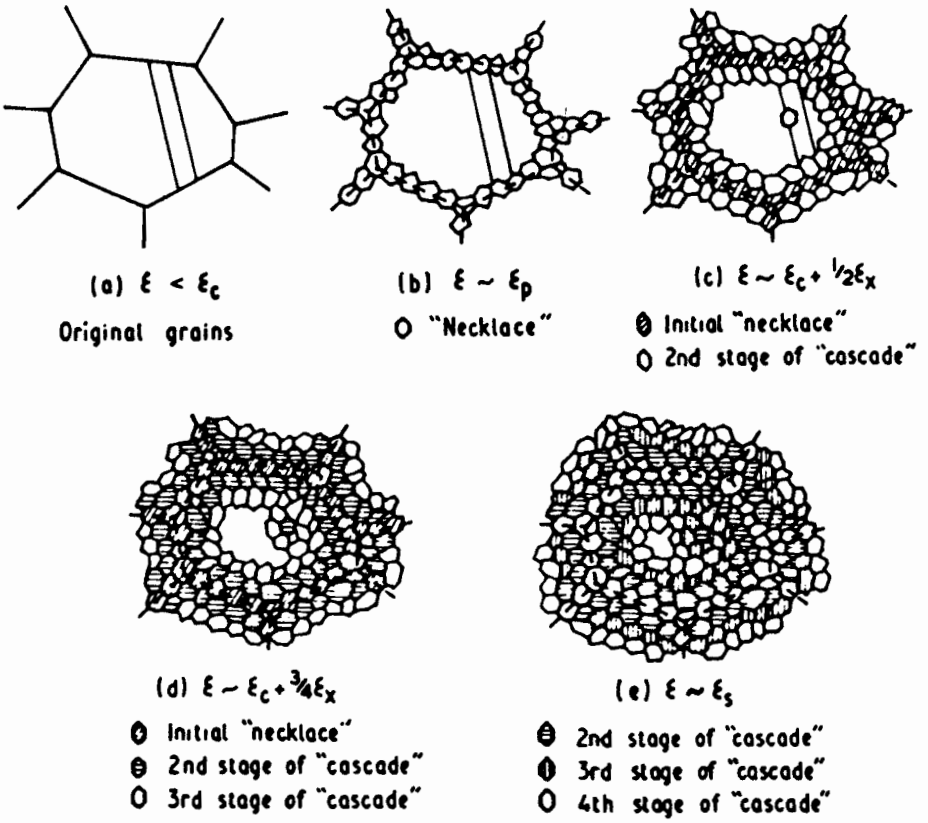

Fig. 5.41 Schematic illustration of the progress of dynamic recrystallization[249].

As in the case of static recrystallization, pre-existing grain boundaries are considered to be major nucleation sites for dynamic recrystallization. Substructures are continuously being established within grains during straining. The dislocation density and misorientation are the highest near the original grain boundaries. When the critical strain (or critical dislocation density) is exceeded, the grain boundaries bulge locally towards the side that has the higher dislocation density. This process continues until the original grain boundaries are completely occupied by strain free nuclei, as shown in Fig. 5.41(b). Nucleation then takes place at the interface between the recrystallized and unrecrystallized material, forming second, third, and fourth generations of nuclei, as illustrated in Figs. 5.41(c), (d) and (e). While the recrystallization front moves gradually into the centre of the unrecrystallized material, the nuclei formed earlier grow and are being deformed

concurrently. The dislocation densities in these grains gradually increase and may reach the critical value again, so that a new generation of nuclei is formed on the grain boundaries of these grains (see Fig. 5.41(e)).

The view that there is repeated nucleation and limited grain growth during dynamic recrystallization is supported by following observations:

a) Dynamically recrystallized grain sizes are independent of initial grain sizes;

b) Dynamic recrystallization grain sizes are almost independent of the recrystallized fraction after the first few percent; and

c) Nb in solution has little effect on the progress of dynamic recrystallization.

The time to deform from the peak to the steady state strain, $t_{0.8}$, decreases with Zener-Hollomon parameter or strain rate, as demonstrated in §5.3.1. This can be readily interpreted in terms of the nucleation mechanism. Strain rate and deformation temperature both influence the dislocation structures of strained materials. Sakai and co-workers[106, 250-252] observed that the dislocation cell size decreases with increasing Z, and the number of potential sites for nucleation per unit volume is proportional to cell size:

$$N_s \propto d^{-2} \qquad (5.21)$$

where d is the dislocation cell size.

This can also be understood by considering the effect of strain rate and deformation temperature on the difference between ε_c and ε_p. For instance, when the strain rate is increased from 0.02 to 2 s^{-1}, the peak strain increases from 0.4 to 0.9 in the 0.07Nb steel deformed at 970 °C. Taking the critical strain $\varepsilon_c = 0.67\varepsilon_p$, then the difference $\Delta\varepsilon = \varepsilon_p - \varepsilon_c$ increases from 0.13 to 0.3 over the same strain rate range, while the deformation time from ε_c to ε_p decreases from 6.5 seconds to 0.15 seconds. Thus, more dislocations are stored in the deforming material at higher than at lower strain rates. If ρ_c is the critical dislocation density for the onset of dynamic recrystallization, and ρ_p is the dislocation density that corresponds to the peak strain, the ratio of ρ_p/ρ_c will increase with strain rate. This suggests that dislocation structures are somewhat supersaturated at high

strain rates, and that these "supersaturated" structures provide more nucleation sites and higher nucleation rates for dynamic recrystallization.

5.3.5 Softening Mechanisms of Metadynamic Recrystallization

The concept of metadynamic recrystallization is due to Djaic and Jonas[74] and Petkovic et al.[104, 234] and involves the growth of dynamically formed nuclei once deformation has ceased. Nucleation takes place during deformation ($\varepsilon > \varepsilon_c$), so that there is no apparent incubation time, and softening is produced directly by the growth of dynamic nuclei into the deformed matrix. Based on this concept, when deformation is interrupted beyond the critical strain, the softening that takes place during holding is mainly attributed to metadynamic recrystallization. Some controversy has recently arisen, however, due to the work of Sakai and co-workers[106, 250-252]. These authors studied the softening mechanisms taking place in pure polycrystalline nickel by means of interrupted tensile tests and microhardness measurements as well as metallographic observations. Their results are reproduced here in Fig. 5.42 and the deformation conditions are also illustrated in this figure. In order to follow the analysis, the softening curve and the plot of the number of fine grains vs. holding time after deformation into the steady state (ε=0.28) are also presented in the same figure.

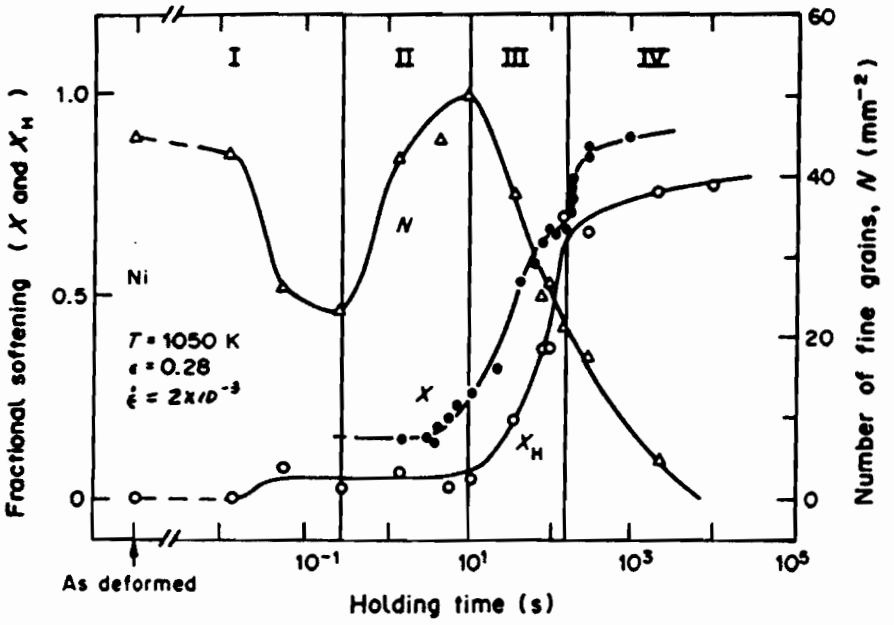

Fig. 5.42 Comparison of the softening curves derived from interrupted tests, X, and from hardness tests, X_H, with the number of fine grains (<12 μm in dia.)[250].

From the softening curve, it can be seen that softening in a DRX matrix can be divided into four regions. In range I, an initial softening of about 15% appears to occur almost instantaneously in 0.3 seconds (their cooling rate during quenching was 2000 Ks^{-1}). The number of fine grains decreases during this time. The level of softening is maintained at 15% over the interval 0.3 to 5 seconds and gradually increases to 20 % at 10 seconds in range II. The number of fine grains now increases with holding time. The fractional softening then increases from 20% to 67% as the holding time is further increased from 10 to 100 seconds in range III. The TEM observations showed that there is a dramatic decrease in the number of fine grains in this interval. The maximum fractional softening of 90% was produced at about 1000 seconds.

The important observations reported by Sakai et al. involve the changes in the number of fine grains within ranges I and II. These authors suggested that the decrease in the number of fine grains in range I is attributable to the rapid growth of DRX nuclei, so that true metadynamic recrystallization is responsible for the softening in this range. The increase in the number of fine grains in range II is due to the nucleation of static recrystallization in the highly deformed dynamically recrystallized grains. This is followed by grain growth in range III, leading to a rapid decrease in the number of fine grains and to an increase in the softening. It can thus be concluded that softening in a DRX matrix is mainly due to static recrystallization rather than to metadynamic recrystallization. This is somewhat in conflict with the kinetics observations; i.e., when deformation is interrupted at strains beyond the transition point, the rate of softening during isothermal holding is strain independent but is strongly strain rate dependent. A possible resolution of this controversy is proposed below by the present author based on a constant number (or density) of nuclei.

As illustrated in Fig. 5.41, dynamic recrystallization nuclei emerge when the critical strain is exceeded. The number of nuclei increases with further straining until "site saturation" takes place, i.e. all the original grain boundaries are occupied by dynamic nuclei. Then the total number of nuclei remains constant during further straining. This appears reasonable since the metadynamic recrystallization grain size is not strain dependent, and can generally be expressed as follows:

$$d_{mdrx} = A' Z^{n'} \qquad (5.22)$$

where A' and n' are constants, and Z is the Zener-Hollomon parameter.

The source of nuclei in the first stage of dynamic recrystallization is the original grain boundaries; then, the interface between the recrystallized and unrecrystallized material becomes the source. As dynamic recrystallization progresses, the interface area per unit volume decreases, so that the number of nuclei from this source decreases. However, the decline in the nucleus density at the interface can be compensated by nucleation in the highly deformed dynamically recrystallized grains. This could happen during deformation (the dynamic case) or after interruption (the static case observed by Sakai et al.). In this way, the nucleus density for post dynamic recrystallization can remain constant from the transition strain ε_T used in the present work to the steady state strain. The rate and resulting grain size of this type of recrystallization will also be strain independent, and so the process can still be termed "metadynamic recrystallization".

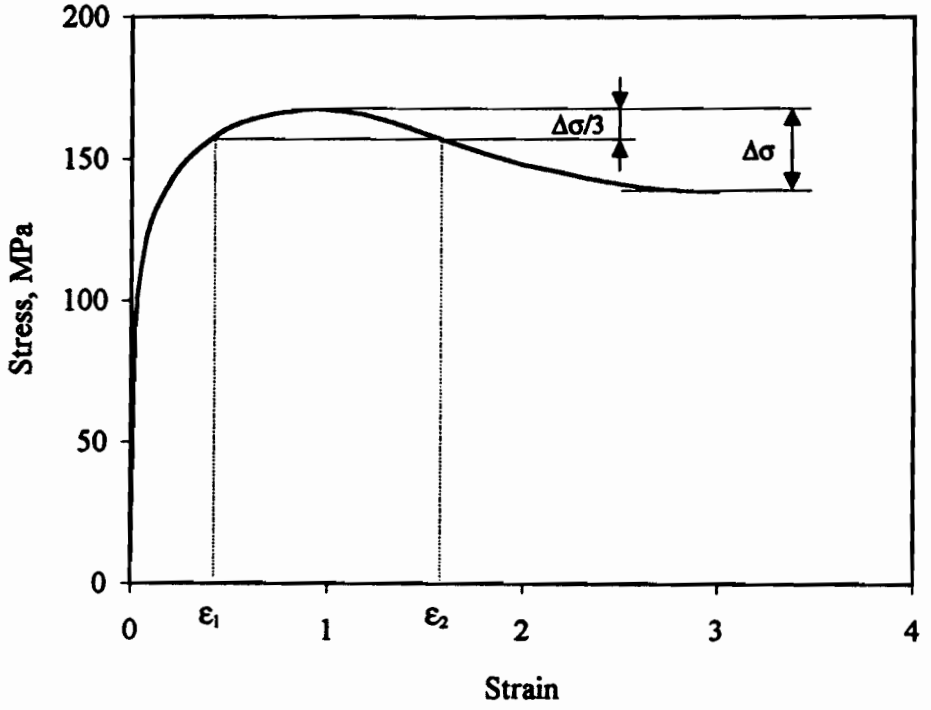

Fig. 5.43 Flow curve of a continuous deformation test.

The above interpretation regarding the difference between metadynamic and static recrystallization is illustrated in Fig. 5.43. It is evident that two strains, ε_1 and ε_2, can be defined, both of which correspond to $\Delta\sigma/3$. The first is well before and the second well after the peak strain. Two tests were interrupted at these strains using interpass times of 1 second. The fractional softening was measured to be 16.4% and 76.8%, and $t_{0.5}$ was evaluated as 3.87 and 0.51 seconds for ε_1 and ε_2, respectively. Thus the rate of softening

at ε_2 was almost one order of magnitude faster than at ε_1. It is also of interest to note that the stresses corresponding to ε_1 and ε_2 are the same, so that the average dislocation densities should be identical. However, the dislocation structure in the latter case was heterogeneous and plenty of dynamically formed nuclei were available to reduce or even eliminate the incubation time for subsequent recrystallization.

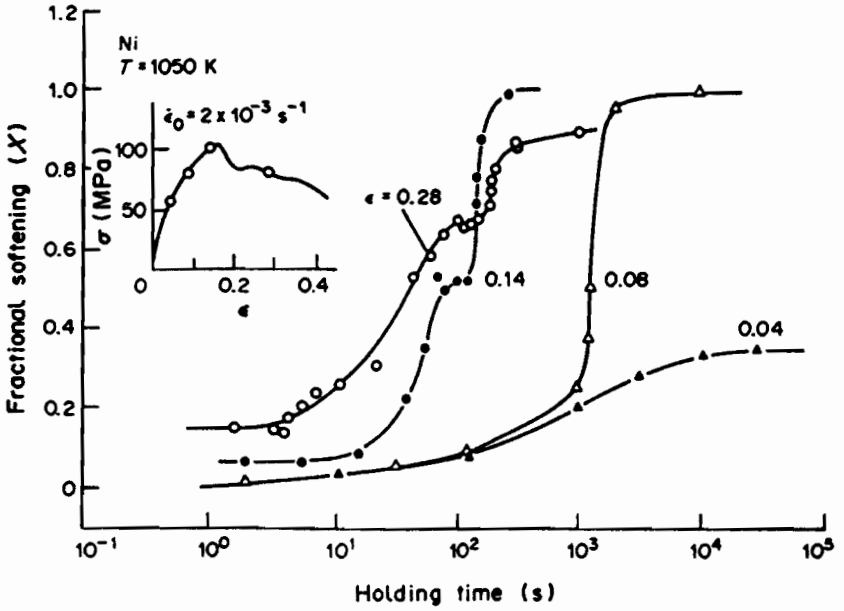

Fig. 5.44 Effect of prior strain on the static softening measured by interrupted tensile testing in hot deformed nickel[250].

The results of Sakai et al. presented in Fig. 5.44 also show the difference between postdynamic (they adopted the term "static" for this process) and static recrystallization. The strain of 0.08 is less than the critical strain and the strain of 0.28 is well into the steady state. It is clear that the rate of softening after deforming to 0.28 ($t_{0.5}$ is around 50 seconds) is much faster than in the 0.08 case ($t_{0.5}$ is over 1000 seconds). Nevertheless, the stresses that correspond to these two strains are nearly the same (~80 MPa). If it is not metadynamic recrystallization that takes place at the interruption strain of 0.28, the dynamically recrystallized matrix must nevertheless provide a "conditioned" and different structure than that normally associated with static recrystallization.

5.3.6 Does Dynamic Recrystallization Take Place under Hot Strip or Rod Mill Rolling Conditions?

Although flow curve peaks (associated with dynamic recrystallization) are commonly observed during *continuous* deformation, the possibility that dynamic recrystallization also takes place under multipass deformation conditions is still being questioned, especially when the strain rate is high. Samuel et al.[51] simulated the Stelco Lake Erie strip mill by means of an average deformation schedule on a hot torsion machine. They observed that the flow curve envelope for the finishing passes displayed a peak for the 0.028Nb steel tested. The grain sizes that resulted from this schedule were as fine as 5 μm. They therefore concluded that dynamic recrystallization took place and was responsible for the grain refinement. Similar observations were also reported by Bowden et al.[253]. Unfortunately, the strain rates used by both authors were 2 s^{-1}, which are much lower than those employed in hot strip mills (these range from 20 to 200 s^{-1}). The importance of metadynamic recrystallization was also ignored by these authors in their analyses. Recently, Roucoules[109] checked the schedule used by Samuel et al. and found that dynamic recrystallization could indeed be initiated under their conditions, but that an appreciable amount of interpass softening also took place. The Lake Erie simulation was thus actually an MDRCR (metadynamic recrystallization controlled rolling) rather than a DRCR (dynamic recrystallization controlled rolling) process.

Their work thus raises questions regarding the process that is responsible for softening and microstructural evolution under strip mill or rod mill rolling conditions. Is this SRX, DRX or MDRX? This is a question that must be answered if accurate models for the prediction of the mill loads and final microstructures are to be developed. To some extent, a response can be given by calculating (at least in the solute drag region) the times for SRX, DRX and MDRX using the models derived in the present work. For this purpose, it is assumed here that the equations derived at laboratory strain rates (~10 s^{-1}) are also valid at the higher strain rates usually employed in strip or rod mills. Thus, equation (5.18) was used to calculate the times for 20% and 80% metadynamic recrystallization, i.e. $t_{0.2}$ and $t_{0.8}$, in the strain rate range 2 to 1000 s^{-1}. According to the Avrami equation, $t_{0.2}$ and $t_{0.8}$ can be estimated as follows:

$$t_{0.2} = k_1 t_{0.5} \qquad (5.23)$$

$$t_{0.8} = k_2 t_{0.5} \qquad (5.24)$$

where k_1 and k_2 are constants. These were found to be 0.32 and 2.32, respectively.

Equation (4.16) was used to estimate the time for static recrystallization by rewriting the equation as follows:

$$t_{0.75} = \left(\frac{88.1\log[Nb]+1156}{T}\right)^{10} \varepsilon^{-1.2}\dot{\varepsilon}^{-0.1} \qquad (5.25)$$

Then $t_{0.2}$ and $t_{0.8}$ were calculated using the following equations:

$$t_{0.2} = k_3 t_{0.75} \qquad (5.26)$$

$$t_{0.8} = k_4 t_{0.75} \qquad (5.27)$$

where k_3 and k_4 are constants. These were found to be 0.16 and 1.16, respectively.

As examples, the peak strains and softening times expected in the 0.023Nb steel were calculated at two temperatures, 1000 and 900 °C. For static recrystallization, two strains, 0.3 and 0.6 were used. The predictions are presented in Tables 5.1 and 5.2 for

Table 5.1 Calculated $t_{0.2}$ and $t_{0.8}$ times for static recrystallization

Strain rate, s^{-1}	ε_p	T=1000 °C, ε=0.3		T=1000 °C, ε=0.6	
		$t_{0.2}$, sec.	$t_{0.8}$, sec.	$t_{0.2}$, sec.	$t_{0.8}$, sec.
2	0.60	0.71	5.15	0.31	2.24
20	0.89	0.56	4.10	0.25	1.78
200	1.31	0.45	3.25	0.20	1.42
1000	1.73	0.38	2.77	0.17	1.21
Strain rate, s^{-1}	ε_p	T=900 °C, ε=0.3		T=900 °C, ε=0.6	
		$t_{0.2}$, sec.	$t_{0.8}$, sec.	$t_{0.2}$, sec.	$t_{0.8}$, sec.
2	1.00	1.67	14.78	0.73	6.43
20	1.47	1.33	11.74	0.58	5.11
200	2.18	1.05	9.33	0.46	4.06
1000	2.87	0.90	7.94	0.39	3.46

Table 5.2 Calculated $t_{0.2}$ and $t_{0.8}$ times for metadynamic recrystallization

Strain rate, s^{-1}	T=1000 °C		T=900 °C	
	$t_{0.2}$, sec.	$t_{0.8}$, sec.	$t_{0.2}$, sec.	$t_{0.8}$, sec.
2	0.0851	0.614	0.1789	1.2906
20	0.0123	0.089	0.0259	0.1865
200	0.0018	0.013	0.0037	0.0270
1000	0.0005	0.003	0.0010	0.0070

SRX and MDRX, respectively. To prevent the initiation of static recrystallization, the interpass times must be shorter than the corresponding $t_{0.2}$'s in the middle columns. To prevent metadynamic recrystallization, the interpass times should be shorter than the corresponding values of $t_{0.2}$ values in Table 5.2.

In the strip mill case, the strain rates in the finishing passes fall in the range 10 to 200 s^{-1}, and interpass times of 0.4 to 4 seconds are observed. When these values are compared with those that are framed in Table 5.1, the $t_{0.2}$ times at a strain of 0.3 at 1000 °C are approximately equal to the mill interpass times. By contrast, the $t_{0.2}$ times that correspond to a strain of 0.6 are shorter. However, finishing is not carried out at such high temperatures. At the more typical temperature of 900 °C, the $t_{0.2}$ times are about 1.1 and 0.5 s, respectively, for prestrains of 0.3 and 0.6, while the $t_{0.8}$ times are 9.3 and 4.1 s, respectively. These times imply that only a small amount of static recrystallization is involved, and large retained strains are produced. When the accumulated strains from successive passes become large enough to initiate dynamic recrystallization, metadynamic recrystallization will take over in the interpass interval, since $t_{0.8}$ is now much shorter than the mill interpass time (as shown in the highlighted frames of Table 5.2).

In order to predict the amount of softening expected in a strip mill from a laboratory simulation carried out at lower strain rates, a 'similarity law' was introduced to correct the interpass time for the difference in strain rate[254]. This can be done because the $t_{0.5}$'s for static and metadynamic recrystallization are inversely proportional to a power of the strain rate. Thus, the hold times t for X percent softening should also follow such a relation. In this way, the hold time t_{mill} for X percent softening at a given mill strain rate

can be related to the hold time t_{lab} for the same amount of softening at a particular laboratory strain rate as follows:

$$t_{mill} = t_{lab}\left(\frac{\dot{\varepsilon}_{mill}}{\dot{\varepsilon}_{lab}}\right)^{n} \qquad (5.28)$$

where $\dot{\varepsilon}_{lab}$ and $\dot{\varepsilon}_{mill}$ are the strain rates in the laboratory and the mill, respectively, and n is the strain rate sensitivity of the time to 50% softening.

It should be noted that the occurrence of dynamic recrystallization was indicated by the flow curve envelopes in Figs. 5.16(a), 5.17(a) and 5.18(a) when interpass times of t= 0.05 second were used at a strain rate of $\dot{\varepsilon} = 2s^{-1}$. If these results are converted into strip mill rates using the similarity law, interpass times as short as 0.002 to 0.015 seconds would be required to avoid the occurrence of metadynamic recrystallization. These interpass times are much shorter than those currently employed in strip mills. Thus it can be concluded that, as long as strain accumulation leads to dynamic recrystallization, metadynamic softening will play an important role when microalloyed steels are rolled in these mills.

In the rod mill case, the strain rates range from 10 to 1000 s^{-1}, and the interpass times fall between 0.015 and 1 second. It is of interest to note that the calculated $t_{0.2}$ times for static recrystallization are shorter than the interpass times during the first few passes at 1000 °C, but not at 900 °C. Thus, a small amount of static recrystallization may be involved in the early stages of finishing. More generally, the strain is expected to accumulate from pass to pass because of the gradual decrease in interpass time. Again, when the accumulated strain exceeds the critical strain, dynamic recrystallization will be initiated, followed by appreciable amounts of metadynamic recrystallization. This is indicated by the rod mill interpass times, which fall between the $t_{0.2}$ and $t_{0.8}$ times listed in Table 5.2.

When the temperature is reduced into the Nb(CN) precipitation region, both static and metadynamic recrystallization are retarded significantly, as indicated by the softening curve for 850 °C in Fig. 5.12(b). The strain will therefore be accumulated from pass to pass. The peak strain increases, however, because Nb(CN) precipitation retards the onset of dynamic recrystallization. For example, the flow curves in Fig. 5.20(d) indicate that the peak strain is about 2.4 when interpass times of t = 8 seconds are employed at a strain rate

of 2 s^{-1} and T= 850 °C. This interpass time is equivalent to those of the strip mill after conversion using equation (5.28). The total strain applied over the finishing passes in the strip mill, however, is only about 2.5; thus the amount of strain accumulated over the finishing passes is not enough to bring about the completion of dynamic recrystallization at the temperature of interest. It can nevertheless be concluded that metadynamic recrystallization is likely to control both the interstand softening process as well as the microstructure prior to transformation, even at temperatures below the P_s temperature.

In rod mills, the total strain applied during the finishing passes can attain 6.4 for 5.5 mm diameter rod and 5.7 for 13 mm diameter bar[82]. This amount of strain would normally ensure the complete dynamic recrystallization of Nb steels if both static and metadynamic recrystallization can be prevented (e.g. in the case of high Nb steels). By contrast, in plain carbon steels, the $t_{0.5}$ for metadynamic recrystallization is as short as 0.0016 seconds[82]. It can therefore be concluded that repeated metadynamic recrystallization is responsible for the final microstructures of plain carbon steel wire rod.

The behaviour of Nb steels in strip mills probably resembles that shown in Figs. 5.16(b), 5.17(b) and 5.18(b). After strain accumulation, dynamic recrystallization is initiated and supplies nuclei for the metadynamic recrystallization that follows. Bearing in mind the heterogeneous nature of dynamic recrystallization, some local areas will always provide dynamic nuclei to contribute to metadynamic recrystallization. However, the nucleation of static recrystallization is also possible in areas free of dynamic nuclei. Thus, both metadynamic and static recrystallization can play a role under these conditions. On the other hand, if the interpass times are long enough to allow metadynamic recrystallization to produce full or nearly full softening, there will be a significant drop in the mean flow stress (or mill load) and strain accumulation will begin all over again during the following pass. This will lead to 'oscillations' in the mean flow stress on the MFS-pass number plot.

Summary

The recrystallization behaviours of three Nb steels (0.023Nb, 0.07Nb and 0.09Nb) were investigated under isothermal conditions. Hot torsion tests were performed using continuous deformation, as well as double twist and multipass deformation schedules. Temperatures of 850 to 1100 °C were employed, together with strain rates of 0.02 s^{-1} to 10 s^{-1}, and interpass times of 0.05 to 100 seconds. Peak and steady state strains were

determined from the continuous deformation flow curves. Two empirical equations were derived from the experimental data; these take into account the effects of the deformation parameters and of the Nb in solution on the peak and steady state strains. The interpass softening data obtained from the double twist tests were analyzed; by this means the effect of Nb in solution on the rate of interpass softening was established. When this model is combined with an equivalent one for static recrystallization, the relative importance of SRX, DRX and MDRX during hot rolling can be deduced.

CHAPTER 6

STRAIN INDUCED TRANSFORMATION

In modern low carbon and ultralow carbon bainitic (ULCB) steels, boron is an important microalloying element that is added to improve the hardenability of the steel[130, 255-261]. By optimizing the boron concentration and processing conditions, boron can be made to segregate on prior austenite grain boundaries, and the γ-to-α transformation is then effectively delayed to the low temperature range in which low carbon bainite is formed. Boron can also form coarse precipitates, which promote the formation of polygonal ferrite by acting as nucleation sites. Thus the form in which boron is present is an important factor affecting the resulting microstructure. In more recent developments, strong carbide and nitride formers, such as Nb and Ti, are added to tie up the C and N and so make the boron available for segregation. The combined effects of Nb, Mo and B on the no-recrystallization temperature were investigated, and the results were presented in Chapter 4. The effects of chemical composition (mostly Nb and B) and of the processing parameters (reheat temperature, amount of deformation, holding time and cooling rate) on the transformation temperature and on the microstructures produced are another important aspect. The experimental results detailed in this part of the investigation are presented in this chapter.

6.1 Experimental Results

6.1.1 Continuous Cooling Transformation

In order to detect the transformation temperatures (A_{r3} and B_s), schedule C illustrated in Fig. 3.15 was employed to perform a series of CCC tests on the Mo-Nb-B, Mo-B, Nb-B and boron steels. The results are presented in the subsections that follow.

The determination of the A_{r3} and B_s temperatures is illustrated in Fig. 6.1. The broken line shows the continuous deformation of austenite in the absence of ferrite formation. Once ferrite begins to form during straining, the flow stress will deviate from the broken line, as shown in the diagram, and deformation continues in the $\alpha+\gamma$ range. The point at which the actual curve deviates from the trend line (broken line) is defined here as A_{r3}. The flow hardening of the austenite is balanced by softening attributable to ferrite formation at the peak; with further decrease in the deformation temperature, the flow stress begins to drop because of the continued formation of ferrite. If only the γ-to-α transformation is taking place, the curve will follow the dotted line. However, when the formation of bainite is initiated, the flow stress will leave the downward trend, go through a minimum, and then increase, as shown. Because of the practical difficulties involved in establishing the precise point of departure from the "ferrite formation" line, here the minimum, located at 605 °C in the example, will be used to define B_s instead. More precisely, the A_{r3} and B_s temperatures can be determined from the $\Phi\,(\partial\sigma/\partial T)$ vs. σ curve using points A and B, respectively, as shown in Fig. 6.2.

6.1.1.1 Effect of Reheat Temperature

Temperatures of 900, 1000, 1100 and 1200 °C were employed to study the effect of reheat temperature on A_{r3} and B_s in the Mo-Nb-B, Mo-B, Nb-64B, Nb-48B, Nb-15B and B steels. For comparison purposes, a C-Mn steel (the base steel) with a composition of 0.03C-1.55Mn-0.02Ti-0.02Al-0.0048N was also used to provide the baseline behaviour. The stress-temperature curves obtained from a series of CCC tests for the above steels are illustrated in Figs. 6.3 through 6.9.

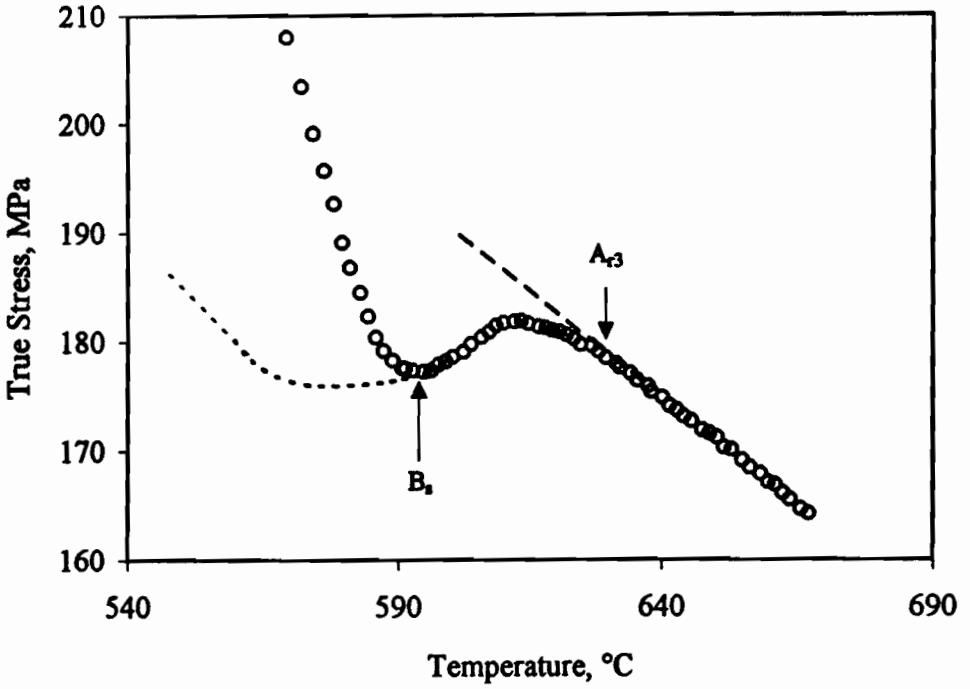

Fig. 6.1 Stress-temperature curve of the Mo-Nb-B steel.

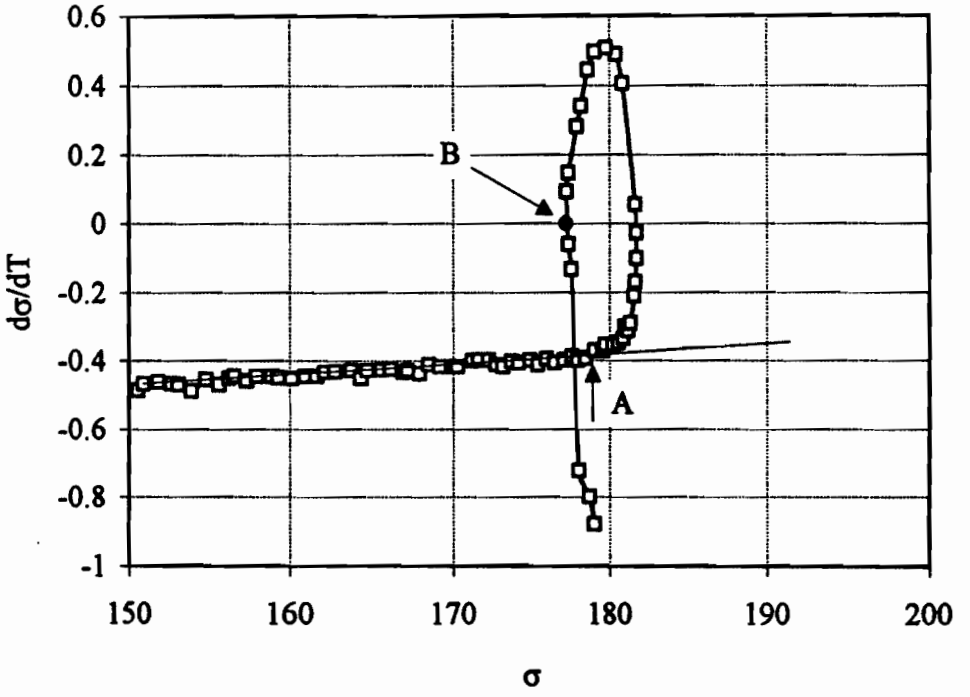

Fig. 6.2 Example of the determination of the A_{r3} and B_s temperatures.

The stress-temperature curves obtained on the base steel reheated at 900 °C and 1200 °C are presented in Fig. 6.3. It can be seen that the measured A_{r3}'s only differ by about 10 °C despite the large difference between the reheated austenite grain sizes at 900 °C and 1200 °C. In the case of the Mo-Nb-B steel (see Fig. 6.4), the flow stress in the austenite region is the highest for the 900 °C reheat temperature because this leads to the finest reheated austenite grain size. The A_{r3} and B_S temperatures were determined in the way described above and are marked by small arrows on the stress-temperature curves. It can be seen that the A_{r3} and B_s values are highest for the samples reheated at 900 °C and both decrease with increasing reheat temperature.

The curves determined on the Mo-B steel are displayed in Fig. 6.5; here it can be seen that the 1000 °C curve is close to the 900 °C one in the austenite range. This is because the reheated grain sizes in these samples were comparable. The measured A_{r3}'s and B_s's for all the reheat temperatures fall in a narrow range. It seems that the transformation temperature is insensitive to reheat temperature (grain size) in this steel.

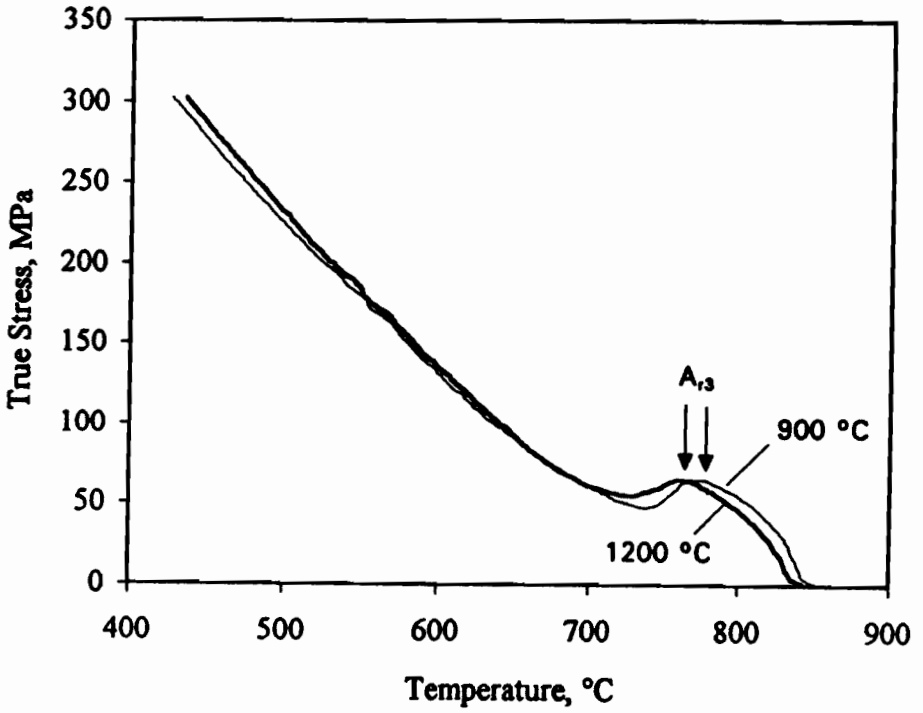

Fig. 6.3 Stress-temperature curves for two different reheat temperatures in the base steel.

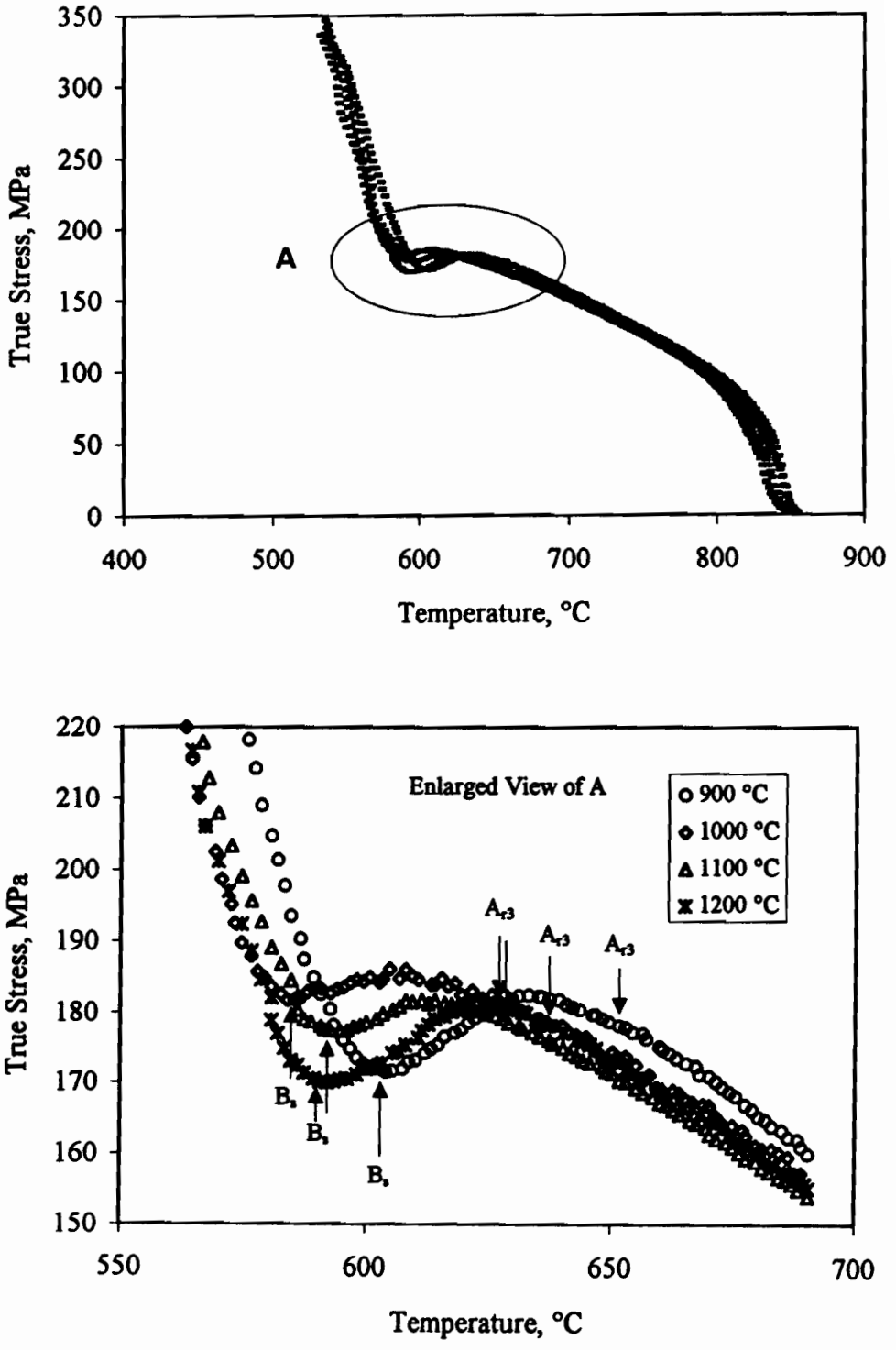

Fig. 6.4 Stress-temperature curves for four different reheat temperatures in the Mo-Nb-B steel.

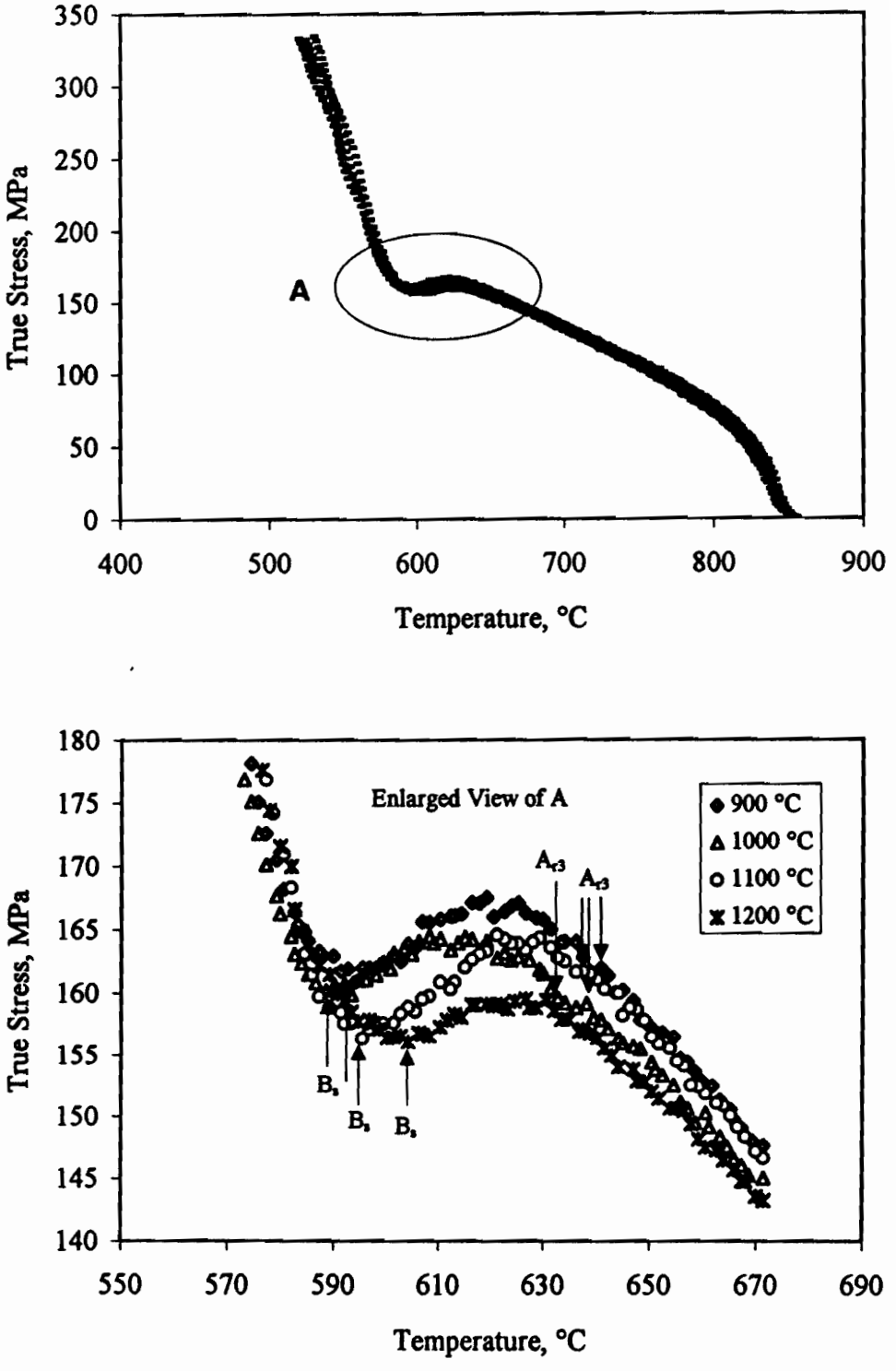

Fig. 6.5 Stress-temperature curves for four different reheat temperatures in the Mo-B steel.

The effect of reheat temperature on transformation behaviour in the Nb-B steels is illustrated in Figs. 6.6 to 6.8. It can be seen from Fig. 6.6 that, unlike the Mo-Nb-B and Mo-B steels, the Nb-64B steel A_{r3} covers a wide range: from 800 °C for the 900 °C reheat temperature to 670 °C for 1200 °C. For the Nb-48B steel (see Fig. 6.7), the transformation behaviours for the 1000, 1100, and 1200 °C reheat temperatures are similar to those for the Mo-Nb-B and Mo-B steels, except for the 900 °C case (the A_{r3} for this reheat temperature is about 700 °C). When the boron concentration is lowered to 15 ppm, i.e. in the Nb-15B steel (see Fig. 6.8), the transformation is again sensitive to reheat temperature, and the measured A_{r3} decreases from 775 °C to 735 °C as the reheat temperature is increased from 900 °C to 1200 °C. The A_{r3}'s are about 120 °C higher in this steel than in the Mo-Nb-B steel, and the transformation is mainly of the γ-to-α type. This will be confirmed later with the aid of the respective microstructures.

The boron steel curves display less sensitivity to reheat temperature (see Fig. 6.9), and the transformation is again of the γ-to-α type in this steel. The measured A_{r3}'s are close to those of the base steel.

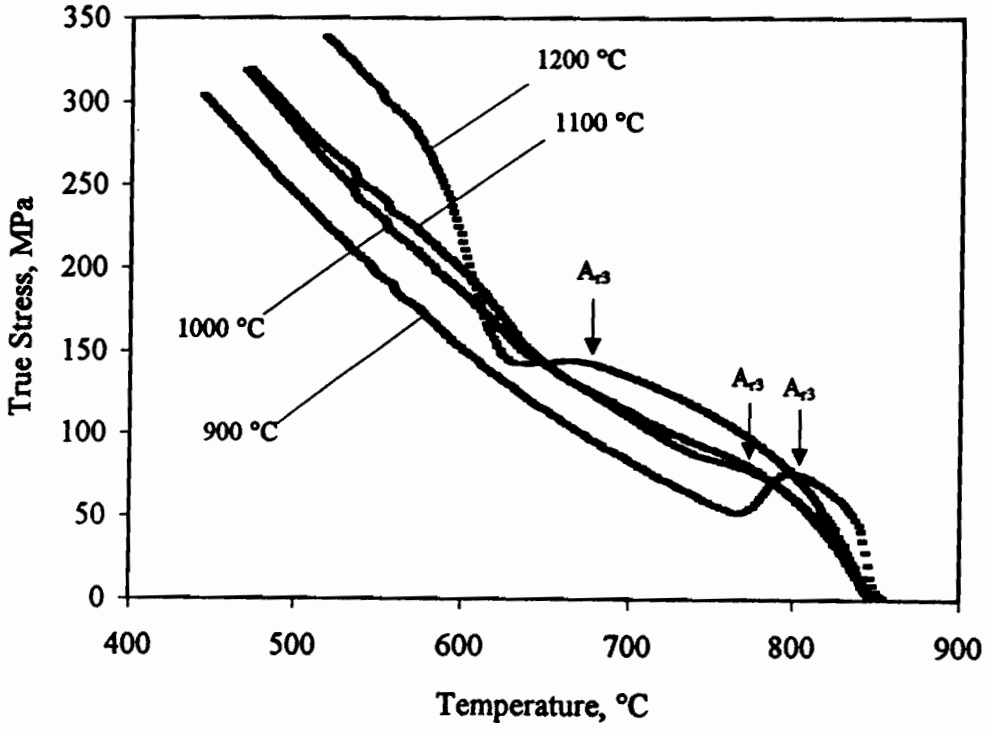

Fig. 6.6 Stress-temperature curves for four different reheat temperatures in the Nb-64B steel.

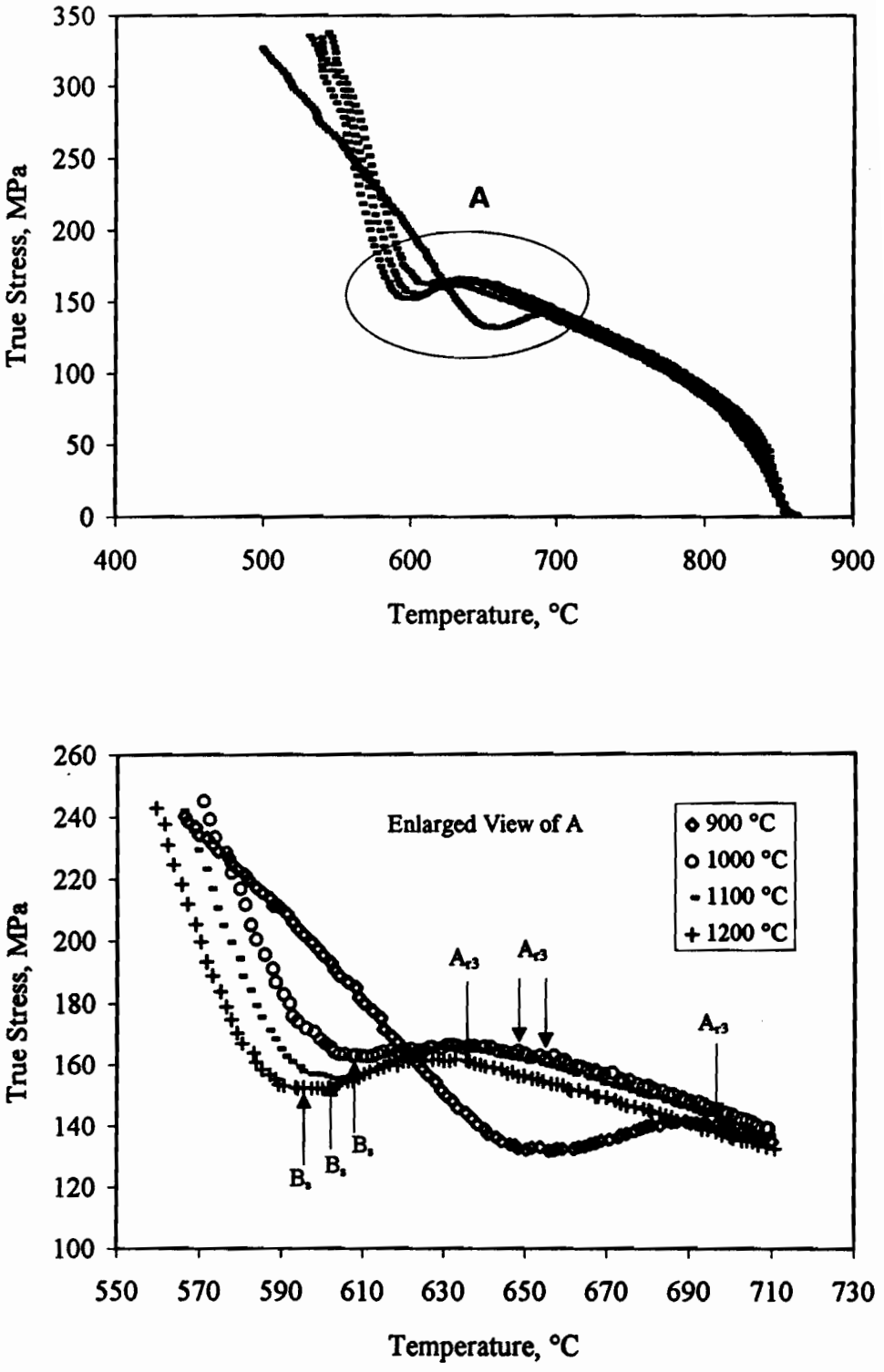

Fig. 6.7 Stress-temperature curves for four different reheat temperatures in the Nb-48B steel.

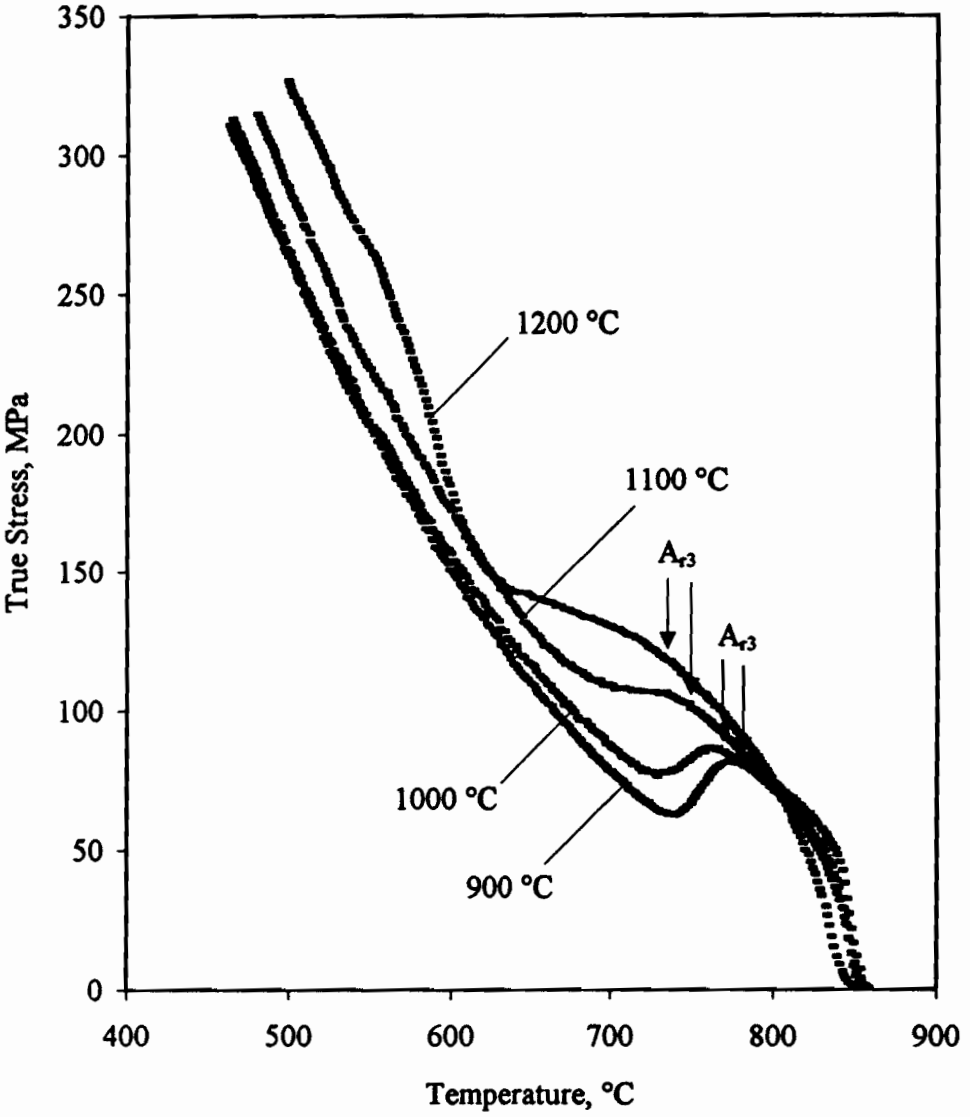

Fig. 6.8 Stress-temperature curves for four different reheat temperatures in the Nb-15B steel.

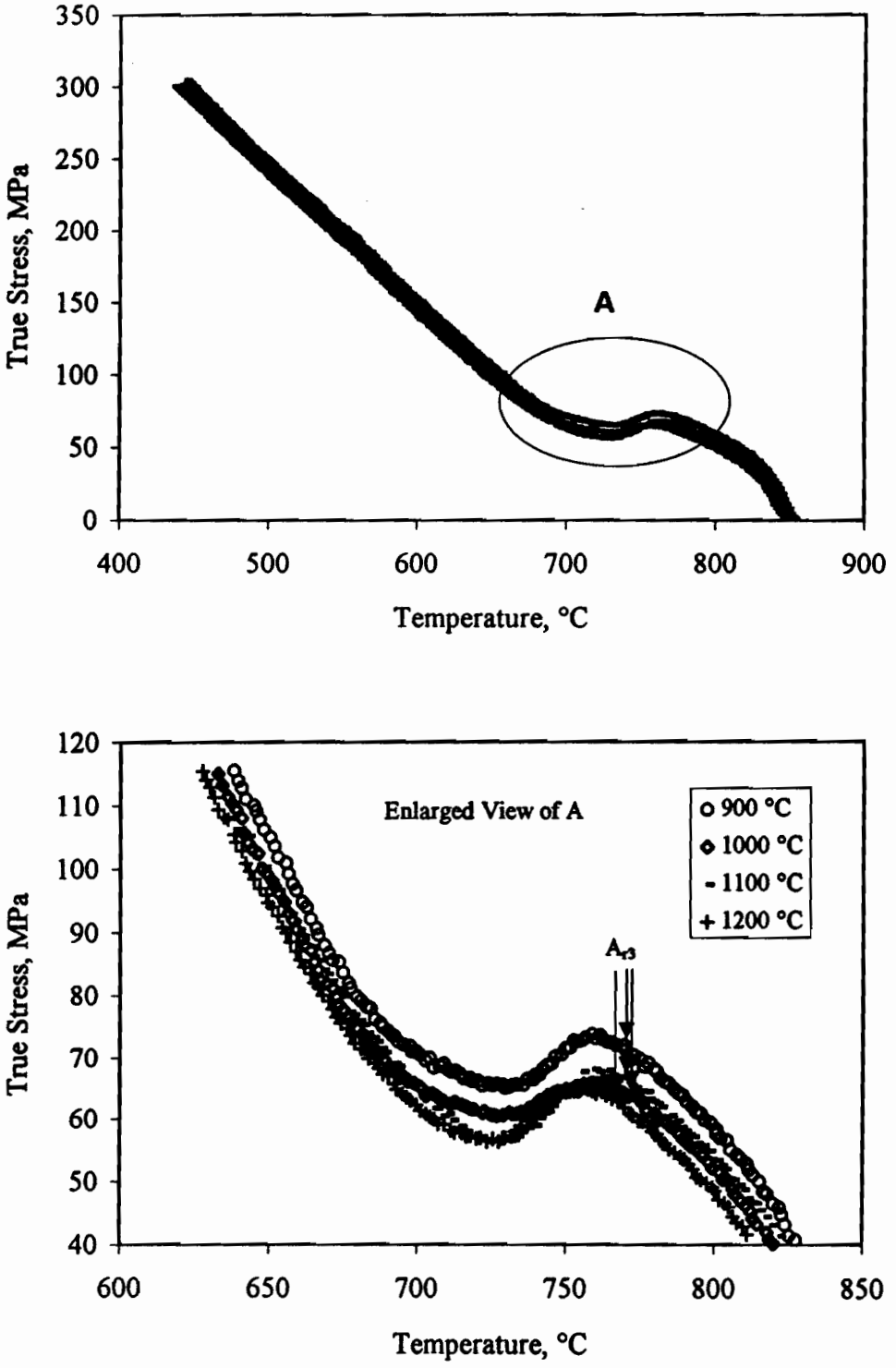

Fig. 6.9 Stress-temperature curves for four different reheat temperatures in the boron steel.

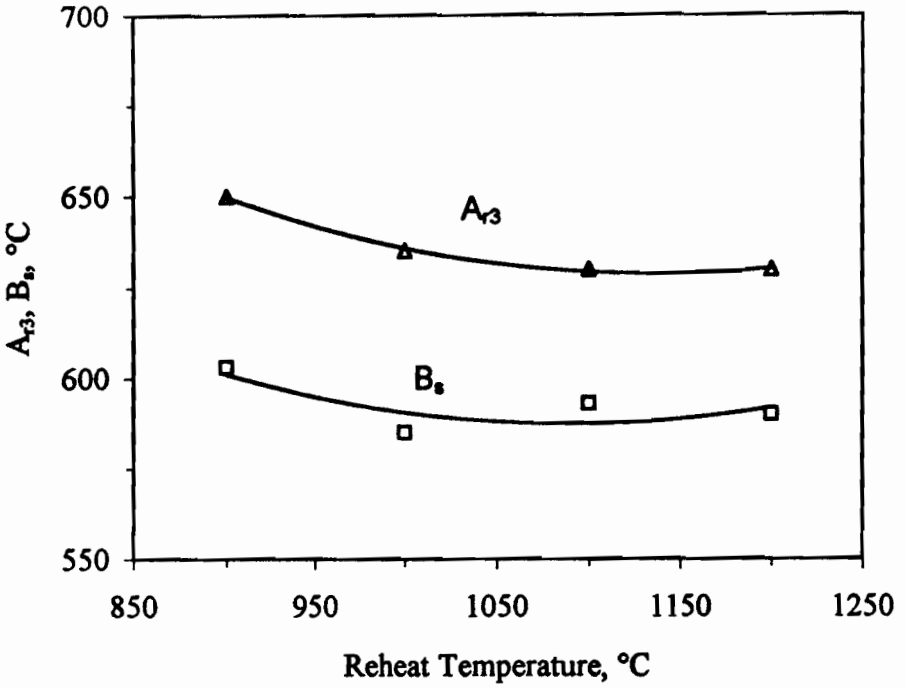

Fig. 6.10 Dependence of the transformation temperature on reheat temperature in the Mo-Nb-B steel.

The dependence on reheat temperature of the transformation temperatures in the Mo-Nb-B steel is illustrated in Fig. 6.10. It can be seen that both the A_{r3} and B_s decrease with increasing reheat temperature, and that the difference between them is about 50 °C. The change in transformation temperature with reheat temperature is related to the amount of Nb and B in solution and the reheated austenite grain size. The effects of Nb and B in solution will be presented in a later subsection.

6.1.1.2 Effect of Composition

The effect of chemical composition on the transformation behaviour will be described in this subsection. Stress-temperature curves for the Mo-Nb-B and Nb-15B steels tested after reheating at 1200 °C are presented in Figs. 6.11 (a) and (b), respectively. Interrupted tests were also performed, in which case specimens were quenched at selected temperatures, labelled by a, b, c and d in the figures. The resulting microstructures are shown in Fig. 6.12 for the Mo-Nb-B and Fig. 6.13 for the Nb-15B steel. It is evident that the microstructures are basically different in the two steels. In the Mo-Nb-B grade, the transformation started at around 635 °C; plate-like ferrite formed

first at the prior austenite grain boundaries and then grew rapidly toward the centres of the grains. When the temperature was decreased, lath-like ferrite was formed and small amounts of retained austenite were trapped between these laths. The room temperature microstructure consists of a mixture of plate-like and lath-like ferrite with retained austenite or martensite (i.e. M/A) islands, and the prior austenite grain boundaries can be readily seen. This type of microstructure is often referred to as *low carbon bainite*.

By contrast, in the Nb-15B steel, the transformation started at a much higher temperature (around 736 °C), and polygonal ferrite formed on the prior austenite grain boundaries. The transformation progressed by the continuous nucleation and growth of this phase into the prior austenite grains. A very small amount of austenite transformed into bainite in the later stages of the reaction. Thus, the resulting microstructure is mainly polygonal ferrite in this case, with a small amount of bainite.

The effect of boron concentration on the transformation behaviour can be further deduced from the results on the three Nb-B steels. Fig. 6.14(a) collects the stress-temperature curves determined after reheating at 900 °C. It can be seen that both the high and low boron containing materials (i.e. the Nb-64B and Nb-15B steels) undergo the γ-to-α transformation, while both the γ-to-α and γ-to-B phase changes take place in the Nb-48B steel. The A_{r3} is about 100 °C higher in the Nb-64B than in the Nb-48B steel. It is also noteworthy that the A_{r3} is about 20 °C higher in the Nb-64B than in the Nb-15B steel. This is probably due to the effect of the borocarbides. The higher boron concentration in the Nb-64B steel promotes the formation of $Fe_{23}(C,B)_6$, and these large borocarbides enhance the formation of polygonal ferrite by acting as nucleation sites. This will be proved later by both optical and TEM microscopy.

The differences among these steels can be further detected from the stress-temperature curves determined after reheating at 1200 °C (see Fig. 6.14(b)). In this case, the measured A_{r3}'s for the three steels are about 50 °C~100 °C lower than when a reheat temperature of 900 °C was employed, and the shapes of all three curves indicate that a mixture of γ-to-α and γ-to-B transformation is taking place.

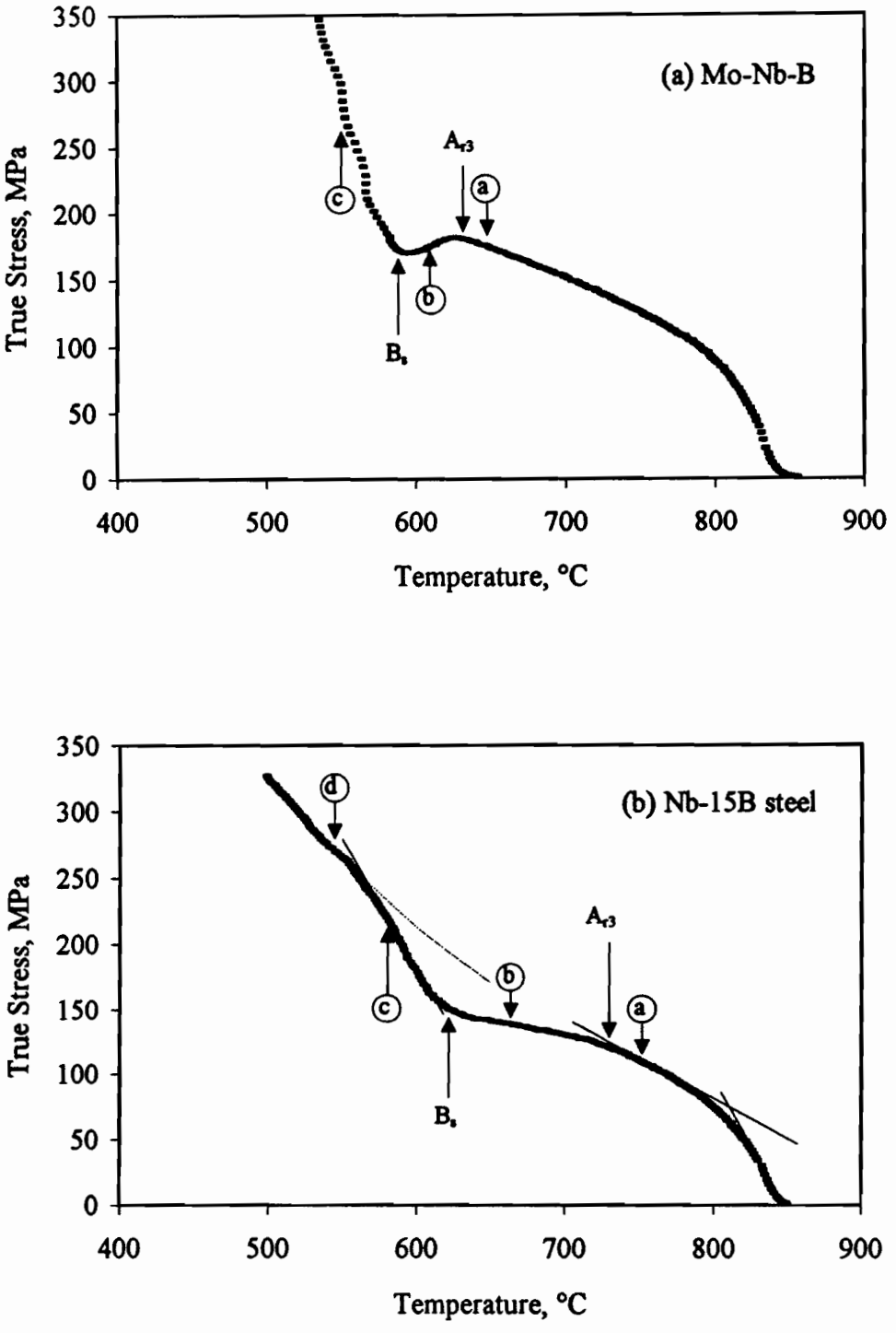

Fig. 6.11 Stress-temperature curves of the (a) Mo-Nb-B steel and (b) Nb-15B steel reheated at 1200 °C.

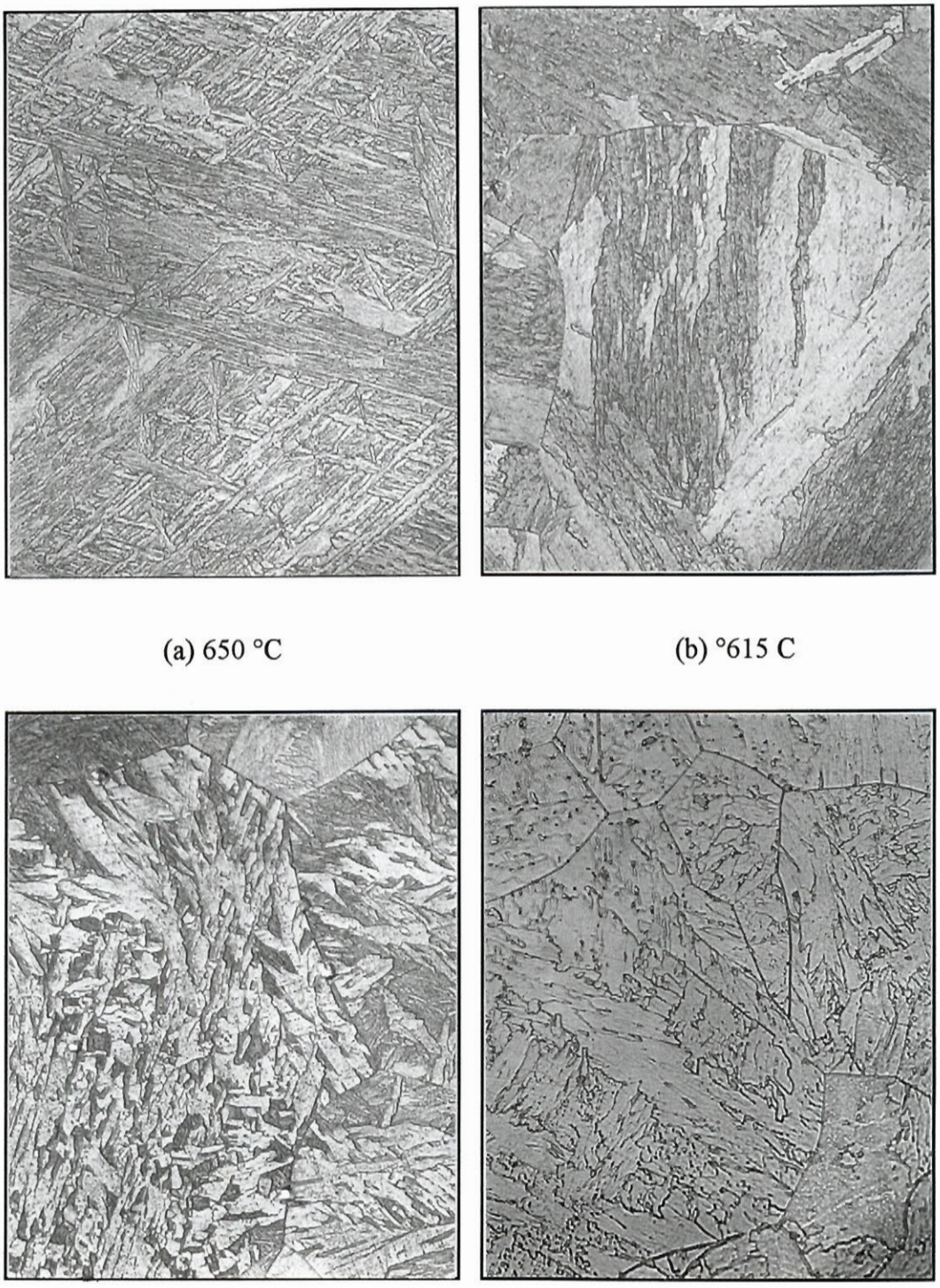

(a) 650 °C (b) °615 C

(c) 540 °C (d) RT

x 630

Fig. 6.12 Microstructure evolution during continuous cooling in the Mo-Nb-B steel.

6.1.1.3 Effect of Deformation

Three sets of CCC tests were performed in order to determine the effect of deformation on transformation behaviour in the Mo-Nb-B and Nb-B steels. In the first set of tests, a prestrain of 0.5 was applied at 980 °C (above the T_{nr}) and at 850 °C (below the T_{nr}) before the CCC tests were initiated. These treatments resulted in the microstructures shown in Fig. 6.15. Recrystallized austenite was produced at 980 °C and a pancaked structure at 850 °C. The stress-temperature curves generated from the CCC tests are shown in Fig. 6.16. The transformation behaviour is similar in the two cases, although the flow stresses pertaining to the 850 °C curve are higher than those associated with the 980 °C curve. The higher flow stress at 850 °C is due to the strain retained from the previous deformation. This indicates that the strained condition of the austenite does not significantly affect the transformation behaviour of the Mo-Nb-B steel during subsequent deformation.

In the second set of tests, prestrains of 0.05 and 0.25 were applied at 900 °C, and the samples were held for 60 seconds at this temperature and then cooled to 850 °C, at which point the CCC tests were initiated. The stress-temperature curves determined on the Nb-48B steel are presented in Fig. 6.17. It can be seen that the transformation temperatures of this steel were increased slightly by increasing the amount of deformation, while the type of transformation was not changed by the deformation.

In the third set of tests, a prestrain of 0.25 was applied at 900 °C and the holding time was increased to 300 seconds; then the samples were cooled to 850 °C, at which point the CCC tests were initiated. The stress-temperature curves generated from the tests on the Nb-15B, Nb-48B and Nb-64B steels are presented in Fig. 6.18. It can be seen that the stress-temperature curve of the Nb-48B steel displays a transformation behaviour similar to the one determined after shorter holding times (shown in Fig. 6.17). The stress-temperature curves of the Nb-15B and Nb-64B steels, however, indicate that deformation produces a large increase in the A_{r3}.

(a)

(b)

Fig. 6.15 Microstructures of the Mo-Nb-B steel deformed to ε=0.5 at (a) 980 °C and (b) 850 °C and quenched at 850 °C. x 400

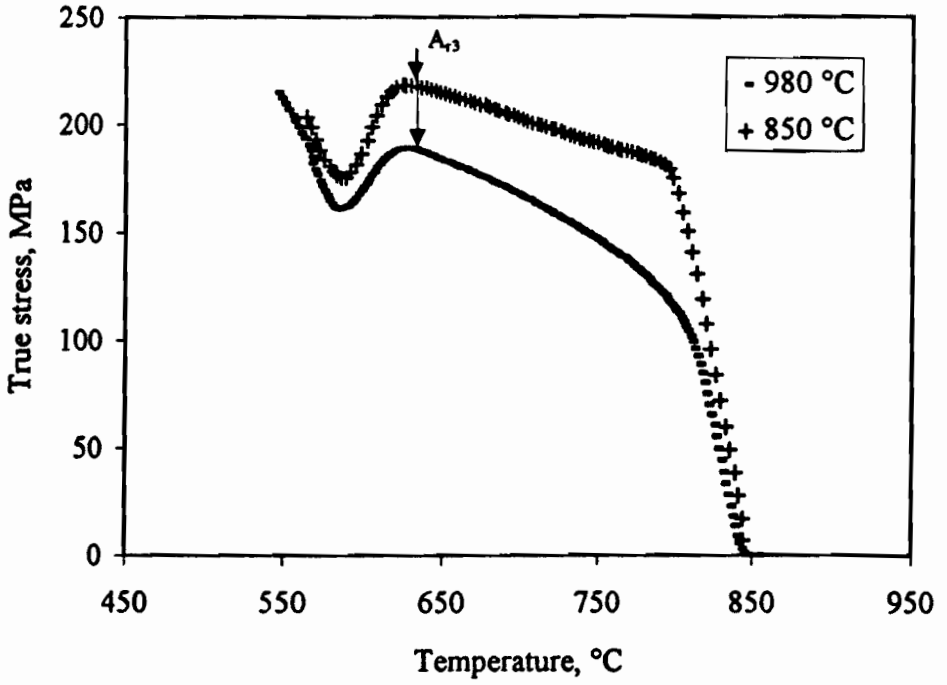

Fig. 6.16 Stress-temperature curves determined on the Mo-Nb-B steel prestrained to ε=0.5 at 850 °C and 980 °C before the CCC tests.

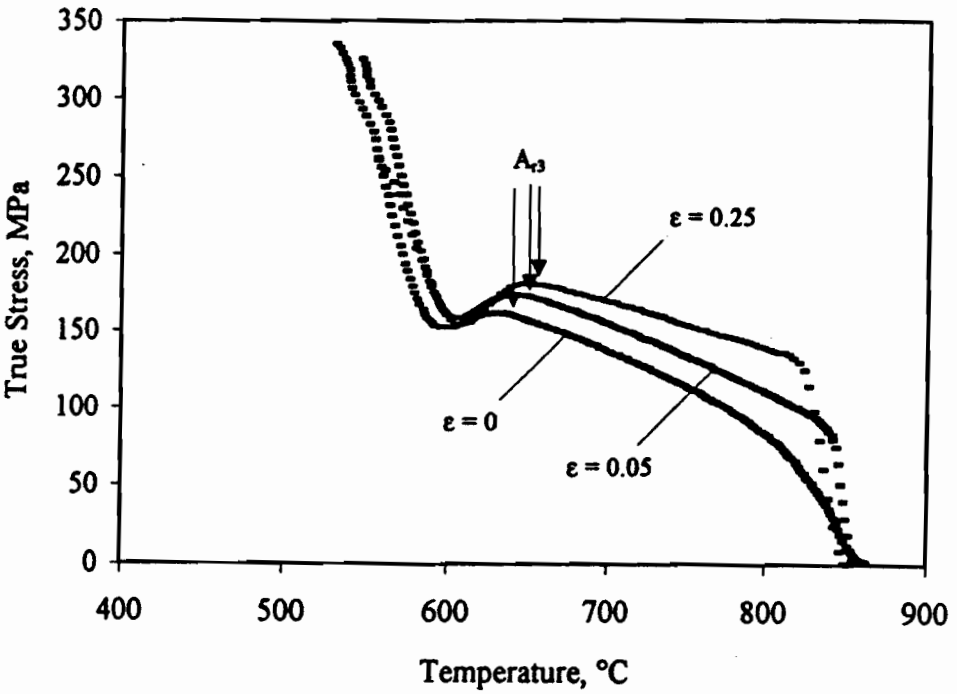

Fig. 6.17 Stress-temperature curves determined on the Nb-48B steel prestrained to ε=0, 0.05 and 0.25 at 900 °C before the CCC tests.

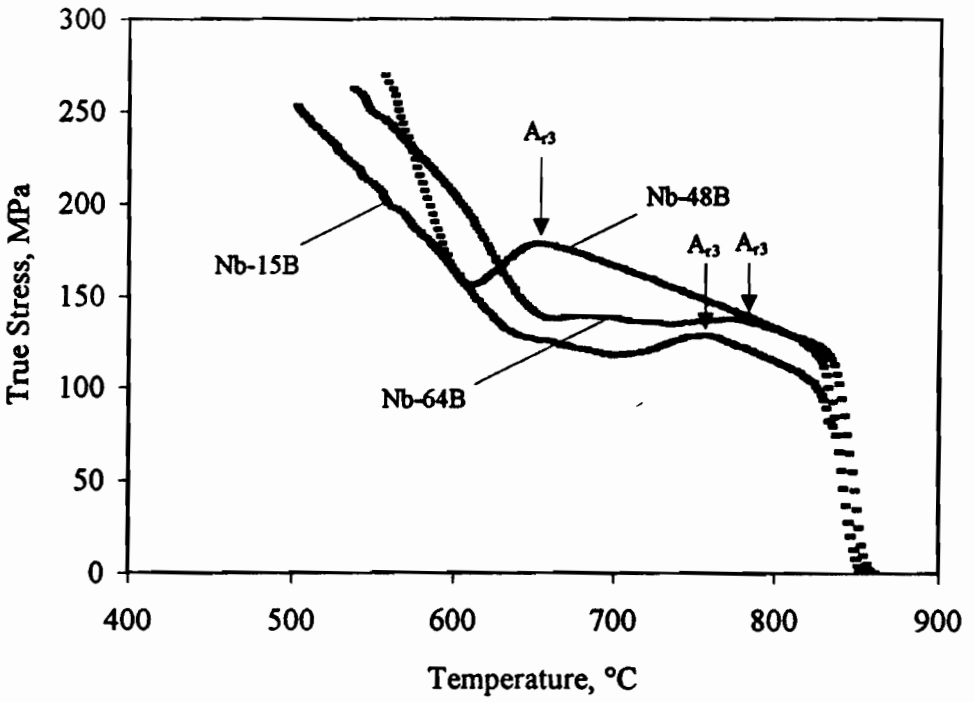

Fig. 6.18 Stress-temperature curves determined on the Nb-15B, Nb-48B and Nb-64B steels prestrained to ε=0.25 at 900 °C and held for 300 seconds before the CCC tests.

6.1.1.4 Effect of Nb and B in Solution

As shown in § 6.1.1.1, the transformation behaviours of the Nb-15B, Nb-48B and Nb-64B steels were significantly influenced by the prior reheat temperature. This could be due in part to the different amounts of Nb and B put into solution at the reheat temperature, and also to the different reheated austenite grain sizes. In order to gain a better understanding of this phenomenon, and to evaluate the relative importance of the two effects, a series of CCC tests was carried out on the Nb-15B and Nb-48B steels.

In the first set of tests, specimens were reheated at 1200 °C for 30 minutes, and then cooled to 900 °C at a cooling rate of 1 °C/s. The specimens were held at this temperature for 30 minutes, and subsequently cooled to 850 °C, at which point the CCC tests were initiated. The 900 °C + 30 min. treatment was employed to reduce the amounts of Nb and B in solution through the precipitation of Nb(CN) and $Fe_{23}(C,B)_6$. The stress-

temperature curves generated from this type of test for the Nb-15B and Nb-48B steels are presented in Figs. 6.19 and 6.20. For purposes of comparison, the curves pertaining to the 900 °C and 1200 °C conventional reheat tests are also included in these figures. It can be seen from Fig. 6.19 that, after the modified 900 °C treatment, the stress-temperature curve of the Nb-15B steel is similar to that of the conventional 900 °C reheat treatment, although a slightly lower A_{r3} is observed. No apparent γ-to-B transformation is indicated by the shape of the curve.

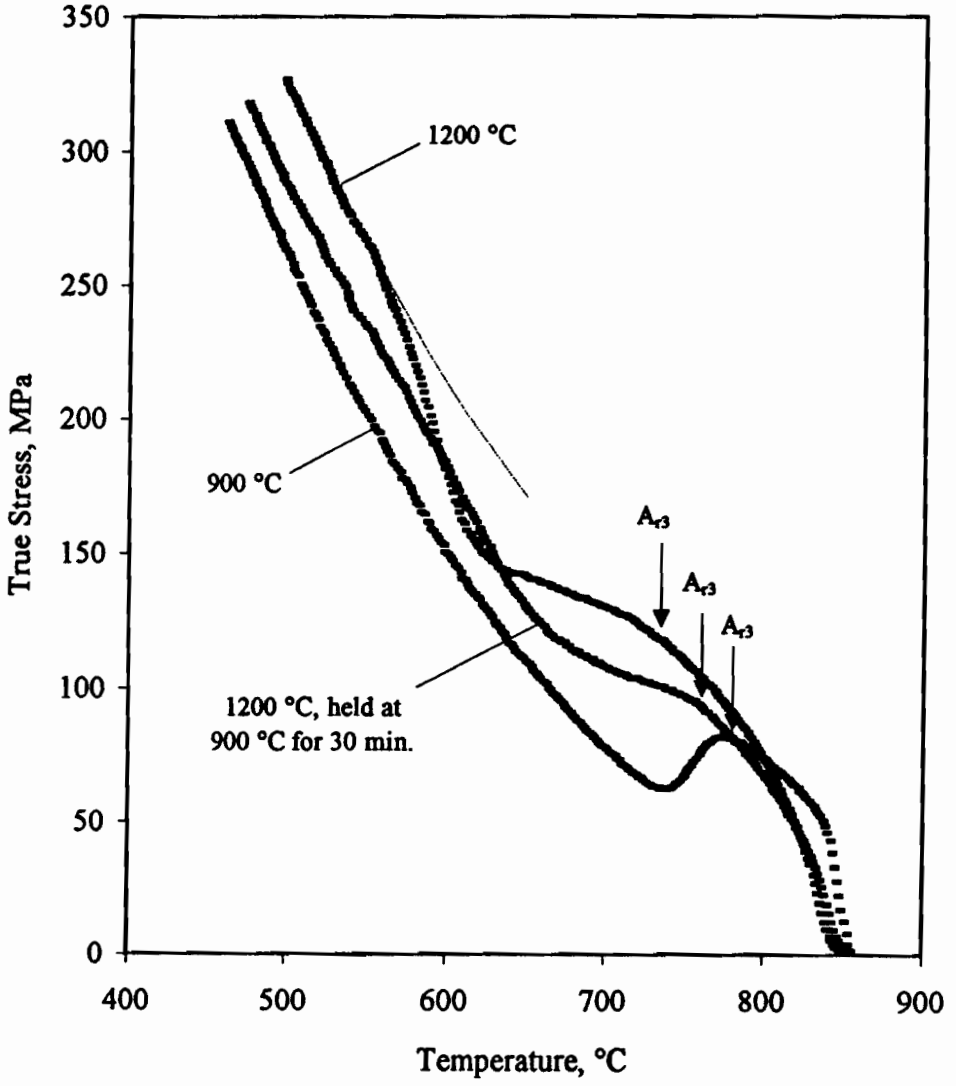

Fig. 6.19 Stress-temperature curve of the Nb-15B steel reheated at 1200 °C and held at 900 °C for 30 minutes prior to testing.

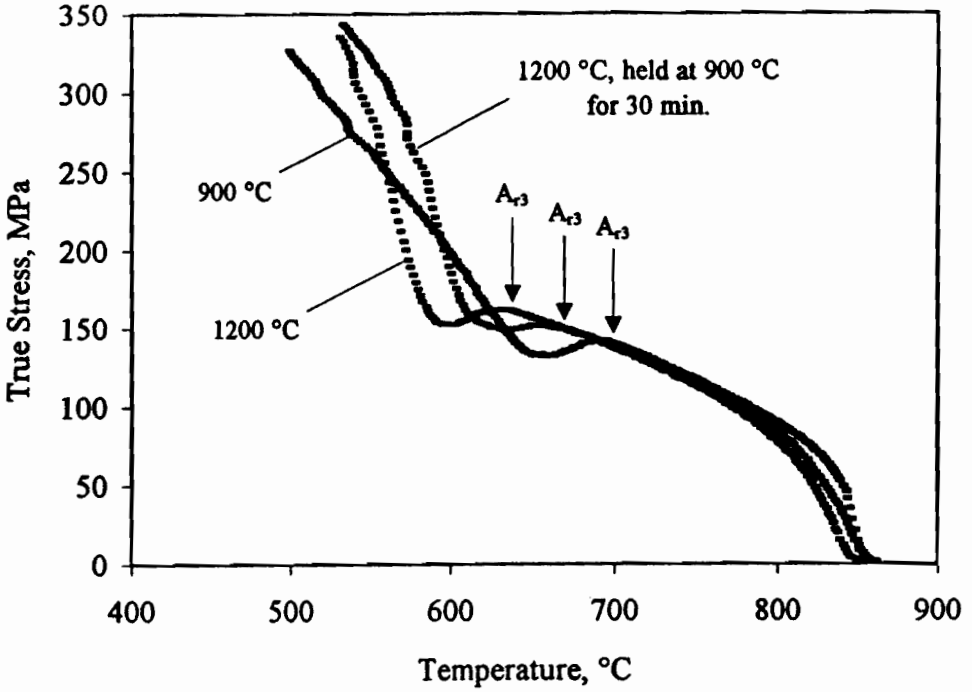

Fig. 6.20 Stress-temperature curve of the Nb-48B steel reheated at 1200 °C and held at 900 °C for 30 minutes prior to testing.

In the case of the Nb-48B steel, however, the stress-temperature curve after holding at 900 °C indicates that the transformation behaviour is similar to that observed after the 1200 °C reheat, although the A_{r3} is increased by about 30 °C by the treatment. This phenomenon can be attributed to the Nb and B in solution since holding at 900 °C for 30 min. did not change the grain size.

In the second set of tests, samples were reheated at 1200 °C for 30 minutes, and then cooled to 900 °C at a cooling rate of 1 °C/s. A prestrain of 0.25 was applied at this temperature and then the samples were held for periods of time ranging from zero to 3600 seconds. At the end of holding, the samples were continuously cooled to 850 °C, at which point the CCC tests were initiated. The stress-temperature curves of the Nb-48B steel samples treated in this way are presented in Fig. 6.21. It can be seen that, in the austenite region, the flow stresses are higher after 60 and 300 seconds of holding than after 0, 1800 and 3600 seconds. This reflects the effect of Nb(CN) precipitation on austenite strength. In fact, Djahazi[133] reported that the P_s and P_f times (the start and finish times for

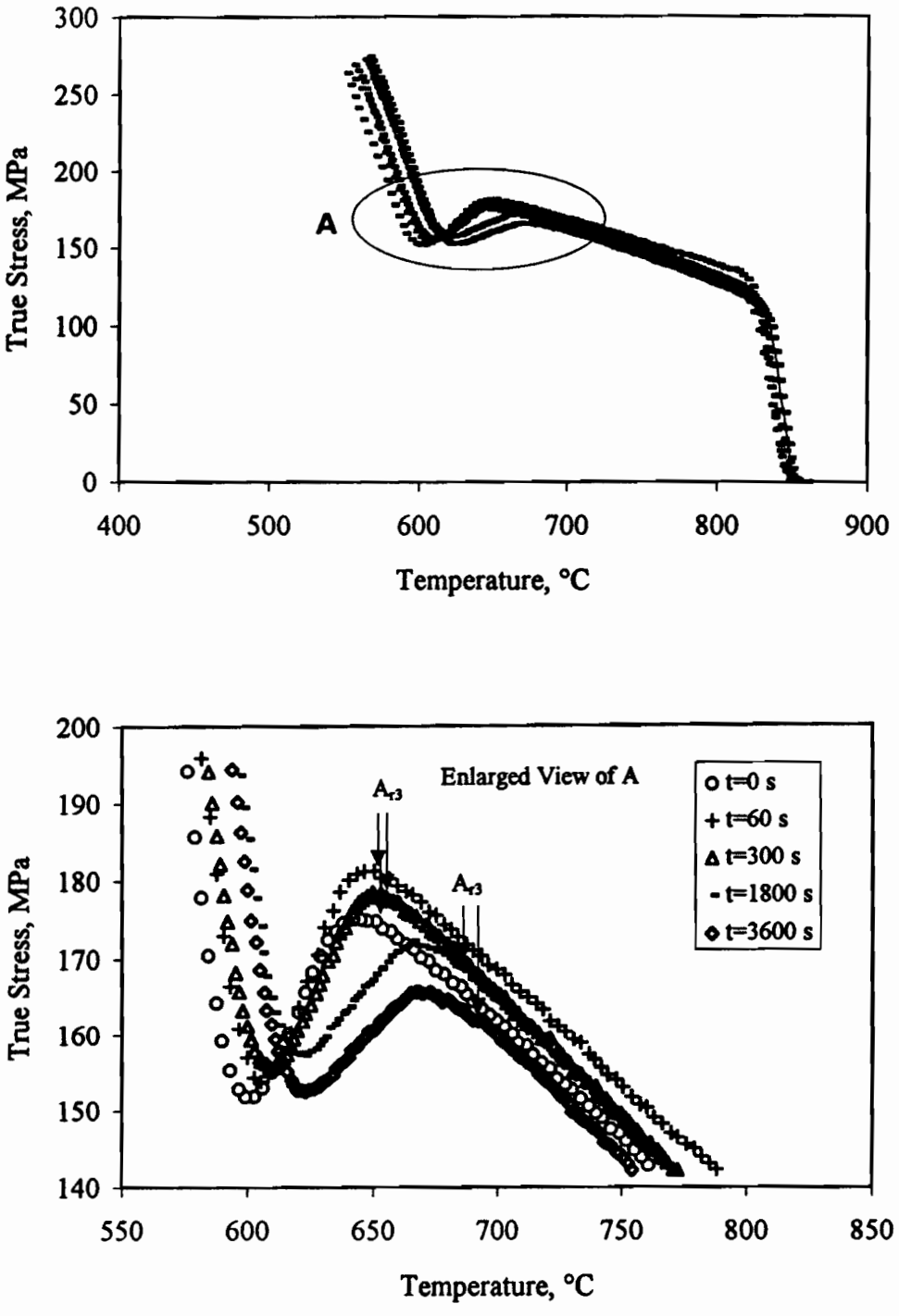

Fig. 6.21 Stress-temperature curves determined on the Nb-48B steel reheated at 1200 °C, prestrained to ε=0.25 at 900 °C, and then held for different times before the CCC tests.

Nb(CN) precipitation) in a steel of similar composition are 10 and 350 seconds after deformation at 900 °C. The 60 and 300 second holding times in the present investigation fall into this range; thus a large number of fine Nb(CN) precipitates are expected to have formed during holding. The austenite was in turn strengthened by these fine precipitates. On further increasing the holding time to 3600 seconds, the Nb(CN) precipitates were coarsened, which eventually lowered the strengthening effect of the precipitates and led to the lower flow stresses in this way.

The transformation temperatures that can be determined from the stress-temperature curves measured after 1800 and 3600 seconds of holding are about 30 °C higher than after the shorter holding times. This can be associated with the reduced amounts of Nb and B in solution, which inhibit the formation of polygonal ferrite.

The combined effects of deformation and holding on the transformation behaviour of the Nb-48B steel are further demonstrated by the curves generated after applying an increased prestrain of 0.5 (see Fig. 6.22). It can be seen that the transformation behaviours that follow 60 and 300 seconds of holding are nearly the same, while the A_{r3} produced by 3600 seconds of holding is about 50 °C higher than after less holding.

The optical micrographs that correspond to the specimens of Fig. 6.22 water quenched at the end of holding are shown in Fig. 6.23. It can be seen that the microstructures associated with holding times of 60 and 300 seconds, shown in Figs. 6.23(a) and (b), are pancaked, while the one after 3600 seconds of holding is partially recrystallized (see Fig. 6.23(c)). The microstructures of the specimens cooled to room temperature are presented in Fig. 6. 24. It is of interest to note that the amount of polygonal ferrite increases with holding time, and about 70% polygonal ferrite was obtained after 3600 seconds of holding (see Fig. 6.24(c)).

In order to have a better understanding of the effect of boron, both optical and TEM investigations were carried out on the quenched samples of Fig. 6.23. In the case of the optical microscopy observations, the samples were prepared using standard methods and etched in 2% nital for 6 seconds, resulting in the micrographs presented in Fig. 6.25. Both intragranular and intergranular precipitates can be seen in the cases of the 60 and 300 second specimens (see Figs. 6.25(a) and (b)). These precipitates were identified by their EDX spectra, as will be seen below (Fig. 6.27).

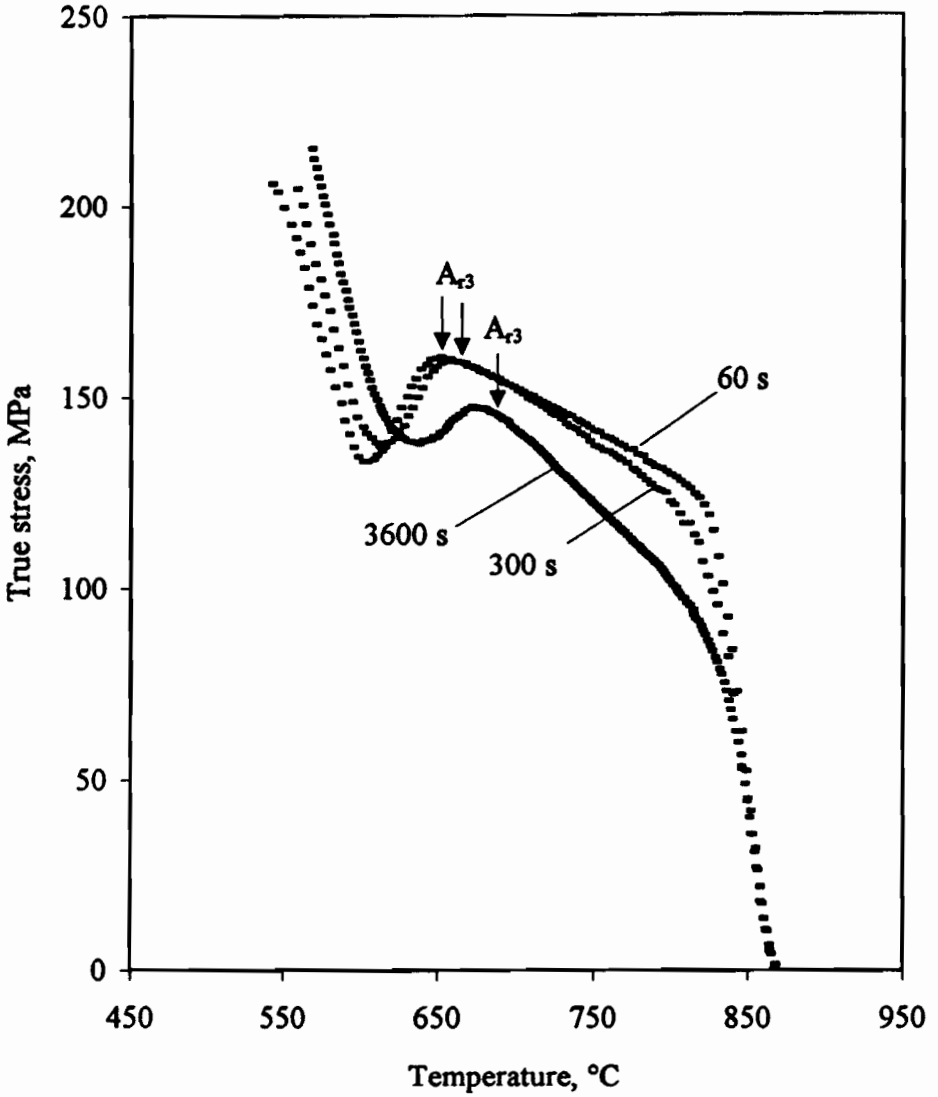

Fig. 6.22 Stress-temperature curve of the Nb-48B steel reheated at 1200 °C, prestrained to ε=0.5 at 900 °C, and held for different times before CCC testing.

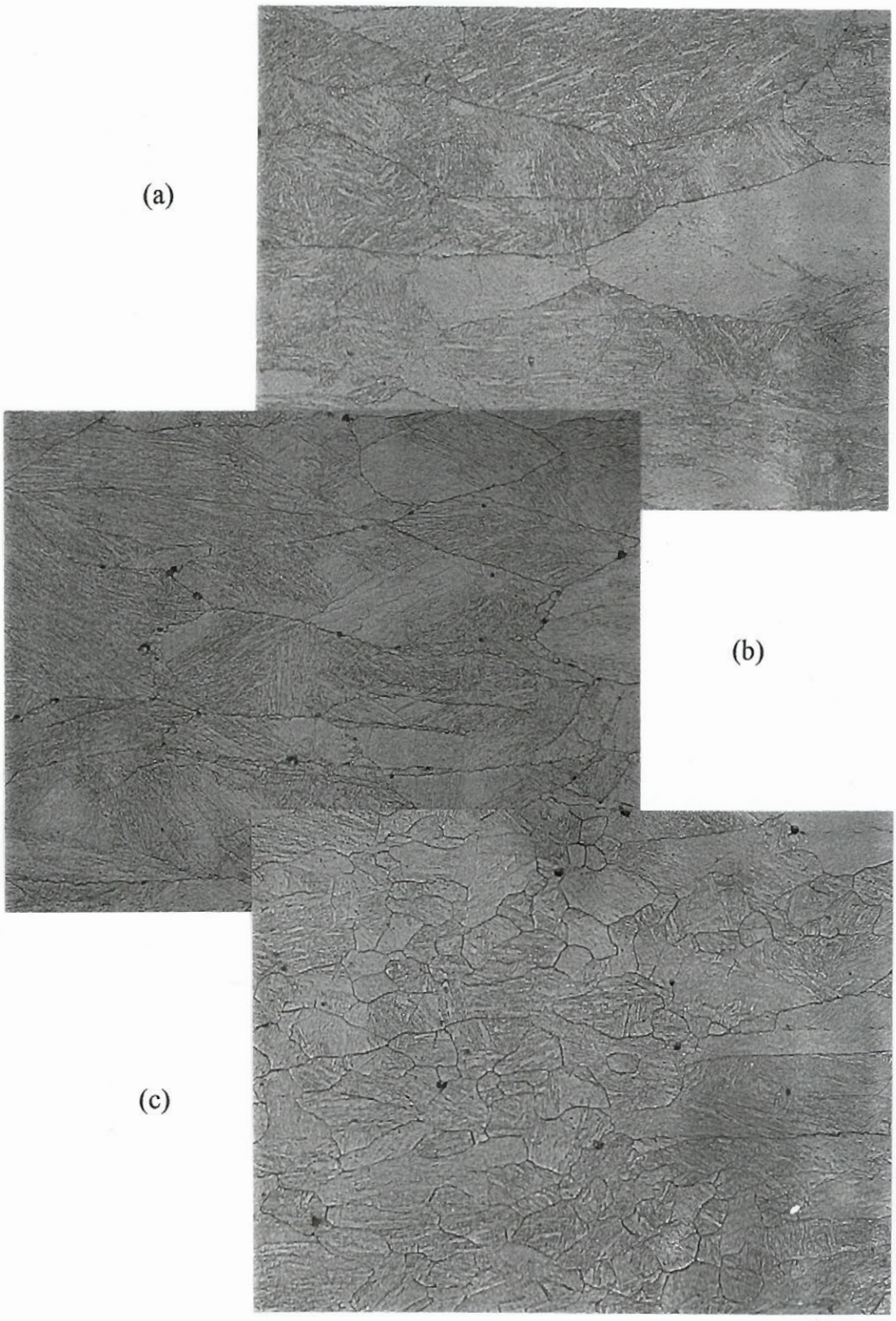

Fig. 6.23 Microstructures of the Nb-48B steel samples of Fig. 6.22: prior to CCC testing, but after holding for: (a) 60 seconds, (b) 300 seconds, (c) 3600 seconds. x 400

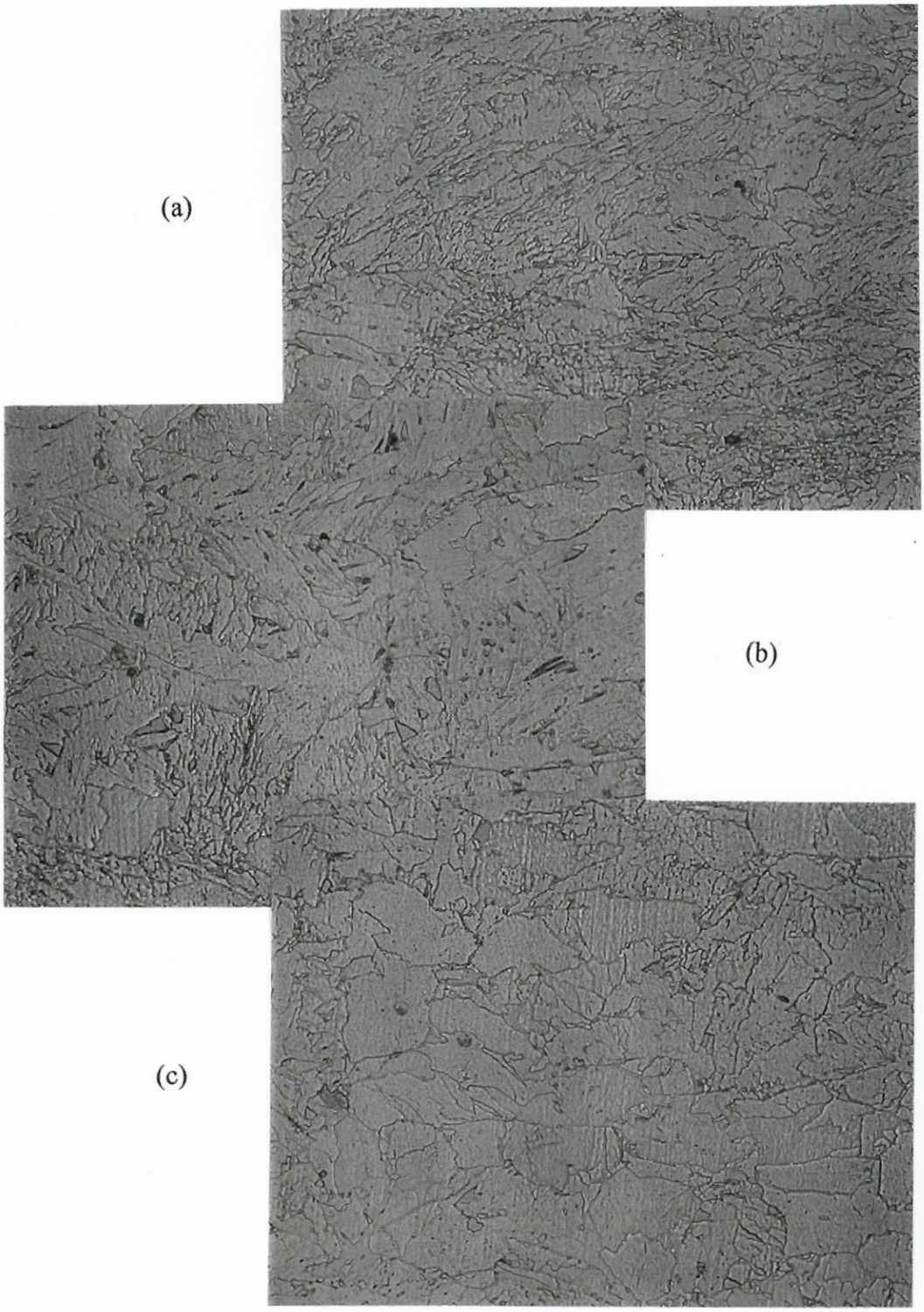

Fig. 6.24 Microstructures of the Nb-48B steel samples of Fig. 6.22 after completion of the CCC tests. These were held for the following times prior to testing: (a) 60 seconds, (b) 300 seconds, (c) 3600 seconds. x 630

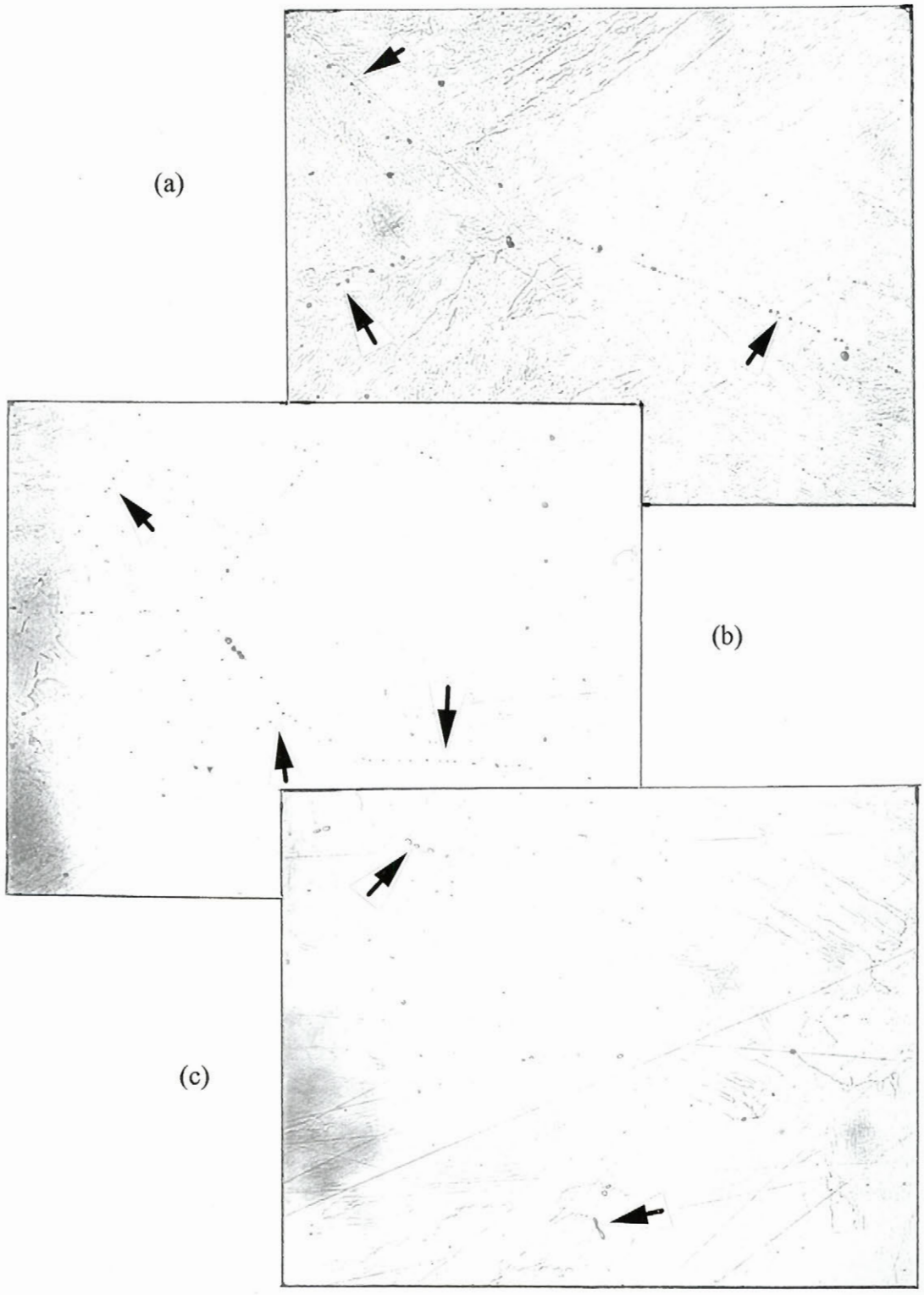

Fig. 6.25 Micrographs showing the sizes and distributions of the precipitates in the Nb-48B steel samples of Fig. 6.22. Prior to testing, these specimens were held at 900 °C for: (a) 60 seconds, (b) 300 seconds, (c) 3600 seconds. x 800

It should be pointed out that the detection of borocarbide precipitates is very difficult because they are readily dissolved in the usual etching and polishing solutions. Light etching (for 6 seconds) in 2% nital apparently either dissolves the particles or releases them from the sample surface. In either event, etch pits are usually all that remain afterwards. The actual sizes of precipitates are therefore smaller than indicated by the optical microscope observations. In order to identify these particles and to have a more accurate assessment of their sizes, surface replicas were prepared from some samples and studied using a TEM.

Two TEM micrographs obtained in this way are presented in Fig. 6.26 and the particles that were analyzed by the EDX spectra are marked by arrows. The EDX analyses are presented in Fig. 6.27; these indicate that four kinds of precipitates are present in the Nb-48B steel after 3600 seconds of holding. These are Ti-rich, (Ti,Nb)-rich, Nb-rich and $M_{23}(C,B)_6$ particles. The Ti-rich precipitates are believed to be undissolved TiN. They usually have a cubic appearance and are of large size (as indicated by the arrow in Fig. 6.26(a)). The (Ti,Nb)-rich particles are formed by first precipitating TiN at high temperatures, and then trapping NbC on their surfaces and growing in this way. Their sizes covered a wide range. Nb-rich particles were also found in the samples and they were probably formed at relatively low temperatures (mostly during holding after the prestrain of 0.5). Their sizes range from 10 to 35 nm and so they are much smaller than the TiN particles. Intragranular and intergranular iron borocarbides were also found in the samples (as indicated by the arrows in Fig. 6.26(b)). These particles have sizes ranging from 0.1 to 1 μm.

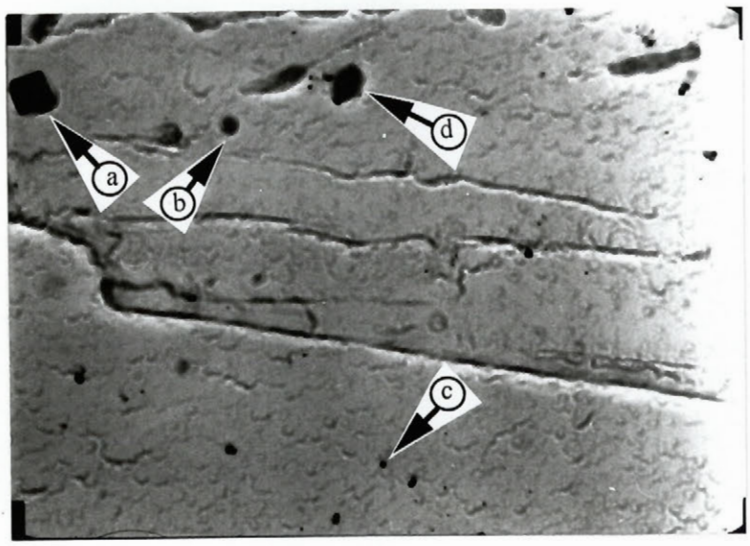

(a) x 19000

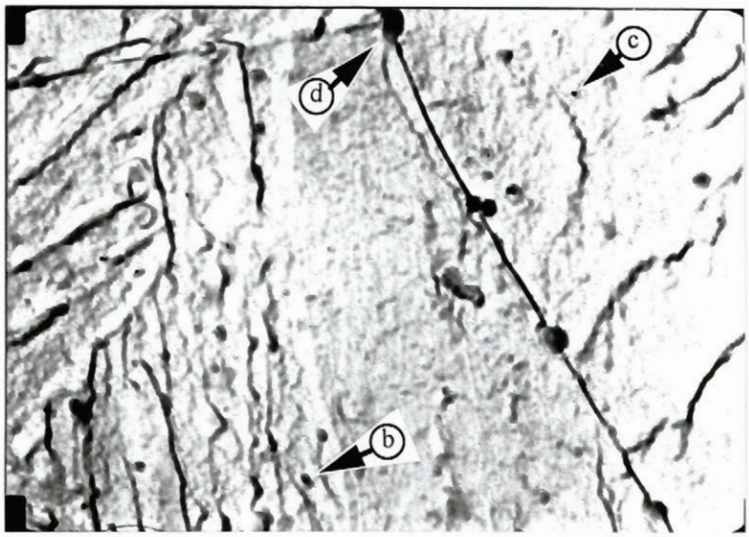

(b) x 14000

Fig. 6.26 Carbon extraction replicas showing the shapes and sizes of the precipitates observed in the Nb-48B steel after 3600 seconds of holding at 900 °C.

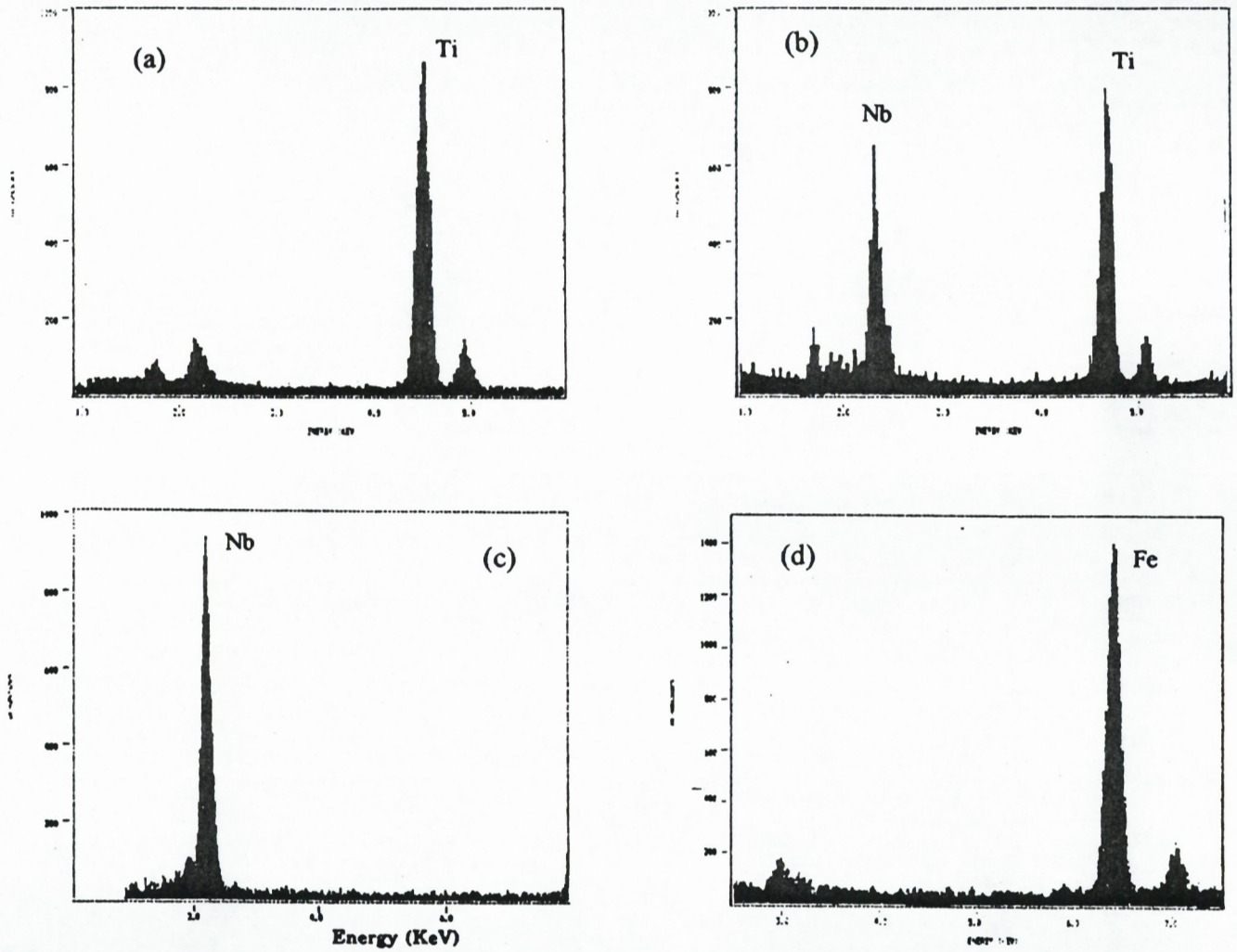

Fig. 6.27 X-ray spectra of the particles shown in Fig. 6.26; the following strong peaks can be seen: (a) Ti, (b) Nb, Ti, (c) Nb, (d) Fe.

6.1.1.5 Effect of Cooling Rate

Cooling rate has a major influence on the transformation behaviour and the final microstructure. Four cooling rates ranging from 0.25 °C/s to 3.5 °C/s were used in the present investigation, and the resulting stress-temperature curves for the Mo-Nb-B steel are shown in Fig. 6.28. It can be seen that the transformation temperature decreases as the cooling rate is increased. The measured A_{r3} and B_s temperatures for this steel are further illustrated in Fig. 6.29, and these decreased by about 75 °C when the cooling rate was increased from 0.25 °C/s to 3.5 °C/s.

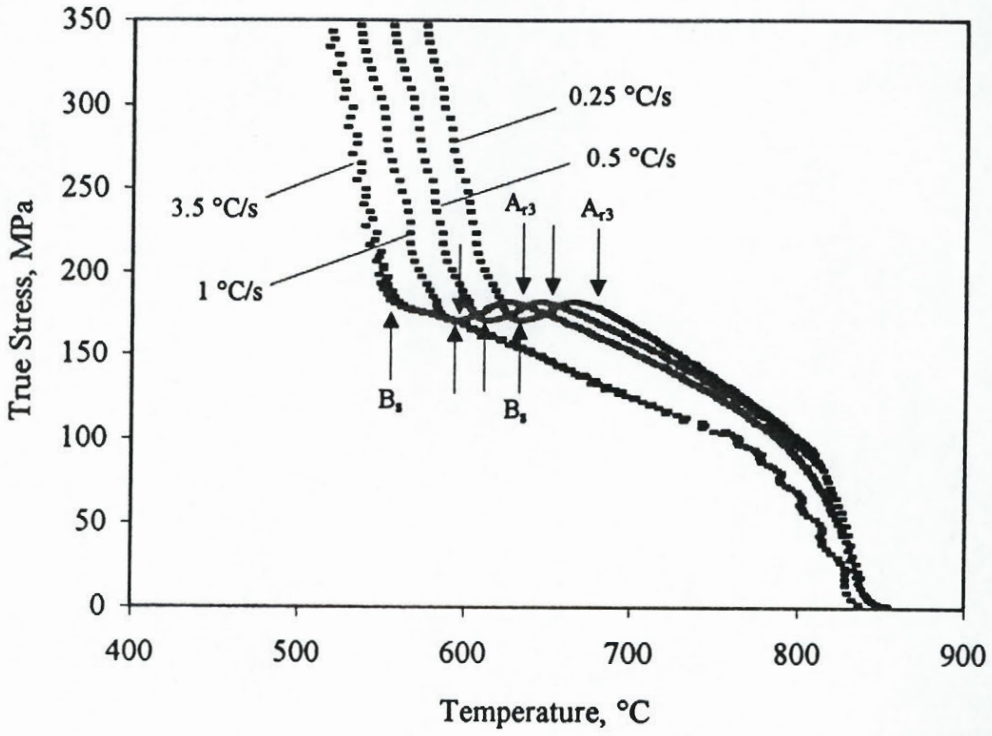

Fig. 6.28 Stress-temperature curves of the Mo-Nb-B steel tested at different cooling rates. The following strain rates were employed: $2x10^{-3}$/s (3.5 °C/s), $1x10^{-3}$/s (1 °C/s), $5x10^{-4}$/s (0.5 °C/s), $3x10^{-4}$/s (0.25 °C/s).

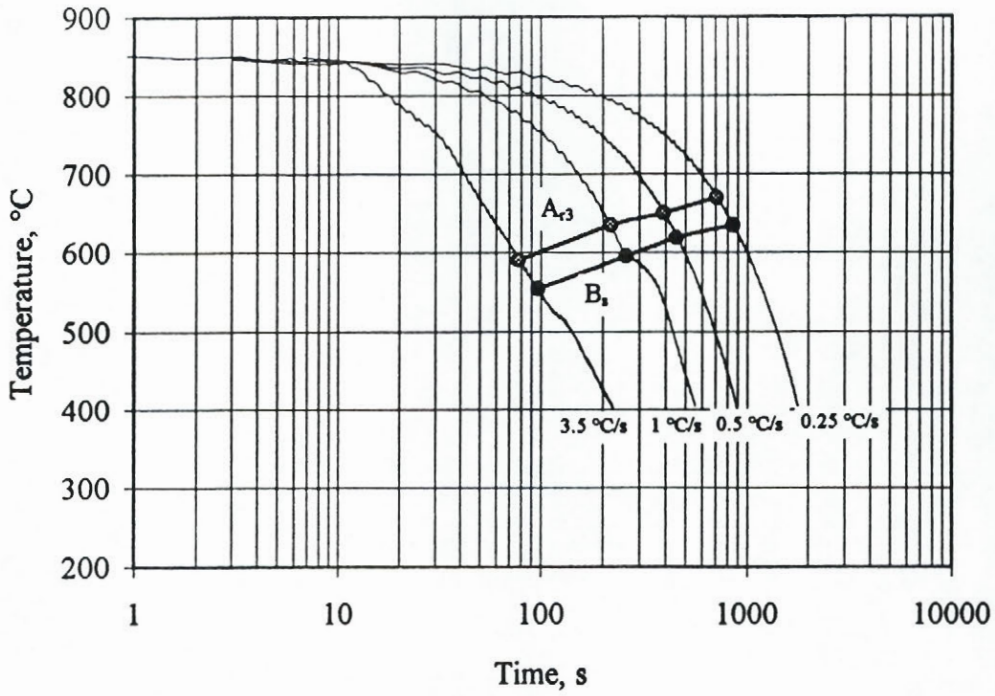

Fig. 6.29 CCT diagram of the Mo-Nb-B steel.

Two microstructures of the Mo-Nb-B steel resulting from cooling at 0.5 and 3.5 °C/s are presented in Fig. 6.30. At the higher cooling rate, the microstructure consists of low carbon bainite, which contains lath-like ferrite and fine intergranular M/A islands. At the lower cooling rate, the microstructure is composed of plate-like and lath-like ferrite and blocky M/A islands. The main difference between these two micrographs involves the sizes of the lath-like ferrite and the M/A constituent. The ferrite laths are narrower and longer at the higher cooling rate than at the lower cooling rate, and the M/A islands are more blocky shaped at the lower cooling rate.

The M/A trapped between the ferrite laths can be further revealed by using LePera's reagent. The solution was made by mixing 1 gram of sodium metabisulfite + 100 ml of water and 4 grams of picric acid + 100 ml ethanol. It reveals the ferrite as a light tan phase, and the retained austenite and martensite as bright white phases, as shown in Fig. 6.31. The thin foils were made from the 3.5 °C/s cooled samples, and the corresponding TEM micrograph is shown in Fig. 6.32. It can be seen that the lengths of the lath ferrite can attain 20 μm and the widths can be as narrow as 0.35 μm.

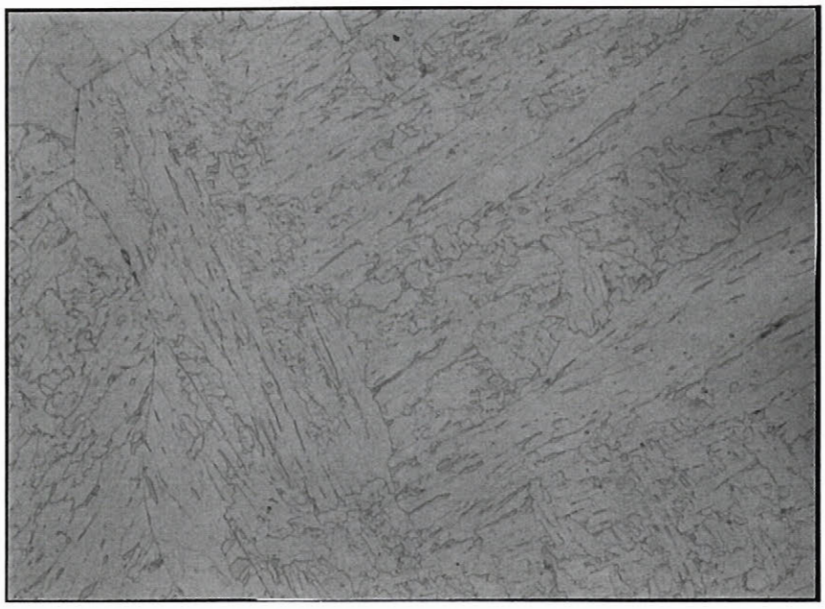

(a)

(b)

Fig. 6.30 Microstructures of the Mo-Nb-B steel cooled at (a) 3.5 °C/s and (b) 0.5 °C/s. x 630

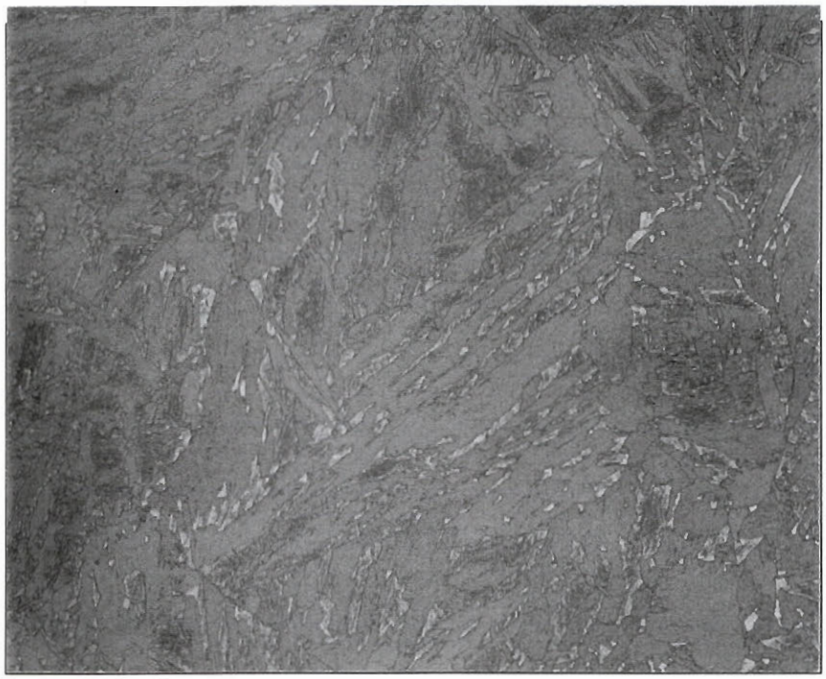

x 630

Fig. 6.31 Microstructure of the Mo-Nb-B steel continuously cooled to 450 °C at 1 °C/s and water quenched immediately. The sample was etched using LePera's reagent, and the white phase is the M/A constituent.

The combined effects of deformation and cooling rate on the microstructures in the Mo-Nb-B, Nb-15B and boron steels are illustrated in Figs. 6.33 through 6.37. In this set of tests, specimens were reheated at 1200 °C for 30 minutes, then cooled to 850 °C at a cooling rate of 1 °C/s. A strain ranging from 0.1 to 0.7 was applied at this temperature and followed by different cooling rates, which ranged from 0.1 °C/s to 50 °C/s. It can be seen that, in the Mo-Nb-B steel, the micrographs associated with smaller deformations and higher cooling rates contain low carbon bainite (see Fig. 6.33 (c) and (d) and Fig. 6.34 (c) and (d)). By contrast, the ones associated with large deformations and lower cooling rates display a mixture of fine grained polygonal ferrite and low carbon bainite (see Fig. 6.35 (a) and (b)). The lengths and widths of the lath-like ferrite vary with the deformation conditions; higher cooling rates produce fine bainite which contains very thin and long

x 19000

Fig. 6.32 TEM micrograph of the specimen cooled at 3.5 °C/s and shown in Fig. 6.30 (a).

lath-like ferrite, separated by linearly aligned small sized M/A particles (see Fig. 6.33(c)). Lower cooling rates result in coarse bainite, which contains shorter and wider lath-like ferrite and large sized needle-like or blocky M/A grains (see Fig. 6.33(a)). The linear alignment of the M/A constituent gradually disappears as the cooling rate is decreased and the appearance changes from needle-like to blocky.

The other obvious feature is that the prior austenite grain boundaries can be clearly seen, and several packets of lath-like ferrite with different orientations occupy individual austenite grains. The orientations of these packets are more aligned at higher cooling rates and more random at lower cooling rates. In some cases, a packet of lath-like ferrite forms at the prior austenite grain boundary, and grows in a particular direction across the grain. This feature is rarely seen in the γ-to-α transformation, but often seen in the γ-to-M transformation.

The microstructures of the Nb-15B steel that resulted from the same test schedule are presented in Fig. 6.36. It can be seen that, at a cooling rate of 1 °C/s, the transformation product is mainly polygonal ferrite. When the cooling rate is increased to 10 °C/s, the resulting microstructure is converted to a mixture of polygonal ferrite and bainite. The grain size of the polygonal ferrite decreases and the volume fraction of bainite increases as the cooling rate is increased. When the micrographs of this steel are compared with those of the Mo-Nb-B grade, less M/A islands are seen to be present and the lath sizes are coarser in the former case.

The microstructures of the boron steel are illustrated in Fig. 6.37. Coarse grained polygonal ferrite was produced at a cooling rate of 1 °C/s, and a small amount of pearlite (~10%) was also present (see Fig. 6.37(a)). When the cooling rate was increased, the shape of the ferrite changed from polygonal to plate-like (see Fig. 6.37(b)), and then to lath-like at still higher cooling rates (Fig. 6.37(c) and (d)). It should also be noted that the prior austenite grain boundaries are rounded, and therefore indicate that the microstructure was recrystallized at 850 °C after the application of a prestrain of 0.5. This is consistent with the T_{nr} results presented in Chapter 4 (the T_{nr} determined for this steel was about 830 °C).

The influence of the amount of deformation and cooling rate on the microstructure in the three steels is summarized in Fig. 6.38. It can be seen that the Mo-Nb-B steel is basically bainitic. At lower strains, a fully bainitic microstructure can be obtained.

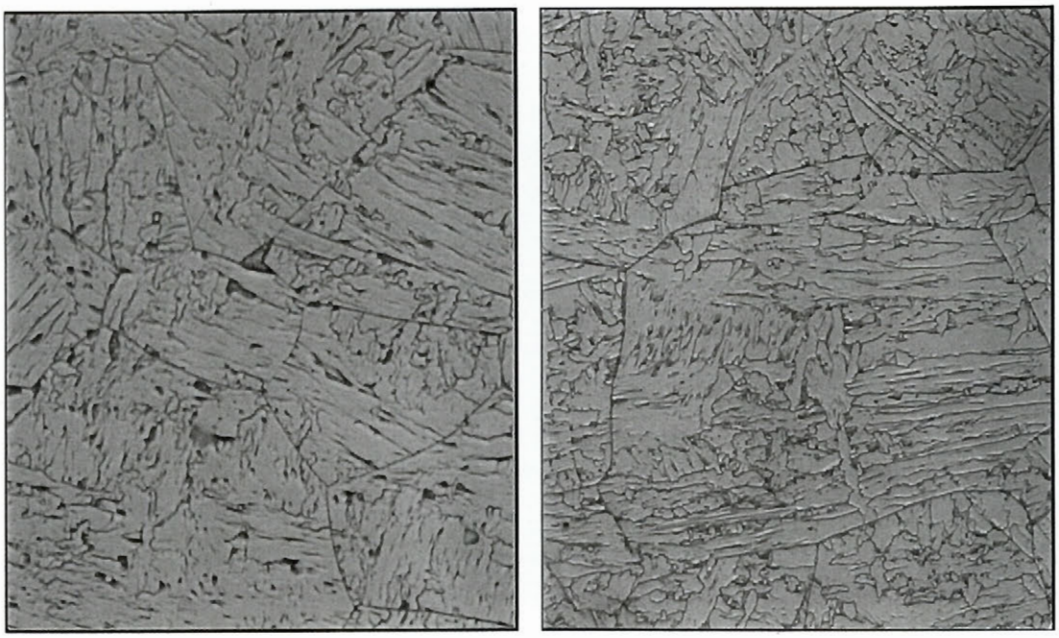

(a) (b)

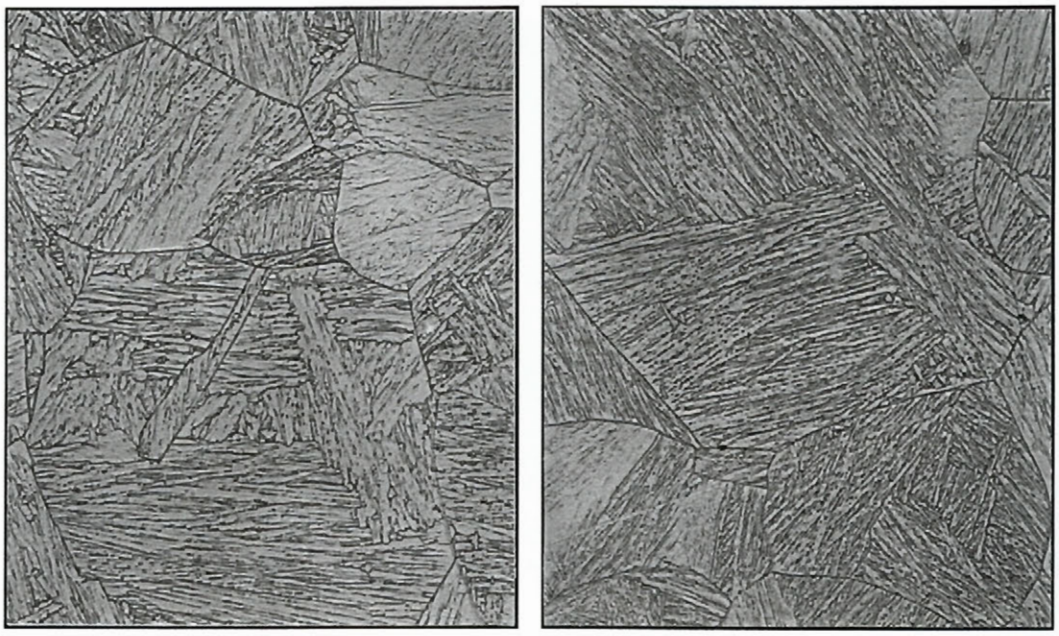

(c) (d)

Fig. 6.33 Microstructures of the Mo-Nb-B steel deformed to ε=0.1 at 850 °C and cooled at (a) 1 °C/s, (b) 10 °C/s, (c) 30 °C/s, (d) 50 °C/s. x 630

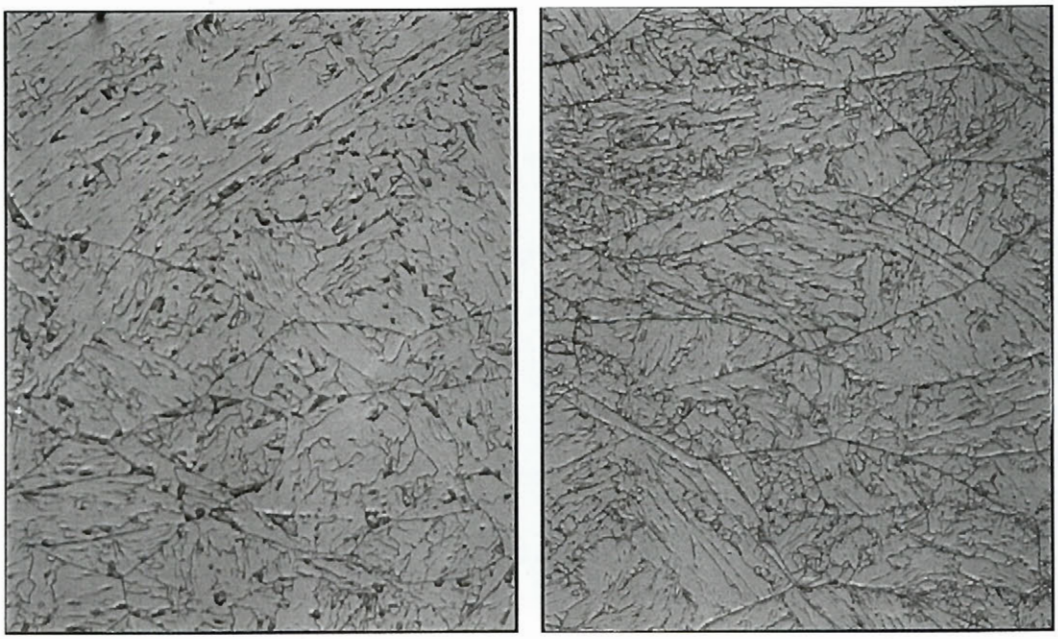

(a) (b)

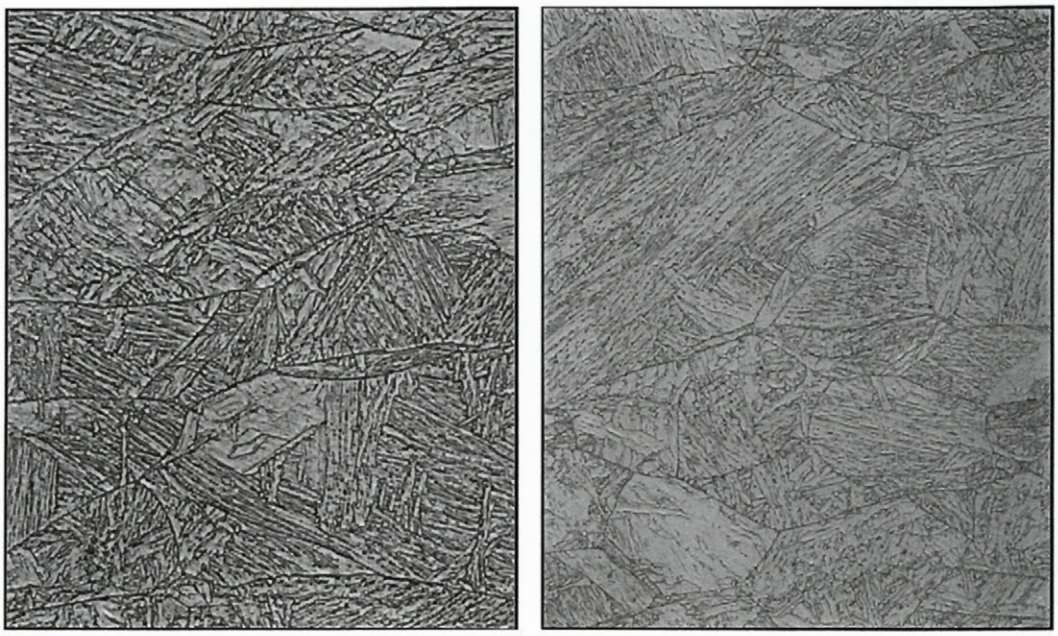

(c) (d)

Fig. 6.34 Microstructures of the Mo-Nb-B steel deformed to ε=0.3 at 850 °C and cooled at (a) 1 °C/s, (b) 10 °C/s, (c) 30 °C/s, (d) 50 °C/s. x 630

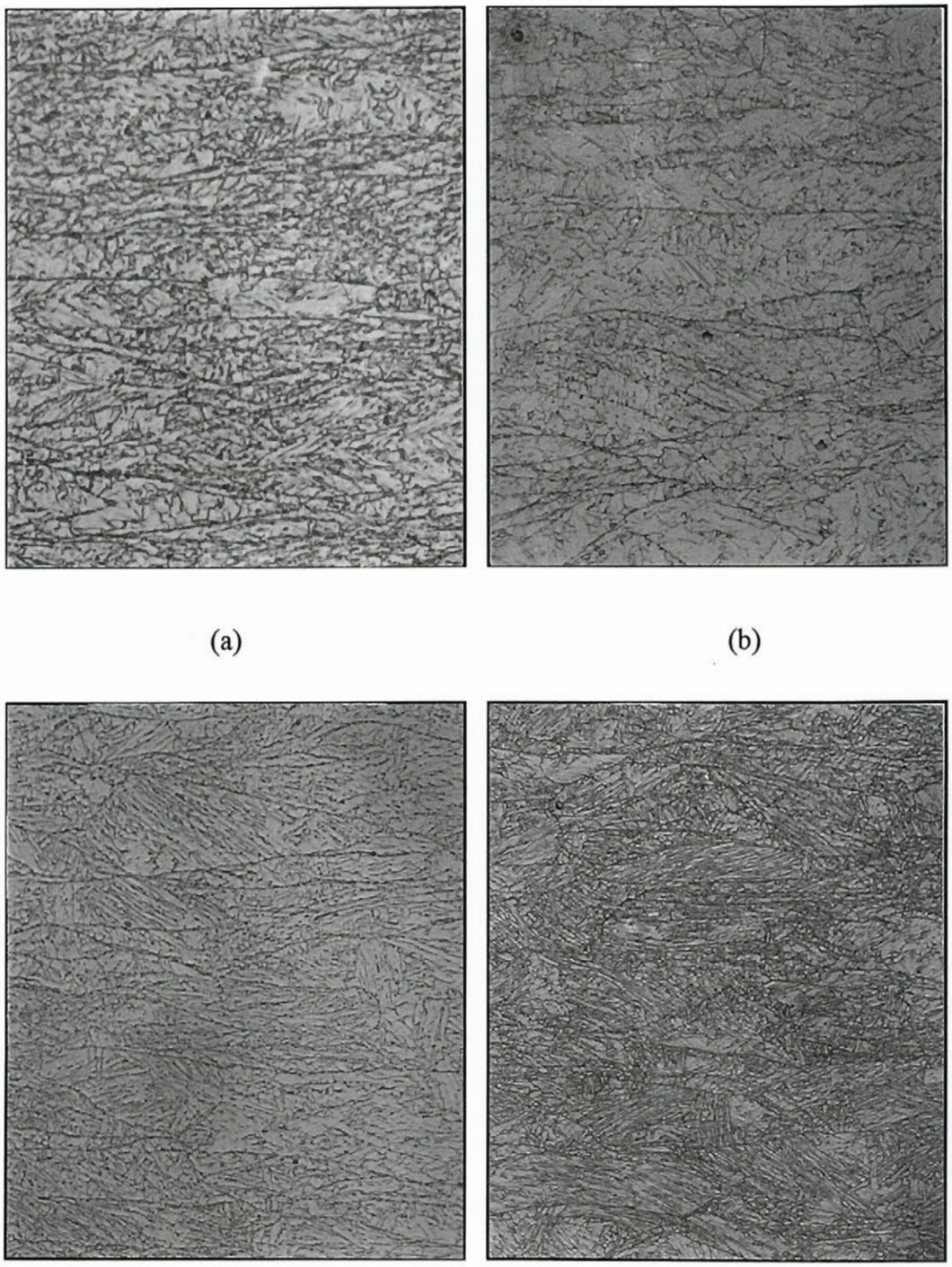

(a) (b)

(c) (d)

Fig. 6.35 Microstructures of the Mo-Nb-B steel deformed to ε=0.7 at 850 °C and cooled at (a) 1 °C/s, (b) 10 °C/s, (c) 30 °C/s, (d) 50 °C/s. x 630

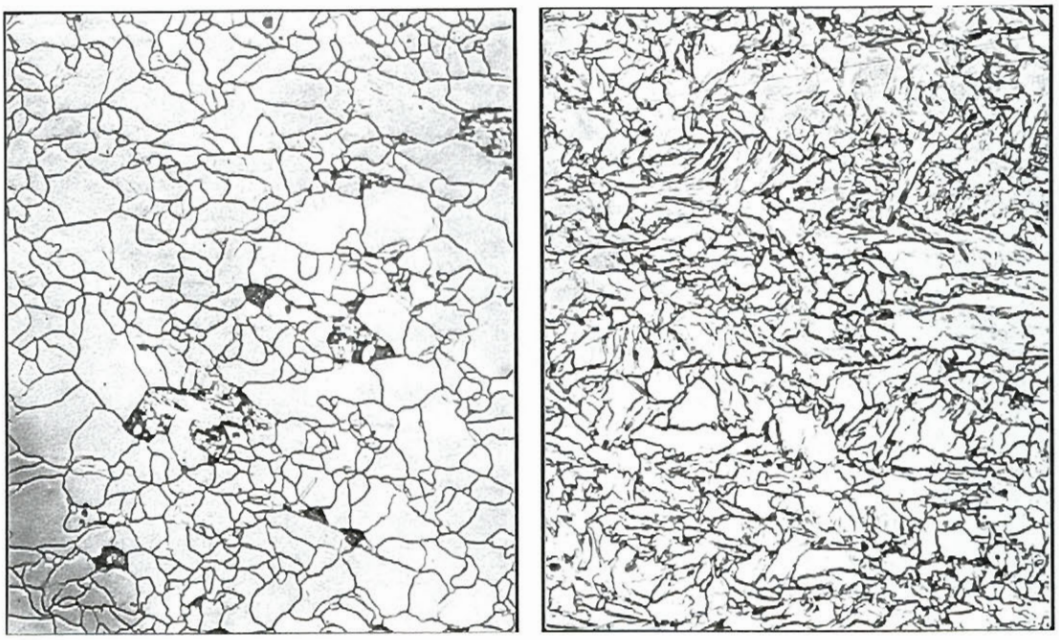

(a) (b)

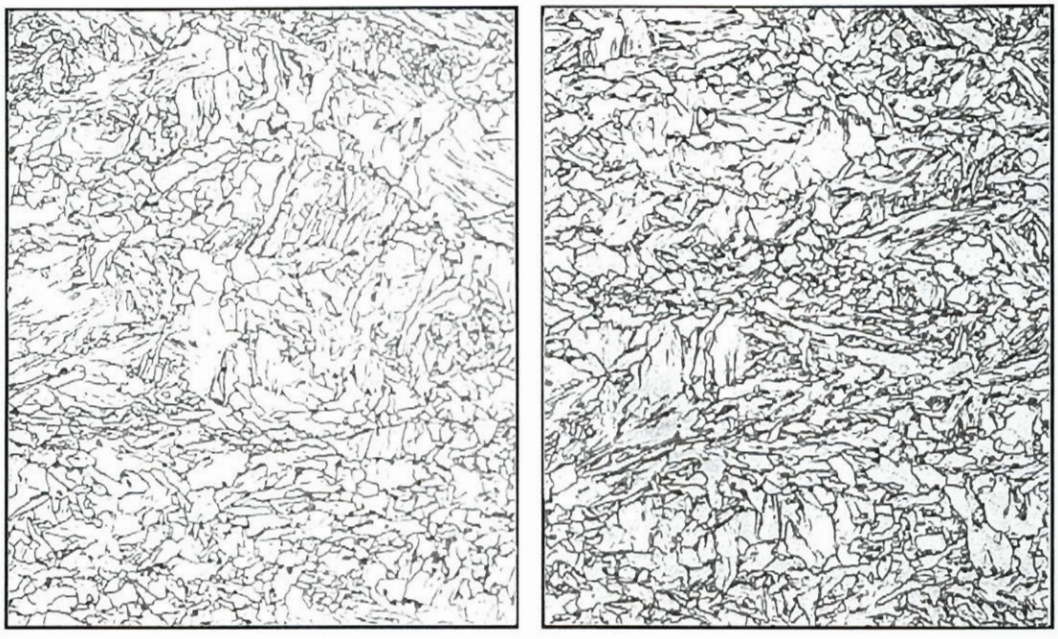

(c) (d)

Fig. 6.36 Microstructures of the Nb-15B steel deformed to ε=0.5 at 850 °C and cooled at (a) 1 °C/s, (b) 10 °C/s, (c) 30 °C/s, (d) 50 °C/s. x 630

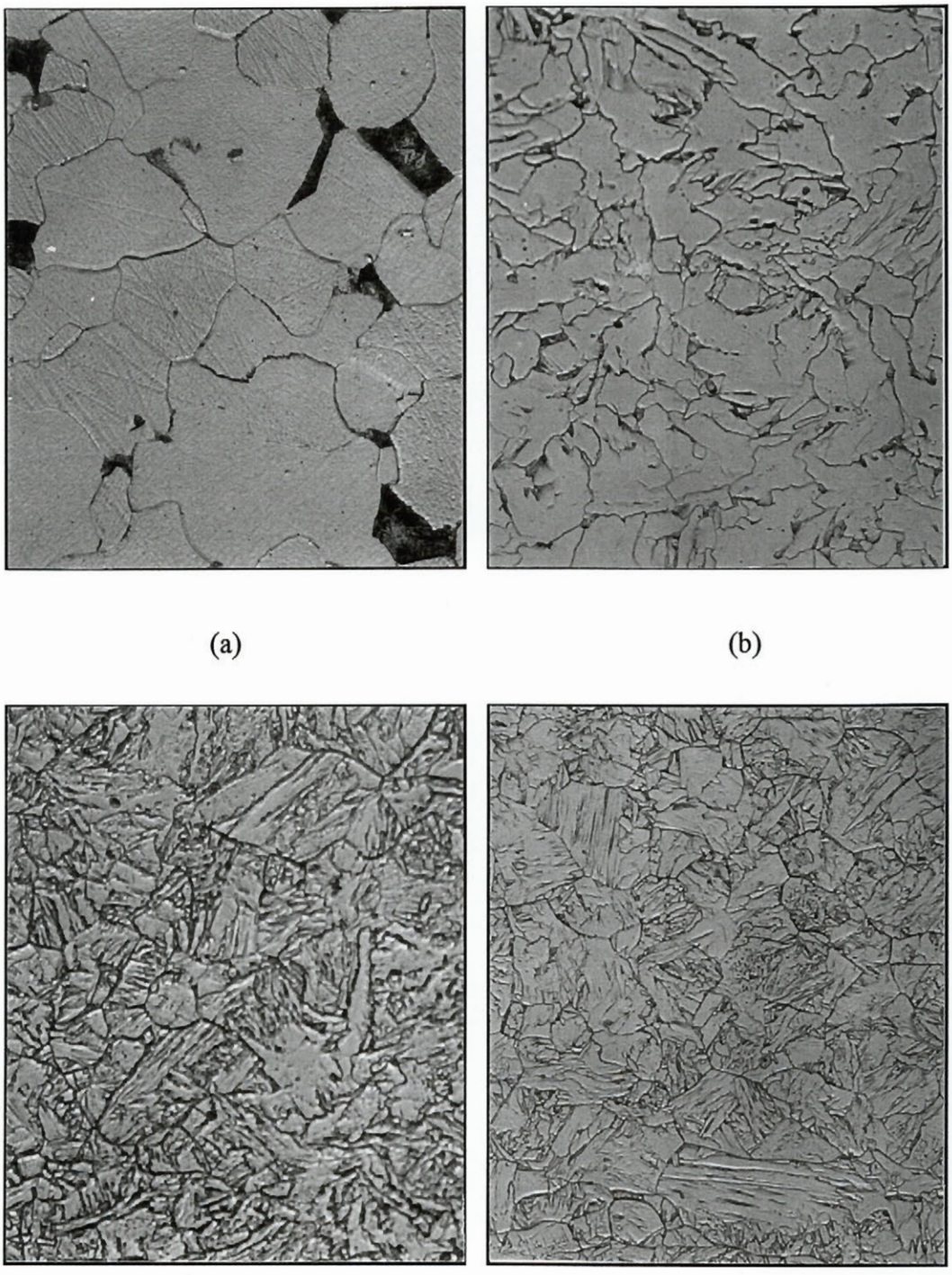

(a) (b)

(c) (d)

Fig. 6.37 Microstructures of the boron steel deformed to ε=0.5 at 850 °C and cooled at (a) 1 °C/s, (b) 10 °C/s, (c) 30 °C/s, (d) 50 °C/s. x 630

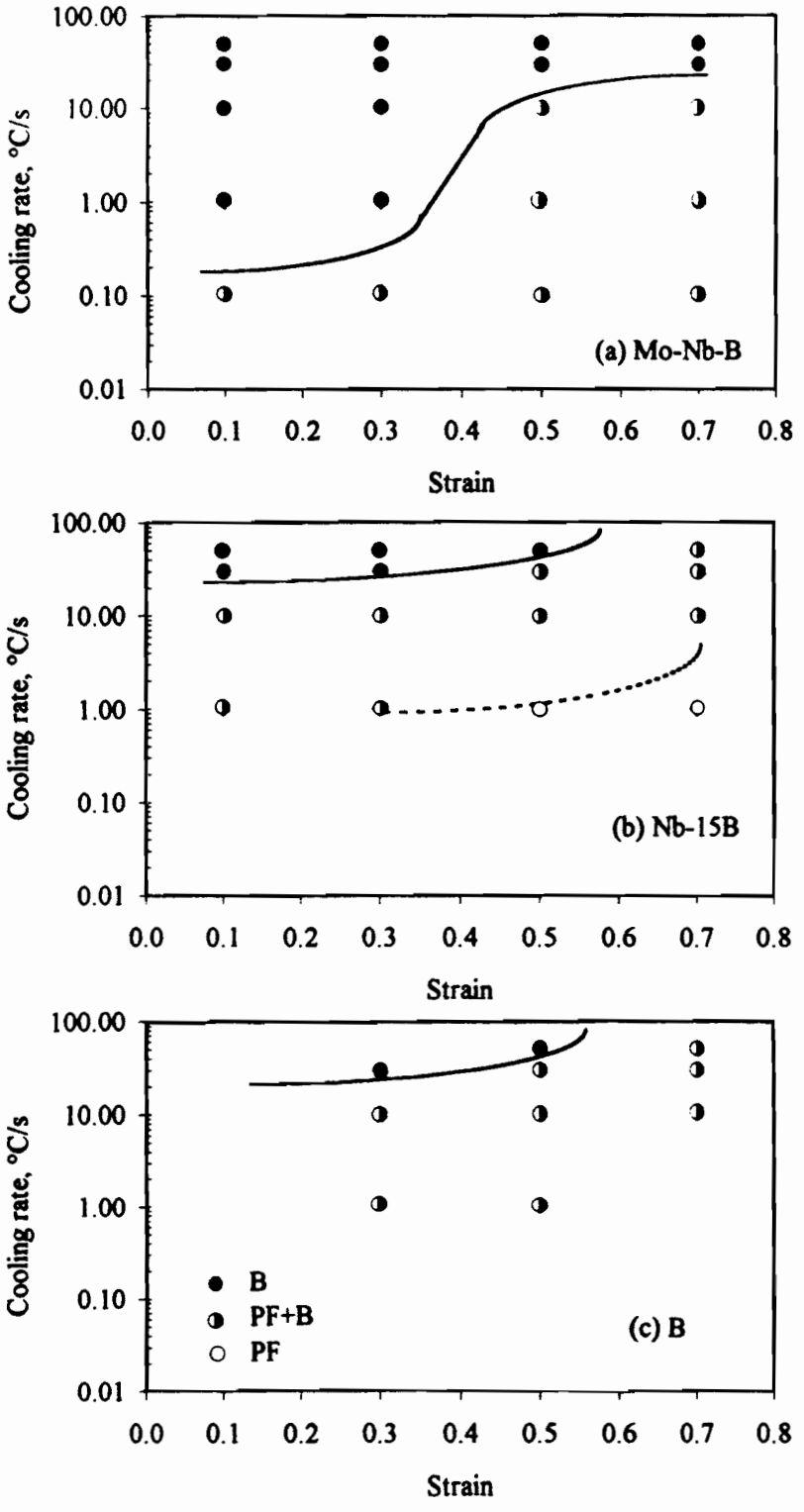

Fig. 6.38 Effect of austenite deformation on the minimum cooling rate for the avoidance of polygonal ferrite formation during continuous cooling of the (a) Mo-Nb-B, (b) Nb-15B, and (c) boron steels.

The minimum cooling rate required to avoid the formation of polygonal ferrite during continuous cooling increases with the amount of deformation. In order to obtain full bainite after hot rolling, cooling rates between 25 °C/s and 35 °C/s can be recommended for the plate rolling of the Mo-Nb-B material. For the Nb-15B steel, the transformation products after continuous cooling include both polygonal ferrite and bainite. For large deformations and low cooling rates, a fully polygonal ferrite microstructure is expected after transformation. In other words, a CCR schedule plus air cooling should produce a 50% polygonal ferrite + 50% bainite microstructure for this particular steel. In the case of the boron steel, mixed microstructures were obtained for most combinations of deformation and cooling rate.

6.1.2 Isothermal Transformation

In order to gather more information about the transformation behaviour of low carbon Nb and B treated steels, isothermal compression tests were carried out on the same MTS machine using a strain rate change testing program. A detailed description of the technique was presented in Chapter 3, and only the experimental results are presented in this subsection.

6.1.2.1 The Stress-Strain Curves

In this set of tests, specimens were cooled from the reheat temperature of 1200 °C to different test temperatures at a cooling rate of 1 °C/s. A prestrain of 0.1 was applied at a strain rate of 0.1 s^{-1}, after which the strain rate was reduced to $5x10^{-4}$ s^{-1} without unloading. The stress-strain curves generated from this kind of test on the base steel at four deformation temperatures are shown in Fig. 6.39.

The prestrain of 0.1 raised the flow stress to a certain level that was mainly a function of the deformation temperature. After the strain rate decrease, the stress dropped abruptly due to the sudden decrease in the Z parameter. Following the strain rate change, the flow stress continued to rise with further straining due to work hardening. Then the flow stress dropped again if either dynamic recrystallization or the γ-to-α transformation took place. Because of their importance, only the low strain rate parts of the flow curves are considered in the following analysis. As shown by the 850 °C flow curve in Fig. 6.39, the flow stress continued to increase with strain until ε= 0.31, which corresponds to a deformation time of 420 seconds; then it started to drop on further straining. When the deformation temperature was decreased to 800 °C, the flow stress started to drop at a much lower strain (ε=0.11), which corresponds to a deformation time of 20 seconds.

Furthermore, when the deformation temperature was decreased to 770 °C (which is close to the transformation temperature determined from the CCC test) or 720 °C (which is lower than the A_{r3}), the flow stress dropped dramatically after a small rise (which was over a strain of less than 0.001). This drop in flow stress is associated with the γ-to-α transformation since the peak strains are too small for the initiation of dynamic recrystallization. Thus the times required for initiation of the γ-to-α transformation at the above temperatures (850 °C, 800 °C, 770 °C and 720 °C) were determined in this way as 420, 20, 2 and 0.6 seconds, respectively. Similarly, the times at which the γ-to-α transformation was finished were determined from the strains at which the flow stress dropped to a minimum. These turned out to be 8, 36 and 120 seconds for deformation temperatures of 720 °C, 770 °C and 800 °C, respectively.

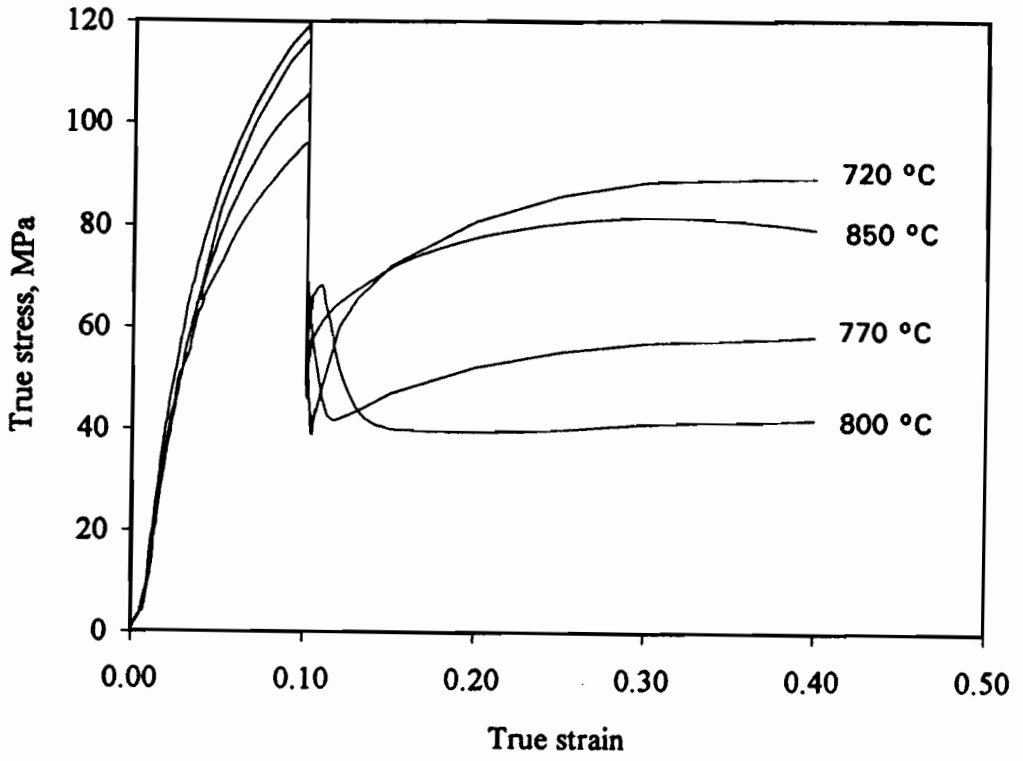

Fig. 6.39 Stress-strain curves of the base steel tested at $\dot{\varepsilon}_1 = 0.1 s^{-1}$ and $\dot{\varepsilon}_2 = 5 \times 10^{-4} s^{-1}$.

The other interesting phenomenon that can be observed on these flow curves is that the work hardening rate in the ferrite depends on the deformation temperature. At 800 °C, after the transformation was finished, the flow stress remained constant on further straining. This is because dynamic recovery at this temperature is very rapid and balances

the work hardening of the ferrite. When the temperature was decreased to 770 °C, the rate of dynamic recovery was decreased; thus work hardening could no longer be offset by dynamic recovery, resulting in an increase in the flow stress. This is still more pronounced at 720 °C because of the further decrease in the ease of dynamic recovery.

The stress-strain curves for the Mo-Nb-B steel are presented in Fig. 6.40. It can be seen that the flow behaviour of this steel differs considerably from that of the base material. The temperatures of 750 °C and 700 °C are well above the transformation temperatures determined by the CCC test (A_{r3} and B_s are 630 °C and 595 °C for this steel); the curves therefore indicate that the austenite is work hardening continuously. At temperatures of 620, 650 and 670 °C, the flow curves display an S-shaped appearance. At 670 °C, the stress initially increased at the same rate as at 700 °C, but then underwent a change to a higher rate when the strain exceeded 0.16, which corresponds to a deformation time of 120 seconds. The flow curve then returned to the 700 °C behaviour when the deformation time exceeded 520 seconds. Defining the first and the second

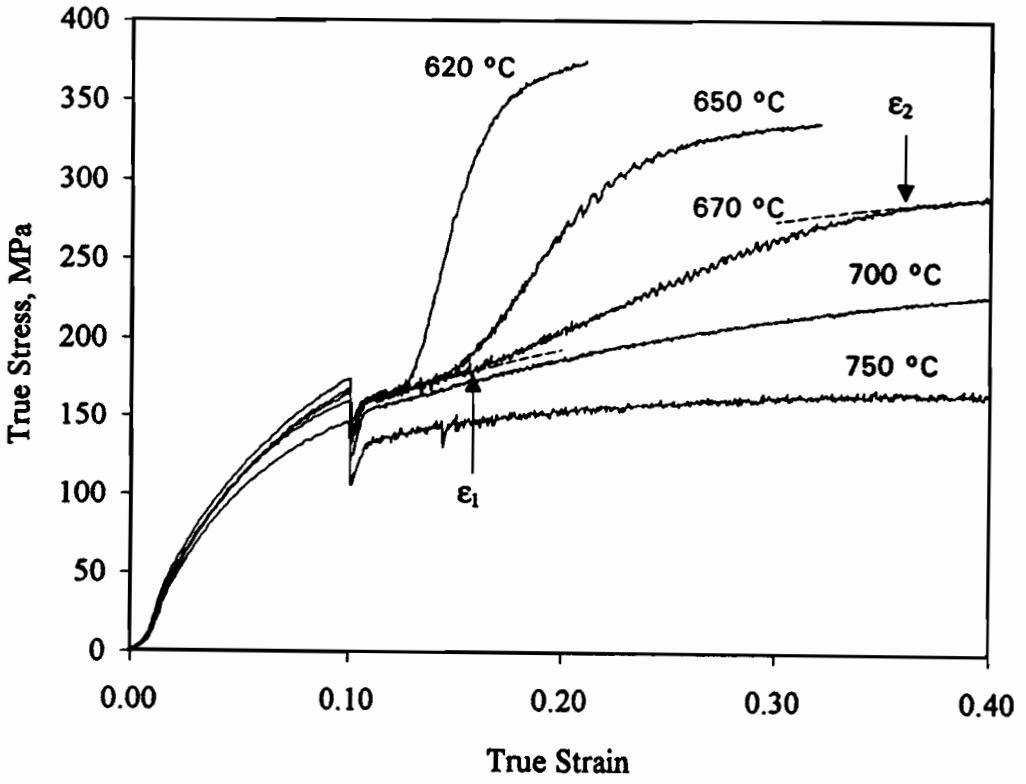

Fig. 6.40 Stress-strain curves of the Mo-Nb-B steel tested at $\dot{\varepsilon}_1 = 0.1 s^{-1}$ and $\dot{\varepsilon}_2 = 5 \times 10^{-4} s^{-1}$.

strains as ε_1 and ε_2 (as indicated on the 670 °C curve), the corresponding deformation times can be referred to as t_s and t_f. The measured t_s and t_f times that correspond to the three temperatures are presented in Table 6.1.

Table 6.1 Measured t_s and t_f times for the Mo-Nb-B steel

T, °C	ε_1	t_s, s	ε_2	t_f, s
620	0.12	40	0.21	220
650	0.14	80	0.29	380
670	0.16	120	0.36	520

The sharp increase in flow stress between ε_1 and ε_2 can be attributed to two alternative causes: i) the austenite transforming to a harder phase, ii) strengthening as a result of NbC precipitation. A more detailed discussion will be presented later, and here the phenomenon will simply be associated with transformation to a harder phase, i.e. to bainite. Thus the t_s and t_f in Table 6.1 can be termed the start and finish transformation times. By contrast, the flow stress *decreases* instead of increases during transformation of the base steel.

It should be noted that the initial parts of the flow curves at 620, 650 and 670 °C display nearly the same stress levels, and that these are close to that of the 700 °C flow curve. This suggests that a small amount of the softer phase (e.g. plate-like ferrite) has been introduced during cooling or after prestraining; the lower rate of flow stress increase could simply indicate that a mixture of ferrite and austenite has a lower work hardening rate.

Another interesting phenomenon involves the serrations on the flow curves at 670 °C and 650 °C; a closer look at the serrations is presented in Fig. 6.41. These irregularities are not considered to consist of test noise since they display typical shapes and have similar magnitudes and frequencies. They could be related to several distinct metallurgical phenomena, such as dynamic strain aging, the formation of strain-induced martensite or bainite, and mechanical twinning. These mechanisms will be discussed in more detail in a later subsection.

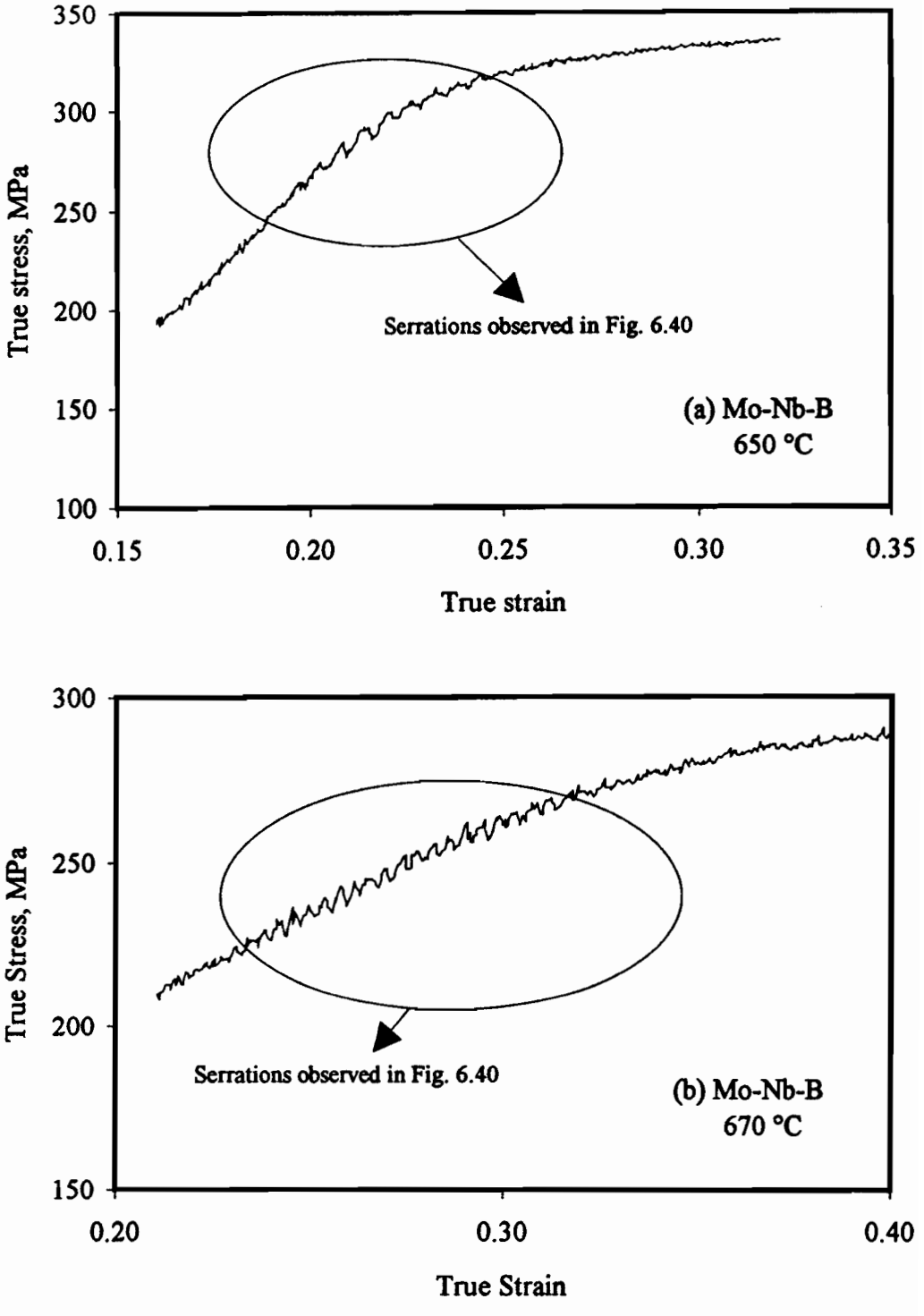

Fig. 6.41 A closer look at the serrations on the flow curves of Fig. 6.40.

The stress-strain curves of the Mo-B steel are presented in Fig. 6.42. The A_{r3} and B_s temperatures determined by CCC testing are 635 °C and 595 °C in this case. The deformation temperature of 700 °C is therefore well above the upper transformation temperature, so that the flow stress increase indicates that the austenite is undergoing work hardening. The shapes of the flow curves at 630, 650 and 670 °C are similar, and the corresponding t_s and t_f times are shown in Table 6.2.

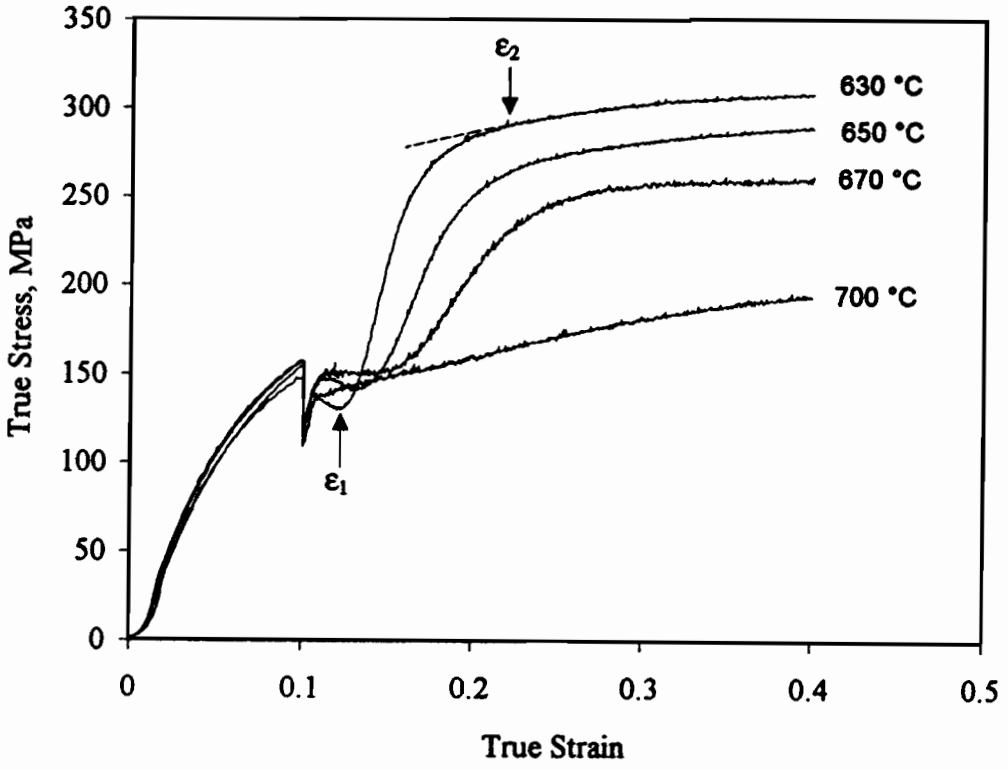

Fig. 6.42 Stress-strain curves of the Mo-B steel tested at $\dot{\varepsilon}_1 = 0.1 s^{-1}$ and $\dot{\varepsilon}_2 = 5 \times 10^{-4} s^{-1}$.

Table 6.2 Measured t_s and t_f times for the Mo-B steel

T, °C	ε_1	t_s, s	ε_2	t_f, s
630	0.12	40	0.22	240
650	0.135	70	0.25	300
670	0.15	100	0.27	340

In the initial stages of the flow curves determined *after* the strain rate change, the flow stresses decrease slightly until ε_1 is reached (as indicated on the 630 °C curve). This is probably due to the formation of plate-like ferrite during straining. It should be noted that the flow stress at 630 °C is less than at 700 °C in the strain range 0.11 to 0.13, indicating the formation of ferrite. The dramatic increase in the flow stress between ε_1 and ε_2 is related to the formation of bainite, since there is no significant strengthening by precipitation in this steel. The transformation behaviour displayed by this grade is similar to that of the Mo-Nb-B steel, which indicates that the γ-to-B transformation is of major importance in this material.

The stress-strain curves determined on the Nb-15B steel are presented in Fig. 6.43. The transformation temperatures determined by the CCC tests for this grade are 740 °C (A_{r3}) and 610 °C (B_s). The austenite-to-polygonal ferrite transformation dominates in this steel, as indicated in Fig. 6.11. At 810 °C, the stress increased continuously with strain until ε=0.14, then decreased gradually with further straining. The flow curve at this temperature displays a peak, and the γ-to-α transformation is considered to start at the peak strain. It can be seen that the peak shifts to the left with decreasing deformation temperature. This suggests that the time required for the initiation of the γ-to-α transformation decreases with decreasing deformation temperature.

As mentioned above, the transformation in the Nb-15B steel is mainly of the γ-to-α type, so that it should become faster at lower temperatures. The flow curves at 750 °C and 710 °C, however, reflect the occurrence of a relatively slow transformation; the flow stresses decreased slightly over a small strain range, then increased slowly on further straining. When the strain reached 0.2, the stresses started to decrease again, but slowly compared to the tests at 810 °C and 780 °C. The sluggish transformation phenomenon at 750 °C and 710 °C will be discussed in more detail later.

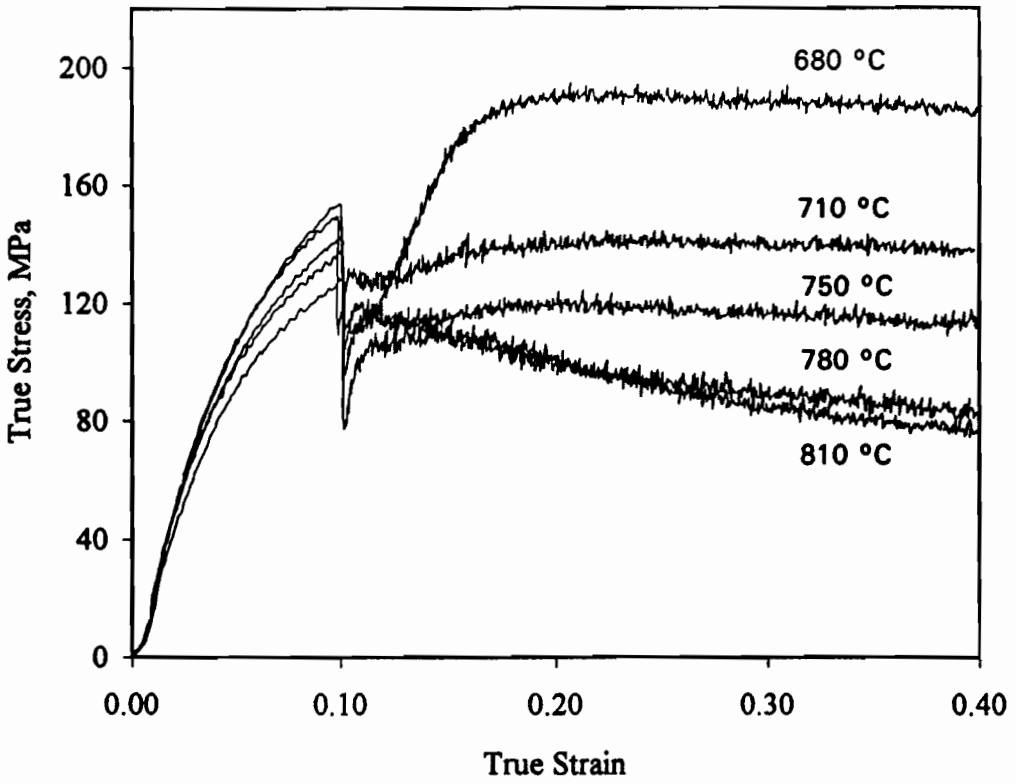

Fig. 6.43 Stress-strain curves determined on the Nb-15B steel tested at $\dot{\varepsilon}_1 = 0.1 s^{-1}$ and $\dot{\varepsilon}_2 = 5 \times 10^{-4} s^{-1}$.

A similar phenomenon is also displayed by the flow curves of the Nb-64B steel shown in Fig. 6.44. At 800 °C, the flow curve peak suggests that the γ-to-α transformation was initiated at ε=0.13. The flat flow curve at 750 °C indicates that transformation is slow at this temperature. Dramatic increases in the flow stress at 700 °C and 660 °C could be caused by precipitation strengthening of the ferrite. This is not related to the austenite-to-bainite transformation, as the γ-to-α transformation is considered to be of primary importance in this steel. This will be demonstrated later when the metallographic results are presented.

In the case of the 900 °C reheat temperature tests, specimens were cooled to the temperatures of interest and deformed according to the same testing program as was used for the 1200 °C reheat experiments. The flow curves generated from these tests are

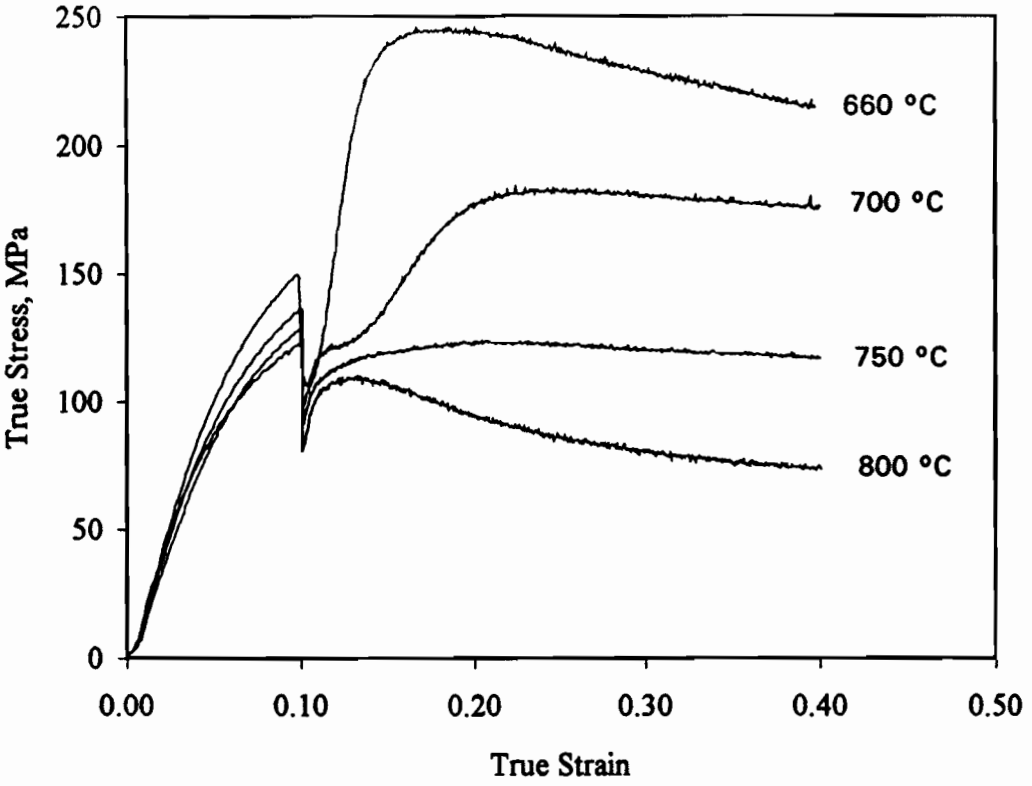

Fig. 6.44 Stress-strain curves determined on the Nb-64B steel tested at $\dot{\varepsilon}_1 = 0.1s^{-1}$ and $\dot{\varepsilon}_2 = 5\times10^{-4}\,s^{-1}$.

presented in Fig. 6.45 for four steels. The deformation temperatures in these cases were chosen to be close to the A_{r3}'s of the steels. It can be seen that the γ-to-α transformation took place in the Nb-15B and Nb-64B steels. At the selected temperatures, dynamic recovery was fast enough to balance the work hardening taking place in these two steels, so that the stress was maintained at low levels. By contrast, for the Nb-48B steel, there is a first peak at ε=0.105, and a second at ε=0.2. The first is related to the start of the γ-to-α transformation, while the second may be associated with precipitate coarsening or dynamic recrystallization of the ferrite. The Mo-Nb-B steel displays similar behaviour, but at a higher stress level and without a second flow curve peak. The higher and continuously increasing flow stress in this steel may also indicate that the transformation is mixed, i.e. that it includes both γ-to-α and γ-to-B components.

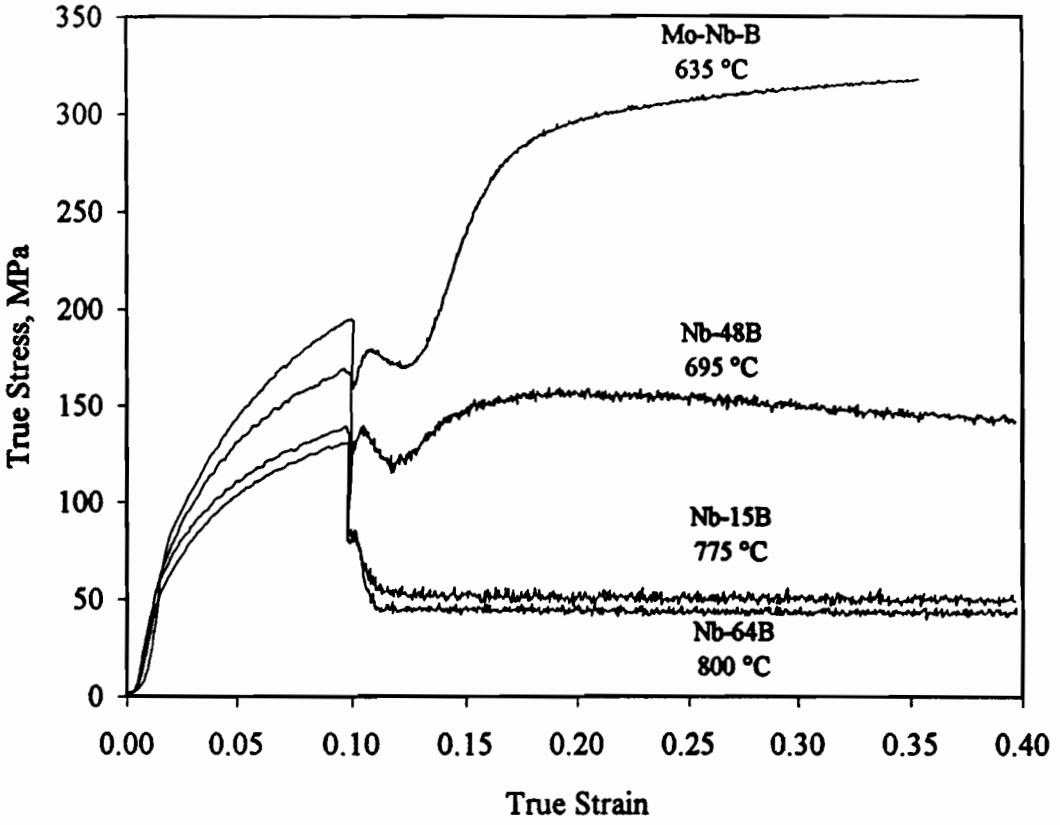

Fig. 6.45 Stress-strain curves determined on the Mo-Nb-B, Nb-15B, Nb-48B, and Nb-64B steels reheated at 900 °C and deformed at $\dot{\varepsilon}_1 = 0.1 s^{-1}$ and $\dot{\varepsilon}_2 = 5 \times 10^{-4} s^{-1}$.

6.1.2.2 Metallographic Observations

In order to reveal the transformation behaviour of the Mo-Nb-B, Nb-15B and Nb-64B steels, several specimens were water quenched after holding intervals of 5, 30, 300 and 600 seconds at several temperatures of interest. The resulting microstructures are illustrated in Figs. 6.46 through 6.48.

The microstructures of the Mo-Nb-B steel quenched at 620 °C (see Fig. 6.46) are typical of a γ-to-B type transformation. Plate-like and lath-like ferrite can be seen to have formed at the prior austenite grain boundaries; it then grew into the austenite grains. Retained austenite or martensite was trapped between the ferrite laths. Transformation in this steel is fairly slow at this temperature, and only about 75% of the austenite has transformed to bainite after 600 seconds of holding. The prior austenite grain boundaries can be seen clearly.

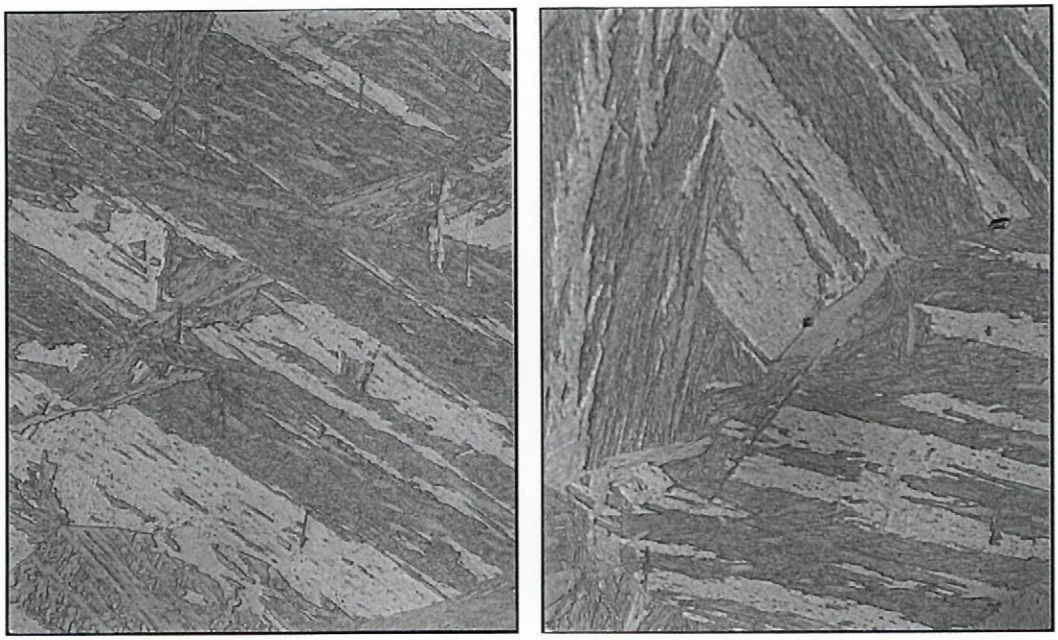

(a) (b)

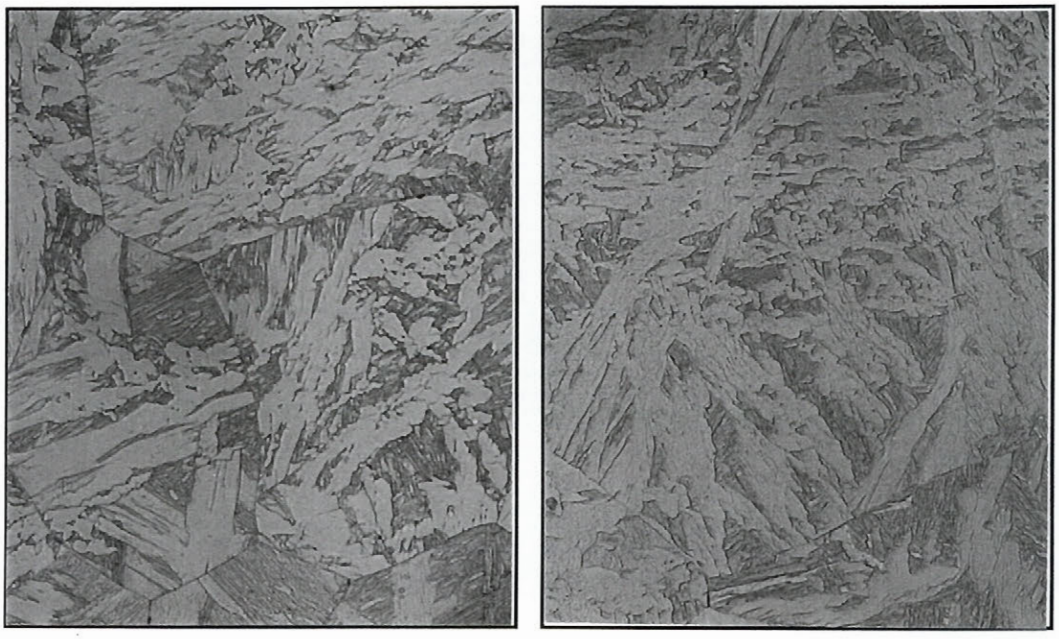

(c) (d)

Fig. 6.46 Microstructural evolution in undeformed samples of the Mo-Nb-B steel held at 620 °C for (a) 5 s, (b) 30 s, (c) 300 s, (d) 600 s. x 630

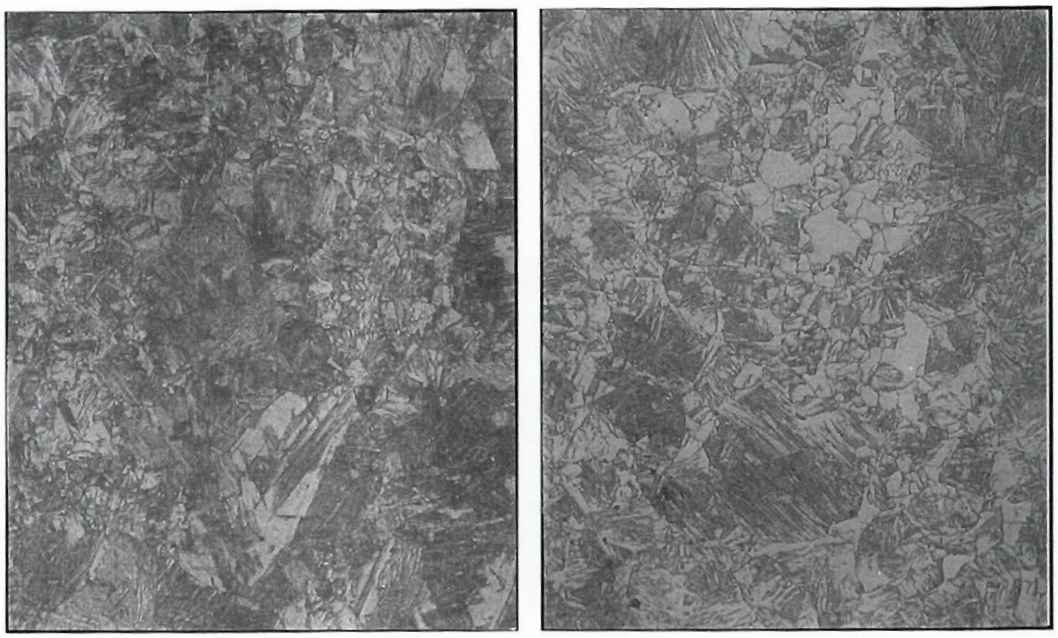

(a) (b)

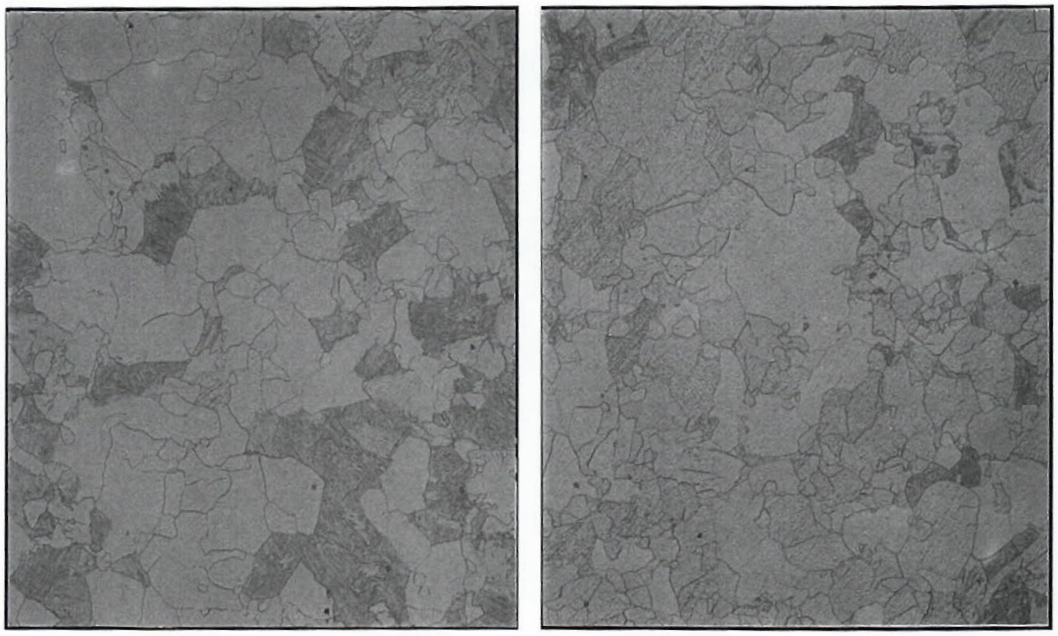

(c) (d)

Fig. 6.47 Microstructural evolution in undeformed samples of the Nb-15B steel held at 700 °C for (a) 5 s, (b) 30 s, (c) 300 s, (d) 600 s. x 250

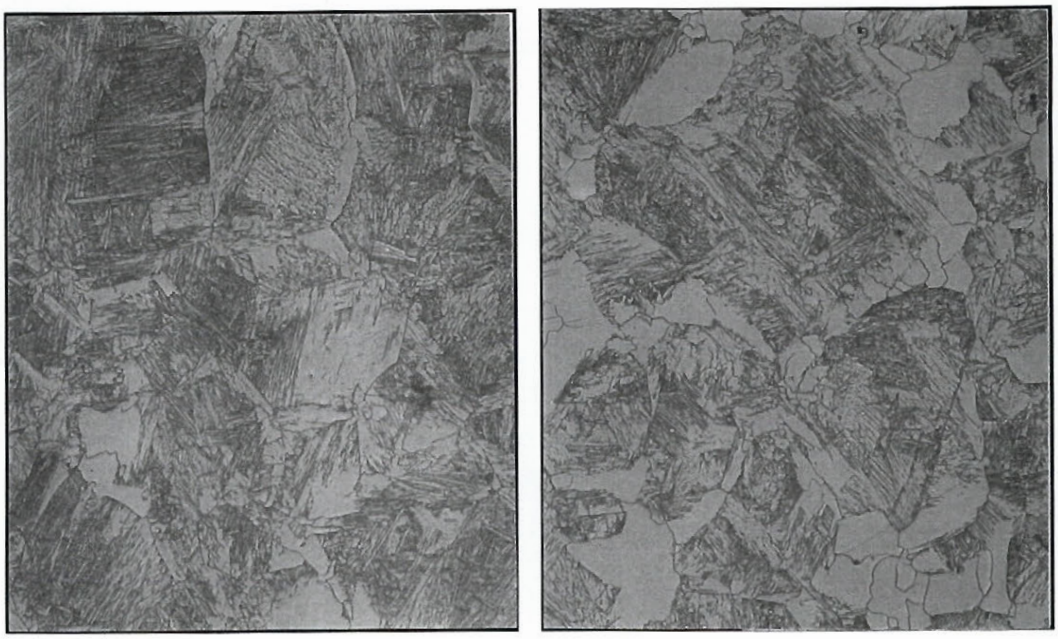

(a) (b)

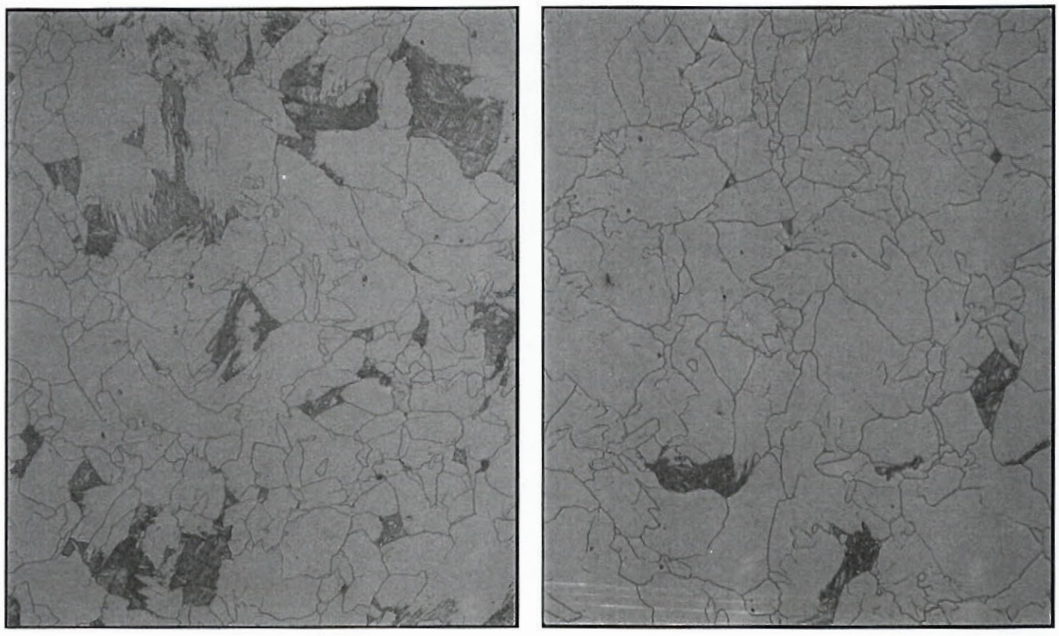

(c) (d)

Fig. 6.48 Microstructural evolution in undeformed samples of the Nb-64B steel held at 660 °C for (a) 5 s, (b) 30 s, (c) 300 s, (d) 600 s. x 250.

By contrast, the transformation products in the Nb-15B and Nb-64B steels are mainly polygonal ferrite. Transformation started at the austenite grain boundaries as before, and progressed by growing into the grains. The rate of transformation in the Nb-64B steel (Fig. 6.47) is faster than that in the Nb-15B steel (Fig. 6.48), while the transformations in both steels are quicker than in the Mo-Nb-B steel. The prior austenite grain boundaries in the former steels could not be revealed by using the same etchant because the austenite grain boundaries were totally covered by ferrite.

6.2 Discussion

The overall aim of this part of the investigation was to clarify the transformation behaviour of Mo-Nb-B, Nb-B and Mo-B steels, and in particular to elucidate the role played by boron in the transformation. The main objective of this chapter is therefore to respond to the following questions:

(1) Does the γ-to-B transformation take place in the present low carbon microalloyed steels?
(2) In what form is boron present during hot deformation and what sort of role does it play in the γ-to-α or γ-to-B transformation?
(3) If the answer to the first question is positive, then what is the mechanism of bainite transformation in the low carbon microalloyed steels employed in this study?

Some appropriate answers to the above questions are presented below, based on the experimental observations made in this investigation.

6.2.1 Does the γ-to-B Transformation Take Place in the Present Low Carbon Microalloyed Steels?

There remain many disagreements concerning some aspects of the mechanism of formation of bainite. Nevertheless, the principal features of bainite microstructures were recognized by Habraken and Economopoulos[22] and Pickering[6] in alloyed low carbon steels, and more recently, by Ohtani et al.[17] and Yun et al.[262] in ultralow carbon Nb-B steels. The carbon levels in the grades studied by these authors were as low as 0.02~0.04 wt%; these are similar to the carbon concentrations pertinent to this study. Most of the above investigations were concerned with the microstructures and hardnesses, and with constructing the transformation diagrams using dilatometric tests. In the present

investigation, both high temperature mechanical tests (CCC and IT) and metallographic examinations were performed, so that more information concerning the transformation behaviour was obtained. To clarify whether or not the γ-to-B transformation took place in the present steels, it is important to single out the factor responsible for the abrupt changes appearing on the CCC and IT flow curves.

6.2.1.1 Analysis of the CCC Flow Curves

The candidate mechanisms responsible for the abrupt increase in flow stress during the CCC tests are the following: (1) precipitation hardening, (2) the γ-to-B transformation, (3) a combined effect of (1) and (2). In order to analyse this phenomenon, some of the present stress-temperature curves are replotted in Fig. 6.49. The equivalent curve for a ferritic stainless steel taken from the work of Moses et al.[263] is superimposed on this figure for comparison purposes.

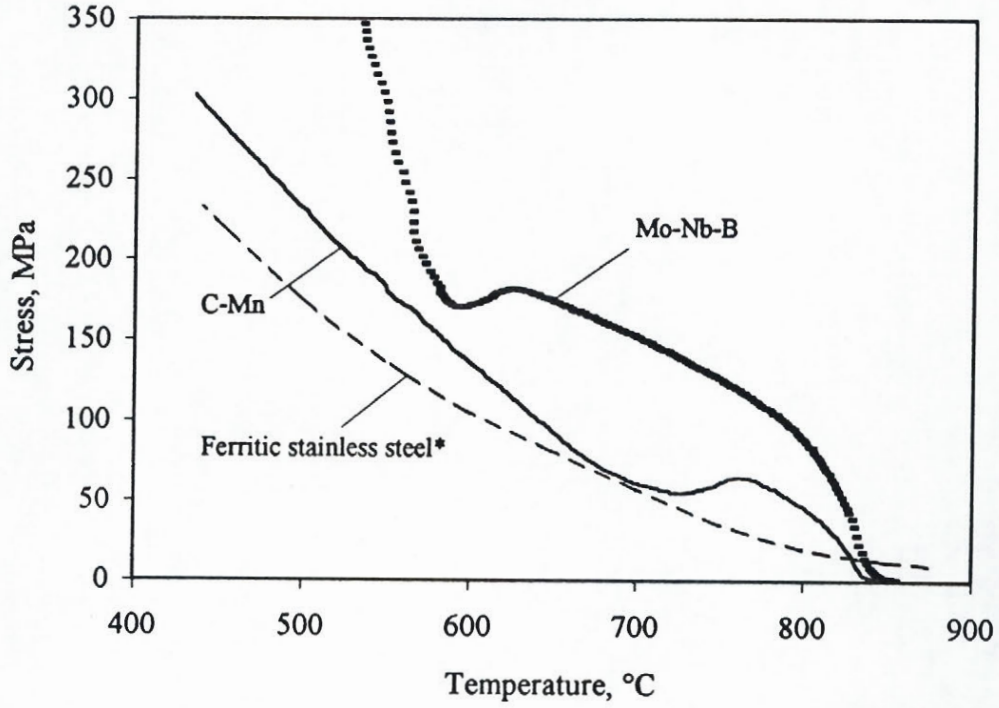

Fig. 6.49 A comparison of the stress-temperature curves determined on three different steels. The broken line shows the behaviour of a Ti-stabilized ferritic stainless steel[263].

It can be seen that when the ferritic stainless steel was subjected to a CCC test, the flow stress increased smoothly, as shown by the broken line. As pointed out by Moses et al., neither precipitation nor phase transformation took place in this steel over the temperature range employed. The increase in flow stress simply indicated that the ferrite was cooling and work hardening simultaneously. This provides a baseline for the present analysis, and any noticeable deviation from such flow behaviour during a CCC test can be related to a microstructural change. As illustrated by the C-Mn steel, the stress drop at around 760 °C indicates the occurrence of the γ-to-α transformation, since ferrite is softer than austenite at the same deformation temperature. After the transformation was finished at around 690 °C, the flow stress increased smoothly with further decrease in temperature in a manner similar to that of the ferritic stainless steel.

By contrast, the stress-temperature curve for the Mo-Nb-B steel displays a very high rate of increase in flow stress with decreasing temperature in the range 595 °C-540 °C. As shown in Fig. 6.50, the dependences of the flow stress on deformation temperature were determined as follows:

$$\sigma = 1.1\times10^{-3}T^2 - 2.16T + 1049.5 \qquad \text{C-Mn steel} \qquad (6.1)$$

$$\sigma = 2.4\times10^{-2}T^2 - 30.57T + 9776.3 \qquad \text{Mo-Nb-B steel} \qquad (6.2)$$

Here T is the deformation temperature in °C.

The rates of increase in flow stress were calculated by taking the first derivatives of the above relations with respect to temperature, i.e. $d\sigma/dT$. The extent to which the rate of increase in flow stress with decreasing temperature was increasing was evaluated by calculating the value of the second derivative; these turned out to be 2.2×10^{-3} and 4.8×10^{-2} for the C-Mn and Mo-Nb-B steels, respectively. It can be seen that the rate of increase in flow stress accelerates about 22 times more quickly in the Mo-Nb-B than in the C-Mn steel over the present temperature range. This dramatic difference in the rate of acceleration in the two steels is due to the occurrence of the γ-to-B transformation in the Mo-Nb-B steel, as demonstrated by the microstructures presented in the previous subsection. However, a component can also be due to precipitation hardening of the ferrite as the solubility of niobium in ferrite is lower than in austenite.

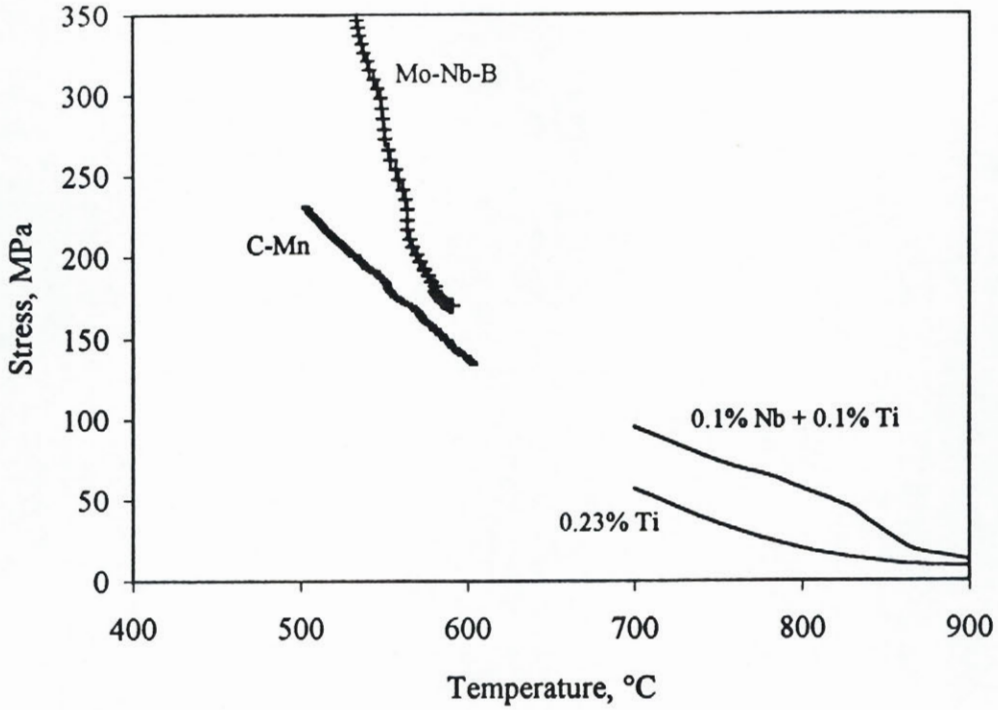

Fig. 6.50 Stress-temperature curves comparing the rate of increase in flow stress in the base and Mo-Nb-B steels. The stress-temperature curves illustrated in the lower right corner are from reference [263].

NbC precipitation in ferrite has been studied by several authors, as reported by Gray et al.[264], Morrison and Woodhead[265], and Irvine and Baker[266] in microalloyed low carbon steels. In the past several years, similar observations have also been made on IF steels[159, 160, 267]. More recently, Moses et al.[263] observed that NbC precipitation takes place in Nb stabilized ferritic stainless steels at around 900 °C. Their CCC test results displayed abrupt changes in slope at temperatures slightly below 900 °C. For comparison purposes, their results are reproduced and presented in the lower right hand corner of Fig. 6.50. The lower curve was generated using a CCC test on a 0.2% Ti stabilized steel; the upper one refers to a 0.1%Nb + 0.1%Ti stabilized steel. It can be seen that the rate of increase in flow stress is much higher in the 0.1%Nb + 0.1%Ti steel than in the 0.23%Ti grade over the temperature range 880 °C-830 °C, the ratio between the two rates of acceleration being about 10. According to those authors, strengthening caused by NbC precipitation was responsible for the higher rate of increase in flow stress in the former material.

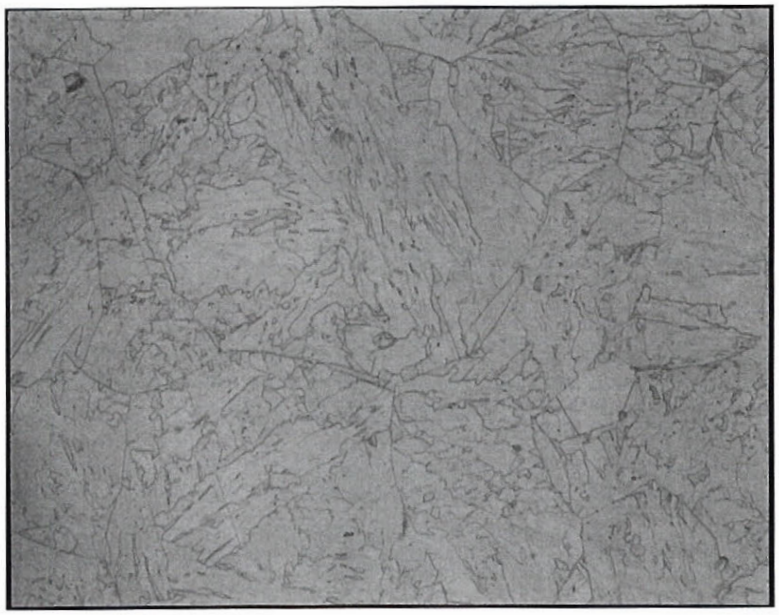

(a)

(b)

Fig. 6.51 Microstructures of undeformed specimens of the (a) Mo-Nb-B steel and (b) Mo-B steel cooled at 1 °C/s. x 630

Although the effect of NbC precipitation may not be as great as in the material studied by Moses et al., (because of the lower Nb contents), it can nevertheless be concluded that the higher rate of increase in flow stress in the Mo-Nb-B and Nb-B steels is partially due to NbC precipitation strengthening. This will be examined more closely below.

In the Mo-B steel, on the other hand, there is no NbC precipitation, although $Fe_{23}(C,B)_6$ and BN precipitation can occur. There was no evidence that strengthening due to this kind of precipitation was taking place. The abrupt changes in slope in this steel can therefore be associated with the γ-to-B transformation. In fact, Mo and B are usually added to this type of steel to suppress the γ-to-α transformation, and thus to produce a bainitic structure. Furthermore, the microstructure of the Mo-B steel cooled from 1200 °C to room temperature at a cooling rate of 1 °C/s is similar to that of the Mo-Nb-B steel, as shown in Fig. 6.51. The common features of these microstructures are: (1) plate-like and lath-like ferrite; (2) well-defined prior austenite grain boundaries; (3) discrete needle-like or blocky retained austenite and/or martensite. These features are more visible at higher cooling rates, as shown in Figs. 6.33 through 6.35. According to Bramfitt and Speer[20], microstructures with these features can be termed as B_3.

6.2.1.2 Analysis of the IT Flow Curves

As demonstrated in §6.1.2, the γ-to-α transformation is accompanied by a continuous drop in flow stress during deformation. At the end of the transformation, the stress will increase with further straining, as long as the temperature is low enough to allow further strain accumulation. However, the results shown in Fig. 6.40 illustrate an opposite trend; the transformation is accompanied by a continuous *increase* in flow stress during deformation. As in the CCC tests, a sharp increase in flow stress over a specific strain range can be due to the same causes as were analyzed in the previous subsection. To clarify the mechanism that is responsible for the abrupt slope change, some flow curves from §6.1.2 are replotted here as Fig. 6.52.

A rapid change in flow stress over a relatively small strain range is a common feature shared by these flow curves. Some differences are also evident. First, the stress levels are different in the three steels; at ε=0.3, for example, the Mo-Nb-B flow stress is the highest, while that of the Nb-64B steel is the lowest. Second, the flow stresses of the Mo-Nb-B and Mo-B steels increase continuously and then level out, while the Nb-64B steel displays a decreasing trend after the initial increase. The rapid flow stress increase in

the Nb-64B steel is mainly attributable to strengthening by NbC precipitation , as the γ-to-α transformation was observed to take place in this steel (see Fig. 6.48). It is harder to explain the flow stress increase in the Mo-B steel, since $Fe_{23}(C,B)_6$ and BN are not strong contributors to precipitation strengthening. Strengthening in the Mo-B steel therefore appears to be due mainly to the transformation of austenite into a harder phase, i.e. to the γ-to-B reaction. The same remark applies to the Mo-Nb-B steel.

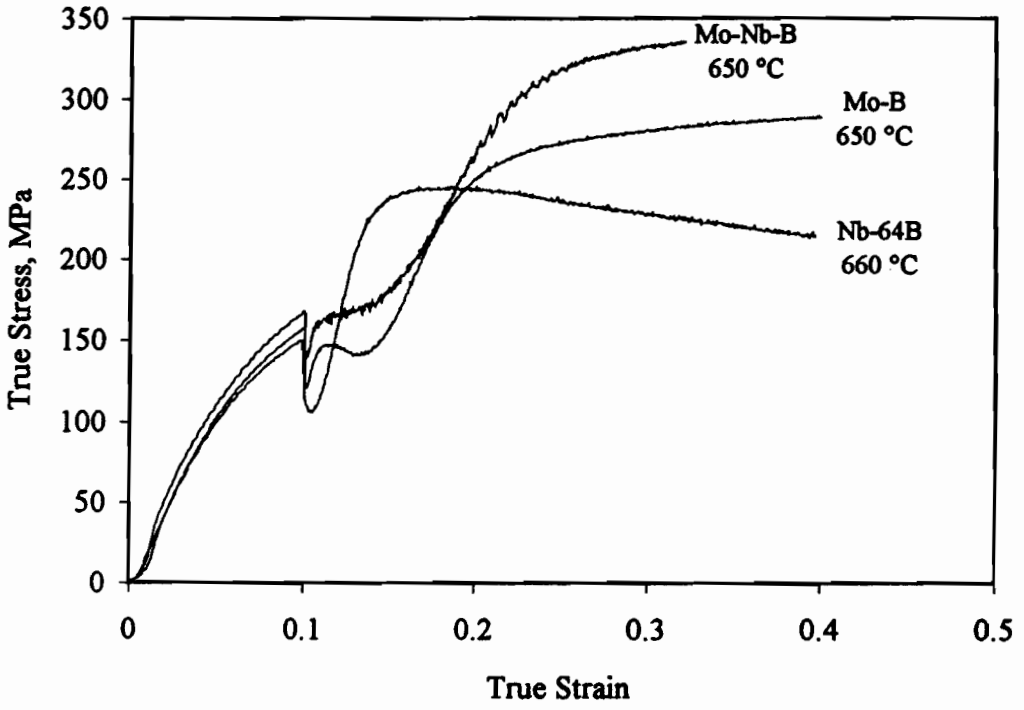

Fig. 6.52 Flow curves determined on the Mo-Nb-B, Mo-B, and Nb-64B steels at 650 and 660 °C.

The rate of increase in flow stress can be correlated with the progress of the transformation by analyzing the flow curves. Fig. 6.53(a) shows the stress-strain curve of the Mo-Nb-B steel in the lower strain rate region when tested at 670 °C. The curve can be divided into three regions according to the local flow hardening rate. The relationship between stress and strain during high temperature deformation can be expressed by a power function[268]:

$$\sigma = k\varepsilon^n \qquad (6.3)$$

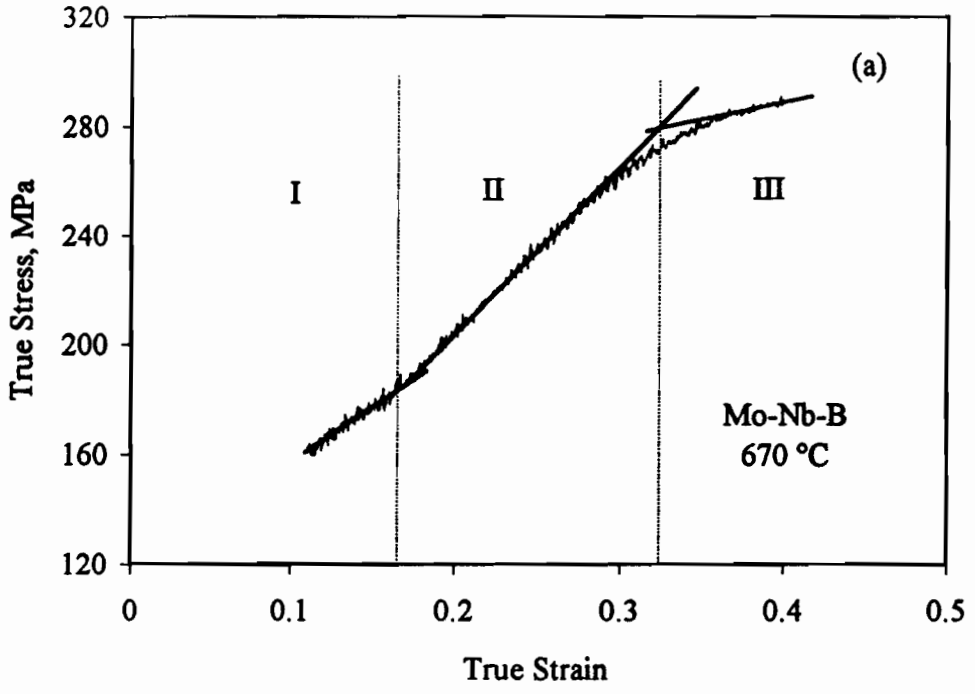

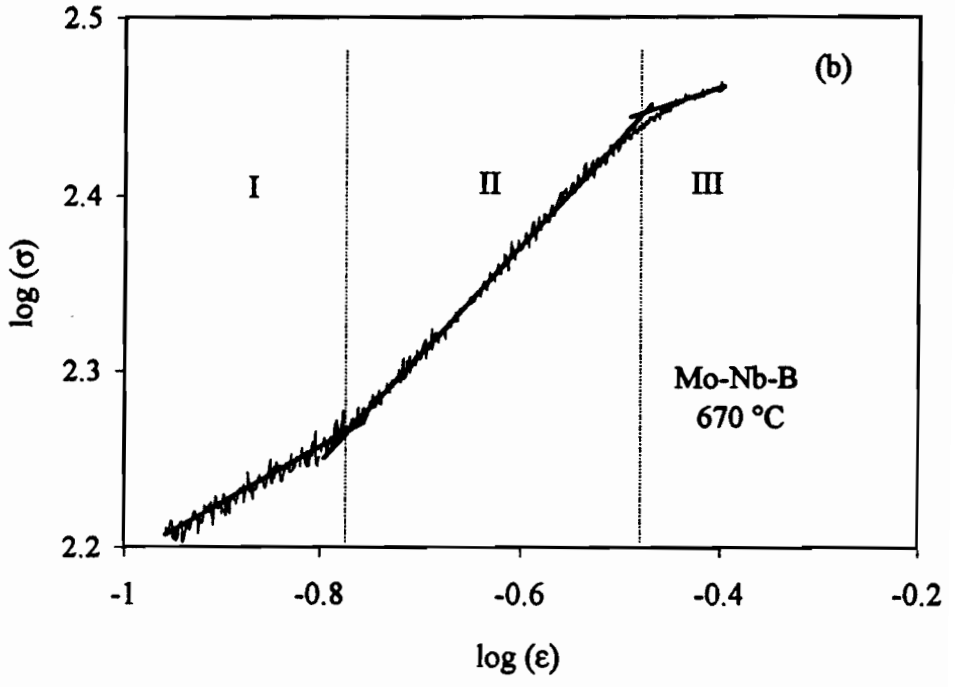

Fig. 6.53 Stress-strain curve of the Mo-Nb-B steel illustrating the three regions of flow behavior.

Here k and n are constants. The value of n is an indication of the flow hardening rate and can be determined by plotting log (σ) vs. log (ε). This is illustrated in Fig. 6.53(b). The log (σ)-log (ε) curve can also be divided into three regions. In range I, the flow hardening rate is low because of the formation of plate-like ferrite. In range II, the flow hardening rate increases dramatically due to the occurrence of the γ-to-B transformation and of precipitation strengthening. In range III, as most of the austenite has already transformed to low carbon bainite, the flow curve simply reflects the rate of work hardening of a single phase. The values determined for n at different temperatures are shown in Table 6.3.

Table 6.3 Values of n determined for the Mo-Nb-B steel

Temperature, °C	n		
	region I	region II	region III
620	0.18	2.86	0.18
650	0.24	1.32	0.17
670	0.31	0.61	0.18
700	0.31	~	~
750	0.25	~	~

As the temperatures of 700 °C and 750 °C are about 65 °C and 115 °C higher than the transformation temperature determined by the CCC test, deformation at these two temperatures is concluded to take place in the austenite region. The estimated n values are about 0.3, and are in good agreement with those reported by other authors for austenite[269-271]. The work hardening rate in region I decreases consistently as the deformation temperature is lowered because of the formation of plate-like ferrite. In region II, however, the n value *increases* when the deformation temperature is lowered. This is because the rate of the γ-to-B transformation increases when the deformation temperature approaches and then exceeds the transformation temperature determined by the CCC test. In region III, n appears to be insensitive to deformation temperature, and a general value of $n \approx 0.18$ was obtained. This value is slightly higher than those reported for ferrite but is lower than the ones for austenite.

The transformation behaviours displayed by the Nb-15B and Nb-64B steels in Figs. 6.43 and 6.44 are more complicated because of the low slopes evident at 750 °C in both cases. At higher deformation temperatures, for example 780 °C and 810 °C for the

Nb-15B steel and 800 °C for the Nb-64B steel, only a single peak is apparent. The peak strain that corresponds to a specific deformation time is associated with the start of the γ-to-α transformation rather than with the initiation of dynamic recrystallization; this is because the peak recrystallization strain estimated for the two steels at 800 °C is about 0.7, which is even higher than the total strain employed in the present investigation. This is consistent with the observations of Essadiqi and Jonas[272].

At 710 °C and 750 °C, the slight drops in flow stress of the Nb-15B steel in the earlier stages of flow indicate the start of the γ-to-α transformation. The flat flow curves observed at the later stages of straining suggest that the transformation is progressing rather slowly. The reasons for this phenomenon are not obvious, but could involve retardation of the moving interfaces by fine NbC precipitates. Another possibility is that the softening due to the γ-to-α transformation is well balanced by precipitation strengthening. The rapid increase in flow stress of the Nb-64B steel at 700 °C indicates that the balance was broken after a short incubation time, which suggests in turn that large numbers of precipitates emerged in the material. More precipitates at 660 °C led to higher rates of work hardening rate during the early stages of flow. It should be noted that the flow stress starts to drop when the strain reaches 0.16. This probably marks the end of precipitation, so that the softening due to the γ-to-α transformation overcomes the precipitation strengthening, resulting in the drop in flow stress.

6.2.2 What Sorts of Roles Do Nb and B Play during High Temperature Deformation?

Nb is a well known alloying element in modern high strength steels, and is usually added: (1) to retard austenite grain growth during reheating; (2) to widen the window between the recrystallization stop temperature and the A_{r3}, which in turn extends the pancaking range; (3) to strengthen the steel by NbC precipitation in the ferrite. Boron is added to steels to improve the hardenability by acting as an inhibitor of polygonal ferrite formation. A large number of investigations have been carried out on Mo-B and Mo-Cr-B systems in the past several decades, and more recently on Nb-B and Mo-Nb-B systems[14, 15, 24, 273]. In Mo-B steels, $Fe_{23}(C,B)_6$ precipitates are often observed to form during hot deformation. In Nb-B and Mo-Nb-B steels, the carbon atoms are taken out of solution by Nb in the form of Nb(CN) at higher temperatures, leaving the boron free to segregate at grain boundaries. Borocarbides are not expected to form if the carbon or boron content is low, as reported by Tamehiro et al.[14].

The types and distributions of the precipitates observed in the Nb-48B steel were illustrated in Figs. 6.25 to 6.27. Four types of precipitate, namely Ti-rich, (Ti, Nb)-rich, Nb-rich, and iron-rich, were present in the specimens deformed at 900 °C and held for different times before quenching. No effort was made to employ EELS (electron energy loss spectroscopy, which is able to detect light elements such as B, C and N) analysis in the present investigation. Thus it is simply assumed (but not proved) that the large iron-rich precipitates located at the prior austenite grain boundaries are composed of $Fe_{23}(C,B)_6$. Surprisingly, the kinetics of $Fe_{23}(C,N)_6$ precipitation are so rapid that numerous particles were observed even after only 60 seconds of holding. The sizes of these particles increase with holding time and their densities decrease correspondingly. These observations go counter to the conclusions drawn by Tamehiro et al.[14] that Nb can eliminate the carbon required for the formation of $Fe_{23}(C,B)_6$, since the carbon level is lower and the Nb level is higher in the present steel than in the steel used by those authors.

On an atomic weight basis, the ratio Nb:C:B is 1.4:4:1 in the present 0.021C-0.06Nb-0.0048B steel. Assuming that the reaction between C and Nb goes to completion, only a small amount of C is tied up by the Nb, since the stoichiometric ratio of C to Nb in NbC is about 1/8. This leaves enough free C in solution for subsequent $Fe_{23}(C,B)_6$ precipitation. Thus the addition of Nb to boron steels can slow down but not prevent the precipitation of $Fe_{23}(C,B)_6$. Actually, $Fe_{23}(C,B)_6$ precipitates were also observed by Tamehiro et al.[15] in a 0.057C-0.046Nb-0.0016B steel. The failure by these authors to detect the $Fe_{23}(C,B)_6$ precipitates in their 0.032C-0.046Nb-0.0011B steel is probably due to their low boron and carbon contents. By contrast, the boron concentration in the present steel is appreciably higher than in the steels studied by Tamehiro et al.

It should be noted that the diffusivities of Nb and B in austenite differ considerably. Their diffusivities were estimated using the following relationship:

$$D = D_0 \exp(-Q/RT) \qquad (6.4)$$

where D_0 is a constant, Q is the activation energy for diffusion, R is the gas constant, and T is the absolute temperature. The first two parameters are listed in Table 6.4 and used in the calculations. The diffusivities of Nb and B turned out to be 1.31×10^{-16} and 9.37×10^{-12} m^2/s at 900 °C. Thus $Fe_{23}(C,B)_6$ should form more readily than NbC at this temperature.

The failure to observe $Fe_{23}(C,B)_6$ precipitates in steels of the present type are thus probably due to the difficulty of their detection.

Table 6.4 Diffusion coefficients and activation energies in γ-iron

	unit	reference
$D_0^{Nb} = 1.4 \times 10^{-4}$	m^2/s	[274]
$Q^{Nb} = 270$	kJ/mol	[274]
$D_0^{B} = 1.9 \times 10^{-4}$	m^2/s	[275]
$Q^{B} = 164$	kJ/mol	[275]

Based on the above analysis, it can be concluded that either the boron content itself, or else the product of the boron and carbon contents as proposed by Taylor and Hansen[230], controls the rate of $Fe_{23}(C,B)_6$ precipitation. The product of the boron and carbon concentrations in the present steel is close to that in the steel investigated by Tamehiro et al. (i.e., the 0.057C-0.046Nb-0.0016B steel).

In what follows, the effects of Nb and B on the γ-to-α or γ-to-B transformation will be discussed in detail. First of all, an increase in the volume fraction of NbC and/or $Fe_{23}(C,B)_6$ precipitate appears to increase the transformation temperature. This is well illustrated by the results in Figs. 6.14, and 6.18-6.22. It can be seen from Fig. 6.14 that lowering the reheat temperature raises the transformation temperatures significantly. The A_{r3} was increased by about 35 °C in the Nb-15B steel, 65°C in the Nb-48B steel, and 115 °C in the Nb-64B steel when the reheat temperature was decreased from 1200 °C to 900 °C. This clearly indicates that Nb and B in solution have an important influence on the transformation temperature since the austenite grain size alone can only cause ~a 10 °C difference.

The large $Fe_{23}(C,B)_6$ particles found in specimens of the Nb-64B steel reheated at 1000 °C are illustrated in Fig. 6.54. These particles not only decreased the amount of boron available for subsequent segregation, but also accelerated the γ-to-α transformation by acting as nucleation sites. In addition, Nb in solution acts as an inhibitor of polygonal ferrite formation. Thus the lower reheat temperature, which decreased the amount of Nb in solution, raised the transformation temperature in turn. The characteristics of the

transformation changed from involving a mixture of the γ-to-α and γ-to-B reactions to consisting of a pure γ-to-α type transformation. This was particularly true in the Nb-64B steel.

x 14000

Fig. 6.54 Carbon extraction replica showing some typical $Fe_{23}(C,B)_6$ precipitates observed in the Nb-64B steel reheated at 1000 °C.

Figs. 6.18-6.20 also illustrated that deformation at 900 °C followed by 300 seconds of holding, or a heat treatment at 900 °C for 30 minutes, also raises the transformation temperature. Taking the A_{r3} measured for the 1200 °C reheat as the reference, the increases in A_{r3}, i.e., ΔA_{r3} for different conditions, are summarized in Table 6.5. It can be seen that the Nb-15B steel is least sensitive to the deformation conditions. The dramatic increase in A_{r3} in the Nb-64B steel is mainly attributable to the formation of the large $Fe_{23}(C,B)_6$ precipitates. The boron concentration or the product of the carbon and boron concentrations in this steel is the highest among the three Nb grades. Therefore, either lowering the reheat temperature or holding at 900°C evidently increased the amount of undissolved or precipitated $Fe_{23}(C,B)_6$. This in turn decreased the amount of boron available for segregation, leading to the increase in A_{r3}. In addition, the observation that the highest A_{r3} in the Nb-64B steel corresponds to the reheat temperature of 900 °C implies that the γ-to-α transformation is enhanced by the presence of large $Fe_{23}(C,B)_6$ particles, which act as nucleation sites.

Table 6.5 Effect of deformation conditions on the A_{r3}

Steel	Condition	A_{r3}, °C	ΔA_{r3}, °C*
Nb-15B	900 °C reheat.	775	+35
	1200 °C reheat + 900 °C, 30 min holding.	770	+30
	1200 °C reheat + 900 °C, ε=0.25, 300 s holding.	750	+10
Nb-48B	900 °C reheat.	700	+65
	1200 °C reheat + 900 °C, 30 min holding.	670	+35
	1200 °C reheat + 900 °C, ε=0.25, 300 s holding.	650	+15
Nb-64B	900 °C reheat.	800	+115
	1200 °C reheat + 900 °C, ε=0.25, 300 s holding.	780	+95

* $\Delta A_{r3} = A^{i}_{r3} - A^{0}_{r3}$ A^{i}_{r3}– the measured transformation temperature under the conditions listed in Table 6.5; A^{0}_{r3}– the measured transformation temperature corresponding to the 1200 °C reheat.

Based on the above analysis, it can be concluded that, in order to produce low and stable transformation temperatures, the boron concentration in low carbon Nb steels should be not lower than 15 ppm and not higher than 40 ppm. Taking the strength and low temperature toughness into consideration, the range of boron concentration can be narrowed still further to 15~30 ppm, as suggested by several other researchers[230, 231, 259]. The desirable Nb concentration range is from 0.02 to 0.06 wt%. Furthermore, the C, B, N and Nb concentrations must all be carefully controlled so as to optimize the mechanical properties.

6.2.3 What Mechanism Is Operative during the γ-to-B Transformation?

The mechanism responsible for the γ-to-B transformation has been under debate for many years, and still remains an unresolved issue. More recently, this transformation has been studied in ultralow carbon high manganese Nb-B steels by Yun et al.[262] and a proposal regarding the mechanism was put forward by these authors. They believe that the nucleation of ferrite occurs by a *diffusional* mechanism under paraequilibium conditions and that longitudinal growth takes place by a *displacive* mechanism in their materials. This interpretation is similar to that advanced by Bhadeshia and Christian[29] for the formation of upper and lower bainite and of acicular ferrite in a recent review The microstructures observed in the present work are similar to those of Yun et al., particularly in the Mo-Nb-B steel cooled at the higher rates. Thus the same set of

transformation mechanisms can be considered to operate in the present low carbon bainitic steels.

It is in fact hard to explain how the packets of lath-like ferrite grow so much more quickly along their long rather than short axes by a diffusional mechanism. In some cases, the packets grow from one side of an austenite grain to the other without interruption. Fig. 6.32 clearly shows a packet of lath-like ferrite with a length of about 20 μm and an average width of about 0.8 μm. Such unidirectional growth requires a particular "atmosphere" which cannot readily be produced by carbon diffusion. The long lath-like ferrite components can be produced instead by a displacive (or martensitic) type of mechanism. Although no efforts were made to study the surface relief characteristic of martensite transformation in the present investigation, the serrations observed on the flow curves (see Fig. 6.55) in the work described here may be related to this type of transformation. In what follows, the discussion will be focused on a possible explanation of the serration phenomenon observed in the present work, which has not received much attention to date.

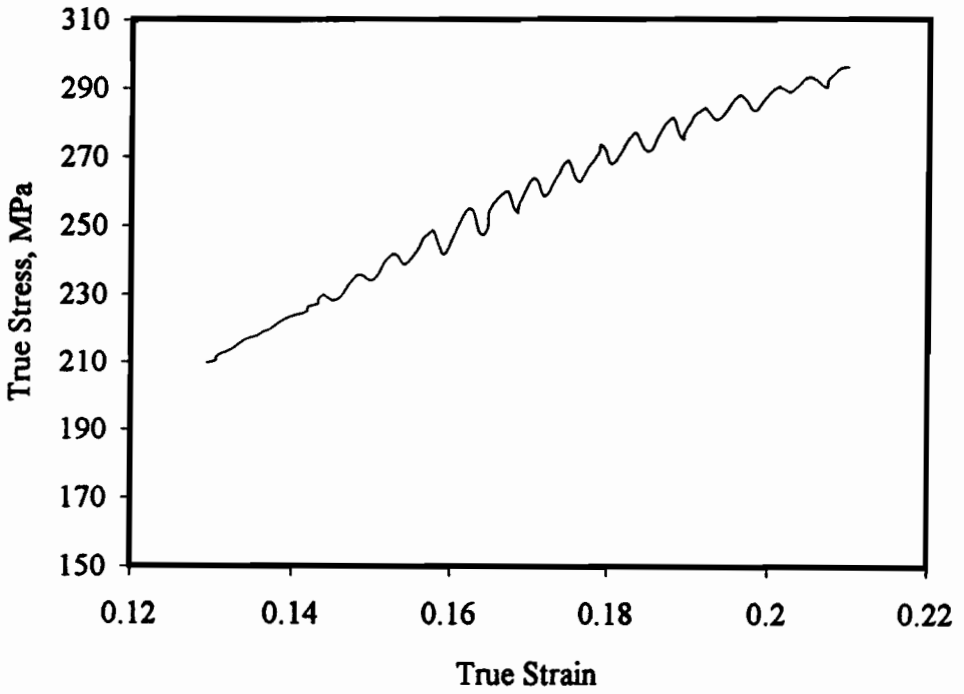

Fig. 6.55 Serrations observed in the Mo-Nb-B steel tested at 650 °C.

It has been reported in the literature that flow curve serrations can result from the operation of mechanisms of the following types:

(i) mechanical twinning;
(ii) thermal instability (localized deformation or adiabatic heating);
(iii) dynamic strain aging;
(iv) strain-induced martensite formation.

The first two mechanisms can be readily eliminated from the list of candidates. Mechanical twinning is often observed in the hexagonal metals, zinc, cadmium and magnesium, in which the number of possible slip systems is severely limited. This mechanism has also been observed in fcc and bcc metals, such as copper[276], silver[277], gold[277], nickel[278] and pure iron[279], but only at relatively low temperatures, e.g., 4 K (-269 °C) and 77 K (-196 °C). Localized deformation heating, the so-called thermal instability, has also been related to presence of serrations on stress-strain curves by Bazinski[280], although his analysis is more generally applicable to low temperatures, where the yield stress is a sensitive function of temperature and the specific heat is low. These conditions obviously do not apply to the present experiments. In the cases of dynamic strain aging and strain-induced martensite formation, the situation is more complicated and has to be considered in more detail.

6.2.3.1 Dynamic Strain Aging

The serrated yielding phenomenon is widely observed on the stress-strain curves produced by the tensile (or compressive) testing of low carbon and alloyed steels. This behaviour, also known as jerky flow or the Portevin-LeChatelier effect, is accompanied by high work hardening rates, negative temperature and strain rate dependence of the flow stress, and reductions in ductility. This phenomenon has been attributed to the occurrence of dynamic strain aging[281, 282]; for this to take place, a solute must be able to diffuse quickly enough to slow down the moving dislocations by forming atmospheres around them. It has been noted that the process is strongly temperature and strain rate dependent, and is thermally activated.

According to Cottrell[283], the minimum diffusion rate D required to produce serrated yielding is given by

$$\dot{\varepsilon} = \rho b v_c = \left(\frac{4b\rho}{h}\right) D \qquad (6.5)$$

where $\dot{\varepsilon}$ is the strain rate, v_c the critical dislocation velocity, ρ the mobile dislocation density, b the Burgers vector of the dislocation, and h the effective radius of the solute atmosphere. The values of $4b\rho/h$ in the equation have been estimated to fall in the range 10^{13}-10^{15} m^{-2} for different solutes[284-286]. The possibility that dynamic strain aging may be taking place in the present steel was assessed as follows. First it should be noted that, at 650 °C and 670 °C, the γ-to-B transformation was occurring during deformation. Thus dynamic strain aging can arise from the diffusion of substitutional solutes in the γ or interstitial solutes in the α. These two distinct cases are considered separately below.

(a) Dynamic strain aging due to interstitial solutes in ferrite

In low carbon steels, interstitial solutes, such as carbon, nitrogen and boron, are considered to be responsible for locking dislocations. At a tensile strain rate of 10^{-4} s^{-1}, the reported temperature range for serrations is 100 °C-350 °C, which is in the pure ferrite region. In the present steel, the interstitial solutes are carbon, nitrogen and boron; their diffusivities at the current deformation temperatures were estimated using equation (6.4) using the parameters shown in Table 6.6. The results obtained in this way are presented in Table 6.7.

Table 6.6 Impurity diffusion parameters in α-iron

Solute	D_0 (m^2/s)	Q (kJ/mol)	Refs
C	6.2×10^{-7}	80	[287]
N	3.0×10^{-7}	76	[287]
B	10^2	260	[288]

Table 6.7 Impurity diffusivities in α-iron

Solute	650 °C (m^2/s)	670 °C (m^2/s)
C	1.83×10^{-11}	2.28×10^{-11}
N	1.49×10^{-11}	1.84×10^{-11}
B	1.90×10^{-13}	3.90×10^{-13}

The strain rate used in the present investigation was 5×10^{-4}; thus the minimum diffusion rate for the occurrence of serrations was estimated to be 5×10^{-18}. It can be seen that the calculated diffusivities of the different candidate solutes are about five to seven orders of magnitude higher than the minimum value. It can therefore be concluded that

the solute atmospheres diffuse too rapidly at these temperatures to produce dynamic strain aging.

(b) Dynamic strain aging due to substitutional solutes in austenite

Dynamic strain aging in austenitic steels is well documented in the literature[289-291]. It is known that the interstitial sites in austenite (γ-iron) are considerably larger than in ferrite. Thus, the binding energy between interstitial solutes and dislocations is expected to be very small, so that serrated yielding, if it occurs, will be caused by substitutional atoms. The substitutional elements in the present steel are Nb, Ti, Mo and Mn; their diffusion parameters in γ-iron are listed in Table 6.8 and the estimated diffusivities at 650 °C and 670 °C are presented in Table 6.9.

It can be seen from Table 6.9 that the estimated diffusivities of the substitutional solutes at a given temperature are about one to three orders lower than the minimum value ($D_{min} \approx 5x10^{-18}$). Nevertheless, as pointed out by Cottrell[295], the diffusivities of substitutional solutes can be raised by about two to five orders of magnitude by the presence of strain induced vacancies[289, 296]. Taking this consideration into account, it may become possible for the diffusion rate of a substitutional atom to be raised sufficiently for it to move at speeds near to those of mobile dislocations. Thus it seems possible that dynamic strain aging could be initiated in this way.

Table 6.8 Impurity diffusion parameters in γ-iron

Solute	D_0 (10^{-4} m^2/s)	Q (kJ/mol)	Refs
Nb	1.4	270	[159]
Ti	0.89	291	[292]
Mo	0.036	240	[293]
Mn	0.178	260	[294]

Table 6.9 Impurity diffusivities in γ-iron

Solute	650 °C (m^2/s)	670 °C (m^2/s)
Nb	$7.21x10^{-20}$	$1.52x10^{-19}$
Ti	$2.85x10^{-21}$	$6.38x10^{-21}$
Mo	$9.27x10^{-20}$	$1.80x10^{-19}$
Mn	$2.01x10^{-20}$	$4.16x10^{-20}$

Although the diffusivities of these solutes are close to one another, the Nb and Ti atoms may not be available, as they will have combined with C and N in the form of NbC and TiN precipitates. This leaves Mo and Mn as candidate solutes for dynamic strain aging. If this is the case, the Mo-B flow curves shown in Fig. 6.42 lead to the following observations. There are no obvious serrations on these curves, while the chemical composition is similar to that of the Mo-Nb-B steel, except for the absence of Nb, which *does* display serrations. Thus it appears that the presence of Mo does not, in itself, lead to serrations. Similar remarks apply in the present instance to Mn addition. Furthermore, the rate of work hardening decreases continuously as the temperature is increased (see Table 6.3 in region II); this is unlike dynamic strain aging, in which case a peak on the θ-T plot is usually observed.

6.2.3.2 Strain Induced Martensite Formation

It is well known that metastable austenite can transform into martensite under load or during straining at room or even lower temperatures. This leads to additional strengthening of the material. This concept is used in the processing of steels such as the ausforming grades, TRIP steels, and certain creep resistant austenitic stainless steels. An interesting phenomenon observed in these materials is jerky flow. Although the factor responsible for serrated yielding at low temperatures is still being debated, the flow curve serrations present at room or higher temperatures have been related to the formation of strain induced martensite[297, 298].

According to the room temperature microstructures, the transformation taking place in the present Mo-Nb-B steel is of the γ-to-B type. If the γ-to-B transformation is at least partially martensitic in nature, then a shape change (or shear) is introduced by the phase change. This can lead to a dilation of the testing specimen along the load axis under a tensile stress or to a contraction under a compressive stress, resulting in a reduction of the stress on the specimen[298, 299].

The influence of deformation on the spatial arrangement of the long axes or habit planes of the transformed products was studied by Zaymovskiy et al.[300]. They found that, in a γ-to-B transformation, packets of crystals are formed under load whose habit surfaces lie preferentially at angles inclined at 45° to the specimen axis. By contrast, transformation in the absence of load produced packets of parallel crystals with more random orientations, such as triangles,"stars", and "tentlike" pairs. They also found that, after a 5% prestrain, the angle between the transformed product and load axes had a

maximum in the range 45°-70°. These observations support the view that bainite formation involves some shear displacements.

It should be pointed out that, although serrated yielding can accompany martensite formation, serrations are not always observed during such transformations. Their appearance seems to be temperature, strain rate and stress field dependent. As pointed out by Fahr[298], a transformation that is stress-induced can take place so readily that the externally applied stress is sufficient to sustain it, without the appearance of any serrations on the flow curve. In the present case, although the transformation mechanism probably involved shear, the flow curve serrations could still be due to some other unknown metallurgical phenomenon. Thus the source of the serrations is worthy of further investigation.

6.3 Summary

The transformation behaviours of six steels containing different microalloying additions were investigated under continuous cooling and isothermal conditions. CCC tests were used to determine the transformation temperatures, while the strain rate change technique was employed to study the transformation kinetics and to analyze the various metallurgical phenomena occurring in the experimental temperature range. The effects of the amount of deformation and of the cooling rate on the final microstructure were also investigated. It was found that the Mo-Nb-B steel is basically a low carbon bainitic grade, and that B_3 microstructures are formed over a large cooling rate range (from 1 °C/s to 50 °C/s). The lengths of the lath-like ferrite sheaths increased and their widths decreased when the cooling rate was increased. The shapes and distributions of the retained austenite changed from being blocky and randomly distributed to fine, more aligned, and needle-like with increasing cooling rate. The precipitates that appeared at 900 °C were examined using a TEM and analyzed with the aid of EDX spectra. Large $Fe_{23}(C,B)_6$ particles were found in the Nb-48B steel after 3600 seconds of holding. These large precipitates are considered to be responsible for increasing the transformation temperature when they appear as well as the proportion of polygonal ferrite in the final microstructure. The mechanism of γ-to-B formation is judged to be displacive in the present case; the serrations evident on the flow curves of the Mo-Nb-B steel are considered to be due to the jerky nature of this transformation.

CHAPTER 7

CONCLUSIONS

In the present work, four related behaviours, namely static recrystallization, dynamic recrystallization, metadynamic recrystallization, and phase transformation, were studied in a series of Nb and Nb-B steels. Based on the experimental results and the discussions presented in Chapters 4 through 6, the following conclusions can be drawn regarding each of these topic areas.

A. Static Recrystallization

In this part, the effect on the T_{nr} of chemical composition and of the processing parameters was investigated in a series of Nb and Nb-B steels. Here multipass deformation was applied under continuous cooling conditions.

1. Chemical composition, pass strain, and interpass time all have a significant influence on the T_{nr} in Nb and Nb-B steels. The strain rate has an order of magnitude less influence on the T_{nr} than the pass strain.

2. The effect of interpass time on the T_{nr} falls into two distinct ranges. In the short interpass time range ($t \leq 12.5$ s), the T_{nr} *decreases* with increasing time because recrystallization is controlled by solute drag. The equivalent solute Nb content, defined as $[Nb]_{eq} = Nb + 0.22Ti + 0.08Al$, can be used to express the effect of

chemical composition on the T_{nr} in this range. In the long interpass time range (t > 12.5), the T_{nr} *increases* with interpass time, and recrystallization is retarded instead by precipitate formation and dislocation pinning. The effect of chemical composition on the T_{nr} can be expressed in terms of the solubility product [Nb][C] in this range.

3. The T_{nr} can be predicted from two relations, one each for short and long interpass times; these express the respective dependences on composition, pass strain, and interpass time.

4. The addition to Nb steels of up to 48 ppm boron increases the T_{nr}. Increasing the boron concentration beyond this range results in a decrease in the T_{nr}.

5. The residual strain that applies to a particular pass can be estimated by comparing the actual pass flow curve (which can display strain accumulation) to the one associated with the absence of strain accumulation. The lowest temperature at which the residual strain ratio λ (ratio of the residual strain to the total effective strain) is zero (i.e. at which recrystallization is complete) is known as the recrystallization limit temperature (RLT). The temperature at which $\lambda = 0.6$ is the highest at which recrystallization is completely absent; it is known as the recrystallization stop temperature (RST). The T_{nr} is associated with incomplete recrystallization and falls between the RLT and RST.

6. The residual strain ratio λ can be predicted from the deformation parameters and chemical composition through their effects on the T_{nr}.

B. Dynamic and Metadynamic Recrystallization

The occurrence of dynamic and metadynamic recrystallization was investigated in three Nb steels (0.023Nb, 0.07Nb and 0.09Nb) using hot torsion tests. The following conclusions can be drawn from these tests.

1. The process of dynamic recrystallization is initiated at a strain below the peak strain and penetrates to the grain interiors at the steady state strain.

2. The abrupt change in the temperature dependence of the peak strain at low temperatures can be attributed to the effect of Nb(CN) precipitation. Higher

concentrations of Nb in solution increase the peak strain ε_p in a manner described by the following relationship:

$$\varepsilon_p = \left(3.34\log[Nb]+9.79\right)\times 10^{-4} D_0^{0.3} Z^{0.17}$$

Here [Nb] is the concentration of Nb in solution, D_0 the initial grain size, and Z the Zener-Hollomon parameter. The advantage of this expression, compared to the ones in the literature, is that it can predict the effect of Nb concentration on the peak strain.

3. The rate (or rapidity) of dynamic recrystallization can be characterized by the "time for dynamic recrystallization" $t_{0.8}$ (defined on p. 176), which represents the deformation time that elapses from the peak to the steady state strain. The $t_{0.8}$ time depends on strain rate and deformation temperature, but only slightly on composition. The following empirical equation can be used to describe this relationship:

$$t_{0.8} = 1.5\times 10^{-5} Z^{-0.73} \exp\left(\frac{392000}{RT}\right)$$

4. When the accumulated strains are less than $1.5\varepsilon_p$, the fractional softening is strongly strain dependent. At strains in excess of $1.5\varepsilon_p$, however, a strong strain rate and temperature dependence is observed. The softening that occurs under the latter conditions is mainly due to metadynamic recrystallization; its kinetics can be described by the relation:

$$t_{0.5} = \left(12[Nb]+0.5\right)\times 10^{-4} Z^{-0.84} \exp\left(\frac{403000}{RT}\right)$$

5. Comparison of the kinetics of static, dynamic and metadynamic recrystallization shows that metadynamic recrystallization is the fastest of the three in Nb steels.

6. At laboratory strain rates (less than 10 s^{-1}), there is little metadynamic recrystallization when the interpass times are less than 0.1 s. At the strain rates employed in rod mills, however, metadynamic recrystallization is much more rapid and becomes the dominant softening process.

C. Transformation in the Mo-Nb-B, Nb-B, Mo-B and Boron Steels

The transformation behaviours of the Mo-Nb-B, Nb-B, Mo-B and boron steels were investigated under continuous cooling and isothermal conditions. CCC tests were used to determine the transformation temperatures and the strain rate change technique was employed to study the transformation kinetics. This part of the investigation led to the following conclusions.

1. The transformation temperatures in the Mo-Nb-B and Mo-B steels are about 150 °C lower than in the base C-Mn steel. These temperatures increase slightly when the reheat temperature is decreased.

2. In the Nb-B steels, the transformation temperatures are clearly sensitive to the reheat temperature. Decreasing the latter from 1200 °C to 900 °C leads to about a 30 °C increase in A_{r3} in the Nb-15B steel, 55 °C in the Nb-48B steel, and 120 °C in the Nb-64B steel. The large increase associated with the Nb-64B steel is due to the undissolved $Fe_{23}(C,B)_6$ particles that act as nucleation sites for the γ-to-α transformation.

3. The transformation temperatures increase slightly with deformation, but more significantly when deformation is followed by holding. A holding interval of about 300 s at 900 °C after a strain of 0.25 raises the transformation temperature of the Nb-64B steel by about 100 °C. This increase is again due to the presence of large $Fe_{23}(C,B)_6$ precipitates.

4. The microstructures of the Mo-Nb-B and Mo-B steels are composed of plate-like and/or lath-like ferrite in association with discrete M/A constituents. This can be classified as a B_3 structure[20]. By contrast, the microstructures of the Nb-B steels depend strongly on the boron content; the Nb-48B steel displays a B_3 type microstructure, while those of the Nb-15B and Nb-64B grades consist of polygonal ferrite.

5. Low carbon bainite can be produced in the Mo-Nb-B steel over a wide range of prior strains and cooling rates. The minimum cooling rate required to avoid the formation of polygonal ferrite increases when deformation is applied. The experiments indicate that cooling rates in the range 25 °C/s-35 °C/s should produce fully bainitic microstructures under plate mill rolling conditions.

6. The high flow hardening slopes observed on certain portions of the isothermal flow curves of the Mo-Nb-B steel are due to the occurrence of both transformation and precipitation strengthening. The serrated flow behaviour displayed at 650 °C and 670 °C in this steel is probably attributable to features of the γ-to-B transformation that are related to the formation of strain induced martensite. This observation indicates that the γ-to-B transformation probably takes place by means of a displacive mechanism.

STATEMENT OF ORIGINALITY AND CONTRIBUTION TO KNOWLEDGE

The static, dynamic and metadynamic recrystallization behaviours of Nb, Nb-B, Mo-B and Mo-Nb-B steels were investigated. Some attention was also paid to their transformation behaviours. The results obtained in this work are of industrial as well as academic interest, and include the following original contributions:

1. For the first time, the effects of chemical composition and of the processing parameters on the no-recrystallization temperature (T_{nr}) were systematically studied in a series of Nb modified steels. The results obtained in this work show that the T_{nr} decreases significantly when the strain is increased, but is affected only slightly when the strain rate is increased. The effect of interpass time on the T_{nr} has been clearly shown to fall into two distinct ranges. In the short interpass time range, recrystallization is retarded by solute drag and the T_{nr} *decreases* with increasing time. In the long interpass time range, the T_{nr} *increases* with increasing time because of the increasing volume fraction of fine precipitates that are formed.

2. The effect of boron addition on the T_{nr} was investigated for the first time in Nb steel deformed using a multipass schedule applied under continuous cooling conditions. It was found that boron alone produces a weak effect on the T_{nr}. The addition of boron to Nb steels increases the T_{nr} continuously until a level of 48 ppm is attained. Increasing the boron concentration beyond this value results in a *decrease* in the T_{nr}.

3. Two empirical equations were derived for prediction of the T_{nr}; these employ the chemical composition and the deformation parameters. The residual strain ratio was deduced by comparing actual pass flow curves to the one associated with an absence of strain accumulation. This original approach led to two empirical equations for estimation of the residual strain ratio. It also enabled the relation between the T_{nr} and the RLT (recrystallization limit temperature) and RST (recrystallization stop

temperature) to be clarified. The approaches described here will make it possible for industrial engineers to improve the accuracy of their rolling load calculations.

4. The present experimental results made it possible to modify the recrystallization and precipitation models of Dutta and Sellars so that they can be applied to the present low carbon Nb steels. The additivity rule was employed to predict the T_{nr} under continuous cooling conditions using the kinetic models derived in this investigation.

5. Expressions were derived to describe the kinetics of dynamic and metadynamic recrystallization in the three low carbon Nb steels. The time for dynamic recrystallization to go to near completion, $t_{0.8}$, has been shown to be relatively insensitive to Nb concentration, while that for metadynamic recrystallization depends on the solute Nb content. It was shown that the rate of recrystallization in the present alloys follows the ascending order: static, dynamic, metadynamic.

6. At laboratory strain rates, multipass simulations have been employed to demonstrate that there is little metadynamic softening when the interpass times are shorter than 0.1 s. At the strain rates employed in rod mills, however, metadynamic recrystallization is accelerated and can produce nearly full softening in the present materials once dynamic recrystallization is initiated. This requires the absence of static recrystallization so that the strain can be accumulated into the vicinity of the peak strain.

7. The transformation behaviours of the Mo-Nb-B, Mo-B, Nb-B and boron steels were investigated using both CCC (continuous cooling compression) and IT (isothermal) tests. The presence of low carbon bainitic microstructures was established in the Mo-Nb-B steel over a wide cooling rate range. The characteristics of the lath-like ferrite that forms in this material together with the serrated flow behaviour evident on the flow curves indicate that the displacive mechanism plays a role in the present transformation.

8. The presence of intergranular and intragranular $Fe_{23}(C,B)_6$ precipitates was established in the Nb-48B and Nb-64B steels deformed at 900 °C (after reheating at 1000 °C). The sizes of these particles ranged from 0.1 μm to 1 μm.

9. The effect of boron concentration was studied in the Nb-B steels. It was shown that both low and high boron concentrations promote the formation of polygonal ferrite. A

low boron concentration (15 ppm) means that there is insufficient boron to produce the segregation on austenite grain boundaries that retards the formation of polygonal ferrite. By contrast, when the boron concentration is high (64 ppm), the large $Fe_{23}(C,B)_6$ particles that form enhance the formation of polygonal ferrite by acting as nucleation sites.

REFERENCES

1. K.J. Irvine: *"Strong, Tough Structural Steels"*, The Iron and Steel Institute, publication 104, (1967), p. 1.
2. W. Barr: *"The Fracture of Metals"*, Institution of Metallurgists, (1950), p. 117.
3. W.E. Bardgett and L. Reeve: *J. Iron and Steel Institute*, 163, (1949), p. 277.
4. K.J. Irvine, F.B. Pickering, W.C. Heselwood, and M. Atkins: *J. Iron Steel Inst.*, 186, (1957), p. 54.
5. K.J. Irvine and F.B. Pickering: *J. Iron and Steel Institute*, 187, (1957), p. 292.
6. F.B. Pickering: *"Transformation and Hardenability in Steels"*, Climax Molybdenum Company Symposium, Ann Arbor, MI, (1967), p. 109.
7. A.J. McEvily: *"Transformation and Hardenability in Steels"*, Climax Molybdenum Company Symposium, Ann Arbor, MI, (1967), p. 179.
8. A.J. McEvily and C.L. Magee: The Iron and Steel Institute, publication 114, (1968), p. 111.
9. Y.E. Smith, A.P. Coldren and R.L. Cryderman: *"Towards Improved Ductility and Toughness,"*, Climax Molybdenum Company Conference, Kyoto, (1971), p. 119.
10. A.P. Coldren, R.L. Cryderman and Y.E. Smith: *"Processing and Properties of Low Carbon Steels"*, AIME, (1973), p. 163.
11. M.R. Krishnadev, S. Dionne, J.T. Bowker and J.T. McGrath: *"THERMEC-88"*, ed. I. Tamura, Tokyo, Japan, (1988), p.511.
12. S. Dionne, M.R. Krishnadev, L.E. Collins and J.D. Boyd: *"Accelerated Cooling of Rolled Steel"*, Proc. of the Metallurgical Society of the CIM, eds. G.E. Ruddle and A.F. Crawley, (1987), p. 71.
13. J.R. Yang, C.Y. Huang, and S.C. Wang: International symposium on "*LOW-CARBON STEELS for the 90's*", eds. R. Asfahani and G. Tither, Pittsburgh, Pennsylvania, (1993), p. 293.
14. H. Tamehiro, M. Murata, R. Habu: *Trans. ISIJ*, 27, (1987), p.120.
15. H. Tamehiro, M. Murata, R. Habu: *Trans. ISIJ*, 27, (1987), p.130
16. M. Babbit, P. Valette and G. Rigaut: Proc. Int. Conf. on *"Processing, Microstructure and Properties of Microalloyed and other High Strength Low alloy Steels"*, ed. A.J. DeArdo, (1991), p. 281.
17. H. Ohtani, S. Okaguchi, Y. Fujishiro and Y. Ohmori: *Metall. Trans. A*, 21A, (1990), p. 877.
18. E.S. Davenport and E.C. Bain: *Trans. AIME*, 90, (1930), p. 117..
19. R.F. Mehl: *Hardenability of Alloy Steels*, ASM, Cleveland, OH, (1939), p. 1.
20. B.L. Bramfitt and J.G. Speer: *Metall. Trans. A*, 21A, (1990), p. 817.
21. L.J. Habraken: Proc. 4th Int. Conf. on "*Electron Microscopy*", Springer-Verlag, Berlin, 1960, p. 621.

22. L.J. Habraken and M. Economopoulos: *"Transformations and Hardenability in Steels"*, Climax Molybdenum, Ann Arbor, MI, (1967), p. 69.

23. S.W. Thompson, D.J. Colvin, and G. Krauss: *Metall. Trans. A*, 21A, 1990, p. 1493.

24. W.W. Cias: *Metall. Trans. A*, 4A, (1973), p. 603.

25. H.I. Aaronson: The Mechanism of Phase Transformations in Crystalline Solids, Monograph and Report Series No. 33, The Institute of Metals, London, 1969, p. 270.

26. H.I. Aaronson and W.T. Reynolds, Jr.: *Scripta Metall.*, 22, 1988, p. 567.

27. H.I. Aaronson and H.J. Lee: *Scripta Metall.*, 21, 1987, p. 1011.

28. G.B. Olson, H.K.D.H. Bhadeshia, and M. Cohen: *Acta Metall.*, 37, 1989, p. 381.

29. H.K.D.H. Bhadeshia and J.W. Christian: *Metall. Trans. A*, 21A, (1990), p. 767.

30. S.A. Khan and H.K.D.H. Bhadeshia: *Metall. Trans. A*, 21A, (1990), p. 859.

31. N.F. Kennon: in *"Optical Microscopy of Carbon Steels"*, L.E. Samuels, ed., ASM, Metals Park, OH, 1980, p. 28.

32. F.B. Pickering: *"Microalloying 75"*, Union Carbide Corporation, New York, NY, (1977), p. 9.

33. J.N. Cordea: Symposium on *"Low Alloy High Strength Steels"*, Nurnberg, RBD, (1970), p. 61.

34. R.W. Vanderbeck: *Weld. J.*, 37, (1958), p. 114.

35. A.J. DeArdo: Proc. Int. Conf. *"THERMEC-88"*, ed. I. Tamura, Tokyo, Japan, ISIJ, (1988), p. 20.

36. S. Yue and J.J. Jonas: *Materials Forum*, 4, (1990), p. 245.

37. J.J. Jonas: *Materials Science and Engineering*, A148, (1994), p. 155.

38. J.J. Jonas and C.M. Sellars: *Sir Robert Honeycombe Commemorative Symposium*, eds. J.A. Charles, G.W. Greenwood and G.C. Smith, The Institute of Materials and the Royal Society, London, 1992, p. 147.

39. M. Cohen and S.S. Hansen: *"HSLA Steels: Metallurgy and Applications"*, Proc. Int. Conf. on HSLA Steels '85, eds. J.M. Gray, T. Ko, S. Zhang, B. Wu and X. Xie, ASM, (1985), p. 61.

40. J.J. Irani, D. Burton, J.D. Jones and A.B. Rothwell: in *"Strong, Tough Structural Steels"*, The Iron and Steel Institute, Publication 104, (1967), p. 110.

41. A.B. Le Bon and L.N. de Saint Martin: *"Microalloying 75"*, ed. M. Korchynski, Union Carbide Corporation, New York, NY, (1977), p. 90.

42. H.J. McQueen and J.J. Jonas: *"Treatise on Materials Science and Technology"*, ed. R.J. Arsenault, Academic Press, New York, NY, 6, (1975), p. 393.

43. I. Kozasu, C. Ouchi, T. Sampei and T. Okita: *"Microalloying 75"*, ed. M. Korchynski, Union Carbide Corporation, New York, NY, (1977), p. 90.

44. T. Tanaka, T. Enami, M. Kimura, Y. Saito and T. Hatomura: *"Thermomechanical Processing of Microalloyed Austenite"*, eds. A.J. DeArdo, G.A. Ratz and P.J. Wray, AIME, Warrendale PA., (1982), p. 195.

45. A.N. Mitra, M.D. Maheshwari, T. Mukherjee and J.J. Irani: Proc. Int. Conf. *"High Strength Low Alloy Steels"*, eds. D.P. Dunn and T. Chandra, Uni. Wollongong, Wollongong, (1984), p. 38.

46. K. Kuribayashi and R. Horiuchi: Proc. Int. Conf. *"THERMEC-88"*, ed. I. Tamura, Tokyo, Japan, ISIJ, (1988), p. 903.

47. *"Accelerated Cooling of Rolled Steel"*, Proc. of the Metallurgical Society of the Canadian Institute of Mining and Metallurgy, eds. G.E. Ruddle and A.F. Crawley, 1987.

48. *"Accelerated Cooling of Steel"*, TMS-AIME, Warrendale, PA.,ed. P.D. Southwick, 1986.

49. W. Roberts: *"HSLA steels: Technology and Application"*, ASM, Metals Park, Ohio, (1984), p. 33.

50. S. Yue, R. Barbosa, J.J. Jonas and P.J. Hunt: *30th Mechanical Working and Steel Processing Conference*, Iron and Steel Society of AIME, Dearborn, (1988), p. 37.

51. F.H. Samuel, S. Yue, J.J. Jonas and K.B. Barnes: *ISIJ International*, 30, (1990), p. 216.

52. L.N. Pussegoda and J.J. Jonas: *ISIJ International*, 31, (1991), p. 278.

53. L.N. Pussegoda, S. Yue and J.J. Jonas: *Metall. Trans. A*, 21A, (1990), p. 153.

54. Dj. Drobnjak and N. Radovic: *"Recrystallization' 92"*, Int. Conf. on Recrystallization and Related Phenomena, San Sebastián, Spain, Materials Science Forum, 113-115, (1993), p. 411.

55. J.J. Jonas and T. Sakai: in *"Deformation, Processing and Structure"*, 1982 ASM Materials Science Seminar, ed. G. Krauss, ASM, Metals Park, Ohio, (1984), p. 185.

56. A. Le Bon et al.:*Mém. Sci. Rev. Métall.*, 57, (1973), p. 577.

57. A. Le Bon, J. Rofes-Vernis and C. Rossard: *Metal Science*, 9, (1975), p. 36.

58. K. Esaka, J. Wakita, M. Takahashi, O. Kawano and S. Harada: *Seitetsu-Kenkyu*, 32, (1986), p. 92.

59. P. Choquet, P. Fabregue, J. Giusti and B. Chamont: Proc. Int. Symp. on *"Mathematical Modelling of Hot Rolling of Steel"*, ed. S. Yue, CIM, Hamilton, Ontario, (1990), p. 34.

60. O. Kwon, K.B. Kang, K.J. Lee, J.K. Lee, K.S. Lee and R.W. Chang: *"The Structure/Property Prediction and Control Model for Plain Carbon Steels"*, RIST, Korea, (1988).

61. P.D. Hodgson and R.K. Gibbs: Proc. Int. Symp. on *"Mathematical Modelling of Hot Rolling of Steel"*, ed. S. Yue, CIM, Hamilton, Ontario, (1990), p. 76.

62. C.M. Sellars: *"Hot Working and Forming Process"*, ed. Sellars and G.J. Davies, The Metals Society, London, (1979), p. 3.

63. A. Laasraoui and J.J. Jonas: *Metall. Trans. A*, 22A, (1991), p. 151.

64. W. Roberts, A. Sandberg, T. Siwecki and T. Werlefors: Proc. Int. Conf. on *"Technology and Applications of HSLA Steels"*, ASM, Philadelphia, (1983), p. 67.

65. P. Choquet, A. Le Bon and C. Perdrix: Proc.ISCMA7-*"Strength of Metals and Alloys"*, eds. H.J. MeQueen, J.J. Jonas, 2, (1985), p. 1025.

66. H. Yada and T. Senuma: J. Jpn. Soc. *Technol. Plast.*, 27, (1986), p. 34.

67. O. Kwon, K. J. Lee, K.B. Kang, J.K. Lee, J.H. Ryu and R. W. Chang: Proc. Int. Conf. *"Recrystallization in Metallic Materials"*, ed. T. Chandra, TMS-AIME, Philadelphia, (1990), p. 843.

68. C.M. Sellars and J.A. Whiteman: *Metal Science*, 14, (1979), p. 187.

69. M. Suehiro, K. Sato, H. Yada, T. Senuma, H. Shigefuji and Y. Yamashita:*"HSLA Steels: Metallurgy and Applications"*, Proc. Int. Conf. on HSLA Steels '85, eds. J.M. Gray, T. Ko, S. Zhang, B. Wu and X. Xie, ASM, (1985), p. 693.

70. T. Senuma and H. Yada: Proc. 7th Risø Conf. *"Annealing Process-Recovery, Recrystallization and Grain Growth"*, ed. N. Hansen et al., Risø Denmark, (1986), p. 547.

71. P. Choquet, B. de Lamberterie, C. Perdrix and H. Biausser: Proc. *4th Int. Conf. on Steel Rolling*, Deauville, France, 1, (1987), p. B5.1.

72. D.R. Barraclough and C.M. Sellars: *Metal Science*, 13, (1979), p. 257.

73. W.B. Morrison: *J. Iron and Steel Institute*, 210, (1972), p. 618.

74. R.A.P. Djaic and J.J. Jonas: *Metall. Trans. A*, 4, (1973), p. 621.

75. R.A.P. Djaic and J.J. Jonas: *J. Iron and Steel Institute*, 210, (1972), p. 256.

76. H.J. Whittaker: Proc. ICSTIS, *Suppl. Trans. Iron and Steel Institute of Japan*, 11, (1971), p. 662.

77. E. Ruibal, J.J. Urcola and M. Fuentes: *Z. Metallkde*, 76, (1985), p. 568.

78. N.D. Ryan and H.J. McQueen: *J. Mech. Work Tech.*, 12, (1986), p. 279.

79. J.J. Jonas, C.M. Sellars and W.J. McG Tegart: *Met. Rev.*, 14, (1969), p. 1.

80. R. Priestner et al.: *J. Iron and Steel Institute*, 206, (1968), p. 1252.

81. H. Weiss, A. Gittins, G.G. Brown and W.J. McG Tegart: *J. Iron and Steel Institute*, 211, (1973), p. 703.

82. P.D. Hodgson: Ph D Thesis, University of Queensland, Austrilia, 1993.

83. E. Anelli, J. Ghersi, A. Mascanzoni, M. Paolicchi, A. Aprile, F. Granato, G. Ligouri, G. Rizzo: *"HSLA Steels: Metallurgy and Applications"*, Proc. Int. Conf. on HSLA Steels '85, eds. J.M. Gray, T. Ko, S. Zhang, B. Wu and X. Xie, ASM, (1985), p. 693.

84. L.J. Cuddy: *"Thermomechanical Processing of Microalloyed Austenite"*, eds. A.J. DeArdo, G.A. Ratz and P.J. Wray, AIME, Warrendale, PA., (1982), p. 129.

85. L.J. Cuddy: 1st Risø International Symposium on *"Metallurgy and Materials Science"*, eds. N. Hansen, A.R. Jones and T. Leffers, Roskilde, Denmark, Risø National Laboratory, (1980), p. 317.

86. W. Roberts: *Scandinavian Journal of Metallurgy*, 9, (1980), p. 13.

87. T. Siwecki: *ISIJ International*, 32, (1992), p. 368.

88. W. Roberts and B. Ahlblom: *Acta Metall.*, 26, (1978), p. 801.

89. C. Rossard and P. Blain: *Rev. Met.*, 55, (1958), p. 573.

90. C. Rossard and P. Blain: *Rev. Met.*, 56, (1959), p. 286.

91. H.P. Stuwe: *"Deformation Under Hot Working Conditions"*, London, The Iron and Steel Institute, Publication, 108, (1968), p. 1.

92. M.J. Luton and C.M. Sellars: *Acta Metall.*, 17, (1969), p. 1033.

93. S. Sakui, T. Sakai and K. Takeishi: *Trans. ISIJ*, 17, (1977), p. 718.

94. T. Sakai, M.G. Akben and J.J. Jonas: *"Thermomechanical Processing of Microalloyed Austenite"*, eds. A.J. DeArdo, G.A. Ratz and P.J. Wray, AIME, Warrendale, PA., (1982), p. 237.

95. T. Sakai and J.J. Jonas: *Acta Metall.*, 32, (1984), p. 189.

96. C. Ouchi and T. Okita: *Tetsu-to-Hagane*, 62, (1976), p. 208.

97. H.J. McQueen and J.J. Jonas: *"Plastic Deformation of Materials"*, ed. R.J. Arsenault, New York, Academic Press, (1975), p. 393.

98. J.P. Sah, G.J. Richardson and C.M. Sellars: *Metal Science*, 8, (1974), p. 325.

99. W. Roberts, H. Boden and B. Ahlblom: *Metal Science*, 8, (1979), p. 195.

100. H.J. McQueen, E. Evangelista and N.D. Ryan: *"Recrystallization' 90"*, ed. T. Chandra, TMS-AIME, (1990), p. 89.

101. X. Xia, H.J. McQueen, N.D. Ryan, B. Li, Q. Meng and Y. Cui: Proc. Int. Symp. on *"Strip Casting, Hot and Cold Working of Stainless Steels"*, eds. N.D. Ryan, A.J. Brown and H.J. McQueen, (1993), p. 117.

102. H.J. McQueen, B. Li, Q. Meng and Y. Cui and N.D. Ryan: Proc. Int. Symp. on *"Strip Casting, Hot and Cold Working of Stainless Steels"*, eds. N.D. Ryan, A.J. Brown and H.J. McQueen, (1993), p. 181.

103. C.M. Sellars: *Materials Science and Technology*, 6, (1990), p. 1072.

104. R.A. Petkovic, M.J. Luton and J.J. Jonas: *Can. Metall. Quart.*, 14, (1975), p. 137.

105. M.J. Luton, R.A. Petkovic and J.J. Jonas: *Acta Metall.*, 28, (1980), p. 329.

106. T. Sakai and Z. Xu: *"Recrystallization' 90"*, ed. T. Chandra, TMS-AIME, (1990), p. 453.

107. T. Sakai and M. Ohashi: *ICSMA7*, (1985), p. 917.

108. Z. Xu and T. Sakai: *Mat. Trans. JIM.*, 32, (1991), p. 174.

109. C. R. Roucoules: Ph D Thesis, McGill University, Montreal, Canada, (1993).

110. C.R. Roucoules, P.D. Hodgson, S. Yue and J.J. Jonas: Proc. Int. Conf. on *"Processing, Microstructure and Properties of Microalloyed and Other Modern High Strength Low Alloy Steels"*, Pittsburgh, PA., (1991), p. 95.

111. P.D. Hodgson, J.J. Jonas and S. Yue: Proc. Int. Conf. on *"Grain Growth in Polycrystalline Materials"*, Rome, Materials Science Forum, 94-96, (1992), p. 715.

112. P.D. Hodgson, J.J. Jonas and S. Yue: *"Recrystallization' 92"*, Int. Conf. on Recrystallization and Related Phenomena, San Sebastián, Spain, Materials Science Forum, 113-115, (1993), p. 473.

113. C.R. Roucoules, S. Yue and J.J. Jonas: Proc. *34th Mechanical Working and Steel Processing Conf.*, ISS-AIME, XXX, (1993), p. 377.

114. C.R. Roucoules, S. Yue and J.J. Jonas: Proc. 1st Int. Conf. on *"Modelling of Metal Rolling Processes"*, The Institute of Materials, London, (1993), p. 165.

115. C.R. Roucoules, S. Yue and J.J. Jonas: *Metall. Trans. A*, 25A, (1994), p. 389.

116. T. Gladman: *"Inclusions"*, ed. F.B. Pickering, The Institution of Metallurgists, London, (1979), p. 172.

117. T. Gladman and F.B. Pickering: *J. Iron and Steel Institute*, 205, (1967), p. 653.

118. T. Gladman: *"Recrystallization of Multiphase and Particle Containing Materials"*, eds. N. Hansen, A.R. Jones and T. Leffers, Risø National Laboratory, Roskilde, Denmark, (1980), p. 183.

119. L.A. Erasmus: *J. Iron and Steel Institute*, 202, (1964), p. 128.

120. R.K. Amin and F.B. Pickering: *"Thermomechanical Processing of Microalloyed Austenite"*, eds. A.J. DeArdo, G.A. Ratz and P.J. Wray, AIME, Warrendale, PA., (1982), p. 1.

121. I. Weiss, G.L. Fitzsimons, K. Mielityinen-Tiitto and A.J. DeArdo: *"Thermomechanical Processing of Microalloyed Austenite"*, eds. A.J. DeArdo, G.A. Ratz and P.J. Wray, AIME, Warrendale, PA., (1982), p. 33.

122. W.X. Cui, W.Y. Yang, H.Y. Cao, W.Z. Lu, T. Chen and Y.K. Ho: *"HSLA Steels: Metallurgy and Applications"*, Proc. Int. Conf. on HSLA Steels '85, eds. J.M. Gray, T. Ko, S. Zhang, B. Wu and X. Xie, ASM, (1985), p. 199.

123. W.J. Liu and J.J. Jonas: Proc. Int. Conf. *"THERMEC-88"*, ed. I. Tamura, Tokyo, Japan, ISIJ, (1988), p. 90.

124. H. Gondoh, H. Nakasagi, H. Matsuda, H. Tamehiro and H. Chino: *Nippon Steel Tech. Rep.*, 14, (1979), p. 55.

125. Z. Chen, M.H. Loretto and R.C. Cochrane: *Materials Science and Technology*, 3, (1987), p. 836.

126. L.J. Cuddy, J.S. Lally and L.F. Porter: *"Technology and Applications"*, Metals Park, Ohio, ASM, (1983), p. 697.

127. C.Y. Hsu: Ph. D. Thesis, MIT, Cambridge, USA, (1984).

128. T. Gladman: Proc. Roy. Soc., 266(A), (1966), p. 298.

129. Ph. Maitrepierre, J. Rofes-Vernis and D. Thivellier: Proc. Int. Conf. on *"Boron in Steel"*, eds. S.K. Banerji and J.E. Morral, TMS-AIME, (1979), p. 1.

130. K. Yamanaka and Y. Ohmori: *Transaction ISIJ*, 17, (1977), p. 92.

131. K. Yamanaka and Y. Ohmori: *Transaction ISIJ*, 17, (1978), p. 404.

132. Y. Ohmori and K. Yamanaka: Proc. Int. Conf. on *"Boron in Steel"*, eds. S.K. Banerji and J.E. Morral, TMS-AIME, (1979), p. 44.

133. M. Djahazi: Ph.D. Thesis, McGill University, Montreal, Canada, (1989).

134. W.E. Duckworth, R. Phillips and J.A. Chapman: *J. Iron and Steel Institute*, 203, (1965), p. 1108.

135. K.J. Irvine, F.B. Pickering and T. Gladman: *J. Iron and Steel Institute*, 205, (1967), p. 161.

136. M. Umemoto, H. Ohtsuka, H. Kato and I. Tamura: Proc. Int. Conf. on *"High Strength Low Alloy Steels"*, eds. D.P. Dunn and T. Chandra, Univ. Wollongong, Wollongong, (1984), p. 107.

137. R.K. Amin and F.B. Pickering: *"Thermomechanical Processing of Microalloyed Austenite"*, eds. A.J. DeArdo, G.A. Ratz and P.J. Wray, AIME, Warrendale, PA., (1982), p. 377.

138. *"Processing and Properties of Low Carbon Steel"*, ed. J.M. Gray, TMS-AIME, New York, NY, 1973.

139. *"Microalloying 75"*, Union Carbide Corporation, New York, NY, 1977.

140. *"The Hot Deformation of Austenite"*, ed. J.B. Ballance, TMS-AIME, New York, NY, 1977.

141. *"Thermomechanical Processing of Microalloyed Austenite"*, eds. A.J. DeArdo, G.A. Ratz and P.J. Wray, AIME, Warrendale, PA., 1982.

142. S.S. Hansen, J.B. VanderSande and Morris Cohen: *Metall. Trans. A*, 11A, (1980), p.387.

143. R. Coladas, J. Masounave and J.P. Bailon: *"The Hot Deformation of Austenite"*, ed. J.B. Ballance, TMS-AIME, New York, NY, (1977), p. 341.

144. M.G. Akben, I. Weiss and J.J. Jonas: *Acta Metall.*, 29, (1981), p. 111.

145. H.L. Andrade, M.G. Akben and J.J. Jonas: *Metall. Trans. A*, 14A, (1983), p. 1967.

146. J.G. Speer and S.S. Hansen: *Metall. Trans. A*, 20A, (1989), p. 25.

147. O. Kwon and A.J. DeArdo: *Acta Metall. and Mater.*, 39, (1991), p. 529.

148. S. Yamamoto, C. Ouchi and T. Osuka: *"Thermomechanical Processing of Microalloyed Austenite"*, ed. A.J. DeArdo, TMS-AIME, New York, NY, (1980), p. 613.

149. S. Akamatsu, T. Senuma and M. Hasebe: *ISIJ International*, 32, (1992), p. 275.

150. T. Senuma and K. Kawasaki: *ISIJ International, Special Issue on Physical Metallurgy of Ultralow Carbon Interstitial Free Steels*, 34, (1994), p.51.

151. R.Yoda, I. Tsukatani, T. Inoue and T. Saito: *ISIJ International, Special Issue on Physical Metallurgy of Ultralow Carbon Interstitial Free Steels*, 34, (1994), p.70.

152. R.K. Ray, J.J. Jonas and R.E. Hook: *Int. Materials Reviews*, 39, (1994), p.

153. G. Krauss, D.O. Wilshynsky and D.K. Matlock: Proc. Int. Symp. on *"Interstitial Free Steel Sheet: Processing, Fabrication and Properties"*, eds. L.E. Collins and D.L. Baragar, CIM, Ottawa, (1991), p. 1.

154. S.V. Subramanian, M. Prikryl and A. Ulabhaje: Proc. Int. Symp. on *"Interstitial Free Steel Sheet: Processing, Fabrication and Properties"*, eds. L.E. Collins and D.L. Baragar, CIM, Ottawa, (1991), p. 15.

155. M. Perera, S. Saimoto and D. Boyd: Proc. Int. Symp. on *"Interstitial Free Steel Sheet: Processing, Fabrication and Properties"*, eds. L.E. Collins and D.L. Baragar, CIM, Ottawa, (1991), p. 55.

156. D.O. Wilshynsky, G. Krauss and D.K. Matlock: Proc. Int. Symp. on *"Interstitial Free Steel Sheet: Processing, Fabrication and Properties"*, eds. L.E. Collins and D.L. Baragar, CIM, Ottawa, (1991), p. 69.

157. S. Akamatsu, M. Hasebe, T. Senuma, Y. Matsumura and O. Akisue: *ISIJ International, Special Issue on Physical Metallurgy of Ultralow Carbon Interstitial Free Steels*, 34, (1994), p.9.

158. N. Yoshinaga, K. Ushioda, S. Akamatsu and O. Akisue: *ISIJ International, Special Issue on Physical Metallurgy of Ultralow Carbon Interstitial Free Steels*, 34, (1994), p.24.

159. S.V. Subramanian, M. Prikryl, B.D. Gaulin, D.D. Clifford, S. Benincasa and I. O'Reilly: *ISIJ International, Special Issue on Physical Metallurgy of Ultralow Carbon Interstitial Free Steels*, 34, (1994), p.61.

160. W.P. Sun, P.R. Cetlin, S. Yue and J.J. Jonas: Proc. *34th Mechanical Working and Steel Processing Conf.*, ISS-AIME, XXX, (1993), p. 61.

161. K. Sato and Y. Ishiguro: *"Physical Metallurgy of IF Steels"*, International Forum, ISIJ, Tokyo, (1994), p. 45.

162. S.V. Subramanian and J. Gao: *"Physical Metallurgy of IF Steels"*, International Forum, ISIJ, Tokyo, (1994), p. 53.

163. G. Tither, C.I. Garcia, M. Hua and A.J. DeArdo: *"Physical Metallurgy of IF Steels"*, International Forum, ISIJ, Tokyo, (1994), p. 293.

164. J.W. Martin and R.D. Doherty: *"Stability of Microstructure in Metallic Systems"*, Cambridge, UK, Cambridge University Press, (1976), p. 40.

165. R.W.K. Honeycombe: *"The Plastic Deformation of Metals"*, 2nd Edition, Metals Park, Ohio, ASM, (1984), p. 287.

166. R.W. Cahn: *"Recrystallization, Grain Growth and Textures"*, ed. H. Margolin, Metals Park, Ohio, ASM, (1966), p. 99.

167. P.A. Beck and P.R. Sperry: *"Effect of Recrystallization Texture on Grain Growth"*, Transaction of the AIME, 185, (1949), p. 240.

168. P.A. Beck and P.R. Sperry: *"Strain Induced Boundary Migration in High Purity Aluminum"*, Journal of Applied Physics, 21, (1950), p. 150.

169. J.E. Bailey and P.B. Hirsch: *"The Recrystallization Process in Some Polycrystalline Metals"*, Proc. of the Royal Society of London, A267, (1962), p. 11.

170. W.C. Leslie: *"The Physical Metallurgy of Steels"*, New York, McGraw Hill Book Company, (1981), p. 43.

171. C. Zener: *"Private communication to C.S. Smith"*, Trans. AIME, 175, (1949), p. 15.

172. H. Nordberg and B. Aronsson: *J. Iron and Steel Institute*, 206, (1968), p. 1263.

173. T.M. Hoogendoorn and M.H. Spanraft: *"Microalloying 75"*, ed. M. Korchynski, Union Carbide Corporation, New York, NY, (1977), p. 75.

174. C. Ouchi, T. Sampei, T. Okita and I. Kozasu: *"The Hot Deformation of Austenite"*, ed. J.B. Ballance, TMS-AIME, New York, NY, (1977), p. 316.

175. H. Watanabe, Y.E. Smith and R.D. Pehlke: *"The Hot Deformation of Austenite"*, ed. J.B. Ballance, TMS-AIME, New York, NY, (1977), p. 140.

176. R. Simoneau, G. Begin and A.H. Marquis: *Metal Science*, 12, (1978), p. 381.

177. J. Barford: *J. Iron and Steel Institute*, 204, (1966), p. 134.

178. S.J. Harris and N.R. Nag: *J. Materal Science*, 10, (1975), p. 1137.

179. S.J. Harris and N.R. Nag: *J. Materal Science*, 11, (1976), p. 1320.

180. B. Dutta and C.M. Sellars: *Materials Science and Technology*, 3, (1987), p.197.

181. W.J. Liu and J.J. Jonas: *Metall. Trans. A*, 20A, (1989), p. 689.

182. S.H. Park, S. Yue and J.J. Jonas: *Metall. Trans. A*, 23A, (1992), p. 1641.

183. M. Djahazi, X.L. He, J.J. Jonas and W.P. Sun: *Metall. Trans. A*, 23A, (1992), p. 2111.

184. J. Geise and C. Herzig: *Z. Metallkd.*, 76, (1985), p. 622.

185. E. Scheil: *Arch. Eisenhüttenwes.*, 12, (1935), p. 565.

186. I. Weiss and J.J. Jonas: *Metall. Trans. A*, 11A, (1980), p. 403.

187. T. Siwecki: Proc. Int. Conf. *"THERMEC-88"*, ed. I. Tamura, Tokyo, Japan, ISIJ, (1988), p. 232.

188. S.F. Medina and J.E. Mancilla: *ISIJ International*, 33, (1993), p. 1257.

189. F. Boratto, R. Barbosa, S. Yue and J.J. Jonas: Proc. Int. Conf. *"THERMEC-88"*, ed. I. Tamura, Tokyo, Japan, ISIJ, (1988), p. 383.

190. A. Najafi-Zadeh, S. Yue and J.J. Jonas: Proc. Int. Symp. on *"Interstitial Free Steel Sheet: Processing, Fabrication and Properties"*, eds. L.E. Collins and D.L. Baragar, CIM, Ottawa, (1991), p. 93.

191. L.T. Mavropoulos and J.J. Jonas: *Canadian Metallurgical Quart.*, 27, (1988), p. 235.

192. L.T. Mavropoulos and J.J. Jonas: *Canadian Metallurgical Quart.*, 28, (1989), p. 159.

193. X.L. He, M. Djahazi, J.J. Jonas and J. Jackman: *Acta Metall. Mater.*, 39, (1991), p. 2295.

194. S.L. Semiatin, G.D. Lahoti and J.J. Jonas: *"Mechanical Testing"*, 8, ASM Metals Handbook, 9th Edition, ASM, Metals Park, Ohio, (1985), p. 154.

195. D.S. Fields and W.A. Backofen: Proc. ASTM. 57, (1975), p. 1259.

196. H.G. Suzuki, S. Nishimura, J. Imamura and Y. Nakamura: *Trans. ISIJ*, 24, (1984), p. 169.

197. P.J. Wray: *Metall. Trans. A*, 15A, (1984), p. 2041.

198. Ch. Liebaut, E. Gautier and A. Simon: *"THERMEC-88"*, ed. I. Tamura, Tokyo, Japan, ISIJ, (1988), p. 146.

199. H. Yada, Y. Matsumura and T. Senuma: Proc. Int. Conf. on *"Martensitic Transformations"*, (1986), p. 515.

200. R. Pandi and S. Yue: *ISIJ International*, 34, (1994), p. 270.

201. A. Zarei Hanzaki, R. Pandi, P.D. Hodgson and S. Yue: *Metall. Trans. A*, 24A, (1993), p. 2657.

202. C.M. Sellars and W.J. McTegart: *Acta Metall.*, 14, (1966), p. 1136.

203. R.A. Petkovic, M.J. Luton and J.J. Jonas: *Hot Deformation of Austenite*, Proc. AIME Symposium, J.B. Ballance, ed., Cincinnati, Ohio, (1977), p. 68.

204. M.G. Akben, B. Bacroix and J.J. Jonas: *Acta Metall.*, 31, (1983), p. 161.

205. B. Migaud: *Hot Working and Forming Processes*, C.M. Sellars and G.J. Davis, eds., Sheffield, England, (1979), p. 67.

206. W. Knudsen, J. Sankar, H.J. McQueen, J.J. Jonas, and D.N. Hawkins: *Hot Working and Forming Processes*, C.M. Sellars and G.J. Davis, eds., Sheffield, England, (1979), p. 51.

207. L.J. Cuddy: *Metall. Trans. A*, 15A, (1984), p. 87.

208. L.J. Cuddy, *Metall. Trans. A*, 12A, (1981), p. 1313.

209. L.J. Cuddy, J.J. Bauwin, and J.C. Raley: *Metall. Trans. A*, 11A, (1980), p. 381.

210. S.V. Subramanian, F. Boratto, J.J. Jonas, and C.M. Sellars: *Microalloyed Bar and Forging Steels*, M. Finn ed., Hamilton, ON, Canada, (1990), p. 120.

211. H.L. Zou and J.S. Kirkaldy: *Metall. Trans. A*, 22A, (1991), p. 1511.

212. C. Ouchi, T. Okita, T. Ichihara, and Y. Ueno: *Iron Steel Inst. Jpn. Int.*, 20, (1980), p. 833.

213. K.C. Russell: *Adv. Colloid Interfaces Sci.*, 13, (1980), p. 205.

214. S. Kurokawa, J.E. Ruzzante, A.M. Hey and F. Dyment: *Metal Science*, 17, (1983), p. 433.

215. H.I. Aaronson and J.K. Lee: in Lectures on the Theory of Phase Transformation, H.I. Aaronson, ed., TMS, Warrendale, PA, (1986), p. 83.

216. I. Weiss and J.J. Jonas: *Metall. Trans. A*, 10A, (1979), p. 831.

217. H.B. Aaron and H.I. Aaronson: *Acta Metall.*, 18, (1970), p. 699.

218. J.G. Williams, C.R. Kilmore and G.R. Harris: *"THERMEC-88"*, ed. I. Tamura, Tokyo, Japan, ISIJ, (1988), p. 224.

219. P.D. Hodgson and R.K. Gibbs: *ISIJ International*, 32, (1992), p. 1329.

220. M. Umemoto, K. Horiuchi and I. Tamura: *Trans. ISIJ*, 22, (1982), p. 854.

221. M. Umemoto, N. Nishioka and I. Tamura: *Trans. ISIJ*, 22, (1982), p. 629.

222. M. Umemoto, K. Horiuchi and I. Tamura: *Trans. ISIJ*, 23, (1983), p. 690.

223. M. Umemoto, N. Nishioka and I. Tamura: Trans. ISIJ, 22, (1982), p. *629.*

224. M. Umemoto, Z.H. Gao and I. Tamura: *Mater. Sci. Technol.*, 3, (1987), p. 249.

225. M. Militzer, W.P. Sun and J.J. Jonas: *Acta Metall.*, 42, (1994), p. 133.

226. X.L. He, Y.Y. Chu and J.J. Jonas: *Acta Metall.*, 37, (1989), p. 147.

226. X.L. He, Y.Y. Chu and J.J. Jonas: *Acta Metall.*, 37, (1989), p. 147.

227. X.L. He, Y.Y. Chu and J.J. Jonas: *Acta Metall.*, 37, (1989), p. 2905.

228. T.M. Williams, A.M. Stoneham and D.R. Harries: *Metal Science*, (1976), p. 14.

229. M. Djahazi, X.L. He, J.J. Jonas and W.P. Sun: *Mater. Sci. Technol.*, 8, (1992), p. 628.

230. K.A. Taylor and S.S. Hansen: *Metall. Trans. A*, 21A, (1990), p. 1697.

231. K.A. Taylor: *Metall. Trans. A*, 23A, (1992), p. 107.

232. A. Laasraoui and J.J. Jonas: *Metall. Trans. A*, 22A, (1991), p. 1545.

233. C. Ouchi and T. Okita: *Trans. ISIJ*, 22, (1982), p. 543.

234. R.A. Petkovic, M.J. Luton and J.J. Jonas: *Metal Science*, (1979), p. 569.

235. C. Roucoules, S. Yue and J.J. Jonas: *Metall. Trans. A*, 26A, (1995), p. 181.

236. A. Laasraoui: Ph.D. Thesis, McGill University, Montreal, Canada, (1990).

237. L.T. Mavropoules: Ph.D. Thesis, McGill University, Montreal, Canada, (1989).

238. G. Anan, S. Nakajima, M. Miyahara, S. Nanba, M. Umemoto, A. Hiramatsu, A. Moriya and T. Watanabe: *ISIJ International*, 32, (1992), p. 261.

239. S. Nanba, M. Kitamura, M. Shimada, M. Katsumata, T. Inoue, H. Imamura, Y. Maeda and S. Hattori: *ISIJ International*, 32, (1992), p. 377.

240. N.D. Ryan and M.J. McQueen: *Can. Met. Quart.* 29, (1990), p. 147.

241. C.M. Sellars: *Czech. J. Phys.* B35, (1985), p. 239.

242. G. Glover and C.M. Sellars: *Metall. Trans.*, 3, (1972), p. 2271.

243. G. Glover and C.M. Sellars: *Metall. Trans.*, 4, (1973), p. 765.

244. A.T. English and W.A. Backofen: *Trans. TMS-AIME*, 230, (1964), p. 396.

245. E. Furubayashi and M. Nakamura: Proc. 6th Int. Conf. *Textures of Materials*, Tokyo, 1981, p. 619.

246. G. Gottstein, D. Zabardjadi and H. Mecking: *Metals Science*, 13, (1979), p.223.

247. G. Gottstein and U.F. Kocks: *Acta Metall.*, 31, (1983), p. 175.

248. T. Ito and Y. Nakayama: Strength of Metals and Alloys, *ICSMA7*, eds. H.J. McQueen et al., (1985), p. 911.

249. C.M. Sellars: *Annealing Processes-Recovery, Recrystallization and Grain Growth*, Proc. 7th Risø Conf., eds. N. Hansen et al., Denmark, (1986), p. 167.

250. T. Sakai, M. Ohashi, K. Chiba and J.J. Jonas: *Acta Metall.*, 36, (1988), p. 1781.

251. T. Sakai and J.J. Jonas: *Annealing Processes-Recovery, Recrystallization and Grain Growth*, Proc. 7th Risø Conf., eds. N. Hansen et al., Denmark, (1986), p. 143.

252. T. Sakai and M. Ohashi: *Mat. Sci. and Tech.*, 6, (1990), p. 1251.

253. J.W. Bowden, F.H. Samuel and J.J. Jonas: *Metall. Trans. A*, 22A, (1991), p. 2947.

254 E. Anelli: ISIJ Int. 32, (1992), p. 440.

255. *"Boron in Steel"*, ed. by S.K. Banerji and J.E. Morral, AIME, Warrendale, (1979).

256. R.A. Grange and J.B. Michell: *Trans. ASM*, 53, (1956), p. 157.

257. B.M. Kapadia, R.M. Brown and W.J. Murphy: *Trans. TMS-AIME*, 242, (1968), p. 1689.

258. M. Ueno and T. Inoue: *Trans. ISIJ*, 13, (1973), p. 210.

259. G.F. Melloy, P.R. Slimmon and P.P. Podgursky: *Metall. Trans. A*, 4, (1973), p. 2279.

260. Ph. Maitrepierre, D. Thivellier and R. Tricot: *Metall. Trans. A*, 6A, (1975), p. 287.

261. R. Habu, M. Miyata, S. Sekino and S. Goda: *Trans. ISIJ*, 18, (1978), p.404.

262. C.J. Yun, K. Nakai, H. Ohtsubo and Y. Ohmori: *ISIJ*, 34, (1994), p. 43.

263. R. Moses, A. Zarei Hanzaki, S. Yue and J.J. Jonas: *35th Mechanical Working and Steel Processing Conference*, Iron and Steel Society of AIME, (1994), p. 435.

264. J.M. Gray, D. Webster and J.H. Woodhead: *J. Iron Steel Inst.*, 203, (1965), p. 812.

265. W.B. Morrison and J.H. Woodhead: *J. Iron Steel Inst.*, 201, (1963), p. 43.

266. J. Irvine and T.N. Baker: Metal Science, (1979), p. 228.

267. N. Yoshinaga, K. Ushioda, S. Akamatsu and O. Akisue: *ISIJ International, Special Issue on Physical Metallurgy of Ultralow Carbon Interstitial Free Steels*, 34, (1994), p.24.

268. J.H. Hollomon: *Trans. AIME*, 162, (1945), p. 268.

269. P.J. Wray: *Metall. Trans. A*, 15, (1984), p. 2009.

270. P.J. Wray: *Met. Technol.*, 12, (1981), p. 466.

271. E.A. Simielli: Ph. D. Thesis, McGill University, Montreal, (1990).

272. E. Essadiqi and J.J. Jonas: Metall. Trans. A, 19A, (1988), p. 417.

273. J.R. Yang, C.Y. Huang, and S.C. Wang: *ISIJ Special Issue*, 35, (1995), p. 1013.

274. S. Kurokawa, J.E. Ruzzante, A.M. Hey and F. Dyment: *Metal Science*, 17, (1983), p. 433.

275. R.P. Agarawala, M.C. Naik, M.S. Anand and A.R. Paul: *J. Nucl. Mater.* 36, (1970), p. 41.

276. T.H. Blewitt, R.R. Coltman and J.K. Redman: *J. Appl. Phys.*, 28, (1957), p. 651.

277. H. Suzuki and C.S. Barrett: *Acta Metall.*, 6, (1958), p. 156.

278. P. Haasen: *Phil. Mag.*, 3, (1958), p. 384.

279. T.L. Altshuler and J.W. Christian: *Acta Metall.*, 14, (1966), p. 903.

280. Z.S. Bazinski and A. Sleeswijk: *Acta Metall.* 5, (1957), p. 176.

281. A.S. Keh, Y. Nakada and W.C. Leslie: *in Dislocation Dynamics*, ed. by W.A. Owen and M.J. Roberts, McGraw Hill, New York, (1968), p. 381.

282. P. Rodriguez: Bull. *Mater. Sci.* 6, (1984), p. 653.

283. A.H. Cottrell: *Phil. Mag.*, 44, (1953), p. 829.

284. B.J. Brindley and P.J. Worthington: *Metallurgical Reviews*, 15, (1970), p. 101.

285. J.D. Baird: *in The Inhomogeneity of Plastic Deformation*, ASM, Metals Park, OH, (1973), p. 191.

286. P.G. McCormick: *Acta Metall.*, 21, (1973), p. 873.

287. "*Steel*", ed. by R.W.K. Honeycombe, Edward Arnold, (1981).

288. "*Yield Point Phenomena in Metals and Alloys*", ed. by E.O. Hall, Plenum Press, new York, (1970).

289. J.T. Barnby: *J. Iron Steel Inst.*, 203, (1965), p. 392.

290. R. Sumerling and J. Nutting: *J. Iron Steel Inst.*, 203, (1965), p. 398.

291. H.J. Harding and R.W.K. Honeycombe: *J. Iron Steel Inst.*, 204, (1966), p. 259.

292. H. Oikawa: *Technology Reports*, Tohoku University, Japan, 47, (1982), p. 67.

293. P.J. Alberry and C.W. Haworth: *Met. Sci.*, 8, (1974), p. 407.

294. S. Tsuji and H. Yamanaka: *J. Japan Inst. Metals*, 34, (1970), p. 486.

295. A.H. Cottrell: *ASM Seminar* "Relation of properties to microstructure", (1953), p. 131.

296. G. Thomas, D. Schnatz and W. Gerberich: *High-Strength Materials*, Procs. of Second Int. Materials Conf. ed. by V.F. Zackay, (1964), p. 251.

297. L. Raymond, W. Gerberich and C.F. Martin: *High-Strength Materials*, Procs. of Second Int. Materials Conf. ed. by V.F. Zackay, (1964), p. 297.

298. D. Fahr: *Metall. Trans. A*, 2, (1971), p. 1883.

299. A. Sato, M. Kato and T. Mori: Martensitic Transformations *ICOMAT 1979*, Procs. of Int. Conf., Massachusetts Institute of Technology, Cambridge, Massachusetts, (1979), p. 331.

300. V.A. Zaymovskiy, I.I. Martinovich, O.N. Samedov and S.A. Faldin: *Phys. Met. Metall.* 61, (1986), p. 122.

APPENDICES

Appendix I Program for the continuous cooling tests

```
BAI10T  28-Aug-94  MTS 773 MU BASIC V02.09

10   REM
20   REM---CONSTANT TRUE STRAIN RATE INTERRUPTED COMPRESSION TEST----
30   REM
40   REM**********DOUBLE-HIT*****************
50   REM
60   REM
70   REM
80   ERASE
90   DIM X(50,1),Y(50,1)
100  COMMON A(350,3),C(350,3),D(350,3),Z(350),T(350)
110  COMMON F(15),E(15)
120  COMMON H0,A0,D1,D2,D5,B,S0,I1,I2,D
130  COMMON C1,S1,S2,L0,A,J,N$,M$,T$
140  PRINT "SAMPLE IDENTIFICATION"; \ INPUT N$
150  PRINT  \ PRINT "MATERIAL"; \ INPUT M$
160  PRINT  \ PRINT "TEST TEMPERATURE"; \ INPUT T$
170  PRINT  \ PRINT "INITIAL HEIGHT (mm)"; \ INPUT H0
180  PRINT  \ PRINT "INITIAL DIAMETER (mm)"; \ INPUT D0 \ A0=PI*(D0)^2/4
190  PRINT  \ PRINT "NUMBER OF DEFORMATIONS:"; \ INPUT D5
200  PRINT  \ PRINT "FIRST DEFORMATION"; \ INPUT D1
205  PRINT  \ PRINT "FIRST STRAIN RATE (1/s)"; \ INPUT S1
207  D2=1 \ S3=1
210  IF D5=1 THEN GO TO 240
220  PRINT  \ PRINT "SECOND DEFORMATION"; \ INPUT D2
235  PRINT  \ PRINT "SECOND STRAIN RATE (1/s)"; \ INPUT S3
240  PRINT  \ PRINT "TIME INTERPASS (s)"; \ INPUT T
250  PRINT  \ PRINT "LOAD RANGE (kip)"; \ INPUT L \ L0=L*4.4482*1000
260  PRINT  \ PRINT "STROKE RANGE (mm)"; \ INPUT S0
270  PRINT  \ PRINT "NO. OF DATA YOU WANT (MAX. 300) "; \ INPUT D \ D9=D/D5
280  ERASE
290  GTIME(,M,H)
300  PRINT "DATE                :"; \ PRINT DAT$
310  PRINT "TIME                :"; \ PRINT H;":"M
320  PRINT
330  PRINT "************************ EXPERIMENTAL DATA ************************"
340  PRINT  \ PRINT
350  PRINT "FILE NAME           :"; \ PRINT N$
360  PRINT "MATERIAL            :"; \ PRINT M$
370  PRINT
380  PRINT "TEST TEMPERATURE      :"; \ PRINT T$
390  PRINT "INITIAL HEIGHT        :"; \ PRINT H0; \ PRINT "   (mm)"
400  PRINT "INITIAL DIAMETER      :"; \ PRINT D0; \ PRINT "   (mm)"
410  PRINT
420  PRINT "NUMBER OF DEFORMATIONS  :"; \ PRINT D5
```

```
430  PRINT "NUMBER OF REQUESTED DATA:"; \ PRINT D
440  PRINT
450  PRINT "FIRST DEFORMATION      :"; \ PRINT D1
455  PRINT "1ST STRAIN  RATE        :"; \ PRINT S1; \ PRINT "  1/SEC"
460  PRINT "SECOND DEFORMATION     :"; \ PRINT D2
475  PRINT "2ND STRAIN  RATE        :"; \ PRINT S3; \ PRINT "  1/SEC"
480  PRINT "TIME INTERPASS        :"; \ PRINT T; \ PRINT "    SEC"
490  PRINT
500  PRINT "LOAD RANGE           :"; \ PRINT L; \ PRINT "    Kip"
510  PRINT "STROKE RANGE          :"; \ PRINT S0; \ PRINT "   (mm)"
520  W=SYS(4)
530  PRINT  \ PRINT
540  PRINT "PRESS RETURN TO START THE TEST"; \ INPUT G$
550  PRINT  \ PRINT
560  PRINT "STARTING THE AUTOMATIC POSITIONING OF THE ACTUATOR"
570  FGARB(1,"R", TIME 100,-.4)
580  ADIMMED(1,A)
590  FGGO
600  IF A<-3.00000E-03 THEN GO TO 620
610  GO TO 580
620  FGSTOP
630  S2=A*L0/A0
640  PRINT  \ PRINT "THE STRESS ON THE SAMPLE IS: "; \ PRINT S2; \ PRINT "MPa"
650  ETIME \ SLEEP(1)
660  ADIMMED(3,B)
670  T1=D1/S1/50 \ T2=D2/S3/50
675  PRINT "T1= ";T1,"T2= ";T2
680  REM
690  FOR I=1 TO 50
700  H1=H0/EXP(D1*I/50)
710  X(I,0)=(H1-H0)/S0+B
720  NEXT I
730  REM
740  H2=H0/EXP(D1)+.254
750  H=(H0-H1)/S0
760  FOR I=1 TO 50
770  H3=H2/EXP(D2*I/50)
780  Y(I,0)=(H3-H2)/S0+.02+(B-H)
790  NEXT I
800  REM
810  CKTIME(1,.01)
820  V1=D1/S1/.01 \ T8=V1/D9 \ IF T8<1 THEN T8=1
830  V2=D2/S3/.01 \ T9=V2/D9 \ IF T9<1 THEN T9=1
880  ADTIMED(1,A,,1,T8,3,4)
890  ADTIMED(2,A,,1,10000,3,4)
900  ADTIMED(3,A,,1,T9,3,4)
910  ADTRIGGER(3,F5,-1)
920  REM----------SET UP  THE SYSTEM----------
930  FGARB(1,"R", TIME T1, ARRAY X)
940  FGARB(1,"R", TIME 1.00000E-03,.02+(B-H))
950  PRINT  \ PRINT "PRESS RETURN TO START THE DEFORMATION"; \ INPUT G$
955  PRINT  \ PRINT "TO INTERRUPT THE TEST, PRESS Ctrl^C, ";
957  PRINT "AND TYPE 'GOTO 1060'  "
960  ADINIT \ FGGO \ ADGO(1)
```

```
970  FGSTATUS(1,W) \ IF W<>0 THEN GO TO 970
980  ADSTOP(1)
990  PRINT  \ PRINT "1ST DEFORMATION DONE"
1000  IF D5=1 THEN GO TO 1060
1010  ETIME \ SLEEP(T)
1020  PRINT  \ PRINT "INTERPASS FINISHED"
1030  FGARB(1,"R", TIME T2, ARRAY Y)
1040  FGGO \ ADGO(3)
1050  FGSTATUS(1,S) \ IF S<>0 THEN GO TO 1050
1060  ADSTOP \ FGSTOP \ CKSTOP
1070  REM
1080  FGIMMED(1,"R", TIME .5,0)
1090  PRINT  \ PRINT  \ PRINT
1100  PRINT "****** THE EXPERIMENT IS FINISHED******"; \ INPUT G$
1105  REM-----C1 IS THE MTS COMPLIANCE----------
1110  FOR I=1 TO A
1130  C2=-ELEVEL(A(I,1))*L0
1140  C1=.198769*(1-EXP(-1.15596E-07*C2^2))+2.00063E-05*C2
1150  Z(I)=H0+(ELEVEL(A(I,2))-B)*S0
1160  REM --- PRINT I,LOG(H0/Z(I))
1170  NEXT I
1180  PRINT  \ PRINT
1190  X0=1.00000E-05
1200  FOR I=10 TO A
1210  X1=LOG(H0/Z(I))
1220  IF X1<X0 THEN 1250
1230  X0=X1
1240  NEXT I
1250  PRINT "I1=";I-1 \ I1=I-1
1254  G2=-ELEVEL(A(I1,1))*L0*Z(I1)/A0/H0
1256  G3=.1*G2
1260  FOR J=I1 TO A
1270  X2=-ELEVEL(A(J,1))*L0*Z(J)/A0/H0
1280  IF X2>G3 THEN 1300
1290  NEXT J
1300  PRINT "I2=";J \ I2=J
1310  J=0
1380  FOR I=0 TO A
1390  IF I>I1 THEN IF I<I2 GO TO 1420
1400  D(J,0)=A(I,0) \ D(J,1)=A(I,1) \ D(J,2)=A(I,2) \ D(J,3)=A(I,3)
1410  J=J+1
1420  NEXT I
1430  REM
1440  ERASE
1450  PRINT  \ PRINT
1460  PRINT "RESULTS FROM THE EXPERIMENT:"
1470  PRINT  \ PRINT
1480  PRINT "INITIAL POSITION:"; \ PRINT B
1490  PRINT "TOTAL NUMBER OF DATA POINTS:"; \ PRINT J
1500  PRINT "NUMBER OF POINTS FOR THE FIRST DEFORMATION:"; \ PRINT I1
1510  F(1)=J \ F(2)=I1
1520  F(3)=I2 \ F(4)=H0 \ F(5)=D0 \ F(6)=D5 \ F(7)=D1 \ F(8)=S1
1530  F(9)=T \ F(10)=D2 \ F(11)=L \ F(12)=S0
1540  F(13)=B \ F(14)=S3
```

```
1550  PRINT \ PRINT \ PRINT
1560  W=SYS(4)
1570  PRINT "DO YOU WANT TO SAVE THE DATA"; \ INPUT G$
1580  PRINT \ PRINT
1590  IF G$="N" THEN GO TO 1650
1600  OPEN "DU1:T"&N$ FOR OUTPUT AS FILE #1
1610  OPEN "DU1:K"&N$ FOR OUTPUT AS FILE #2
1620  FOUT(1,D(0,0),,0,F) \ CLOSE #1
1630  FOUT(2,F(1),,0,F) \ CLOSE #2
1640  REM ---
1650  PRINT \ PRINT "DO YOU WANT TO SEE THE DATA"; \ INPUT G$
1660  IF G$="N" THEN GO TO 1910
1670  OPEN "DU1:T"&N$ FOR INPUT AS FILE #1
1680  OPEN "DU1:K"&N$ FOR INPUT AS FILE #2
1690  FINP(1,C(0,0),,0,F) \ CLOSE #1
1700  FINP(2,E(1),,0,F) \ CLOSE #2
1710  J=E(1) \ I1=E(2) \ I2=E(3) \ H0=E(4)
1720  D0=E(5) \ D5=E(6) \ D1=E(7) \ S1=E(8)
1730  T=E(9) \ D2=E(10) \ L=E(11) \ S0=E(12) \ B=E(13)
1740  REM ---
1750  T(0)=0
1760  FOR I=1 TO J
1770  T(I)=C(I,0)*.01+T(I-1)
1780  NEXT I
1790  L0=L*4.4482*1000
1800  A0=PI*(D0)^2/4
1810  PRINT \ PRINT "TEST= ";N$
1820  PRINT \ PRINT "TIME(sec) ;","HEIGHT(mm) ;","LOAD(kN) ;","TEMP(C)"
1830  FOR I=1 TO J
1840  H1=H0+(ELEVEL(C(I,2))-B)*S0
1850  PRINT T(I);";",
1860  PRINT H1;";",
1870  PRINT ELEVEL(C(I,1))*L*4.4482;";",
1880  PRINT ELEVEL(C(I,3))*2794-25
1890  NEXT I
1900  PRINT \ PRINT "B=";E(13),"J=";E(1),"I1=";E(2)
1910  PRINT \ PRINT "DO YOU WANT TO SEE THE GRAPHICS"; \ INPUT F$
1920  IF F$="Y" THEN CHAIN "BAI5T.BAS" LINE 270
1930  END
```

Appendix II Program for the strain rate change tests

```
DQ2T  28-Aug-94  MTS 773 MU BASIC V02.09

10   REM--MULTISPEED HOT COMPRESSION--
20   ERASE
25   COMMON M$,T$,N,J,V,T0,T1,B0,N$
28   COMMON Z(12),H(12)
30   DIM Q(10),T(12),F(12)
40   DIM E(12,4),S(12),E1(12,4),D(12,4)
50   DIM X(50,1),A(900,2),B(900,3),Y(15,1)
60   PRINT "ID FOR SAMPLE (FILE NAME) :"; \ INPUT N$
70   PRINT "MATERIAL :"; \ INPUT M$
80   PRINT "TEMPERATURE :" \ INPUT T$
100  PRINT "INITIAL HEIGHT, DIAMETER (MM): "; \ INPUT S(1),S(2)
110  E(1,4)=S(1)
120  V=S(1)*(S(2)/2)^2*3.1416
140  PRINT "INITIAL STRAIN, STRAIN RATE (1/SEC.): "; \ INPUT E(1,1),E(1,2)
145  PRINT "NUMBER OF POST STEPS: "; \ INPUT N
150  IF N=0 GO TO 240
160  E1(1,1)=E(1,1)
170  PRINT "POST STRAIN AND STRAIN RATE :"
180  FOR J=2 TO N+1
190  PRINT "STEP ";J;" :"; \ INPUT E(J,1),E(J,2)
200  T(J)=E(J,1)/E(J,2)
204  E1(J,1)=E1(J-1,1)+E(J,1)
210  NEXT J
240  PRINT "SET LOAD RANGE TO 5 kip AND STROKE RANGE TO 0.5 in."
250  PRINT "ARE ALL PARAMETERS OK?"; \ INPUT J$
260  IF J$="N" GO TO 20
270  PRINT "PRESS ENTER TO POSITION PISTON"; \ INPUT J$
290  REM--POSITION PISTON--
300  ADIMMED(3,J)
310  FGARB(1,"R", TIME 25,J-.4)
320  PRINT  \ PRINT "POSITIONING PISTON - ",1
330  FGGO
340  ADIMMED(1,J)
350  IF J<-2.00000E-03 GO TO 370
360  GO TO 340
370  FGSTOP \ B0=J*5*4448.2*S(1)/V
375  PRINT  \ PRINT "INITIAL STRESS: "; \ PRINT B0; \ PRINT "MPA"
380  ADIMMED(3,J)
390  D(1,1)=J
400  REM--U=D(1,1)+5.00000E-03
410  REM--FGARB(1,"R", TIME 2,U)
420  REM--FGGO
430  REM--FGSTATUS(1,J)              \ REM--IF J<>0 GO TO 430
440  REM--FGSTOP
500  PRINT "PRESS ENTER TO START TEST"; \ INPUT J$
510  REM--WRITE PISTON POSITIONS TO ARRAY--
520  T1=E(1,1)/E(1,2)/50
530  FOR J=1 TO 50
```

```
540  H=E(1,4)/EXP(E(1,1)*J/50)
550  X(J,0)=(H-E(1,4))/12.7+D(1,1)
560  NEXT J
565  F(1)=INT(10*E(1,1)/E(1,2))
570  REM--T0(5.00000E-03/15)*T1/(X(1,0)-X(2,0))
580  REM--FOR J=1 TO 15
590  REM--Y(J,0)=U-J*5.00000E-03/15
600  REM--NEXT J
610  REM--SET UP DATA AQUISTION--
620  CKTIME(1,1.00000E-03)
621  REM FOR J=2 TO N+1
622  REM F(J)=INT(5*E(J,1)/E(J,2))
623  H(2)=E(1,4)/EXP(E1(2,1))
624  Z(2)=(H(2)-E(1,4))/12.7+D(1,1)
625  ADTIMED(2,A,,3,1000,1)
626  F(2)=1000
627  REM F(N+1)=1
628  REM ADTIMED(N+1,A,,3,1,1)
630  ADTIMED(1,A,,3,F(1),1)
632  ADTRIGGER(2,X(50,0),-1)
633  FOR J=2 TO N
635  ADTRIGGER(J+1,Z(J),-1)
636  NEXT J
640  REM--START TEST--
650  REM--FGARB(1,"R", TIME T0, ARRAY Y)
660  FGARB(1,"R", TIME T1, ARRAY X)
740  ADINIT \ ADGO(1)
750  FGGO
760  FGSTATUS(1,C)
770  IF C<>0 GO TO 760
775  ADSTOP(1)
781  FOR J=2 TO N+1
782  FGARB(1,"R", TIME T(J),Z(J))
783  ADGO(J)
784  FGSTATUS(1,C) \ IF C<>0 GO TO 784
785  ADSTOP(J)
786  NEXT J
790  FGARB(1,"R", TIME .5,Z(N+1)+.2)
800  FGSTATUS(1,C) \ IF C<>0 GO TO 800
810  FGSTOP
820  ETIME
840  ADSTOP \ CKSTOP
850  FGIMMED(1,"R", TIME .5,0)
860  REM--SAVE/MANIPULATE DATA--
870  PRINT  \ PRINT  \ PRINT "ALL OVER RED ROVER"
880  FOR J=1 TO A
890  B(J,1)=LOG(S(1)/(S(1)+12.7*(ELEVEL(A(J,1))-D(1,1))))
900  B(J,2)=-ELEVEL(A(J,2))*5*4448.2
910  B(J,3)=B(J,2)/(V/(S(1)+12.7*(ELEVEL(A(J,1))-D(1,1))))
920  NEXT J
925  GO TO 1020
1020 PRINT "SHOW DATA ON SCREEN?"; \ INPUT J$
1030 IF J$="N" GO TO 1150
1040 FOR J=1 TO A
```

```
1050  PRINT J;";";B(J,1);";";B(J,3);";";ELEVEL(A(J,1));";";B(J,2);";";A(J,0)
1060  NEXT J
1070  FOR J=1 TO N+1
1090  PRINT J;"  E(J,X)";E(J,1);";",E(J,2)
1095  PRINT "0.001*F(J)",1.00000E-03*F(J)
1110  NEXT J
1150  END
```